



HAL
open science

Mechanistic and structural basis for tuning of myosin activity

Louise Canon

► **To cite this version:**

Louise Canon. Mechanistic and structural basis for tuning of myosin activity. Cellular Biology. Université Paris sciences et lettres, 2022. English. NNT : 2022UPSLS064 . tel-04250726

HAL Id: tel-04250726

<https://theses.hal.science/tel-04250726>

Submitted on 20 Oct 2023

HAL is a multi-disciplinary open access archive for the deposit and dissemination of scientific research documents, whether they are published or not. The documents may come from teaching and research institutions in France or abroad, or from public or private research centers.

L'archive ouverte pluridisciplinaire **HAL**, est destinée au dépôt et à la diffusion de documents scientifiques de niveau recherche, publiés ou non, émanant des établissements d'enseignement et de recherche français ou étrangers, des laboratoires publics ou privés.

Mechanistic and structural basis for tuning of myosin activity

Base mécanistique et structurelle pour la régulation de l'activité de la myosine

Soutenue par

Louise CANON

Le 19 Octobre 2022

Ecole doctorale n°515

Complexité du vivant

Spécialité

Biochimie et biologie moléculaire

Composition du jury :

Carine, TISNE Directrice de recherche, IBPC	<i>Présidente du jury</i>
Françoise, OCHSENBEIN Directrice de recherche, CEA	<i>Rapporteuse</i>
Christopher, TOSELAND Senior Lecturer, University of Sheffield	<i>Rapporteur</i>
Pierre, LEGRAND Scientifique de ligne, Synchrotron SOLEIL	<i>Examineur</i>
Dietmar, MANSTEIN Professor, Medizinische Hochschule Hannover	<i>Examineur</i>
Christophe, LAMAZE Directeur de recherche, Institut Curie	<i>Examineur</i>
Anne, HOUDUSSE Directrice de recherche, Institut Curie	<i>Directrice de thèse</i>

À ma famille



Remerciements /Acknowledgments

First, I would like to thank my PhD supervisor: **Anne HOUDUSSE** for welcoming me in this team, for giving me the opportunity to perform a PhD in her team, for supervising me during these four years, for her encouragements and for all her great advises she provides me with.

I am really grateful to **Françoise OCHSENBEIN, Christopher TOSELAND, Pierre LEGRAND, Carine TISNE, Dietmar MANSTEIN** and **Christophe LAMAZE** for agreeing to be part of my PhD jury and for accepting to evaluate my thesis. I would also like to thank **Patricia BASSEREAU, Patrick ENGLAND** and **Laure STROCHLIC** for agreeing to be part of my PhD comity, for the scientific discussions, for their advises and guidance.

Thanks to our collaborators, **Lee SWEENEY, András MALNASI-CSIZMADIA** and their teams, for all the scientific discussions and thanks for showing me your confidence. Thanks to **Mate GIYMESI** for the discussions on blebbistatin derivatives, to **Tianming LIN** for all these ATPase assays on Myo6 and **Xiaoyan LIU** for all the bacculo viruses.

Thanks to the **structural motility team, present and past members**, for training me, providing me with good advises, supporting me during these four years and for all and for all the good time and laughs that we shared together:

À **Guillaume**, pour m'avoir transmis les bases du clonage, de la production et caractérisation de protéines recombinantes lorsque je suis arrivée en stage de M2. Merci aussi pour ta patience, ta bonne humeur et gentillesse (go chicken go !).

À **Léonid**, merci pour ta bonne humeur, tes conseils et tes digressions philosophiques ! Merci aussi pour toutes les protéines purifiées sans oublier toutes les MST.

À **Franck**, pour toutes les expériences de biologie cellulaire, pour son implication et pour ta bonne humeur.

À **Elena**, merci de m'avoir formé à la cristallisation et au SAXS. Merci pour ton aide, ta bonne humeur et tout le temps passer à cloner !

À **Carlos**, merci de m'avoir enseigné le traitement de données cristallographiques, merci pour ta gentillesse et tes conseils scientifiques.

À **Livia**, pour ses conseils en cristallisation et ses numéros de danses.

To **Lena** and **Moutse**, my office neighbors, thank for all your advises and discussions, thanks for helping me with Pymol, Coot and Buster!

À **Amandine**, merci pour ta bonne humeur et bien sûr merci pour tous les gâteaux !

À **Mona** et **Emma**, mes deux stagiaires, pour leur motivation, leur sérieux et leur bonne humeur.

À **Vincent**, pour les discussions scientifiques et tous les voyages au synchrotron !

Enfin, à **Leila**, mon indispensable bras droit ! Merci pour tout ton travail, ta motivation et ta gentillesse.

Thanks to the PX1, PX2 and SWING staff, **Aurélien THUREAU**, **Serena SIRIGU**, **Pierre MONTAVILLE**, **Bill SHEPARD**, **Andrew THOMPSON**, **Tatiana ISABET** and **MARTIN SAVKO** for providing me with great advises and helps for collecting and processing my data.

Thanks to La Ligue contre le cancer for funding my work.

Enfin merci à **ma famille et à mes amis** pour leur confiance, leur patience et tout leur soutien ! Merci de croire en moi !

Abstract

The eukaryotic cell nanomotors are able to perform complex mechanical tasks, necessary for tension generation in precise cellular locations. Vesicles formation and transport in the endocytic and secretory pathways can for example result from it. Among these motors, myosins are able, from the hydrolysis of ATP, to generate force in association with actin filaments. Myosins are divided into many classes involved in a wide range of functions and pathologies. Their dysfunction can lead to many diseases including spasticity, asthma, cardiomyopathy, deafness or many cancers... (Coluccio 2020).

Thus, the thesis project is centered on the one hand **(I)** on the study of the regulation of myosin VI (Myo6), a nanomotor involved in deafness as well as many cancers (Dunn *et al.* 2006; Li *et al.* 2015; Ma *et al.* 2015; You *et al.* 2018; Yang 2019; Yang *et al.* 2021). Myo6 is unique among all members of the myosin superfamily because it moves on actin filaments in the opposite direction to all other myosins. This specificity allows it to perform unique cellular roles that cannot be performed by any other myosin. **(II)** On the other hand, the thesis project focused on the study of the blebbistatin pocket (Straight *et al.* 2003), an inhibitor pocket within the myosin Motor domain, in order to explore its potential for the development of specific inhibitors.

This thesis therefore contributes to:

(I) Understanding the processes regulating the activity of Myo6 via an approach combining structural biology, biophysical tests and cell biology.

Such regulation involves the existence of an auto-inhibited state of Myo6 (Spink *et al.* 2008; Fili *et al.* 2017; 2020), a state in which the latter consumes little ATP and diffuses freely into the cytosol so that the motor is activated only at the site required for its recruitment. The biophysical study of this state has made it possible to better understand how to stabilize or destabilize it *in vitro* and has enabled us to obtain a first model of the auto-inhibited state using negative staining electron microscopy. This study also allowed us to better understand the differential role of cellular partners of Myo6 for its activation. Mutants promoting the activation or formation of the auto-inhibited state of Myo6 have been developed based on this study. Their ability to be recruited by different partners of Myo6 could thus be studied in human melanoma cells (MNT-1), these tests confirm a differential recruitment by the partners and suggest non-specific recruitment of mutants promoting activation.

(II) Understanding the origin of the specificity of the MPH-220, an allosteric modulator derived from the well-known myosin inhibitor blebbistatin and able to specifically inhibit skeletal Myosin-2 from a crystallographic approach.

This study describes that the specificity of this inhibitor with high potential for the development of new treatment against spasticity is based on a single non-conserved residue in the Blebbistatin allosteric pocket of the other myosins-2 (Gyimesi *et al.* 2020).

Abbreviations

ADP	adenosine diphosphate
ATP	adenosine triphosphate
P _i	inorganic phosphate
VO ₄	orthovanadate
F-actin	actin filament
MD	Motor domain
Ins2	Insert-2
IQ	light chain binding motif
CaM	calmodulin
ELC	essential light chain
RLC	regulatory light chain
3HB	triple helix bundle
LAE	Lever arm extension
SAH	single alpha helix
DT	distal Tail
CBD	cargo binding domain
FL	full-length
aa	amino acid
K _d	dissociation constant
KO	knock-out
NMR	nuclear magnetic resonance
EM	electron microscopy
HPLC	high performance liquid chromatography
SDS-PAGE	sodium dodecyl sulphate polyacrylamide gel electrophoresis
SAXS	small-angle light scattering
MALS	multi-angle light scattering
SEC	steric exclusion chromatography
MST	microscale thermophoresis
MTOC	microtubule-organizing center
LI	long insert
SI	small insert
R _g	radius of gyration

CONTENT

Remerciements /Acknowledgements	5
Abstract	7
Abbreviations	8
List of figures	12
List of tables	14
General introduction	15
A. The molecular motors	15
B. The Myosin superfamily	16
C. Structural organization of the myosins	18
C.1. The motor domain.....	18
C.2. The Lever arm.....	20
C.3. Tail	22
D. Kinetic cycle of myosin motors	24
Chapter 1: Mechanistic and structural basis for tuning of myosin VI activity	26
Introduction	26
A. Hearing loss and deafness	26
B. Myo6 unique features	29
B.1. Myo6 head	29
B.2. Myo6 Lever arm	33
B.3. Myo6 Tail	36
C. Wide range of cell partners links Myo6 to various functions and diseases	41
C.1. WWY partners	42
C.2. RRL partners	45
C.3. OFD1	48
C.4. Clathrin.....	48
C.5. Ubiquitin	49
C.6. Lipid	52
C.7. DNA.....	53
C.8. Fine differences in the interaction surface can modulate partner binding to Myo6.....	53
D. Myo6, a multifunctional motor in cells	56
D.1. Myo6 in trafficking/signaling events	56
D.2. Degradation pathways.....	63
D.3. Structure maintenance and organization	64
D.3.d. Myo6 association with cell-cell junctions	65
D.4. In Transcription	67
D.5. Myo6 links microtubule and actin tracks.....	67
D.6. Myo6 in cancers	68
E. Myo6 versatile mechanical properties	70
E.1. Actin organizer.....	72
E.2. Myo6 can dimerize at high concentration to perform transport and anchoring functions.....	72
E.3. Myo6 travelling along actin	73

E.4. Load sensitivity and anchoring	74
E.5. Large steps for a short Lever arm	76
E.6. Two dimerization models were proposed to address this question	76
F. Regulation of the Myo6 active/inactive pool equilibrium by an auto-inhibited state.....	80
F.1. Engaging large amount of active Myo6 is deleterious, control of myo6 activation is necessary.....	80
F.2. An auto-inhibited state	81
F.3. Myo6 activation.....	83
G. Modulation of the mechanical properties of the activated Myo6.....	86
G.1. Cargo nature	86
G.2. Cargo stiffness.....	91
H. Interest of having several partners interacting at once.....	91
Objectives	94
Results and discussion	95
A. Myosin VI activation: from the auto-inhibited state to its active forms	95
A.1. Methodology.....	95
A.2. Paper.....	106
A.3. Limits of the study and perspectives	157
Conclusions	175
Chapter 2: Inhibition of Myosin motor by small molecules binding in the 50 kDa cleft	178
Introduction	178
A. Conventional myosins (Myo2): therapeutical targets.....	178
A.1. Sarcomeric Myo2.....	179
A.2. Smooth muscle Myo2.....	181
A.3. Non-muscle Myo2	181
B. Targeting myosin motors against diseases	182
B.1. Five allosteric pockets found in myosin motor domain	183
B.2. Myosin modulators overview.....	184
C. Blebbistatin	186
C.1. Specificity.....	186
C.2. Solubility and permeability	187
C.3. Fluorescence	188
C.4. Blebbistatin stability and toxicity.....	188
C.5. Blebbistatin degradation mechanism	189
C.6. Blebbistatin inhibition mechanism	192
C.7. Blebbistatin site.....	194
C.8. Developing efficient blebbistatin inhibitors	197
Objectives	201
Results and discussion	202
A. Study of MPH-220: a specific SkMyo2 inhibitor	202
A.1. Crystallization of the promising specific skeletal inhibitor: MPH220	202
A.2. Article describing MPH-220 specificity and potential for spasticity treatment.....	208
A.3. MPH-220 may induce rearrangements within the Myo2 motor	235
B. Perspectives.....	237

B.1. Potential of blebbistatin derivatives for specific myosin targeting	237
B.2. Blebbistatin pocket entrance: a parameter than still requires investigation	239
Conclusions	241
General conclusion.....	243
Bibliography.....	245
Résumé	268
Abstract	269

List of figures

Figure 1: Simplistic view of the organization of the cytoskeleton and molecular motors in cells.....	p.15
Figure 2: Unrooted phylogenetic tree of the 40 human myosin genes sorted in classes.....	p.16
Figure 3: Myosin classes can adopt various conformations enabling them for diverse functions.....	p.17
Figure 4: Diagram of myosin general organization.....	p.18
Figure 5: Myosin head organization.....	p.19
Figure 6: IQ motif among myosins.....	p.20
Figure 7: Lever arm conformational change during the last step of the powerstroke.....	p.21
Figure 8: Scallop Myo2 Lever arm.....	p.22
Figure 9: Myosins general organization.....	p.23
Figure 10: kinetic cycle of a myosin motor.....	p.24
Figure 11: sensory hair cell degenerescence upon Myo6 loss.....	p.27
Figure 12: deafness/hearing loss mutation reported for Myo6.....	p.28
Figure 13: Overall organization of the Myo6 motor.....	p.29
Figure 14: ATPase cycle of Myo6.....	p.31
Figure 15: Myo6 P _i release.....	p.32
Figure 16: Leu310 hinders ATP binding due to the presence of Insert-1.....	p.32
Figure 17: Ins2 reorientates Myo6 converter towards the minus end of actin filament.....	p.33
Figure 18: Converter rearrangement between the pre-powerstroke and the rigor-like state reorients Insert-2.....	p.34
Figure 19: Myo6 can undergoes a particularly large stroke due to converter rearrangement.....	p.35
Figure 20: Myo6 Lever arm.....	p.36
Figure 21: Myo6 triple helix bundle is stabilized by hydrophobic interactions.....	p.36
Figure 22: sequence alignment of SAH domain among species.....	p.37
Figure 23: DT domain organization.....	p.38
Figure 24: localization of Myo6 isoforms in MDCK cells.....	p.39
Figure 25: sequence alignment of human Myo6 Tail (998-end) isoforms.....	p.39
Figure 26: Distal Tail and Cargo binding domain, key platforms for Myo6 recruitment.....	p.40
Figure 27: Diagram of Myo6 interactome.....	p.41
Figure 28: Dab2 fragment 675-711 form a 2:2 complex with Myo6 CBD ^c	p.42
Figure 29: TOM1 fragment 436-462 form a 1:1 complex with Myo6 CBD ^c	p.44
Figure 30: GIPC1 GH2 domain forms long oligomers when bound to the CBD ⁿ fragment.....	p.46
Figure 31: Clathrin organization.....	p.48
Figure 32: CLCa fragment bound to CBD ⁿ fragment.....	p.49
Figure 33: Ubiquitin chains linkage.....	p.50
Figure 34: K63-diUbiquitin bound to the CBD ⁿ fragment.....	p.51
Figure 35: Myo6 CBD binds to PIP2 resulting in conformational changes.....	p.52
Figure 36: DNA binding motif.....	p.53
Figure 37: CBD ⁿ organization.....	p.54
Figure 38: Increasing number of elongated vesicles suggest the role of Myo6 for fission.....	p.61
Figure 39: sensory ear hair cell organization and Myo6 distribution.....	p.65
Figure 40: Myo6 behavior switches mode under load.....	p.75
Figure 41: Distal dimerization.....	p.77
Figure 42: SAH mediated dimerization.....	p.79
Figure 43: Proximal dimerization.....	p.79
Figure 44: Myo6 auto-inhibited state model.....	p.82
Figure 45: Myo6 oligomeric states instruct this motor for specific, distinct mechanical properties.....	p.87
Figure 46: Myo6 oligomeric state induced by binding of various partners.....	p.90
Figure 47: Characterization of Myo6 auto-inhibited state using FLMyo6 SI pig-mouse chimera.....	p.96

Figure 48: Myo6 sequence alignment.....	p.98
Figure 49: Surface residues conservation between pig and mouse Myo6.....	p.98
Figure 50: Myo6 pig-mouse chimera opens more easily upon salt concentration.....	p.99
Figure 51: GIPC1 organization.....	p.102
Figure 52: GIPC1 auto-inhibited state prevents binding to Myo6	p.103
Figure 53: TOM1 organization.....	p.104
Figure 54: Dab2 organization.....	p.105
Figure 55: Main interactions stabilizing the Myo6 auto-inhibited.....	p.157
Figure 56: CBD ^c loop mutant (D1148V, Y1150D, D1152R and Q1154V) has only little impact on Myo6 compacity <i>in vitro</i>	p.158
Figure 57: DNA binding motifs and CBD ^c loop mutant (D1148V, Y1150D, D1152R and Q1154V) within CBD ^c	p.159
Figure 58: D1148V, Y1150D, D1152R and Q1154V mutations disrupt Myo6 CBD recruitment to melanosomes.....	p.159
Figure 59: Jo-Myo6-In crystallization drops without seeding (right) and with seeding (left).....	p.160
Figure 60: Jo-Myo6-In is a multidomain protein.....	p.161
Figure 61: Model of the active FL Myo6 proximal dimer.....	p.164
Figure 62: Model of the active FL Myo6 proximal dimer with modelization of the R849-E875 region	p.165
Figure 64: Model of the GIPC1-Myo6 complex that could either form a single dimer or a large oligomer of dimers.....	p.167
Figure 65: interferometric scattering mass spectrometry principle.....	p.170
Figure 66: Sequence alignment of the 851-949 (human gene numbering) amino acids among species.	p.171
Figure 67: K63-diUbiquitin is unable to increase the Myo6 ATPase rate	p.173
Figure 68: Myo2 subfragments.....	p.178
Figure 69: Overall sarcomere organization.....	p.179
Figure 70: Relative abundance of Myo2 isoforms in human muscles	p.180
Figure 71: Allosteric binding pockets within the myosin motor.....	p.183
Figure 72: (-)-Blebbistatin scaffold.....	p.186
Figure 73: Blebbistatin IC ₅₀ for various Myo2 isoforms.....	p.187
Figure 74: Blebbistatin photodegradation.....	p.190
Figure 75: Putative photochemical mechanism for blebbistatin photo-inactivation upon 416 nm illumination	p.191
Figure 76: Blebbistatin binding site.....	p.195
Figure 77: Blebbistatin tunnel within the DictyMyo2 pre-powerstroke motor.....	p.196
Figure 78: Identification of most promising positions for A-ring substitution.....	p.197
Figure 79: A-ring derivatives from Verhasselt <i>et al.</i> (2017).....	p.198
Figure 80: The Arg238 backbone is close to the blebbistatin C-ring and was proposed as a potential way to mediate additional polar contact in the allosteric pocket.....	p.198
Figure 81: D-ring derivatives of blebbistatin.....	p.199
Figure 82: Comparison between blebbistatin and MPH-220.....	p.200
Figure 83: Degraded MPH-220 within the SkMyo2 motor.....	p.201
Figure 84: MPH-220 fitted in SkMyo2 blebbistatin allosteric pocket (6YSY).....	p.204
Figure 85: Absorption of 10 μM blebbistatin in water or SkMyo2 buffer.....	p.205
Figure 86: Absorption of 10 μM blebbistatin supplemented with various reagents after 18h in white light.....	p.206
Figure 87: Example of crystallization drops for SkMyo2 MPH-220 crystals with (right) and without (left) DTT.....	p.206
Figure 88: Superimposition of SkMyo2 allosteric pocket with MPH-220 (PDB:6YSY) and without MPH-220.....	p.235
Figure 89: Superimposition of SkMyo2 with MPH-220 (PDB: 6YSY) and without MPH-220.....	p.235

Figure 90: comparison of skeletostatin and blebbistatin.....	p.236
Figure 91: Inhibition of different Myo2 subclasses by blebbistatin, paraNitroBlebbistatin and Amino-Blebbistatin.....	p.237
Figure 92: Residues variability at the entrance of the 50 kDa cleft.....	p.239

List of tables

Table 1: structure of Myo6 motor in different states of the ATPase cycle.....	p.30
Table 2: Dab2-Myo6 affinity reported in the literature.....	p.43
Table 3: TOM1-Myo6 affinity reported in the literature.....	p.45
Table 4: NDP52-Myo6 affinity reported in the literature.....	p.47
Table 5: TAX1BP1-Myo6 affinity reported in the literature.....	p.47
Table 6: Ubiquitin-Myo6 affinity reported in the literature.....	p.51
Table 7: DNA-Myo6 affinity reported in the literature.....	p.53
Table 8: link between mechanical properties and cell functions.....	p.71
Table 9: Myo6 proximal dimerization.....	p.78
Table 10: GIPC1 interaction with the Myo6 CBD.....	p.104
Table 11: TOM1 interaction with Myo6 CBD.....	p.105
Table 12: TOM1 and Dab2 interaction with Myo6 CBD.....	p.106
Table 13: K63-diUbiquitin binding to the Myo6 CBD.....	p.173
Table 14: clinical trials studies on myosin modulators	p.182
Table 15: Data collection and refinement statistics of the crystal structure of SkMyo2 bound to degraded MPH-220.....	p.202
Table 16: Data collection and refinement statistics of the SkMyo2 pre-powerstroke state crystal	p.234
Table 17: Conservation of key residues for blebbistatin binding between conventional myosins and unconventional Myo6.....	p.238

General introduction

A. The molecular motors

Molecular motors are key proteins able to generate force upon ATP hydrolysis when associated with the cytoskeleton. Force generated by these motors notably result in cell motility, trafficking, division and muscle contraction; key processes for eukaryotic cell integrity and functions.

Among these molecular motors, we can find the kinesins and the dyneins that generate force when associated to microtubules and the myosins that generate force when associated with actin filaments. Cytoskeleton filaments are dynamic and polarized structures with a minus end (slow growth) and a plus end (fast growth) that constrain nanomotors to exert their force in a specific direction. Indeed, while most kinesins and myosins move toward the plus end, some move in the opposite direction (Endres *et al.* 2006; Wells *et al.* 1999), dyneins move toward the minus end of the microtubules (Figure 1).

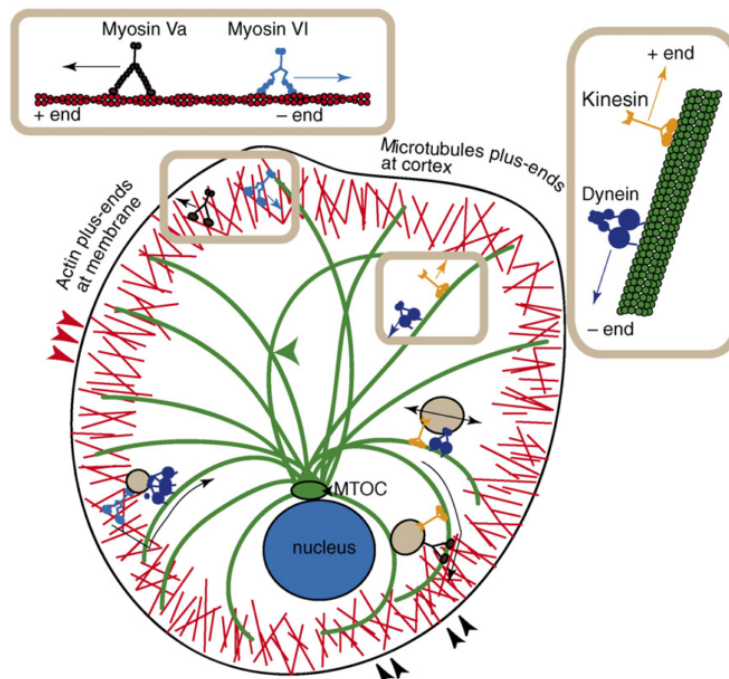


Figure 1: Simplistic view of the organization of the cytoskeleton and molecular motors in cells (Ross, Ali, and Warshaw 2008)

Actin filaments (in red) are found at the cell periphery while microtubules (green) radiate from microtubule-organizing centers (MTOC). In cartoon: myosin Va (dark brown) and myosin VI (light blue) moving towards the plus or minus ends of the actin filaments (respectively). Kinesins (yellow) and dyneins (dark blue) moving towards the plus or minus end of the microtubules (respectively). Contacts between actin filaments and microtubules allow collaboration. In particular, vesicles (sand) can thus switch from actin-based motion to microtubule-based motion or from microtubule-based motion to actin-based motion thanks to collaboration between the molecular motors.

Moreover, the spatial distribution of microtubules and actins filaments differs. Microtubules are large (25 nm diameter) filaments which are anchored in centrosomes at the minus end) and radiate out of the centrosomes at the plus end (Figure 1). So doing, the microtubule network allows cytoplasm organization and cargo transport on the microtubule track from cell periphery to nucleus. In contrast, actin filaments are thin (6 nm diameter) fibers mostly found in the cell cortex where they support specialized structures such as microvilli and can mediate local transport (Figure 1). These nanomotors thus complemented each other, offering the possibility to perform a variety of functions notably offering the possibility of active transport of cargoes at precise location on cytoskeleton tracks upon ATP hydrolysis.

B. The Myosin superfamily

The myosin superfamily is a collection of actin-dependent molecular motors. In human, 40 myosin genes are expressed and divided in 12 classes of myosins (class I, II, III, V, VI, VII, IX, X, XV, XVI, XVIII, and XIX) (Odriontz and Kollmar 2007; Quintero, Moore, and Yengo 2012) (Figure 2). Most of them are ubiquitously expressed in cells.

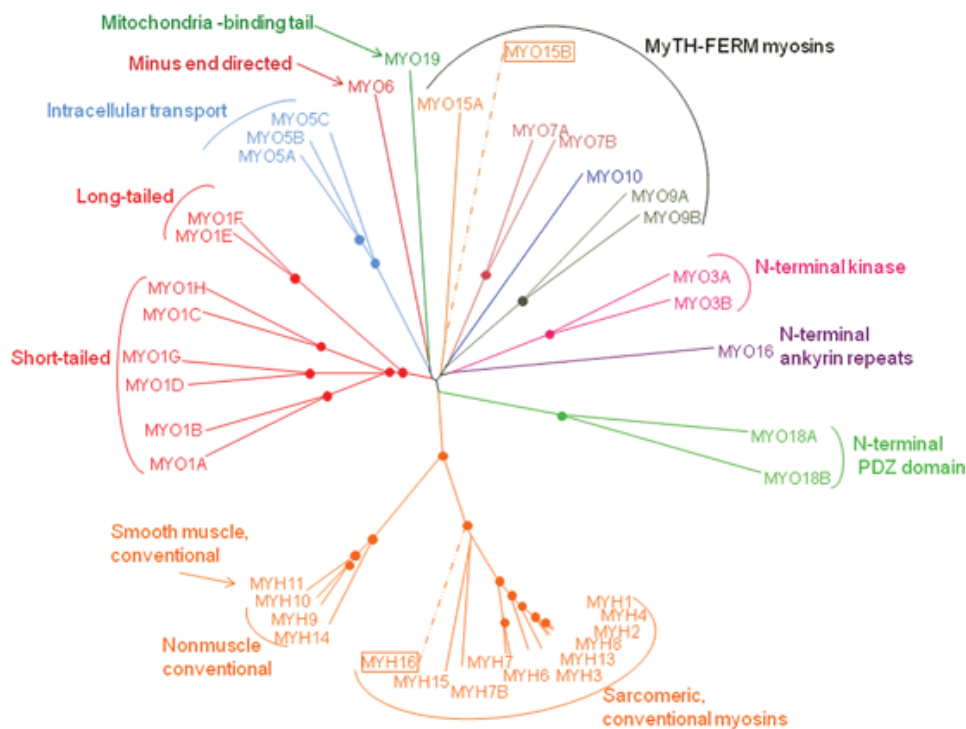


Figure 2: Unrooted phylogenetic tree of the 40 human myosin genes sorted in classes (Quintero, Moore, and Yengo 2012)

Myosins sorted according to their motor sequence identity. Myosin gene name correspond to their official HUGO human gene name. Unconventional myosin genes are named “MYO” and conventional myosin (also known as myosin II) genes are named “MYH”.

Myosins of class II (Myo2) were historically the first myosins discovered by high salt extraction of a muscle extract by Kühne in 1864 (reviewed in [Szent-Györgyi 2004](#)) and nowadays, it is the most diverse class with 15 genes in total in human. Myo2 are thus known as conventional myosins that among myosins, have the unique ability to associate in long filaments able to slide along actin filaments ([Figure 3](#)). This ability is notably crucial for muscle contraction and cytokinesis ([Alonso-Matilla, Thiyagarajan, and O'Shaughnessy 2019; Powers et al. 2021](#)). In contrast, the remaining myosin classes, unable to associate into myosin filament assemblies, constitute the unconventional myosins and can associate to membrane for intracellular organization like Myo1 or use their force for transporting cargo along actin filaments like Myo5 ([Figure 3](#)).

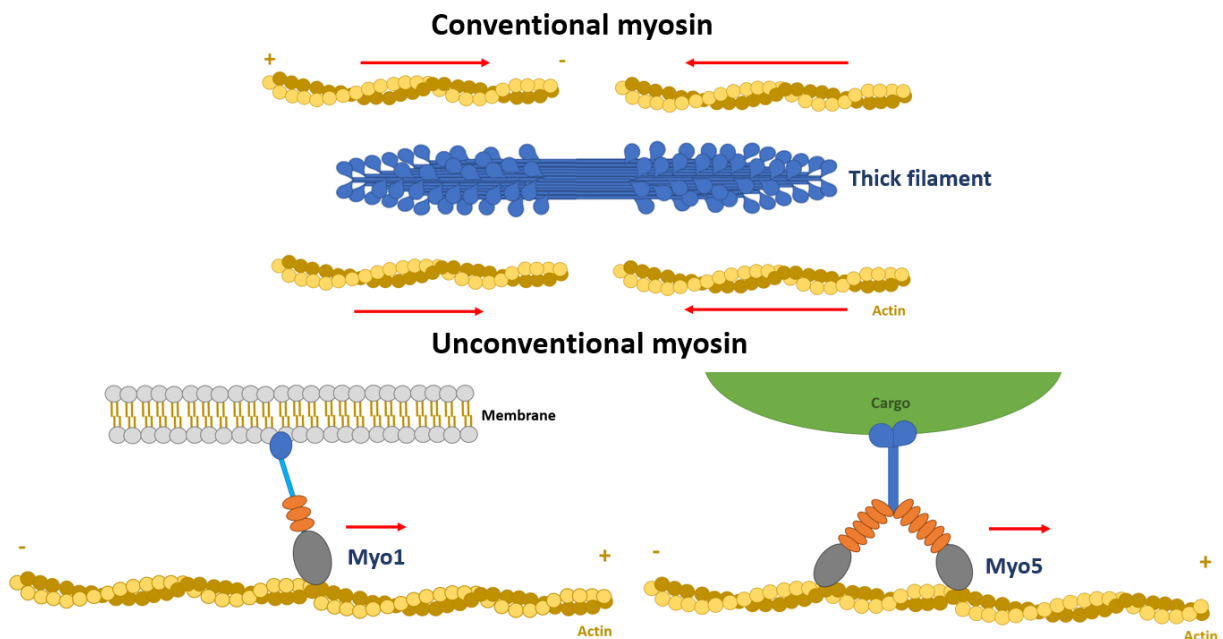


Figure 3: Myosin classes can adopt various conformations enabling them for diverse functions **(Top)** Conventional Myo2 (in blue) associate in thick filaments through their coiled coil Tail and slide along actin filaments (yellow) **(Bottom)** Unconventional myosins; **(right)** Myo1 associates with the membrane through its Tail (blue) and interacts with the actin filaments through its Motor domain (grey). So doing Myo1 can participate in cell organization. **(left)** Myo5 binds cargo (green) and associates as a dimer through its Tail (blue) to take processive steps on the actin track (yellow). Light chains in the neck region are depicted in orange, note that their number vary depending on the myosin isoform.

C. Structural organization of the myosins

Myosins present overall the same organization; they contain (from N-terminus to C-terminus) a Motor domain that generate force, a Lever arm and a divergent Tail (Figure 4).

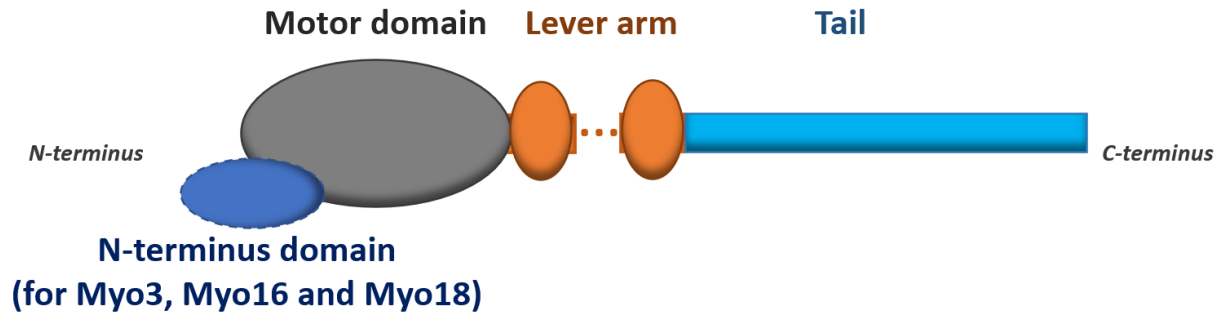


Figure 4: Diagram of myosin general organization

Simplified representation of the general organization of a myosin with from N-terminus to C-terminus a Motor domain (grey) (preceded by an N-terminus domain for Myo3, Myo16 and Myo18) a Lever arm (orange) and a divergent Tail (light blue).

C.1. The Motor domain

Myosins are characterized by a conserved Motor domain usually located at the N-terminus (with notably the exception of Myo3, Myo16 and Myo18 that contains an additional N-terminus domain prior to the Motor and Myo1, Myo9 and Myo15 that exhibit an unstructured region prior to the Motor domain). This domain is responsible for ATP hydrolysis and interaction with actin.

Through all the myosin classes, it exhibits conserved structural elements allowing conserved mode of force production among myosins. Indeed, the Motor generates force by undergoing several conformational states along the ATPase cycle that depend both on the nucleotide- and actin- binding. Since the first atomic description of a myosin Motor, thanks to the X-ray crystallography structure of chicken skeletal Myo2 at 2.8 Å (Rayment *et al.* 1993), a large amount of myosin Motor atomic structures have been solved allowing a detailed description of the different features composing a myosin Motor (reviewed in Sweeney, Houdusse, and Robert-Paganin 2020; Schröder 2020) (Figure 5).

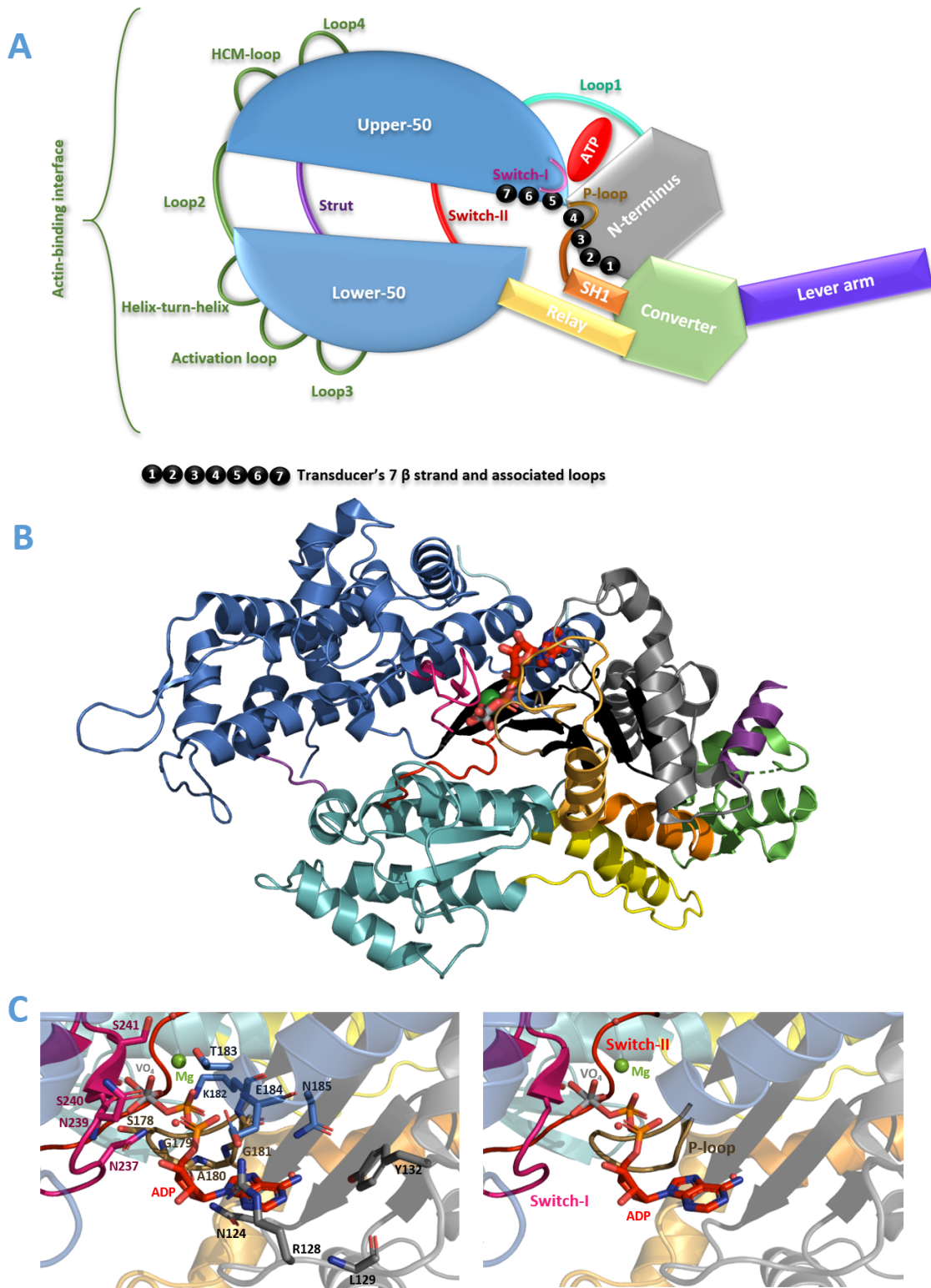


Figure 5: Myosin head organization

(A) Simplified organization of myosin Motor domain and neck. Color code pictured on the figure (B) Motor domain of scallop Myo2 bound to Mg₂ADP.VO₄ (P_i analog) solved by X-ray crystallography at 2.6 Å (PDB: 1QVI; (Gourinath et al. 2003)). Color code as in (A) (C) close up on scallop Myo2 active site. The key nucleotide binding residues are highlighted as sticks.

The myosin Motor domain is composed of four major subdomains: the N-terminus, the lower-50 and upper-50 that separate an inner cleft and the converter. These subdomains are linked together by highly conserved connectors: switch-II, relay, strut and SH1-helix (reviewed in [Robert-Paganin et al. 2020](#)):

- Upper and lower-50 can mediate actin binding to the myosin Motor through the actin binding loops and the helix-turn-helix of the lower-50. The affinity for actin is increased upon closure of the inner cleft (50 kDa cleft) that separate the two subdomains, assisted by the strut connector ([Coureux et al. 2003](#); [Coureux, Sweeney, and Houdusse 2004](#)).
- Switch-II, near the P_i binding site, changes conformation depending on the nucleotide bound and can play the role of a door keeper controlling phosphate release ([Llinas et al. 2015](#))
- Switch-I and P-loop are part of the active site of the myosin Motor.
- As a central β -sheet, the transducer is directly affected by conformational changes at the active site or at the actin-binding interface and is thus critical for structural rearrangement transduction across the Motor.
- Rearrangements are transmitted to the converter through the connectors: SH1-helix and relay.
- The converter, which is the most mobile subdomain can then amplify movement thus drives force generation by the myosin Motor.

C.2. The Lever arm

Consensus	...	I ₁	Q ₂	X ₃	X ₄	X ₅	R ₆	G ₇	X ₈	X ₉	X ₁₀	R ₁₁	...
M1	IQ1	I	Q	A	A	W	R	G	F	H	W	R	
	IQ3	A	Q	T	I	R	R	L	I	R	G	F	
M2	IQ1	T	Q	A	R	C	R	G	F	L	M	R	
	IQ2	I	Q	Y	N	V	R	S	F	M	M	V	
M5	IQ2	L	Q	N	N	I	K	G	F	I	I	R	
	IQ4	L	Q	K	K	I	R	K	E	L	K	Q	
M6	IQ1	M	Q	K	T	I	R	M	W	L	C	K	
M7	IQ3	L	Q	A	L	H	R	S	R	K	L	H	
M10	IQ3	F	Q	K	Q	L	R	G	Q	I	A	R	
M14	IQ2	V	Q	A	H	I	R	K	K	M	A	V	

Figure 6: IQ motif among myosins ([Heissler and Sellers 2014](#))

IQ sequence from myosin I, II, V, VI, VII, X, XIV. First position is occupied by a hydrophobic residue, position 2 is occupied by a conserved Gln, position 6 is occupied by a positively charged residue and position 11 is preferentially occupied by a positively charged residue.

Following the converter, the neck region is found. It is a helical region containing consensus sequence (IQxxxRGxxxR), i.e., IQ motif ([Figure 6](#)). These motifs mediate association of the myosin heavy chain to the light chains, which rigidifies the neck region. The ensemble constitutes the Lever arm, whose structure was solved at 2 Å in 1996 ([Houdusse and Cohen 1996](#)). This rigidified Lever arm allows force generation by amplifying the structure rearrangement of the Motor domain along the force production cycle (H. Lee Sweeney and Houdusse 2010) ([Figure 7](#)). The number of IQ motifs depends on the myosin classes from a short neck region containing only 1 IQ for Myo6 to a long Lever arm containing 6 IQs for Myo5.

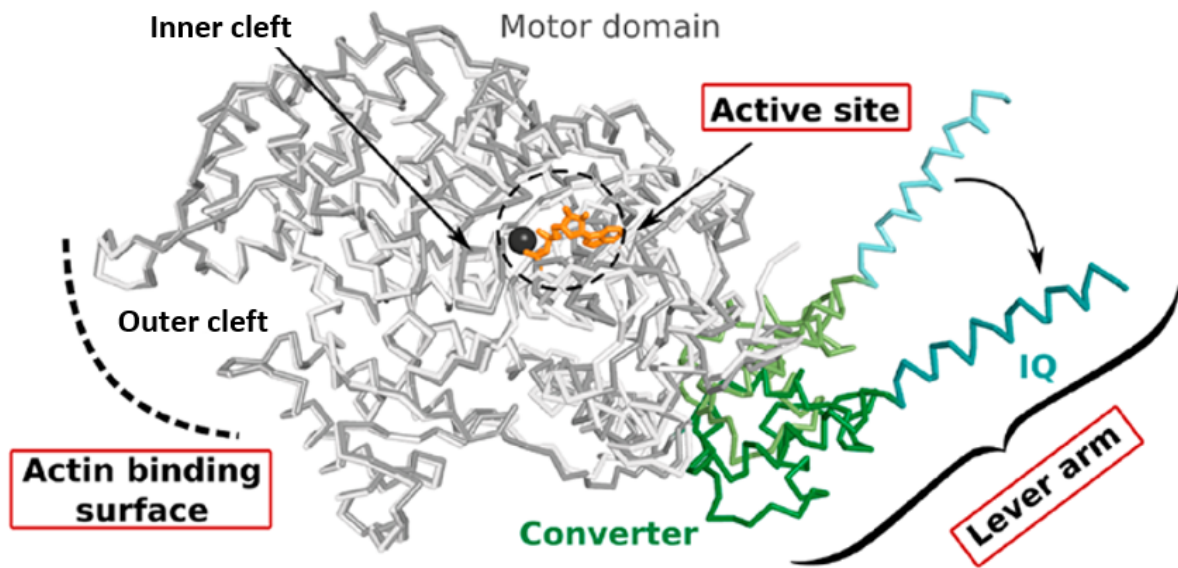


Figure 7: Lever arm conformational change during the last step of the powerstroke (Robert-Paganin *et al.* 2020)

Comparison between *Myo1b* in strong-ADP (PDB: 6C1H, Mentés *et al.* 2018) and rigor state (PDB: 6C1C, Mentés *et al.* 2018). Motor domain is in grey, the converter is in green and the IQ is in blue. An arrow emphasizes the swing performed by the Lever arm in between strong-ADP and rigor state.

Light chains are calmodulin (CaM) and CaM related proteins. Generally speaking, the essential light chain (ELC) binds the first IQ (closest to the Motor domain) of the conventional myosins, the regulatory light chain (RLC) binds to the second IQ and the CaMs bind to the Lever arm of unconventional myosins, although it should be noted that native light chain has not been clearly identified for all myosin motors; some unconventional myosin motors were reported to be able to bind ELC or RLC and some atypical light chains were found to bind unconventional myosin as well (reviewed in Heissler and Sellers 2014).

CaM is a highly conserved protein of ~16 kDa composed of two globular regions (N-lobe and C-lobe) attached together through linker. Each lobe is composed of two EF-hands (helix-turn-helix) able to interact with divalent cations, preferentially Ca^{2+} which coordinate the two helices together through interaction with the central loop, preferentially to adopt various conformations (open, *i.e.*, EF-hand helices perpendicular, semi-open, *i.e.*, intermediate between open and closed, closed, *i.e.*, EF-hand helices anti-parallel, uncoupled, *i.e.*, EF-hand helices separated) notably depending on the cation and the protein bound to it. When a CaM lobe adopts a close conformation, its affinity with the IQ motif became lower. CaM conformational changes can thus be an important element of myosin activity regulation. ELC and RLC are 16-25 kDa proteins that exhibit a structure very similar to CaM with 2 lobes and 4 EF-hands, yet they exhibit several degenerated EF-hands that have partially and completely lost

their Ca^{2+} binding properties (Houdusse and Cohen 1995; reviewed in Heissler and Sellers 2014) (Figure 8). As for CaM, they can adopt extended or compact conformations that impact their affinity for myosin heavy chain. Additionally, phosphorylation of the RLC has been shown to be a key parameter for regulation of the activity of several conventional myosin (Craig, Smith, and Kendrick-Jones 1983).

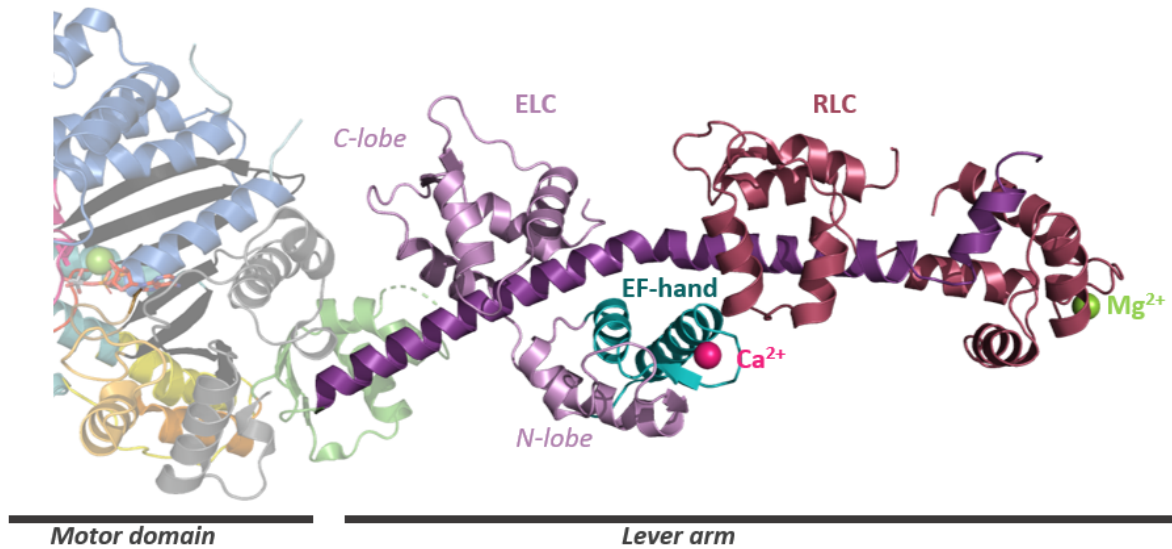


Figure 8: Scallop Myo2 Lever arm

Lever arm of scallop Myo2 solved by X-ray crystallography at 2.6 Å (PDB: 1QVI; Gourinath et al. 2003). Neck region of myosin heavy chain in purple, ELC in lila, RLC in burgundy. Mg^{2+} ion in green and Ca^{2+} ion in pink. One of the four EF-hands of the ELC is highlighted in blue.

C.3. Tail

The Tail is a highly divergent part that sets the different myosin classes apart. It can contain various structural elements such as MyTH4-FERM domain, Lever arm extension or single α -helix and often mediate binding to cell partners and dimerization (Figure 9).

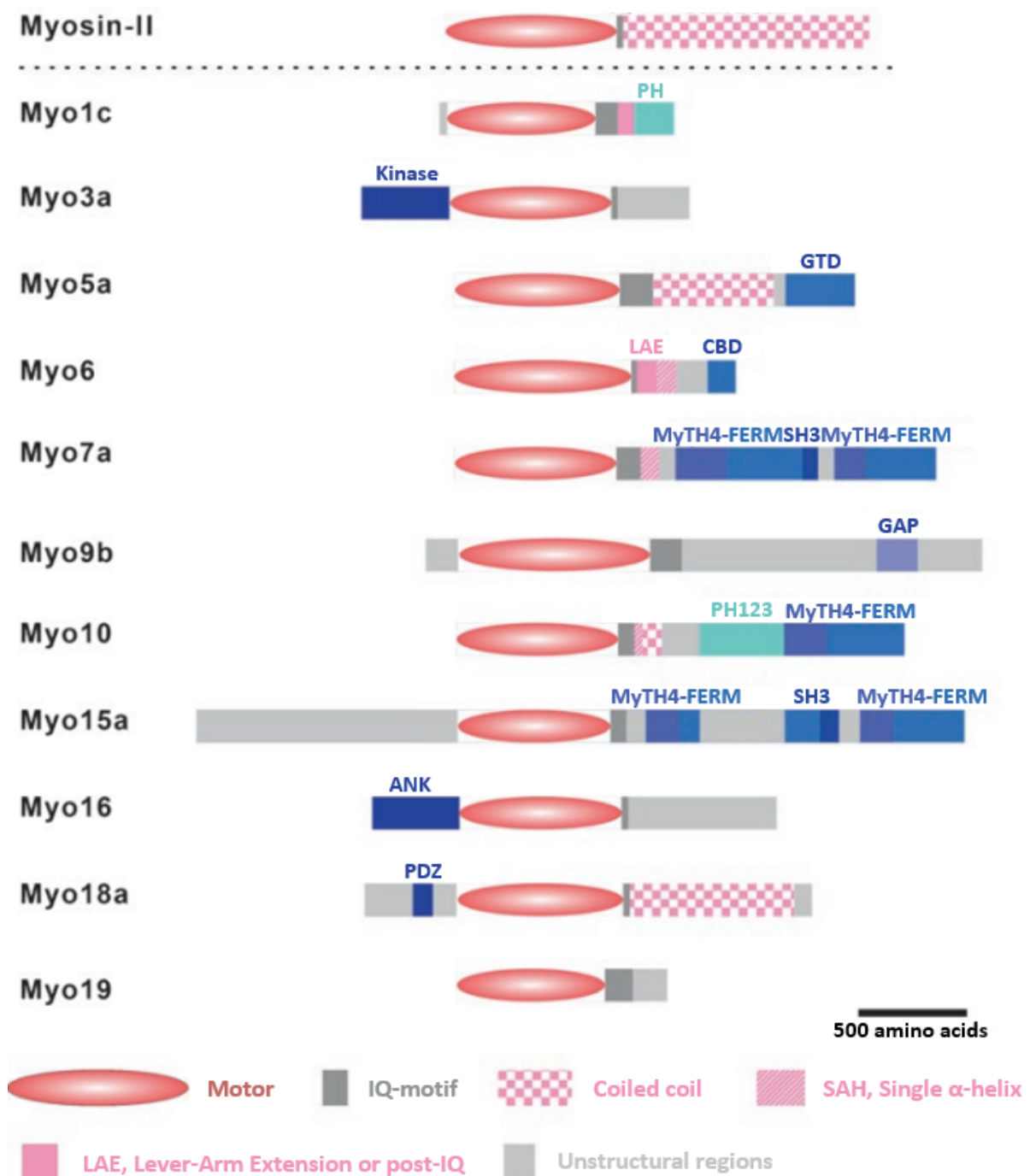


Figure 9: Myosins general organization (Li and Zhang 2020)

General organigram of the 12 different myosins found in human. Domains are colored depending on their nature with the conserved Motor domain in red; the IQ motifs in dark grey (note that the number of IQ motifs varies depending on the myosin class); coiled coil, single α -helix, Lever arm extension in pink; the unstructured regions in light grey and the structured domains in blue (GTD: globular Tail domain, CBD: cargo binding domain, SH3: SRC homology 3 domain, MyTH4-FERM: myosin Tail homology 4-band 4.1, ezrin, radixin, moesin, GAP: GTPase-activating protein, ANK domain: ankyrin domain, PH: pleckstrin homology domain).

D. Kinetic cycle of myosin motors

Force is generated during the ATPase cycle in which the Motor undergoes various conformations depending on its nucleotide state and actin binding. This motor cycle has been extensively characterized through transient kinetic experiments, while biophysical experiments, including optical trapping, have characterized the force produced by these motors (Sweeney and Houdusse 2010). Moreover, atomic structures of myosins in different states of the cycle have been solved using X-ray crystallography and cryo-electron microscopy (Sweeney, Houdusse, and Robert-Paganin 2020; Schröder 2020) allowing a good understanding of the way myosins transform chemical energy from ATP hydrolysis into mechanical work (Figure 10).

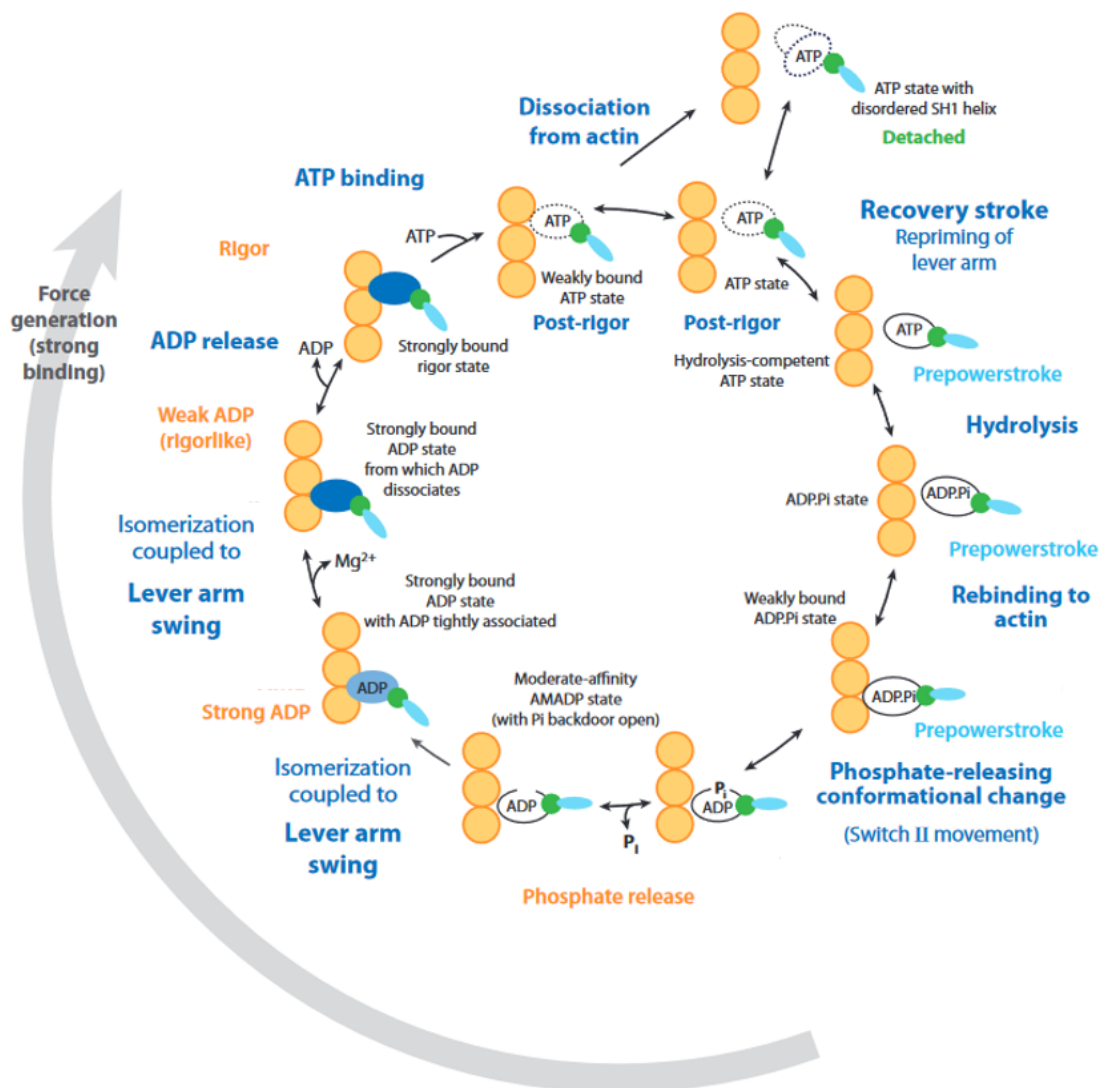


Figure 10: kinetic cycle of a myosin motor (Sweeney and Houdusse 2010)

Schematic representation of myosin ATPase cycle. Actin is represented as yellow dots, myosin Motor domain as an oval either white circled in black when it exhibits a low actin affinity or blue when it exhibits a high actin affinity, the converter is represented in green and the Lever arm is represented in light blue and switch position along the ATPase cycle.

Force is produced during the **powerstroke** of the cycle in which the Motor is bound to the actin filament following ATP hydrolysis. Actin binding induces conformation changes allowing P_i release (**P_i release state**) (Llinas *et al.* 2015) and larger rearrangements resulting in the closure of the inner cleft that increases actin affinity and promote the wide swing of the Lever arm responsible of force generation in the mechanical work (**strong ADP state**). Finally, ADP is released from the Motor after a transition to populate the so-called **Rigor state**. The Motor then detaches from actin upon ATP binding which triggers conformational rearrangements of the transducer and opening of the cleft, constituting the post-rigor state of the myosin Motor (Coureux, Sweeney, and Houdusse 2004). During the following **recovery stroke**, the Motor performs a rapid isomerization that ends up populating the **pre-powerstroke state** in which ATP hydrolysis can be facilitated. This state possesses a low affinity for actin and a primed Lever arm ready to perform its next swing once the Motor will rebind actin to start a new cycle.

Myosins are thus refined machines that generate force, according to a rather conserved mechanism. Yet strong structural divergence in the Tail, the addition of an extra N-terminus domain as well as subtle differences in the Motor domain, notably in the actin loops (Robert-Paganin *et al.* 2020), instruct the different myosin classes to various functions from muscle contraction (Sweeney and Hammers 2018) to gene expression (Louvet and Percipalle 2009) and drug-associated memory (Briggs *et al.* 2017). Myosins are also associated with several diseases or disorders like hypertrophic cardiomyopathy, deafness, spasticity and several cancers (Coluccio 2020). This makes the study of myosin motors of particular interest both for the characterization of the many intracellular processes they are involved in as well as for the development of targeted treatments when diseases are linked to myosin malfunction or overexpression.

Chapter 1: Mechanistic and structural basis for tuning of myosin VI activity

Introduction

The unconventional myosin of class VI (Myo6) was first identified from F-actin column chromatography on an embryonic drosophila melanogaster extract (Kellerman and Miller 1992). It was named 95F MHC at the time. Myo6 was then identified through PCR screening on RNA isolated from human and porcine cell extracts (Caco-2BBE, LLC-PK1, human peripheral blood leukocyte and human liver) (Bement *et al.* 1994) as well as from organisms from various phylogenetic groups such as urchins, fishes and C. Elegans (Terasaki, Ohnuma, and Mabuchi 1997; Kelleher *et al.* 2000; Coffin *et al.* 2007).

Myo6 is ubiquitously expressed and can be found at several cell localizations. It was reported to localize on a variety of cell compartments including: vesicles, membrane ruffles, microvilli, Golgi apparatus (Buss *et al.* 1998) and nucleus (Vreugde *et al.* 2006).

By performing *in vitro* motility assays, Wells *et al.* (1999) demonstrate that as opposed to all other myosin motors, Myo6 moves towards the minus end of the actin filament, which suggests that Myo6 may perform functions that can't be easily compensated by any other myosin. For example, as opposed to Myo5, in cultured rat neurons or in zebrafish *in vivo*, Tail truncated (1-993) Myo6 can travel across the actin barrier that filters the proteins and vesicles able to travel across the axon (Balasanyan *et al.* 2017). This is likely related to its unique ability to move towards the minus end of actin filaments as actin is predominantly oriented with their plus end facing the cell body.

A. Hearing loss and deafness

In 1995, Myo6 was identified as a "deafness gene" (Avraham *et al.* 1995) through genetical mapping of the Snell's Waltzer mice (sv/sv) that suffer from recessive deafness (first described in Deol *et al.* 1966).

Immunofluorescence on sections of the mouse organ of Corti shows that Myo6 normally concentrates within the inner and outer hair cells of the sensory epithelium of the cochlea, while in sv/sv mouse, no Myo6 was detected and hairs cells degeneration with hair cell stereocilia fusion was seen after only 3 weeks post-birth (Avraham *et al.* 1995). At six weeks of age, they found a complete loss of both inner and outer hair cells within the organ of Corti (Avraham *et al.* 1995) and formation of giant stereocilia 20 days after birth (Self *et al.* 1999) resulting in deafness (Figure 11).

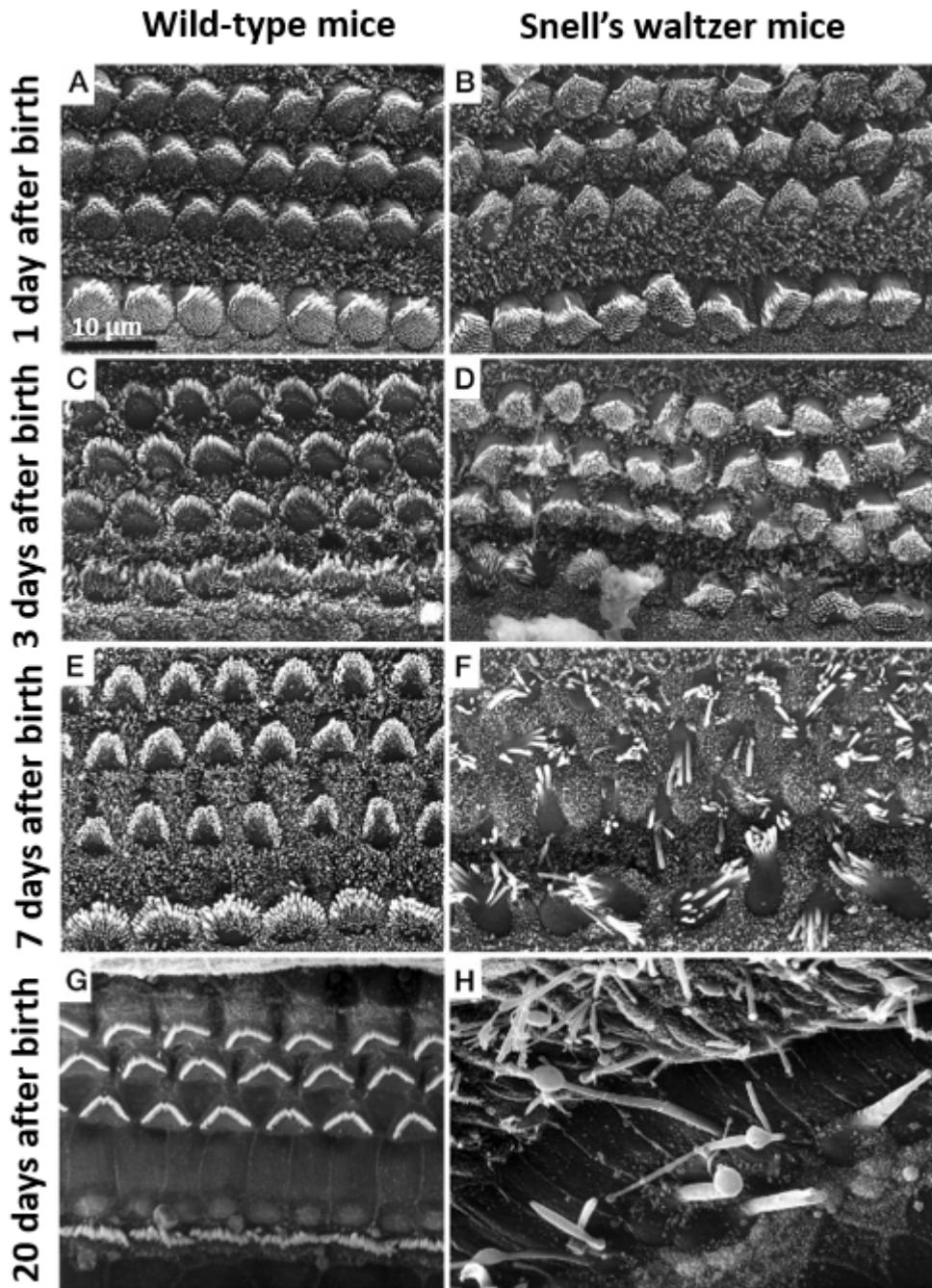


Figure 11: sensory hair cell degenerescence upon Myo6 loss (Self *et al.* 1999)

Scanning electron microscopy of sensory hair cells of wild-type (A, C, E, G) or Snell's Waltzer (*Myo6*-null) (B, D, F, H) mice cochlea from 1 to 20 days after birth. On the left part of the figure, we can clearly see that the hair cells degenerate to form giant stereocilia in *Myo6*-null mice as opposed to wild-type mice on the right.

Melchionda *et al.* (2001) then confirmed that *Myo6* dysfunction was also responsible for hearing loss in human. Since then, an ever-growing number of pathogen mutations and genetics anomaly were found in the human and mouse *Myo6* gene, causing either dominant or recessive genetic hearing loss (Figure 12).

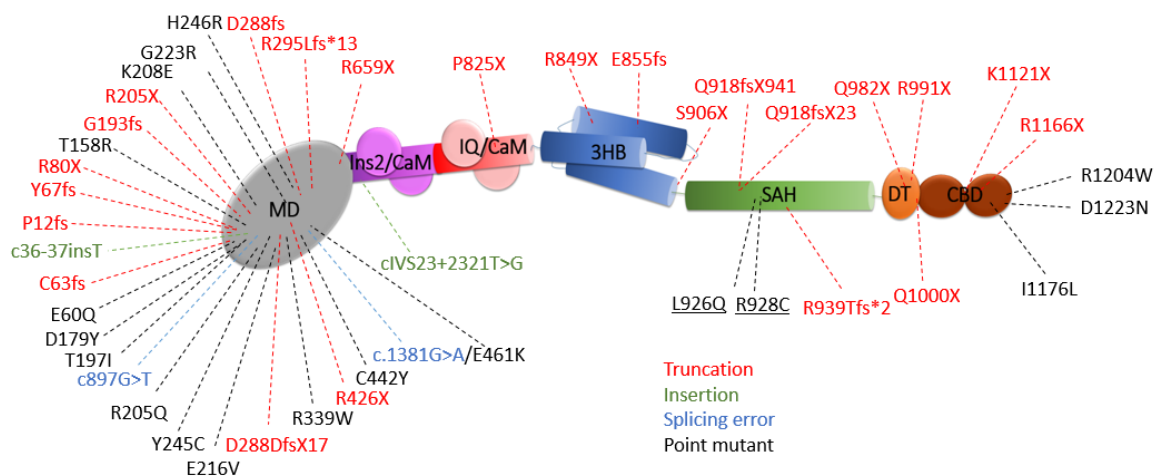


Figure 12: deafness/hearing loss mutation reported for Myo6

Myo6 diagram with the Motor domain (MD) in grey, the Insert-2/calmodulin (*Ins2/CaM*) in purple, the IQ motif/calmodulin (*IQ/CaM*) in red, the triple helix bundle (3HB) in blue, the single α -helix (SAH) in green, the distal Tail (DT) in orange and the cargo binding domain (CBD) in brown. Deafness mutations are indicated on the full-length *Myo6* diagram. fs stands for frame shift, fs* indicates the position of the translation termination, c. stand for coding DNA, > indicates nucleotide substitution, ins indicates an Insertion, X indicates a stop. Mutations from Alkowari et al. 2017; Brownstein et al. 2014; Wu et al. 2020; Venugopal et al. 2020; Melchionda et al. 2001; Ahmed et al. 2003; Seki et al. 2017; Sampaio-Silva et al. 2018; Kim et al. 2018; Alimardani et al. 2019; Wang et al. 2019; Wu et al. 2020; Tian et al. 2018; Talebi et al. 2017; Oka et al. 2020

Fluorescence *in situ* hybridization (FISH) and sequencing experiments have shown that hereditary cochlear aplasia is linked to additional *Myo6* copies in genomes (Sun et al. 2020). In contrast *Myo6* haploinsufficiency results in progressive hearing loss (Seki et al. 2021). Mutations resulting in *Myo6* severe truncation (Sampaio-Silva et al. 2018; Wu et al. 2020) or aberrant splicing (Brownstein et al. 2014; Seki et al, 2017) were also found to cause moderate to profound hearing loss or deafness. If most of the point mutations are located either in the Motor domain or in the cargo binding domain, suggesting an impact on the motor activity or proper recruitment through cellular partners binding to the cargo binding domain. Only two of them: the L926Q (Brownstein et al. 2014) and the R928C (Talebi et al. 2017) mutations were identified in the rest of the *Myo6* molecule, and their precise effect on *Myo6* function thus remains to be determined.

A recent study achieves auditory rescue of *Myo6*^{WT/C442Y} mice up to 5 months by reintroducing *Myo6* through *in vivo* CripCas9 assessing the importance of the MYO6 gene in hearing loss and deafness and raising the possibility of a future treatment through gene editing (Xue et al., 2022).

In parallel, a closer look at the Snell's Waltzer mice phenotype reveals symptoms related to *Myo6* in addition to hearing loss suggesting the versatility of *Myo6* motor:

- Fertility problems for male Snell's Waltzer mice (Avraham *et al.* 1995; Zakrzewski, Lenartowska, and Buss 2021)
- Hypertrophic cardiomyopathy (Hegan *et al.* 2015)
- Renal defects and proteinuria (Gotoh *et al.* 2010)

B. Myo6 unique features

Myo6 exhibits a typical organization for a myosin motor with a Motor domain, a Lever arm and a Tail but unique features set Myo6 apart (Figure 13):

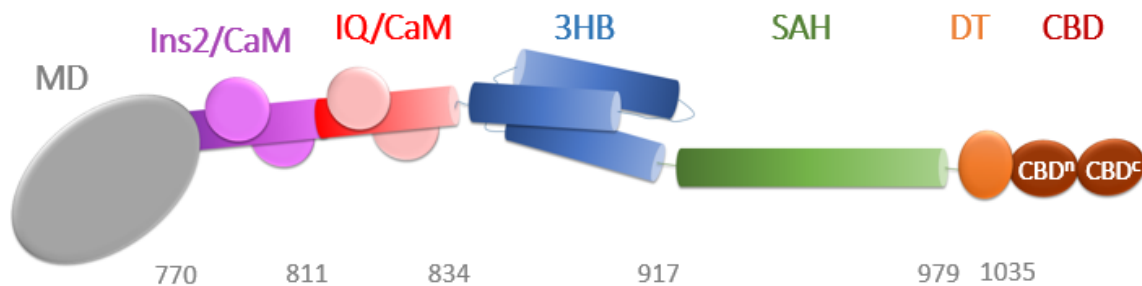


Figure 13: Overall organization of the Myo6 motor

Myo6 organization diagram: From the N-terminus to C-terminus, Myo6 contains a Motor domain (MD) in grey, the Insert-2 (Ins2) in purple bound to a Ca²⁺-CaM in lila, the IQ motif with its associated calmodulin in red, the triple helix bundle (3HB) in blue, the single α -helix (SAH) in green, the distal Tail (DT) in orange and the cargo binding domain (CBD) in brown

B.1. Myo6 head

Sequence analysis shows good conservation of the N-terminus Motor domain typical of a myosin motor (Kellerman *et Miller* 1992). Determination of structures of the Myo6 motor (wild-type or mutants) in six different states of the ATPase cycle allows a deTailed comprehension of the Myo6 cycle making the Myo6 cycle the most well described among myosins (Table 1). This shows that, despite directing its force towards the minus-end of actin filaments and despite the slower ATP binding compared to other myosins, the Motor domain conformational changes along the cycle are very similar with the other myosins (Gurel *et al.* 2017; Ménétrey *et al.* 2005; 2007; 2008; 2012) (Figure 14).

ATPase cycle state	Method	PDB code	Resolution
Pi release (no actin bound)	X-ray diffraction	4PFO, 4PJM, 4PJN, 4PFP, 4PJL,	1.75 Å, 2.05 Å, 2.00 Å, 2.32 Å, 2.10 Å
Strong ADP (actin bound)	Electron microscopy	6BNQ, 6BNW	5.50 Å, 5.50 Å
Rigor (actin bound)	Electron microscopy	6BNP, 6BNV	4.60 Å, 4.60 Å
Rigor-like (no actin bound)	X-ray diffraction	2BKH, 2BKI, 2X51, 3L9I, 4DBP	2.40 Å, 2.90 Å, 2.20 Å, 2.20 Å, 2.20 Å
Post-rigor	X-ray diffraction	2VB6, 2VAS, 4DBQ, 4PJJ	2.30 Å, 2.40 Å, 2.60 Å, 2.40 Å
Intermediate recovery stroke	X-ray diffraction	5O2L	2.20 Å
Pre-powerstroke	X-ray diffraction	2V26, 4ANJ, 4DBR, 4E7S, 4E7Z, 4PK4	1.75 Å, 2.60 Å, 1.95 Å, 2.25 Å, 2.30 Å, 2.78 Å

Table 1: structure of Myo6 Motor in different states of the ATPase cycle

Structures from [Llinas et al. 2015](#); [Gurel et al. 2017](#); [Ménétreay et al. 2005](#); [Pylypenko et al. 2011](#); [2015](#); [Ménétreay et al. 2007](#); [2008](#); [Blanc et al. 2018](#); [Ménétreay et al. 2012](#)

Uniquely, the Myo6 Motor was crystallized in an intermediate state between the post-rigor and the pre-powerstroke characterized by an open switch-II (as for post-rigor) but a relay and a SH1 helix close to the pre-powerstroke conformation and a partially reprimed converter. Structure analysis and molecular dynamics thus offer unique insights on the Myo6 recovery stroke (and probably on the recovery stroke of all myosins). It suggests that the Lever arm repriming is not coupled with switch-II closure (as previously proposed from molecular dynamics), but rather be driven by thermal fluctuations ([Blanc et al. 2018](#)). The Myo6 P_i release state is also particularly well characterized. Indeed, a serie of Myo6 crystals soaked with P_i for different times revealed that Myo6 can adopt a state exhibiting a primed converter (as in the pre-powerstroke) but an actin binding interface and an open switch-II allowing P_i to escape ([Llinas et al. 2015](#)). This state was thus proposed to constitute the P_i release state of Myo6. The different crystals describe different positions of P_i within the Myo6 Motor depending on the time they were soaked in P_i which traces the putative P_i route to escape the Motor. Moreover, deTailed analysis of the structures together with kinetic studies of Myo6 mutants designed to impair the actin binding or cleft closure suggest that P_i release must occur before the cleft closure and Lever arm swing but after a conformational change occurring due to actin binding, offering deTailed insights on the force generation mechanism of Myo6 and possibly other myosin motors ([Llinas et al. 2015](#)) ([Figure 15](#)).

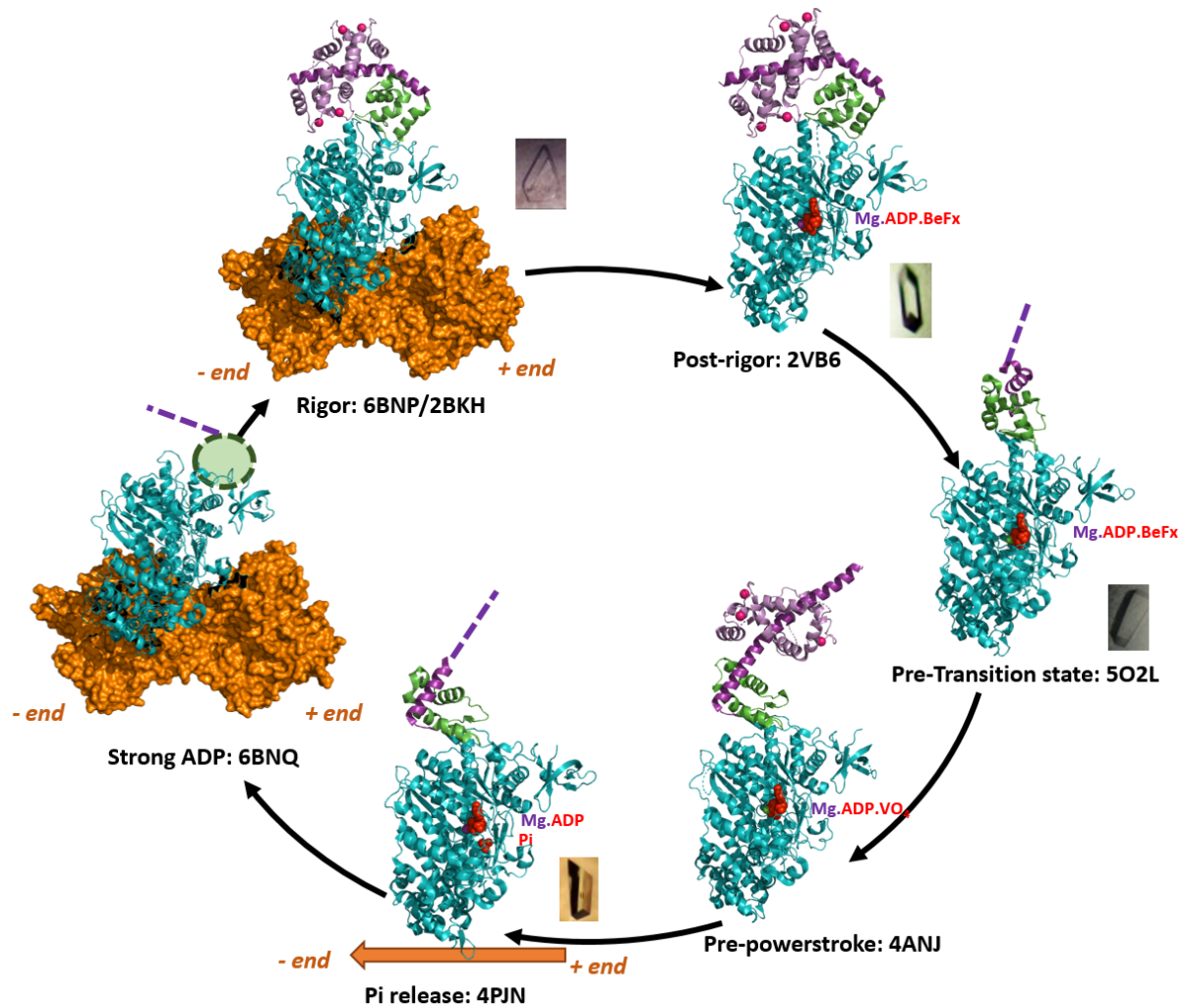


Figure 14: ATPase cycle of Myo6

Motor domain in blue, converter in green, Lever arm in purple, actin in orange. When not present in the experimental structure, putative position of the converter is depicted as a green circle and the putative position of the Insert-2, at the basis of the Lever arm as a purple dotted line. X-ray structures of the P_i release (PDB: 4PJN, [Llinas et al. 2015](#)), the post rigor (PDB: 2VB6, [Ménétrety et al. 2008](#)), the pre-transition state (PDB: 5O2L, [Blanc et al. 2018](#)) and the pre-powerstroke (PDB: 4ANJ, [Ménétrety et al. 2012](#)) are depicted. The electron microscopy structure of the ADP strong state which is incomplete (PDB: 6BNQ, [Gurel et al. 2017](#)) is depicted. The rigor state is obtained here by alignment of the electron microscopy structure of the Myo6 Motor domain bound to actin (PDB: 6BNP, [Gurel et al. 2017](#)) and the rigor-like structure where Myo6 is detached from actin but contains the converter and the Insert-2 (PDB: 2BKH, [Ménétrety et al. 2005](#)).

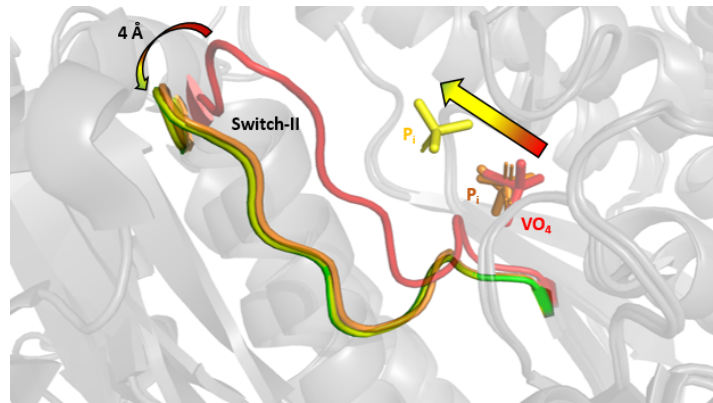


Figure 15: Myo6 P_i release

Superimposition of crystal structures of Myo6 pre-powerstroke (PDB: 2V26, [Ménétreay et al. 2007](#), switch-II and P_i analog: VO_4 are highlighted in red), Myo6 P_i release with short P_i soaking (4PJM, [Llinas et al. 2015](#), switch-II and P_i are highlighted in orange), Myo6 P_i release with very short P_i soaking (4PJN, [Llinas et al. 2015](#), switch-II and P_i are highlighted in yellow) and Myo6 P_i release with no P_i soaking (4PJN, 4PJM, 4PFO, [Llinas et al. 2015](#), switch-II is highlighted in green). From pre-powerstroke to P_i release, switch-II moves from ~ 4 Å opening a back-door and P_i moves out of the active site.

Finally, sequence analysis revealed the presence of a unique 25 amino acid insert within Myo6 Motor domain (residues 316-329 in porcine Myo6) ([Hasson and Mooseker 1994](#)). This so-called “Insert-1” is localized near the actin binding element switch-I ([Ménétreay et al. 2005](#)) and slows down the Myo6 ATP binding rate compared to other myosins by repositioning Leu310 and creating selective steric hindrance for ATP but not ADP binding ([Pylypenko et al. 2011](#)) (Figure 16).

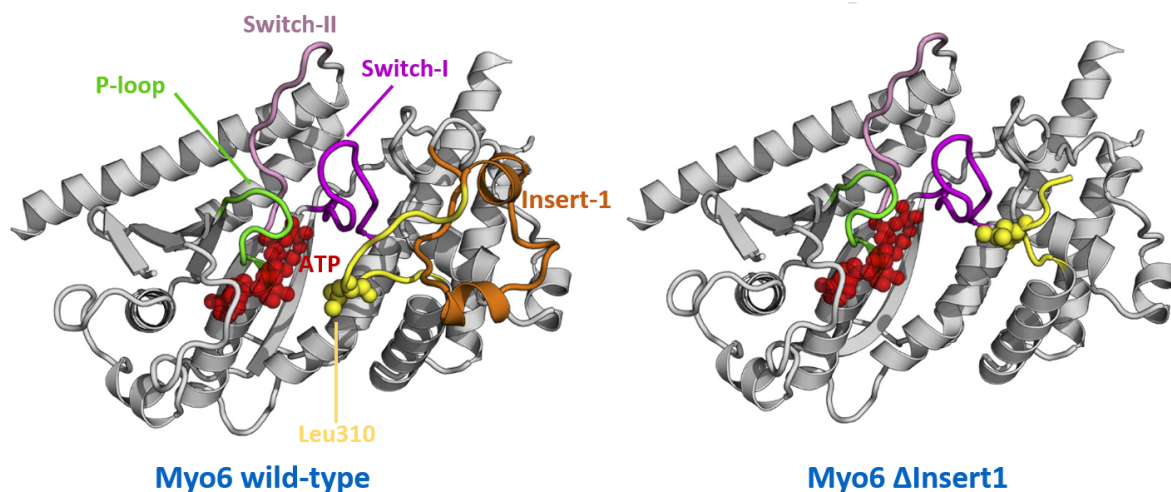


Figure 16: Leu310 hinders ATP binding due to the presence of Insert-1 ([Pylypenko et al. 2011](#))

Myo6 active site with or without Insert-1 in rigor-like state (ATP modeled in X-ray crystallography structures). In wild-type Leu310 is closer to the ATP binding pocket generating hindrance and slowing-down its binding while upon removal of Insert-1, Leu310 moves out of the pocket resulting in faster ATP binding ([Pylypenko et al. 2011](#))

B.2. Myo6 Lever arm

The Myo6 Lever arm was thought to be particularly short as only 1 IQ motif can be found within the Myo6 neck (Kellerman et Miller 1992, Hasson et Mooseker 1994). Yet, uniquely, a ~50 amino acid insert (the Insert-2 or Ins2) distances the IQ from the Motor domain (Hasson and Mooseker 1994) which is unexpected for a myosin motor where the IQ is usually directly connected to the converter. Interestingly, although it does not contain a canonical CaM binding motif (Hasson and Mooseker 1994), it was discovered to be a Ca^{2+} -CaM binding element (Bahloul et al. 2004).

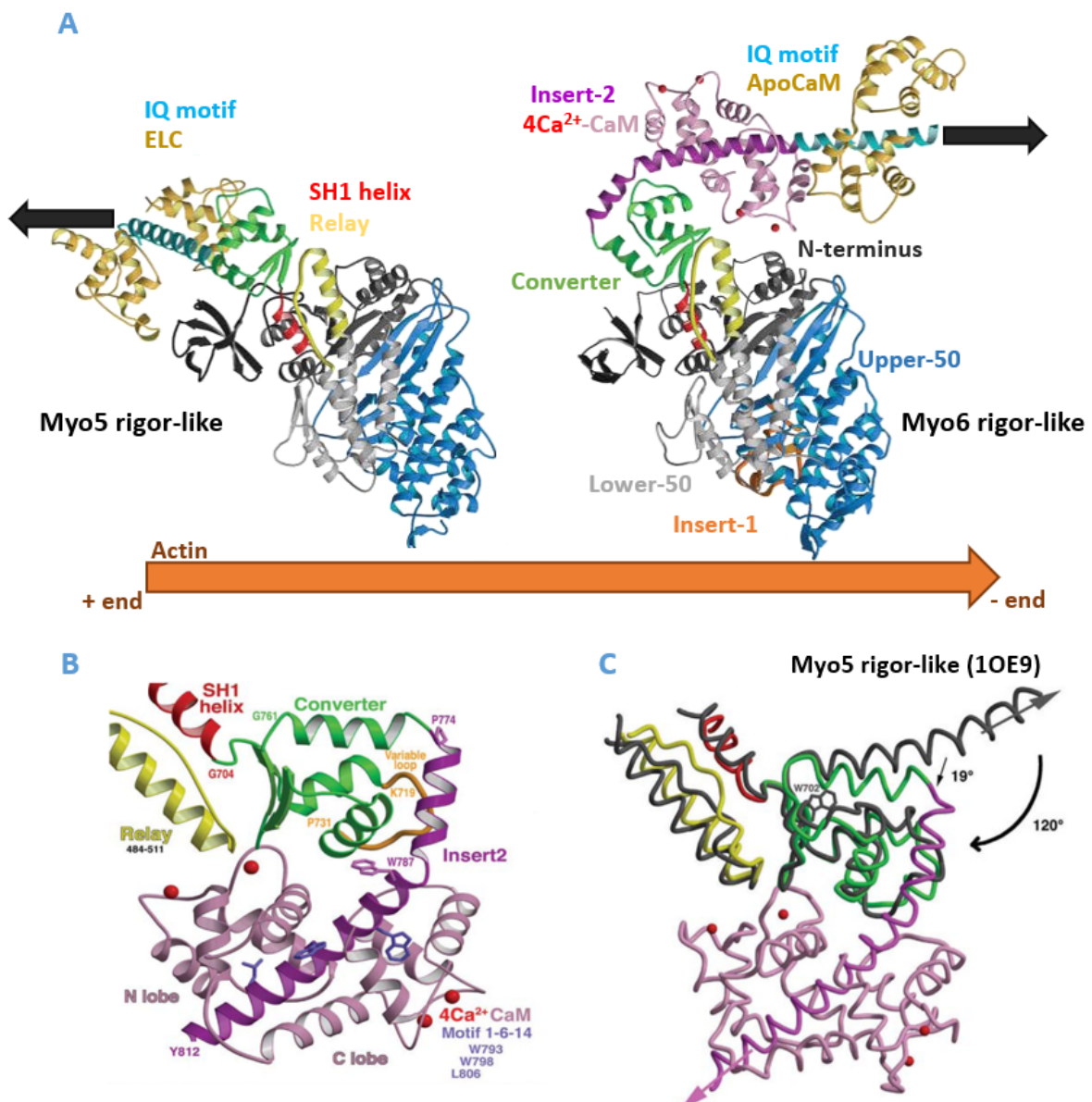


Figure 17: Ins2 reorientates Myo6 converter towards the minus end of actin filament (adapted from Ménétrey et al. 2005).

(A) Model of Myo5 (Coureux et al. 2003) and Myo6 (Ménétrey et al. 2005) on actin filament. Myo5 Lever arm is directed towards the plus end and Myo6 Lever arm toward the minus end due to interaction between converter

(green) and Insert-2 (purple) shifting the Lever arm direction of 120° compared to Myo5 (B) Close up on Myo6 Insert-2/ converter interface. (C) Superimposition of Myo5 and Myo6, Myo5 is in black and Myo6 in colors.

The crystal structure of the Motor domain with Ins2/Ca²⁺-CaM in rigor state confirmed the ability of Ins2 to bind to CaM light chain with four Ca²⁺ ions (Ménétreay *et al.* 2005). Furthermore, this crystal structure revealed that in rigor state, Ins2-CaM complex interacts with the converter resulting in its reorientation of 120° compared to plus-end myosins allowing force generation toward the minus-end of the actin filament (Ménétreay *et al.* 2005) (Figure 17). Consistently, motility assays revealed that the removal of Ins2 or its replacement by a conventional IQ motif makes Myo6 a plus-end directed motor further confirming that this unique Insert-2 is at the origin of the reverse directionality of Myo6 (Park *et al.* 2007; Bryant, Altman, and Spudich 2007).

Then, in 2007, a crystal structure of Myo6 was obtained in the pre-powerstroke state (PDB: 2V26, Ménétreay *et al.* 2007). This structure, which contains the Motor domain, the converter and the first helix of the Insert-2, revealed that Myo6 converter undergoes conformational rearrangements between the pre-powerstroke and the rigor-like state which is unexpected for a myosin motor (Ménétreay *et al.* 2007) (Figure 18).

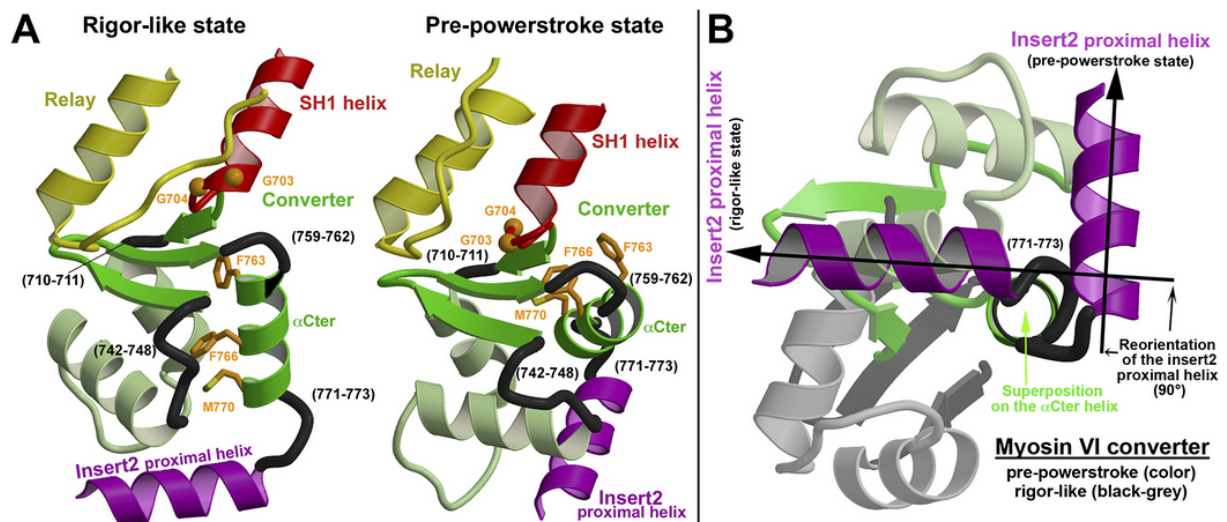


Figure 18: Converter rearrangement between the pre-powerstroke and the rigor-like state reorients Insert-2 (Ménétreay *et al.* 2007)

(A) Comparison of the converter (green) and Insert-2 (purple) position in the rigor like and in the pre-powerstroke state. If the position of the central β -sheet of the converter is rather conserved, the hinges (black) and the helices adopt very different conformations resulting in the repositioning of Insert-2. (B) Superimposition of Myo6 in the rigor-like (black) and pre-powerstroke (color) states highlights the 90° repositioning of the Insert-2 between the two states.

The first helix of the Insert-2 is reorientated by 90° between the two states. As a consequence, Myo6 is able to perform a particularly large stroke compared to other myosins that would not be possible without rearrangement of the converter (Ménétreay *et al.* 2007). Myo6 powerstroke is thus quite unique among myosins as the powerstroke does not only rely on Lever arm swing but also the rearrangements within the converter (Figure 19).

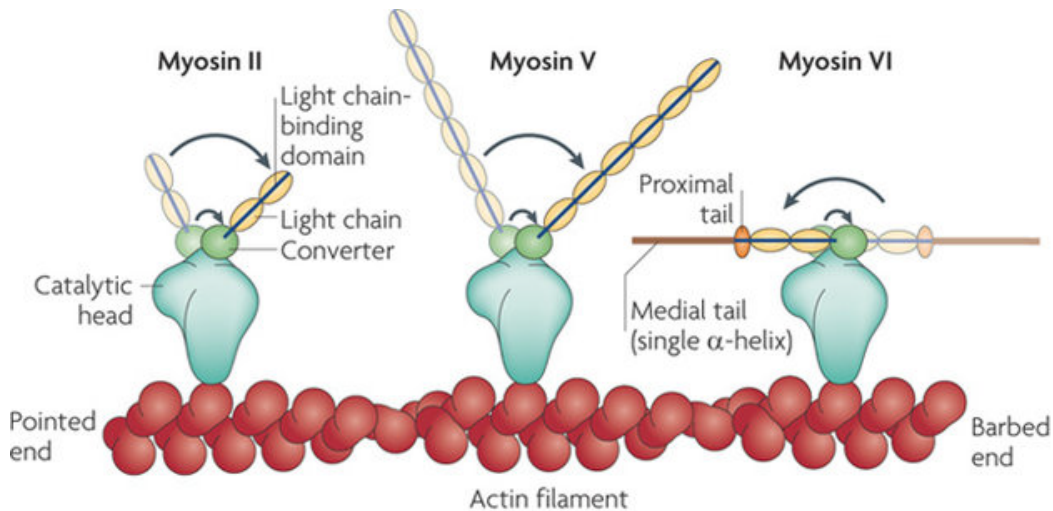


Figure 19: Myo6 can undergoes a particularly large stroke due to converter rearrangement (Spudich and Sivaramakrishnan 2010)

Schematic representation of Myo2, Myo5 and Myo6 strokes with the Motor domain in blue, the converter in green and the neck in dark blue bound to light chains in yellow. Myo6 Tail is depicted in orange and actin is depicted in red. Position of the Lever arm in the pre-powerstroke (before the stroke) and the rigor states (after the stroke) are displayed. Lever arm position in the pre-powerstroke is shown in transparency. Myo2 and Myo5 undergoes a ~70° stroke while Myo6 undergoes a ~180° stroke.

Finally, a crystal structure of the Myo6 Lever arm containing both the Ins2 and IQ motif was obtained in 2009 (3GN4; Mukherjea *et al.* 2009) (Figure 20). Consistently, Ins2 binds to Ca²⁺-CaM while the IQ motif binds to apoCaM (no Ca²⁺ bound to it), (3GN4, Mukherjea *et al.* 2009). However, titration experiments show that the IQ motif is able to bind to CaM at both low and high calcium concentration but with higher affinity at high calcium concentrations. Moreover, a study by electron microscopy suggests that conformational changes occur for the second CaM upon Ca²⁺ binding (Batters *et al.* 2016). Ca²⁺ was thus proposed as a regulatory element of the Myo6 force production.

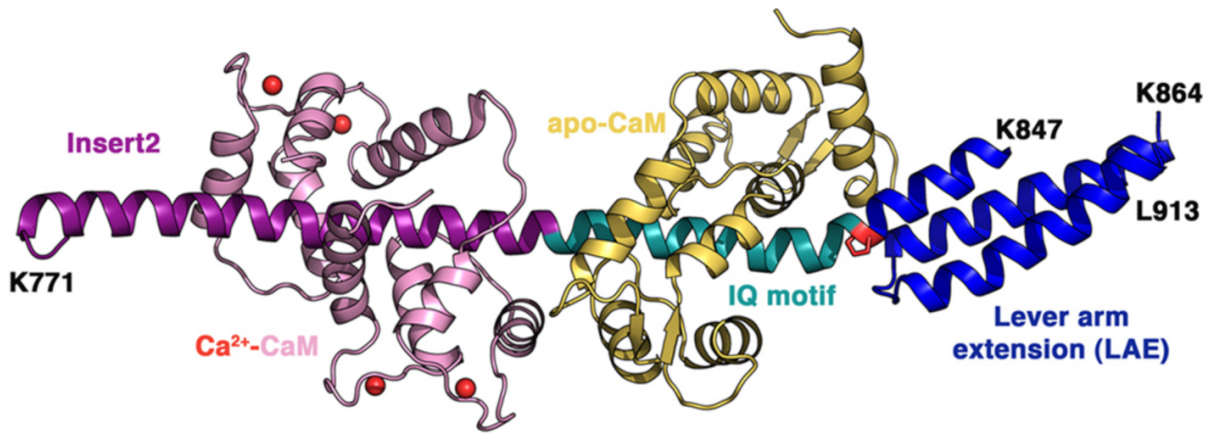


Figure 20: Myo6 Lever arm (Mukherjea *et al.* 2009)

Myo6 Lever arm with *Ins2* in purple bound to Ca^{2+} -CaM in lila and IQ motif in cyan bound to apoCaM. A triple helix bundle (blue) follows the IQ motif and has been proposed to unfold and act as a Lever arm extension (Mukherjea *et al.* 2009) by revealing a new CaM binding site (Mukherjea *et al.* 2009; Batters *et al.* 2016)

B.3. Myo6 Tail

The structure of the proximal region of the Myo6 Tail (aa 834-917) has been described as a **triple helix bundle (3HB)** stabilized by hydrophobic interactions by NMR in isolation (PDB: 2LD3; Yu *et al.* 2012) (Figure 21) and by X-ray crystallography (PDB: 3GN4, Mukherjea *et al.* 2014) in the context of the Lever arm (see above).

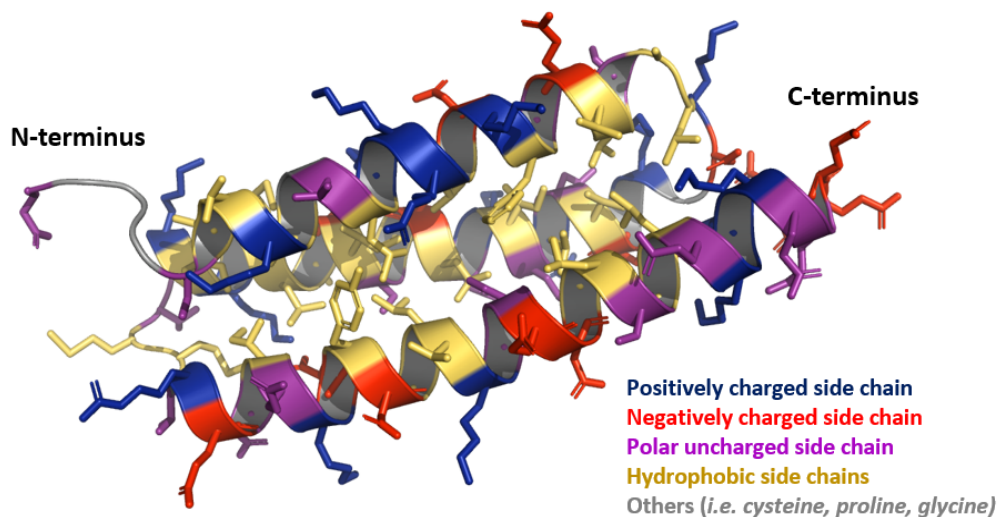


Figure 21: Myo6 triple helix bundle is stabilized by hydrophobic interactions

The NMR structure of the Myo6 3HB (PDB: 2LD3; Yu *et al.* 2012) is similar to the structure solved in the context of the whole Lever arm (PDB: 3GN4, Mukherjea *et al.* 2009). The only difference is that the NMR structure proposes a conformation for the loop region that is disordered in the crystal structure. Residues are coloured depending on their charges: residues with positively charged side chains are in blue, residues with negatively charged side chains

are in red, residues with polar uncharged side chains are in purple and others are in grey. Charged residues are found exposed at the surface of the bundle while hydrophobic residues interact with each other inside the bundle.

Rhodamine fluorescence quenching (Mukherjea *et al.* 2009) and NMR (Yu *et al.* 2012) experiments demonstrated the ability of 3HB to unfold to adopt an extended conformation upon artificial dimerization of Myo6 or DPC micelles addition (respectively), highlighting the putative 3HB role for Myo6 regulation and more specifically as a Lever arm extension. Indeed, Mukherjea *et al.* 2014 and Batters *et al.* 2016 show the ability of residues 834-875 and 833-856 (respectively) positioned at the N-terminus of Myo6 3HB to bind to a CaM supporting the 3HB potential to act as a Lever arm extension following 3HB unfolding. The precise role and composition of this Lever arm extension remains to be clarified. Mukherjea *et al.* 2014 proposed a recruitment of a third CaM in EGTA conditions (specific Ca²⁺ chelator) would allow to extend a linear Lever arm while Batters *et al.* 2016 proposed that the 833-856 region would fold back on the CaM bound to the IQ upon Ca²⁺ addition (pCa 4). Both propositions result in a rigidification of the 3HB N-terminus upon its unfolding (also see section E.6.b).

Following the 3HB, the sequence corresponds to a **single α -helix domain (SAH or medial Tail) (aa917-978)**. Interestingly, a few apolar residues are found within the helix in particular at its N-terminus and around the residue 955 that do not perfectly follow a (i, i+4) distribution (Figure 22). An NMR study of the SAH domain shows that it corresponds to a stiff α -helix with a persistent length of ~200 Å (PDB: 6OBI, Barnes *et al.* 2019).

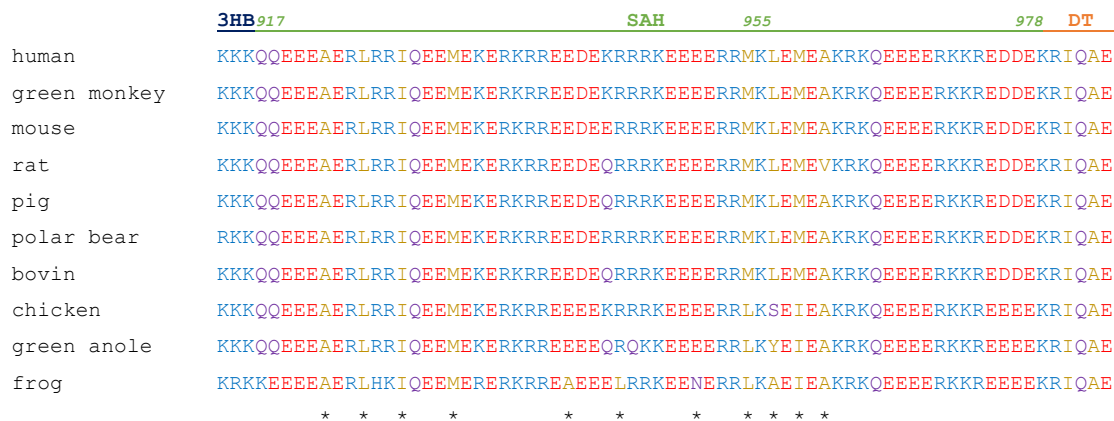


Figure 22: sequence alignment of SAH domain among species

Residues are colored depending on their charges: residues with positively charged side chains are in blue, residues with negatively charged side chains are in red, residues with polar uncharged side chains are in purple. * marks all the hydrophobic residues found within the SAH domain

The distal Tail (979-1034) has been proposed to constitute a domain of 3 nm of diameter when associated to SAH based on a SAXS study (Spink *et al.* 2008). On the basis of a Rosetta prediction,

Spink *et al.* 2008 thus proposed that the DT domain would be constituted by three helices interacting with each other's (Figure 23). However, an NMR study of the 998-1071 fragment reveals that alone the DT domain is a succession of helices with high flexibility (He *et al.*, 2016) (Figure 23). Perhaps the DT domain can be stabilized by other elements of the Tail in the context of FLMyo6, thus further studies are required to conclude on the structure and dynamics of this domain. The DT domain was also shown to bind ubiquitin (MIU domain) through its distal amino acids 998-1031 (Penengo *et al.*, 2006).

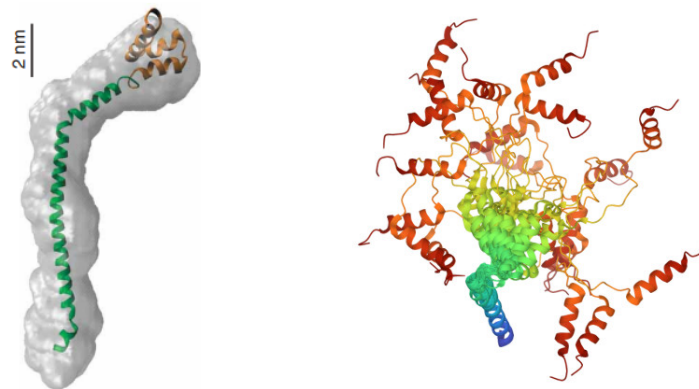


Figure 23: DT domain organization

(Left) SAXS envelope of a Myo6 fragment containing the SAH and the DT domain. Structure of SAH and DT comes from Rosetta prediction. SAH is in green and DT in orange (Spink *et al.* 2008). **(Right)** Top 20 conformers found by NMR for the 998-1071 fragment containing a portion of the DT domain. High variability between the conformers shows a high flexibility of the fragment when purifies alone (PDB: 2N11, Wollscheid *et al.* 2016)

Finally, the Myo6 C-terminus consists in the **cargo binding domain (CBD)** that greatly diverges from other myosin Tails. Alternative splicing of the CBD has been described: a large insert (LI) of either 32 or 23 amino acids can be found between the DT and the CBD and a small insert (SI) of 9 amino acids is found in between two subdomains of the CBD: the CBDⁿ (aa 1069-1146) and the CBD^c (aa 1166-end) (Figure 25 and 26). These different insertions result in the existence of several kinds of Myo6 isoforms:

- Myo6 LI that only contains the long insert
- Myo6 SI that only contains the small insert
- Myo6 LI + SI that contains both inserts
- Myo6 NI that does not contain any insert

Interestingly, transfection of each isoform in MDCK cells shows a differential localization for the Myo6 LI isoform, highlighting the importance of this alternative splicing for Myo6 function determination (Figure 24).

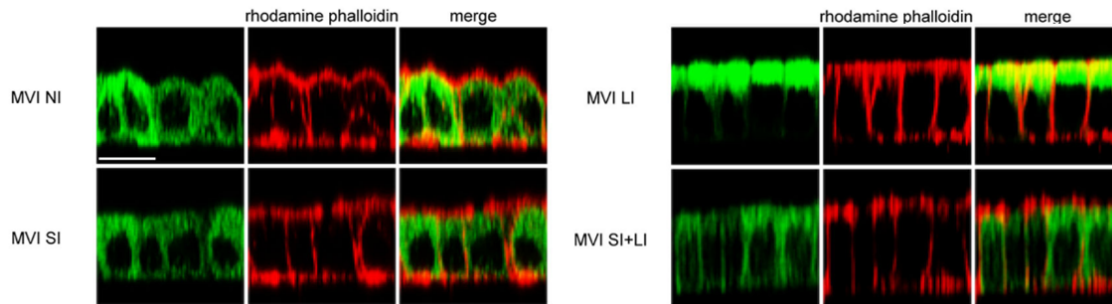


Figure 24: localization of Myo6 isoforms in MDCK cells (adapted from [Au et al. 2007](#))

Location of ^{GFP}Myo6 in MDCK cells of Myo6 isoforms (NI, SI, LI and SI+LI). Myo6 location is plotted in green (left panels) and actin (stained using rhodamine phalloidin) is plotted in red (middle panels). Merged images of Myo6 and actin are pictured in the right panels. Scale bar: 10 μ m.

	MIU	LI	
iso1	QQQAVLEQERRDRELALRIAQSEAELISDEAQADLALRR-----	NDGTRPKMTPEQMAKEMSEFLSRGPAVLATKAAAG	1071
iso2	QQQAVLEQERRDRELALRIAQSEAELISDEAQADLALR-----	-----RGPVLATKAAAG	1048
iso3	QQQAVLEQERRDRELALRIAQSEAELISDEAQADLALRRSLDSYPVSKNDGTRPKMTPEQMAKEMSEFLSRGPAVLATKAAAG		1080
iso4	QQQAVLEQERRDRELALRIAQSEAELISDEAQADLALRRSLDSYPVSKNDGTRPKMTPEQMAKEMSEFLSRGPAVLATKAAAG		1080
iso5	QQQAVLEQERRDRELALRIAQSEAELISDEAQADLALR-----	-----RGPVLATKAAAG	1048
iso6	QQQAVLEQERRDRELALRIAQSEAELISDEAQADLALRRSLDSYPVSKNDGTRPKMTPEQMAKEMSEFLSRGPAVLATKAAAG		1080
	MyUb	SI	
iso1	TKKYDLSKWKYAE LRDTINTSCDIELLAACREEFH RRL KVYHA WKS KN KKR NTETEQRAPKSVTDYDFAPFLNNSPQQNPAAQ		1154
iso2	TKKYDLSKWKYAE LRDTINTSCDIELLAACREEFH RRL KVYHA WKS KN KKR NTETEQRAPKSVTDYDFAPFLNNSPQQNPAAQ		1131
iso3	TKKYDLSKWKYAE LRDTINTSCDIELLAACREEFH RRL KVYHA WKS KN KKR NTETEQRAPKSVTDYDFAPFLNNSPQQNPAAQ		1163
iso4	TKKYDLSKWKYAE LRDTINTSCDIELLAACREEFH RRL KVYHA WKS KN KKR NTETEQRAPKSVTDY-----PQQNPAAQ		1154
iso5	TKKYDLSKWKYAE LRDTINTSCDIELLAACREEFH RRL KVYHA WKS KN KKR NTETEQRAPKSVTDY-----PQQNPAAQ		1122
iso6	TKKYDLSKWKYAE LRDTINTSCDIELLAACREEFH RRL KVYHA WKS KN KKR NTETEQRAPKSVTDY-----AQQPAAQ		1154
iso1	IPARQREIEMNRQORFFRIPFIRPADQYKDPQ SKKKG W W Y AHFDGWPWIARQME LHDPKPPILLVAGKDDMEMCELNLEETGLT		1237
iso2	IPARQREIEMNRQORFFRIPFIRPADQYKDPQ SKKKG W W Y AHFDGWPWIARQME LHDPKPPILLVAGKDDMEMCELNLEETGLT		1214
iso3	IPARQREIEMNRQORFFRIPFIRPADQYKDPQ SKKKG W W Y AHFDGWPWIARQME LHDPKPPILLVAGKDDMEMCELNLEETGLT		1246
iso4	IPARQREIEMNRQORFFRIPFIRPADQYKDPQ SKKKG W W Y AHFDGWPWIARQME LHDPKPPILLVAGKDDMEMCELNLEETGLT		1237
iso5	IPARQREIEMNRQORFFRIPFIRPADQYKDPQ SKKKG W W Y AHFDGWPWIARQME LHDPKPPILLVAGKDDMEMCELNLEETGLT		1205
iso6	IPARQREIEMNRQORFFRIPFIRPADQYKDPQ SKKKG W W Y AHFDGWPWIARQME LHDPKPPILLVAGKDDMEMCELNLEETGLT		1237
iso1	RKR GAEILPRQFEEIWERC GGIQYLQNAIESRQARPTYATAMLQSLK		1285
iso2	RKR GAEILPRQFEEIWERC GGIQYLQNAIESRQARPTYATAMLQSLK		1262
iso3	RKR GAEILPRQFEEIWERC GGIQYLQNAIESRQARPTYATAMLQSLK		1294
iso4	RKR GAEILPRQFEEIWERC GGIQYLQNAIESRQARPTYATAMLQSLK		1285
iso5	RKR GAEILPRQFEEIWERC GGIQYLQNAIESRQARPTYATAMLQSLK		1253
iso6	RKR GAEILPRQFEEIWERC GGIQYLQNAIESRQARPTYATAMLQSLK		1285

Figure 25: sequence alignment of human Myo6 Tail (998-end) isoforms

All the six isoforms found in the UNIPROT databank for human Myo6 are aligned. Inserts are highlighted in green and the different sequence/domains reported to mediate interaction with partners are highlighted in colors.

The CBD can interact with a variety of cargos through different binding sites: two sequence motifs: the RRL motif within the CBDⁿ and the WWY motif within the CBD^c have been identified as critical for Myo6 interaction with various proteins, while the WKSKNKKR motif has been proposed to constitute a lipid binding site (Spudich *et al.* 2007). An ubiquitin binding site (MyUb) has also been identified close to the RRL motif. It exhibits higher affinity for ubiquitin than the MIU (He *et al.* 2016). The CBD^c TRTK and SKKK motif have been proposed to participate in DNA binding (Fili *et al.* 2017). Finally, a clathrin interaction binding site overlaps with the RRL motif and requires the LI insert (Biancospino *et al.* 2019).

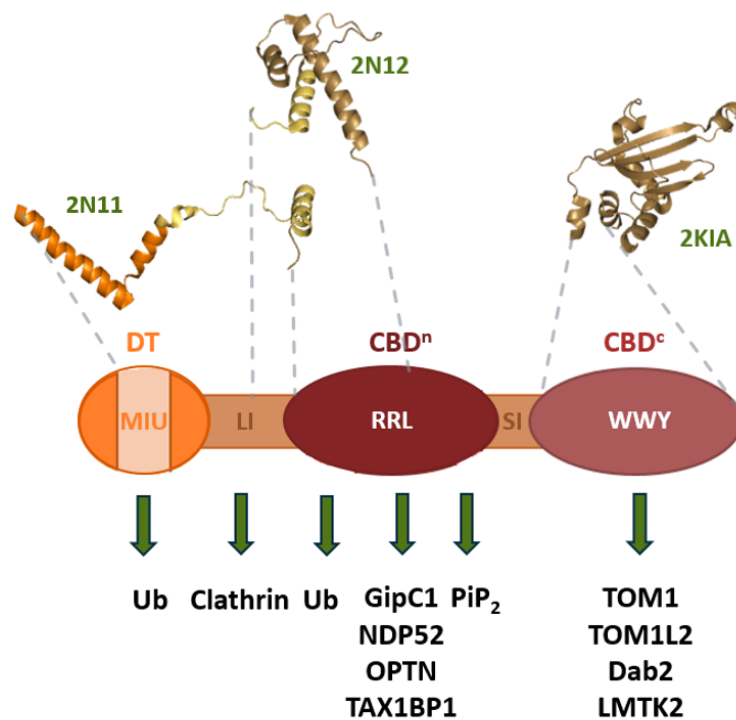


Figure 26: Distal Tail and Cargo binding domain, key platforms for Myo6 recruitment

Diagram representing the different domains of the most distal part of the Myo6 Tail. The distal Tail, that contains the ubiquitin binding motif (MIU) (Penengo *et al.* 2006) is depicted in orange. The cargo binding domain (CBD) is pictured in brown, it contains the CBDⁿ that mediates binding (from the N-terminus to the C-terminus) to ubiquitin through its MyUb domain (He *et al.* 2016), to several protein partners such as GIPC1 through its RRL motif and to the PiP₂ lipid through its WKSKNKKR motif (Spudich *et al.* 2007). The CBD also contains CBD^c that can mediate interactions with partners such as Dab2 and TOM1 through its WWY motif and to DNA through its SKKK and TRTK motifs. CBDⁿ and CBD^c can be separated by a small insert (SI) in certain spliced isoforms and a long insert (LI) can be found between the distal Tail and the CBDⁿ in certain spliced isoforms and can mediate interaction with clathrin (Biancospino *et al.* 2019). Although no structure containing the whole CBD domain is currently available, structures of several fragments were solved by NMR (Yu *et al.* 2009; Wollscheid *et al.* 2016). The structures available are depicted above the diagram with their corresponding PDB code.

Several NMR structures described portions of the cargo binding domain. Yet, up to date, no structure of the complete cargo-binding domain has been described (Figure 26). Thus, parts of the CBDⁿ structure remains unresolved, probably due to the difficulty in purifying a stable CBD construct (Shang *et al.* 2017; Yu *et al.* 2009; Spudich *et al.* 2007). Moreover, it is unknown from the literature if CBDⁿ and CBD^c interact with each other in a folded domain or if it consists in two independent Myo6 domains.

C. Wide range of cell partners links Myo6 to various functions and diseases

Through the various interaction sites within the CBD and the DT, Myo6 has the ability to interact with a wide range of proteins and even with lipids (Spudich *et al.* 2007) and DNA (Fili *et al.* 2017)). O’Loughlin, Masters, and Buss (2018) used proteomics to provide a map of the wide Myo6 interactome (Figure 27). These partners were for several of them already characterized as key in many cellular processes and diseases (Qiu *et al.* 2022; Ogbu *et al.* 2021; Viret, Rozières, and Faure 2018; Katoh 2013). This emphasizes the potential of Myo6 as a multifunctional motor.

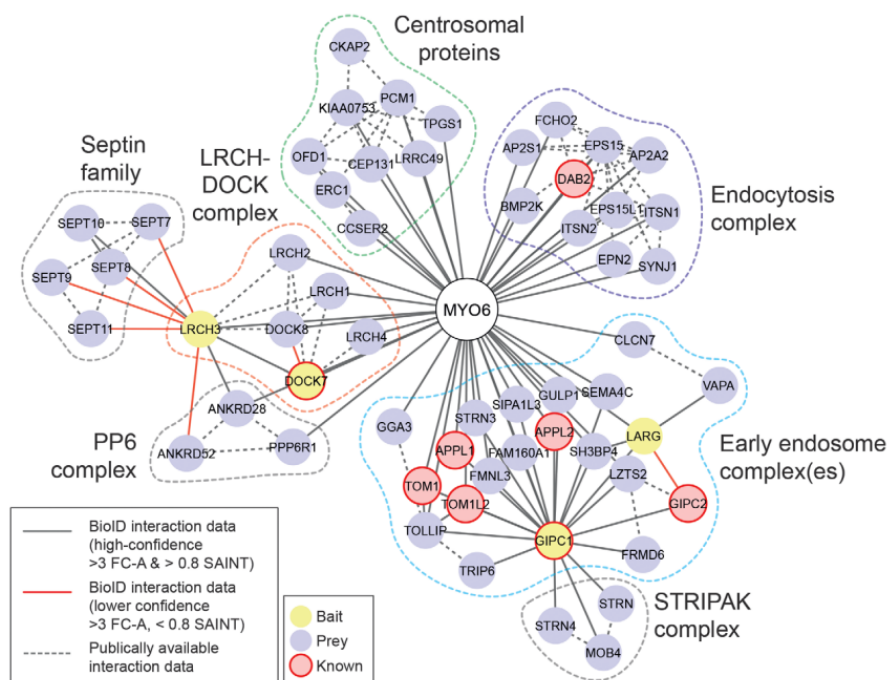


Figure 27: Diagram of Myo6 interactome (O’Loughlin, Masters, and Buss 2018)

Diagram of Myo6 interaction network identified by BioID. Myo6 (white circle) is represented in the middle of the diagram. Partners are gathered in groups according to their subcellular locations. GIPC1, LARG, DOCK7 and LRCH3, that were used as baits in secondary BioID screens in O’Loughlin, Masters, and Buss (2018) study, are represented in yellow. Interactions identified by BioID are represented with a solid line. The diagram was completed with the interactions (represented through dashed lines) reported in the literature prior to the O’Loughlin, Masters, and Buss (2018) study.

C.1. WWY partners

C.1.a. Dab2

Dab2 is present on clathrin-coated structures at the plasma membrane and can interact with cell surface receptors as well as many proteins (AP2 (Mishra *et al.* 2002), ITSN1 (Teckchandani *et al.* 2012), EPS15 (Teckchandani *et al.* 2012) and FCHO2 (Mulkearns and Cooper 2012)). These are involved in clathrin endocytosis and were also found to interact with Myo6 through *in situ* proximity labelling (O'Loughlin, Masters, and Buss 2018). Dab2 interacts with Myo6 through the WWY motif (Inoue *et al.* 2002)(Table 2) and thus mediates Myo6 recruitment to clathrin coated structures suggesting a role of the complex in the transport of vesicles along the actin cytoskeleton (Spudich *et al.* 2007; Morris *et al.* 2002). The crystal structure of Dab2 in complex with the Myo6 CBD^c provides a detailed description of the interaction surfaces showing that Dab2 interacts with Myo6 through two interfaces and confirming the role of the WWY motif (Yu *et al.* 2009) (Figure 28) (also see section G.1.).

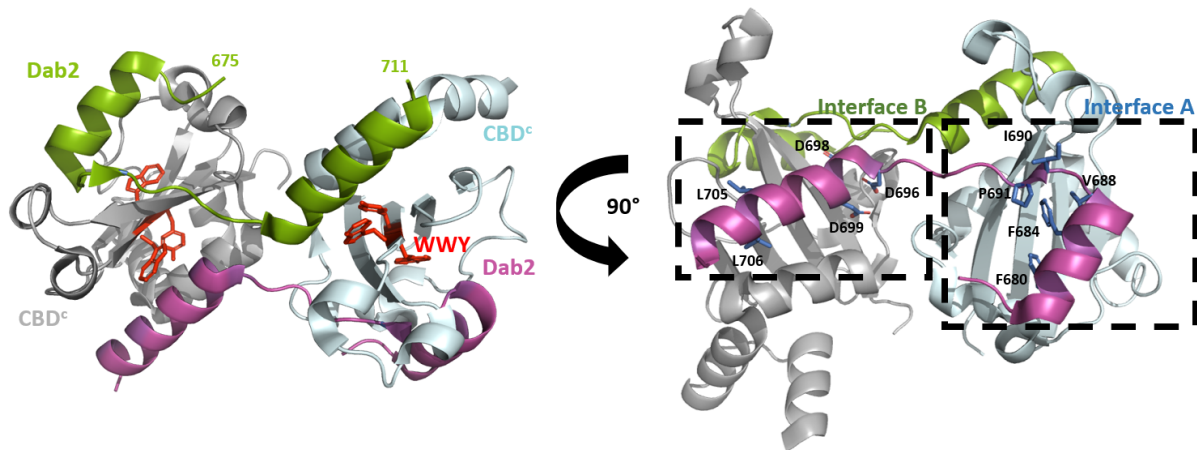


Figure 28: Dab2 fragment 675-711 form a 2:2 complex with Myo6 CBD^c

*Crystal structure of the Dab2 (675-711) - CBD^c complex (PDB: 3H8D, Yu *et al.* 2009). Dab2 interaction with Myo6 involved the WWY motif. Myo6 and Dab2 interacts together through two interfaces thanks to whom Dab2 can mediate indirectly Myo6 CBD^c dimerization.*

Mutation of the WWY motif results in loss of Dab2 localization on clathrin coated structures (O'Loughlin, Masters, and Buss 2018). Yet the integrity of the WWY motif is not required for the localization of the Myo6 LI isoform on clathrin coated structures (Wollscheid *et al.* 2016). Finally, Dab2 was described as a tumor suppressor (see section D.6.).

Publication	K _D	Dab2 construct	Myo6 construct	Technic used
Yu et al. 2009	50 nM 54 nM 80 nM 420 nM	450-768 -rat 627-768 – rat 675-713 – rat 675-695 - rat	CBD ^c - mouse (1137-end)	ITC 25°C in 50 mM (pH 6.5) phosphate buffer
Fili et al. 2020	3.5 μM (vs LI) 11.6 uM (vs NI)	650-end - human	IQ-end NI or LI - human (814-end)	FRET 25°C in 50 mM Tris·HCl (pH 7.5), 150 mM NaCl and 1 mM DTT
Rai et al. 2021	184 nM	675-713 - human	MIU-CBD LI/SI - human (991-end)	FRET 20 mM Imidazole (pH 7.5), 25 mM KCl, 4 mM MgCl ₂ , 1 mM EGTA, 1 mM DTT

Table 2: Dab2-Myo6 affinity reported in the literature

C.1.b. LMTK2

Lemur Tyrosine Kinase 2 (LMTK2) is an ubiquitous transmembrane serine/threonine kinase ([Wang et Brautigam 2002](#)) that was found to mostly localize near the Golgi complex ([Kesavapany et al. 2003](#)). It is notably involved in endocytosis trafficking and apoptosis and is linked to diseases such as neurodegenerescence, infertility and cancers ([Cruz, Farinha, and Swiatecka-Urban 2019](#)). LMTK2 was identified as a Myo6 binding partner through a yeast 2-hybrid screen and a GST-pull-down. This shows that LMTK2 binds Myo6 through its C-terminus cytoplasmic domain. Furthermore, mammalian 2-hybrid using Myo6 mutants show that LMTK2 is a WWY motif binder ([Chibalina et al. 2007](#)). They were also found to co-localize and co-precipitate together from HeLa cells. Like Myo6, LMTK2 localizes on Rab5 positive early endosomes ([Chibalina et al. 2007](#)). But as opposed to Myo6, LMTK2 does not seem to play a key role in secretory pathways as SEAP secretion is impaired by Myo6 knockdown but not by LMTK2 knockdown ([Chibalina et al. 2007](#)). Both Myo6 and LMTK2 knockdown result in formation of abnormal large endosome structures, impairment of transferrin receptor recycling in perinuclear recycling vesicles from early endosomes ([Inoue et al. 2008; Chibalina et al. 2007](#)).

C.1.c. TOM1 and TOM1L2

The target of Myb1 (TOM1) and TOM1-like2 (TOM1-L2) proteins are early members of the Endosomal Sorting Complexes Required for Transport (ESCRT), which are required for degradation of ubiquitynilated cargos. TOM1 and TOM1-L2 are able to interact with clathrin ([Seet and Hong 2005; Katoh et al. 2006](#)) and ubiquitinilated cargos ([Yamakami, Yoshimori, and Yokosawa 2003; Katoh et al. 2006](#)). TOM1 binds also endofin, mediating clathrin recruitment to endosomes ([Seet and Hong 2005](#)). TOM1 interaction with Tollip results in a loss of the interaction of Tollip with phosphatidylinositol-3-phosphate ([Xiao et al. 2015](#)), so that is is ready to bind cargos ([Mitra et al. 2013](#)). TOM1 has also been identified as a binding partner of phosphatidylinositol 5 phosphate (PI5P), which is implicated in the

endosomal sorting of the epidermal growth factor receptor (EGFR). Its recruitment by TOM1 induces a delay in EGFR degradation and fluid-phase bulk endocytosis. The more PI5P is concentrated in the membrane, the slower is the endosomal maturation (Boal *et al.* 2015).

TOM1 and TOM1-L2 were found to be Myo6 partners (Table 3) based on pull-down and mammalian 2-hybrid experiments. Use of different truncation and mutagenesis shows that TOM1 interact with the Myo6 WWY site within its last 107 amino acids (Tumbarello *et al.* 2012). Recently, the crystal structure of the CBD^c and a small helix of TOM1 was solved offering a precise description of the binding interface (Hu *et al.* 2019) (Figure 29).

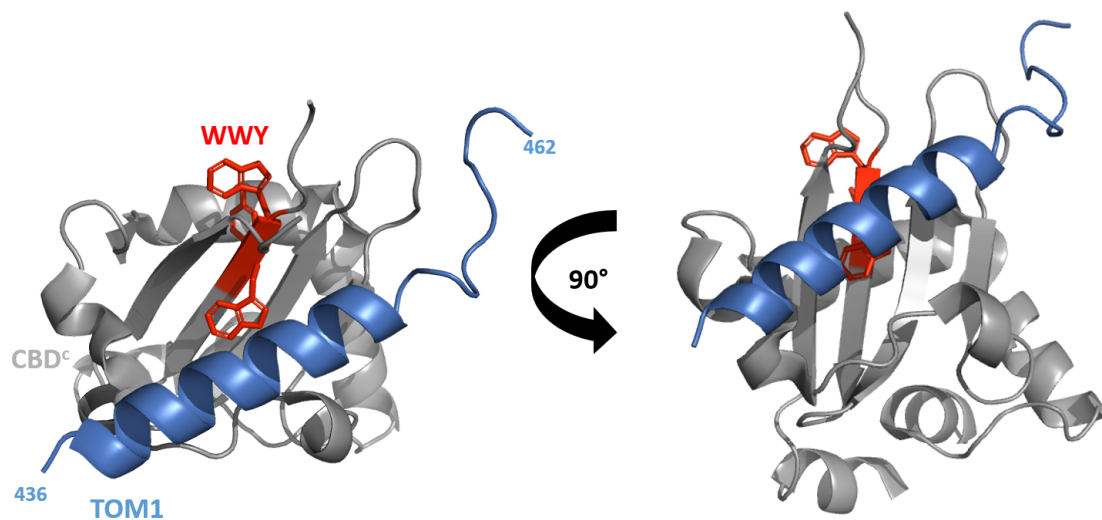


Figure 29: TOM1 fragment 436-462 form a 1:1 complex with Myo6 CBD^c

*Crystal structure of the TOM1 (436-462 – numbering according to human TOM1 canonical isoform) - CBD^c complex (PDB 6J56, Hu *et al.* 2019). Dab2 interaction with Myo6 involved the WWY motif. Contrary to Dab2, TOM1 interacts with Myo6 CBD^c via a unique interface resulting in the formation of a 1:1 complex.*

TOM1-L2 was found to colocalize with Myo6 on tubulobulbar complex and APPL1/Rab5 positive endosomes during spermatid maturation and Myo6 depletion results in loss of TOM1-L2 localization on these specialized structures although the function of the Myo6-TOM1-L2 complex is unclear (Zakrzewski *et al.* 2020). Interestingly, TOM1 depletion in RPE cells mimics the Myo6 depletion phenotype on autophagy: it delays autophagosome fusion with lysosomes for their degradation (Tumbarello *et al.* 2012), suggesting a common role for autophagy regulation, notably through correct addressing of Myo6 to endosomes by TOM1, as TOM1 depletion results in loss of Myo6 localization to endosomes (Tumbarello *et al.* 2012). Furthermore, TOM1 silencing, similarly to Myo6 silencing, results on the accumulation of Rab5 endosomes on nuclear periphery on HeLa cells suggesting that the spatial organization of endosomes depends on TOM1-Myo6 interaction (Master *et al.* 2017).

Publication	K _d	TOM1 construct	Myo6 construct	Technic used
Hu et al. 2019	2.13 ± 0.12 μM 0.93 ± 0.09 μM 0.76 ± 0.04 μM 0.76 ± 0.04 μM 0.67 ± 0.03 μM	215-493 – human iso2 392-493 – human iso2 392-463 – human iso2 437-493 – human iso2 437-463 – human iso2	1157-1285(CBD ^c short LI SI isoform numerotation, human)	ITC 25 °C in 20 mM Tris (pH 7.9), 100 mM NaCl, and 1 mM DTT

Table 3: TOM1-Myo6 affinity reported in the literature

Moreover, TOM1 play a key role in amyloid-β clearance. In Alzheimer disease, amyloid-β neurotoxic accumulation in dystrophic neurites causes memory loss ([Gwon et al. 2018](#)). Thereby, TOM1 knockdown from sick mice result in an aggravation of Alzheimer disease but was rescued by increase in TOM1 expression ([Martini et al. 2019](#)). Although the importance of the Myo6-TOM1 complex has not been clearly established in this context, Myo6 was found to colocalize with TOM1 in dystrophic neurites suggesting a role of the motor for amyloid-β trafficking ([Makioka et al. 2016](#); [Feuillette et al. 2010](#)).

C.2. RRL partners

C.2.a. GIPC

The GIPC family consists in an ensemble of highly conserved proteins GIPC1, GIPC2 and GIPC3. GIPC contributes to the endocytosis process by facilitating the formation of clathrin coated pits and ligand clustering in these pits ([Hasson 2003](#)). It is also involved in receptor recycling, signaling, angiogenesis and cytokinesis ([Katoh 2013](#)). Through its PDZ domain, GIPC1 can interact with a wide variety of proteins including transmembrane proteins like TGFβR3 (transforming growth factorβ receptor type III) signaling proteins like RGS19 (regulator of G-protein signaling 19) and even viral proteins like HPV-18 E6 (human papillomavirus type 18 protein E6 ([Katoh 2013](#))). GIPC1 has also been described as a therapeutical target in cancers (see section D.6.).

Yeast 2-hybrid assays first show that GIPC1 can interact with Myo6 ([Bunn, Jensen, and Reed 1999](#)). The crystal structure between CBDⁿ and GIPC1 and GIPC2 confirmed GIPC as a Myo6 partner that binds through the Myo6 RRL motif and provided a deTailed description of the complex as an oligomer ([Shang et al. 2017](#)) ([Figure 30](#)), although this oligomerization capacity is controversial (see section G.1.).

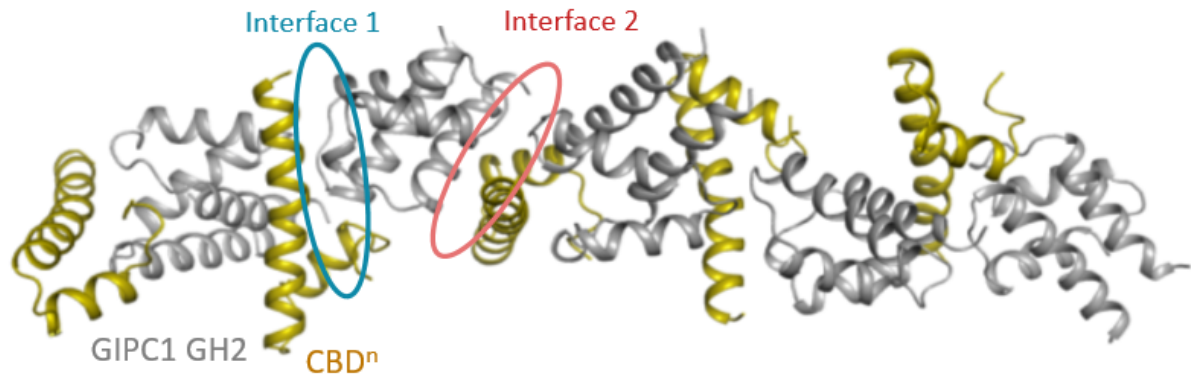


Figure 30: GIPC1 GH2 domain forms long oligomers when bound to the CBDⁿ fragment

Crystal structure of the GIPC1 – CBDⁿ complex (PDB 5V6E, Shang et al. 2017). GIPC1 and CBDⁿ form oligomers through two interfaces

GIPC1 colocalizes with Myo6 on endocytic uncoated vesicles and APPL1-positive endosomes in several cell lines (NRK, ARPE-19 and COS-7 cells) (Dance et al. 2004), supporting a role in endocytosis. Moreover, GIPC1 can also form a ternary complex with Myo6 and LARG, an actin network regulator, thus GIPC1 could play a role in endocytosis and actin organization when associated with Myo6 (O’Loughlin, Masters, and Buss 2018). As GIPC1 is able to localize on uncoated vesicles in Snell’s Waltzer Myo6-null mice kidney cells, Myo6 is not required for GIPC1 localization on uncoated vesicles (Naccache, Hasson, and Horowitz 2006), perhaps thanks to direct interaction between APPL1 and GIPC1 PDZ domain. Indeed, transfection of a GIPC1 construct lacking the GIPC1 PDZ domain failed to colocalize with uncoated vesicles (Naccache, Hasson, and Horowitz 2006) and interestingly failed to coprecipitate with Myo6 even if the Myo6 binding domain is present (Naccache, Hasson, and Horowitz 2006). These results suggest that GIPC1 localization on APPL1 positive endosomes/vesicles is required for its binding to Myo6.

C.2.b. Autophagy receptors: Optineurin, NDP52 and TAX1BP1

Optineurin (OPTN, Sahlender et al. 2005), nuclear dot protein 52 (NDP52, Morriswood et al. 2007, Table 4) and Tax1-binding protein 1 (TAX1BP1, Morriswood et al. 2007, Table 5) were all found to interact with Myo6 using a yeast 2-hybrid screen although affinity with TAXBP1 was later found to be rather low in ITC (~30 μM, Hu et al. 2018). They all contain a zinc finger domain that was shown to mediate interaction with Myo6 in the case of TAX1BP1 through an NMR study (Hu et al. 2018).

Optineurin (OPTN) has been described as a key protein in Golgi organization and vesicle trafficking (Ryan and Tumbarello 2018; Sahlender et al. 2005) and OPTN mutations are associated with glaucoma and amyotrophic lateral sclerosis (Swarup and Sayyad 2018).

Through their interaction with LC3 and ubiquitinated cargos, these proteins were described as autophagy receptors (Qiu *et al.* 2022; J. White *et al.* 2022; Viret, Rozières, and Faure 2018) and were found to colocalize with Myo6 on autophagosomes suggesting a collaboration between these proteins in autophagy (Tumbarello *et al.* 2012; 2015).

In addition to a cooperation with Myo6 in autophagy, NDP52 was also shown to interact with Myo6 in the nucleus to modulate RNA polymerase II (RNAPII) transcription (Fili *et al.* 2017). NDP52 seems to interact with RNAPII as it partially colocalizes with it in dots and co immunoprecipitates with it (HeLa cells). Moreover, using a HeLaScribe extract, transcription levels have been shown to decrease by ~50% upon NDP52 depletion (Fili *et al.* 2017).

Publication	K _D	NDP52 construct	Myo6 construct	Technic used
Fili <i>et al.</i> 2017	NI => 3.2 ± 1.2 μM ARL => 4.6 ± 1.2 μM RAL => 55 ± 23 μM RRA => 21 ± 11 μM LI => 9.8 ± 4.3 μM	Alexa555-FLNDP52	FITC-IQ-end – human (814-end)	FRET 25°C in 50 mM Tris (pH 7.5), 150 mM NaCl and 1 mM DTT

Table 4: NDP52-Myo6 affinity reported in the literature

Publication	K _D	TAX1BP1 construct	Myo6 construct	Technic used
Hu <i>et al.</i> 2018	93.9 ± 10.8 μM 30.7 ± 1.2 μM 90.0 ± 11.4 μM	725-789 - UBZ1+2-human 754-789 – UBZ2 human 725-753 – UBZ1 - human	R1036-T1135 LI-CBD ⁿ human L1073-K1119 ^{short Nter} CBD ⁿ human	ITC 25°C in 20 mM Tris (pH 7.5), 100 mM NaCl and 1 mM DTT

Table 5: TAX1BP1-Myo6 affinity reported in the literature

C.2.c. DOCK7 and the guanine nucleotide exchange factors DOCK180 family

DOCK180 activates Rho GTPases by catalyzing their binding to GTP (Côté and Vuori 2002). DOCK7 can be mainly found in nervous system where it regulates Schwann cell migration, myelination (Yamauchi *et al.* 2008) and neurite outgrowth (Watabe-Uchida *et al.* 2006). DOCK7 was first described as a partner of Myo6 in neural cells PC12 (Majewski *et al.* 2012). It was then further established that this interaction occurs through the RRL motif of Myo6 and is also important for neurite outgrowth (Sobczak *et al.* 2016).

The DOCK180 family has also been involved in cytoskeleton remodeling. Interestingly, DOCK7 has been shown to interact with Rac1 and CDC42, two key regulators of the actin network (Zhou *et al.* 2013). Strikingly, it was proposed that DOCK7 forms a complex with LRCH3 and Myo6 (DISP complex) that could result in a strong remodeling of the septin cytoskeleton as coexpression of LRCH3 and DOCK7 results in a dramatic increase in septin structures in cells (O’Loughlin, Masters, and Buss 2018).

C.3. OFD1

Oral-facial-digital syndrome 1 (OFD1) is specifically localized at centriole and centriolar satellites in cells (Magistrati *et al.* 2022) where it regulates centriole elongation and promotes the recruitment of distal appendage proteins (Singla *et al.* 2010; Wang *et al.* 2018). Its defect results in facial, oral and digital malformations as well as brain malformation and polycystic kidney disease in some cases (Ko *et al.* 2022).

Immunofluorescence and proximity ligation assays show that OFD1 colocalizes with Myo6 on centriole constituting a link between Myo6 and the microtubule cytoskeleton. Immunoprecipitation and pull down further confirm that OFD1 and Myo6 can interact together independently of the Myo6 isoform. Pull-down using point mutants and/or truncations demonstrate that the OFD1 coiled coil interacts with the Myo6 Tail; CBD^c seems critical for its binding as its truncation results in loss of OFD1 binding although usual WWY motif mutation WLY does not impact its binding. Notably, CBD^c seems to need to collaborate with more proximal regions of the Tail for optimal binding (Magistrati *et al.* 2022) which emphasizes the importance to obtain structures with larger Tail fragment to understand how different parts of the Tail can collaborate together for optimal binding of partners.

C.4. Clathrin

Clathrin is a key component of clathrin-mediated endocytosis where it assembles in polyhedral cages to shape vesicular and tubular carriers (Wood and Smith 2021) (Figure 31).

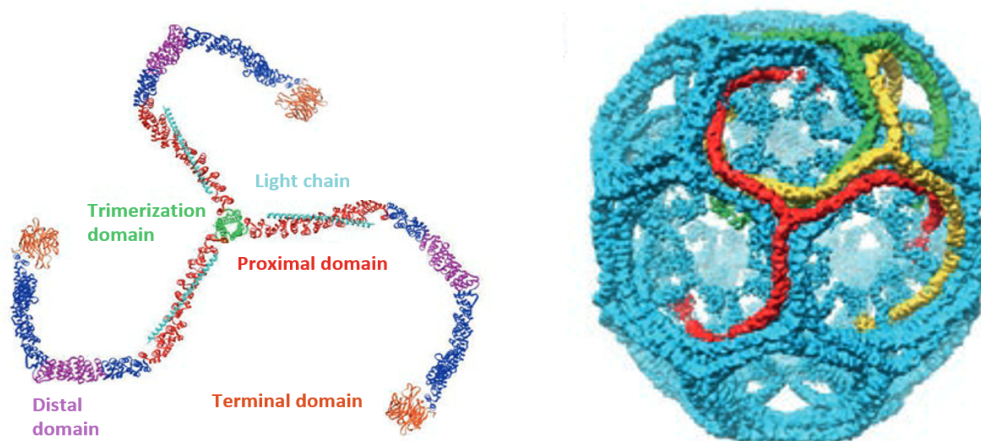


Figure 31: Clathrin organization (Haleblian, Morris, and Smith 2017)

*Left: Structure of a clathrin triskelion from cryoEM model (PDB: 3IYV, Fotin *et al.* 2004). Right: CryoEM map of a clathrin cage with triskelions pictured in red, blue and yellow (PDB: 3IYV, Fotin *et al.* 2004)*

Clathrin was first found to colocalize with Myo6 LI isoform in polarized CACO-2 cells on clathrin coated vesicles (Buss *et al.* 2001). Biancospino *et al.* (2019) have shown that Myo6 LI directly binds to residues 46-61 of the clathrin light chain α , CLCa₄₆₋₆₁ by GST pull-down, ITC, immunoprecipitation and co sedimentation. The NMR structure of the complex reveals key contacts between Myo6 and CLCa. The authors notably identified mutants that could impair this interaction: M1058E, Y1121A and W1124E in Myo6 and I54D in CLCa (Biancospino *et al.* 2019) (Figure 32). Clathrin is thus uniquely a Myo6 LI specific partner. This specificity may explain the unique localization of the Myo6 LI in polarized cells on clathrin coated vesicles near the plasma membrane.

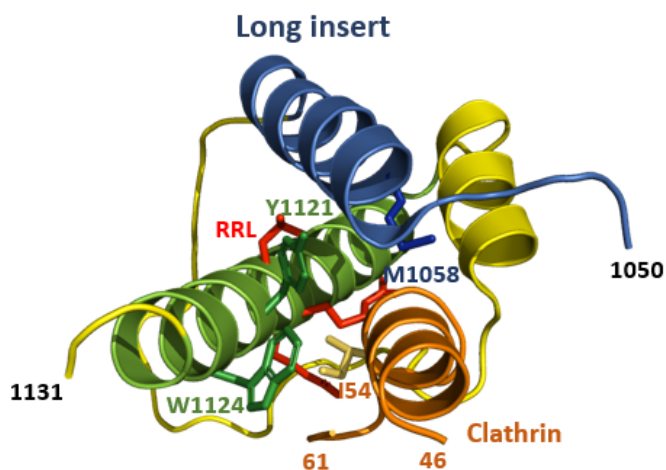


Figure 32: CLCa fragment bound to CBDⁿ fragment

*NMR structure of the CLCa (46-61) – CBDⁿ (1050-1131) complex (PDB 6E5N, Biancospino *et al.* 2019). Clathrin bound with Myo6 through two helices: the helix G1080-R1131 (green) which is also involved in interaction with partners of Myo6 RRL motif and the last helix of the long insert (blue) making its binding isoform specific.*

Of note, Myo6 cannot interact with clathrin light chain b (CLCb) which may suggest different functions for CLCa and CLCb. Indeed, although both are involved in clathrin mediated endocytosis, CLCa is preferentially involved in cell spreading and migration (Tsygankova and Keen 2019). CLCb exhibits 40% sequence identity with CLCa and is expressed at various levels depending on the tissues as opposed to CLCa which is ubiquitously expressed. CLCb overexpression in lung cancer causes aberrant growth factor signaling (Chen *et al.* 2017).

C.5. Ubiquitin

Ubiquitin is a highly conserved protein involved in signaling and degradation pathways. Ubiquitin can form polyubiquitin chains and can covalently bind to proteins and form long ubiquitin

chains to address them to degradation pathways. Ubiquitin chains (polyubiquitin) are either linear (M1) (Ubiquitin C-terminus bound to N-terminus of the following ubiquitin) or branched through bonds between the ubiquitin C-terminus and a lysine side chain of the following ubiquitin (K6, K11, K27, K29, K33, K48 or K63) (Akutsu, Dikic, and Bremm 2016; Komander and Rape 2012) (Figure 33). Each kind of ubiquitin chain links the ubiquitinated proteins to a specific fate, K11 and K48 chains mediate protein degradation at proteasome (Akutsu, Dikic, and Bremm 2016; Komander and Rape 2012) while K63 can mediate interaction between two proteins (Akutsu, Dikic, and Bremm 2016; Komander and Rape 2012).

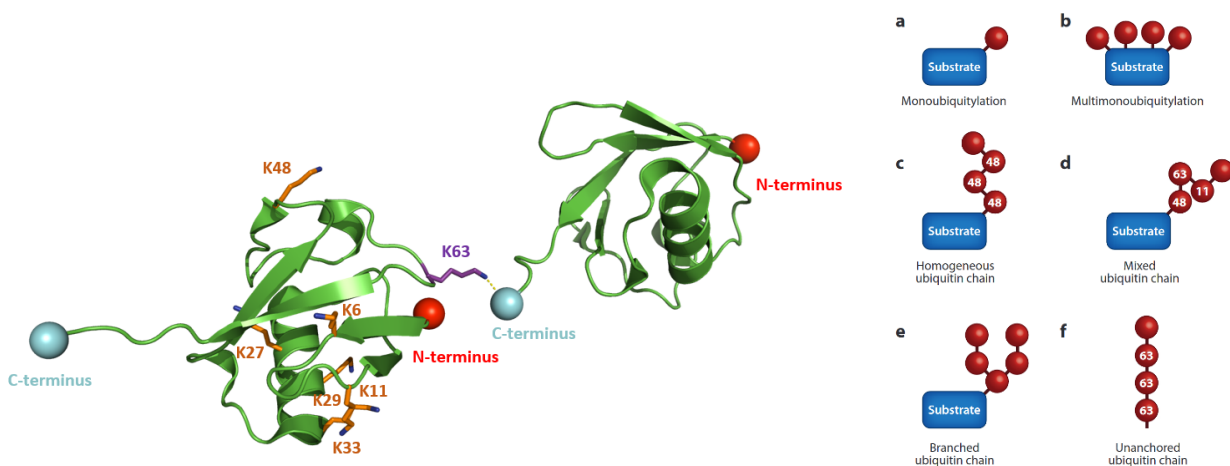


Figure 33: Ubiquitin chains linkage

Left: X-ray crystal structure of K63-diUbiquitin (PDB: 3H7P, Weeks et al. 2009). Lys63 is colored in purple, all the other lysines able to give rise to another kind of ubiquitin linkage (Lys6, Lys11, Lys27, Lys29, Lys33 and Lys48) are colored in orange. Right: example of ubiquitin linkages extracted from Komander and Rape 2012. Ubiquitins are represented as red spheres that carried a number corresponding to the type of linkage (48 for K48 linkage, 63 for K63 linkage and 11 for K11 linkage)

The Myo6 MyUb domain interacts with K48, K63, K29 and K11 linked ubiquitin chains, with a clear preference for the latter three. The NMR structure of the complex between the CBDⁿ fragment and K63-diUbiquitin revealed that ubiquitin can interact with Myo6 through two different binding interface within the MyUb, key residue for ubiquitin binding on MyUb domain I1072 (number according to the NI isoform of Myo6) was thus identified through pull-down (He et al. 2016) (Figure 34).

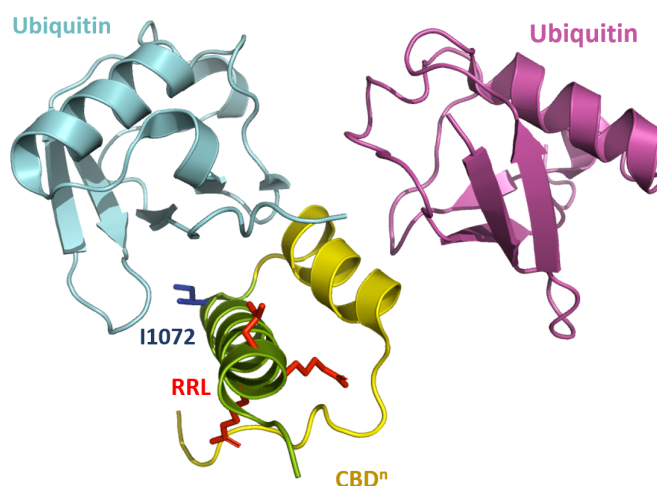


Figure 34: K63-diUbiquitin bound to the CBDⁿ fragment

The NMR structure of the K63-diUbiquitin / CBDⁿ complex (1080-1122) (PDB 2N13, He et al. 2016). Ubiquitin binds through two interfaces that involve two different helices of the CBDⁿ. The Key residue for binding I1072 (blue) is found in one of the two interfaces.

Although no structure is available for the MIU-Ubiquitin complex, MIU was first identified in Rabex (for which the structure of the MIU domain and ubiquitin was solved by NMR) and characterized as a conserved motif found on several proteins. The A1013G mutation was thus identified, which prevents the MIU's interaction to ubiquitin (Penengo et al. 2006; He et al. 2016). The MIU-binding motif shows no affinity or preference towards ubiquitin linkages; however, in cooperation with the MyUb domain, it seems to specifically support K11-linked ubiquitin binding (Penengo et al. 2006; He et al. 2016) (Table 6).

Publication	K _D	Ubiquitin construct	Myo6 construct	Technic used
He et al. 2016	2.1 ± 0.8 μM	K63-diUb	MyUb	Fluorescence polarization assay 22°C in 20 mM Tris pH 7.6, 200 mM NaCl, and 5% glycerol
	13.5 ± 2.0 μM		MIU-MyUb Iso1	
	2.0 ± 1.0 μM		MIU-MyUb Iso2	
	2.7 ± 0.4 μM		MIU-MyUb Iso2	
	11.4 ± 11.4 μM		A1013G	
	5.2 ± 1.5 μM	K11-diUb	MIU-MyUb Iso3	
	3.9 ± 0.1 μM		MyUb	
	0.8 ± 0.4 μM		MIU-MyUb Iso1	
	4.9 ± 1.0 μM		MIU-MyUb Iso2	
	6.1 ± 1.5 μM		MIU-MyUb Iso2	
	20.1 ± 1.1 μM	K48-diUb	A1013G	
	45.8 ± 5.1 μM		MIU-MyUb Iso3	
	14.5 ± 8.5 μM		MyUb	
	-		MIU-MyUb Iso1	
	44.5 ± 8.5 μM		MIU-MyUb Iso2	

Table 6: Ubiquitin-Myo6 affinity reported in the literature

C.6. Lipid

Myo6 was proposed to bind to liposomes through its CBDⁿ region as it coprecipitates with liposomes. More precisely, liposomes were proposed to bind through WSKSNKKR, aa 1115-1122, since the WASANNR mutant disrupts lipid binding (Spudich *et al.* 2007). Using liposomes of different compositions, it appears that Myo6 binds specifically to liposomes containing phosphatidylinositol-4,5-bisphosphate (PI(4,5)P₂ or PIP₂) (Spudich *et al.* 2007) (Figure 35).

Interestingly, addition of liposomes to Myo6 CBD results in significant changes in the Myo6 circular dichroism profile indicative of conformational changes upon liposome binding (α -helix formation) (Spudich *et al.* 2007) (Figure 35), highlighting the potential of lipid binding for Myo6 regulation. Moreover, FLMyo6 is able to coprecipitate with liposomes only if calcium is added (Spudich *et al.* 2007; Batters *et al.*, 2016). As calcium does not change the ability of CBD to bind liposomes, this is likely due to Ca²⁺ inducing FLMyo6 wider conformational changes that will make the lipid binding site available.

Uniquely, lipids seem also able to bind to the proximal Tail of Myo6 as addition of liposomes to the Myo6 proximal Tail results in significant structural rearrangements suggesting putative interaction between the Myo6 3HB and lipids and confirming the importance of lipid binding for Mo6 regulation (Yu *et al.* 2012).

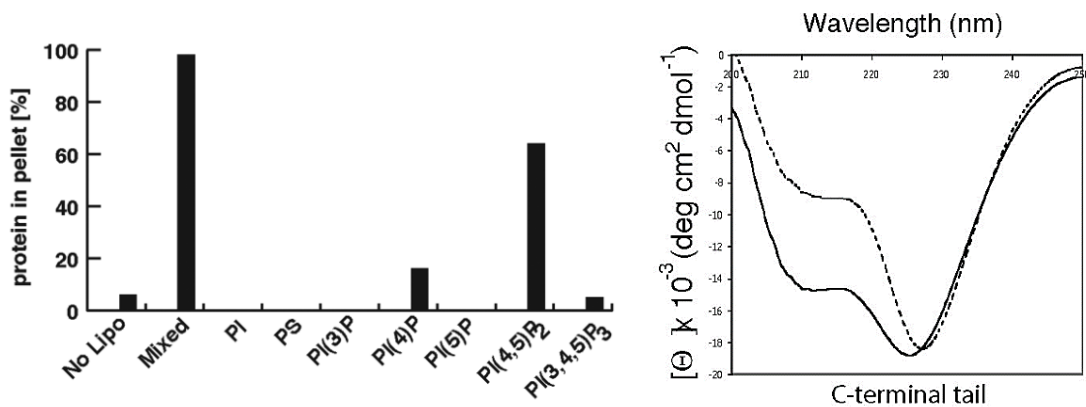


Figure 35: Myo6 CBD binds to PIP₂ resulting in conformational changes

Left: The Myo6 Tail sedimentation with mixed brain liposomes or liposomes specifically containing phosphoinositides (PI), phosphatidylserine (PS), phosphatidylinositol-3-phosphate (PI(3)P), phosphatidylinositol-4-phosphate (PI(4)P), phosphatidylinositol-5-phosphate (PI(5)P), phosphatidylinositol-4,5-bisphosphate (PI(4,5)P₂ or PIP₂) or phosphatidylinositol (3,4,5)-trisphosphate (PI(3,4,5)P₃). Right: Circular dichroic spectra of the Myo6 Tail with mixed brain liposomes addition (dashed line) or without (solid line)

C.7. DNA

DNA was also identified as a partner of Myo6. While it seems to be able to weakly bind to the Myo6 IQ-CBDⁿ, highest affinity was found for CBD^c and two sequence motifs were found to be particularly important for its binding as their depletion results in 5 or 7-fold decrease in its affinity for DNA (Fili *et al.* 2017) (Table 7, Figure 36). In cells, this binding is particularly important for the ability of Myo6 to regulate RNAPII transcription (Fili *et al.* 2017) (see section D.4).

Publication	K _D	DNA construct	Myo6 construct	Technic used
Fili <i>et al.</i> 2017	3.5 ± 0.7 μM	DNA (40 pb)	FLMyo6 (1-1253)	Anisotropy fluorescence, 25 °C in 50 mM Tris pH 7.5, 150 mM NaCl and 1 mM DTT
	2.5 ± 0.4 μM		IQ-end (814-1253)	
	1.2 ± 0.35 μM		IQ-DT (814-1060)	
	0.1 ± 0.02 μM		CBD (1060-1253)	
	1.3 ± 0.7 μM		CBD ⁿ (1060-1120)	
	0.12 ± 0.03 μM		CBD ^c (1121-1253)	
	0.5 ± 0.18 μM		CBDc ΔTRKR (1121-1253)	
	0.7 ± 0.15 μM		CBDc ΔSKKK (1121-1253)	

Table 7: DNA-Myo6 affinity reported in the literature

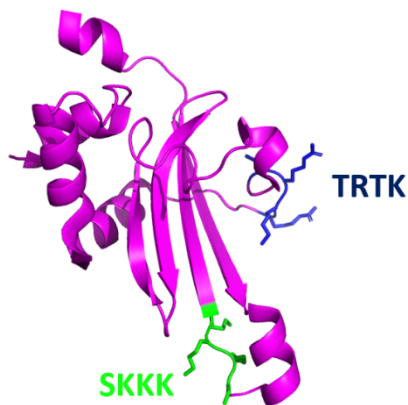


Figure 36: DNA binding motif

NMR structure of CBD^c (PDB: 2KIA, Yu *et al.* 2009) is pictured in magenta. The TRTK (blue) and SKKK (green) motifs, whose depletion result in 5/7-fold decrease in affinity for DNA thus could be implicated in DNA binding to Myo6.

C.8. Fine differences in the interaction surface can modulate partner binding to Myo6

C.8.a. RRL partners interact with the RRL motif in different fashions

The correct interaction surface remains to be properly characterized for many Myo6 partners and may be slightly different for each of them.

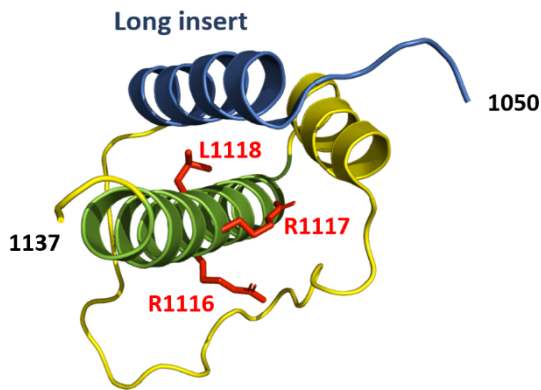


Figure 37: CBDⁿ organization

NMR structure of Myo6 CBDⁿ fragment 1050-1137 (PDB: 2N12, [Wollscheid et al. 2016](#)) containing the last helix of the long insert and the first two helices of CBDⁿ. Long insert is colored in blue, key helix for CBDⁿ partner binding is colored in green, it contains the RRL motif, colored in red. Note that the long insert folds on the RRL motif, provoking hindrance for binding of RRL partners

Even if several partners seem to share the same RRL binding motif, comparison of chemical shifts in Myo6 NMR spectrum upon partner addition further confirm that although OPTN, NDP52 and TAX1BP1 are RRL partners whose binding occurs mainly on the CBDⁿ helix 1071–1122 ([Figure 37](#), helix in green), key binding residues differ ([Biancospino et al. 2019](#)). A mutagenesis analysis through a GST-pull-down assay from HEK293T cells using GST-Myo6 CBDⁿ (G1080-R1131) lacking the long insert has shown that Myo6 point mutation R1116A (i.e. “ARL”) and L1118A (i.e. “RRA”) strongly impact OPTN and GIPC1 binding but impact only weakly NDP52 and TAX1BP1 binding ([Wollscheid et al. 2016](#)). Further characterization through mammalian two-hybrid from RPE cells shows the relative contribution of R1116A and L1118A for GIPC1 and NDP52: using R1116A, GIPC1 binding to Myo6 goes down to ~70% compared to WT while using L1118A, it goes down to ~40%. For NDP52, using R1116A, affinity only goes down to 80-90% while L1118A does not impair the binding at all ([Arden et al. 2016](#)). Yet, these findings are controversial: different conclusions were reported by [Fili et al. \(2017\)](#) using a FRET assay with Myo6 (814-end). In this case, R1116A has barely any effect on NDP52 binding while L1118A reduced it by 4-fold.

Furthermore, several studies have used the R1117A (i.e., RAL) mutant or the ¹¹¹⁶RRL₁₁₁₈ to AAA mutant (i.e., AAA) to study interaction of RRL partners with Myo6. Yet, R1117A disrupts the CBDⁿ structural integrity according to circular dichroism ([Wollscheid et al. 2016](#)). Thus, data obtained using these mutants should be carefully considered as they don’t show specifically the importance of interaction of Myo6 with RRL partners but rather point out at the importance of the CBDⁿ as a whole.

C.8.b Long insert regulates partner binding

The long insert also plays a key role in the regulation of partner binding. In situ proximity labelling using either CBD NI or LI shows that NI and LI isoforms shared 39 interactions while LI has 16 specific interaction and NI 47 ([O’Loughlin, Masters, and Buss 2018](#)).

Interestingly, the CBDⁿ partner binding is isoform dependent. Indeed, the presence of the long insert between the Myo6 DT and CBD domains drastically reduced NDP52, TAX1BP1, OPTN, K63- diUb and GIPC1 binding to Myo6. Actually, the NMR structure of CBDⁿ (PDB: 2N12, [Wollscheid et al. 2016](#)) reveals that the LI insert can fold on the CBD, masking the RRL site ([Wollscheid et al. 2016](#)) and impairing thus the bindings of several CBDⁿ partners to the Myo6 isoforms containing the long insert ([Figure 36](#)). In contrast, the long insert is crucial for clathrin binding as it directly participate to its binding site ([Biancospino et al. 2019](#)). Thus, binding of partners on Myo6 RRL motif and binding of clathrin seem to mutually exclude each other.

Although WWY partners were shown to bind both NI and LI isoforms, some of them seem to show a preference for the LI isoform. Indeed, LMTK2 shows a slight preference for the Myo6 LI isoform over the NI isoform in mammalian 2-hybrid assays ([Chibalina et al. 2007](#)) and Dab2 has a strong preference for the LI isoform in fluorescence resonance energy transfert (FRET) using Myo6 814-end ([Fili et al. 2020](#)).

Myo6 has a wide range of partners that could cooperate or compete with each other with the potential to link Myo6 to various functions notably in the context of diseases.

D. Myo6, a multifunctional motor in cells

Its unique features and its many cellular partners allow Myo6 to perform a wide range of functions for exocytosis, endocytosis, cell motility, organelle morphology and transcription.

D.1. Myo6 in trafficking/signaling events

D.1.a. Exocytic/secretory pathway

Once synthesized at the endoplasmic reticulum, the proteins must be transported in tubular/vesicular carriers to the Golgi complex for maturation, they are then sorted for correct delivery to organelles or plasma membrane. By transfecting the protein secretion reporter : secreted form of alkaline phosphatase (SEAP) into immortal fibroblastic cell lines of Snell's Waltzer Myo6-null mice, [Warner et al. \(2003\)](#) revealed that Golgi secretion was reduced by 40% in the absence of Myo6 suggesting a role for Myo6 in the secretory pathway. Further studies took a close look at the impact of Myo6 on this process and proposed a role for it at different steps of the secretory process.

D.1.a.i Myo6 at the trans-Golgi

Golgi is an important crossroad in the secretory pathway as it allows protein maturation and sorting. Myo6 was found to localize to vesicles in the perinuclear region around the Golgi complex independently of its Motor domain ([Buss et al. 1998](#); [Warner et al. 2003](#)). On Golgi, Myo6 nicely colocalizes with TGN38 showing a localization at the trans Golgi and trans Golgi network in fluorescence and electron microscopy of NRK cells ([Warner et al. 2003](#); [Buss et al. 1998](#)). This localization of Myo6 seems mediated by its partner OPTN as OPTN silencing results in loss of Myo6 localization at the Golgi ([Sahlender et al. 2005](#)).

Interestingly, using immortal fibroblastic cell lines of Snell's Waltzer mice, it was established that the size of the Golgi was reduced by 40% compared to wild-type while Myo6 overexpression nicely rescues Golgi morphology ([Warner et al. 2003](#)). However, in contrast, a more recent study found that Myo6 results in a ~25% Golgi decompaction using HeLa cells ([Capmany et al. 2019](#)). Actually, they pointed out that heterogenous outcomes can be obtained depending on cell types, cell spreading and imaging techniques (2D or 3D) ([Capmany et al. 2019](#)). Thus, effect of Myo6 on Golgi morphology remains to clarify ([Capmany et al. 2019](#)).

D.1.a.ii Cargo sorting in polarized cells

Once mature, the proteins must be sorted prior to their secretion. This is particularly important in polarized cells as cell polarity requires differential addressing of newly synthesized proteins either to the basolateral or apical region of the cell (Eaton and Martin-Belmonte 2014). Myo6 NI isoform expression was found to be crucial for basolateral addressing; indeed, pulse-chase experiment shows that overexpression of the Myo6 NI Tail results in missorting of VSVG (basolateral sorted protein used as a reporter). Mutagenesis shows that intact CBDⁿ is required for sorting of VSVG to basolateral domain suggesting of role of a CBDⁿ partners in this process (Au *et al.* 2007). The authors suggest that the RRL partner OPTN could be involved as electron microscopy shows colocalization of Myo6 and OPTN on clathrin coated vesicles (Au *et al.* 2007).

D.1.a.iii Transport to the plasma membrane

To address potential roles of Myo6 for vesicles transport from the Golgi, the temperature sensitive VSV-G construct was transfected in NRK cells allowing its accumulation in Golgi on precise temperature conditions. Transferring cells at 32°C results in their secretion from the trans Golgi to the plasma membrane. In these conditions, immunostaining clearly shows colocalization of Myo6 with VSV-G vesicles secreted by the Golgi on their path to the plasma membrane suggesting a role of Myo6 in their delivery to the plasma membrane (Warner *et al.* 2003).

D.1.a.iv Myo6 SI may ensure replenishment of secretory granules by tethering

Vesicles carrying signals must accumulate at the plasma membrane prior to their release at appropriate time (replenishment). In neurosecretory cells, secretory granules are key for diffusion of neuropeptides and hormones upon calcium signaling and Myo6 seems to be involved in their replenishment. Indeed, looking by mass spectroscopy at proteins associated to purified secretory granules, Myo6 was found to interact with the granules in the presence of calcium (Tomatis *et al.* 2013). TIRF microscopy on PC12 cells reveals that Myo6 knockdown results in the defect in secretory granule retention near the plasma membrane without affecting their speed or biogenesis suggesting a tethering role for Myo6 (Tomatis *et al.* 2013). Interestingly, PC12 cells express both SI and NI isoforms but only Myo6 SI isoform is able to rescue secretory granule exocytosis upon Myo6 knockdown, suggesting a unique role of the small insert in this secretory function. Interestingly, the small insert contains a tyrosine phosphorylation site (DYD) that can be phosphorylated by Src kinase. Addition of a Src kinase inhibitor in PC12 cells results in loss of Myo6 mediated exocytosis revealing a possible role of the phosphorylation of the Myo6 DYD motif for secretory granule exocytosis (Tomatis *et al.* 2013).

A key partner in this process seems to be the ENA/VASP protein: Mena as relocalization of Mena to mitochondria results in reduction of Myo6 localization to secretory granules and reduction of secretory granules near the plasma membrane (Tomatis *et al.*, 2017).

D.1.a.v Myo6 at the plasma membrane for fusion

Myo6 and OPTN colocalize with secretory vesicles at the plasma membrane. TIRF microscopy reveals that depletion of either OPTN or Myo6 results in less vesicle fusion events at the plasma membrane but does not seem to impact vesicles biogenesis at the trans Golgi (Bond *et al.* 2011) suggesting a role of Myo6 for vesicle fusion perhaps by tethering Myo6 near the plasma membrane as described in the previous section.

D.1.a.vi Tubular carrier fission

Myo6 was also involved in tubular secretion necessary for maturation of a specialized organelle: Melanosomes. Melanosomes synthesize and store melanin pigments in their lumen and are involved in protein recycling through tubular carriers (Dennis *et al.* 2016). Finally, once matured, they are secreted to epidermal keratinocytes (Delevoe 2014; Wu and Hammer 2014), where they assure photoprotection of the epidermis. In this process, Myo6 was proposed to play an additional role during maturation: fission of tubular carriers (Ripoll *et al.* 2018).

Actually, Myo6 NI colocalizes with melanosomes in punctate at the basis of tubular carrier without the need of the Motor. Interestingly, live cell imaging and EM microscopy reveals that depletion of Myo6 or of its cellular partner OPTN seems to decrease tubular carrier fission. Precisely, tubules can form normally but their basis are larger and fissions event are much rarer suggesting a role of Myo6 for constriction at the tubule basis required for their fission. Interestingly, both Arp2/3 and WASH (branched-actin nucleation factors) depletion also reduce melanosome tubular carrier constriction, as seen with Myo6 depletion (Ripoll *et al.* 2018), highlighting the importance of branched actin for tubular carrier fission. In this context, Myo6 could participate in branched actin network formation or act as an anchor that would exert a precise force at the basis of tubules for their fission.

D.1.b. Myo6 in endocytosis

Endocytosis allows cells to internalize various particles in vesicles from outside the cells. Soluble molecules can be internalized through pinocytosis, membrane receptors can be internalized in clathrin coated vesicles and large particles, such as pathogens, are internalized in phagosomes. Eventually, the endocytosis pathway can also be hijacked by parasites. Internalized vesicles are then

addressed to the early endosomes for either recycling or degradation after endosome maturation. This process thus requires accumulation of a substance at the plasma membrane, membrane deformation to form the vesicles, fission of the formed vesicle, transport towards the endosomal compartments and fusion. As for secretion pathways, Myo6 was found to be implicated in many steps of the endocytic process.

D.1.b.i Myo6 is required for cargo internalization in clathrin mediated endocytosis

Accumulating evidence emphasize the importance of Myo6 motor for cargo entrance and receptor recycling through clathrin-mediated endocytosis, impacting intestinal absorption (Ameen and Apodaca 2007; Collaco *et al.* 2010), cell homeostasis (Blaine *et al.* 2009), renal excretion (Gotoh *et al.* 2010) and synapse plasticity (Wagner *et al.* 2019).

Indeed, comparison of Myo6-null (Snell's Watzler) mice and normal mice cerebellum in super resolution microscopy reveals that Myo6 clathrin mediated endocytosis participate in synapse plasticity through removal of AMPA receptors from the cell surface (Wagner *et al.* 2019). In Myo6 and Dab2 KO mice, cystic fibrosis transmembrane conductance regulator (CFTR) accumulate at the surface of the enterocytes suggesting that Myo6 and Dab2, its partner on clathrin-mediated endocytosis, are required for proper endocytosis at the apical region of enterocytes (Ameen and Apodaca 2007; Collaco *et al.* 2010). In Myo6 KO mice kidney proximal tubules, mislocalization of Dab2 and clathrin and a reduced absorption of HRP (endocytosis marker) can be noticed. Moreover, protein excretion is much higher in Myo6 KO mice compared to wild type control. These data suggest a defect in clathrin mediated endocytosis of proteins in kidney resulting in proteinuria (Gotoh *et al.* 2010). Myo6 has also been proposed to regulate renal proximal tubule homeostasis as Myo6 is required for Na/Pi cotransporter removal from microvilli of renal brush border membrane as expression of Myo6 Tail (dominant negative) inhibits Na/Pi cotransporter removal in TIR-FM (total internal reflection fluorescence microscopy) on cells derived from marsupial kidney proximal tubule: OKP cells (Blaine *et al.* 2009). Na/H exchanger, which is present in the microvilli membrane of enterocytes, can move down to the microvilli basis through endocytosis upon chemical stimulation. Myo6 knockdown in Caco-2 and Bbe cells inhibits this movement assessing a key role of Myo6 either for vesicles formation or for their transport (Chen *et al.* 2014).

It is thus clear that Myo6 is required for cargo internalization, although it is undetermined through these experiments whether Myo6 is key for cargo accumulation at the plasma membrane, membrane deformation to form the vesicles or vesicle fission.

Studies of CACO-2 polarized cells further established the importance of the Myo6 LI isoform in the endocytic pathway. Indeed, the Myo6 LI isoform was shown to localize on clathrin coated structures (Buss *et al.* 2001) where it can directly interact with clathrin both free triskelia and cages through an LI isoform specific insert as described above in section C.4. (Wollscheid *et al.* 2016; Biancospino *et al.* 2019). In NRK cell lines expressing stably Myo6 LI Tail as a dominant negative, transferrin uptake was reduced by ~70%, showing the importance of Myo6 motor for normal transferrin uptake through clathrin dependent endocytosis (Buss *et al.* 2001) while no effect on transferrin uptake were seen in NRK cells stably expressing the Myo6 NI Tail (Buss *et al.* 2001).

D.1.b.ii Membrane ruffling

To internalize an element from the outside, membrane needs to deform to ultimately catch it into a vesicle. In the very specific context of Salmonella invasion where the endocytic pathway is hijacked by a parasite to allow its entrance in the cell, Myo6 was found to be required for these membrane deformations. Indeed, Myo6 knockout from HeLa cells results in a 60% decrease of Salmonella invasion, a reduction of membrane ruffling from 65% to 45% and a reduction of PI3P in macropinocytic cups from 70% to 33%. Myo6 is found to localize to Salmonella induced membrane ruffles. Myo6 recruitment to membrane ruffles depends on its phosphorylation on T405 through PAK. Indeed, the T405A mutant mimicking the dephosphorylated state cannot be recruited while the T405E mutant mimicking the phosphorylation state is strongly recruited to membrane ruffle (Brooks *et al.* 2017).

These findings highlight the potential of Myo6 for deep membrane reshaping for endocytosis of large elements although there is no clear evidence of membrane reshaping by Myo6 in the context of a normal endocytosis.

D.1.b.iii Myo6 can mediate endocytic vesicles fission

A detailed study shows that Myo6 binds to CLCa₄₆₋₆₁ (see section C.4.) in competition with binding to the actin remodeling protein Hip1R (GST pull-down) (Biancospino *et al.* 2019). Lack of Myo6 binding to CLCa (CLC knockdown or CLCa I54D mutant) results in aberrant clathrin-coated pits in Caco-2 cells. An increased number of pits exhibit an elongated shape suggesting that Myo6 binding to clathrin may thus provide the force required for constriction and fission (Figure 38).

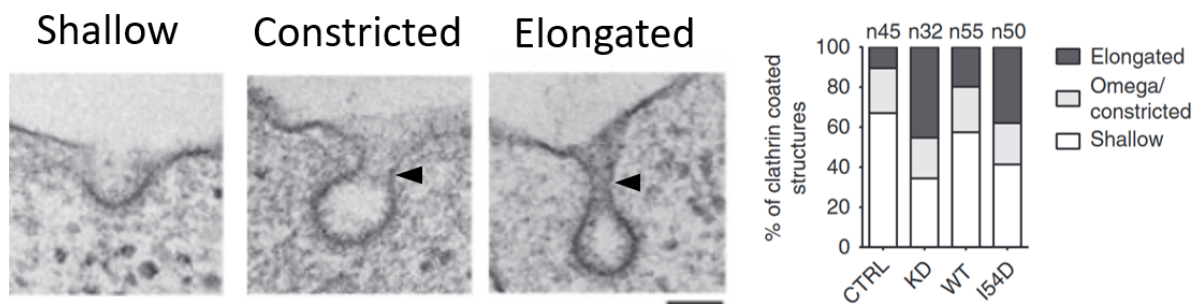


Figure 38: Increasing number of elongated vesicles suggest the role of Myo6 for fission (Biancospino *et al.* 2019)

(Left) Representative electron microscopy images of different morphology of clathrin coated pits. Scale bar: 100 nm. **(Right)** Bar graph representing the number of each kind of clathrin coated structures found in different conditions (CTRL: no clathrin transfected, KD: CLCa knockdown, WT: transfection of wild-type CLCa after CLCa knockdown and I54D: transfection of CLCa I54D mutant (unable to bind Myo6) after CLCa knockdown. Accumulation of elongated vesicles when Myo6 is no longer able to bind CLCa (I54D mutant) suggests the importance of Myo6-clathrin interaction for fission.

The authors thus proposed that, during vesicle invagination Myo6 will bind to CLCa and compete out Huntingtin interacting protein 1-related protein (Hip1R) promoting Hip1R dissociation from the cages and recruitment by epsins at the uncoated neck where Hip1R regulates actin filament polymerization, then Dab2 may bind Myo6 into an active dimer leading to fission.

D.1.b.iv Vesicle transport

Following vesicle fission, Myo6 still seems to have a role to play for transport. Indeed, single particle tracking reveals that microsphere speed is slowed down by overexpression of the Myo6 Tail (as a dominant negative) when phagocytosis of microspheres are studied in ARPE-19 cells (Hewage and Altman 2018). Moreover, a Myo6 mutant directed to the + end of actin filament results in redirecting endosomes to the cell cortex creating clusters at filopodia basis assessing the importance of myo6 directionality for proper localization and transport of endosomes in cells (Masters and Buss 2017).

D.1.b.v Myo6 NI localizes on uncoated vesicles to allow substance entrance

Even if Myo6 LI was the one specifically found on clathrin coated vesicles, Myo6 NI seems to also have its role to play in the endocytic process but in later stages of the process. Indeed, Myo6 NI colocalizes with transferrin receptors whose transport is mediated by clathrin-mediated endocytosis. Yet, intriguingly, Myo6 NI does not colocalize with clathrin coated structures (like Myo6 LI) or with

EEA1-positive endosomes. Rather Myo6 NI colocalizes with transferrin receptor on Rab5 positive endosomes suggesting its recruitment after vesicles uncoating but before fusion with EEA1 early endosomes. In this context, Myo6 does not colocalize with Dab2 but colocalize with GIPC1 and the overexpression of the dominant negative: Myo6 NI Tail results in delay in transferrin uptake (Aschenbrenner, Lee, and Hasson 2003).

D1.b.vi Myo6 seems to control early endosome localization and maturation

Myo6 colocalizes in a large majority of APPL1-positive signaling endosomes along the actin filaments on the cell cortex (structured illumination microscopy on HeLa cells) (Masters *et al.* 2017). In contrast, EEA1-positive (more mature) endosomes do not colocalize with Myo6 although they are surrounded by actin filaments. Upon Myo6 silencing, APPL1-positive endosomes relocate to the nuclear periphery together with an accumulation of actin filaments, assessing the importance of Myo6 for proper localization of these signaling endosomes (Masters *et al.* 2017). Analysis of the content of these perinuclear endosomes notably through the biosensor GFP-PX reveals a change of endosomes composition upon Myo6 depletion. A high density of PI3P and EEA1 was found which indicates that more endosomes have started their maturation process. Interestingly, addition of the microtubule depolymerizer: nocodazole on SiMyo6 HeLa cells results in loss of perinuclear localization, although it does not rescue the wild-type phenotype (i.e., cell periphery localization). Thus the authors proposed that Myo6 would tether signaling endosomes at cell periphery preventing their displacement through microtubule for maturation (Masters *et al.* 2017).

D.1.b.vii Endocytosis defects may result in infertility in male mice

Defect in Myo6 mediated endocytosis may be at the origin of Snell's Walzer male mice (Myo6 KO) fertility problems. In late phasis of spermatogenesis, in WT mice, MYO6, GIPC1 and TOM1-L2 are recruited to the bulbar region of the apical tubulobulbar complexes (TBCs), a highly specialized endocytic structure that correspond to double-membrane invagination of Sertoli cells to the spermatid stabilized by actin (Zakrzewski *et al.* 2020). It associates to Rab5 and APPL1 positive early endosomes but are not present in EEA1-positive (more mature) sorting endosomes, as previously reported (Master *et al.* 2017). Myo6 KO changes the overall TBCs orientation, Rab5/APPL1-positive vesicles and EEA1 early endosomes distribution, actin organization and the localization of Arp3 and Cortactin (actin binding proteins) as well as Myo6 adaptors (GipC1, TOM1-L2) distribution (Zakrzewski *et al.* 2020) resulting in defects in endocytosis in spermatogenesis probably responsible of infertility issues in Myo6-null mice.

D.2. Degradation pathways

D.2.a. Autophagy

Autophagy is a key degradation pathway that can maintain cell homeostasis and growth on starvation condition (non-selective autophagy) and ensure degradation of large structures tagged with ubiquitin such as pathogens and large protein aggregates (selective autophagy). In this process, autophagosomes fused with early endosomes to form the amphisome (maturation process) prior to its fusion with lysosomes for acidic degradation. Autophagosome membranes contain LC3 that allow their binding to autophagy receptors, able to capture ubiquitinated cargos.

Actually, Myo6 is key for both selective and non-selective autophagy as shown in HeLa, RPE cells and MEFs and primary cortical neurons derived from Myo6 KO mice. MYO6 together with its partner TAX1BP1 was also found to be able to recognize ubiquitinated *Salmonella typhimurium* in infected cells thus playing a role for the autophagy-dependent clearance of pathogens (Tumbarello *et al.* 2015). Its depletion results in an accumulation of autophagosomes and lack of protein aggregate clearance due to a defect in fusion of autophagosomes with lysosomes (monitoring LC3 lipidation and colocalization between autophagosomes and lysosomes) as well as a delay in the formation of amphisomes (Tumbarello *et al.* 2012). In this context, Myo6 may be involved in short movement, and tethering of compartment together for fusion.

D.2.b. Mitophagy

Clearance of damaged mitochondries is essential for cell homeostasis. Damaged mitochondries can be taken in charge by a specialized autophagy process called mitophagy. Parkin is recruited upon membrane potential changes and strongly ubiquitinylates outer membrane proteins including the Myo6 partners OPTN, NDP52 and TAX1BP1 that link damaged mitochondria to autophagosomes through LC3 binding (Onishi *et al.* 2021). Shortly after membrane depolarization, mitochondries are encaged in a dense actin network isolating the damaged mitochondria from the rest of the network until their degradation (Kruppa *et al.* 2018).

Cells deprived from Myo6 exhibit a large number of autophagosomes containing mitochondries which may suggest delay in autophagosomes fusion with lysosomes as previously described in autophagy processes (Tumbarello *et al.* 2012) and a defect in mitochondrial respiration (Kruppa *et al.* 2018). Moreover, upon chemically induced mitophagy, Myo6 was found to translocate from a cortex location to a mitochondria membrane where it colocalizes with the mitophagy marker parkin in HEK293 cells. Interestingly, this translocation is independent of OPTN, NDP52 and TAX1BP1

as their knockdown does not affect Myo6 localization. In contrast, I1072A mutation known to abolish Myo6 MyUb domain binding to ubiquitin (He *et al.* 2016), results in loss of Myo6 translocation to mitochondria. Thus, ubiquitin chains may be the bridge between Myo6 and mitophagy receptors in this context. Despite the fact that lack of motor activity does not impair Myo6 localization to mitochondria, overexpression of the Myo6 Tail (no motor activity) in HEK293 cells, results in disorganization of the actin cage surrounding the damaged mitochondria and reintroduction of the damaged mitochondria in the healthy mitochondrial network (Kruppa *et al.* 2018).

D.3. Structure maintenance and organization

D.3.a. Organelle organization

Myo6 was also found to be key for correct organelle positioning and shaping in neurons. Through interaction with Syntaphilin (SNPH), Myo6 can recruit and anchor mitochondria in presynaptic region of neurons. Indeed, Myo6 knockdown results in loss of the presynaptic localization of the mitochondria while its overexpression increased it. Moreover, Myo6 colocalizes on mitochondria with the mitochondria anchoring protein SNPH and ability to recruit mitochondria to presynaptic region was lost upon SNPH knock out (Li *et al.* 2020). Myo6 seems also essential for endoplasmic reticulum (ER) extension towards the axon as addition of Myo6 inhibitor (TIP) reduces dynamic movement of the ER (Deng *et al.* 2021).

D.3.b. Assembly of Cx43 GAP junctions

Immunohistochemistry on mouse frozen heart sections, immunofluorescence on HeLa cells or NRK cells as well as primary ventricular myocytes from rats show that Myo6 can colocalize with Cx43 (connexin-43) GAP junction plaques (Waxse *et al.* 2017; Piehl *et al.* 2007). Interestingly, if Cx43 is still expressed in similar amount in fibroblast cells lacking Myo6, the GAP junction plaque size is smaller (Waxse *et al.* 2017) and intercellular communication across GAP junction is reduced (Waxse *et al.* 2017). Photobleaching experiments revealed that even if Cx43 amount is not impaired, fibroblasts lacking Myo6 have more difficulties to integrate free Cx43 to GAP junction plaque (Waxse *et al.* 2017).

ED.3.c. Cilia/microvilli formation and maintenance

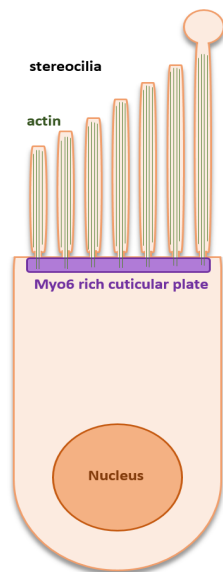


Figure 39: sensory ear hair cell organization and Myo6 distribution.

Myo6 accumulates in the actin rich cuticular plate at the basis of the stereocilia

In Myo6-null (deaf) mice cochlea, 20 days after birth, many hair cells have died and the remaining are degenerated with abnormal giant stereocilia containing diffuse actin (Self *et al.* 1999). Interestingly, in wild-type Guinea pig, no Myo6 can be detected in inner and outer hair cell stereocilia. Myo6 concentrates instead in the cuticular plates (Figure 39) and vestibular organs (Hasson *et al.* 1997). Taken these data together, Frank, Noguchi, and Miller (2004) proposed that Myo6 could keep the actin organization of the cuticular plate together preventing undesired cell components entrance in the stereocilia and maintaining the basis of stereocilia in place.

Myo6 was also found to be critical for cilia/microvilli formation and maintenance in other cell types. Myo6 depletion was also found to impair primary cilium formation (that normally originate from centriole) probably by preventing the centriole protein ODF1 degradation through autophagy upon starvation conditions which essential for primary cilliogenesis (Magistrati *et al.* 2022). Although it is less dramatic than ear hair cell stereocilia changes, enterocytes from Snell's Waltzer mice exhibit abnormal microvilli with irregular length and implantation (Collaco *et al.* 2010)

D.3.d. Myo6 association with cell-cell junctions

D.3.d.i Tissues morphogenesis

Abnormal neuron morphology has been described in Myo6 depleted cells in mice and drosophila models (Osterweil, Wells, and Mooseker 2005; Yoong *et al.* 2020). Thereby, *in vivo* time-lapse imaging of Drosophila adult sensory neuron differentiation demonstrate the importance of Myo6 for morphogenesis of primary branched dendrites by controlling actin filament extension (Yoong *et al.* 2020). Similarly, in drosophila embryos, Myo6 depletion results in an increase of cell area and a decrease of cell elongation upon development highlighting the importance of Myo6 for cell tissues morphogenesis through actin network organization (Dye *et al.* 2021). Actually, Myo6 depletion can even lead to severe epithelial organization defect and death of certain drosophila larvae and embryos (Millo *et al.* 2004).

Myo6 has thus been proposed to be part of the Rho-dependent signaling pathway that participate to actin cytoskeleton reorganization in response to mechanical stress. In this pathway, Myo6 seems to act as a force sensor as its association with E-cadherin at cellular junctions increased upon mechanical stress resulting in the activation of RhoA signaling required for maintenance of tissues integrity (Acharya *et al.* 2018; Mangold *et al.* 2012).

D.3.d.ii Migration

Myo6 interaction with cellular junctions was also described in the context of cell migration: Myo6 depletion was found to reduce cell migration of C2C12 myoblast (Karolczak *et al.* 2015) and drosophila melanogaster ovarian border cells (Geisbrecht and Montell 2002). In both cases, this could come from defect in cell adhesions which is essential for cell migration (Huttenlocher, Sandborg, and Horwitz 1995). Indeed, in myoblast, Myo6 concentrates in adhesion sites together with talin and vinculin (Karolczak *et al.* 2015). Moreover, Myo6 depletion leads to a lower expression level of proteins involved in cell-cell contacts: E-cadherin and the β -catenin (Armadillo) in Drosophila ovarian brush border (Geisbrecht and Montell 2002) and talin, FAK/pFAK, M-cadherin and drebrin in mice myoblast (Lehka *et al.* 2020). Actually, Myo6 depletion results in an even wider change in the expression level of several key proteins involved in myoblast differentiation (Pax7, MyoD and myogenin), in the cytoskeleton organization (α -actinin, desmin, myosin heavy chains and γ -actin), and in myoblast membrane fusion (myomaker and myomerger) (Lehka *et al.* 2020). Yet in myoblast, Myo6 is not expressed in nuclei (Lehka *et al.* 2020; Karolczak *et al.* 2015) making a direct effect of Myo6 on transcription level unlikely in this context. Instead, Geisbrecht and Montell (2002) proposed that interaction between cell adhesion proteins and Myo6 helps stabilizing each other at the cell-cell junction level as Myo6 protein level is also reduced in brush border cells upon E-cadherin or Armadillo depletion and interaction between these three proteins is found by immunoprecipitation (Geisbrecht and Montell 2002).

Beside its importance for proper cell-cell adhesion, Myo6 was also proposed to interact and support the formation of migratory cell leading edge. Indeed, in A431 cells, upon ruffling stimulation through EGF addition, Myo6 is phosphorylated and goes from a juxtannuclear localization to ruffles location at leading edges within minutes (Buss *et al.* 1998). Myo6 depletion in HeLa or A549 cells through siRNA or crisprCas9 significantly decrease ruffling upon EGF addition (Buss *et al.* 1998; Chibalina *et al.* 2010). Interestingly, Myo6 truncated from the Tail can localize to membrane ruffles while, in contrast, neither Myo6 Tail nor Myo6 K157R (rigor mutant strongly bound to actin) were able to localize to ruffles when overexpressed (Masters *et al.* 2017), assessing the importance of a correctly functioning motor for Myo6 localization to ruffles.

Further evidence suggest that Myo6 may control leading edge ruffling by controlling protein delivery to leading edge, indeed, it was shown that Myo6 or OPTN depletion results in loss of EGFR and RAC delivery to the leading edge of the A549 cells thus preventing ruffling and formation of lamellipodia (Buss *et al.* 1998; Chibalina *et al.* 2010).

D.4. In Transcription

In addition to its many roles in the cytoplasm, Myo6 is expressed in the nucleus in several cell types: in hippocampal neurons (Kneussel *et al.* 2021), in adrenal medulla cells (Majewski *et al.* 2018; 2011), in native CD4 T cells (Zorca *et al.* 2015) and HeLa cells (Vreugde *et al.* 2006; Fili *et al.* 2017) where it colocalizes with its partner NDP52 (Fili *et al.* 2017) and RNA polymerase II (RNAPII) (Vreugde *et al.* 2006; Fili *et al.* 2017). More precisely Myo6 was found to localize mostly in chromatin free regions and near the nuclear envelope (Vreugde *et al.* 2006; Majewski *et al.* 2018) and upon cell stimulation (through addition of high external concentration of KCl), Myo6 can translocate to the nucleus where its colocalization with RNAPII and transcription factors SP1, SC35, PML and RNAPII mediated transcription activity are increased (Majewski *et al.* 2018). Actually, Myo6 depletion even results in loss of normal localization of RNAPII (Hari-Gupta *et al.* 2022). Furthermore, in fluorescence anisotropy, Myo6 CBD^c was found to bind DNA with an affinity of ~0.1 μ M compatible with a role of Myo6 in transcription (Fili *et al.* 2017).

Using an in vitro transcription system (HeLaScribe[®] Nuclear extract), it has been shown that transcription level decreases by ~25 % upon Myo6 depletion (using anti-Myo6 antibody) while addition of 1 μ M of FLMyo6 partially rescue the transcription level (Fili *et al.* 2017). In contrast, addition of CBD results in transcription decrease in a CBD concentration dependent manner suggesting a competition between FLMyo6 already present in the sample and the exogenous CBD. Thus, a key role of the CBD to address Myo6 to its transcription function is revealed. Transcription level increases further by 2-fold when 5 μ M of the Myo6 nuclear partner NDP52 is added, assessing the importance of this partner in transcription (Fili *et al.* 2017).

D.5. Myo6 links microtubule and actin tracks

D.5.a. Myo6 and dynein can collaborate with each other

Dynein coprecipitates with Myo6 from whole brain lysate and both can coprecipitate with the muskelin protein. Interestingly, Myo6 ability to coprecipitate with dynein is significantly reduced upon muskelin knockout suggesting that muskelin may constitute a bridge between the two motors (Kneussel *et al.* 2021). Dynein inhibitor: ciliobrevin D results in ~13% loss of nuclear Myo6 intensity in hippocampal neurons and muskelin knockout results in ~22% loss assessing the role of dyneins and

muskelin for Myo6 translocation to the nucleus and highlighting a collaboration between the microtubule based motor dynein and the actin based motor Myo6 (Kneussel *et al.* 2021).

Such a crosstalk between microtubules and actin filaments through dynein and Myo6 has also been reported in the context of influenza virus infection: this virus moves from the cell periphery to the perinuclear region by switching from actin to microtubule tracks transportation. Single virus tracking shows that the switch from actin to microtubules require Myo6 and dynein motors (Zhang *et al.* 2018).

D.5.b. Myo6 is involved in centrosomes localization

EM and immunofluorescence microscopy confirmed that Myo6 can localize at the centriole (Magistrati *et al.* 2022). Moreover, while Myo6 depletion from RPE-1 cells does not seem to impair the centriole's structure, it impairs centrosome localization (centriole moves further away from the plasma membrane). Myo6 depletion also induces accumulation of its partner OFD1 at mother and daughter centrioles even though the overall level of expression of OFD1 is not impaired. Super resolution microscopy reveals that OFD1, which normally concentrates at the tips of the centrioles, adopt a general localization all over the centrioles when Myo6 is depleted. Actually, FRAP reveals that an OFD1 pool stayed immobilized at the centriole surface instead of being translocated at the centriole tips (Magistrati *et al.* 2022). Thus, Myo6 may act as a regulator of the microtubules cytoskeleton by impacting centrosome location and ODF1 organization.

D.6. Myo6 in cancers

Myo6 seems to have an impact on various signaling pathways related to cancer cells notably transcription, migration, receptor surface expression and autophagy, a key process for cell survival under stress conditions (White 2015). Precisely, when interacting with APPL1+ signaling endosomes, Myo6 can enhance EGFR signaling and AKT phosphorylation, a key pathway in cancer progression (Masters *et al.* 2017; Polo, Di Fiore, and Sigismund 2014). Moreover, the impact of Myo6 on signaling protein phosphorylation has been reported in several cancer models. Notably, Myo6 *in vitro* knockdown decreases ERK1/2 phosphorylation (cell proliferation and cell death modulator) in lung (Yu *et al.* 2015) and prostate cancer (Wang *et al.* 2016). Myo6 has also been proposed to be coupled with nuclear receptor expression: indeed, Myo6 Tail can directly interact with estrogen receptor, moreover, in estrogen receptor positive MCF7 cells, Myo6 Tail expression drastically reduced the expression level of estrogen receptor target PS2 and GREB1. Given the key role of estrogen receptor in breast cancer growth (Fili *et al.* 2017), this shows the potential of Myo6 in regulation of cancer related signaling pathway.

The key role of Myo6 for tumor development has been shown using several cancer cell models: oral squamous carcinoma (Zhang *et al.* 2016), ovarian carcinoma (Yoshida *et al.* 2004), lymphoid leukemia (Jbireal *et al.* 2010), melanoma (Li *et al.* 2015), hepatocellular carcinoma (Ma *et al.* 2015), lung cancer (Yu *et al.* 2015), gastric cancer (Wang *et al.* 2016), colorectal cancer (You *et al.* 2016; Wang *et al.* 2022) and prostate cancer (Dunn *et al.* 2006; Puri *et al.* 2010; Wang *et al.* 2016). *In cell cultures* Myo6 knockdown drastically decreases cell proliferation and increases apoptosis in cell models of colorectal cancer (You *et al.* 2016; Wang *et al.* 2022), oral squamous cell carcinoma (Zhang *et al.* 2016), melanoma (Li *et al.* 2015), hepatocellular carcinoma (Ma *et al.*, 2015) and gastric cancers (Yang *et al.* 2021). In lymphoid leukemia, *in vitro* Myo6 knockdown results in the reduction of cell migration (Jbireal *et al.*, 2010). Myo6 is overexpressed in high-grade ovarian carcinoma. Moreover, *in vitro*, Myo6 knockdown drastically reduced cells spreading and migration (Yoshida *et al.*, 2004). In prostate cancer cells, Myo6 knockdown decreases cell migration, growth (Dunn *et al.*, 2006) and proliferation *in vitro* (Wang *et al.*, 2016) and significantly decreases PSA (biomarker in prostate cancer) and VEGF (growth factor that stimulate vascularization and tumor angiogenesis) secretion (Puri *et al.*, 2010). Furthermore, it was reported that Myo6 is overexpressed, and the overall survival of patients is affected (Kaplan-Meier plotter) in gastric cancer. In this cancer, *in vitro* knockdown of Myo6 significantly decreases cell migration and proliferation and downregulates cell cycle activators (Wang *et al.*, 2016). In lung cancer, immunohistochemical staining on human tissues reveals that Myo6 expression is higher in lung cancer tissues than in adjacent normal tissues. Interestingly, the highest level of Myo6 expression was seen in the lymph nodes upon metastasis. *In vitro* Myo6 knockdown results in a significant reduction of cell proliferation (Yu *et al.* 2015).

Developing Myo6 specific inhibitors of the motor function for investigation in cells and development of potential anti-tumor drugs is thus of high interest. Currently, only one Myo6 inhibitor: has been reported: [TIP: 2,4,6-triiodophenol] (Heissler *et al.*, 2012). However, although it is an interesting tool to study Myo6 functions, the druggability of TIP is quite poor as it has a rather low affinity (μM range). Moreover, its mechanism of action is unknown and as it is a very small molecule, it could result in off-target effects.

Myo6 partners also link Myo6 to cancer; GIPC1 was found to be a promising therapeutical target in cancer, it is notably highly overexpressed in prostate and ovarian cancers and has been associated with proliferation and cell survival (Chittenden *et al.* 2010; Westbrook *et al.* 2016). Peptides preventing GIPC1 interaction with its PDZ partners have been developed as an anti-tumoral treatment. They result in decrease in proliferation, and increase in apoptosis in pancreas cancer (Patra *et al.* 2012; Pal *et al.* 2014).

In contrast, DNA fingerprinting of normal and cancerous ovarian cell lines reveals that Dab2 is downregulated in ovarian cancer (Mok *et al.* 1994) and has the ability to inhibit tumor growth *in vitro* and *in vivo* (Mok *et al.* 1994; 1998). It was found later that Dab2 expression was decreased in many other cancers including breast cancer (Martin, Herbert, and Hocevar 2010), colorectal cancer (Kleeff *et al.* 2002), gastric cancer (Wang *et al.* 2020) and squamous cell cancers (Wang *et al.* 2016). In contrast, decreasing Dab2 expression through miRNA has been found to promote cancer invasiveness and proliferation in prostate cancer cell lines (Yang 2019). These findings highlight Dab2 possible roles as a tumor suppressor (Ogbu *et al.* 2021). Although the « tumor suppression » mechanisms are not clearly established, Dab2 expression level has been shown to regulate several signaling pathways that may be a reason for its tumor suppressor activity. Dab2 downregulation is notably responsible of activation of the Ras/MAPK or Wnt/ β -catenin signaling cascade resulting in EMT promotion (Wang *et al.* 2020; Martin, Herbert, et Hocevar 2010).

To that extent, understanding Myo6 regulation and how partners can orientate Myo6 towards pro or anti-cancer functions is of particular interest. Typically, in the context of breast cancer (MCF-7 cells), Dab2 expression levels is particularly low and its transfection in MCF-7 cells decrease estrogen receptor transcription level thus tumorigenicity, similarly to Myo6 depletion. This is consistent with the ability of Dab2 to block Myo6 ability to bind DNA (fluorescence anisotropy) and to block its *in vitro* transcription ability in HeLa cells (Fili *et al.* 2020). Fili *et al.* (2020) thus proposed that the tumor suppressor role of Dab2 would be a down regulation of Myo6 action in the nucleus, in particular an attenuation of estrogen receptor expression.

E. Myo6 versatile mechanical properties

A large range of cellular functions and partners have thus been identified. In the course of characterizing the wide range of functions of Myo6, several mechanical roles have been proposed for Myo6, as an anchor, a transporter or an organizer of the actin network (Table 8). Gathering knowledge on the Myo6 cell functions, it is possible that in complex processes, such as mice spermatogenesis, different Myo6 mechanical roles could collaborate (Zakrzewski *et al.* 2020): first in association with GIPC1, Myo6 could transport APPL1-endosomes towards the cell cortex (Aschenbrenner, Lee, and Hasson 2003), then Myo6 could tether them at the cortex to prevent their maturation (Masters *et al.* 2017). Finally, Myo6 could participate in organization of the actin network by interacting with LARG, Arp3 and cortactin (Noguchi, Lenartowska, and Miller 2006; O'Loughlin, Masters, and Buss 2018). However, the mechanical role Myo6 performs in several cellular functions remains to be determined.

Cell function		Proposed mechanical role(s)	Myo6 partner(s) identified	References
Secretory pathway	Localization at Golgi	?	OPTN	Buss et al. 1998 ; Warner et al. 2003 Sahlender et al. 2005 and Capmany et al. 2019
	Cargo sorting	?	OPTN ?	Au et al. 2007
	Vesicles transport after their secretion by the Golgi apparatus	Transport	?	Warner et al 2003
	Vesicles replenishment	Tethering	Mena	Tomatis et al. 2013 and Tomatis et al., 2017
	Vesicle fusion at the membrane	?	OPTN	Bond et al. 2011
Melanosome maturation	Tubular carrier constriction and fission	Tethering or/and actin organization	OPTN	Ripoll et al. 2018
endocytosis	Coated vesicles constriction and fission	Tethering or/and actin organization	Clathrin/Dab2	Biancospino et al. 2019
	Vesicle transport	Transport	GIPC1	Hewage and Altman 2018 and Masters and Buss 2017
	Parasite invasion	Membrane ruffling	?	Brooks et al. 2017
	Early endosomes localization	Tethering	?	Masters et al. 2017
spermiogenesis	Vesicle transport out of the TBC	Transport, tethering and actin organization	GIPC1/TOM1-L2	Zakrzewski et al., 2020
	TBC maintenance			Zakrzewski et al., 2020
autophagy	Amphisome formation	tethering	TOM1/NDP52/TAX1BP1/OPTN	Tumbarello et al. 2012 ; 2015
mitophagy	Actin cage formation	Actin organization	NDP52/TAX1BP1/OPTN	Kruppa et al. 2018
Organelle organization	Mitochondria and endoplasmic reticulum correct positioning	tethering	?	Li et al. 2020 and Deng et al. 2021
GAP junction trafficking	Cx43 addressing to GAP junction plaque	?	?	Waxse et al., 2017
Hair cell maintenance	Stereocilia maintenance	Actin organization and/or tethering	?	Avraham et al. 1995 , Hasson et al. 1997 , Self et al. 1999 and Frank, Noguchi, and Miller 2004
Tissues morphogenesis	Cellular junctions function	?	?	Osterweil, Wells, and Mooseker 2005 ; Yoong et al. 2020 Dye et al. 2021 Millo et al. 2004 Acharya et al. 2018 and Mangold et al. 2012
				Karolczak et al. 2015 and Geisbrecht and Montell 2002
Migration	Leading edge shaping and EGFR delivery	?	OPTN	Buss et al. 1998 , Masters et al. 2017 and Chibalina et al. 2010
	Transcription	RNAPII localization and mediated transcription	Tethering	NDP52/DNA
Microtubule and actin crosstalk	Myo6-dynein collaboration	?	Muskelin ?	Kneussel et al. 2021 and Zhang et al. 2018
	Centrosome organization	?	OFD1	Magistrati et al. 2022

Table 8: link between mechanical properties and cell functions

Thus, how the same motor might adapt to different mechanical properties is of outstanding importance to understand how Myo6 functions in cells. Mechanical properties enabling Myo6 to perform these functions have thus been pursued.

E.1. Actin organizer

As Myo6 has been found to impact the morphology of cells and organelles, the motor was suspected to act as an actin network organizer (Frank, Noguchi, and Miller 2004).

Myo6 was found to maintain the actin-dependent organization of the tubulobulbar complexes required for endocytosis during mouse spermiogenesis (Zakrzewski *et al.* 2020), to participate in actin cage formation during mitophagy (Kruppa *et al.* 2018) and to maintain actin network supporting stereocilia in cochlear (Frank, Noguchi, and Miller 2004). Profound defects in actin cytoskeleton organization were also found in PC12 cells upon Myo6 depletion (Majewski *et al.* 2011). Moreover, Myo6 ability to associate with several actin modulators, including LRCH1 and LRCH3 (O'Loughlin, Masters, and Buss 2018) as well as DOCK7 and LARG (Wollscheid *et al.* 2016; O'Loughlin, Masters, and Buss 2018) further supports its possible role as an actin organizer.

However, it should be noted that actin organization is not the only way Myo6 could undergo membrane reshaping, indeed, using a fluid supported bilayer lipid model, it was found that Myo6 on its own induces lipid surface remodeling pointed out to possible membrane reshaping through direct contact between Myo6 and lipid instead of indirect contact through actin cytoskeleton (Rogez *et al.* 2019).

E.2. Myo6 can dimerize at high concentration to perform transport and anchoring functions

To take several steps on actin without detaching, which is necessary for performing a transporter function, Myo6 need to be at least a dimer so that one head remains attached to actin while the other is detached. Actually, even for anchoring function, having two myosin heads working together is more efficient (Sweeney and Houdusse 2007).

But surprisingly, gel filtration and sucrose density centrifugation show that recombinant full length Myo6 as well as Myo6 from cell extracts are monomeric (Lister *et al.* 2004). Actually, Myo6 remains monomeric even after addition of the zero-length cross linker as an attempt to stabilize weak dimers (Lister *et al.* 2004). Strikingly, despite being monomeric *in vitro*, Myo6 were found to be a dimer in cells: Myo6 dimerization study through homoFRET in ARPE-19 cells shows that, when bound to clathrin coated vesicles, a high FRET signal is recorded, as FRET required specific orientation between donor and acceptor, FRET signal increase is unlikely to be due to high monomer concentration in random orientation, rather these results pointed out a possible dimerization of the motor on these vesicles (Altman *et al.* 2007).

Further investigation demonstrates that actually, at high concentration Myo6 can dimerize even *in vitro*. High concentration can be reached *in vitro* by Myo6 saturation on actin dense network

or ^{Flag}Myo6 saturation on an anti-flag column, the Myo6 is then released using ATP or flag peptide (respectively). Rotary shadowing electron microscopy shows that after these treatments 17% of Myo6 is stably dimerized for a few hours (Park *et al.* 2006). These dimers are able to move processively for ~1.1 μm runs (Park *et al.* 2006). The authors thus proposed that Myo6 dimerization can be reached and regulated by partner binding. Partners would address Myo6 to clusters creating a high local Myo6 concentration allowing dimerization or even oligomerization. Indeed, formation of such large Myo6-partner clusters were reported by several groups (Dos Santos *et al.* 2022; Karolczak *et al.* 2015; Shang *et al.* 2017). Moreover, Myo6 dimerization (Spudich *et al.* 2007; Phichith *et al.* 2009; Yu *et al.* 2009; Fili *et al.* 2020) or oligomerization (Shang *et al.* 2017) upon partners binding has been reported by several teams.

Overall, Myo6 seems to be indeed able to function as a dimer in cells, but because of the difficulty to form a stable dimer for *in vitro* experiments, an artificial Myo6 dimer has been extensively used to investigate Myo6 dimer mechanical properties. Artificial dimerization is reached by the addition of a leucine zipper (Lumb, Carr, and Kim 1994) in place of the cargo binding domain usually at aa 992. Using single molecule motility assays, comparison of the artificially dimerized Myo6 to FLMyo6 formed though actin saturation shows that both constructs are processive and take steps of identical size but it should be noted that run length drops from 1.1 to 0.3 μm when the artificially dimerized Myo6 is used (Park *et al.* 2006). Caution must thus be raised upon studies of chimeric motors in the absence of structural knowledge of how Myo6 motors dimerize.

E.3. Myo6 travelling along actin

When artificially dimerized through a leucine zipper (introduced at aa 992), Myo6 acts as a slow processive motor able to take several steps on actin filaments without detaching in single molecule motility and optical trapping assays (Rock *et al.* 2001). Intriguingly, Myo6 takes irregular steps of 30-36 nm (Rock *et al.* 2001) which is unusual compare to the processive motor Myo5 (Rief *et al.* 2000).

Proper stepping requires specific adaptation of the motor, indeed, a processive motor needs:

- high duty ratio (*i.e.*, the motor must spend most of its kinetic cycle on actin so that the dimer does not detach too easily)
- coordination between the two heads of the dimer (called lead and rear heads) must be established to keep one head interacting with actin when the other is detached.

Kinetic studies show that Myo6 has a poorer affinity for ATP compared to Myo5 but it has a good affinity for ADP making the ADP state, in which Myo6 is bound to actin, the most populated state

of the cycle and ADP release the limiting step of the Myo6 cycle (De La Cruz, Ostap, and Sweeney 2001). These data are consistent with a high duty ratio for Myo6 compatible with its transport function.

Coordination between the lead and rear heads of the motor has been described for Myo5 through a « gating » in which the lead head and the rear head coordinate with each other through intramolecular strain (Rosenfeld and Sweeney 2004). However, Myo6 cannot gate using the same mechanism as this mechanism relies on the directionality of Myo5 Lever arm. This suggests a unique gating mechanism for Myo6 (Sweeney and Houdusse 2007). For the Myo6 artificial dimer (leucine zipper introduced at aa 992), the ADP release rate is twice as big as the ATPase rate per head while both are similar for the monomer, suggesting indeed a collaboration between the two heads of the dimer (Morris *et al.* 2003). A mechanism for Myo6 stepping has thus been proposed: the lead head stay bound to ADP.Pi and only weakly binds to actin until the rear head can detach (Robblee, Olivares, and de la Cruz 2004). Alternatively, it was proposed that the lead head would be the one strongly attached to actin allowing longer run in an hand-over-hand stepping mechanism (Park *et al.* 2006; Sweeney and Houdusse 2007) (Figure 40).

Performing *in vitro* motility assay on keratocyte actin network with either artificially dimerized Myo6 or multiple Myo6 monomers linked together through a nanosphere, Sivaramakrishnan and Spudich (2009) showed that a Myo6 monomer ensemble is able to be processive, indicating that dimerization might not be required for this. Monomer ensemble moves at a speed similar to the dimer and is able to transport cargos on long trajectories of $\sim 10 \mu\text{m}$ (Sivaramakrishnan and Spudich 2009) perhaps due to the fact that it is more likely to have at least one head remaining attached to the actin track in the context of an ensemble of motor compare to a dimer. Such oligomer assembly may be best suited for long distance trafficking while dimers will be able to transport cargo on $\sim 1 \mu\text{m}$ distance.

Overall, Myo6 seems indeed well suited for cargo transport function.

E.4. Load sensitivity and anchoring

Actually, it was shown using optical trap experiments that Myo6 is force sensitive and can switch from a transport function to an anchoring function when force higher than 2 pN is applied to the motor (Altman, Sweeney, and Spudich 2004; Chuan, Spudich, and Dunn 2011). When a resisting load is applied to Myo6, the motor becomes a much better ADP binder and a poorer ATP binder. Thus, until the resisting load is released, the strong ADP conformation of the motor is favored and the motor stays more stably attached to the actin filament (Altman, Sweeney, and Spudich 2004), which clearly promotes high capacity for this motor to anchor a cargo/organelle to the actin cytoskeleton.

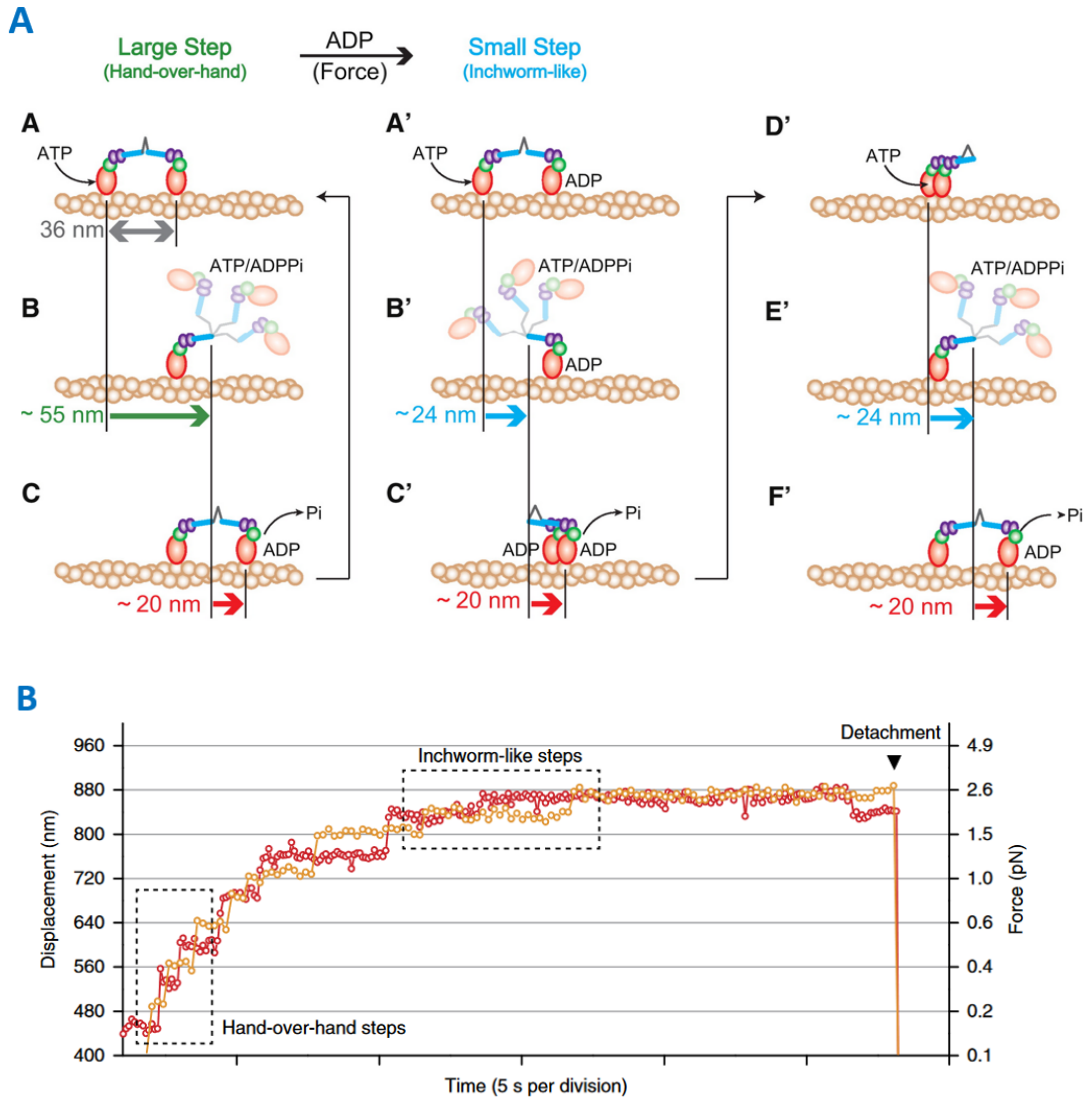


Figure 40: Myo6 behavior switches mode under load (Nishikawa *et al.* 2010; Iwaki *et al.* 2016)

(A) Model of Myo6 stepping mechanism on actin (brown). Myo6 Motor domain is colored in red, its converter is in green and its Lever arm in blue. CaM are colored in purple. Left: hand-over-hand mechanism resulting in 36 nm steps. Right: Inchworm-like mechanism resulting in 10–22 nm steps (Nishikawa *et al.* 2010). (B) Example of the trajectory of each head of a Myo6 dimer on actin in optical trapping assay coupled with DNA nanospring. Step size and behavior clearly evolved with load (Iwaki *et al.* 2016).

Interestingly, using Myo6 constructs truncated and artificially dimerized at residue 1021 either by addition of a portion of a Myo2 dimerization domain or by addition of a flag-tag that will mediate dimerization through binding to oligonucleotides (respectively), Nishikawa *et al.* (2010) and Iwaki *et al.* (2016) found that Myo6 can change its stepping mode upon load and ADP addition. Indeed, through *in vitro* motility assays, they monitored the movement on actin of each head of a Myo6 artificial dimer upon increasing load. They found that the Myo6 motor can switch from a non-adjacent binding mode (\sim 36 nm between the two head of the dimer) under low load to an adjacent binding mode (\sim 22 nm

(Nishikawa *et al.* 2010) or ~10 nm (Iwaki *et al.* 2016) between the two head of the dimer) when load is applied. The non-adjacent stepping mode at low load is typical of a hand-over-hand mechanism associated with Myo6 transport function while the adjacent binding mode is typical of an Inchworm-like stepping behavior and could correspond to a transition between Myo6 transport and anchoring functions (Figure 40).

E.5. Large steps for a short Lever arm

When processive, Myo6 undergoes ~30-36 nm steps towards the minus end of the actin filaments which is surprisingly large considering the length of the Myo6 canonical Lever arm (Spudich 2001). It should be noted that ~11 nm steps were also observed in the other direction although they are 3.5-fold less frequent (Rock *et al.* 2001; Nishikawa *et al.*, 2002).

Myo6 has only one conventional IQ motif in its Lever arm, while Myo5, that similarly performs ~36 nm steps, has 6 IQ (Rosenfeld and Sweeney 2004). The Ins2 sequence constitutes a second CaM binding site that increases the Myo6 Lever arm length. Moreover, during its powerstroke, the Myo6 Lever arm undergoes a very large swing (180°) compared to Myo5 (70°) (see section B.2.). But only considering the length of the Ins2-IQ motif as the Myo6 Lever arm and applying a 180° swing during the powerstroke, a 12 nm stroke is generated, which is in agreement with what has been measured on optical traps (Ménétreay *et al.* 2007). However, the way the Myo6 dimer can extend to cover the remaining 24 nm is still unclear and controversial.

It was first tested whether the Myo6 Ins2, unlike conventional IQ motif, would allow more flexibility of the motor allowing to cover the missing 24 nm. But 30-36 nm steps can also be achieved when Ins2 is replaced by one of the IQ motif found in Myo5 (Park *et al.* 2007), thus the Myo6 large steps cannot be explained by the singularity of Ins2 alone and the Tail must play an important role for this. Thereby, a combination of TIRF single motility assays and optical trapping experiments have shown that randomization of the proximal Tail sequence results in shorter steps and reduced velocity of artificially dimerized Myo6 (leucine zipper at aa 992) assessing the importance of the proximal region for Myo6 correct stepping (Spink *et al.* 2008). However, the way this proximal region would contribute to the Myo6 Lever arm stiffness or to the dimerization of the motor remains unclear and at least two models of the active dimer have been proposed.

E.6. Two dimerization models were proposed to address this question

E.6.a. Distal dimerization

As the addition of the proximal region to the Myo6 S1 fragment does not significantly increase the working stroke of the motor, Rock *et al.* (2005) proposed that the proximal Tail does not constitute

a rigid Lever arm, instead, it may act as a flexible linker that will reach the 36 nm via a diffusive process. Zimmermann *et al.* (2015) show that on ADP-actin filaments, Myo6 binds to specific spots spaced from ~36 nm suggesting that preferential binding sites could be reached by Myo6 through diffusion allowing 36 nm steps, in support to the hypothesis proposed by Rock *et al.* (2005). Consistently, Spink *et al.*, (2008) proposed that Myo6 would dimerize through the distal cargo binding domain (at the CBD level) and thus both the 3HB and the SAH would be part of a flexible Lever arm. They were indeed unable to find a clear indication of Myo6 dimerization upon characterization of the proximal and distal Tails with SEC-MALS.

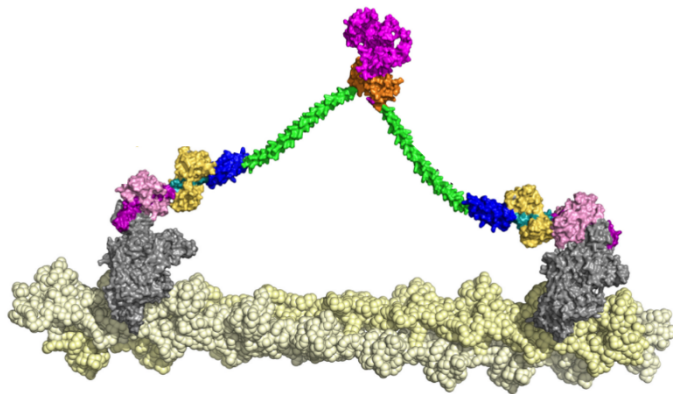


Figure 41: Distal dimerization (Mukherjea *et al.* 2009)

Myo6 distal dimerization. The Motor domain is colored in grey, the Insert-2 in purple, the IQ in cyan, the folded 3HB in blue, the SAH in green, the DT in orange and the CBD in purple. Actin is colored in yellow. The two Myo6 molecules interact with each other at the level of the CBD.

In support of this hypothesis, Yu *et al.* (2009) have shown that the Myo6 partner Dab2 is able to dimerize the CBD of Myo6 by X-ray crystallography. In this context, Dab2 constitutes a link that connects the two CBDs together without direct interaction between them (see section C.1.a.) (Figure 41).

CBD does not seem able to dimerize on its own, as addition of the zero-length cross linker in CBD at 12 μ M results in no dimerization (Spudich *et al.* 2007). Based on that, Yu *et al.* (2009) proposed a general scheme for the formation of the dimer that would be highly dependent on partner binding : the so-called cargo-mediated dimerization in which distal dimerization of the Myo6 CBD via partner binding results in a dimer exhibiting flexible Lever arms.

E.6.b. Proximal dimerization

In vitro motility assays using a Myo6 (1-991 and 1-1050) motor without any CBD sequence (Park *et al.* 2006) have shown that Myo6 is still dimeric and is able to make 30-36 nm steps on actin suggesting that a proximal dimerization of Myo6 could occur. Further studies in fact showed that an even more truncated Myo6 (1-940) construct was sufficient to make such big steps (Mukherjea *et al.* 2009). When Myo6 is truncated up to 917 or 920, processivity of the motor is lost (Parks *et al.*, 2006)

assessing the importance of including the 920-940 region for internal dimerization (Table 9). Thereby, replacement of the 922-935 sequence with a perfect single alpha helix sequence (SAHmimic mutant) results in loss of Myo6 proximal dimerization in electron microscopy and loss of processivity in single molecule motility assays (Mukherjea *et al.* 2014). This further supports the regulatory role of the aa 920-940 region in this process.

	% processive molecules (dimers)	Average step size (nm)	Average run length (μm)
MVI-839 (S1)	0	0	0
MVI-917	0	0	0
MVI-940	12	27.2 ± 9.7	0.9
MVI-991	10	27.1 ± 8.7	0.6
MVI-991-GCN4	>98	27.6 ± 9.8	0.3
MVI-1050	90	30.2 ± 12.6	0.9
MVI FL	15-30	27.6 ± 8.6	1.1

Table 9 : Myo6 proximal dimerization

*Single molecule motility of Myo6 constructs as assessed by fluorescence imaging with one nanometer accuracy (FIONA) (after actin saturation in rigor) (Park *et al.* 2006; Mukherjea *et al.* 2014); The FIONA method can track the position of a single fluorophore with ~ 1.5 nm resolution*

Using molecular dynamic on Myo6 907-980 then 907-940, (Kim *et al.* 2010) proposed a dimerization of the SAH domain based on formation of salt bridges upon low salt condition (Figure 42). Yet peptides that include the SAH domain (with residues 920-940) remain monomeric at high concentration ($45.6 \mu\text{M}$ in SEC-MALS: Spink *et al.* 2008; 1 mM in NMR: Barnes *et al.* 2019) excluding a role for this region as triggering proximal dimerization.

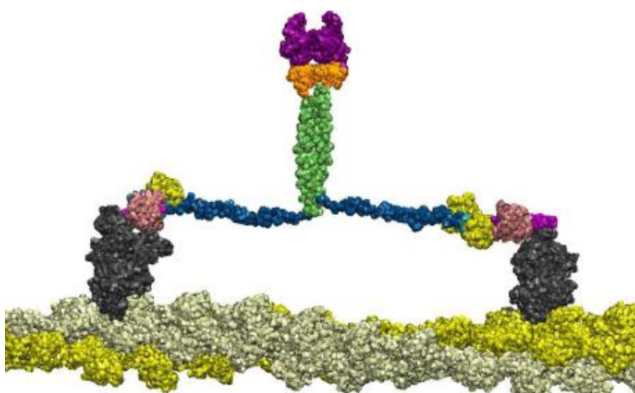


Figure 42: SAH mediated dimerization (Kim *et al.* 2010)

Myo6 dimerized through SAH association thanks to the formation of salt bridges. The Motor domain is colored in grey, the Insert-2 in purple, the IQ in cyan, the unfolded 3HB in blue, the SAH in green, the DT in orange and the CBD in purple. Actin is colored in yellow.

Mukherjea *et al.* (2009) have proposed instead a model involving 3HB ability to unfold to reach 36 nm step size. 3HB N-terminus will then act as a third CaM binding site that extend to form a Myo6

rigid Lever arm as shown by Microscale thermophoresis (Mukherjea *et al.* 2014) while the C-terminus part may participate to proximal dimerization (Mukherjea *et al.* 2009; 2014) (Figure 43).

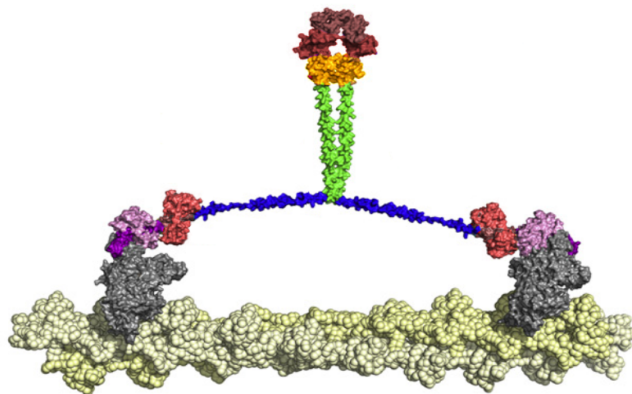


Figure 43: proximal dimerization (Mukherjea *et al.* 2009)

Myo6 dimerized in between SAH and 3HB domain upon unfolding of the 3HB. The Motor domain is colored in grey, the Insert-2 in purple, the IQ in red, the unfolded 3HB in blue, the SAH in green, the DT in orange and the CBD in brown. Actin is colored in yellow.

Proximal dimerization thus results in a rigid Lever arm with three CaM binding motif per motor and a long-constrained dimerization structure that promotes coordination between the two heads and is critical to allow reaching two actin-binding sites distant by ~ 30 nm for each of the heads of the dimer.

Finally, co sedimentation of FLMyo6 and Myo6 Tail 814-end on actin shows its ability to intrinsically dimerize although the affinity is very low (Fili *et al.* 2017) making internal dimerization of Myo6 very unlikely to happen in cells without a regulatory signal that would enhance Myo6 dimerization which could be partner binding (see section G.1.).

To check whether the Myo6 proximal dimerization is important for Myo6 cellular functions, SAHmimic was transfected in fibroblasts derived from Snell's Waltzer mice to investigate on its ability to rescue Myo6-mediated endocytosis following transferrin uptake (Mukherjea *et al.* 2014). As opposed to FLMyo6, SAHmimic is unable to rescue Myo6 mediated transferrin uptake even when dimerization is forced by the addition of a leucine zipper at residue 994. These findings support the importance of a proper proximal dimerization for Myo6 functions (Mukherjea *et al.* 2014) and emphasizes the importance of the configuration of the dimeric active motor in order to correctly serve its cellular roles. While the proximal dimerization model is more constrained and exhibit a stiffer Lever arm favouring gating between the heads, it is currently unclear whether the distal dimerization model that exhibits much more flexible Lever arms could be better suited for other Myo6 functions.

In an artificial context, a +end Myo6 mutant, in which the Ins2 and the rest of the Lever arm is replaced by two Myo5 IQ motifs is able to translocate cargo from the basis to the tips of filopodia in which it accumulates, although proximal dimerization cannot occur. This suggests that transport may not require the formation of a proximal dimer but rather leave open the question whether in this

context Myo6 serve the role of a transporter as an ensemble of monomeric forms of a vesicle or whether distal dimerization plays a role for this cellular role.

Overall, the mechanical role of Myo6 has been well explored with single molecule biophysical studies, indicating the role the motor may fulfill in cells. Although Myo6 can exist as a compact monomer (Lister *et al.* 2004), it has been demonstrated that the motor is able to dimerize in high concentration conditions (Parks *et al.* 2006), which can notably be reached when the motor clusters on vesicles (Altman *et al.* 2007). Characterization of the Myo6 dimer using *in vitro* motility assays demonstrated that the motor can take processive runs and can switch to an anchoring function under resisting load (Altman, Sweeney, and Spudich 2004; Chuan, Spudich, and Dunn 2011). Uniquely, the steps that Myo6 takes were found to be irregular and larger than expected. If progress has been made in understanding how Myo6 can take such large steps (Ménétrety *et al.* 2005; Ménétrety *et al.* 2007), the precise architecture of the Myo6 dimer remains debated and several models are currently coexisting (Mukherjea *et al.* 2009; 2014; Kim *et al.* 2010; Yu *et al.* 2009; Spink *et al.* 2008). More precise description of the architecture of the Myo6 dimer(s) is thus of high relevance. This could greatly help understanding why this motor takes irregular steps and how load can constrain it to adopt an anchoring function. Indeed, the lack of knowledge on the architectures of Myo6 processive dimer(s) and anchoring dimer(s) greatly limit our ability to specifically study these Myo6 functions, in particular in cells.

F. Regulation of the Myo6 active/inactive pool equilibrium by an auto-inhibited state

F.1. Engaging large amount of active Myo6 is deleterious, control of myo6 activation is necessary

In cells, Myo6 localizes in two pools in several cell lines. Indeed, despite its ability to interact with actin, Myo6 does not always colocalize with actin rich structures, rather Myo6 can be seen as either diffuse across the cytosol or in punctate in the cytoplasm in LLC-PK1 (pig proximal tubule cells of the kidney), HeLa, NRK (Hasson and Mooseker 1994) and Caco-2BBE (human intestinal epithelial line) (Peterson, Bement, and Mooseker 1993). Punctates have been proposed to correspond to the active pool of Myo6 while diffused pool could constitute a Myo6 auto-inhibited pool waiting for its recruitment at appropriate time and place.

When unregulated, Myo6 over-dimerization can have deleterious effects for the cell and may possibly hijack other motor functions. Indeed, when artificially dimerized through an optogenetic or

chemical approach, Myo6 was targeted to Rab5-positive early endosomes. Individual tracking of endosomes reveals that inducing Myo6 dimer engagement slows down endosome displacement and makes it irregular probably by competing with microtubule transport. Within minutes, endosomes morphology is altered. Ultimately, the endosomes fused together. In contrast, endosomes are not impaired when additional monomeric Myo6 are recruited (Ritt and Sivaramakrishnan 2018). Thus, the amount, location and timing of activated dimers/oligomers recruitment must be finely regulated in cells to avoid over recruitment.

F.2. An auto-inhibited state

Regulation of unconventional myosins in cells often requires an auto-inhibited state with:

- (1) a low ATPase rate, avoiding ATP consumption when force is not needed
- (2) a low affinity for actin so the motor can diffuse freely across the actin network until it reaches the place where and when its recruitment is needed

Such a state has already been characterized as a back-folded dimer for Myo5 (Liu *et al.* 2006; Thirumurugan *et al.* 2006) or as a back-folded monomer for Myo10 (Umeki *et al.* 2011) and Myo7 (Umeki *et al.* 2009; Sakai *et al.* 2015). Similarly, to Myo10 and Myo7, Myo6 can adopt a back-folded conformation as shown in SAXS (Spink *et al.* 2008) and negative staining (Song *et al.* 2010; Lister *et al.* 2004) experiments in which the Myo6 Tail was proposed to form intra-molecular interactions in order to form a compact back-folded conformation (Song *et al.* 2010; Spink *et al.* 2008) (Figure 44). Back-folding of the Tail could then prevent motor activity and recruitment, thus constituting the auto-inhibited state of Myo6. The existence of such a back-folded conformation, in which the Myo6 N-terminus and C-terminus are close to each other, has been confirmed in cells where a FRET signal between GFP and RFP can be measured upon transfection with GFP-FLMyo6-RFP (Fili *et al.* 2017). It has already been proposed as key for the regulation of Myo6 activity since back-folding impedes Myo6 binding to DNA making it a key element in the regulation of Myo6-mediated transcription (Fili *et al.* 2017).

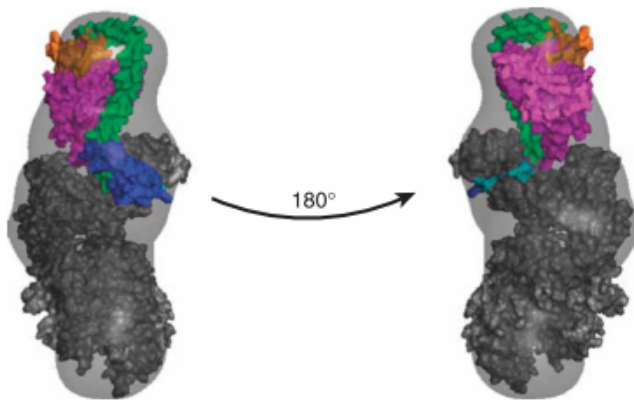


Figure 44: Myo6 auto-inhibited state model (Spink *et al.* 2008)

Model of a back-folded Myo6 build based on SAXS study of FLMyo6 in nucleotide free state. The Motor domain, the Ins2 and the IQ are colored in grey, the 3HB in blue, the SAH in green, the DT in orange and the CBD in magenta. In this model, the Tail folds on itself near the neck region

Thus, the detailed description of the Myo6 back-folded structure would be of great interest to understand how this conformation enables Myo6 for appropriate activation. To characterize the regions interacting with each other in this back-folded state, FRET and pull-down experiments have shown the ability of the CBD to interact with the IQ-DT region with an affinity of $4.5 \mu\text{M}$ (Fili *et al.* 2017) independently of the presence of the long insert (Dos Santos *et al.* 2022). Rai *et al.* (2022) further confirmed the importance of the structural integrity of the CBDn for Myo6 back-folding, by showing that the mutation of the RRL motif to AAA, known to disrupt CBDn folding (Wollscheid *et al.* 2016), results in Myo6 unfolding. While pull down and microscale thermophoresis experiments had also proposed interactions between CBDn with a CaM bound to the IQ motif (Batters *et al.* 2016), Fili *et al.* (2017) demonstrated the ability of CBD to pull-down with MD^{Ins2} region acknowledging the importance of an other region of the neck and a possible contribution of the Motor domain in the stabilization of the auto-inhibited state of Myo6.

Taken together these studies established the ability of Myo6 to fold-back (Spink *et al.* 2008; Fili *et al.* 2017) and indicated the key importance of the CBD. This C-terminal domain was indeed shown to be capable of interaction with CaM (Batters *et al.* 2016), with the IQ-DT fragment or with the MD^{Ins2} fragment (Fili *et al.* 2017), which could play a role in the stabilization of the Myo6 offstate. Yet these studies were performed using Myo6 truncations, thus the key structural elements stabilizing the Myo6 back-folded conformation in the context of the full-length motor remain to be explored. In particular, the contribution of the Motor compared to the contribution of the neck, in the context of a full-length motor, remains to be established. Moreover, the importance of the nucleotide state of the Motor to stabilize the auto-inhibited state has not been clearly explored yet as well as possible contribution of the proximal and of distal Tail. Detailed understanding of interactions going on in the auto-inhibited state and the way to disrupt them would greatly help dissecting Myo6 activation in cells.

F.3. Myo6 activation

Signals enabling Myo6 to switch from a back-folded auto-inhibited state to an unfolded activated one have been explored and several factors have been proposed, some are shared with other unconventional motors and others are unique to Myo6.

F.3.a. Ca^{2+} ions

It has been well established in several myosin motors such as Myo1 and Myo5, as well as Myo6, that the CaM bound to the IQ motif is sensitive to Ca^{2+} ions (Bahloul *et al.* 2004; Manceva *et al.* 2007; Kremmentsov, Kremmentsova, and Trybus 2004). The role of Ca^{2+} ions in the destabilization of the back-folded state of Myo6 was explored by Batters *et al.* (2016) who proposed that the CaM bound on the IQ motif previously identified as Ca^{2+} sensitive (Bahloul *et al.* 2004), would regulate the back-folded state. They indeed identified that its interaction with the CBDⁿ depends on Ca^{2+} concentration by a pull-down experiment. The interaction is lost when Ca^{2+} is added (Batters *et al.* 2016). Metal shadow electron microscopy suggests even more that upon calcium addition, CaM could detached from the IQ (Song *et al.* 2010) supporting previous experiments from Bahloul *et al.* 2004 and the hypothesis that a conformational change in this Calmodulin could trigger unfolding (Batters *et al.* 2016). But Fili *et al.* (2017) showed by pull-down assays that MD^{Ins2} can interact with CBD with or without Ca^{2+} , suggesting that unfolding regulation upon calcium may not be a relevant mechanism in the context of FLMyo6 since even if CaM CBD^N interactions are lost, some remaining contact may keep the folded state together. Yet, in presence of ATP and a 10-fold excess of actin, intramolecular FRET suggests the ability of calcium (pCa 4) to unfold Myo6 when the motor is in a specific condition where it can bind to actin and cycle (Rai *et al.* 2022). In this context, Ca^{2+} may facilitate Myo6 activation in actin rich regions of the cell but the importance of calcium in on/off regulation thus needs further investigation.

While it is still unclear whether Ca^{2+} ions are sufficient to open Myo6, it can modulate the strength of the interaction between Myo6 and its partners, and thus influence the recruitment of Myo6 in cells. Fat blot and cosedimentation with liposomes show that Myo6 interacts much better with lipids at high calcium concentration (Batters *et al.* 2016). Moreover, Biancospino *et al.* (2019) shows through immunoprecipitation that addition of 2 mM $CaCl_2$ increased Myo6-clathrin binding. They also pointed out that clathrin interacts with Myo6 through CLCa₄₆₋₆₁ (Biancospino *et al.* 2019) which is a flexible and unfolded part of the clathrin light chain but folded as an helix when bound to Myo6. As the conformation of the CLCa₄₆₋₆₁ has been reported to be reversibly modulated by Ca^{2+} ions, they proposed calcium as a key regulator of the Myo6-clathrin interaction (DeLuca-Flaherty *et al.* 1990). Although these studies (Batters *et al.* 2016; Biancospino *et al.* 2019) highlighted that Ca^{2+} ions can

improve the interactions between Myo6 and certain partners, it is not clear from these data whether Ca^{2+} ions directly increase the affinity between the Myo6 Tail and certain partners or whether they indirectly enhance Myo6 ability to bind partners by relieving auto-inhibition.

In any case, high Ca^{2+} concentrations can only be transient so that the motor would unfold and undergo recruitment. Low Ca^{2+} concentrations are required for the Myo6 motor to function properly: Indeed, direct impact of calcium on Myo6 motor activity has been investigated. At high calcium concentration (pCa 5), Myo6 S1 ATPase rate is significantly reduced compared to low calcium condition (pCa 9). In contrast, artificially dimerized Myo6 (leucine zipper at aa 994) ATPase rate remains unchanged. Yet ADP release and actin filament sliding rate decreases in a calcium concentration dependent manner. The decrease upon reducing Ca^{2+} concentrations is even stronger for the artificially dimerized Myo6. The authors thus proposed decoupling of the two heads of the dimer at high Ca^{2+} concentration ([Morris et al. 2003](#)).

F.3.b. Phosphorylation

Phosphorylation of myosin motors has been described as a way to regulate the activity of several myosin motors. Phosphorylation of non-muscle and smooth Myo2s regulatory light chain results in important conformational changes, resulting in a shift from the inactive backfolded motor to the unfolded active form ([Craig, Smith, and Kendrick-Jones 1983](#)).

Moreover, Myo1 and Myo2 actin-activated ATPase are greatly enhanced by phosphorylation of the motor in the myosin-actin interface ([Brzeska and Korn 1996](#)). In Myo6, a threonine was identified at the corresponding location ([Hasson and Mooseker 1994](#)) (Thr405 in human) and its phosphorylation has been shown to influence Myo6 localization. In A431, Myo6 motor domain T405 phosphorylation occurs upon EGF stimulation, simultaneously, Myo6 relocates to membrane ruffles ([Buss et al. 1998](#)). Similarly, Myo6 recruitment to Salmonella induced ruffles required T405 phosphorylation ([Brooks et al. 2017](#)). Phosphorylation can be seen on T405 *in vitro* using PAK enzyme (known to control actin filament turnover) ([Buss et al. 1998](#); [Brooks et al. 2017](#)). Yet, effect of T405 phosphorylation on Myo6 mechanical properties is unclear, this phosphorylation does not enhance Myo6 ability to cosediment with F-actin ([Buss et al. 1998](#)). Moreover, its phosphorylation does not impair Myo6 ATPase rate, either using S1 or HMM fragment and does not impact actin sliding capacity ([Morris et al. 2003](#); [Sweeney and Houdusse 2007](#)).

But T405 is not the only site phosphorylated by the PAK enzyme, indeed, mass spectroscopy analysis of Myo6 immunoprecipitated from A431 cells revealed two Thr phosphorylation sites in the

Myo6 CBD within the TINT motif (Sahlender *et al.* 2005). These phosphorylation sites can also be mediated by PAK *in vitro*. Mammalian two hybrids using either the phosphomimetic EINE mutant or the antiphosphorylation mutant AINA revealed that phosphorylation prevent binding to binding partners OPTN, thus TINT phosphorylation could have a role for addressing Myo6 to correct location by preventing Myo6 binding to specific cellular partners (Sahlender *et al.* 2005). Moreover, the TINT motif is present in the CBD. Since the CBD is involved in stabilization of the auto-inhibited state, the TINT phosphorylation could regulate Myo6 opening/back folding equilibrium.

In addition, phosphorylation of the SI isoform specific Tyr phosphorylation site (CBD DYD motif) was also found to be a key regulator of Myo6 mediated secretory granule exocytosis in PC12 cells although its precise role in this process is unknown (Tomatis *et al.* 2013).

Overall, Myo6 phosphorylation appears as a key parameter for proper Myo6 localization but it remains unclear if these phosphorylations impact Myo6 auto-inhibition by unfolding the motor, by modulating binding to partners or by regulating force generation. Phosphorylation thus remains an interesting parameter to look at for studying how the role Myo6 plays in cells is finely tuned.

F.3.c. Actin track (concentration, age and composition)

High concentration of actin could constitute a regulation signal as well since ATPase assays show that FLMyo6 ATPase activity increased upon actin addition (Dos Santos *et al.* 2022). Actin being essentially found near the membranes; this parameter could control the locations where the motor will be activated in cells although it could also depend on the age and composition of the actin tracks:

Actin filaments are dynamic structures in which new ATP-actin monomers bind to the filament plus-end which are in general the closest to the membrane surface. Once the monomer is incorporated in the filament, ATP is hydrolyzed resulting in ADP-actin, which is less stiff and less stable. At the minus end, ADP bound actin form the “old” filament while at the + end, the youngest part of the filament is formed with ATP actin (Merino *et al.* 2018). Interestingly Zimmermann *et al.* (2015) show through *in vitro* motility assays that Myo6 undergoes as a single molecule processive motor longer run length on ADP-rich actin filament (while Myo5 binds preferentially to ADP.Pi-rich filaments). Actin + end being usually oriented near the plasma membrane, actin “age” could thus be a parameter that control Myo6 activation on precise location.

Actin track composition has been shown to modulate their association with myosins motors; six actin isoforms can be found in mammalian cells and despite presenting a high sequence identity, non-muscle Myo2A and B associate preferentially with α -actin, non-muscle Myo2C with β -actin and

Myo7A with γ -actin, highlighting possible regulation of motor recruitment by actin through actin isoform (Müller *et al.* 2013). Moreover, the actin binding tropomyosin was also found to modulate the ability of diverse myosin motors to bind to distinct actin tracks (Sckolnick *et al.* 2016; Gateva *et al.* 2017; Manstein *et al.* 2020). Although there is no evidence showing that actin track composition could modulate Myo6 recruitment, as pointed out by de Jonge *et al.* (2019), it could be an interesting aspect to explore.

F.3.d. Partners

Regulation of the Myo6 auto-inhibition could also directly be driven by its cellular partners. Using FRET experiments, Fili *et al.* (2017; 2020) show that partners NDP52 and Dab2 can unfold Myo6 (814-end) and Rai *et al.* (2022) shows that GIPC1 can unfold FLMyo6. Moreover Fili *et al.* (2017; 2020) demonstrate that partners NDP52, DNA and Dab2 can sequester the CBD and prevent its interaction with Myo6 Tail (Fili *et al.*, 2017; 2020) suggesting that once Myo6 unfold, partners could have the ability to stabilize the active form of Myo6.

French, Sosnick, and Rock (2017) show that artificial recruitment of Myo6 to peroxisomes through Dab2 significantly slow down peroxisome movement on microtubule tracks showing the ability of Dab2 to recruit a competent motor on this cellular compartment. In contrast, single molecule tracking in HeLa cells shows that Myo6 diffuses randomly in the cytosol when partner binding is disabled by mutation within the CBD (Dos Santos *et al.*, 2022). These findings assess the potential of partners for Myo6 activation.

Thanks to the recent findings described above (Fili *et al.* 2017; 2020; Dos Santos *et al.* 2022; Rai *et al.*, 2022), partner binding appears as a key parameter for Myo6 activation. Several of them have been proposed to be able to unfold Myo6. Yet, main evidence of Myo6 unfolding by partners have been assessed with FRET titrations that used the Myo6 Tail 814-end, and not the full length motor. The only study that used a full length motor has been published in 2022 (Rai *et al.*) and has shown the role of GIPC1 in this process but whether all partners are able to do so in the context of a full-length motor remains to clarify.

G. Modulation of the mechanical properties of the activated Myo6

G.1. Cargo nature

Partners play critical roles in addressing the motor to precise cellular locations (Fili *et al.* 2017, Tumbarello *et al.* 2012, Sahlender *et al.* 2005). They also have been proposed to trigger the unfolding

of the motor to activate it (see section F.3.d.). But considering the variety of mechanical roles and oligomeric states proposed for Myo6 (see section E), it is of outstanding interest to explore the potential of Myo6 partners to instruct Myo6 for a precise mechanical role, facilitating either anchoring, transporting or organizing actin among other functions (Figure 45). To that aim, understanding which partners can induce Myo6 oligomerization, dimerization or stabilize Myo6 as a monomer following its unfolding is of particular interest. Myo6 partners themselves exhibit various oligomeric states: Dab2 is monomeric while OPTN, NDP52 and GIPC1 are dimeric (Phichith *et al.* 2009; Kim *et al.* 2013; Shang *et al.* 2017; Dos Santos *et al.* 2022), ubiquitin can form long oligomeric chains (Akutsu, Dikic, and Bremm 2016) and clathrin can assemble in trikele or even cages (Halebian, Morris, and Smith 2017). This stoichiometry can also influence the way partners will instruct Myo6 for its function, attaching Myo6 monomeric motors together without direct contact between them or inducing direct dimerization between Myo6 molecules.

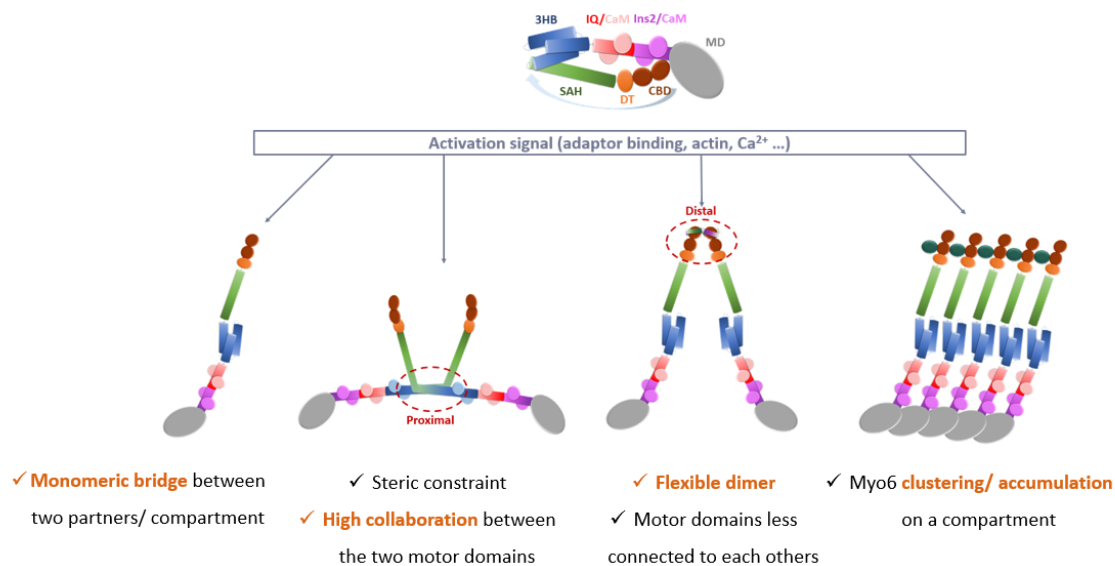


Figure 45: Myo6 oligomeric states instruct this motor for specific, distinct mechanical properties. Myo6 is represented in different conformations. The motor domain is colored in grey, the Insert-2 in purple, the IQ in red, the 3HB in blue, the SAH in green, the DT in orange and the CBD in brown. Once unfolded, Myo6 was proposed to adapt various conformation to perform its function. Myo6 was proposed to function as a monomeric bridge linking cargoes together (Hu *et al.* 2019), as a proximal dimer (Mukherjea *et al.* 2009; 2014), as a distal dimer (Yu *et al.* 2009) or as an assembly of monomers (Shang *et al.* 2017). Due to their different conformations and stoichiometries each of them could lead to a different function of Myo6. A more detailed characterization of these models is now required to determine which are relevant in Myo6 functions in cells, note that several of them could exist but would fulfill different mechanical functions.

Single molecule motility assays show that the **OPTN** dimer is able to make Myo6 processive (Phichith *et al.* 2009) and rotary shadowing confirmed that Myo6 is dimeric upon OPTN binding.

The X-ray structure of **Dab2** (675-713) with Myo6 CBD^c reveals that despite being monomeric, Dab2 can mediate indirect Myo6 dimerization through binding on two distinct binding sites of the CBD^c, promoting the formation of a 2:2 complex. ITC using a variety of Myo6 and Dab2 mutants and truncations reveals that the first interaction site results in high affinity (~310 nM) through hydrophobic interactions and a second binding site of lower affinity alone (>13 μM) that, when combined with the first binding site results in increased affinity (50-80 nM) and indirect dimerization (Yu *et al.* 2009). These results pointed out to a **distal dimerization** (Figure 45 and 46). More recently, FRET titration confirmed the ability of Dab2 to dimerize Myo6 814-end fragment (Fili *et al.* 2020) and seems to promote gating of the FLMyo6 upon increasing concentration of actin (Dos Santos *et al.*, 2022). It has been further confirmed in gliding filament assays that Dab2 activates Myo6 and makes the motor processive (Phichith *et al.* 2009; French, Sosnick, and Rock 2017; Rai *et al.* 2021) similarly to what was seen with OPTN (Phichith *et al.* 2009). Electron micrography consistently shows that Dab2 dimerizes FLMyo6.

But, even if both **OPTN and Dab2** can dimerize, in rotary shadowing only 2% of dimer were seen in Dab2 while 17 % were seen with OPTN in similar conditions (Phichith *et al.* 2009) which pointed out to the weaker ability of Dab2 to form dimers compared to OPTN. Consistently with low dimerization level using Dab2, single molecule and ensemble molecule motility assays show that Myo6 dimerized by Dab2 behaves differently than the artificially dimerized Myo6 (leucine zippered dimer, i.e., 100% dimers). Although the run lengths are similar, with Dab2, less motile events occurred with bigger pauses between them, showing that Dab2 enables Myo6 for a sparse processive motility. Interestingly, when either Dab2 mediated dimer or zippered dimers are observed on a minimal actin cortex, zippered dimer generates actin foci while Dab2 mediated dimers do not impact the overall organization of the actin network (Rai *et al.* 2021).

As a dimeric partner, we would expect **NDP52** to promote distal dimerization as proposed for OPTN. Yet, a FRET-based assay shows that if CBD dimerization can occur through binding to its dimeric partner NDP52, this is much weaker compared to the dimerization that NDP52 can promote with Myo6 814-end, suggesting a strong contribution of residues within the IQ-DT region for promoting Myo6 dimerization (Fili *et al.*, 2017). Fili *et al.*, 2017 proposed thus that **both distal and proximal dimerization** could occur upon NDP52 binding and that the type of dimer could be modulated by the variation of Myo6 partner concentration.

These comparisons highlight thus the potential of partners to modulate both the nature and the number of Myo6 dimers formed with thus a great potential for fine tuning of Myo6 mechanical properties.

In parallel, using a severely truncated fragment of Myo6 (1052-1096), [Shang et al. \(2017\)](#) has proposed that the **GIPC1** GH2 domain can interact with the Myo6 CBDⁿ forming oligomers using two opposite interfaces (5V6E). In AUC, the complex seems to oligomerize up to 5:5 complex (reached at 150 μM). They proposed that the two proteins could thus form long chains in an assembly of motors. In our hands, only very short fragments of Myo6 have this property. This kind of oligomerization could then allow Myo6 to perform a transporter role as a motor ensemble enabling very long processive runs ([Sivaramakrishnan and Spudich 2009](#)). Yet, this result might be an artefact since experiments from our lab demonstrate that longer Myo6 CBD fragments form a **1:1 complex** by multi-angle light scattering (MALS). [Rai et al. \(2022\)](#) supported in contrast that FLMyo6 and GIPC1 can form a 1:1 non processive complex, although the difference in stoichiometry may be due to the very low concentration of Myo6 used in the motility assays (pM) ([Figure 45 and 46](#)). Still, they found that GIPC1 was able to greatly enhance Myo6 motor velocity (2.5-fold increase compared to Myo6 alone) and to decrease dwell time in motility assays. In multiple motor motility assays, they even found that GIPC1-Myo6 ensembles display fast, smooth, processive movement on cellular actin networks showing the potential of the complex for transport. They proposed using FRET experiments that GIPC1 binding could result in 3HB opening. They thus proposed that GIPC1 may increase flexibility of the motor by opening 3HB and in so doing increase its velocity. But preliminary data of the Houdusse team ([Figure 46](#)) suggests that once unfolded, 3HB can also mediate proximal dimerization possibly orienting the motor towards anchoring functions. Overall, the impact of GIPC1 or Dab2 binding to the Myo6 motor remains to be clarified although it clearly appears that Dab2 and GIPC1 partners have very different impact on the Myo6 motor function in similar experimental set ups ([Rai et al. 2021; 2022](#)).

In contrast, **TOM1** (6J56; [Hu et al. 2019](#)), **clathrin light chain A** (6E5N; [Wagner et al. 2019](#)) were proposed to form a 1:1 complex with Myo6 on the basis of their crystallographic or NMR structure, although these studies did not look at the impact of these partners on the functional motility properties or the impact on possible proximal dimerization. Finally, a FRET study revealed DNA inability to dimerize Myo6 814-end excluding both proximal and distal dimerization upon DNA binding. [Hu et al. \(2019\)](#) thus hypothesized that, as a non processive monomer, Myo6 plays the role of a **bridge between between cellular compartments** ([Figure 45 and 46](#)), linking for example endosomes (via TOM1) and autophagy receptors through two different binding interfaces.

From various oligomeric states to various dimer architectures of Myo6 upon partner binding, all the results obtained on the study of Myo6-partner binding characterization (see above) highlight the unique ability of Myo6 partners to instruct the motor for a specific architecture and oligomeric state, which can result in various mechanical properties thus likely in various cellular mechanistic roles. Actually, this diversity of Myo6-partners complex structures could at least in

part explain why one single motor such as Myo6 can fulfill a wide range of cellular functions switching for example from an anchoring function to a transport function depending on the partner bound to the motor.

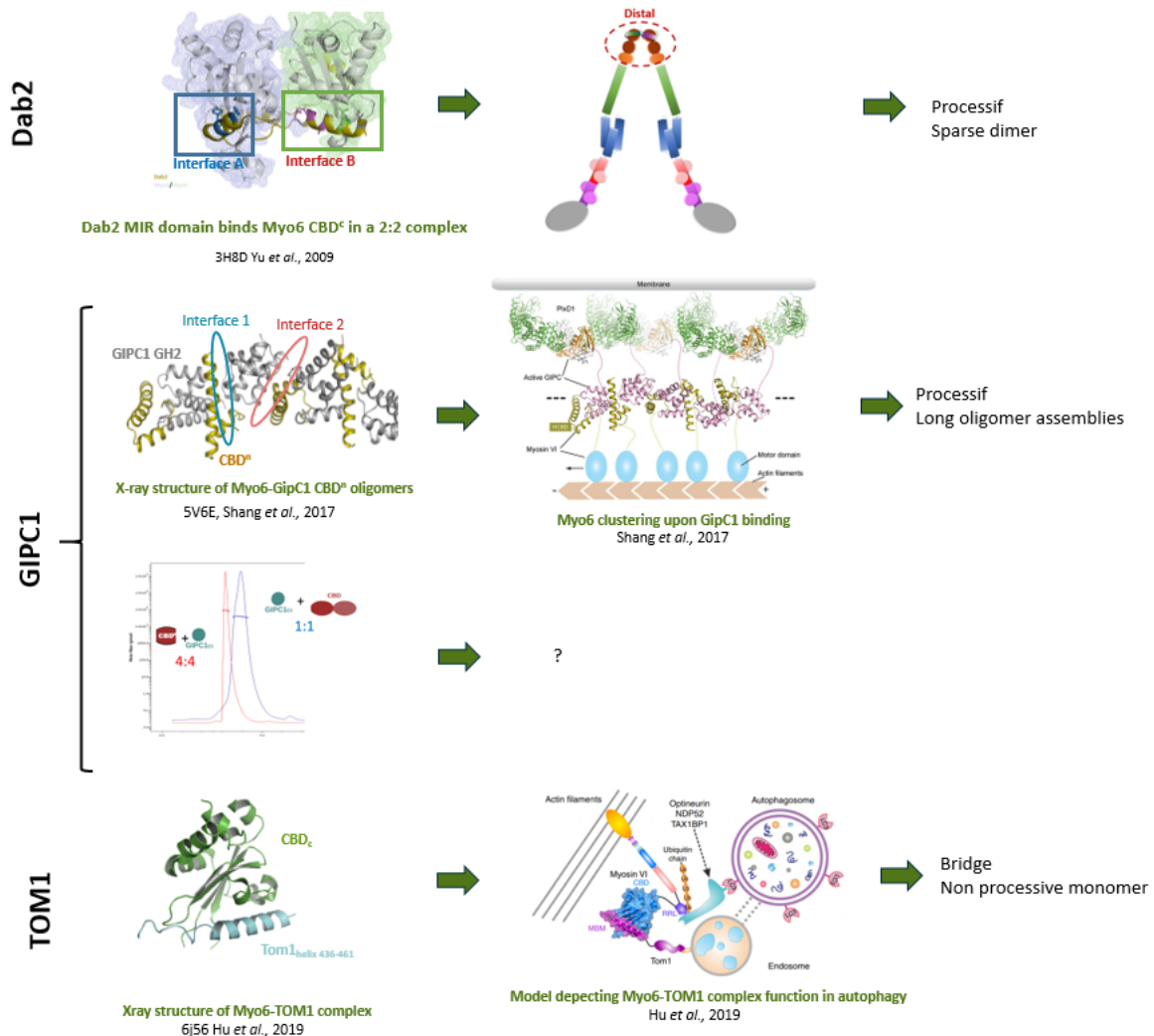


Figure 46: Myo6 oligomeric state induced by binding of various partners

(Top) Crystal structure of the 2:2 complex between Myo6 CBD^c and Dab2 fragment 675-713, each Dab2 interacts with the two CBD^c through two helices (interface A and interface B) (Yu et al. 2009). This 2:2 complex between Dab2 and CBD^c has been proposed to mediate distal dimerization (although an additional proximal dimerization remained to be explored and has been proposed using rotary shadowing (Phichith et al. 2009). The complex can mediate sparse processive motility (Rai et al. 2021).

(Center) Crystal structure of GIPC1 GH2 domain through 2 interfaces (Shang et al, 2017). In this context, it was proposed that GIPC1-Myo6 could function as large cluster of motors in cells. Such clusters have been shown to be able to mediate long processive run. Yet in contrast, SEC-MALS study of the GIPC1-Myo6 complex in our lab has shown that if CBD^c-GIPC1 can form oligomers, only 1:1 complex can form using longer Myo6 Tail fragment (979-end), (experiments carried out in Superdex 10/300 in 20 mM Tris pH 7,5; 100 mM KCl; 3 mM NaN₃ by former PhD

student Vicente Planelles-Herrero). A recent study proposed also a 1:1 complex between FLMyo6 and GIPC1 in biophysical assays (Rai et al. 2022) but the assays were carried out at low concentration. In this context, more studies are required to identify whether GIPC1 and FLMyo6 act as a 1:1 complex and whether a proximal dimerization can form after association of GIPC1 to FLMyo6.

(Bottom) Crystal structure of TOM1 436-461 with CBD^c, the two proteins interact as a 1:1 complex through an interface similar to one of the two binding sites of Dab2 on CBD^c: the so-called interface A. In this context, Myo6 has been proposed to act as a non-processive bridge able for example to reunite endosome (bound to TOM1) and autophagosome (bound to autophagy adaptors NDP52, OPTN or TAX1BP1) for fusion during autophagy (Hu et al. 2019). However, no evidence has been collected to support that such ability of a FLMyo6 monomer or dimer to bind two partners has yet been collected.

G.2. Cargo stiffness

Once unfolded, the stiffness of the cargo bound to Myo6 could also contribute to dictate mechanical properties of the motor to orient it towards a transport or anchoring function (Shrivastava et al. 2019). Indeed, in an optical trap, attaching artificially dimerized Myo6 (leucine zipper at aa992) to DNA origami using DNA linker of different lengths can mimic Myo6 attachment to either stiff (short DNA linker) or flexible (long DNA linker) cargos. These experiments reveal that under load >2pN, both Myo6 linked to flexible or stiff cargo can take steps on the actin track. However, steps are bigger (28 ± 13 nm) with the flexible cargo, while the time between the steps is smaller and the run length is longer suggesting that a flexible linkage between Myo6 and its cargo would facilitate its transport function. In contrast, under load, Myo6 associated with a stiff linkage exhibit longer stall events suggesting that load induced anchoring could be facilitated by stiff cargo binding to Myo6 (Shrivastava et al. 2019) reinforcing the importance of cargo in dictating the mechanical role of Myo6. Yet it should be noted that this study was performed using DNA origami to mimic cargo stiffness and not actual Myo6 cargoes. Thus, to complete this study it would be of great interest to extend it using various Myo6 binding partners.

H. Interest of having several partners interacting at once

Since the Myo6 Tail contains several, distinct sites of interaction with partners, this raises the possibility of having several partners interacting at once with Myo6. Moreover, Myo6 NI isoform colocalizes with both TOM1 and GIPC1 on APPL1-positive signaling endosomes (Tumbarello et al., 2012). In mice, during spermatid maturation, Myo6 localizes with two partners at once: GIPC1 and TOM1-L2 that localizes with it to the bulbar region of the TBCs and associates to Rab5 and APPL1 positive early endosomes (Zakrzewski et al. 2020). Although DOCK7 has been reported to bind to the RRL motif and TOM1L2 the WWY motif, a recent study shows that depletion of the WWY motif results

in loss of the DOCK7 interaction and loss of the RRL motif results in the loss of TOM1L2 interaction in RPE cells (O'Loughlin, Masters, and Buss 2018), suggesting a possible collaboration between the different partners being required for localization.

Actually, even if the localization is similar, the function pursued by the partners can vary; TOM1 and GIPC1 both colocalize with Myo6 on endosomes but immuno-cytochemistry in RPE cells shows that TOM1 depletion results in a dramatic loss of Myo6 on endosomes while with GIPC1 depletion, Myo6 localization loss is only partial (Tumbarello *et al.* 2012).

Thenceforth, the interest of having several partners collaborating should be pursued. With such collaboration, cellular roles could be smooth transition from one mechanical role to another as proposed in Zakrzewski *et al.* (2020), enhancing the mechanical properties of the motor or assuring redundancy.

Fili *et al.* (2017) highlights an important distinction between DNA and NDP52; while both can sequester the CBD prior to its binding to the rest of the Tail, only NDP52 can disrupt the interaction and promote unfolding of Myo6 814-end fragment once its interaction is formed. In this context, they proposed that Myo6 would need first to be opened by its nuclear partner NDP52 prior to DNA binding (Fili *et al.* 2017). They then pursue the relevance of this hypothesis in the context of Myo6 transcription function. As described in section D.4., addition of Myo6 or NDP52 to HeLaScribe extract increase the transcription level but strikingly, competition with Myo6 CBD^{NI} or CBD^c results in transcription decrease while the use of either the CBD^{LI}, CBDⁿ and CBD^{RAL} mutant does not decrease transcription supporting the fact that a partner is required for the recruitment to this localization. Intriguingly, this suggests a greater role of CBD^c than CBDⁿ in transcription whereas NDP52 has been reported to be a CBDⁿ partner suggesting that while NDP52 can enhance transcription, it may not mediate Myo6 interaction with RNAPII. Actually, immunoprecipitation of Myo6 and RNAPII shows using different Myo6 truncations that Myo6 CBD^c can nicely interact with RNAPII while CBDⁿ can only very weakly interact with it (Fili *et al.* 2017). Overall, it seems that Myo6 unfolding occurs through the RRL binding partners which free the CBD^c making its interaction with RNAPII possible through binding of DNA.

Possible collaboration between partners for assuring smooth transition between function was also proposed in prostate cancer LNCaP cells, both GIPC1 and LMTK2 were identified as Myo6 partners (Puri *et al.* 2010). Considering the localization of GIPC1 on APPL1 early endosomes and the role of LMTK2 in the delivery of endosomes to multivesicular bodies (Chibalina *et al.* 2007), the authors proposed that GIPC1 would first recruit Myo6 to early endosomes, then LMTK2 will address Myo6 to the perinuclear recycling compartment (Puri *et al.* 2010).

In autophagy, Myo6 can form a ternary complex with TOM1 and the autophagy receptors TAXBP1, NDP52 or OPTN according to immunoprecipitation from HEK293T cells (Hu *et al.* 2019). The SiTOM1 phenotype nicely mimics that of Myo6 depletion which results in defects in fusion of

autophagosomes with lysosomes and a delay in amphisomes formation ([Tumbarello et al. 2012](#)). Interestingly, NDP52, OPTN, T6BP depletion do not mimic this phenotype. Actually, as opposed to Myo6 depletion, the depletion of autophagy receptors impairs autophagosomes biogenesis. As, the Ubiquitin and Myo6 binding site overlaps on these adaptors, they may first link ubiquitinated cargo to LC3-autophagosomes and interact afterwards with Myo6 for autophagosomes fusion with lysosomes. The authors thus proposed that Myo6 is recruited to endosomes through TOM1. Then Myo6 will address the TOM1-positive early endosomes to autophagosomes through autophagy adaptor interaction (NDP52, OPTN, T6BP). Delay in fusion may be the result of an incorrect maturation of the autophagosomes (i.e., lack of TOM1-endosomes docking on autophagosomes).

Finally, in melanocytes (MNT-1), if OPTN seems to be important as a Myo6 associated partner for the constriction of tubular carriers, its depletion does not impair Myo6 localization at melanosomes ([Ripoll et al. 2018](#)) suggesting the existence of an addition unknown Myo6 partner to address Myo6 to melanosomes.

Overall, Myo6 location and mechanical properties are likely dictated by a collection of successive or simultaneous interactions with cargo proteins, lipids and actin network. Thus, cellular Myo6 works under various load, oligomeric states and concentration conditions, and this makes this motor able to perform a wide range of functions.

Objectives

This chapter explores structural insights of Myo6 mechanic regulation enabling its multifunctionality. Indeed, even if progress has been made in understanding how Myo6 function can be modulated through various signals (partners binding, calcium), mechanism that constricts full-length Myo6 selection, substitution and releases of cargos is not clearly established. Moreover, identification of key parameters able to orientate Myo6 mechanical characteristic towards anchoring, transporter or actin organizer function is still an on-going process: stiffness, the nature of the partner bound or the local Myo6 concentration has been proposed as key parameters.

Considering the growing importance of Myo6 in pathologies such as cancers and deafness, answering such questions is of particular interest as they are necessary to describe the precise role Myo6 plays in pathogenous processes, which can lead to the development of therapies targeting Myo6 in the future.

We thus aimed at providing further insights on the Myo6 auto-inhibited state properties via a structural and functional approach. Specifically, we aimed to explore the importance of the Motor domain nucleotide state and identify the relative contribution of interactions within the Tail or in between the CBD and the Motor to be able to determine precise conditions or pathogenous mutations favoring Myo6 opening and activation. In particular, the potential of partners for differential Myo6 activation has been explored. A particular focus of our research concerned the proximal dimerization. Indeed, while the potential of partners such as Dab2 to promote distal dimerization has been established, there is no clear evidence of Myo6 proximal dimerization upon partners binding or upon other activation pathways in a physiological context.

Our structural insights have been completed by experiments in cells to assess the relevance of our findings in a physiological context. In particular, we highlight the importance of the Myo6 auto-inhibition and dimerization in the context of endocytosis and melanosome maturation.

Results and discussion

A. Myosin VI activation: from the auto-inhibited state to its active forms

A.1. Methodology

A.1.a. Identifying the conditions stabilizing either a compact or an open conformation

As the Myo6 auto-inhibited state has been proposed to be a compact back-folded monomer, combination of SEC-MALS (steric exclusion chromatography multi angles light scattering) and SEC-SAXS (steric exclusion chromatography small angles light scattering) were used to determine Myo6 compacity and oligomeric state in several buffer conditions. Indeed, for a given molecular weight, elution time in SEC column is already indicative of the compacity of a protein and allows rather quick screening of buffer conditions for their impact on Myo6 compacity. MALS then allows precise measurement of the molecular weight of the protein allowing reliable estimation of the oligomeric state while SAXS provides information on the shape (Figure 47) and dimension of the protein. Microscale thermophoresis (MST) then allows *in vitro* estimation of K_D between different Myo6 fragments.

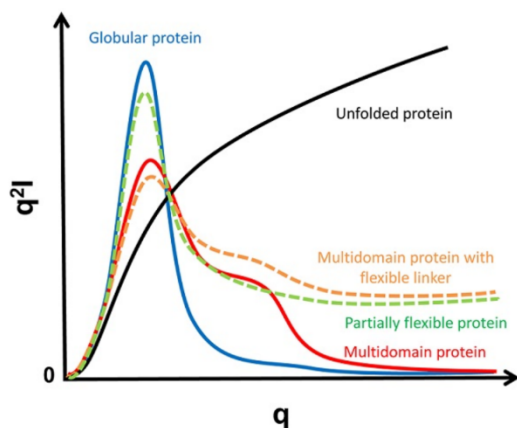


Figure 47: How to read a Kratsky plot (Stanford.edu)

Theoretical kratsky plot that can be obtained from SAXS for proteins of different shapes. q is the scattering vector $q=4\pi \sin(\vartheta)/\lambda$ with λ the radiation wavelength and 2ϑ the scattering angle.

Before I arrived in the team, using a combination of these techniques, preliminary data using a chimeric FL Myo6 construct (Motor domain from *Sus Scrofa* in fusion with the Tail domain from *Mus Musculus*, Figure 49) suggested that Myo6 is indeed able to adopt a compact and monomeric conformation upon addition of Mg.ADP.VO₄. (VO₄ is a P_i analog that stabilizes the myosin Motor in the MgADP.P_i state (i.e., pre-powerstroke state). In contrast, the open form of Myo6 is stabilized upon nucleotide removal in high salt (400 mM NaCl). Moreover, preliminary microscale thermophoresis experiments (MST) had revealed that when supplemented with Mg.ADP.VO₄, a Myo6 construct containing the Motor domain, the CaM binding motifs and the 3HB (1-917) can interact with the CBD with high affinity while addition of four point-mutations in a highly exposed CBD^c loop (D1157V, Y1159D, D1161R and Q1163V) was sufficient to lose the interaction (Figure 48). This loop had been reported to mediate Myo6 binding to DNA (Fili *et al.* 2017). Based on these data, a constitutively back-

folded Myo6 construct was engineered by fusing at the Myo6 N-terminus and C-terminus two subdomains (“Jo” and “In”) able to recognize each other and subsequently undergo strong attachment while a covalent bound would be created between them (Bonnet *et al.* 2017)(Jo-Myo6-In construct).

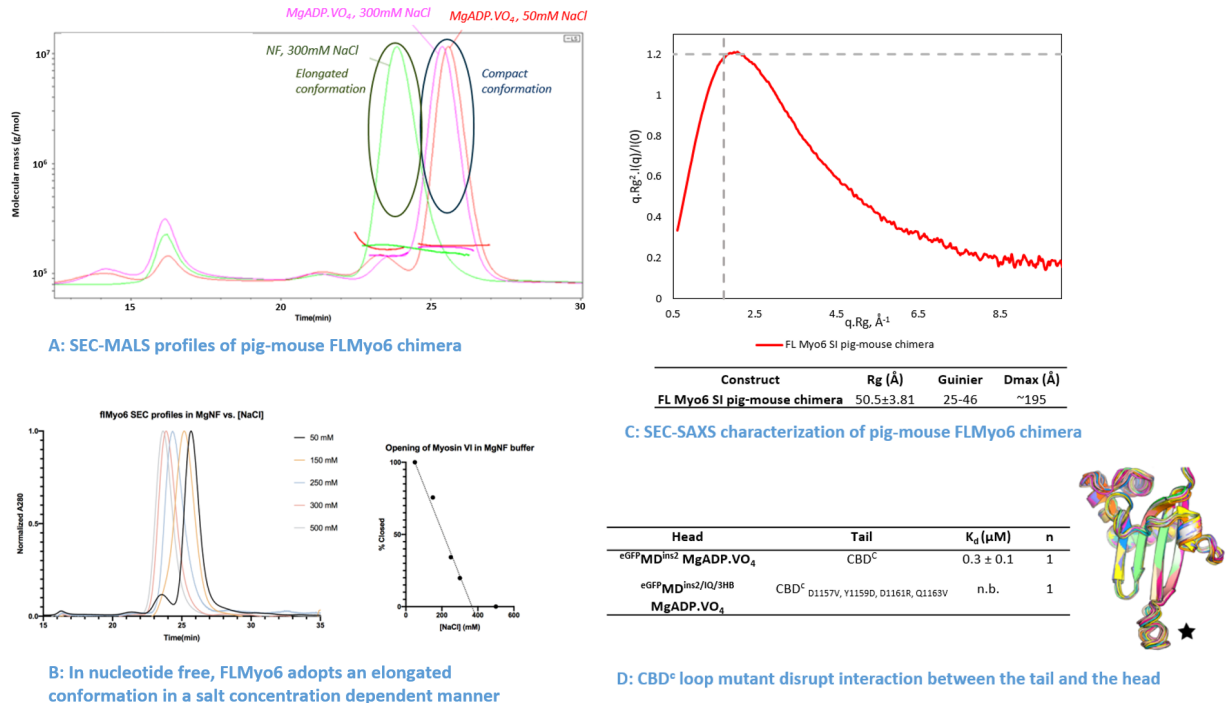


Figure 48: Characterization of Myo6 auto-inhibited state using FLMyo6 SI pig-mouse chimera

(A) SEC-MALS profiles of FL Myo6 SI pig mouse chimera in either MgADP.VO₄ buffer: 20 mM Hepes; 2 mM MgCl₂; 1 mM NaADP; 1 mM NaVO₄; 0.1 mM EGTA; 0.5 mM TCEP, 50 mM or 300 mM NaCl, pH 7.5 or NF buffer: 20 mM Hepes; 2 mM MgCl₂; 0.1 mM EGTA; 0.5 mM TCEP, 300 mM NaCl, pH 7.5. Myo6 remained monomeric in all buffers but switch from a compact state in Mg.ADP.VO₄ to an elongated one upon nucleotide removal in high salt condition. **(B)** (left) Normalized SEC profiles of full-length Myosin VI in different elution buffers. MgNF buffer: 20 mM Hepes; 2 mM MgCl₂; 0.1 mM EGTA; 0.5 mM TCEP, 50 to 500 mM NaCl, pH 7.5. (right) normalized elution volumes plotted against [NaCl] shows linear relationship between opening of FLMyo6 and salt concentration. Dashed line: arbitrary (visual) linear regression. Maximum opening of Myosin VI is expected to occur at ~380 mM NaCl in MgNF buffer. **(C)** (Top) Dimensionless Kratsky plot representation. Intersection of the dotted lines ((qRg)²l(q)/I(0) = 1.104 and qRg = √3) highlights the theoretical maximum of a folded protein. Full-length Myo6 in the presence of MgADP.AIF₄ (red) results in a bell-shape spectrum with a maximum close to (√3:1.104), which is typical of a globular folded protein. (Bottom) Table exhibiting Gyration radius and maximal diameter of Myo6 as calculated from SEC-SAXS data using the Guinier approximation **(D)** microscale thermophoresis table of CBD^c either WT or D1157V, Y1159D, D1161R and Q1163V mutant against Myo6 head fragments in 10 mM HEPES pH 7.5, 50 mM NaCl, 1 mM TCEP, 1 mM Na₃, 1mM MgADP, 1 mM VO₄ and 0.05% Tween-20. D1157V, Y1159D, D1161R and Q1163V mutations results in loss of binding. On the left, NMR structure of CBD^c (2KIA, Yu *et al.* 2009).

A black star highlights the highly conserved CBD^c loop that was mutated in this study (Vicente planelles-Herrero, Virginie Ropars, Carlos Kikuti and Inigo Urrutia).

But surface residues of the Tail and Motor domain-Lever arm regions are not fully conserved in between mouse and pig which may affect the way Myo6 back-folds (Figure 49 and 50). We thus first decided to repeat these experiments using the human FL Myo6 construct.

	Motor domain	
Human 1	MEDGKPVWAPHPTDGFQGNIVDIGPDSLTIIEPLNQKGTFLALINQVFPAAEDSKKDVEDNCSLMYLNEATLLHNKIVRYSKDRIYTYV	90
Pig 1	MEDGKPVWAPHPTDGFQGNIVDIGPDSLTIIEPLNQKGTFLALINQVFPAAEDSKKDVEDNCSLMYLNEATLLHNKIVRYSKDRIYTYV	90
Mouse 1	MEDGKPVWAPHPTDGFQGNIVDIGPDSLTIIEPLNQKGTFLALINQVFPAAEDSKKDVEDNCSLMYLNEATLLHNKIVRYSKDRIYTYV	90
Human 91	ANILIAVNPYFDIPKIYSS EA IKSYQGKSLGTRPPHVFAIADKAFRDMKVLK MS QSIIVSGESGAGKTENTKFLVRLYLTESYGTGQDIDD	180
Pig 91	ANILIAVNPYFDIPKIYSS EA IKSYQGKSLGTRPPHVFAIADKAFRDMKVLK LS QSIIVSGESGAGKTENTKFLVRLYLTESYGTGQDIDD	180
Mouse 91	ANILIAVNPYFDIPKIYSS DT IKSYQGKSLGTRPPHVFAIADKAFRDMKVLK MS QSIIVSGESGAGKTENTKFLVRLYLTESYGTGQDIDD	180
Human 181	RIVEANPILLEAFGNAKTVRNNSSRFGKFVEIHFNKSSVVGGFVSHYLLEKSRI CVQGKEERNYHIFYRLCAGASEDIRE KL LHLSSPDN	270
Pig 181	RIVEANPILLEAFGNAKTVRNNSSRFGKFVEIHFNKSSVVGGFVSHYLLEKSRI CVQGKEERNYHIFYRLCAGASEDIRE KL LHLSSPDN	270
Mouse 181	RIVEANPILLEAFGNAKTVRNNSSRFGKFVEIHFNKSSVVGGFVSHYLLEKSRI CVQGKEERNYHIFYRLCAGASEDIRE KL LHLSSPDN	270
Human 271	FRYLNRGCTRF F ANKETDKQILQNRKSP EY L K AGS K KDPLDDHGDFIRMC T AMKKIGLDDEEKLDLFRVAVGLHLGNIDFEEAGSTSG	360
Pig 271	FRYLNRGCTRF F ANKETDKQILQNRKSP EY L K AGS K KDPLDDHGDFIRMC T AMKKIGLDDEEKLDLFRVAVGLHLGNIDFEEAGSTSG	360
Mouse 271	FRYLNRGCTRF F ANKETDKQILQNRKSP EY L K AGS K KDPLDDHGDFIRMC T AMKKIGLDDEEKLDLFRVAVGLHLGNIDFEEAGSTSG	360
Human 361	GCNLKKNK SA Q S LEYCAELGLDQDDLRLVSLTRVMLT T AGG K GTVIK V PLK VE QANNARDALAKTVYSHLFDHVNRV N Q CF PFETSSY	450
Pig 361	GCNLKKNK ST Q A LEYCAELGLDQDDLRLVSLTRVMLT T AGG K GTVIK V PLK VE QANNARDALAKTVYSHLFDHVNRV N Q CF PFETSSY	450
Mouse 361	GCNLKKNK SA P S LEYCAELGLDQDDLRLVSLTRVMLT T AGG K GTVIK V PLK VE QANNARDALAKTVYSHLFDHVNRV N Q CF PFETSSY	450
Human 451	FIGVLDIAGFEYFEHNSFEQFCINYCNEK L Q Q FFNERILKE E QELYQKEGLGVNEVHYVDNQDCIDLIEA K LVGILDILDEENR L PQPSD	540
Pig 451	FIGVLDIAGFEYFEHNSFEQFCINYCNEK L Q Q FFNERILKE E QELYQKEGLGVNEVHYVDNQDCIDLIEA R LVGILDILDEENR L PQPSD	540
Mouse 451	FIGVLDIAGFEYFEHNSFEQFCINYCNEK L Q Q FFNERILKE E QELYQKEGLGVNEVHYVDNQDCIDLIEA V LVGILDILDEENR L PQPSD	540
Human 540	QHFT S AVH Q KHKDH F RL I PRK S KLAV H R N TRDDEGFII R H F AGAVCYET T Q F VEK N DALHMSLES L ICES R DK F IR E L F ES S TNN K D	630
Pig 541	QHFT S AVH Q KHKDH F RL I PRK S KLAV H R N TRDDEGFII R H F AGAVCYET T Q F VEK N DALHMSLES L ICES R DK F IR E L F ES S TNN K D	630
Mouse 540	QHFT S AVH Q KHKDH F RL I PRK S KLAV H R N TRDDEGFII R H F AGAVCYET T Q F VEK N DALHMSLES L ICES R DK F IR E L F ES S TNN K D	630
Human 631	TKQKAGKLSFI SVGNKFKTQLNLLDKLRSTGASFIRCIKPNLKMTSHHFEGAQILSQ L QCSGMVSVL D LMQGG F PSRAS F HELYNMY K	720
Pig 631	TKQKAGKLSFI SVGNKFKTQLNLLDKLRSTGASFIRCIKPNLKMTSHHFEGAQILSQ L QCSGMVSVL D LMQGG F PSRAS F HELYNMY K	720
Mouse 631	TKQKAGKLSFI SVGNKFKTQLNLLDKLRSTGASFIRCIKPNLKMTSHHFEGAQILSQ L QCSGMVSVL D LMQGG F PSRAS F HELYNMY K	720
Human 721	YMP K LARLD P RL F CKAL F KAL G LN E Y D YK F GL T K V F R PG K FA E FD Q IM K SD P D H LAE L V K R V N H W L CS R W K K V Q W C S L S V I K L K N K I	810
Pig 721	YMP K LARLD P RL F CKAL F KAL G LN E Y D YK F GL T K V F R PG K FA E FD Q IM K SD P D H LAE L V K R V N H W L CS R W K K V Q W C S L S V I K L K N K I	810
Mouse 721	YMP K LARLD P RL F CKAL F KAL G LN E Y D YK F GL T K V F R PG K FA E FD Q IM K SD P D H LAE L V K R V N L W L CS R W K K V Q W C S L S V I K L K N K I	810
Human 811	KYRAEACIK M Q T IR M W L C K R R H K PRIDGLVKG T L K R L DK F NE V S V L K D G K E P E M N K Q T K N L E I S I D L M A K I K S T M T T R E Q I Q K E Y D	900
Pig 811	KYRAEACIK M Q T IR M W L C K R R H K PRIDGLVKG T L K R L DK F NE V S V L K D G K Q E M S K Q V K D L E I S I D L M A K I K S T M T T R E Q I Q K E Y D	900
Mouse 811	KYRAEACIK M Q T IR M W L C K R R H K PRIDGLVKG T L K R L DK F NE V S V L K D G K E P E V N R Q T K N L E I S I D L M A K I K S T M T T R E Q I Q K E Y D	900
Human 901	ALVKSS E LL S AL Q KK Q EEEAER L RR I Q E EM E K E R K R R E D E R RR R KE E E E RR M K L E M E A K R K Q E E E R K K R E D E K R I Q A E V E A Q L A	990
Pig 901	ALVKSS AV LL S AL Q KK Q EEEAER L RR I Q E EM E K E R K R R E D E R RR R KE E E E RR M K L E M E A K R K Q E E E R K K R E D E K R I Q A E V E A Q L A	990
Mouse 901	ALVKSS E LL S AL Q KK Q EEEAER L RR I Q E EM E K E R K R R E D E R RR R KE E E E RR M K L E M E A K R K Q E E E R K K R E D E K R I Q A E V E A Q L A	990
Human 991	R Q R E E S Q Q AV L Q E R R DR E L A L R I A C S E A E L I S D E A Q A D L A L R R G P A V Q A T K A A A G T K K D L S K W K Y A E L R D T I N T S C D I E L L A A C R E	1080
Pig 991	R Q R E E S Q Q AV L Q E R R DR E L A L R I A C S E A E L I S D E A Q A D P L L R R G P A V Q A T K A A A G T K K D L S K W K Y A E L R D T I N T S C D I E L L A A C R E	1080

```

Mouse 991  RQREESQQALIVLLIQEQCRDRELALRIAQNESELISDEAQLISDLIALRRGPAVLIATKAAAGTKKLIDLSKWKYAELILRDTINTSCDIELLAACRE 1080
                                     SI *
Human 1081  EFHRRLLKVYHAWKSKNKKRNTETEQRAPKSVTDYDFAPFLNNSPQQNPALIQLIPARQLIEEILIEMNRQLIRRFFRIPFIRPADQYKDPQLIKKKGLIWW 1170
Pig 1081  EFHRRLLKVYHAWKSKNKKRNTETEQRAPKSVTDYDFAPFLNNSAQQNPALIQLIPARQLIEEILIEMNRQLIRRFFRIPFIRPADQYKDPQLIKKKGLIWW 1170
Mouse 1081  EFHRRLLKVYHAWKSKNKKRNTETEQRAPKSVTDYDFAPFLNNSPQQNPALIQLIPARQLIEEILIDMKRQLIRRFFRIPFIRPADQYKDPQLIKKKGLIWW 1170

Human 1171  YAHFDGPWIARQLIMELHDPKPPILLVAGKDDMEMCELNLEETGLTRKGALIEILPRQLIFEEIWERCGGIQYLILQNAIESRQARPTYATAMLILQLIL 1260
Pig 1171  YAHFDGPWIARQLIMELHDPKPPILLVAGKDDMEMCELNLEETGLTRKGALIEILPRQLIFEEIWERCGGIQYLILQNAIESRQARPTYATAMLILQLIL 1260
Mouse 1171  YAHFDGPWIARQLIMELHDPKPPILLVAGKDDMEMCELNLEETGLTRKGALIEILPRQLIFEEIWERCGGIQYLILQSAIESRQARPTYATAMLILQLIL 1260

Human 1261  LK 1262
Pig 1261  LK 1262
Mouse 1261  LK 1262

```

Pig: A0A4X1V1K9 Human: Q9UM54-3 Mouse: V9GX76

||: switch from pig to mouse Myo6 in the pig-mouse FL Myo6 chimera

|: LI position

Figure 49: Myo6 sequence alignment

Sequence is colored depending on the domains. * marks the surface residues that differs between the human Myo6 and the pig-mouse Myo6 construct used in the preliminary experiments

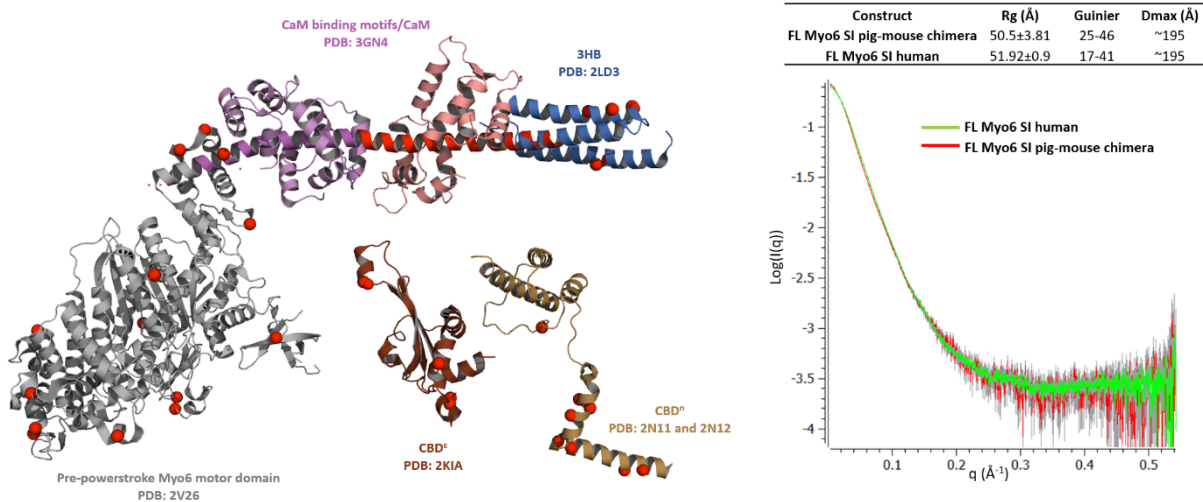


Figure 50: Surface residues conservation between pig and mouse Myo6

(Left) NMR and crystallographic structures of Myo6 1-917 and CBD fragments are represented in cartoon and orientated and positioned using overlapping parts of the structures (Ins2 is used as a reference to align 3GN4 and 2V26 together while LI is used as a reference to align 2N11 and 2N12). Non-conserved surface residues are represented as red spheres. (Right) SEC-SAXS on Superdex 3.2/300 column pre-equilibrated in 20 mM hepes; 200 mM NaCl; 2 mM MgCl₂; 1 mM NaADP; 1 mM AlF₄ (P_i analog), 0.1 mM EGTA, 1 mM DTT

I thus performed a SAXS study that shows that human FL Myo6, overall, behaves the same as pig-mouse Myo6: the protein remains closed in MgADP.VO₄ and opens upon nucleotide removal in high salt. SEC-SAXS data collected on buffers containing the Mg.ADP.P_i analog comparing the human and chimera Myo6 compact conformation: no significant changes are found. Yet, gel filtration suggests that human Myo6 back-folded conformation would be more stable than the pig/mouse chimera as 400 mM NaCl was found to be sufficient to fully shift the Myo6 pig-mouse chimera elution peak, while it is not the case for the human Myo6: a second and significant peak corresponding to a compact conformation can be seen at 13.8 mL (although the main peak at 12 mL corresponds to the elongated conformation) (Figure 51). Comparison of pig-mouse chimera and human Myo6 sequence highlights differences in polarity/charge of several surface residues between the two constructs that could be responsible of weaker polar contacts within the chimera enabling easier opening upon salt addition.

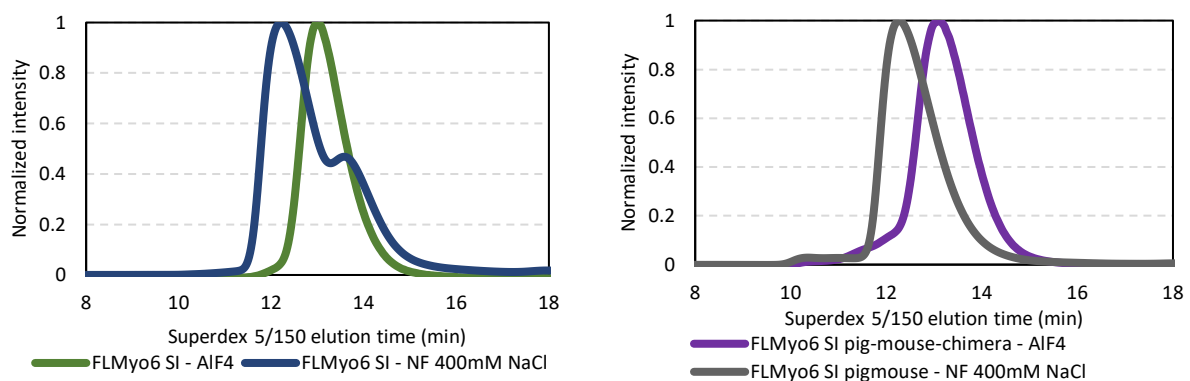


Figure 51: Myo6 pig-mouse chimera opens more easily upon salt concentration

SEC profiles on Superdex 3.2/300 column pre-equilibrated in 20 mM Hepes; 200 mM NaCl; 2 mM MgCl₂; 1 mM NaADP; 1 mM AIF₄ (P_i analog), 0.1 mM EGTA, 1 mM DTT or in 20 mM Hepes; 400 mM NaCl; 2 mM MgCl₂; 0.1 mM EGTA, 1 mM DTT. FLMyo6 elution peak shifts upon nucleotide removal in high salt concentration conditions. This suggests that Myo6 adopt a more elongated shape. For the human FLMyo6 (left panel), upon nucleotide removal in high salt concentration conditions, a small peak can be seen on the SEC profile at ~14mL in addition of the main peak at ~12mL. This suggests that a fraction of the human FLMyo6 remains closed even upon nucleotide removal in high salt concentration conditions.

Additionally, triplicate affinity measurements were performed between the CBD and the Myo6 MD^{Ins2-IQ-3HB} (1-917) in microscale thermophoresis to confirm the preliminary results and get a reliable estimation of the K_D. Additionally, we looked at the affinity of the CBD against either MD (1-789), MD^{Ins2} (1-816) and Ins2-IQ-3HB (1-917) to gain greater insights on the relative influence of all the structural elements proposed to maintain the Myo6 back-folded conformation.

Thanks to all the knowledge gathered on Myo6 opened and closed conformations, a combination of SEC-SAXS and SEC-MALS could finally be applied to the characterization of (1) the Myo6 engineered construct designed to be constitutively back-folded (Jo-Myo6-In) and (2) mutants suspected to trigger Myo6 opening. My role in the project was to perform all biochemical steps, in particular for the FL motors and partners in order to eliminate fully the proteolysis fragments that are sometimes present in a preparation. In addition, I took in charge the SEC-SAXS study while Carlos Kikuti, a research engineer in our time took in charge the SEC-MALS experiments. Additionally, Carlos Kikuti, the research engineer in our team pushed forward the characterization of the Jo-Myo6-In in negative staining, thanks to a collaboration with Daniel Levy's team (Institut Curie), to get more detailed information of the overall shape and organization of the Myo6 back-folded conformation.

To complete this structural study, we collaborated with Cédric Delevoye (Institut Curie) and Lee Sweeney's team (University of Florida) to set up functional assays. Lee Sweeney's team performed actin-based ATPase activity measurements on the Myo6 to pursue the impact of back-folding and opening on Myo6 activation while I took in charge the purification optimization of Myo6 and partners constructs needed for these experiments. For the cell-based assays, I participated in analyzing the cell-based assays on melanosomes that were performed by Franck Mayeux, an engineer in our team under the guidance of Cédric Delevoye, a researcher notably specialized in melanosomes. These cell-based assays allowed us to monitor the co-distribution of either constitutively open or back-folded Myo6 in cells with melanosome markers to gain insight on the impact of back-folding dysregulation on Myo6 recruitment in cells. I was also in charge of animating with Anne Houdusse and Lee Sweeney the working group that was gathering on meetings once a week. The goal of these meetings was to make sure of the quality and the reproducibility of the data the teams had obtained, proposing new experiments when needed, so that the results from our multi-disciplinary approaches would be organized in a manuscript.

A.1.b. Proximal dimerization

Before I joined the research on Myo6's ability to dimerize on its own, SEC-MALS was used to determine the oligomeric state of several Myo6 fragments in the 3HB-SAH area as [Mukherjea et al. \(2009\)](#) had pointed out that the Myo6 1-940 fragment was sufficient to allow processivity, thus highlighting the existence of this proximal dimerization region. The peptide identified as sufficient to allow proximal dimerization was crystallized and its structure was determined. These studies were performed by Elena Sirkia and Carlos Kikuti, engineers in our lab. Based on this structure, the triple mutant T888D, R892E and V903D was designed to disrupt proximal dimerization (without affecting the stability of the folded 3HB) and its efficiency was confirmed in SEC-MALS.

But all these results were performed on peptides *in vitro*, so finally, to confirm the relevance of this model of proximal dimerization in a more physiological context, we introduced the mutations T888D, R892E and V903D within the FLMyo6 to check its impact on Myo6 motility using single-molecule assays through a collaboration with Lee Sweeney's lab. Finally, through this collaboration, we also checked the impact of these mutations T888D, R892E and V903D on transferrin uptake in HeLa cells.

A.1.c. Recruitment and activation of Myo6 by its partners

Our model of the Myo6 auto-inhibited state suggests that the ability of the protein adaptor to interact with Myo6 could depend on its binding site on the motor. To challenge this hypothesis, we explored the ability of RRL and WWY adaptors to differentially recruit Myo6 and activate it either as an active monomer or dimer.

Pull-down assays were first carried out to explore the ability of the various partners to bind Myo6 in conditions favoring either opening or back-folding *in vitro*. Then, the ability of partners to recruit Myo6 in cell was explored using MNT-1 cells (human melanoma cells). To design this assay, we took advantage of the work of a former Post-Doctoral researcher in our team: Karl Petersen that had revealed that addition to FLMyo6 NI of a point mutation I1072A previously reported to prevent the interaction between the MIU domain and ubiquitin (He *et al.* 2016) results in loss of Myo6 endogenous recruitment to melanosome. We thus decided to fuse the Myo6 adaptor with a melanosome targeting tag (MST, Ishida *et al.* 2014) enabling their addressing to melanosome and looking at their ability to rescue Myo6 recruitment to melanosome. These experiments were performed by the cell biologist engineer of our team, Franck Mayeux.

Finally, the ability of the Myo6 adaptor to activate Myo6 as either a functional monomer or a dimer was monitored by Tianming Lin from Lee Sweeney's lab via performing actin-based ATPase. Indeed, ATPase assays was a very clear way to monitor whether binding of adaptors unfolds (releases auto-inhibition) and thus increases Myo6 ATPase rate. In addition, it gives an indirect information on the possibility of gating between the two heads when Myo6 forms a dimer. As described above (see section E), formation of a Myo6 dimer results in an unusual "gating" enabling coordination between the two heads of the Myo6 dimer which results in a 2-fold decrease of Myo6 ATPase rate per head compared to a Myo6 monomer.

These assays were carried out with partners Dab2, TOM1 and GIPC1 and we used their Myo6 binding region to avoid domains that might regulate exposure of the minimal interaction domain for the binding of Myo6 (MIR).

CBDⁿ partner: GIPC1

GIPC1 is a CBDⁿ RRL motif adaptor (section C.2.a.) containing an N-terminus GH1 domain allowing dimerization, a PDZ domain allowing binding to various cellular partners notably APPL1, which mediate its recruitment to APPL1-positive endosomes, finally a GH2 domain that mediates its interaction with Myo6 (Figure 52).



Figure 52: GIPC1 organization

GIPC1 contains a N-terminus GH1 domain allowing dimerization, a PDZ domain allowing binding to various cellular partners notably APPL1 and a GH2 domains able to mediate interaction with Myo6.

Although the GIPC1-Myo6 complex was presented as an oligomer based on AUC and the co-crystal structure of GIPC1 with a highly truncated CBDⁿ, preliminary data gathered by the Houdusse team before I joined the team suggests that GIPC1 may not oligomerize Myo6 but rather promote Myo6 internal dimerization (see section G.1.). GIPC1 was thus an adaptor of particular interest to look at the ability of an RRL adaptor to unfold full-length Myo6 and to challenge and complete our model of Myo6 proximal dimer.

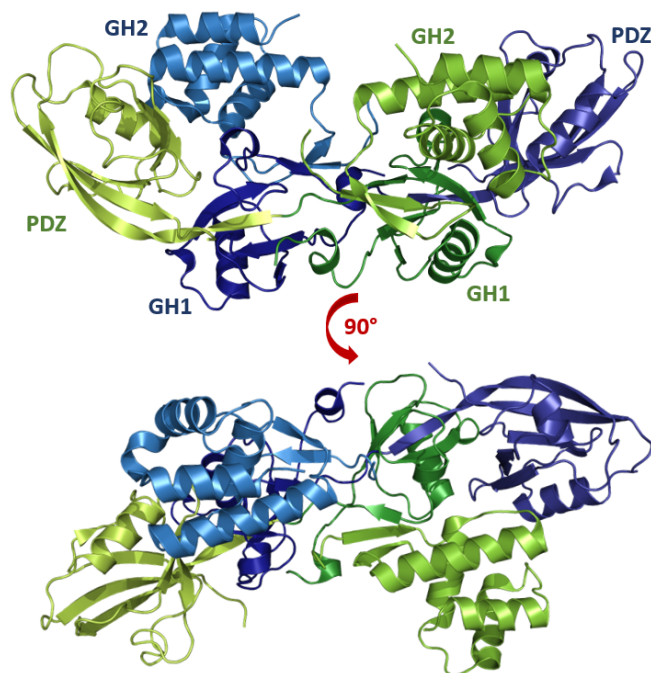


Figure 53: GIPC1 auto-inhibited state prevents binding to Myo6

The GIPC1 dimer (PDB: 5V6B; Shang et al. 2017), with one copy in Green and the other one in blue. GH1 of the first dimer is found to interact with the PDZ of the second one resulting in the formation of a dimer.

Importantly, the GIPC1 52-333 crystal structure reveals the organization of the GIPC1 dimer as a swapped dimer in which GH1 and PDZ interact together (PDB: 5V6B, [Shang et al. 2017](#)) ([Figure 53](#)). The GH2 domain folds on the PDZ hindering the Myo6-GIPC1 binding interface. This dimer has thus been proposed to constitute an auto-inhibited state of GIPC1 in which GIPC1 cannot bind to Myo6 ([Shang et al. 2017](#)). They additionally proposed that binding of a PDZ partner would be required to destabilize the GIPC1 dimer enabling Myo6 binding. Indeed, GIPC1 52-333 was co-crystallized with the PDZ partner plexin D1 and although GIPC1 was not degraded according to SDS page gels of the crystals, the GH2 domain could not be seen in the electron density, the authors thus proposed that GH2 is flexible and possibly more available for Myo6 due to GIPC1 conformational changes occurring upon plexin D1 binding ([Shang et al. 2017](#)). Moreover, addition of a PDZ partner improves Myo6-GIPC1 binding in pull-down ([Naccache, Hasson, and Horowitz 2006](#)).

Due to the existence of this GIPC1 auto-inhibited state and the possible reduction in binding affinity for the FL GIPC1 in its capacity to interact with Myo6, we decided to work with GIPC1 constructs containing only the GH2 domain to ensure Myo6 binding in our assays. The ability of GIPC1 GH2 to bind Myo6 was then confirmed by microscale thermophoresis in our hands ([Table 10](#)). Finally, as I1072 is present in CBDⁿ near the GIPC1 binding site, we confirmed with this assay that the mutation I1072A does not impair GIPC1 binding. Note that the I1072A mutation was extensively used to monitor the Myo6 recruitment on melanosome in MNT-1 cells.

	Adaptor	Myo6 Tail	K _D	n
Interaction with Gipc1	Gipc1 _{GH2 255-end}	YFP ⁺ CBD	164 ± 51 nM	3
	Gipc1 _{GH2 255-end}	YFP ⁺ CBD _{I1072A}	90 ± 34 nM	2

Table 10: GIPC1 interaction with the Myo6 CBD

MST done in 20 mM BisTris pH6.5, 100 mM KCl, 1 mM DTT, 0.05% tween or in 20 mM BisTris pH6.5, 100 mM KCl, 1 mM DTT, 0.05 % tween

CBDc partner: TOM1

TOM1 is a CBD^c WWY motif adaptor (section C.1.c) containing an N-terminus VHS domain and a GAT domain which mediates interaction with TOLLIP and ubiquitin. Moreover, TOM1 C-terminus can bind clathrin through residues 300-366 ([Seet and Hong 2005](#)) and double hybrid assays suggest that TOM1 binds Myo6 within its last 104 amino acids ([Tumbarello et al. 2012](#)) ([Figure 54](#)).

VHS domains are found in several proteins that are thought to be key in trafficking events. The VHS domain could facilitate membrane association ([Wang et al. 2010](#)). Although the VHS domain

structure has been solved at 1.5 Å for TOM1 (1ELK; [Misra, Beach, and Hurley 2000](#)), its exact function is not clear despite the fact that it mediates key interaction(s) in trafficking events. As it does not participate to Myo6 binding, we thus excluded this domain from our study.



Figure 54: TOM1 organization

TOM1 contains a N-terminus VHS domain, a GAT domain allowing binding to various cellular partners notably TOLLIP and a myosin binding motif (MBM) within its C-terminus.

For cell-based assays, we opted for TOM1 299-end as its interaction with Myo6 was reported in [Tumbarello et al. 2012](#). For biophysical and biochemical assays, we first generated a serie of TOM1 C-terminus truncations to confirm their stability and ability to bind Myo6 *in vitro* ([Table 11](#)). I characterized the affinity for Myo6 of all these constructs using microscale thermophoresis and kept Tom1₂₀₇₋₄₉₂ for our pull-down assays as this construct exhibits the highest affinity for Myo6 and colors nicely in coomassie blue.

Tom1	Myo6	K _D (nM)	n
Tom1 ₃₉₄₋₄₆₁	^{yfp} Myo6 _{1035-fin}	878 ± 321	2
Tom1 ₄₀₈₋₄₆₁	^{yfp} Myo6 _{1035-fin}	4024 ± 1836	1
Tom1 ₂₀₇₋₄₉₂	^{yfp} Myo6 _{1035-fin}	444 ± 135	2
Tom1 ₂₀₇₋₄₆₁	^{yfp} Myo6 _{1035-fin}	554 ± 180	2

Table 11: TOM1 interaction with Myo6 CBD

MST done in 20 mM BisTris pH6.5, 100 mM KCl, 1 mM DTT, 0.05 % tween or in 20 mM BisTris pH 6.5, 100 mM KCl, 1 mM DTT, 0.05 % tween

During the course of my PhD, a crystal structure of the Myo6 CBD^c bound to TOM1 revealed that the Myo6 binding motif (MBM) of TOM1 forms a single helix between residues 436 and 461 that able to interact with Myo6 in a 1:1 complex with a K_D of ~630 nM (determined through ITC) ([Hu et al. 2019](#)). For ATPase assays we thus switched for this well characterized TOM1 fragment instead (^{yfp}TOM1₄₃₆₋₄₆₁).

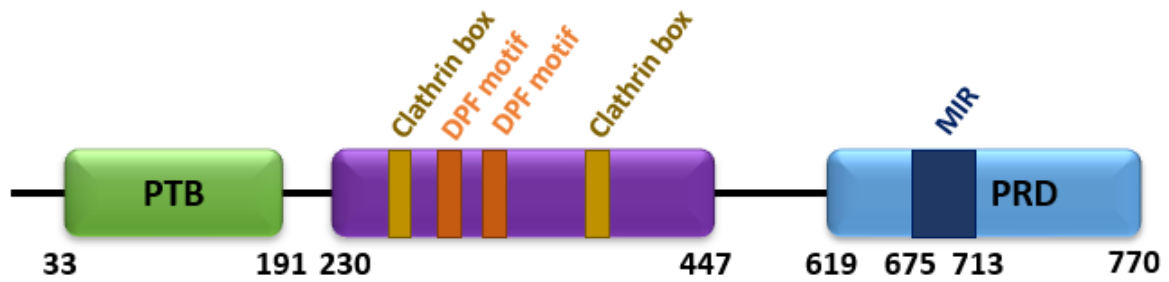


Figure 54: Dab2 organization

Dab2 contains a N-terminus phosphotyrosine-binding (PTB) domain. The region between residues 230 and 447 is only present in isoform p96 and contains clathrin box and Asp-Pro-Phe (DPF) motifs. *Dab2* C-terminus is a proline rich domain (PRD) that notably mediates interaction with Myo6 through the Myo6 interacting region (MIR).

Dab2 contains a phosphotyrosine-binding (PTB) domain at its N-terminus that mediates binding to PtdIns(4,5)P(2) and a proline rich (PRD) C-terminus. As opposed to the p96 isoform, the p67 isoform lacks residues 230-447 that mediates interaction with clathrin (clathrin box) and with α -adaptin (DPF motif) in clathrin-coated pits. Both isoforms can interact with Myo6 through the Myo6 interacting region 675-713 (MIR) (Figure 54). For our study, we used the Dab2 650-end construct, which was used in Fili *et al.*, 2020 and was a kind gift of the Toseland lab. In our hand, this construct exhibits submicromolar affinity in the same range as the TOM1 construct (Table 12).

	Adaptor	Myo6 Tail	K _D	n
Interaction with Dab2	Dab2 _{650-end}	YFP ^{CBD}	408 ± 236 nM	2
Interaction with TOM1	Tom1 ₂₀₇₋₄₆₁	YFP ^{CBD}	554 ± 180 nM	2

Table 12: TOM1 and Dab2 interaction with Myo6 CBD

MST done in 20 mM BisTris pH6.5, 100 mM KCl, 1mM DTT, 0.05 % tween or in 20 mM BisTris pH 6.5, 100 mM KCl, 1 mM DTT, 0.05 % tween

A.2. Paper

How Myosin VI Traps its Off-State, is Activated and Dimerizes

Louise Canon¹, Carlos Kikuti¹, Vicente J. Planelles-Herrero¹, Tianming Lin², Franck Mayeux¹, Helena Sirkia¹, Young il Lee², Leila Heidsieck¹, Léonid Velikovskiy¹, Amandine David¹, Xiaoyan Liu², Dihia Moussaoui¹, Emma Forest^{1,3}, Peter Höök², Karl J. Petersen¹, Aurélie Di Cicco⁴, Julia Sires-Campos⁵, Daniel Lévy⁴, Cédric Delevoye⁵, H. Lee Sweeney^{2,*}, Anne Houdusse^{1,*}

¹ Structural Motility, UMR 144 CNRS/Curie Institute, PSL Research University, 26 rue d'Ulm, 75258 Paris cedex 05, France

² Department of Pharmacology & Therapeutics and the Myology Institute, University of Florida College of Medicine, PO Box 100267, Gainesville, Florida 32610-0267, United States.

³ École Nationale Supérieure de Chimie de Montpellier, 240 Avenue du Professeur Emile Jeanbrau, 34090, Montpellier, France.

⁴ Institut Curie, Université PSL, Sorbonne Université, CNRS UMR168, Laboratoire Physico-Chimie Curie, 75005 Paris, France

⁵ Structure et compartimentation membranaire, UMR 144 CNRS/Curie Institute, PSL Research University, 26 rue d'Ulm, 75258 Paris cedex 05, France.

* co-corresponding authors: anne.houdusse@curie.fr; lsweeney@ufl.edu

Abstract

Myosin VI (Myo6) is the only minus-end directed nanomotor on actin, allowing it to uniquely contribute to numerous cellular functions. As for other nanomotors, proper functioning of Myo6 relies on precise spatio-temporal control of motor activity via a poorly defined off-state and interactions with partners. Our structural, functional, and cellular studies reveal key features of myosin regulation and indicate that not all partners can activate Myo6. TOM1 and Dab2 cannot bind the off-state while, GIPC1 binds Myo6, releases its auto-inhibition and triggers proximal dimerization. Myo6 partners thus differentially recruit Myo6. We solved a crystal structure of the proximal dimerization domain, and show that its disruption compromises endocytosis in HeLa cells, emphasizing the importance of Myo6 dimerization. Finally, we show that the L926Q deafness mutation disrupts Myo6 auto-inhibition and indirectly impairs proximal dimerization. Our study thus demonstrates the importance of partners in the control of Myo6 auto-inhibition, localization, and activation.

Introduction

Myosin motor proteins generate force and/or movement from ATP hydrolysis when associated with actin filaments. Conformational changes in the motor as it progresses from ATP hydrolysis to release of inorganic phosphate and ADP on actin are amplified into large movements via a calmodulin (CaM) or light chain binding region referred to as the “Lever arm” (Fig. 1A). To control the functions of myosin motors in cells, the ATPase activity of the motor and its ability to interact with actin must be regulated both spatially and temporally. Thirteen different classes of myosin motors serve diverse cellular functions in mammalian cells¹. The regulation of their motor activity is however poorly characterized. A general theme for the control of motor activity is the formation of intra-molecular interactions involving the C-terminal Tail region and the Motor domain of these motors. In the active form of the motor, the Tail region interacts with itself or cellular partners. The best understood is the case of the dimeric myosin II (Myo2) class² and myosin V (Myo5) class³. In cardiac muscle, impairment in the stabilization of the myosin off-state leads to severe cardiomyopathies⁴. Whether lack of regulation of unconventional myosins can also lead to pathology has not been demonstrated.

Perhaps the most divergent form of regulation is emerging for Class VI (Myo6), VIIa (Myo7a), and X (Myo10) myosins, which all contain regions of extended stable single alpha helices (SAH). Indeed, while they are back-folded monomers in their inactive form⁵⁻⁸, these motors can self-associate to form active dimers upon activation⁹⁻¹². How back-folding is stabilized is unknown and the nature of the dimerization following unfolding has only been elucidated for Myo10^{10,12}, which forms an anti-parallel coiled-coil immediately following the SAH. The SAH thus extends the Lever arm in the case of Myo10^{9,13}. Whether this is also the case for the dimeric Myo6 is debated and requires elucidation of its dimerization region^{12,14-18}. The manner in which the motor is dimerized and the composition of its Lever arm greatly influence its function. A distinctive dimerization region in Myo10 allows the dimer to easily reach out for neighboring actin tracks and participate in filopodia formation¹³, unlike the vesicle transporter, Myo5, that makes multiple steps on a single actin track.

As a minus-end directed actin motor, Myo6 performs unique cellular roles (reviewed in¹⁹), including endocytic vesicle trafficking and maturation, stereocilia maintenance²⁰ and melanosome maturation²¹, among many others. For these cellular functions, Myo6 must associate with different binding partners, such as Dab2, GIPC1 and TOM1 in distinct endosomal compartments²²⁻²⁴ and NDP52 in autophagy and in RNA Polymerase II transcription²⁵. Initially characterized as a deafness gene²⁰, Myo6 is also overexpressed in aggressive cancers^{26,27} and its depletion reduces cell migration and proliferation^{26,27}.

Full-length Myo6 (FLMyo6) was characterized as a back-folded monomer *in vitro*^{7,8}, which was confirmed to exist in cells by FLIM (Fluorescence lifetime imaging microscopy)²⁵. TOM1 and Dab2 bind Myo6 through its WWY motif on the C-terminus part of its cargo-binding domain (CBDⁿ; Fig. 1A) while GIPC1 and NDP52 bind the RRL motif on the CBDⁿ (Fig. 1A). FRET studies showing that these partners can unfold constructs lacking the Myo6 Motor domain (MD) led to the proposition that all partners could activate Myo6 upon binding^{25,28,29}. However, whether the WWY and RRL motifs are both accessible in the FLMyo6 back-folded state is unknown. Detailed studies of Myo6 recruitment are required to investigate the role of partners in the spatio-temporal regulation of its cellular activity.

The configuration of the Myo6 active state, the nature of its Lever arm and its oligomeric state can make critical differences in the way the force produced by the motor is used^{17,30,31}. In fact, Myo6

is well adapted to transport as well as to anchor, depending on the load it is working against, according to single molecule assays³². Although the capacity of partners to favor either monomeric, dimeric or oligomeric assemblies has been described^{14,25,28,29,31,33-35}, the active configuration required to perform the different cellular roles of Myo6 is unknown. *In vitro* studies have identified a proximal dimerization region^{12,18}, but its role for the cellular function of Myo6 is not established, nor is the structure of this region. Furthermore, it is not known whether the dimerization occurs following partner binding, and whether all partners lead to the same motor configuration, which ultimately will determine the nature of the effective Lever arm and mechanical performance of the motor.

A detailed description of the Myo6 off-state, a structural characterization of the proximal dimerization region, and the role of partners in Myo6 regulation are all essential to understand how Myo6 function is regulated in cells. Here we used structural and functional assays to thoroughly investigate these properties of Myo6. We demonstrate that not all partners can relieve Myo6 auto-inhibition since not all binding sites are accessible, and importantly we solved the structure of the proximal dimerization domain and demonstrate its validity.

Results

ADP.P_i bound to the motor strongly stabilizes the off-state conformation of Myo6

Previous biophysical characterizations of the Myo6 back-folded state identified contacts between the Myo6 Lever arm and CBD (Fig. 1A)^{25,36}. However, a possible role of the Motor domain in back-folding remains to be clarified. *Size Exclusion Chromatography coupled with Multi-Angle Light Scattering* (SEC-MALS) and *SEC coupled with Small-Angle X-ray Scattering* (SEC-SAXS) experiments (Sup Fig. 1A-C; Fig. 1B) indicate that FLMyo6 adopts a compact conformation in the presence of ADP.P_i analogs (Radius of gyration (Rg) = 49.23 ± 0.92 Å) (Fig. 1B-C; Sup Fig. 1C) even at high salt concentration (~425 mM NaCl) (Sup Fig. 1A-B). In contrast, when no nucleotide is present (nucleotide-free (NF) condition), FLMyo6 shifts from a compact to an elongated conformation in a salt concentration-dependent manner (at high salt, Rg = 84.18 ± 4.33 Å, elution 1 mL earlier from SEC-MALS) (Fig. 1B; Sup Fig. 1A-C). Overall, high salt dependency of FLMyo6 opening, combined with the lack of salt dependency in presence of a nucleotide, suggests that the Lever arm and the Tail are held together *via* electrostatic interactions, while the interactions that keep the Tail back-folded on the Head require the Motor domain to be in a nucleotide-bound state of its cycle (Fig. 1D). At very low salt (10 mM KCl) and in the presence of actin, FLMyo6 consumes ATP ~10 fold slower than the Tail-less construct MD^{Ins2} (Fig. 1A; Sup Fig. 1D), indicating that the back-folded state is auto-inhibited.

3D reconstruction of the Myo6 off-state

To further characterize the Myo6 off-state, negative staining electron microscopy (EM) of FLMyo6 in ADP.VO4 (ADP.P_i analog) resulted in heterogeneous 2D classes, likely due to the intrinsic flexibility of the protein particles. Previous FLIM demonstrated that fusion of the N- and C-termini to fluorescent proteins is compatible with Myo6 back-folding²⁵. Thus, we fused the N- and C-termini of Myo6 to two covalent bonding subdomains of *Streptococcus pneumoniae* pilus adhesin RrgA: Jo and In³⁷ (the Jo-Myo6-In construct) to attempt to limit the inherent flexibility of the back-folded monomer.

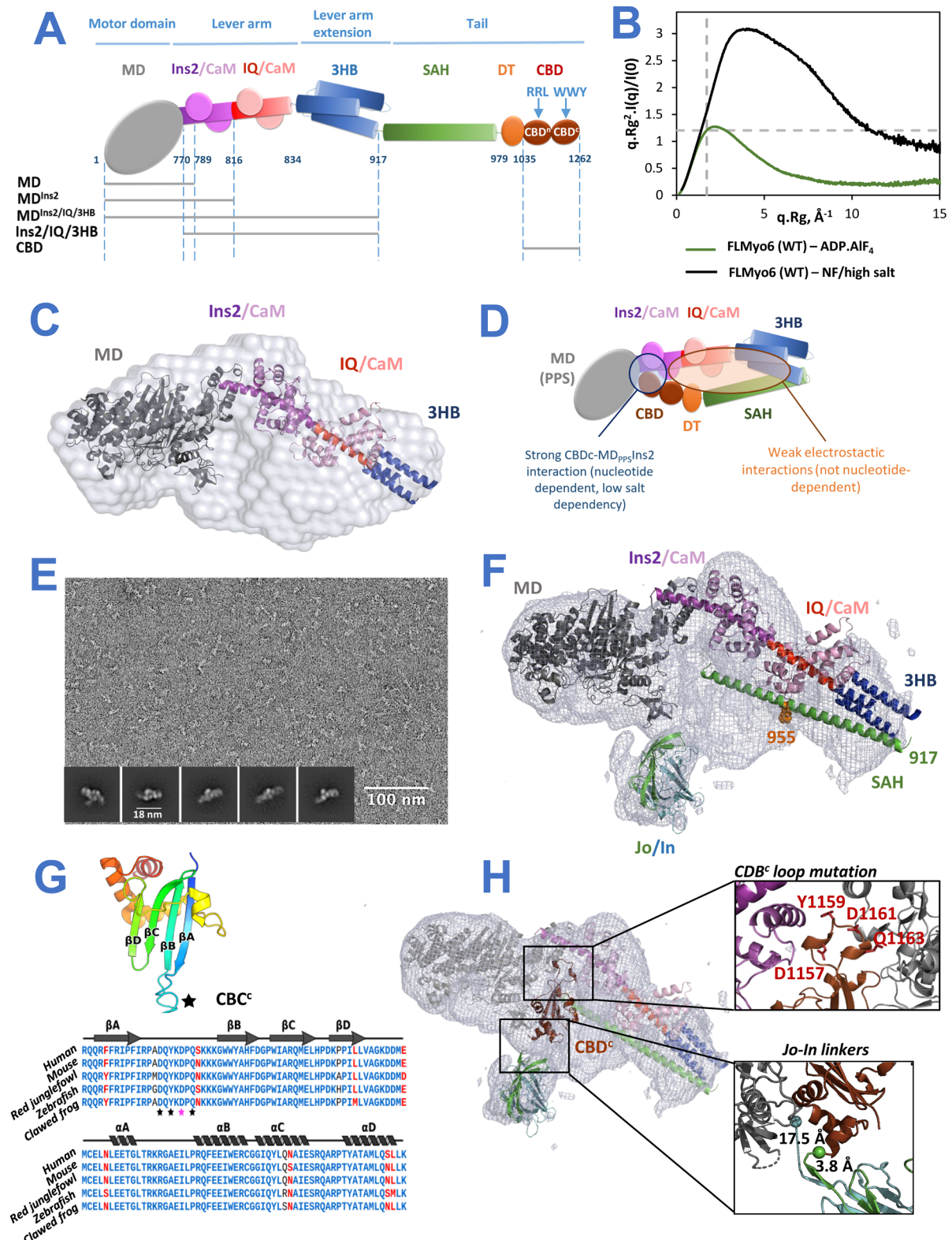


Figure 1 – Importance of ADP.P_i for the compact, back-folded Myo6 conformation.

(A) Schematic representation of FLMyo6 with the Motor domain (MD, grey), CaM binding sites (Ins2/IQ, purple/red), CaM (lilac/pink), 3-helix bundle (3HB, blue), single alpha helix (SAH, green), distal Tail (DT, orange) and CBD (brown). Residue numbers correspond to human Myo6, Uniprot entry Q9UM54-2. **(B)** Dimensionless Kratky plot representation from SEC-SAXS. FLMyo6 in the presence of ADP.AIF₄ (green) results in a bell-shape spectrum with a maximum close to the intersection of the dashed lines

(*v3:1.104*), typical of a globular protein. The spectrum for FLMyo6 in NF/high salt (black) suggests a much more elongated shape. See buffer compositions in Methods. **(C)** Representation of the ab initio SAXS envelope (light gray) with MD^{Ins2-IQ-3HB} docked. **(D)** Scheme representing the interactions stabilizing the Myo6 back-folded state. **(E)** Example of a negative staining micrograph of Jo-Myo6-In in ADP.VO₄, with selected 2D classes. **(F)** EM density for Jo-Myo6-In (grey mesh) obtained by negative staining. Docking of Myo6 fragments and Jo-In (see Methods). **(G) (Top)** Crystal structure of the Myo6 C-terminus (CBD^c) (PDB: 3H8D¹⁴). Star: highly conserved and exposed loop between the β_A and β_B strands. **(Bottom)** Alignment of Myo6 CBD^c domain (aa 1143 to 1262 in Q9UM54-2) from different species. Strictly conserved and similar residues are shown in blue and red, respectively. Stars: residues implicated in binding to the Myo6 Head (Table 1). **(H)** CBD^c (brown) added to the model pictured in **(F)** (see Methods).

To show that the fusion does not disrupt the Myo6 back-folding, we confirmed that the Jo-Myo6-In heavy chain could bind to two CaM using SDS-PAGE and that the Jo-Myo6-In behaved as a compact folded protein, even in NF/high salt condition using SEC-MALS and SEC-SAXS (Sup Fig. 2A-C). An actin-activated stopped-flow experiment revealed a low P_i release rate for Jo-Myo6-In compared to FLMyo6 wild-type (WT), indicating that the conformational changes required to release P_i were greatly slowed (Sup Fig. 2D). Finally, negative staining EM images of Jo-Myo6-In in ADP.VO₄, low salt were collected (Fig. 1E). The 3D reconstruction of the Myo6 off-state at ~17 Å resolution (Fig. 1F, Sup Movie 1) is consistent in shape and dimensions with SAXS data of FLMyo6 (Fig. 1C, F).

Structural model of the Myo6 off-state

The distinct EM density for the Jo-In fusion clearly defines the position of the N- and C-termini of FLMyo6 and demonstrates how it can lock the off-state. We used available Myo6 crystallographic structures to build a model inside the 3D reconstruction (Fig. 1F, see details in Methods). By defining the orientation of the Lever arm, the model revealed that the flexible joint allowing back-folding must be localized around aa 912-918 prior to the SAH. The ~10 nm long SAH ends up close to the Myo6 N-terminus and Converter, where the rest of the Tail can also participate in stabilizing interactions. Importantly, only the pre-powerstroke structure of the Motor domain (which traps ADP.P_i), not the Rigor (NF) structure leads to good model-to-map agreement (Fig. 1F, Sup Fig. 2E). We challenged this model by measuring affinities between Myo6 CBD^{1035-end} and Myo6 Head fragments (Table 1, Sup Fig. 3). The CBD binds to the Motor domain with low affinity, and the strongest interaction (K_D ~150 nM) was measured for MD^{Ins2/IQ/3HB}. Removal of the IQ-3HB region (MD^{Ins2}) reduces the affinity by 2-fold. Last, the interaction between Myo6 CBD and MD^{Ins2/IQ/3HB} drops from K_D ~150 nM to ~750 nM upon nucleotide removal (Table 1, Sup Fig. 3). These data indicate an interaction of the CBD with both the Motor domain and the Lever arm and highlight the importance of the nucleotide state for optimal interaction.

To define the CBD region that interacts with the MD^{Ins2/IQ/3HB}, we introduced four missense mutations (D1157V.Y1159D.D1161R.Q1163V: CBD^c loop mutant) in a conserved and exposed loop of the CBD (Fig. 1G). These mutations abolished the ability of the CBD to bind to MD^{Ins2/IQ/3HB}, suggesting a key role of the CBD^c, and this specific loop, in the interaction (Table 1). When this information is used to dock the CBD^c, the Myo6 C-terminus is oriented towards the surface, close to the N-terminus consistent with our Jo-Myo6-In model (Fig. 1H, Methods).

Head	Tail	Motor state	K_D (nM)	n
MD ^{Ins2/IQ/3HB}	YFP CBD	ADP.VO ₄	144 ± 61	3
MD ^{Ins2}	YFP CBD	ADP.VO ₄	343 ± 197	3
MD	YFP CBD	ADP.VO ₄	3920 ± 1453	3
Ins2/IQ/3HB	YFP CBD	-	250 ± 86	4
MD ^{Ins2/IQ/3HB}	YFP CBD	NF	726 ± 480	2
MD ^{Ins2/IQ/3HB}	YFP CBD _{D1157V.Y1159D.D1161R.Q1163V}	ADP.VO ₄	n.b.	3

Table 1 – Main contacts that stabilize the back-folded conformation

Dissociation constant (K_D) ± K_D confidence determined by microscale thermophoresis of Myo6 Head constructs against Myo6 Tail constructs (constructs schematized in Fig. 1A). Microscale thermophoresis profiles are presented in Sup Fig. 3.

Auto-inhibition of Myo6 and hearing loss

The back-folded model predicts that a sharp kink occurs at the junction between the 3HB and the SAH (Fig. 1F). The N-terminus region of the SAH (aa 922-935) is thus positioned alongside the 3HB and could participate in the stabilization of the Myo6 off-state via apolar residues found in its atypical sequence (Fig. 2A). The importance of the sequence following the 3HB for back-folding was characterized using the previously published Myo6 (SAHmimic) mutant¹⁷, in which all apolar residues in the SAH were replaced by charged residues to match the i, i+4 alternance of a “perfect SAH sequence” (Fig. 2A). SEC-SAXS and SEC-MALS experiments indicated that FLMyo6 (SAHmimic) adopts an elongated conformation, even upon addition of an ADP.P_i analog, confirming the importance of the residues 922-935 for stabilization of the Myo6 off-state (Fig. 2B-C and Sup Fig. 4A).

Interestingly, a missense mutation present in this region of the SAH (L926Q) leads to deafness in humans³⁸. Positioned away from the Motor domain or from Tail regions involved in recruitment (Fig. 2A), the effect of the mutation on Myo6 function had remained elusive. SEC-MALS (Sup Fig. 4A) and SEC-SAXS experiments (Fig. 2B-C) indicate that the L926Q mutation destabilizes the back-folded state. Both FLMyo6 (L926Q) and FLMyo6 (SAHmimic) mutants display higher ATPase rates ($2.86 ± 0.12$ and $4.83 ± 0.11$ s⁻¹.Head⁻¹ respectively) than the wild-type ($0.65 ± 0.08$ s⁻¹.Head⁻¹) (Fig. 2D), which confirms the destabilization of the off-state.

We then investigated the impact of back-folding misregulation in the human pigmented melanoma cell line (MNT-1). Myo6 localizes to dot-like subdomains on the surface of pigmented melanosomes to promote membrane constriction and fission for the release of tubular carriers²¹. MNT-1 cells were transiently co-transfected with plasmids encoding (1) fluorescent components associated with pigmented melanosome ^{iRFP}VAMP7^{21,39} and ^{mCherry}MST⁴⁰, and with (2) either FLMyo6 WT, SAHmimic, L926Q or Jo-Myo6-In, all fused to GFP. All ^{GFP}Myo6 constructs localize as dots on melanosomes (Sup Fig. 4C), although at distinct levels (Sup Fig. 4B). The co-distribution of ^{GFP}FLMyo6 (SAHmimic) or ^{GFP}FLMyo6 (L926Q) with melanosomal components was greater than that of the ^{GFP}FLMyo6 (WT) (~1.2 fold increase, p ≤ 0.001, Sup Fig. 4B). However, the co-distribution of ^{GFP}Jo-Myo6-In with melanosomes was reduced ~3-fold compared to ^{GFP}FLMyo6 (Sup Fig. 4B) and the associated cytosolic and diffuse fluorescent signal was more readily observed (Sup Fig. 4C).

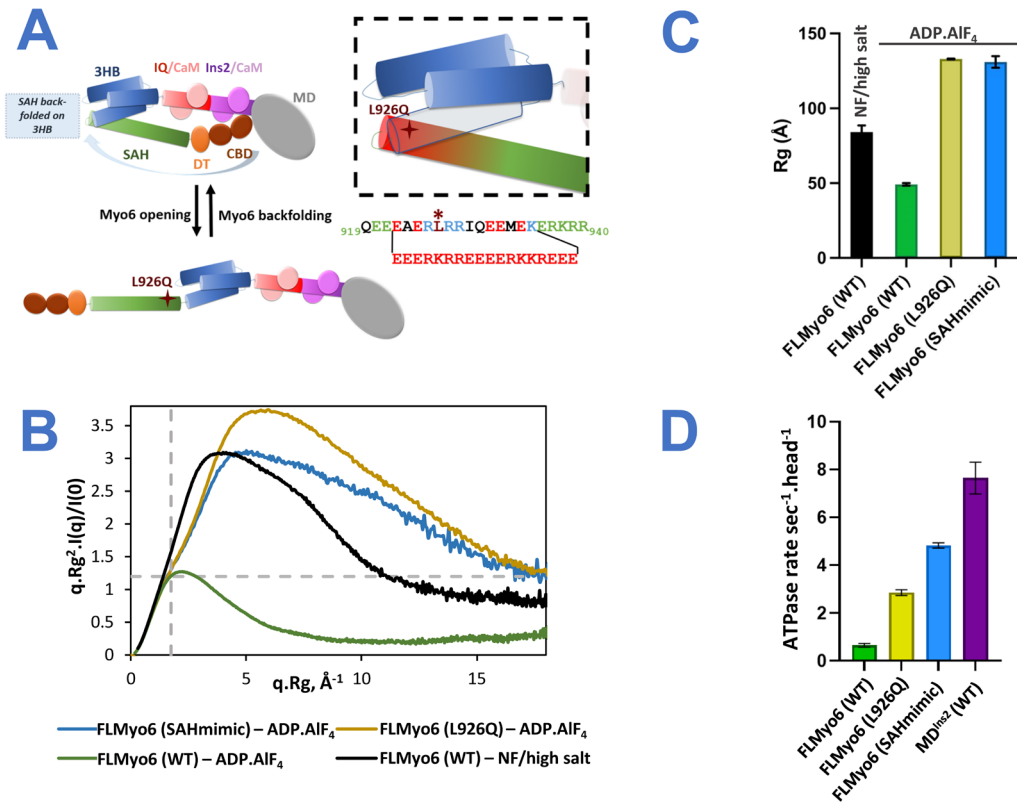


Figure 2 – Role of the proximal Myo6 sequence in the stabilization of the Off-state.

(A) Model of Myo6 opening/back-folding. Back-folding requires the SAH to fold back on the 3HB. The L926 residue (red cross) leads to deafness when mutated into Gln³⁸. (Insert) Mutations of the apolar residues at the N-terminus of the SAH to convert it into a « perfect SAH» sequence (SAHmimic) turn Myo6 into a constitutive monomer¹⁷. (B) (Top) Dimensionless Kratky plot representation from SEC-SAXS. FLMyo6 in NF/high salt is pictured in black. In the presence of ADP.AIF₄, FLMyo6 (L926Q) (yellow) and FLMyo6 (SAHmimic) (light blue) spectrums correspond to an elongated shape, as opposed to FLMyo6 WT (green). (Bottom) Rg of FLMyo6 WT, L926Q and SAHmimic determined by SEC-SAXS experiments in the presence of ADP.AIF₄ and FLMyo6 in NF/high salt. (C) Rg of FLMyo6 WT, L926Q and SAHmimic determined by SEC-SAXS experiments in the presence of ADP.AIF₄ and FLMyo6 in NF/high salt. Rg values were extracted from linear fits of the Guinier plots shown in Sup Fig. 1C using primusqt (ATSAS suite³⁹). (D) Actin-activated ATPase rate of FLMyo6 WT, L926Q, SAHmimic and MD^{Ins2} (n=6).

Collectively, these data indicate that Myo6 auto-inhibition drastically reduces endogenous recruitment to melanosomes while impairment of Myo6 back-folding can result in over-recruitment. These results highlight the importance of the 3HB-SAH region for Myo6 auto-inhibition since the deafness L926Q mutation is sufficient for over-recruitment of the motor. Thus, destabilization of the off-state can lead to pathology.

Differential binding and activation of FLMyo6 by distinct cellular partners

We next aimed at distinguishing whether partners can bind to FLMyo6 in the back-folded state and if binding depends on the specific binding site. Partners interacting either with the RRL motif (GIPC1³⁴) or the WWY motif (TOM1³⁵ and Dab2¹⁴) (Fig. 1A) were examined as our model suggests that in the FL off-state, the WWY motif of the CBD^c is buried and unavailable for binding (Fig. 3A-B). We first looked at the ability of His⁵GIPC1 and His⁵TOM1 to bind FLMyo6 using an anti-His pull-down assay on

purified proteins, in conditions promoting either Myo6 back-folding (addition of ADP.VO₄) or opening (NF, use of the SAHmimic mutant, or addition of Ca²⁺ as previously proposed^{33,36}) (Fig. 3D, Sup Fig. 5). Both TOM1 and GIPC1 were able to retain Myo6 in conditions that favor Myo6 opening. In contrast, upon ADP.VO₄ addition, the interaction of Myo6 with GIPC1 is maintained, but the interaction with TOM1 is weakened, suggesting that binding of TOM1 requires Myo6 opening.

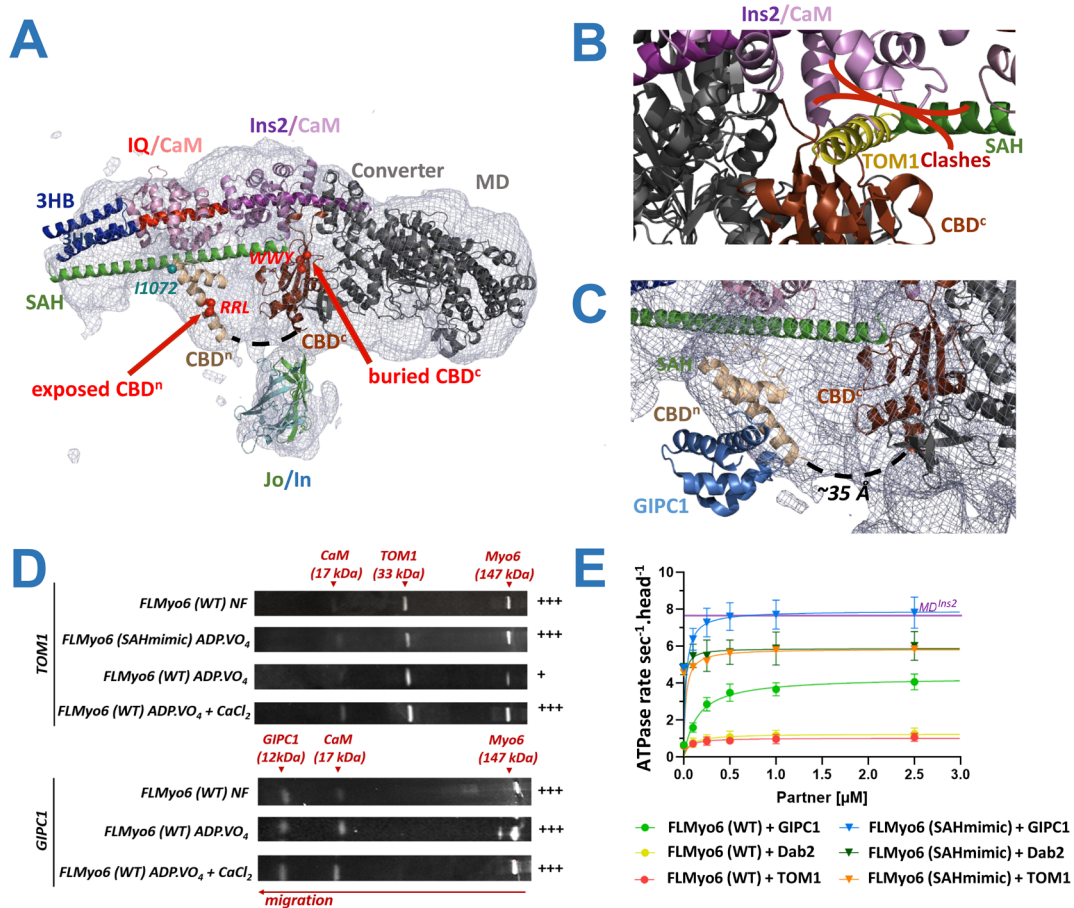


Figure 3 – GIPC1 can bind to and activate the back-folded form of Myo6, while Dab2 and Tom1 can only bind Myo6 once the motor has been primed open.

(A) EM density for the Jo-Myo6-In (grey mesh) obtained by negative staining, as in Fig. 1H and Sup Movie 1. The WWY motif (red spheres) of CBD^c is buried. The CBDⁿ fragment (beige) (PDB: 5V6E³⁴) is positioned in the remaining, uninterpreted part of the density so that the RRL motif (red spheres) on CBDⁿ and the I1072 (blue sphere) that has been proposed to mediate interaction between ubiquitin and Myo6⁴¹ are both exposed. Note that no experimental model exists for 36 missing residues between the CBDⁿ and CBD^c (dashed lines). **(B)** Fitting of CBD^c-TOM1 structure (PDB: 6J56³⁵) with CBD^c (brown) in the model presented in Fig. 1H, TOM1 (yellow) needs to bind in a poorly exposed area and would clash with SAH (green) and CaM (lilac). **(C)** Fitting of CBDⁿ (beige)-GIPC1 (light blue) structure (PDB: 5V6E³⁴) as for CBDⁿ alone. GIPC1 binding seems compatible with the back-folded conformation of Myo6 on a highly exposed binding site. **(D)** Anti-His pull-down assays. His-tagged Myo6 partners TOM1 and GIPC1 against FLMyo6 (WT) or (SAHmimic) revealed using SYPRO⁴² (Input and last wash pictured in Sup Fig. 5). Crosses: quantification of retained Myo6 (Image-Lab software, Bio-Rad) followed by stoichiometric normalization based on partner concentration (n=4). + means less than 10% Myo6 retained; +++ means more than 20% Myo6 retained. **(E)** ATPase rates of FLMyo6 (WT) and FLMyo6 (SAHmimic) with 40 μM

F-actin and increasing concentrations of GIPC1, TOM1 or Dab2 (n=6). Purple line: ATPase rate of MD^{Ins2} at 40 μM actin (n=6) for reference.

Next, we assessed the ability of GIPC1, Dab2 and TOM1 to stimulate the ATPase activity of FLMyo6 (Fig. 3E), and found that GIPC1 increases the Myo6 ATPase rate in a concentration-dependent manner, while addition of Dab2 or TOM1 has little impact. Note that partner affinities for Myo6^{YFP}CBD are all in the submicromolar range (*i.e.*, sufficient to ensure binding in our ATPase assays) (Sup Fig. 6). Lack of activation by TOM1 and Dab2 must thus be due to inaccessibility of the WWY motif in the back-folded FLMyo6. Interestingly, TOM1 and Dab2 increase the ATPase rate of the FLMyo6 (SAHmimic) mutant, as does GIPC1, which indicates that all partners can bind to and stabilize the unfolded state (Fig. 3E).

In this context, we postulate that the RRL motif required for GIPC1 binding to CBDⁿ (Fig. 1A) must be exposed on the surface of the back-folded Myo6, as opposed to the WWY motif. The CBDⁿ fragment (PDB: 5V6E³⁴) was thus positioned in the unexplained density lying in continuity to CBD^c in our Jo-Myo6-In 3D reconstruction (Fig. 3A-C, Sup Movie 1).

Collectively, these results demonstrate that not all partners can induce activation of Myo6. Partners Dab2 and TOM1 require another factor promoting Myo6 opening prior to their binding. In contrast, GIPC1 can directly activate FLMyo6, consistent with a previous study³³.

Assessing the specific recruitment of Myo6 to native organelles by distinct partners

If some partners can relieve Myo6 from auto-inhibition, we reasoned that artificial targeting of these partners to specific cellular membranes would lead to massive recruitment of Myo6. We thus decided to artificially drive GIPC1, TOM1 and Dab2 to melanosome membranes by fusing them to the melanosome-targeting tag (MST)⁴⁰ (Sup Fig. 7) and verifying their ability to recruit either open (SAHmimic and L926Q) or locked (Jo-Myo6-In) Myo6. To do so with an optimized signal to noise measurement, we introduced the point mutation I1072A in our Myo6 constructs since it drastically reduces endogenous recruitment of Myo6 to the melanosomes (GFPFLMyo6 (I1072A), 3.7-fold reduction ($p > 0.0001$) compared to GFPFLMyo6; Fig. 4A; Sup Fig. 8A-B, 9A), while it is not part of the interface with either GIPC1 (Sup Fig. 6), TOM1 or Dab2. Hence, the I1072A mutation provides an easy way to reduce endogenous recruitment to melanosomes and offers a powerful tool to test the ability of distinct exogenous partners to recruit Myo6.

We transiently transfected MNT-1 cells with plasmids encoding for mCherryMST-GIPC1, mCherryMST-TOM1, or mCherryMST-Dab2 for melanosome targeting. Co-transfection with plasmid encoding for GFPMyo6 (I1072A), GFPJo-Myo6-In (I1072A), GFPFLMyo6 (SAHmimic.I1072A) or GFPFLMyo6 (L926Q.I1072A) provided a quantitative way to compare the ability of these partners to recruit Myo6 to specific organelles such as the melanosomes in cells (see Methods).

Expression of mCherryMST-GIPC1 resulted in ~90% of Myo6-positive melanosomes for all the Myo6 constructs tested (Fig. 4B, E; Sup Fig. 9B), indicating that exogenous GIPC1 can recruit Myo6 to melanosomes independently of Myo6 being open or closed. In contrast, expression of mCherryMST-TOM1 or mCherryMST-Dab2 did not significantly increase the amount of GFPJo-Myo6-In (I1072A) positive melanosomes ($p = 0.5005$ and $p = 0.344$ respectively). This confirms the ineffectiveness of WWY partners in recruiting back-folded FLMyo6. Yet, their expression results in a 1.3/1.4-fold increase of melanosomes containing active Myo6 mutants GFPFLMyo6 (SAHmimic.I1072A) and GFPFLMyo6 (L926Q.I1072A) ($p = 0.003$ or lower) (Fig. 4C-E; Sup Fig. 9C-D).

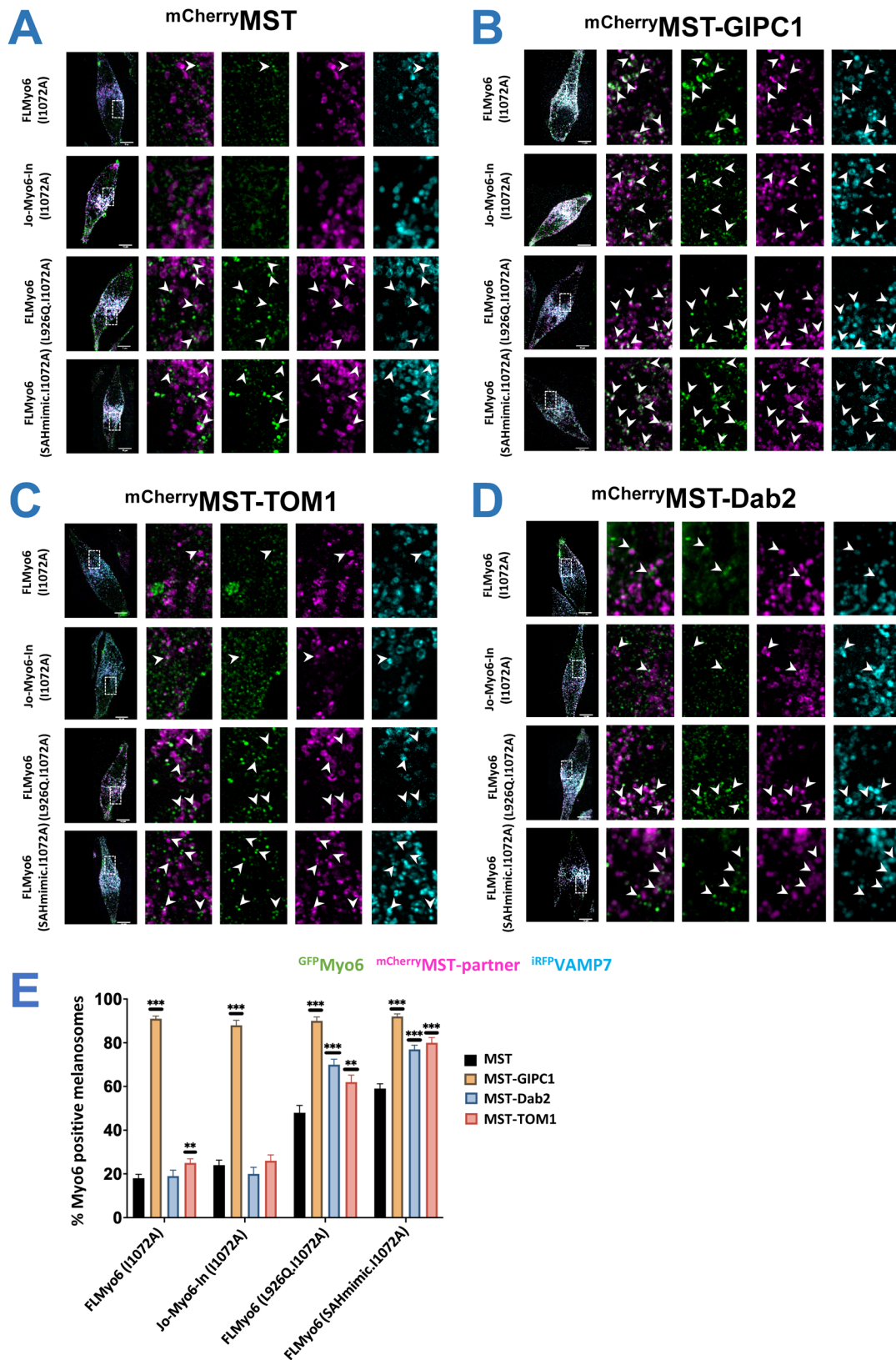


Figure 4 – GIPC1 recruits Myo6 to melanosomes independently of Myo6 closure; Dab2 and TOM1 can only recruit Myo6 after the motor has been primed open.

(A) Representative fixed MNT-1 cells co-expressing different ^{GFP}Myo6 (I1072A), ^{mCherry}MST and ^{iRFP}VAMP7 constructs. (B) Representative fixed MNT-1 cells co-expressing different ^{GFP}Myo6 (I1072A) constructs with ^{mCherry}MST-GIPC1 and ^{iRFP}VAMP7. (C) Representative fixed MNT-1 cells co-expressing

different ^{GFP}Myo6 (I1072A) constructs with ^{mCherry}MST-TOM1 and ^{iRFP}VAMP7. (D) Representative fixed MNT-1 cells co-expressing different ^{GFP}Myo6 (I1072A) constructs with ^{mCherry}MST-Dab2 and ^{iRFP}VAMP7. (A-D) Green: Myo6 GFP; Cyan: ^{iRFP}VAMP7; Magenta: ^{mCherry}MST partner. From left to right: entire cell, 3 channels merged; 8x zoom on boxed region: ^{GFP}Myo6 / ^{mCherry}MST-partners merged, then individual channels. Scale bars: 10µm. Arrowheads: recruitment of Myo6 on melanosomes. (E) Myo6-positive melanosomes quantification of different ^{GFP}Myo6 mutants when different ^{mCherry}MST tagged partners are expressed (n=3, total cell number~30). Myo6-positive melanosomes are expressed in percentage and normalized to the total number of VAMP7-positive melanosomes. Cells were fixed 48h post-transfection then imaged and processed for quantification. Data are presented as the mean ± SEM. Significant stars: ***, P < 0.001; **, P < 0.01; *, P < 0.05, n.s., not significant (unpaired t test with Welch's correction), for each ^{GFP}Myo6 construct, significance of experiments with partners compared to the control without partner (in black on the graph).

Interestingly, I1072A moderately affects the recruitment of Myo6 mutants impaired in auto-inhibition. Compared to ^{GFP}FLMyo6 (SAHmimic) and ^{GFP}FLMyo6 (L926Q), we observe reductions of 1.4 and 1.7-fold in the co-distribution with melanosome components for ^{GFP}FLMyo6 (SAHmimic.I1072A) and ^{GFP}FLMyo6 (L926Q.I1072A), respectively (Fig. 4A, 4E; Sup Fig. 4B-C), which are interestingly similar to the 1.6-fold reduction in recruitment observed for the CBD alone carrying the mutation I1072A (Sup Fig. 8C-D). We thus conclude that the I1072A mutation must reduce the affinity of the CBD for partner(s) responsible for Myo6 endogenous recruitment to melanosomes. In addition, the drastic reduction in ^{GFP}FLMyo6 (I1072A) recruitment evidences the role of endogenous partners to promote Myo6 unfolding and indicates the major role of the I1072 residue in this process.

These results illustrate the importance of the recognition of the inactive state, and the distinct ways signaling factors can trigger association or activation of the back-folded state in a compartment for spatial and timely control of motor activity.

A hinge that dimerizes

While we have demonstrated the key role of the sharp kink (hinge) at the 3HB/SAH junction for Myo6 auto-inhibition (Fig. 2; Sup Fig. 4), previous evidence by single molecule motility assays^{12,17} already suggested that this region is key for Myo6 proximal dimerization. Since Myo6 proximal dimerization might be critical for a number of functional properties, we wanted to elucidate the structure of the dimerization region.

SEC-MALS with six fragments derived from the 3HB/SAH junction (Sup Fig. 10A, C-E) indicated that a rather conserved region (aa 875-940) can self-dimerize with K_D^{App} of ~19 µM obtained from titration (Sup Fig. 10A, C). This minimal region corresponds to the last half of the 3HB (*i.e.*, the 2nd and 3rd helix) and the first part of the SAH (Sup Fig. 10A-B). In contrast, no dimerization was observed when peptides included the whole 3HB domain, even when peak concentration of 30 µM was reached for the 834-955 peptide (Sup Fig. 10A, D). This data is consistent with previous findings indicating that proximal dimerization requires unfolding of the 3HB (¹⁷, Sup Fig. 11A).

Crystals of the 875-940 peptide diffracted to 2.1 Å resolution (Fig. 5A; Sup Table 1). Clear electron density for all residues from 876 to 937 indicates that they form an extended helix that dimerizes in an anti-parallel manner (Fig. 5B; Sup Fig. 12). This anti-parallel dimerization is stabilized by multiple apolar contacts involving 13 residues from each helix, and six polar contacts involving R892 with D900, and T888 with S906 (*via* a water molecule) (Fig. 5A; Sup Fig. 10B).

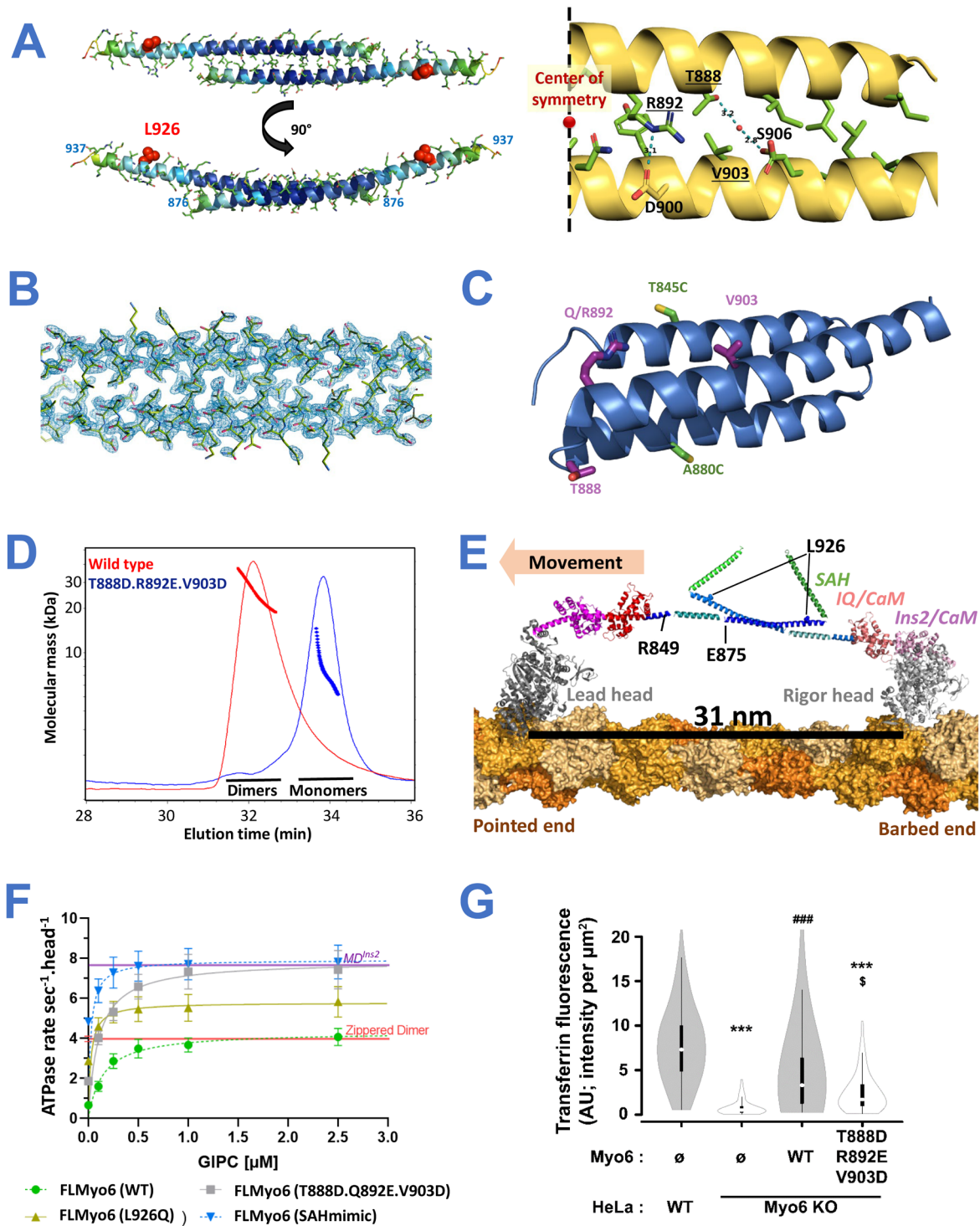


Figure 5 – Myo6 can form an anti-parallel dimer through residues 875-940 which allow large steps.

(A) (Left) X-ray crystallography structure of mouse Myo6 875-940 antiparallel dimer colored according to B-factor from 18.60 Å² (dark blue) to 150.81 Å² (red). **(Right)** Key residues for dimer stabilization. Apolar contacts are mediated by residues I878, L881, I885, T888, R892, I895, Q896, Y899, V903, E907, L909, L910, L913 (pictured in green). Dotted blue line: polar contacts. Residues mutated in our triple mutant (T888D.R892E.V903D) are underlined. **(B)** Close-up of the dimerization interface of Myo6 875-940 (crystallographic dimer) in the electronic density. **(C)** Triple helix bundle (PDB: 2LD3⁴³) domain. T888, R892, V903, T845C and A880C pictured as sticks are surface residues. **(D)** SEC-MALS profiles of

*Myo6 875-940 WT (red) and T888D.R892E.V903D mutant (blue), following injection of 50 μ l at 10 mg/mL in 10 mM Tris-HCl pH 7.5; 50 mM NaCl; 5 mM NaN₃; 0.5 mM TCEP. WT elutes as dimers (32 μ M at the peak) and T888D.R892E.V903D mutant elutes as monomers (43 μ M at the peak). Measured molecular weight is heterogeneous due to the small size of the peptides through elution (low light scattering signal), but at the peaks it coincides with the expected masses. (E) Model of active FLMyo6 dimer (see Methods). (F) ATPase rates of FLMyo6 (WT) (green), FLMyo6 (T888D.Q892E.V903D) (grey), FLMyo6 (SAHmimic) (blue) and FLMyo6 (L926Q) (yellow) at 40 μ M F-actin and increasing concentrations of GIPC1 (from 0 to 2.5 μ M) (n=6). ATPase rates of MD^{Ins2} and zippered HMM dimer^{12,44} with no partner added (n=6) are plotted as purple and red thick lines (respectively) as references for monomeric and dimeric Myo6. (G) Fluorescence intensity of internalized transferrin was measured for each of the conditions after treatment with genistein (minimum 58 cells analyzed per condition). Expression of FLMyo6 (WT) construct restored transferrin uptake to wild-type levels, while the FLMyo6 (T888D.R892E.V903D), fails to rescue the defect. Data shown as violin plot (generated with BoxPlotR⁴⁵) ($p < 0.001$, ANOVA; Tukey post-hoc comparisons: *** $p < 0.001$ vs WT, \$ $p < 0.05$ vs Myo6 KO + FLMyo6 (WT)).*

At the center of the interface, the structure highlights how residues T888, R892 and V903 contribute to the dimerization (Fig. 5A; Sup Fig. 10B). Three mutations (T888D.R892E.V903D) were introduced into the 875-940 peptide to assess their ability to disrupt proximal dimerization. Importantly, these residues were chosen on the surface of the 3HB so that the mutations would not disturb the bundle (Fig. 5C). (Note that residue 892 can be a Gln or an Arg depending on the species (Sup Fig. 10B) but both are compatible with the formation of the dimer). SEC-MALS confirms that the T888D.R892E.V903D mutant stays monomeric even up to 43 μ M (peak concentration in the SEC-MALS experiment) while the WT counterpart is dimeric in similar conditions (Fig. 5D). In addition, motility assays indicated that no movement could be detected when the triple mutant construct is used in single molecule assays, which contrast to robust motility observed for the FLMyo6 (WT) (run length = $0.74 \pm 0.26 \mu$ m (N=82)).

Finally, a model of the active dimeric configuration of Myo6 bound to F-actin including this crystal structure was built (Fig. 5E, see Methods). The inter-head distance is indeed compatible with the large (~30 nm) stepping previously reported when Myo6 walks processively^{12,44}. Taken together, our results strongly support that proximal dimerization requires the formation of an extended anti-parallel coiled coil, which can form following destabilization of the 3HB.

GIPC1 promotes unfolding of the Myo6 monomer and proximal dimerization

We further characterized this proximal dimerization region and investigated the ability of partners to promote proximal dimerization of Myo6 using an actin-based ATPase assay. Such dimerization indeed leads to “gating”, *i.e.* coordination between the two Heads of the dimer that translates into slowing of ATP binding to the lead Head while the rear Head is attached⁴⁶. This results in a 50% drop of ATPase rate per Head when Myo6 is dimerized compared to a monomer. The ATPase rate of zippered HMM (Myo6 truncated at R991 followed by a leucine zipper⁴⁷ to create a constitutive dimer) in which gating has been characterized⁴⁶ is indeed ~50% that of the monomeric MD^{Ins2} ATPase rate (Fig. 5F).

Indeed, upon addition of GIPC1, we found a ~50% reduction in the maximal ATPase activity per Head for FLMyo6 (WT) compared to MD^{Ins2} (Fig. 5F), consistent with GIPC1 promoting proximal

dimerization of FLMyo6. In contrast, addition of GIPC1 to the FLMyo6 (SAHmimic) mutant is similar to that measured with MD^{Ins2}, consistent with a role of GIPC1 in fully freeing the Motor domain from Tail inhibition upon stabilizing an extended, monomeric conformation. Importantly, the FLMyo6 (T888D.Q892E.V903D) exhibits ~2-fold higher maximal ATPase rate upon GIPC1 addition, consistent with loss of gating (Fig. 5F).

This additional evidence strongly validates the role of these residues in antiparallel proximal dimerization, and the role of this region in controlling motor mechanical properties. Furthermore, we demonstrate for the first time that proximal dimerization (involving 3HB unfolding) can be triggered upon GIPC1 binding.

The L926Q deafness mutation indirectly impairs proximal dimerization

Interestingly, when we used GIPC1 to activate the FLMyo6 (L926Q) construct (Fig. 5F), the maximal ATPase activity that we found was intermediate between monomeric and dimeric FLMyo6. Since our proximal dimerization structure indicates that the L926Q missense mutation does not impact the anti-parallel coiled-coil region itself (Sup Fig. 11B), and since we found that 3HB unfolding is essential for proximal dimerization, we hypothesized that L926Q impairs Myo6 dimerization by perturbing the unfolding of the 3HB. This was previously reported for the FLMyo6 (SAHmimic) mutant¹⁷.

To monitor 3HB unfolding, we introduced cysteines at two positions of the 3HB surface (T845 and A880), for tetramethylrhodamine (TMR) labelling (Fig. 5C, Sup Fig. 11A). As previously described¹⁸, a low TMR fluorescence ratio is found when 3HB is folded (fluorescence quenching due to stacking of the rhodamine rings; MD^{Ins2/IQ/3HB} T845C, A880C). This value increases upon 3HB opening (Sup Fig. 11A), and a high TMR fluorescence ratio indicative of 3HB unfolding has been reported for the Myo6 zippered HMM T845C, A880C¹⁸. Introducing the L926Q mutation in this zippered construct led to an intermediate fluorescence intensity, indicating limited unfolding of the 3HB for the deafness mutant compared to control (Table 2). This suggests a role for the L926Q mutation in limiting the conformational changes of the 3HB required for dimerization, in addition to its effect in destabilizing the off-state.

Construct	Fluorescence Ratio without Actin + ATP	Fluorescence Ratio with Actin + ATP	Molar Ratio of Labeling per Myosin Head
MD^{Ins2/IQ/3HB} T845C	256.1 ± 24.4	243.8 ± 14.5	1.03
MD^{Ins2/IQ/3HB} T845C, A880C	22.5 ± 5.8	22.6 ± 7.2	2.10
zippered HMM A880C	238.2 ± 23.7	232.3 ± 30.4	1.11
zippered HMM T845C, A880C	206.5 ± 19.6	214.3 ± 12.6	2.22
Zippered HMM T845C, A880C, L926Q	147.53 ± 30.4	164.6 ± 18.7	2.14

Table 2 – L926Q stabilizes the 3HB.

Fluorescence observed by TMR labeling of one or two cysteine residues inserted into the three-helix bundle of monomers (MD^{Ins2/IQ/3HB}) and dimers (zippered HMM). Fluorescence was analyzed by a ratio of the emission values to that of the absorption values for each construct from four independent measurements (n=4). Mean values (±SD) are reported. The molar ratio was calculated by comparing the myosin concentration to the concentration of the incorporated TMR.

Importance of proximal dimerization in cells

To further demonstrate that proximal dimerization of Myo6 occurs via the anti-parallel coiled-coil seen in our structure, we compared the ability of FLMyo6 (WT) and FLMyo6 (T888D.R892E.V903D) to rescue Myo6-mediated transferrin uptake¹⁷ in HeLa cells whose Myo6 was knocked out for Myo6 by using CRISPR/Cas9 (Sup Fig. 13A). FLMyo6 (WT) and the FLMyo6 (T888D.R892E.V903D) were transiently expressed, and the transferrin internalized during a 10 min pulse was quantified. As summarized in Fig. 5G and Sup Fig. 13B, expression of the T888D.R892E.V903D mutant, unable to form the proximal dimer, profoundly decreases the rate of uptake of endocytic vesicles, providing evidence for the need of proximal dimerization to optimize Myo6 function during endocytosis. Furthermore, this also strengthens the evidence that proximal dimerization occurs via an anti-parallel coiled-coil as depicted in our crystal structure.

Discussion

Despite the significance of controlling where and when myosin motors generate forces and move cargoes in cells, careful investigation of how the function of myosin motors is regulated has only been performed for a few classes of myosin^{2,3,48,49}, and most extensively for Myo2. The results of this study highlight the importance of regulated inhibition of the Myo6 motor until it reaches its target in a cell and it is activated. Myo6 must cross actin-rich regions in order to diffuse and reach its binding partners which selectively activate motor activity (Fig. 6A). If the motor was not blocked from interacting with and cycling on actin, Myo6 would bind to actin filaments throughout the cell, retarding diffusion to its target sites at the cell membrane. The fact that the L926Q mutant disrupts the folding and regulation of Myo6 (Fig. 2) and causes deafness in humans³⁸ attests to the critical need for the regulation of this class of myosin motors.

Our structural and functional studies provide a more precise model to account for the interactions stabilizing Myo6 back-folding (Fig. 1H, Table 1). Among the major differences compared to previous models^{7,36}, we show that **(1)** ADP.P_i bound to the Motor domain is essential to lock Myo6 in its back-folded state (Fig. 1B, Table 1); **(2)** back-folding involves a specific loop of the CBD^c (Table 1), which was previously predicted to be external to the folded complex by AlphaFold^{50,51} (Sup Fig. 14); and **(3)** the 3HB/SAH junction acts as a critical hinge to control the equilibrium between on/off states of the motor (Fig. 1G-H, Fig. 2). Earlier studies of the folded monomers^{25,28,29,36} focused only on interactions within a full-length construct in the absence of nucleotide or within a Motor-less construct, and thus did not fully represent what is happening with the full-length Myo6 monomer saturated with nucleotide.

Intriguingly, a single amino acid change (L926Q) causes deafness³⁸ and is in fact sufficient to destabilize the back-folded monomer (Fig. 2). This SAH mutation flanks the hinge region that we identified as essential for the off-state of this motor. To further investigate the impact of Myo6 back-folding in myosin recruitment, we used the FLMyo6 (L926Q) and FLMyo6 (SAHmimic) mutants to probe their impact on Myo6 recruitment on melanosomes. What was observed (Sup Fig. 4B-C) was that both constructs lead to greater recruitment than the FLMyo6 (WT). This is not a gain of function, but rather a loss of regulation as, **(1)** the normal cellular control over the spatial and temporal recruitment of Myo6 has been lost, and **(2)** fluorescence quenching assays show that both SAHmimic¹⁷ and L926Q (Table 2) mutations impair proximal dimerization and thus Myo6 function. Deafness due to the L926Q

mutation in humans may therefore result from the inability of Myo6 monomers to reach their target sites in hair cells due to loss of folded regulation.

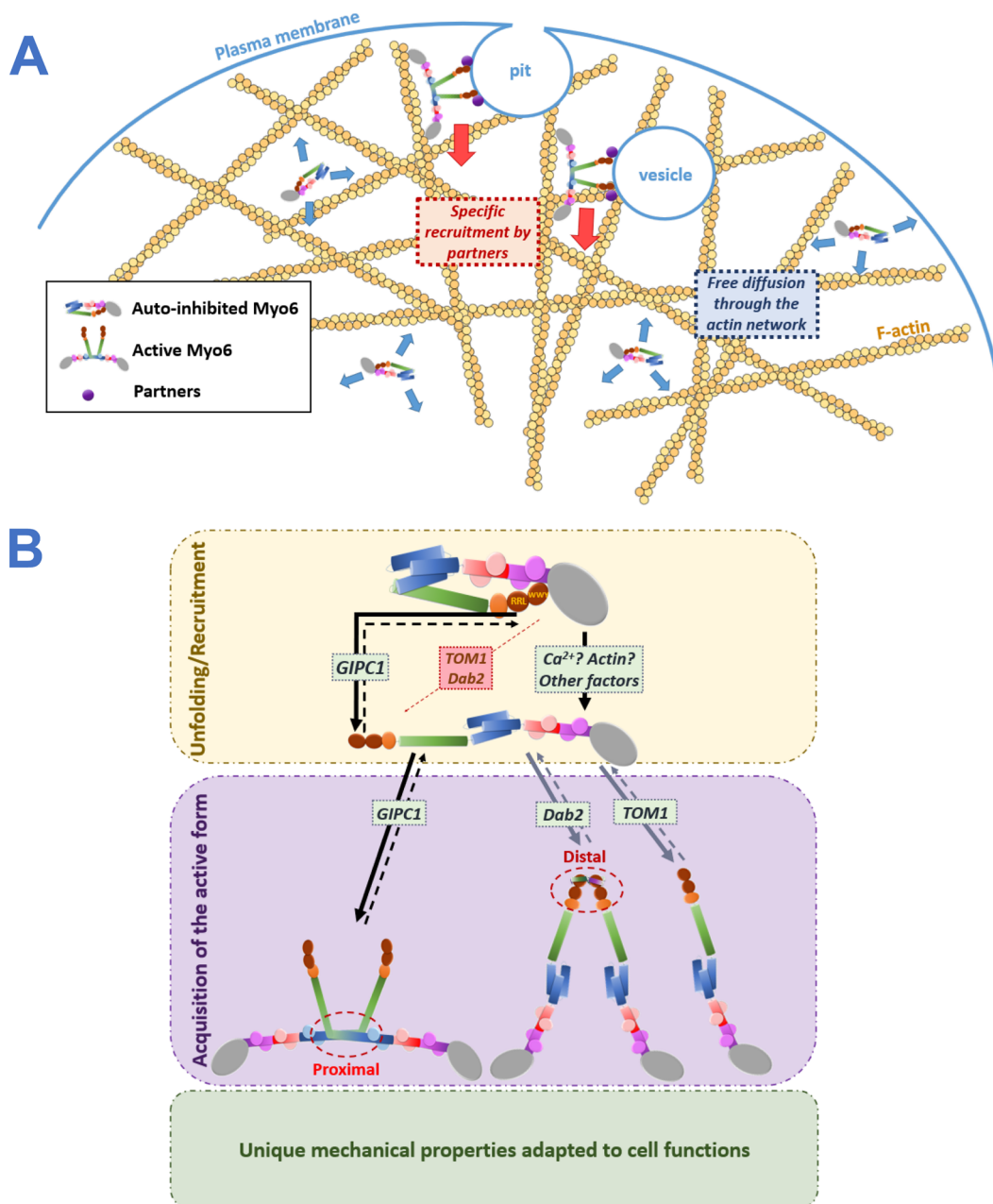


Figure 6 – Importance of a folded monomer for regulation.

(A) When auto-inhibited, Myo6 can diffuse across actin-rich regions without interacting with actin. Once recruited by a partner, Myo6 is activated and starts performing its cellular function. **(B)** Scheme representing possible activation mechanisms for Myo6. Myo6 MD is pictured in grey, Ins2/CaM in purple, IQ/CaM in red/pink, 3HB in blue, SAH in green, DT in orange and CBD in brown. Partner binding sites are labeled in garnet. The binding site (WWY) for Dab2 and TOM1 is blocked, preventing recruitment of Myo6 without a prior unfolding signal prior to unblock their binding. GIPC1 can bind the accessible RRL motif resulting in Myo6 recruitment and opening. Other signals can act as unfolding factors such as Ca²⁺, which can allow TOM1 to bind to Myo6. Such an activation cascade was previously proposed³⁶. Once unfolded, Myo6 potentially acts as a monomer, as previously proposed³⁵ upon TOM1 binding; or it can dimerize²⁹ through proximal dimerization, as demonstrated in this study with GIPC1

binding; or it dimerizes through distal dimerization upon Dab2 binding¹⁴, which may lead to proximal dimerization.

We next examined the ability of some of the Myo6 binding partners that recognize different regions of the CBD to induce unfolding and recruitment of Myo6. Folding not only prevents cycling of the motor on actin until the cellular target has been reached, but as shown by our actin-activated ATPase (Fig. 3D), pull-down (Fig. 3E) and recruitment assays on melanosomes (Fig. 4), the folding can also prevent interaction with a subset of cellular partners until unfolding occurs, by either a different class of partners, or potentially by a spike in cellular Ca²⁺ concentration^{33,36} or PIP₂ recognition^{43,52}. We thus propose a model of the folded off-state of FLMyo6 in which the GIPC1 binding site is available for binding, while the TOM1/Dab2 site is masked (Fig. 3A-C). Interestingly, this demonstrates that not all partners are equivalent in their potential for binding the auto-inhibited form of the motor and to activate Myo6.

While TOM1 and Dab2 cannot trigger Myo6 initial unfolding, once bound they prevent the formation of the off-state due to their incompatibility with it, as previously proposed^{25,28}. Depending on the nature of the partner and its distribution, binding will activate the Myo6 motor and could drive either proximal dimerization (Fig. 5F), distal dimerization^{14,15} or maintain an activated, monomeric form³⁵. Taken together, these results suggest unique roles for partners not only in Myo6 localization, but also in the control of Myo6 activation and function (Fig. 6B).

Once unfolded, binding to its cargo brings two unfolded Myo6 monomers into close apposition, favoring its dimerization^{12,14,15,17,18,25}. The experiments summarized in Fig. 5 provide the previously unknown structure of the proximal dimerization region. We present both *in vitro* and cellular evidence in support of the structure. This structure reveals the dimerization region to be an anti-parallel coiled-coil, as for Myo10^{9,11,13}. Mutations of three of the amino acids that stabilize this coiled-coil structure (T888D.Q892E.V903D) abolish dimer formation in *in vitro* assays, but with no impact on back-folding of the monomer (Fig. 5F). Furthermore, introduction of this Myo6 triple mutant into cells fails to rescue endocytosis (Fig. 5G), providing evidence for the need of proximal dimerization to optimize this cellular function of Myo6.

Myo7A, Myo10 and Myo6 exist as folded monomers in cells until they are activated and recruited by their partners. Formation of an antiparallel dimer may be the mode of dimerization for the three classes that appear to undergo this folded monomer to dimer transition. The structure of the active form of Myo6 has been a long-debated issue^{13,15,17,11}, which is resolved by our structure for the proximal dimerization region. As shown in Fig. 5E, Myo6 is unique in that its antiparallel coiled-coil and Lever arm in the dimer are derived from unfolding of a 3HB, with contribution of the SAH. The resulting Lever arm formed by the CaM binding region and the unfolded 3HB (half of which contributes to the coiled-coil) is sufficiently long to account for the ability of Myo6 to take steps that average ~30nm on actin^{12,44}. These findings provide a structural framework that can be applied to understanding how motors are recruited and how partners influence motor functions in cells.

Methods

Constructs cloning, expression and purification

Details on protein cloning and purification can be found in Supplementary Methods.

SEC-SAXS

SAXS data were collected on the SWING beamline at synchrotron SOLEIL (France)⁵³ in HPLC mode at $\lambda = 1.0332150494700432 \text{ \AA}$ using a Dectris EIGER-4M detector at a 2 m distance. Protein samples were injected at 0.1 mL/min on Superdex 3.2/300 column pre-equilibrated in 20 mM HEPES; 200 mM NaCl; 2 mM MgCl₂; 1 mM NaADP; 1 mM AlF₄, 0.1 mM EGTA, 1 mM DTT; or 20 mM HEPES; 400 mM NaCl; 2 mM MgCl₂, 0.1 mM EGTA, 1 mM DTT; pH 7.5 prior to data acquisition in the SAXS capillary cell. 150 frames of buffer scattering (before the void volume), then 719 frames of elution sample scattering were collected. Exposure time was 1990 ms/frame. Images were processed using the Foxtrot 3.5.10-3979⁵³ developed at the SOLEIL synchrotron: buffer averaging, buffer subtraction from the corresponding frames at the elution peak, and sample averaging were performed automatically. Further data analysis to obtain R_g, I(0), D_{max} and molecular weight estimation was done with PRIMUS from ATSAS suite⁵⁴. Dimensionless Kratky plot ((q.R_g)².I(q)/I(0) versus q.R_g) was generated using Microsoft Excel based on I(0) and R_g values found with PRIMUS. 20 envelopes were generated independently with GASBOR⁵⁵ and averaged with DAMAVER⁵⁶.

SEC-MALS

For SEC-MALS analysis, samples were injected in a Superdex 200 10/300 Increase (GE Life Sciences) previously equilibrated in the corresponding buffer, and developed at 0.5 ml/min. Data collection was performed every 0.5 sec with a Treos static light scattering detector, and a t-Rex refractometer (both from Wyatt Technologies). Concentration and molecular mass of each data point were calculated with the software Astra 6.1.7 (Wyatt Technologies).

Microscale Thermophoresis measurements between Myo6 Tail and Head

Microscale thermophoresis experiments were performed on a Monolith NT.115 system (NanoTemper Technologies) using YFP-fusion proteins.

The non-fluorescent protein was first treated with 0.5 mM EGTA (+/- 2 mM MgADP; 2 mM Na₃VO₄ for some experiments); then dialysed against 20 mM Hepes pH 7.5, 50 mM NaCl, 2.5 mM MgCl₂, 1 mM TCEP and 0.05% (v/v) Tween-20 (+/- 2 mM MgADP; 2 mM Na₃VO₄ for some experiments). Two-fold dilution series (16 in total) of the non-fluorescent protein (« Head » sample) were performed at 25° in the same buffer. The YFP-fused partner was kept at a constant concentration of 100 nM. The samples were loaded into premium capillaries (Nanotemper Technologies) and heated for 30 sec at 60% laser power. All experimental points were measured twice. The affinity was quantified by analyzing the change in thermophoresis as a function of the concentration of the titrated protein using the NTAanalysis software provided by the manufacturer.

Microscale Thermophoresis measurements with Myo6 partners

Two-fold dilution series (16 in total) of the non-fluorescent protein (Myo6 partner) were performed at 25°C in the MST buffer: 20 mM Bis-Tris pH 6.5, 100 mM KCl, 1 mM DTT and 0.05% (v/v) Tween 20. The YFP-fused partner was kept at a constant concentration of 100 nM. Microscale thermophoresis

experiments were then performed in similar conditions as above in 20 mM Bis-Tris pH 6.5, 100 mM KCl, 1 mM DTT and 0.05% (v/v) Tween 20. Capillaries were heated for 30 sec at 50% laser power.

ATPase assays.

ATPase assays were performed as previously described⁵⁷. ATPase rate determined from 2-3 preps with 2-3 independent assays per prep. F-Actin was used at 40 μ M and Myo6 at 150 nM with 2.5 μ M additional CaM in all our experiments. The experiments were all carried out in 10 mM MOPS pH 7.0; 10 mM KCl; 1 mM DTT; 1 mM MgCl₂; 1 mM EGTA.

P_i release experiments

Actin-activated phosphate release from Myo6 constructs was monitored using the 7-diethylamino-3-(((2-maleimidyl)ethyl)amino)carbonyl coumarin labeled phosphate binding protein (MDCC-PBP) as in⁵⁷. Experiments were conducted under single turnover conditions where the substrate was rate-limiting. Actin-stimulated phosphate release was measured in a double-mixing experiment where Myo6 was mixed with a substoichiometric concentration of ATP, aged for 30 seconds, and subsequently mixed with actin and MDCC-PBP (final reaction conditions: 0.5 μ M Myo6, 0.25 μ M ATP, 14 μ M actin, 5 μ M MDCC-PBP). Fluorescence was monitored by excitation at 425 nm, and emitted light was collected through a 455 nm long pass glass filter. Myosin solutions were clarified by centrifugation (550k x g_{max}, 10 minutes, 4°C) after thawing and buffer exchange.

Anti-His Pull-down assay

FLMyo6 SI (WT) or (SAHmimic) were used alone or mixed with partner GIPC1 (*His-rTEV-GIPC1 255-end*) or TOM1 (His-TOM1 207-492) in a ratio (1/1) (10 μ M) and 1 μ M of extra Calmodulin was added in a total volume of 20 μ L. The input was incubated with 40 μ L of Ni²⁺ beads from cOmplete column (Roche), which were previously equilibrated either in ADP.VO₄ Buffer (10 mM HEPES pH 7.5; 100 mM NaCl; 5 mM NaN₃; 1 mM MgCl₂; 0.1 mM TCEP; 1 mM NaADP; 1 mM Na₃VO₄; 0.1 mM EGTA; 4 mM imidazole) or ADP.VO₄-CaCl₂ Buffer (10 mM HEPES pH 7.5; 100 mM NaCl; 5 mM NaN₃, 1 mM MgCl₂, 0.1 mM TCEP, 1 mM NaADP; 1 mM Na₃VO₄; 4 mM imidazole; 1 mM CaCl₂) or NF Buffer [10mM HEPES pH 7.5; 100 mM NaCl; 5 mM NaN₃; 1 mM MgCl₂; 0.1 mM TCEP; 0.1 mM EGTA; 4 mM imidazole]. All steps were performed at 4°C. Beads were washed by centrifugation after 1 hour of gentle agitation. Bound proteins were eluted in 600 mM imidazole in the corresponding buffer.

Electron Microscopy

Purified Jo-Myo6-In at 50 μ g/ml in 10 mM HEPES; 80 mM NaCl; 1 mM MgCl₂; 0.1 mM TCEP; 0.1 mM ADP; 0.2 mM Na₃VO₄; 0.1 mM EGTA, pH 7.5 was transferred to Carbon Film 300 mesh copper grids (Electron Microscopy Sciences), then stained with 2% uranyl acetate. A total of 284 images were collected with a 200 kV Tecnai G2 microscope under low dose condition with a 4Kx4K F416 TVIPS camera at 0.213 nm/px and treated with the software CryoSPARC⁵⁸. Following CTF determination, template picking was carried out using an initial set of 100 manually picked particles. The resulting 711,671 particles were submitted to a few rounds of 2D classification from which 93,293 particles were selected. These were used in the ab-initio reconstruction that produced the map at 17 Å resolution (FSC).

Model of the Myo6 off-state

We first positioned the Motor domain-Lever arm (residues 1-917) in the Jo-Myo6-In maps from SAXS and EM. Best model-to-map agreement was obtained with PDB 4ANJ⁵⁹ (Motor domain and insert-2/Ca²⁺-CaM with ADP.P_i analog bound, in PPS state). The Lever arm from PDB 3GN4¹⁸ was then superimposed to PDB 4ANJ by using the insert-2/Ca²⁺-CaM region, present in both structures, as reference. In the negative staining reconstruction, Jo-In PDB 5MKC³⁷ was placed in the distinct density that corresponds to it, as expected, with the N- and C-termini pointing towards the center of the main density body occupied by Myo6. The structure of the C-terminal half of the CBD from PDB 3H8D¹⁴ was placed according to structural and biochemical restrictions as follows: (1) the CBD^c C-terminus must be near the N-terminus of the fusion protein In; (2) residues D1157, Y1159, D1161 and Q1163 are in contact with the MD^{Ins2}; (3) there is still density to be filled close to the N-terminus of the CBD^c, that can be filled by CBDⁿ. (Note that this proposed position is opposite to that currently predicted by AlphaFold^{50,51} for uniprot entry : Q9UM54, due to lack of data for the intermolecular interactions when that model was built). At last, the NMR structure of the SAH domain (residues 919-998; PDB: 6OBI⁶⁰) was accommodated in the density. This density is narrow up to residue ~955 and then becomes much larger to account for the rest of the model, in which no distinct subdomain can be identified. Thus, our current model lacks the distal Tail (a compact domain of 3 nm in diameter⁷) and CBDⁿ, for which there seems to remain enough density to be fitted. Model and figure were prepared with Pymol⁶¹.

MNT-1 cell transfection

MNT-1 cells were cultured in DMEM supplemented with 20 % FBS, 10 % AIM-V medium, 1 % sodium pyruvate, 1 % nonessential amino acids, and 1 % penicillin-streptomycin. For plasmid transfection, 400 000 MNT-1 cells were transfected using nucleofection (NHEM kit, Lonza) on Amaxa device 2 (program T20) with 1.5 µg of ^{iRFP}VAMP7 plasmid; 1 µg of ^{mCherry}MST plasmid and 3 µg of ^{GFP}FLMyo6 plasmid. After transfection cells were seeded in fluorodish containing 1 mL RPMI medium, then 1 mL of complete MNT-1 medium supplemented by 10 % FBS was added 6 h post-transfection. Medium was changed 1-day post-transfection by complete medium then cells were fixed with 4 % PFA at 48 h post-transfection. Cells were stored in the dark at 4 °C in PBS medium until imaging. Fluorescence intensity of each ^{mCherry}MST construct was analyzed to ensure equivalent expression levels between the different partners (Sup Fig. 15).

Super resolution imaging and analysis

Samples were imaged in fluorodish using a 100x/1.4 NA oil immersion objective on an inverted Spinning disk confocal microscope (Inverted Eclipse Ti-E Nikon, Spinning disk CSU-X1, Yokogawa) equipped with a Photometrics sCMOS Prime 95B Camera (1200 x 1200 pixels). Z images series were acquired every 0.2 µm. Images were processed with a Live super Resolution module (Live-SR; Gataca systems) based on structured illumination with optical reassignment technique and online processing leading to a two-time resolution improvement⁶². For the figures, Z maximum projection and a subtract background (50 pixels) were applied on SR images using the FIJI software. Analysis was done on raw SR images. Melanin pigments (black spots) were automatically detected in a defined region of interest (ROI) (here, cell outlines that were manually drawn) in BrightField images by creating a MIN-intensity z-projection and considering the lowest values, defined using the 'Find Maxima' function of Image J/Fiji and whose spatial coordinates were recorded. To quantify the percentage of melanosomes containing ^{iRFP}VAMP7 / ^{mCherry}MST / ^{GFP}Myo6 proteins at the membrane, additional ROIs

centered around each individual detected pigment were generated whose size was defined (0.350 μm diameter). Then, for each detected brightfield spot, an additional automatic detection in the fluorescent channel(s) of interest was performed by creating a MAX intensity z-projection in the ROI around the pigments and considering the highest values. Detected pigments were considered positive for the marker of interest above a threshold (defined by Triangle's automatic thresholding method, calculated on the MAX intensity projection, or manual thresholding in the case of cells expressing the lowest GFP-Myo6), and the percentage of which was calculated. Pigments that were automatically detected very close to each other (within 4 pixels in XY and 2 pixels in Z) and that had overlapping ROIs were automatically removed and eliminated from the analysis to avoid data duplication. Moreover, automatically detected pigmented that were negative for $i\text{RFP}^{\text{VAMP7}}$ and/or $m\text{Cherry}^{\text{MST}}$ fluorescent signal were excluded from the analysis because not considered as pigmented melanosomes (positive for membrane-associated components). For each cell, a percentage of Myo6 positive melanosome was calculated and normalized to the total number pigmented melanosomes (co-positive for pigment and $i\text{RFP}^{\text{VAMP7}}$ and/or $m\text{Cherry}^{\text{MST}}$).

Proximal dimer Crystallization, Data Collection, and Structure Determination

The Myo6 875-940 construct was crystallized by hanging drop vapor diffusion at 290 K by mixing 1 μL of 9.8 mg/mL protein solution with 1 μL of reservoir solution (27% PEG 4000, 10 mM MgCl_2 and 0.2 M imidazole / malate, pH 6.0). Crystals grew spontaneously as rods 1 to 7 days after. After additional 3 weeks, they were cryo-cooled in liquid nitrogen in a solution containing 28% PEG 4000, 10 mM MgCl_2 , 0.2 M imidazole / malate, pH 6.0, and 27% ethylene glycol. One exploitable X-ray dataset was collected at the Proxima 1 beamline (Synchrotron Soleil, Gif-Sur-Yvette) and processed with Autoproc⁶³. Diffraction limits after treatment with Staraniso⁶⁴ with cut-off of 1.2 I/sI were 2.566 \AA in two directions, and 2.077 \AA in one direction. Initial structure factors were obtained by molecular replacement with Phaser⁶⁵ using a helix comprised of 30 serine residues as search model. Initial sequence attribution was obtained with Phenix AutoBuild⁶⁶, followed by several cycles of iterative edition with Coot⁶⁷ and refinement with Buster⁶⁸. Resolution was automatically cut by Buster to 2.2 \AA based on model-map cross-correlation. The dimer is defined by one of the 2-fold symmetry axis, with crystal contacts between the N-terminus of one dimer and C-terminus of neighboring dimers (Sup Fig. 12B-C, Sup Movie 2). When the carbons are colored according to B-factors (Fig. 5A), the lowest values are found between residues 885 and 913, suggesting that the dimerization interface is comprised within those boundaries.

Single-molecule assays

Biotin labeled CaM was used to selectively exchange only one of the two myosin VI CaMs in the motor domains of the wild-type or the mutant proteins for the single molecule studies as described before⁶⁹. Potential processive movements of FLMyo6, and FLMyo6 (T888D, R892E, V903D) were observed on 20 μL flowcells using Total Internal Fluorescence Microscope (TIRFM) as described⁷⁰. First, 20 μL of N-ethyl maleimide (NEM)-modified myosin (0.5 mg/ml) in Buffer A (25 mM imidazole, pH 7.4, 4 mM MgCl_2 , 1 mM EGTA, 300 mM KCl, 10 mM DTT) was introduced for 2 min to create the attachment sites for actin filaments. To remove the unbound NEM-modified myosin, the flow chamber was washed with buffer B (25 mM imidazole, pH 7.4, 4 mM MgCl_2 , 1 mM EGTA, 50 mM KCl, 10 mM DTT) containing 1 mg/ml BSA and incubated for 2 minutes. Then 100 nM actin filaments in buffer B were infused into the flowcell and incubated for 2 min. The flowcell was washed with buffer B and 150 nM of the full-length myosin monomers, FLMyo6 or FLMyo6(T888D, R892E, V903D), in buffer B were introduced into the

flow cell without ATP. Under these conditions, the actin filaments were saturated by Myo6 monomers, which allowed the monomers to be in close proximity for dimerization, as previously described¹². Then, Streptavidin Qdots (100 nM; emission at 655 nm) were infused into the flow cell. The Qdots bound specifically to the exchangeable biotinylated-CaM in the IQ domain of myosin VI. Finally, buffer B containing 2 mM ATP and 1 mg/ml BSA was infused into the flow cell. In this step, Myo6-monomers and unbound Qdots were removed from the flow cell while Myo6 dimers showed processive movement along actin filaments.

Model of the Myo6 proximal dimer

The cryoEM structure of Myo6 bound to actin (PDB: 6BNP⁷¹) was used as basis for placing two Myo6 Motor domains in rigor and PPS states (grey) at the desired 31 nm distance (Fig. 5E). On each side, the N-terminus of the Lever arm bound to two light chains (pink, PDB: 3GN4¹⁸) was aligned to the corresponding residues in the Converter. The crystallized dimerization domain (blue) was then placed with minimal distance from the two Lever arms, leaving a gap of 4.6 nm from each side. This gap needs to be filled by a stretch of 26 amino acid residues that would make 3.9 nm if in a theoretical helix, or up to 9.9 nm if fully extended. SAH (green) (PDB: 6OBI⁶⁰) was connected to the C-terminus of the dimerization region *via* a putative kink. Model and figure were prepared with Pymol⁶¹.

Bundle Unfolding Assay

As previously described¹⁸, cysteine residues were introduced to replace T845 and A880 in Myo6-917 and Myo6-991-GCN4 constructs with no reactive cysteines. Control constructs contained one reactive cysteine, T845C. One mg of each protein was labeled with a 10-fold molar excess of TMR 5-iodoacetamide (5-TMRIA; Anaspec, San Jose, CA) per cysteine (from a stock concentration of 20 mM in dimethylformamide) at 4°C for 1–3 hr. Unbound rhodamine was removed by gel filtration and overnight dialysis. Absorption spectra were measured in a HP Diode Array Spectrophotometer, and fluorescence spectra were obtained in a PTI QM3 luminescence spectrofluorometer. The excitation and emission spectra were measured at 552 and 575 nm, respectively.

Generation of Myo6 null HeLa cells

The Myo6 gene of HeLa cells (ATCC CCL-2) was inactivated by CRISPR/Cas9 gene editing approach. Briefly, HeLa cells were transfected using a combination of three human Myo6 CRISPR plasmid variants (Santa Cruz Biotech SC-401815) – each driving expression of Cas9, GFP and one of the following human Myo6-specific 20-nucleotide gRNAs (5'-3': taatatcaaagttcgatata, acattctgattgcagtgaatc, ccaagtgttctcgcagaag). Clones of transfected HeLa cells were selected on the basis of GFP fluorescence, and PCR of isolated DNA using primers flanking the targeted genomic sequences. Loss of Myo6 expression was confirmed by western blot.

Transferrin Endocytosis Assay

Normal and Myo6 null HeLa cells were grown in multi-well tissue culture plates on coverslips coated with rat collagen I (Corning). FLMyo6 (WT) or FLMyo6 (T888D.Q892E.V903D) were tagged with a C-terminal mApple for identification of expressing cells. Transfections were performed using the XtremeGENE 9 DNA transfection reagent (Sigma-Aldrich) following the manufacturer's instructions. Cells were serum starved, but otherwise maintained in normal growth conditions – at 37°C with 5% CO₂, by incubation in serum-free Dulbecco's modified Eagle's medium for 2.5 h. Serum-free medium was supplemented with genistein (600 μM, Cayman Chemical Company) to inhibit caveolae-mediated

uptake of transferrin following Myo6 depletion as previously reported¹⁷. During the final 10 min of serum starvation, Alexa fluor 488-conjugated transferrin (ThermoFisher) was added to the culture medium at 25 µg/ml. Following serum starvation, plates were placed on ice and washed twice with 10 mM HCl and 150 mM NaCl to remove cell surface-bound transferrin. The cells were fixed with ice-cold 4 % paraformaldehyde for 20 min and stained with rabbit anti-dsRed antibody (Takara Bio) and Alexa fluor 568-conjugated anti-rabbit secondary antibody to identify cells expressing mApple-tagged Myo6. Image acquisition was performed with a Leica Application Suite X software on Leica TSC-8 confocal system using a 40X oil immersion objective lens (n.a. = 1.3). Transferrin uptake was determined using ImageJ software: the total transferrin-conjugated fluorescence intensity from sum slice projections of individual cells was subsequently normalized by cell size. Comparative samples were stained, imaged, and processed simultaneously under identical conditions. Data were subjected to one-way analysis of variance with Tukey post-hoc comparison of individual groups to determine statistical significance.

Data availability.

The atomic model of the Myo6 proximal dimer is available on the PDB⁷² under the accession code 8ARD. The other data supporting the findings of this study are available from the corresponding author upon request.

References

1. *Myosins: A Superfamily of Molecular Motors*. vol. 1239 (Springer International Publishing, 2020).
2. Heissler, S. M., Arora, A. S., Billington, N., Sellers, J. R. & Chinthalapudi, K. Cryo-EM structure of the autoinhibited state of myosin-2. *Sci Adv* **7**, eabk3273 (2021).
3. Niu, F. *et al.* Autoinhibition and activation mechanisms revealed by the triangular-shaped structure of myosin Va. *Sci Adv* **8**, eadd4187 (2022).
4. Robert-Paganin, J., Auguin, D. & Houdusse, A. Hypertrophic cardiomyopathy disease results from disparate impairments of cardiac myosin function and auto-inhibition. *Nat Commun* **9**, 4019 (2018).
5. Umeki, N. *et al.* The tail binds to the head-neck domain, inhibiting ATPase activity of myosin VIIA. *Proc Natl Acad Sci U S A* **106**, 8483–8488 (2009).
6. Umeki, N. *et al.* Phospholipid-dependent regulation of the motor activity of myosin X. *Nat Struct Mol Biol* **18**, 783–788 (2011).
7. Spink, B. J., Sivaramakrishnan, S., Lipfert, J., Doniach, S. & Spudich, J. A. Long single alpha-helical tail domains bridge the gap between structure and function of myosin VI. *Nat Struct Mol Biol* **15**, 591–597 (2008).
8. Lister, I. *et al.* A monomeric myosin VI with a large working stroke. *EMBO J* **23**, 1729–1738 (2004).
9. Caporizzo, M. A. *et al.* The Antiparallel Dimerization of Myosin X Imparts Bundle Selectivity for Processive Motility. *Biophys J* **114**, 1400–1410 (2018).
10. Liu, R. *et al.* A binding protein regulates myosin-7a dimerization and actin bundle assembly. *Nat Commun* **12**, 563 (2021).
11. Lu, Q., Ye, F., Wei, Z., Wen, Z. & Zhang, M. Antiparallel coiled-coil-mediated dimerization of myosin X. *Proc Natl Acad Sci U S A* **109**, 17388–17393 (2012).
12. Park, H. *et al.* Full-length myosin VI dimerizes and moves processively along actin filaments upon monomer clustering. *Mol Cell* **21**, 331–336 (2006).
13. Ropars, V. *et al.* The myosin X motor is optimized for movement on actin bundles. *Nat Commun* **7**, 12456 (2016).
14. Yu, C. *et al.* Myosin VI undergoes cargo-mediated dimerization. *Cell* **138**, 537–548 (2009).
15. Phichith, D. *et al.* Cargo binding induces dimerization of myosin VI. *Proc Natl Acad Sci U S A* **106**, 17320–17324 (2009).
16. Kim, H., Hsin, J., Liu, Y., Selvin, P. R. & Schulten, K. Formation of salt bridges mediates internal dimerization of myosin VI medial tail domain. *Structure* **18**, 1443–1449 (2010).
17. Mukherjee, M. *et al.* Myosin VI must dimerize and deploy its unusual lever arm in order to perform its cellular roles. *Cell Rep* **8**, 1522–1532 (2014).
18. Mukherjee, M. *et al.* Myosin VI dimerization triggers an unfolding of a three-helix bundle in order to extend its reach. *Mol Cell* **35**, 305–315 (2009).
19. de Jonge, J. J., Batters, C., O’Loughlin, T., Arden, S. D. & Buss, F. The MYO6 interactome: selective motor-cargo complexes for diverse cellular processes. *FEBS Lett* **593**, 1494–1507 (2019).
20. Avraham, K. B. *et al.* The mouse Snell’s waltzer deafness gene encodes an unconventional myosin required for structural integrity of inner ear hair cells. *Nat Genet* **11**, 369–375 (1995).
21. Ripoll, L. *et al.* Myosin VI and branched actin filaments mediate membrane constriction and fission of melanosomal tubule carriers. *J Cell Biol* **217**, 2709–2726 (2018).
22. Tumbarello, D. A. *et al.* Autophagy receptors link myosin VI to autophagosomes to mediate Tom1-dependent autophagosome maturation and fusion with the lysosome. *Nat Cell Biol* **14**, 1024–1035 (2012).
23. Morris, S. M. *et al.* Myosin VI binds to and localises with Dab2, potentially linking receptor-mediated endocytosis and the actin cytoskeleton. *Traffic* **3**, 331–341 (2002).
24. Naccache, S. N., Hasson, T. & Horowitz, A. Binding of internalized receptors to the PDZ domain of GIPC/synectin recruits myosin VI to endocytic vesicles. *Proc Natl Acad Sci U S A* **103**, 12735–12740 (2006).
25. Fili, N. *et al.* NDP52 activates nuclear myosin VI to enhance RNA polymerase II transcription. *Nat Commun* **8**, 1871 (2017).
26. Yoshida, H. *et al.* Lessons from border cell migration in the Drosophila ovary: A role for myosin VI in dissemination of human ovarian cancer. *Proc Natl Acad Sci U S A* **101**, 8144–8149 (2004).
27. Wang, D. *et al.* MYO6 knockdown inhibits the growth and induces the apoptosis of prostate cancer cells by decreasing the phosphorylation of ERK1/2 and PRAS40. *Oncol Rep* **36**, 1285–1292 (2016).
28. Fili, N. *et al.* Competition between two high- and low-affinity protein-binding sites in myosin VI controls its cellular function. *J Biol Chem* **295**, 337–347 (2020).
29. Dos Santos, Á. *et al.* Binding partners regulate unfolding of myosin VI to activate the molecular motor. *Biochem J* **479**, 1409–1428 (2022).
30. Hariadi, R. F., Cale, M. & Sivaramakrishnan, S. Myosin lever arm directs collective motion on cellular actin network. *Proceedings of the National Academy of Sciences* **111**, 4091–4096 (2014).
31. Rai, A., Vang, D., Ritt, M. & Sivaramakrishnan, S. Dynamic multimerization of Dab2-Myosin VI complexes regulates cargo processivity while minimizing cortical actin reorganization. *J Biol Chem* **296**, 100232 (2021).

32. Altman, D., Sweeney, H. L. & Spudich, J. A. The mechanism of myosin VI translocation and its load-induced anchoring. *Cell* **116**, 737–749 (2004).
33. Rai, A. *et al.* Multimodal regulation of myosin VI ensemble transport by cargo adaptor protein GIPC. *J Biol Chem* **298**, 101688 (2022).
34. Shang, G. *et al.* Structure analyses reveal a regulated oligomerization mechanism of the PlexinD1/GIPC/myosin VI complex. *Elife* **6**, e27322 (2017).
35. Hu, S. *et al.* Structure of Myosin VI/Tom1 complex reveals a cargo recognition mode of Myosin VI for tethering. *Nat Commun* **10**, 3459 (2019).
36. Batters, C., Brack, D., Ellrich, H., Averbek, B. & Veigel, C. Calcium can mobilize and activate myosin-VI. *Proc Natl Acad Sci U S A* **113**, E1162–1169 (2016).
37. Bonnet, J. *et al.* Autocatalytic association of proteins by covalent bond formation: a Bio Molecular Welding toolbox derived from a bacterial adhesin. *Sci Rep* **7**, 43564 (2017).
38. Brownstein, Z. *et al.* Novel myosin mutations for hereditary hearing loss revealed by targeted genomic capture and massively parallel sequencing. *Eur J Hum Genet* **22**, 768–775 (2014).
39. Dennis, M. K. *et al.* BLOC-1 and BLOC-3 regulate VAMP7 cycling to and from melanosomes via distinct tubular transport carriers. *J Cell Biol* **214**, 293–308 (2016).
40. Ishida, M., Arai, S. P., Ohbayashi, N. & Fukuda, M. The GTPase-deficient Rab27A(Q78L) mutant inhibits melanosome transport in melanocytes through trapping of Rab27A effector protein Slac2-a/melanophilin in their cytosol: development of a novel melanosome-targeting tag. *J Biol Chem* **289**, 11059–11067 (2014).
41. He, F. *et al.* Myosin VI Contains a Compact Structural Motif that Binds to Ubiquitin Chains. *Cell Rep* **14**, 2683–2694 (2016).
42. Berggren, K. *et al.* Background-free, high sensitivity staining of proteins in one- and two-dimensional sodium dodecyl sulfate-polyacrylamide gels using a luminescent ruthenium complex. *Electrophoresis* **21**, 2509–2521 (2000).
43. Yu, C. *et al.* Membrane-induced lever arm expansion allows myosin VI to walk with large and variable step sizes. *J Biol Chem* **287**, 35021–35035 (2012).
44. Rock, R. S. *et al.* Myosin VI is a processive motor with a large step size. *Proceedings of the National Academy of Sciences* **98**, 13655–13659 (2001).
45. Spitzer, M., Wildenhain, J., Rappsilber, J. & Tyers, M. BoxPlotR: a web tool for generation of box plots. *Nat Methods* **11**, 121–122 (2014).
46. Sweeney, H. L. & Houdusse, A. What can myosin VI do in cells? *Curr Opin Cell Biol* **19**, 57–66 (2007).
47. Lumb, K. J., Carr, C. M. & Kim, P. S. Subdomain folding of the coiled coil leucine zipper from the bZIP transcriptional activator GCN4. *Biochemistry* **33**, 7361–7367 (1994).
48. Heissler, S. M. & Sellers, J. R. Various Themes of Myosin Regulation. *J Mol Biol* **428**, 1927–1946 (2016).
49. Fili, N. & Toseland, C. P. Unconventional Myosins: How Regulation Meets Function. *Int J Mol Sci* **21**, E67 (2019).
50. Jumper, J. *et al.* Highly accurate protein structure prediction with AlphaFold. *Nature* **596**, 583–589 (2021).
51. Varadi, M. *et al.* AlphaFold Protein Structure Database: massively expanding the structural coverage of protein-sequence space with high-accuracy models. *Nucleic Acids Res* **50**, D439–D444 (2022).
52. Spudich, G. *et al.* Myosin VI targeting to clathrin-coated structures and dimerization is mediated by binding to Disabled-2 and PtdIns(4,5)P2. *Nat Cell Biol* **9**, 176–183 (2007).
53. Thureau, A., Roblin, P. & Pérez, J. BioSAXS on the SWING beamline at Synchrotron SOLEIL. *J Appl Cryst* **54**, 1698–1710 (2021).
54. Manalastas-Cantos, K. *et al.* ATSAS 3.0: expanded functionality and new tools for small-angle scattering data analysis. *J Appl Crystallogr* **54**, 343–355 (2021).
55. Svergun, D. I., Petoukhov, M. V. & Koch, M. H. Determination of domain structure of proteins from X-ray solution scattering. *Biophys J* **80**, 2946–2953 (2001).
56. Volkov, V. V., Svergun, D. I. & IUCr. Uniqueness of ab initio shape determination in small-angle scattering. *Journal of Applied Crystallography* vol. 36 860–864 <http://scripts.iucr.org/cgi-bin/paper?S0021889803000268> (2003).
57. De La Cruz, E. M., Ostap, E. M. & Sweeney, H. L. Kinetic mechanism and regulation of myosin VI. *J Biol Chem* **276**, 32373–32381 (2001).
58. Punjani, A., Rubinstein, J. L., Fleet, D. J. & Brubaker, M. A. cryoSPARC: algorithms for rapid unsupervised cryo-EM structure determination. *Nat Methods* **14**, 290–296 (2017).
59. Ménétrey, J. *et al.* Processive steps in the reverse direction require uncoupling of the lead head lever arm of myosin VI. *Mol Cell* **48**, 75–86 (2012).
60. Barnes, C. A. *et al.* Remarkable Rigidity of the Single α -Helical Domain of Myosin-VI As Revealed by NMR Spectroscopy. *J Am Chem Soc* **141**, 9004–9017 (2019).
61. Schrödinger, L. & DeLano, W. PyMOL. Retrieved from <http://www.pymol.org/pymol>. (2020).
62. Roth, S. & Heintzmann, R. Optical photon reassignment with increased axial resolution by structured illumination. *Methods Appl Fluoresc* **4**, 045005 (2016).

63. Vonrhein, C. *et al.* Data processing and analysis with the autoPROC toolbox. *Acta Crystallogr D Biol Crystallogr* **67**, 293–302 (2011).
64. Tickle, I. J. *et al.* STARANISO. Cambridge, United Kingdom: Global Phasing Ltd. (2018).
65. McCoy, A. J. *et al.* Phaser crystallographic software. *J Appl Cryst* **40**, 658–674 (2007).
66. Terwilliger, T. C. *et al.* Iterative model building, structure refinement and density modification with the PHENIX AutoBuild wizard. *Acta Crystallogr D Biol Crystallogr* **64**, 61–69 (2008).
67. Emsley, P. & Cowtan, K. Coot: model-building tools for molecular graphics. *Acta Crystallogr D Biol Crystallogr* **60**, 2126–2132 (2004).
68. Bricogne, G. *et al.* BUSTER version X.Y.Z. Cambridge, United Kingdom: Global Phasing Ltd. (2017).
69. Yildiz, A. *et al.* Myosin VI steps via a hand-over-hand mechanism with its lever arm undergoing fluctuations when attached to actin. *J Biol Chem* **279**, 37223–37226 (2004).
70. Ali, M. Y. *et al.* Myosin Va and myosin VI coordinate their steps while engaged in an in vitro tug of war during cargo transport. *Proc Natl Acad Sci US A* **108**, E535-541 (2011).
71. Gurel, P. S. *et al.* Cryo-EM structures reveal specialization at the myosin VI-actin interface and a mechanism of force sensitivity. *Elife* **6**, e31125 (2017).
72. Berman, H., Henrick, K. & Nakamura, H. Announcing the worldwide Protein Data Bank. *Nat Struct Biol* **10**, 980 (2003).

Acknowledgments

The authors greatly acknowledge the Cell and Tissue Imaging (PICT-IBiSA) – Institut Curie, member of the French National Research Infrastructure France-BioImaging (ANR10-INBS-04) and in particular Anne Sophie Macé for her help in the quantification of the results; the CurieCoreTech Mass Spectrometry Proteomics and Recombinant protein; the beam line scientists of PX1 and SWING (SOLEIL synchrotron) for excellent support during data collection; Pierre-Damien Coureux for preliminary experiments in negative staining electron microscopy; Margaret Titus for her help with Jo-Myo6-In cloning and comments on the manuscript; Virginie Ropars for her help in SAXS data optimization, Guillaume Jousset for its advises in biochemistry and Christopher Toseland for accepting to provide us with Dab2 DNA.

Funding

H.L.S. was supported by National Institutes of Health Grant DC009100. A.H. is supported by grants from CNRS and ANR-19-CE11-0015-02. A.H. and C.D. were supported by grants from ANR-17-CE11-0029-01. The A.H., D.L. and C.D. teams are part of the Labex Cell(n)Scale ANR-11-LBX-0038 and IDEX PSL (ANR-10-IDEX-0001-02-PSL). K.P. is a recipient of a Marie Curie fellowship 797150 MELANCHOR. V.P.-H. and L.C. are recipient of a PhD fellowship from Ligue contre le cancer GB/MA/SC-12630 and IP/SC-16058.

Author contributions

A.H. and H.L.S. designed and directed the research. L.C., V.J.P.-H., K.J.P. and C.D. were involved in project management. H.S., X.L., L.H., L.C., T.L., C.K., L.V., A.D., E.F., P.H., V.J.P.-H., D.M. cloned, produced and purified constructs. L.C., T.L., C.K., H.S., L.H., A.D., L.V., P.H., V.J.P.-H., D.M. performed biophysical and biochemical assays. C.K. performed grid optimization for negative staining EM that were collected by ADC. D.L. provided access to the 200kV microscope. C.K. analyzed the negative staining data and performed the 3D reconstruction. H.S. characterized the limits of the proximal dimerization region, crystallized it and C.K. solved the structure. F.M., Y.I.L. and K.J.P. performed the cell-based assays. L.C., C.K., A.H., H.L.S., F.M., Y.I.L., H.S., L.H., A.D., L.V., K.J.P. and V.J.P.-H. analyzed the data. J. S.-C. provided technical help in quantification of the cell-based assays. L.C., A.H., C.D., C.K. and H.L.S. wrote the initial version of the paper, with the help of F.M. and V.J.P.-H. and all authors reviewed it. A.H. and H.L.S. provided fundings.

Competing interests

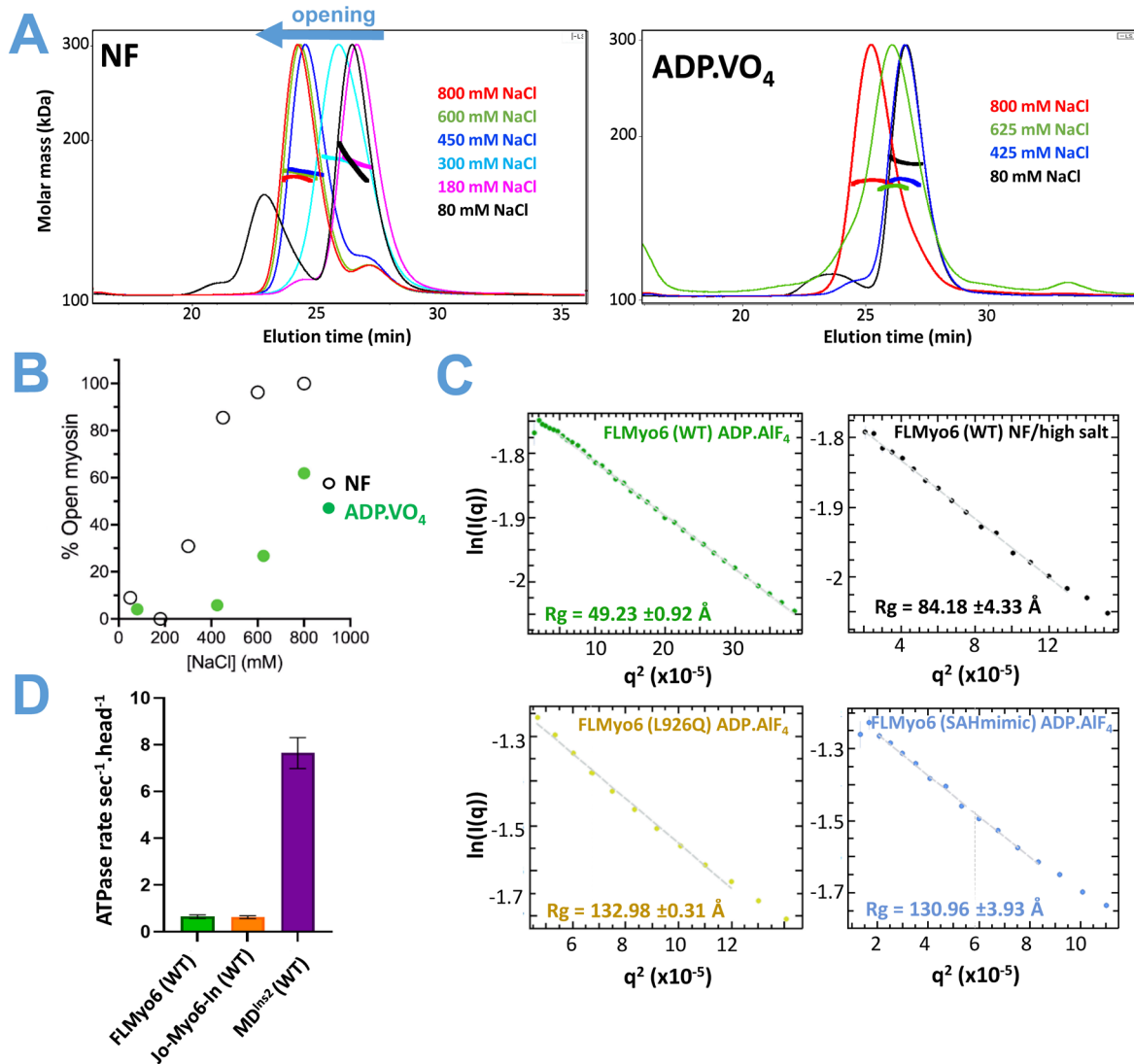
The authors declare no competing financial interests.

Supplementary information

How Myosin VI Traps its Off-State, is Activated and Dimerizes

Louise Canon¹, Carlos Kikuti¹, Vicente J. Planelles-Herrero¹, Tianming Lin², Franck Mayeux¹, Helena Sirkia¹, Young il Lee², Leila Heidsieck¹, Léonid Velikovskiy¹, Amandine David¹, Xiaoyan Liu², Dihia Moussaoui¹, Emma Forest^{1,3}, Peter Höök², Karl J. Petersen¹, Aurélie Di Cicco⁴, Julia Sires-Campos⁵, Daniel Lévy⁴, Cédric Delevoye⁵, H. Lee Sweeney^{2,*}, Anne Houdusse^{1,*}

Supplementary Figures



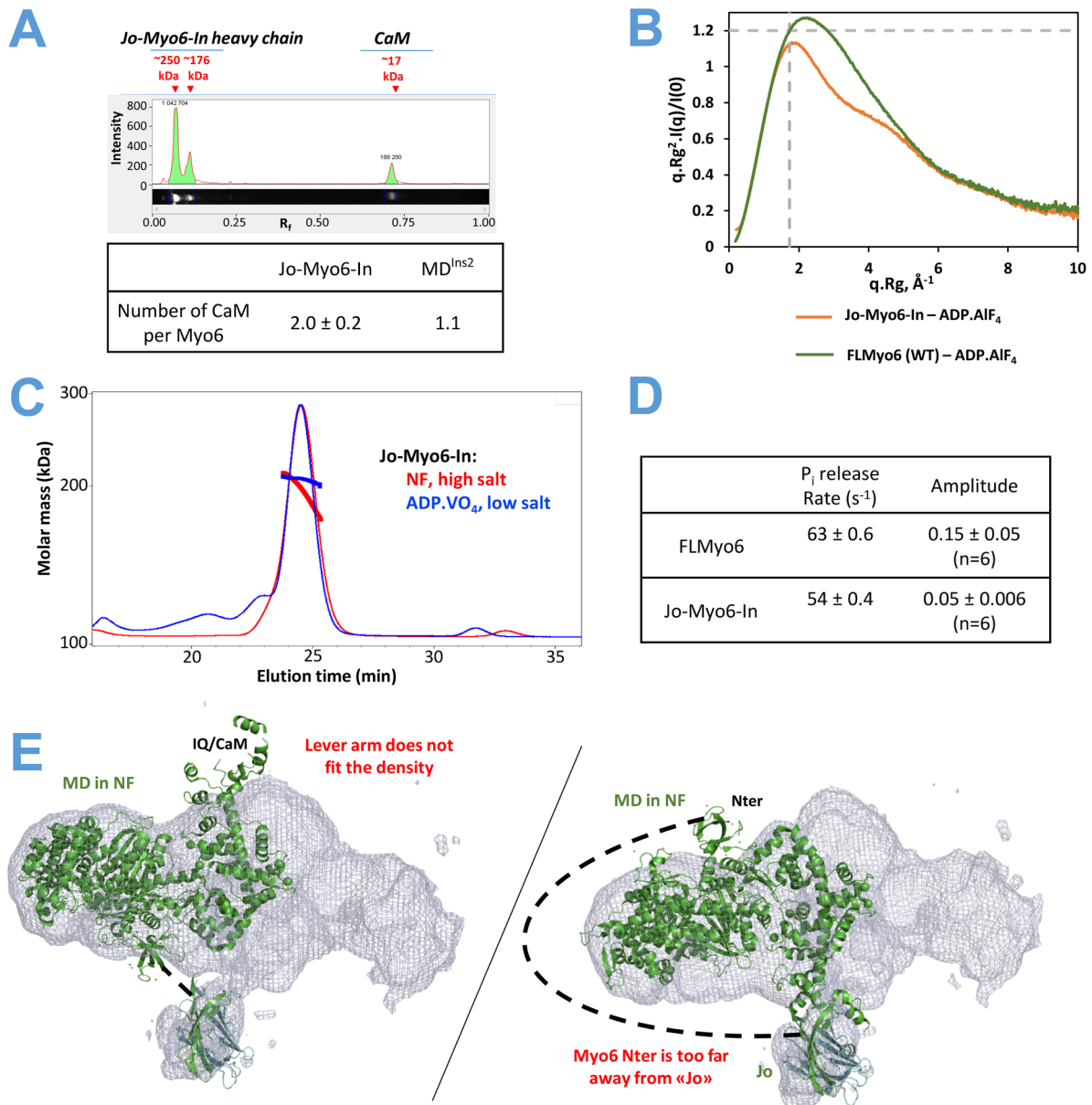
Supplementary Figure 1 – ATP is required for the compact, back-folded conformation of Myo6.

(A) Normalized SEC-MALS profiles of FLMyo6 in different elution buffers. Thin lines: normalized static light scattering; Thick lines: molecular mass as determined for each 0.5 second experimental point by Astra (Wyatt technology). ADP.VO₄ buffer: 20 mM Hepes; 2 mM MgCl₂; 1 mM NaADP; 1 mM NaVO₄; 0.1 mM EGTA; 0.5 mM TCEP, pH 7.5 + indicated NaCl concentration; NF buffer: 20 mM Hepes; 2 mM MgCl₂; 0.1 mM EGTA; 0.5 mM TCEP, pH 7.5 + indicated NaCl concentration.

(B) Percentage of open FLMyo6 as a function of [NaCl] in ADP.VO₄ or NF conditions, as determined by SEC-MALS. The earliest and latest elution times for Myo6 monomers were taken as 100% and 0% open, respectively.

(C) Guinier plot of FLMyo6 WT, SAHmimic and L926Q in ADP.AIF₄ or in NF/high salt. R_g values were extracted from the linear fit (dashed line) using primusqt (ATSAS suite¹).

(D) Actin-activated ATPase rate of 150 nM FLMyo6 (WT), Jo-Myo6-In, and MD^{Ins2} (n=6) at 40 μ M F-actin.



Supplementary Figure 2 – The Jo-In fusion stabilizes the off-state with no effect on its conformation.

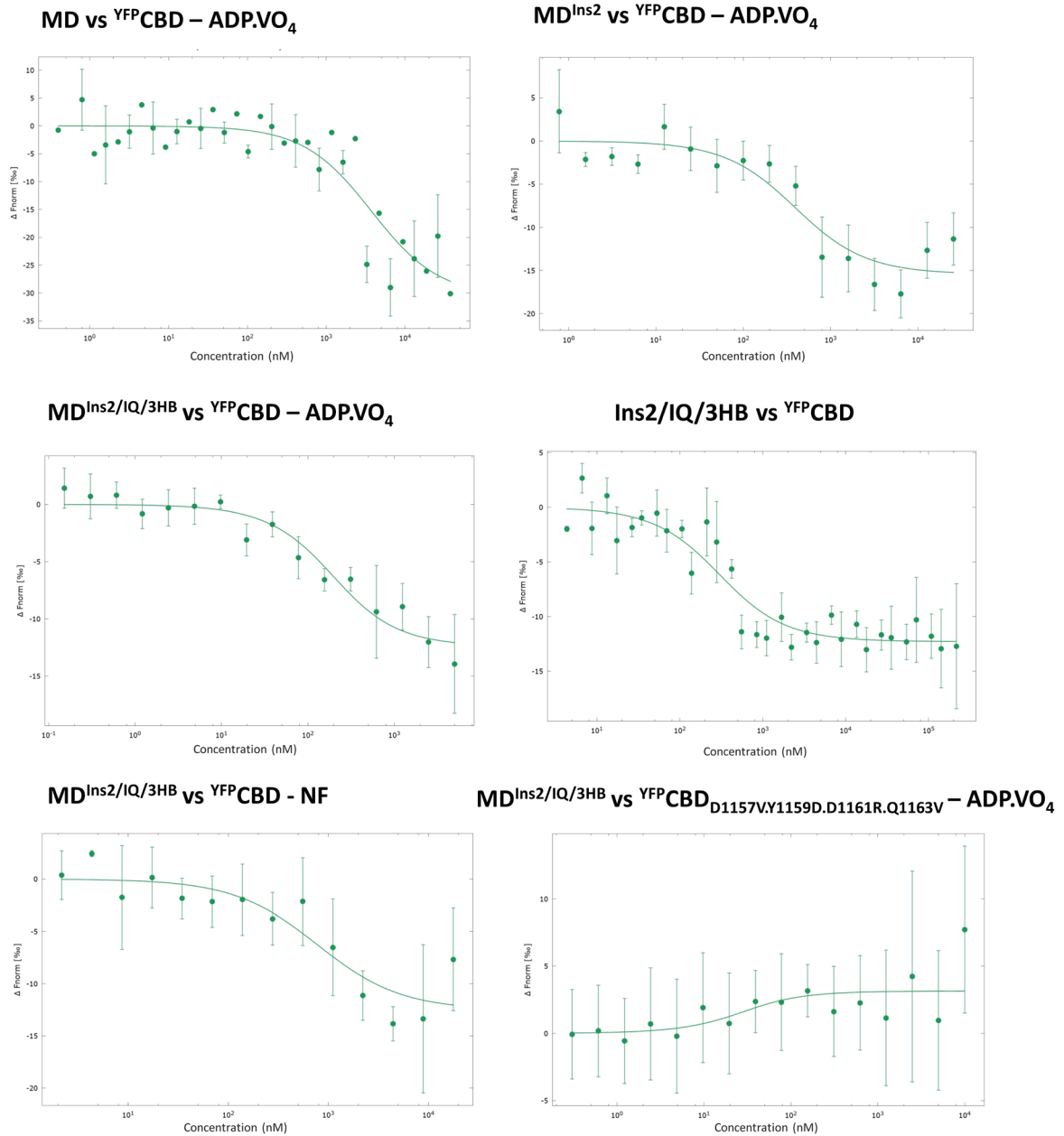
(A) SDS-PAGE profile of Jo-Myo6-In stained with SYPRO². The estimated molecular weight based on SDS-PAGE is given in red. The CaM/FLMyo6 molar ratio was determined from the intensities of the corresponding bands (Table: mean ± standard deviation from 4 replicates). Intensity of Myo6 and CaM bands were estimated on ImageLab software (Bio-Rad). Ratio CaM/FLMyo6 was estimated by calculating (CaM band intensity)/(Myo6 band intensity) and normalized by theoretical molecular weight to get a molar ratio. MD^{Ins2} was used as a control as it binds 1 CaM per Myo6³. Note that, on SDS-PAGE, purified Jo-Myo6-In-Flag appears as two distinct bands, one at its expected molecular weight 176 kDa, and another band around 250 kDa. On SEC, the faster band was found to elute slightly earlier, in a broader peak merged to the one corresponding to the slower band. LC-MS concluded that both bands correspond to Jo-Myo6-In with 68.5% sequence coverage. Exactly the same peptides were found in both bands, and the Jo and In peptides containing the expected covalent Lys-Asn bond could not be found. Therefore, we assume that the slower band corresponds to the protein whose covalent Lys-Asn bond is correctly formed (=“locked”), whereas the faster band is composed by folded, but not locked, protein (=“closed”).

(B) Dimensionless Kratky plot representation. Dotted lines $((qR_g)^2 I(q)/I(0) = 1.104$ and $qR_g = \sqrt{3}$) intersection highlight the theoretical maximum of a globular protein. In the presence of ADP.AIF₄, FLMyo6 (green) and Jo-Myo6-In (orange) spectra result in a bell-shape curve (with a shoulder in the case of Jo-In) with a maximum close to $(\sqrt{3}:1.104)$, suggesting that both proteins are rather globular and well folded. The shoulder in the Jo-Myo6-In profile is typical of multi-domain proteins consistent with the addition of the Jo-In tag.

(C) Normalized SEC-MALS profiles of Jo-Myo6-In in conditions that favor opening (red, NF) or closure (blue, ADPVO₄). NF buffer: 20 mM Hepes; 300 mM NaCl; 2 mM CaCl₂; 0.1 mM EDTA; 0.5 mM TCEP, pH 7.5. ADP.VO₄ buffer: 20 mM Hepes; 80 mM NaCl; 2 mM MgCl₂; 1 mM NaADP; 1 mM NaVO₄; 0.1 mM EGTA; 0.5 mM TCEP, pH 7.5.

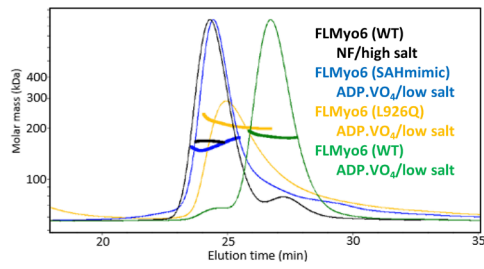
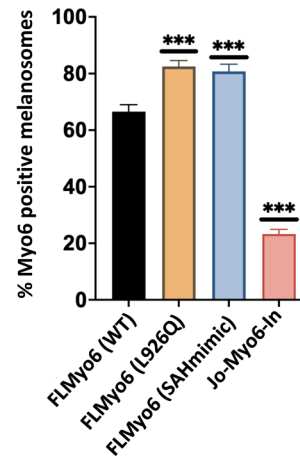
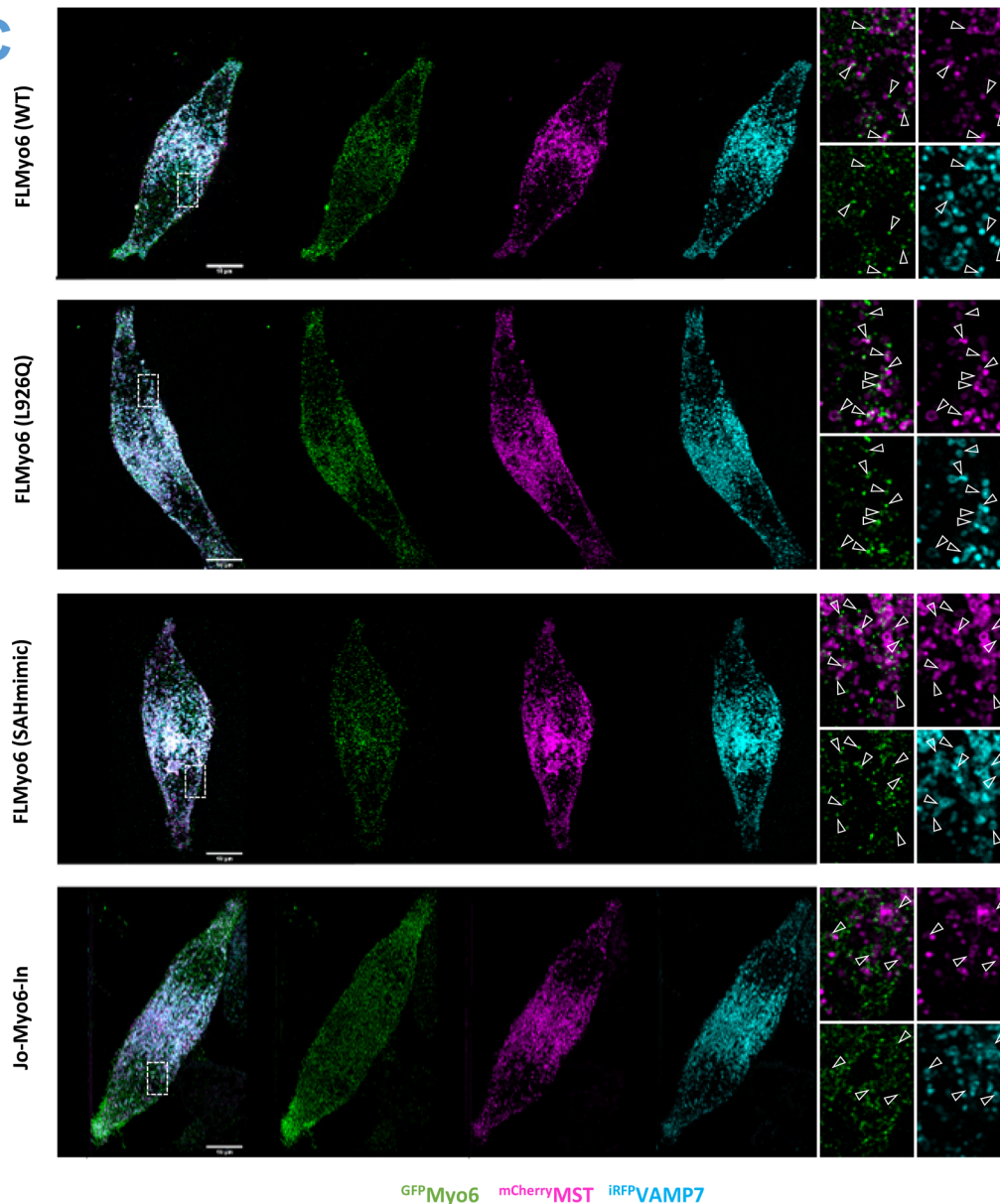
(D) Myo6 P_i release rates and amplitudes from stopped-flow experiments.

(E) Docking of nucleotide-free Myo6 MD^{Ins2/IQ} (PDB: 2BKI³) and Jo-In (PDB: 5MKC⁴) in the negative staining map. The structure of the Motor domain devoid of nucleotide doesn't fit the map: **(left)** if the connection between the N-terminus of Myo6 and the C-terminus of Jo is respected, the Lever arm does not fit in the envelope; **(right)** if the Lever arm is positioned inside the 3D reconstruction, the distance between the Myo6 N-terminus and the fusion subdomain Jo is prohibitive.



Supplementary Figure 3 – Affinity of the Myo6 CBD for different Myo6 Head or Neck constructs.

Microscale thermophoresis profiles and fits corresponding to the data exposed in [Table 1](#).

A**B****C**

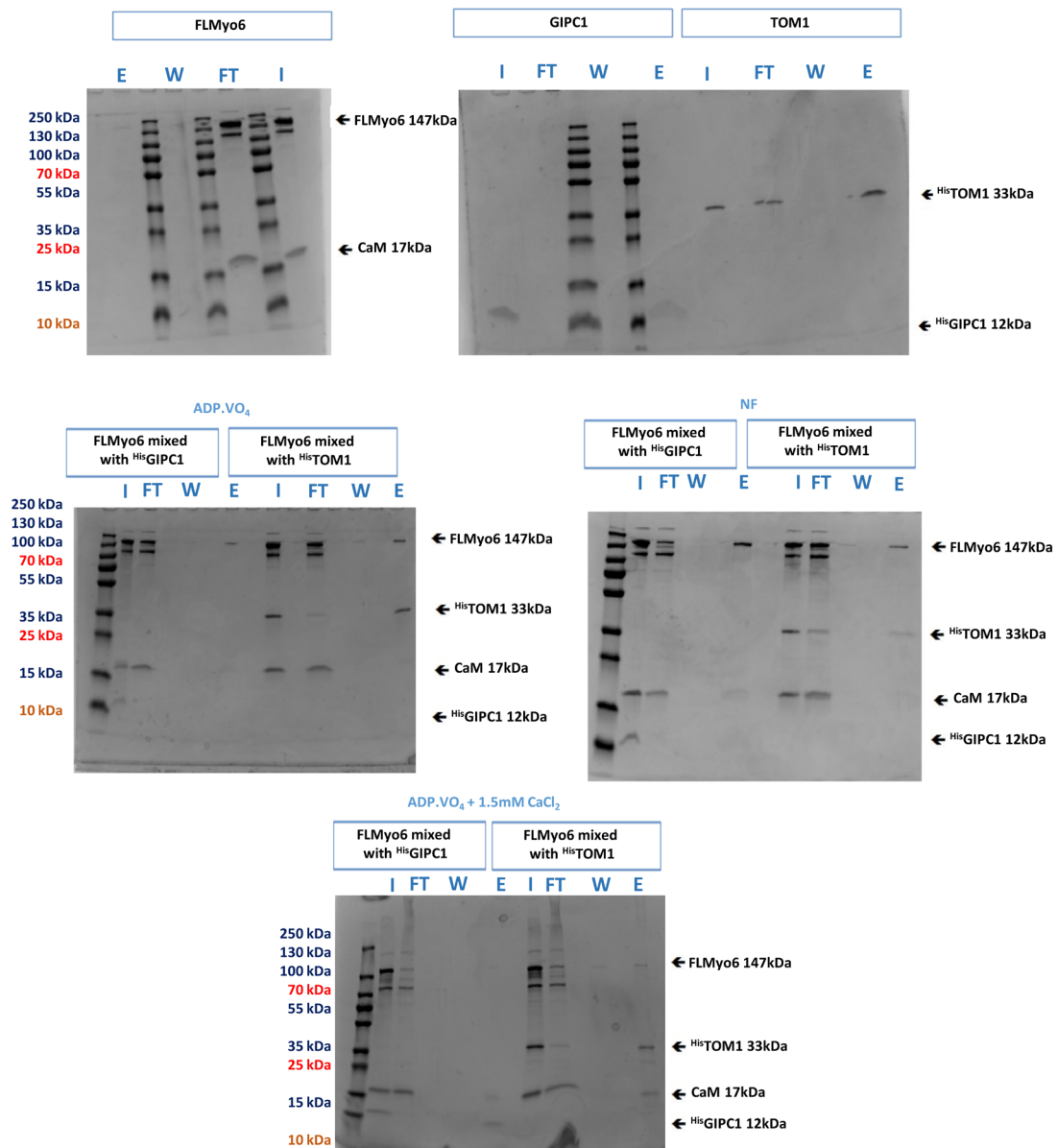
Supplementary Figure 4 – Role of the proximal Myo6 sequence in the stabilization of the off-state.

(A) Normalized SEC-MALS profiles of FLMyo6 (SAHmimic) (blue) and FLMyo6 (L926Q) (yellow) mutants, plus FLMyo6 (WT) in conditions that favor opening (black) or closure (green), as references.

Experimental conditions were similar to those described for [Sup Fig 1](#). Here, “High salt” means 800 mM NaCl; “low salt”, 80 mM.

(B) Quantification of Myo6-positive melanosomes for ^{GFP}FLMyo6 (L926Q), ^{GFP}FLMyo6 (SAHmimic), ^{GFP}Jo-Myo6-In, and ^{GFP}FLMyo6 (WT) (n=3, total cell number ~30). Significance: ***, P < 0.001 (unpaired t test with Welch’s correction).

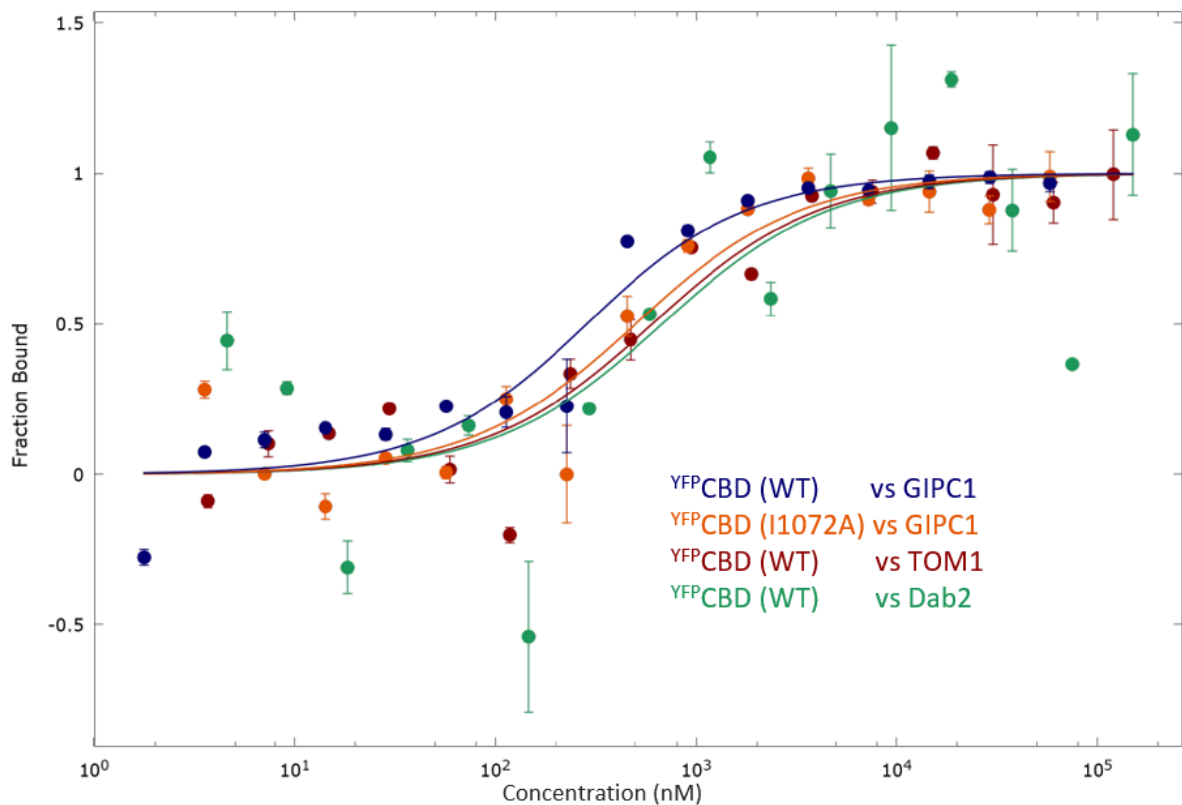
(C) Representative fixed MNT-1 cells co-expressing ^{GFP}FLMyo6 (WT), ^{GFP}Jo-Myo6-In, ^{GFP}FLMyo6 (SAHmimic) or ^{GFP}FLMyo6 (L926Q) with ^{mCherry}MST and ^{iRFP}VAMP7. ^{mCherry}MST and ^{iRFP}VAMP7 are melanosome-associated components. MNT-1 cells were fixed 48h post-transfection, then imaged and processed for quantification. Green: ^{GFP}Myo6; Magenta: ^{mCherry}MST; Cyan: ^{iRFP}VAMP7. From left to right: Entire cell: 3 channels merge and individuals; 8x zoom of the boxed region: merged ^{GFP}Myo6 / ^{mCherry}MST, individual channels. Scale bars: 10 μm.



Supplementary Figure 5 – SDS-PAGE stained with colloidal blue corresponding to Anti-His pull-down in Fig. 3D.

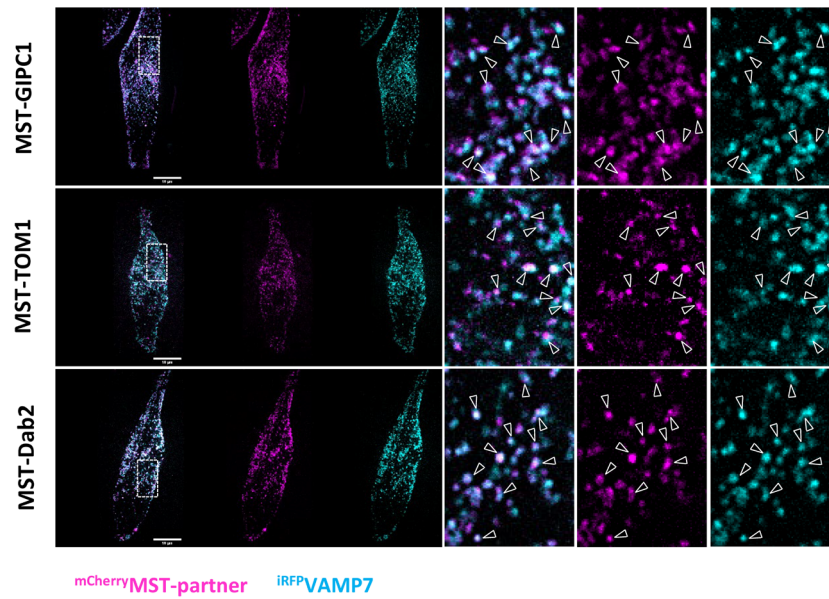
Input (I), flow through (FT), last wash (W) and elution (E) fractions corresponding to anti-His pull-down pictured in Fig. 3D.

	Partner	Myo6 Tail	K_D	n
Interaction with GIPC1	His ⁶ GIPC1	YFP ¹⁻¹⁰⁰ CBD (WT)	214 ± 144 nM	2
	His ⁶ GIPC1	YFP ¹⁻¹⁰⁰ CBD (I1072A)	227 ± 108 nM	2
Interaction with Dab2	His ⁶ Dab2	YFP ¹⁻¹⁰⁰ CBD (WT)	423 ± 346 nM	2
Interaction with TOM1	His ⁶ TOM1	YFP ¹⁻¹⁰⁰ CBD (WT)	445 ± 135 nM	2

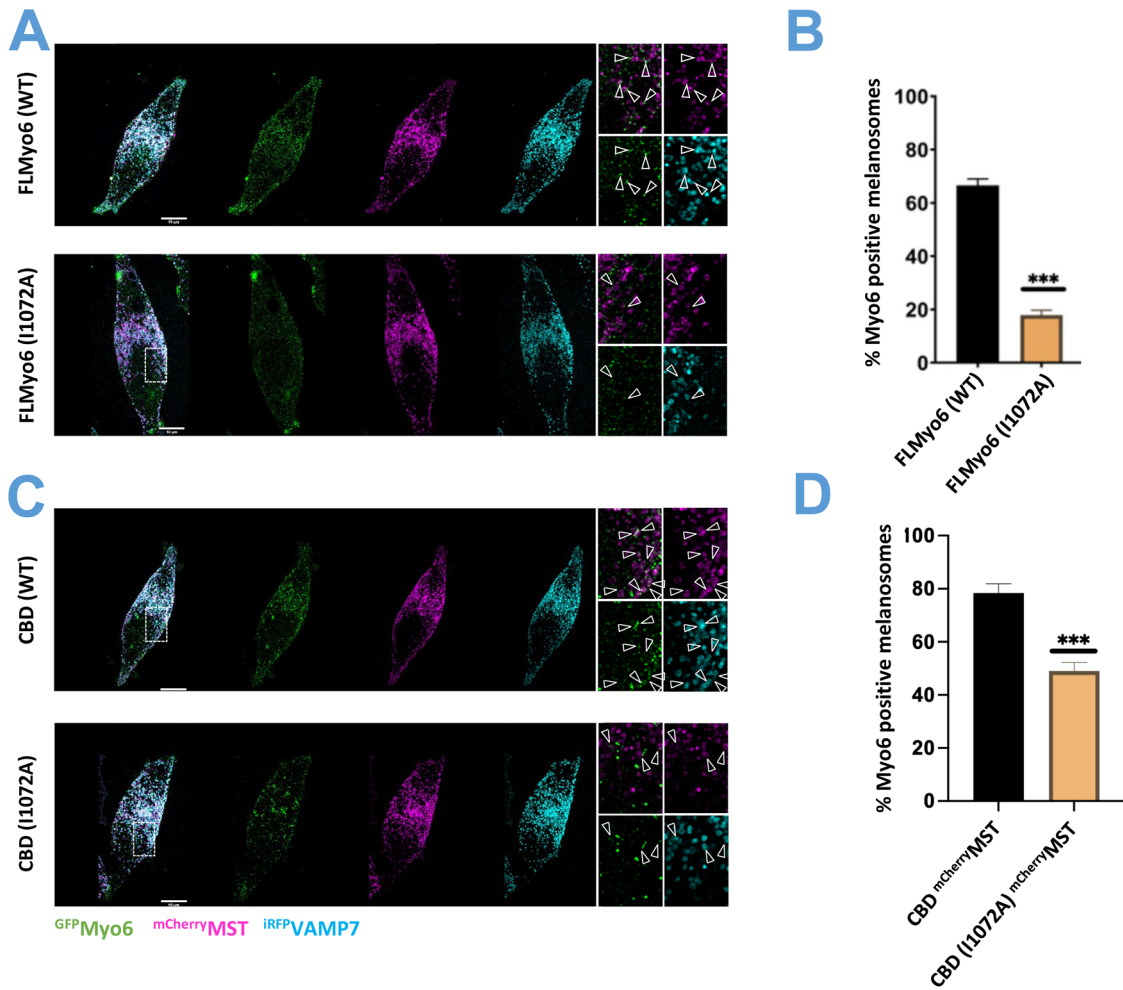


Supplementary Figure 6 – Affinity of the Myo6 tail for partners by Microscale Thermophoresis.

(Top) Dissociation constant (K_D) ± K_D confidence determined by microscale thermophoresis of Myo6 CBD constructs against Myo6 partners. **(Bottom)** Integration of thermophoresis profiles against concentration of partners (nM) for one replicate shown as an example. The affinity was quantified by analyzing the change in thermophoresis as a function of the concentration of the titrated protein using the NTAanalysis software provided by the manufacturer. Error bars: standard deviation. Fit: “Kd model” equation from NTAanalysis.



Supplementary Figure 7 – Localization of MST-partners at melanosomal membrane in MNT-1 cells.
 Representative MNT-1 cells co-expressing ^{mCherry}MST-partners and ^{iRFP}VAMP7. MNT-1 were fixed 48h post-transfection then imaged. In order: ^{mCherry}MST-GIPC1, ^{mCherry}MST-TOM1, ^{mCherry}MST-Dab2. Magenta: ^{mCherry}MST-partners; Cyan: ^{iRFP}VAMP7. From left to right: entire cell (3 channels merged, individual channels); zoom 8x boxed region (^{mCherry}MST-partners / ^{iRFP}VAMP7 merged, individual channels). Results show colocalization of ^{mCherry}MST-partners all around the ^{iRFP}VAMP7 melanosomes.



Supplementary Figure 8 – I1072 is key for Myo6 specific recruitment on melanosomes.

(A) Representative fixed MNT-1 cells co-expressing ^{GFP}Myo6 +/- I1072A mutation with ^{mCherry}MST and ^{iRFP}VAMP7. ^{mCherry}MST and ^{iRFP}VAMP7 are melanosome-associated components. MNT-1 cells were fixed 48h post-transfection then imaged and processed for quantification. Note that the control FLMMyo6 (WT) is the same as in [Sup Fig. 4B](#).

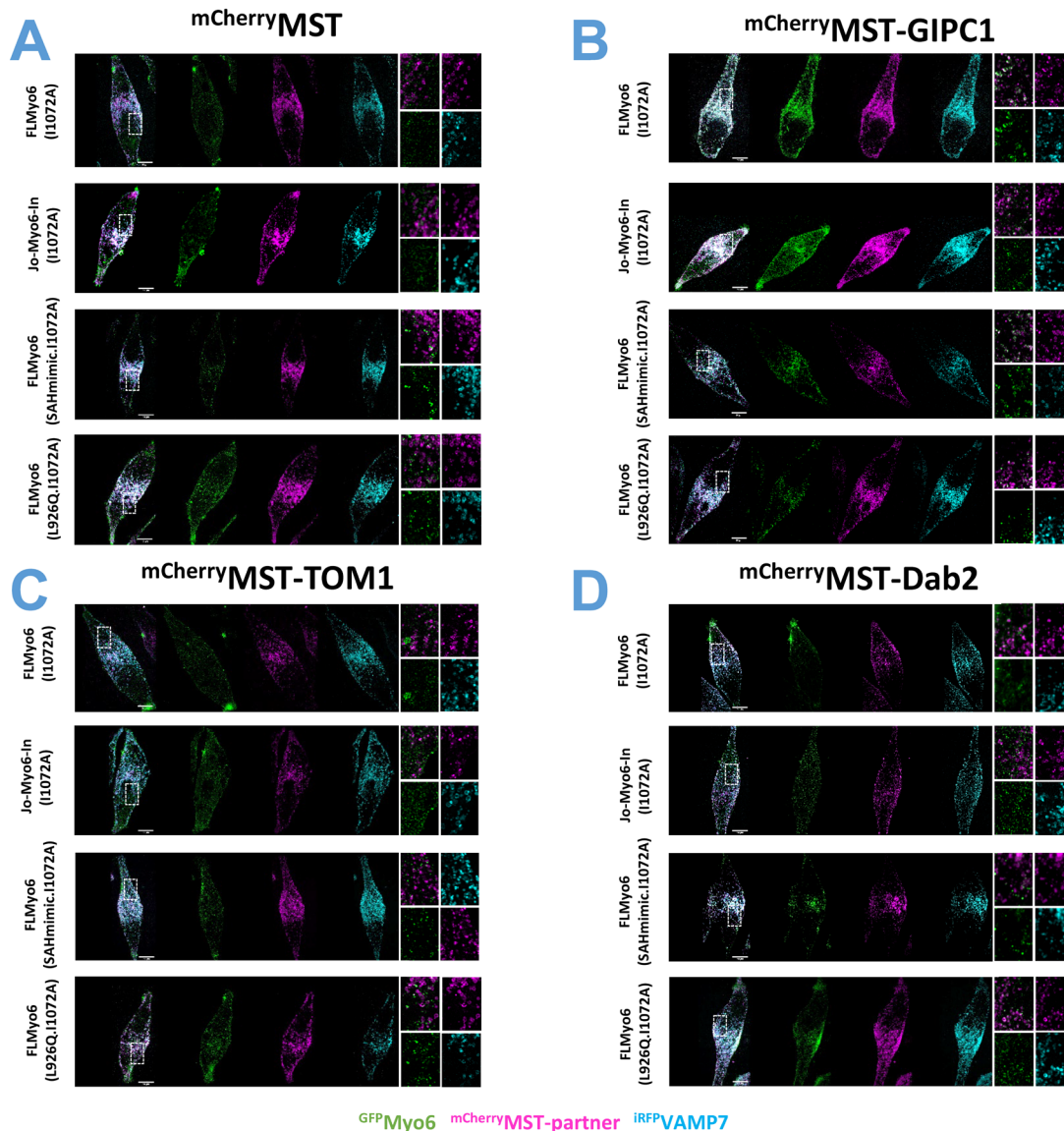
(B) Quantification of Myo6-positive melanosomes for ^{GFP}FLMMyo6 (WT) and ^{GFP}FLMMyo6 (I1072A) in MNT-1 cells (n=3, total cell number ~30).

(C) Representative MNT-1 cells co-expressing Myo6 CBD +/- I1072A mutation with ^{mCherry}MST and ^{iRFP}VAMP7. ^{mCherry}MST and ^{iRFP}VAMP7 are melanosome-associated components. MNT-1 cells were fixed 48h post-transfection then imaged and processed for quantification.

(D) Quantification of Myo6-positive melanosomes for ^{GFP}CBD (WT) and ^{GFP}CBD (I1072A) in MNT-1 cells (n=2, total cell number ~20).

(A, C) Green: ^{GFP}Myo6 constructs; Cyan: ^{iRFP}VAMP7; Magenta: ^{mCherry}MST-partner. Entire cell merge 3 channels and individuals. Zoom (8x boxed region): merge ^{GFP}Myo6 / ^{mCherry}MST-partner, individual channels. Scale bars: 10µm.

(C, D) Myo6-positive melanosomes are expressed in percentage and normalized to the total number of VAMP7-positive melanosomes. Significance: ***, P < 0.001 (unpaired t test with Welch's correction), for each ^{GFP}Myo6 construct, significance of experiments with partners compared to the control without partner (in black on the graph).



Supplementary Figure 9 – GIPC1 can bind the back-folded Myo6 state and activate it, while Dab2 and Tom1 can only bind to Myo6 once the motor has been primed open.

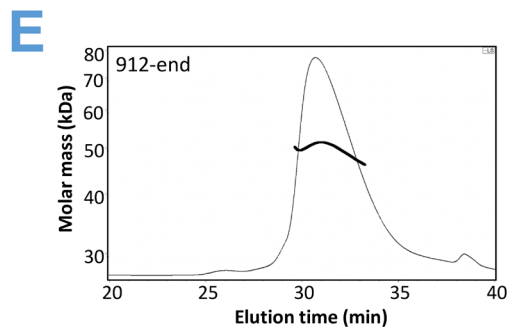
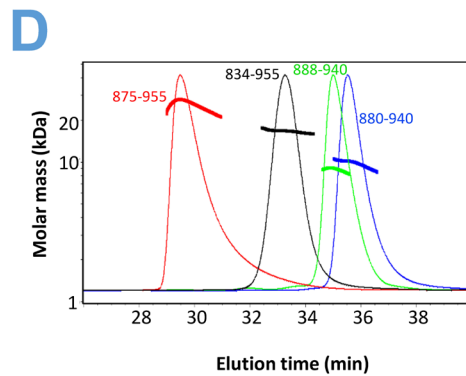
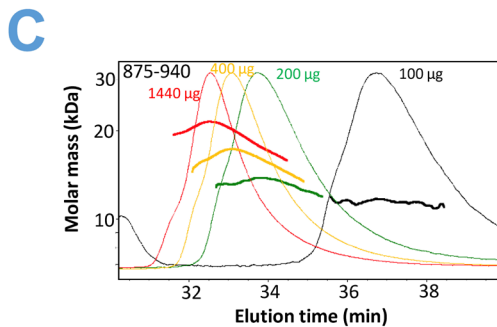
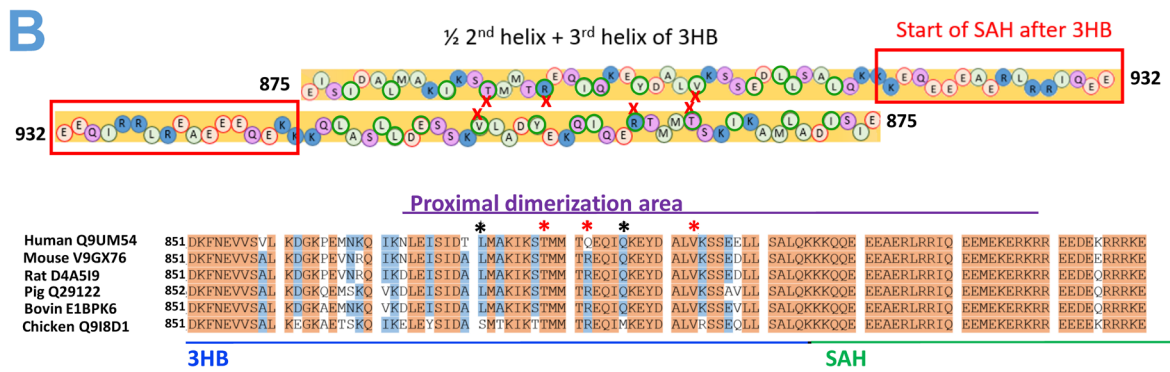
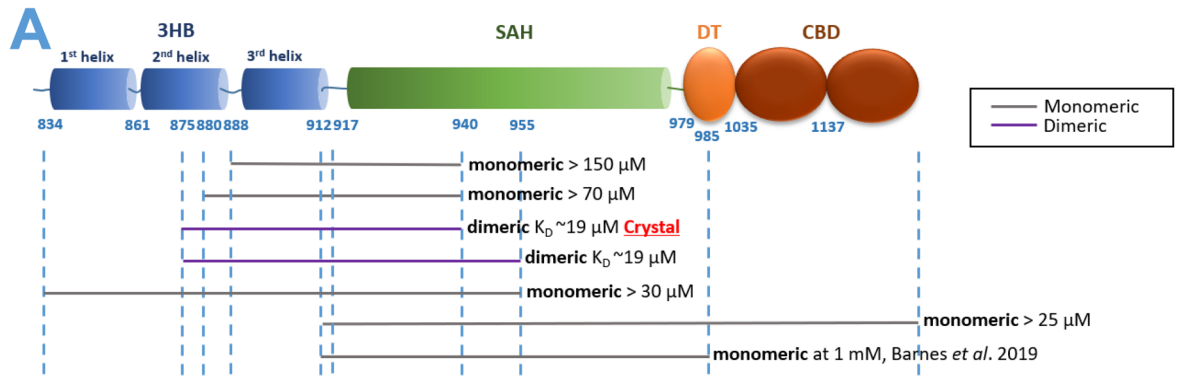
Representative entire MNT-1 cells corresponding to the zooms in Fig. 4. Left to right: merge of 3 channels, individual channels. Zoom (8x boxed region): merge $GFP^{Myo6} / mCherry^{MST-partners}$, individual channels. Scale bars: 10 μ m. GFP^{FLMyo6} constructs: GFP^{FLMyo6} (I1072A), GFP^{FLMyo6} (SAHmimic.I1072A), GFP^{FLMyo6} (L926Q.I1072A), Jo-Myo6-In (I1072A).

(A) Representative fixed MNT-1 cells co-expressing different GFP^{FLMyo6} (I1072A) constructs with control $mCherry^{MST}$ and $iRFP^{VAMP7}$.

(B) Representative fixed MNT-1 cells co-expressing different GFP^{FLMyo6} (I1072A) constructs with $mCherry^{MST-GIPC1}$ and $iRFP^{VAMP7}$.

(C) Representative fixed MNT-1 cells co-expressing different GFP^{FLMyo6} (I1072A) constructs with $mCherry^{MST-TOM1}$ and $iRFP^{VAMP7}$.

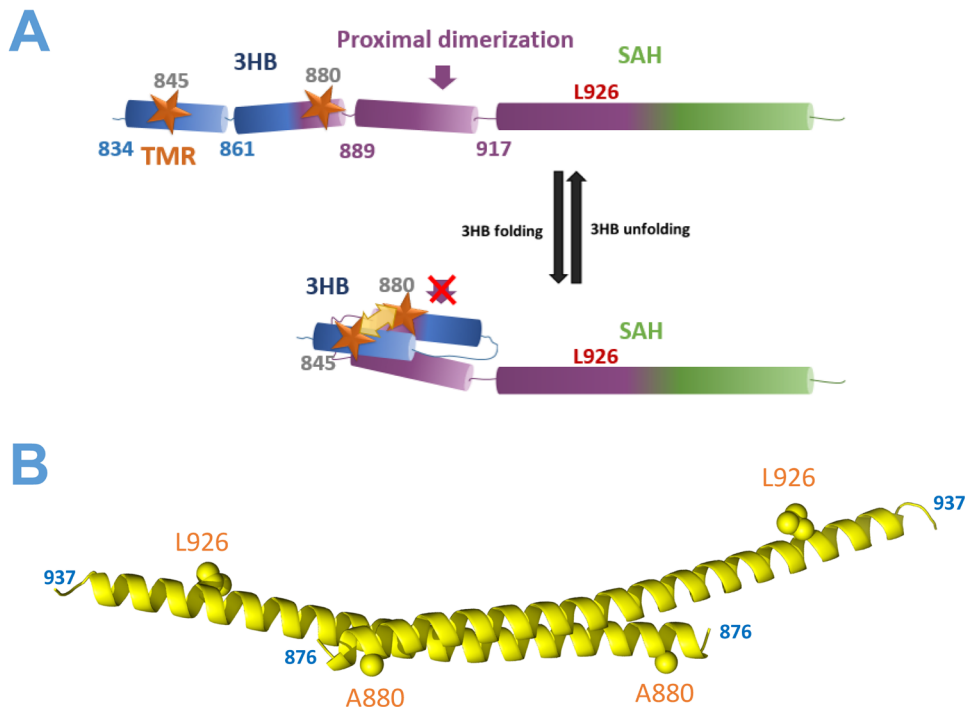
(D) Representative fixed MNT-1 cells co-expressing different GFP^{FLMyo6} (I1072A) constructs with $mCherry^{MST-Dab2}$ and $iRFP^{VAMP7}$.



Supplementary Figure 10 – Characterization of the dimerization of proximal region by MALS.

The 875-940 fragment is sufficient for dimerization. Importantly, a peptide missing the first 5 aa (aa 880-940) failed to dimerize even when its peak concentration was higher than 70 μM , which emphasised the key role of residues 875-880 for the stability of the dimerization. Additionally, in line with a recent study⁵, no dimerization was found via the SAH, unlike previously proposed by molecular dynamics simulations⁶. Indeed, no dimerization was observed via the Tail fragment aa 912-end, (containing the whole SAH), even when its peak concentration was 25 μM .

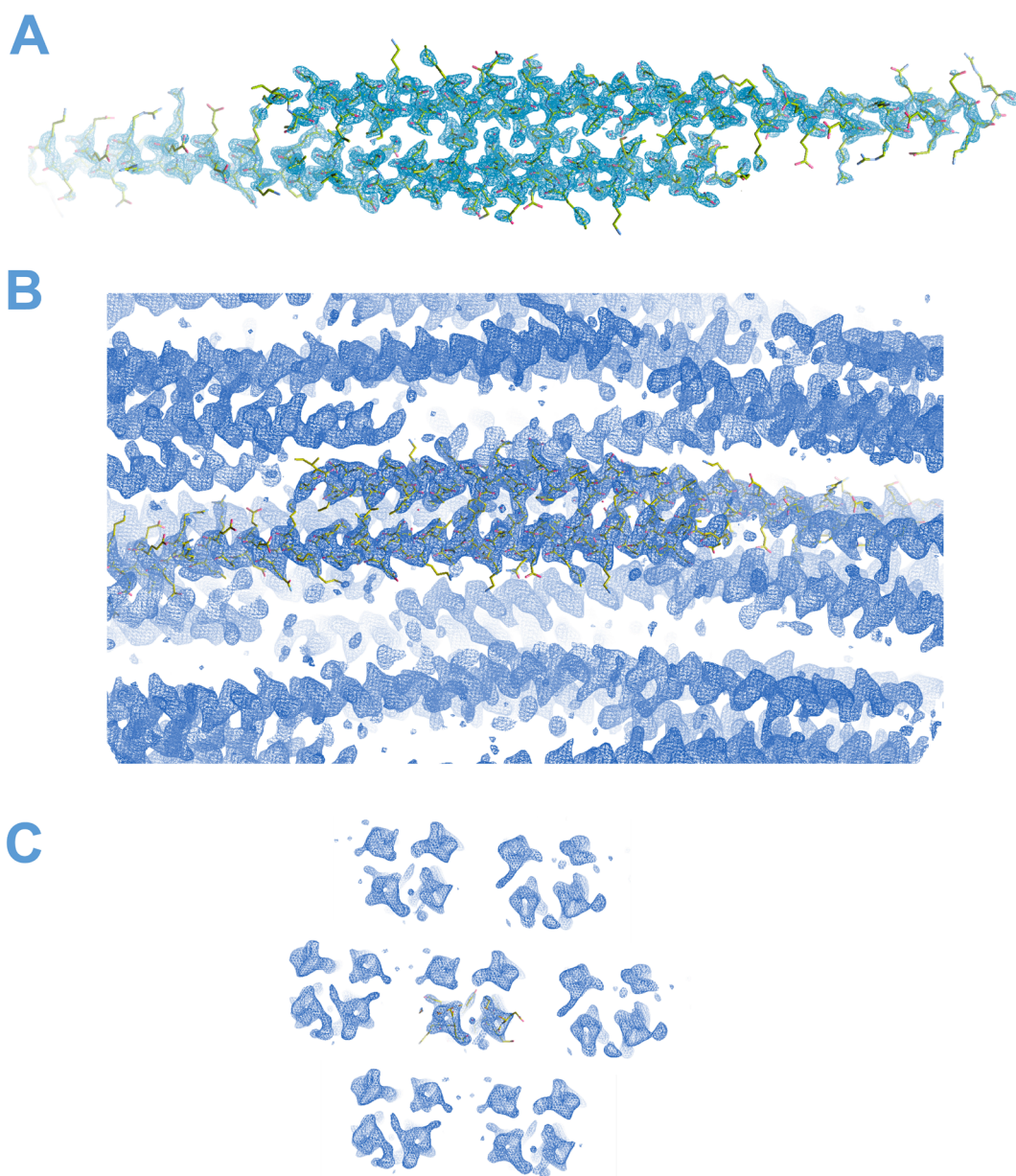
- (A)** Scheme of the Myo6 Tail showing the oligomerization states found for different constructs using SEC-MALS in 10 mM Tris pH 7.5; 50 mM NaCl; 5 mM NaN₃; 0.5 mM TCEP.
- (B) (Top)** schematic representation of the dimer crystal structure. Negatively charged residues are circled in red, positively charged residues are circled in blue, hydrophobic residues are circled in green and polar, uncharged residues are circled in purple. Residues involved in apolar contacts are circled in green. Three residues found to be essential for dimerization (T888D, R892E, V903D) are marked with a red cross. **(Bottom)** Sequence alignment of 851-949 (human protein numbering). Red: conserved residues; blue: conserved in 5 out of 6 species. *: residues inside the dimerization area that are not 100% conserved (S881 and M896). In the structure, M896 faces itself and seems compatible with the crystallized dimer. *: residues mutated in this study to disrupt proximal dimerization. Residues T888 and V903 are well conserved. The crystal structure shows that the replacement of R892 by Q in the human sequence should be compatible with proximal dimerization.
- (C)** Titration of the 875-940 fragment by SEC-MALS in 10 mM Tris pH 7.5; 50 mM NaCl; 5 mM NaN₃; 0.5 mM TCEP. Thin lines: light scattering (normalized); thick lines: molecular masses. A K_D^{App} of ~19 μ M was calculated from a fit of molecular weight against the concentration at the peak from each profile – the affinity is probably underestimated because of the size exclusion resin.
- (D)** Normalized SEC-MALS profiles of the 834-955, 880-940 and 888-940 constructs (concentration at the peak stated on [Sup Fig. 10A](#)) found to be monomeric in 10 mM Tris pH 7.5; 50 mM NaCl; 5 mM NaN₃; 0.5 mM TCEP, unlike the dimeric 875-955 construct (red).
- (E)** Normalized SEC-MALS profile of the 912-end construct (25 μ M at the peak) found to be monomeric in 10 mM Tris pH 7.5; 50 mM NaCl; 5 mM NaN₃; 0.5 mM TCEP.



Supplementary Figure 11 – Proximal dimerization is regulated by 3HB unfolding which is impaired by the pathogenic L926Q deafness mutation.

(A) Scheme representing Myo6 SAH (green) and 3HB (blue), with the proximal dimerization area (875-940) shown in purple. Stars: TMR fluorescent spots. Their proximity promotes quenching when the 3HB is folded.

(B) Crystal structure of the proximal dimer pictured in cartoon, residues A880 and L926 are shown as spheres.

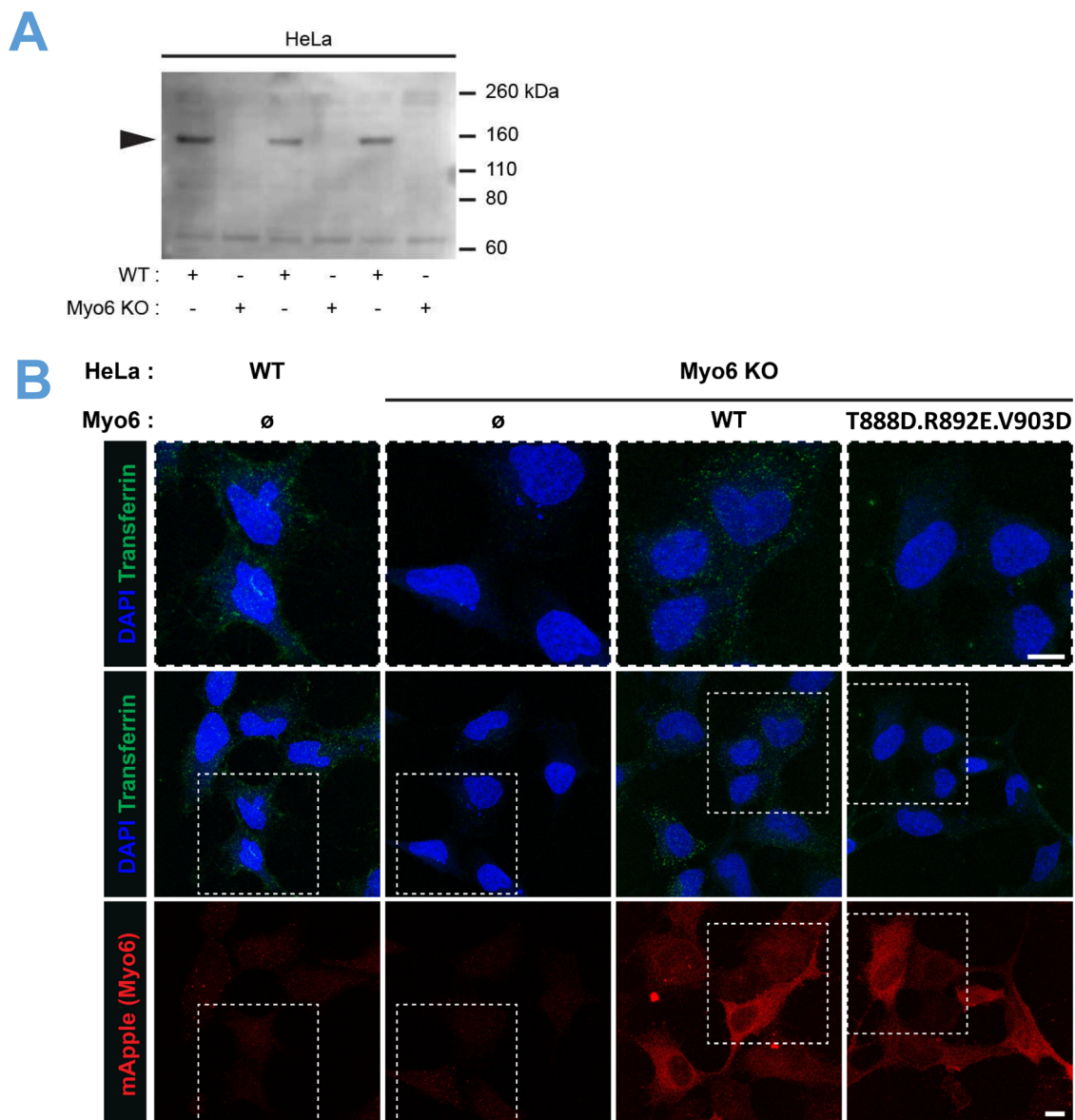


Supplementary Figure 12 – Electron density of the Myo6 875-940 crystal structure.

(A) Electron density corresponding to the 875-940 dimer (2Fo-Fc map contoured at 1.0 RMSD).

(B) View of the 2-fold axis that defines the antiparallel dimer.

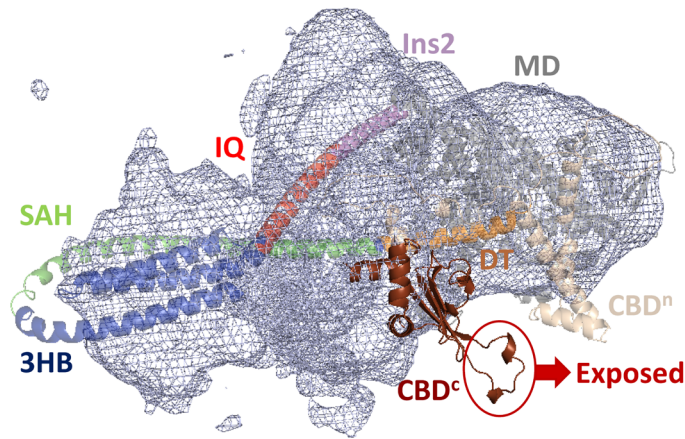
(C) View of the 6-fold axis. Although a high number of copies can be seen in the asymmetric unit, the 875-937 helix makes extensive contacts over 11.5 turns with another helix. The rest of the crystal contacts made by the helix are negligible in comparison ([Sup. Movie 2](#)). Images prepared with Coot 0.9.8.1⁷.



Supplementary Figure 13 – Endocytosis is impaired if Myo6 cannot dimerize through its proximal region

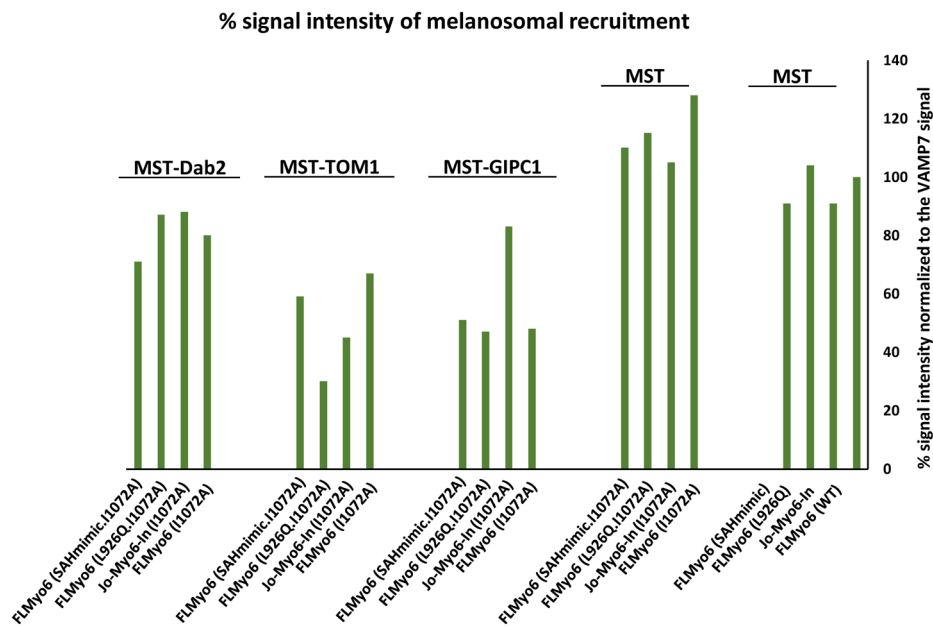
(A) Confirmation of Myo6 null HeLa cells by western blot.

(B) Endocytic uptake of fluorescently-labeled transferrin by WT and Myo6 null HeLa cells. Internalized transferrin appears in green, HeLa cell nuclei (DAPI) in blue, and expression of ^{mApple}Myo6 constructs in red. Representative maximum-intensity projection images demonstrate a marked reduction in internalized transferrin in Myo6 mutant HeLa cells compared to wild-type cells. Forced expression of FLMyo6 (WT), but not of FLMyo6 (T888D.R892E.V903D, triple mutant), restores the ability of Myo6 null HeLa cells to uptake transferrin. Scale bar: 10 μ m.



Supplementary Figure 14 – AlphaFold^{8,9} predicts a back-folded FLMYo6 with an exposed CBD^c

AlphaFold modelisation of FLMYo6 (UNIPROT: Q9UM54) was manually docked within our 3D reconstruction of Jo-Myo6-In (grey mesh). CBD^c is found outside of the electron density, with residues D1157, Y1159, D1161, Q1163 highly exposed (red circle), inconsistently with our experimental data.



Supplementary Figure 15 – Fluorescence of MST-partners localized on melanosomes, normalized to the VAMP7 signal.

Quantification of the fluorescence signal of ^{mCherry}MST-partners on melanosomes in MNT-1 cells expressing different Myo6 constructs. Global intensities were calculated by using the macro described in Methods, normalized to the ^{iRFP}VAMP7 signal (total melanosomal surface area).

Space group	P6 ₅ 22
Cell constants a, b, c, α, β, γ	29.39 Å, 29.39 Å, 295.65 Å 90.00°, 90.00°, 120.00°
Resolution	49.27 Å - 2.22 Å
Data completeness in resolution range	66.9 %
R_{merge}	0.17
I/s(I)	1.02 at 2.22 Å
R, R_{free}	0.304, 0.343
Wilson B-factor	39.2 Å ²
Average B, all atoms	55.0 Å ²
Total number of atoms	1051
Unique reflections	2977
R_{free} test set	301 reflections (10.1%)
Ramachandran outliers	0
Sidechain outliers	8.8%
Solvent content*	45.1%

Supplementary Table 1 – Crystallographic structure of the Myo6 dimerization domain – data and refinement statistics.

* Solvent content estimated by *Matthews_coef*¹⁰

Construct	IMAC	SEC
Ins2/IQ/3HB*	20 mM Tris pH 7.5; 150 mM NaCl; 1 mM DTT (+ 4 and 300 mM Imidazole for binding/washing and elution, respectively)	20 mM HEPES, pH 7.5; 50 mM NaCl; 2.5mM MgCl ₂ ; 1 mM TCEP
^{YFP} CBD (WT and mutant)	20 mM Tris pH 7.5; 150 mM KCl; 40 mM Imidazole pH 7.5; 5% Glycerol; 1mM DTT (+300 mM NaCl in the washing step; and 100 mM KCl; 300 mM imidazole; 1 mM TCEP for elution)	20 mM Tris pH 7.5; 100 mM KCl; 1 mM TCEP
GIPC1	20 mM HEPES pH 7.5; 150 mM NaCl; 1 mM DTT (+4 or 200 mM Imidazole for binding/washing and elution, respectively)	50 mM HEPES pH 7.5; 150 mM or 50 mM NaCl; 1 mM DTT
TOM1	20 mM Tris pH 7.5; 300 mM NaCl; 1 mM DTT (+4 or 300 mM Imidazole for binding/washing and elution, respectively)	20 mM HEPES pH 7.5; 150 mM NaCl; 1 mM DTT
Dab2	20 mM Tris pH 8.5; 300 mM NaCl; 1 mM DTT (+4 or 200 mM Imidazole for binding/washing and elution, respectively)	20 mM Tris pH 8.5; 150 mM NaCl; 1 mM DTT
Myo6 875-940, 875-955**, 880-940, 888-940** and 834-955	20 mM Tris, pH7.5; 150 mM NaCl (+4 or 200 mM Imidazole for binding/washing and elution, respectively)	10 mM Tris, pH7.5 ; 50mM NaCl
Myo6 875-940 triple mutant**	20 mM Tris, pH7.5; 600 mM NaCl (+4 or 200 mM Imidazole for binding/washing and elution, respectively)	10 mM Tris, pH7.5 ; 300mM NaCl

Supplementary Table 2 – Purification buffers used for constructs expressed in E. Coli

* presence of 2 CaM bound was confirmed by SEC-MALS (not shown).

** Ion exchange in MonoQ 5/50 GL prior to SEC.

*** Ion exchange in MonoS 5/50 GL prior to SEC.

(For constructs including a rTEV cleavage site, homemade rTEV was added 1:50 m/m, and a second passage through IMAC was performed before SEC)

Supplementary Movies

Supplementary Movie 1

3D view of the Myo6 off-state docked in the negative staining reconstruction (from Fig 3A).

Supplementary Movie 2

Representation of the crystal packing of the dimerization Myo6 fragment 875-937 as calculated with PyMol. Each crystallographic dimer is represented in a different color.

Supplementary Material and Methods

Cloning, expression and purification from SF9/baculovirus system.

The full-length wild-type Myo6 (FLMyo6) was generated using human Myo6 cDNA splice form without the large insertion (Q9UM54-2 in UNIPROT). The small insert was removed through sub cloning to obtain a FLMyo6 construct without any spliced insert (corresponding to isoform Q9UM54-5). The FLMyo6 (no inserts) construct was then used in all *in vitro* experiments requiring a full-length construct except for the Anti-His pull-down experiment, for which the small insert isoform was used.

The deafness mutant (L926Q) and triple mutant (T888D.Q892E.V903D - R892 in mouse corresponds to Q892 in human, see [Sup Fig. 10B](#)) in the anti-parallel dimerization region were produced from FLMyo6 with no inserts by reverse PCR. As previously described¹¹, a mutant FLMyo6 (SAHmimic) was made where the residues from Glu922 to Glu935 (EAERLRRIQEEMEK) were replaced with alternate acidic and basic residues (EERKRREEEERKKREEE) to match the (i, i+4) phasing observed in the predicted Myo6 SAH domain.

For microscale thermophoresis and ATPase assays, previously described constructs were used: MD (1-789)¹², MD^{Ins2} (2-816)³, MD^{Ins2/IQ/3HB} (1-917)¹³. The Myo6 zippered dimer was created by truncation at R991 followed by a leucine zipper (PDB: GCN4¹⁴) as previously described¹⁵.

For the bundle unfolding experiments, a monomeric “cys-lite” construct was made by C-terminal truncation at amino acid Q919 and introduction of C321S, C362S, and C611A. To this construct, either a T845C mutation alone, or the combination of T845C and A880C mutations was introduced for rhodamine labeling, as previously described¹³. A dimeric “cys-lite” construct was made by introduction of the C321S, C362S, C611A mutations in the Myo6 zippered dimer¹⁵. Into this construct, either a T845C mutation alone, or the combination of T845C and A880C mutations were introduced for rhodamine labeling, as previously described¹³, with or without the addition of a deafness-causing mutation (L926Q).

Each of these constructs had a Flag tag (GDYKDDDDK) at its N-terminal end to facilitate purification. Expression in baculovirus system and purification were performed as previously described¹⁶.

Jo and In-Flag sequences⁴ were synthesized (Eurofins genomics) and fused to Myo6 N-terminus (linker Gly-Ser) and C-terminus (linker Gly), in pVL1392 for expression in Sf9 cells. Purification was achieved using the published protocol for FLMyo6¹⁶ except that, for EM studies, purification was performed by replacing ATP with ADP.VO₄ in the lysis buffer. For increased purity, a SEC step was performed using a Superdex 200 Increase column (Cytiva) developed in 10 mM Hepes; 80 mM NaCl; 5mM NaN₃; 1 mM MgCl₂; 0.1 mM TCEP; 0.1 mM ADP; 0.2 mM VO₄; 0.1 mM EGTA; pH 7.5.

Constructs cloning, expression and purification from Escherichia coli

Cloning Myo6 constructs

Ins2/IQ/3HB was generated using our human FLMyo6 NI construct (see previous section), DNA sequence encoding for aa783-917 was transferred into pPROX-HTB plasmid containing in N-terminus 6XHis tag and a TEV cleavage sequence (coding for ENLYFQG).

Myo6^{YFP}CBD was generated through several round of subclonings from cDNA mouse Myo6 (E9Q3L1 in UNIPROT). Myo6 was incorporated in pET14 plasmid containing in N-terminus 6XHis-tag, yellow fluorescent protein (YFP) and a TEV cleavage sequence. Finally, Myo6 was truncated in N-terminus at position corresponding to aa M1032 through reverse PCR. The^{YFP}CBD (D1157V.Y1159D.D1161R.

Q1163V) mutant was generated through point mutations addition using reverse PCR on the ^{YFP}CBD (WT) construct.

Cloning partner constructs

In order to avoid partner (GIPC1, TOM1 and Dab2) degradation and auto-inhibition as previously reported^{17,18}, we used truncations containing the published Myo6-binding domains¹⁸⁻²¹ instead of FL constructs.

For microscale thermophoresis assays and his-pull-down assays, ^{His}GIPC1 construct was generated using cDNA full length mouse GIPC1 (UNIPROT Q9Z0G0). GIPC1 was incorporated in pProEX-HTb plasmid containing in N-terminus 6XHis-tag and a TEV cleavage sequence. Finally, GIPC1 was truncated in N-terminus at position corresponding to aa D255 through reverse PCR in order to keep only the GH2 domain which is sufficient for mediated interaction with Myo6¹⁸.

For ATPase assays, we used GIPC1 in fusion with the mNeonGreen tag: GIPC1 DNA sequence encoding for residues 238-end was incorporated in the pET28 plasmid containing in the N-terminus 6XHis-tag and a mNeonGreen tag using homemade Gibson Assembly mix²².

For microscale thermophoresis and his-pull-down assays, a non-fluorescent ^{His}TOM1 construct was generated using cDNA full length human TOM1 (UNIPROT O60784-1). TOM1 207-end was incorporated into pET14 in-frame with an N-terminus 6XHis-tag and a TEV cleavage sequence using homemade Gibson Assembly mix²².

For ATPase assays, we used the TOM1 436-461 peptide described as the minimal sequence required for TOM1 binding to Myo6²¹. DNA sequence coding for aa436-461 was incorporated in pET14 plasmid containing in N-terminus 6XHis-tag, yellow fluorescent protein (YFP) and a TEV cleavage sequence.

Dab2 His-650-end (tDab2¹⁷) was a kind gift of Christopher Toseland.

To identify the minimal sequence involved in proximal dimerization, several Myo6 truncations were generated from mouse Myo6 cDNA (UNIPROT: E9Q3L1). Constructs encoding for aa 875-940 and 875-955 were cloned with a N-terminal 6xHis-tag into pET14 plasmid. The construct encoding for aa 834-955 was cloned into pET14 with a N-terminal 6xHis-tag followed with a Thrombin cleavage site (coding for LVPRGSH). Constructs encoding for aa 880-940 and 888-940 were cloned with a C-terminal 6xHis-tag into pET14 by PCR and blunt-end ligation. The 912-end construct was cloned into pProEX-HTb with a N-terminal 6xHis-tag through several rounds of sub cloning. For crystallization assays, the construct encoding for aa 875-940 was generated with a N-terminal 6xHis-tag and a TEV cleavage sequence into pProEX-HTb using homemade Gibson Assembly mix²². The point mutations T888D, R892E, V903D were added in the backbone encoding for his-rTEV-875-940, all by Quickchange²³.

Protein expression and purification

Constructs were expressed in E.coli BL21 (DE3) cells (NEB). Cells were grown in 2xYT media until OD₅₆₀~0.8, expression was then induced by addition of 200 μM isopropyl β-D-1-thiogalactopyranoside (except for Dab2 expression, where 1 mM isopropyl β-D-1-thiogalactopyranoside was used). Cells were lysed by sonication. For purification, the lysate soluble fraction was loaded on an IMAC column (cOmplete 5mL, Roche for all constructs except ^{YFP}CBD (WT and mutant) for which HisTrap-FFcrude 5mL, Cytiva was used instead), and proteins were eluted with 200 mM or 300 mM Imidazole. Purest fractions were identified by SDS-PAGE. If needed, pooled fractions were concentrated using Vivaspin concentrators (Sartorius) up to ~5 mL. Concentrated samples were injected in Superdex 200 or 75 16/600 columns (Cytiva) depending on the molecular weight of the target protein. Purest fractions and the final sample were concentrated by ultrafiltration, and protein concentration was determined using

Nanodrop 2000 (ThermoScientist). The final sample containing concentrated protein was flash-frozen in liquid nitrogen and stored at -80°C.

For proteins containing a TEV cleavable His-tag, prior to the gel filtration, His-tag was removed by incubation with homemade rTEV protease overnight in a 1/50 mass ratio. The incubate was passed through the cOmplete His-Tag Purification Column again to remove rTEV and the uncleaved fraction, then concentrated and loaded in a Superdex 75-16/60 gel filtration column.

Purification buffers are detailed in [Sup Table 2](#).

Constructs cloning for expression in MNT-1 cells

For expression in MNT-1, FLMyo6 was generated from cDNA of full length human Myo6, no inserts isoform (UNIPROT: Q9UM54-5) with shRNA resistance. DNA was transferred to the pEGFP-C1 vector via a XbaI restriction enzyme site. SAHmimic mutations (Glu922 to Glu935 (EAERLRRRIQEEMEK) replaced with alternate acidic and basic residues (EERKRREEEERKKREEE) were introduced by reverse PCR. The L926Q mutation was introduced using Quickchange²³. Transfer of Jo-Myo6-In from baculovirus vector to P-EGFP-C1 was ordered from GenScript. Myo6 CBD was generated by transferring DNA encoding G1037-end from human Myo6, no inserts isoform (UNIPROT: Q9UM54-5) into pEGFP-C1 plasmid using the XbaI restriction enzyme site.

I1072A was introduced in previously cloned constructs (see above) using reverse PCR.

Mouse GIPC1 (239-end), human TOM1 (299-end as described in¹⁹) and human Dab2 (650-end) were transferred in a modified pmCherry-C1 plasmid containing in N-terminus a melanosome-targeting tag (MST tag, aa 1-139 from Mouse MREG – UNIPROT: Q6NVG5) as described in²⁴. The MST tag and mCherry are separated by a GGSGGTGG linker. In the ^{mCherry}MST-partners constructs, mCherry and GIPC1, TOM1 or Dab2 sequences are separated by the polylinker multiple cloning site SGLRSRAQASNSLTSK.

References

1. Manalastas-Cantos, K. *et al.* ATSAS 3.0: expanded functionality and new tools for small-angle scattering data analysis. *J Appl Cryst* **54**, 343–355 (2021).
2. Berggren, K. *et al.* Background-free, high sensitivity staining of proteins in one- and two-dimensional sodium dodecyl sulfate-polyacrylamide gels using a luminescent ruthenium complex. *Electrophoresis* **21**, 2509–2521 (2000).
3. Ménétrey, J. *et al.* The structure of the myosin VI motor reveals the mechanism of directionality reversal. *Nature* **435**, 779–785 (2005).
4. Bonnet, J. *et al.* Autocatalytic association of proteins by covalent bond formation: a Bio Molecular Welding toolbox derived from a bacterial adhesin. *Sci Rep* **7**, 43564 (2017).
5. Barnes, C. A. *et al.* Remarkable Rigidity of the Single α -Helical Domain of Myosin-VI As Revealed by NMR Spectroscopy. *J Am Chem Soc* **141**, 9004–9017 (2019).
6. Kim, H., Hsin, J., Liu, Y., Selvin, P. R. & Schulten, K. Formation of salt bridges mediates internal dimerization of myosin VI medial tail domain. *Structure* **18**, 1443–1449 (2010).
7. Emsley, P. & Cowtan, K. Coot: model-building tools for molecular graphics. *Acta Crystallogr D Biol Crystallogr* **60**, 2126–2132 (2004).
8. Jumper, J. *et al.* Highly accurate protein structure prediction with AlphaFold. *Nature* **596**, 583–589 (2021).
9. Varadi, M. *et al.* AlphaFold Protein Structure Database: massively expanding the structural coverage of protein-sequence space with high-accuracy models. *Nucleic Acids Res* **50**, D439–D444 (2022).
10. Matthews, B. W. Solvent content of protein crystals. *J Mol Biol* **33**, 491–497 (1968).
11. Mukherjea, M. *et al.* Myosin VI must dimerize and deploy its unusual lever arm in order to perform its cellular roles. *Cell Rep* **8**, 1522–1532 (2014).
12. Ménétrey, J., Llinas, P., Mukherjea, M., Sweeney, H. L. & Houdusse, A. The structural basis for the large powerstroke of myosin VI. *Cell* **131**, 300–308 (2007).
13. Mukherjea, M. *et al.* Myosin VI dimerization triggers an unfolding of a three-helix bundle in order to extend its reach. *Mol Cell* **35**, 305–315 (2009).
14. Lumb, K. J., Carr, C. M. & Kim, P. S. Subdomain folding of the coiled coil leucine zipper from the bZIP transcriptional activator GCN4. *Biochemistry* **33**, 7361–7367 (1994).
15. De La Cruz, E. M., Ostap, E. M. & Sweeney, H. L. Kinetic mechanism and regulation of myosin VI. *J Biol Chem* **276**, 32373–32381 (2001).
16. Sweeney, H. L. *et al.* Kinetic tuning of myosin via a flexible loop adjacent to the nucleotide binding pocket. *J Biol Chem* **273**, 6262–6270 (1998).
17. Fili, N. *et al.* Competition between two high- and low-affinity protein-binding sites in myosin VI controls its cellular function. *J Biol Chem* **295**, 337–347 (2020).
18. Shang, G. *et al.* Structure analyses reveal a regulated oligomerization mechanism of the PlexinD1/GIPC/myosin VI complex. *Elife* **6**, e27322 (2017).
19. Tumbarello, D. A. *et al.* Autophagy receptors link myosin VI to autophagosomes to mediate Tom1-dependent autophagosome maturation and fusion with the lysosome. *Nat Cell Biol* **14**, 1024–1035 (2012).
20. Yu, C. *et al.* Myosin VI undergoes cargo-mediated dimerization. *Cell* **138**, 537–548 (2009).
21. Hu, S. *et al.* Structure of Myosin VI/Tom1 complex reveals a cargo recognition mode of Myosin VI for tethering. *Nat Commun* **10**, 3459 (2019).
22. Gibson, D. G. *et al.* Enzymatic assembly of DNA molecules up to several hundred kilobases. *Nat Methods* **6**, 343–345 (2009).
23. Liu, H. & Naismith, J. H. An efficient one-step site-directed deletion, insertion, single and multiple-site plasmid mutagenesis protocol. *BMC Biotechnol* **8**, 91 (2008).
24. Ishida, M., Arai, S. P., Ohbayashi, N. & Fukuda, M. The GTPase-deficient Rab27A(Q78L) mutant inhibits melanosome transport in melanocytes through trapping of Rab27A effector protein Slac2-a/melanophilin in their cytosol: development of a novel melanosome-targeting tag. *J Biol Chem* **289**, 11059–11067 (2014).

A.3. Limits of the study and perspectives

A.3.a. Two kinds of contacts participate in the off-state stability

The study of the Myo6 auto-inhibited state described above allows us to identify important parameters for the maintenance of the Myo6 back-folded conformation. We show that both the NF and Mg.ADP.VO₄ bound Motors could adopt a compact conformation at low salt concentration (80 mM NaCl). Yet, in the presence of Mg.ADP.VO₄, Myo6 remains compact up to 425 mM NaCl while in the NF condition, Myo6 is more sensitive to salt and opens progressively upon salt addition: thus, more than 80 % of the Myo6 molecules are opened at 425 mM NaCl. Moreover, in microscale thermophoresis, the affinity of the MD^{ins2/IQ/3HB} construct for the CBD drops from 144 ± 61 nM to 726 ± 480 nM upon nucleotide removal.

We thus proposed that two kinds of interactions stabilizes Myo6 in its auto-inhibited state: (1) nucleotide-dependent interactions near the Motor domain that can lock Myo6 in its back-folded conformation in a salt independent manner and (2) salt dependent interactions along the rest of the Myo6 molecule that mediates back-folding of Myo6 when no nucleotide is bound (Figure 56) and probably explains why Myo6 is able to fold back even when the Motor is absent as previously reported (Fili *et al.* 2020; 2017; Dos Santos *et al.* 2022).

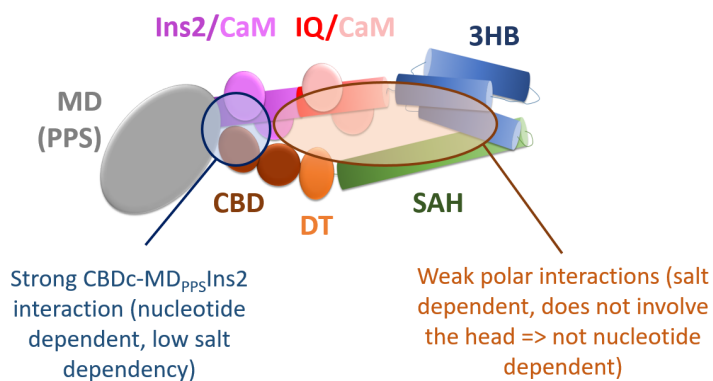


Figure 56: Main interactions stabilizing the Myo6 auto-inhibited state (see section A.2.)

The existence of polar contacts within the Myo6 Tail could explain why, in the context of FL Myo6, point mutations within the CBD have only little impact on the Myo6 compacity as measured from analytical gel filtration. In contrast, mutations within the SAH can have a large impact. Indeed, analytical gel filtration revealed that the human FL Myo6 (D1148V, Y1150D, D1152R and Q1154V) elutes only 0.4min earlier than FL Myo6 (WT) while FL Myo6 (L926Q) elutes 1.6min earlier in Superdex 3.2/300 (Figure 57).

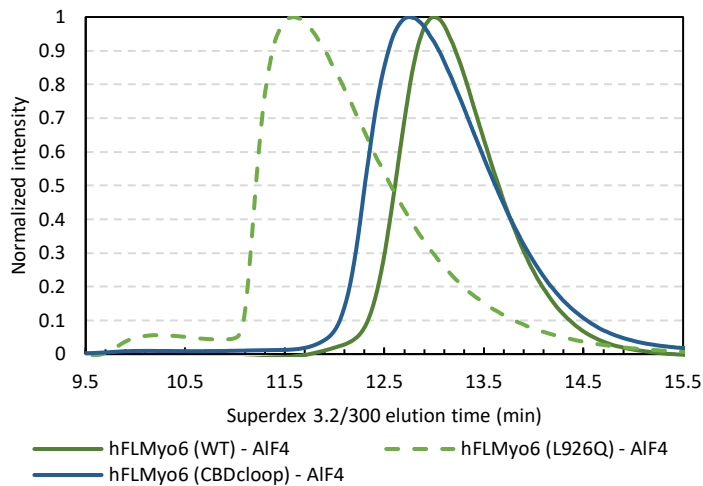


Figure 57: CBD^c loop mutant (D1148V, Y1150D, D1152R and Q1154V) has only little impact on Myo6 compacity *in vitro*

SEC profile on Superdex 3.2/300 column pre-equilibrated in 20 mM hepes; 200 mM NaCl; 2 mM MgCl₂; 1mM NaADP; 1mM AIF₄ (P_i analog), 0.1mM EGTA, 1mM DTT

Yet, shift towards opening as seen with the FLMyo6 L926Q mutant may not be necessary to enable Myo6 recruitment: Loss of nucleotide-dependent contacts within the auto-inhibited state of Myo6 could be sufficient. Indeed, in our pull-down assays, at 100 mM NaCl, nucleotide removal was sufficient to enhance TOM1 binding in conditions in which Myo6 was found to be compact in SEC-MALS in similar conditions. In this context, the Myo6 NF – high salt state was an interesting tool to characterize the polar interactions that must be going on within the Myo6 Tail.

The use of the FLMyo6 D1148V, Y1150D, D1152R and Q1154V mutant remained quite limited for studying Myo6 activation upon partner binding. Indeed, these mutations take place in the CBD^c and could strongly impair Myo6 interaction with certain partners. In particular, DNA binding to this mutant is very unlikely as fluorescence anisotropy revealed that depletion of the SKKK motif near residues D1148V, Y1150D, D1152R and Q1154V results in a 7-fold decrease Myo6 affinity for DNA (Fili *et al.* 2017). It should be noted that in this context, our results are fully consistent with the results reported by Fili *et al.* 2017, that suggest that DNA cannot bind to the Myo6 auto-inhibited state since mutations within the same loop decrease binding between the CBD and DNA (see section C.7.) (Figure 58).

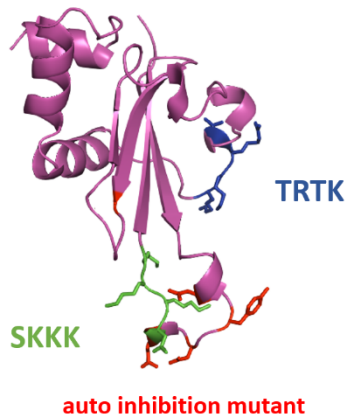


Figure 58: DNA binding motifs and CBD^c loop mutant (D1148V, Y1150D, D1152R and Q1154V) within CBD^c

CBD^c NMR structure (PDB: 2KIA, *Yu et al. 2009*) is pictured in magenta, TRTK and SKKK motif found to be involved in DNA binding are highlighted in blue and green respectively. D1148, Y1150, D1152 and Q1154 are highlighted in red

Additionally, transfection of CBD D1148V, Y1150D, D1152R and Q1154V in MNT-1 cells results in loss of Myo6 recruitment to melanosome highlighting that these D1148V, Y1150D, D1152R and Q1154V mutations likely prevent endogenous recruitment of Myo6 to melanosomes ([Figure 59](#)).

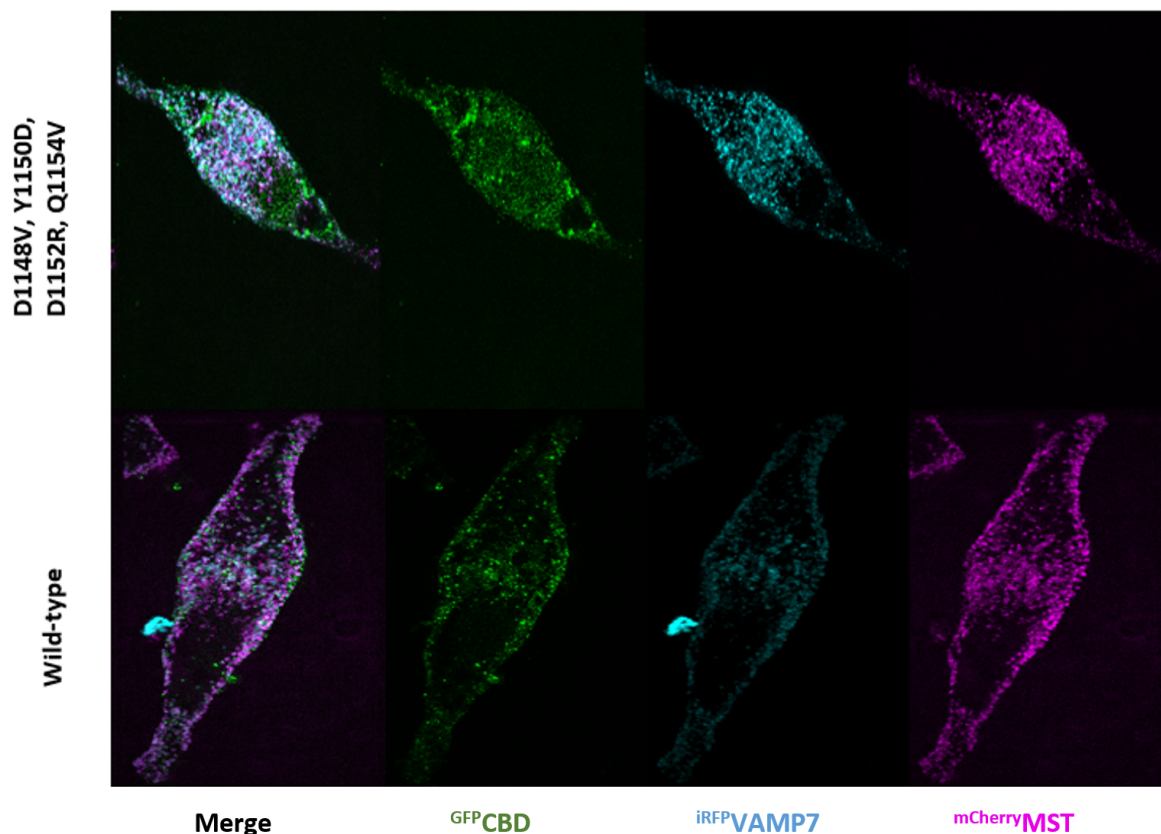


Figure 59: D1148V, Y1150D, D1152R and Q1154V mutations disrupt Myo6 CBD recruitment to melanosomes

Representative fixed MNT-1 cells co-expressing different GFP^{CBD} (WT) or GFP^{CBD} (D1148V, Y1150D, D1152R and Q1154V) constructs with control mCherry^{MST} and iRFP^{VAMP7}

A.3.b. Determination of the atomic structure of the Myo6 auto-inhibited state

Our paper thus brings insights on the way the Myo6 auto-inhibited state might be stabilized, yet atomic description of the auto-inhibited state is still missing to get a clearer understanding of Myo6 regulation by the description of the key contacts that Myo6 maintains in its auto-inhibited state. Additionally, the structure of Myo6 in its auto-inhibited state will bring detailed structural information on the Myo6 distal Tail and CBD subdomains that are still currently unreported and that could lead to a greater understanding on the way Myo6 interacts with its partners. Such structure could also lead to the discovery of new allosteric pockets within the back-folded Myo6 structure that could be of great interest to develop Myo6 modulators.

I thus performed crystallization assays in order to solve the structure of the FL Myo6 auto-inhibited state. To that aim, I used our Jo-Myo6-In construct. Indeed, crystallization of FL Myo6 had been extensively screened without success by a former PhD student of the team: Vicente Planelles-Herrero. Perhaps the Myo6 Tail still explores several conformations in the crystallization drops resulting in heterogeneity in between the Myo6 and making the formation of crystals disfavored.

In contrast, Jo-Myo6-In is trapped in the back-folded conformation as Jo and In subdomains limit the movement of the Tail with respect for the Motor. Crystallization assays were performed in the presence of Mg.ADP.VO₄ and EGTA. Jo-Myo6-In appears to give tiny nuclei in basic conditions whose size slightly improved using seeding (Figure 60). Yet, despite extensive optimization, these crystals remained too small and of poor-quality: no diffraction could be measured at the synchrotron beamline proxima 2.



Figure 60: Jo-Myo6-In crystallization drops without seeding (right) and with seeding (left)

Perhaps Jo-Myo6-In reluctance to crystallize could actually result from the fact that addition of the subdomains Jo and In in fusion with Myo6 results in a formation of an additional domain that

can vibrate with respect to Myo6 and this could make nucleation and growth of the crystal more difficult (Figure 61).

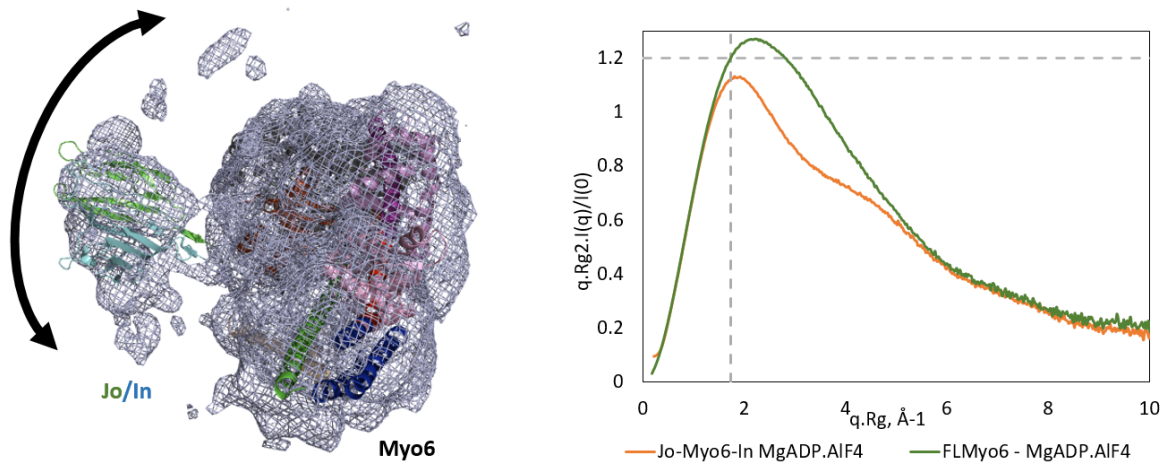


Figure 61: Jo-Myo6-In is a multidomain protein

(Left) 3D-reconstruction of Jo-Myo6-In construct based on negative staining electron microscopy. Jo-Myo6-In is modeled with the density (see section A.2). Density is less defined for Jo and In domains suggesting flexibility
(Right) Dimensionless Kratsky plot representation, dotted lines ($((qRg)2I(q)/I(0) = 1.104$ and $qRg = \sqrt{3}$) intersection highlight theoretical maximum of folded proteins. SEC-SAXS was carried out on Superdex 3.2/300 column pre-equilibrated in 20 mM hepes; 200 mM NaCl; 2 mM MgCl₂; 1 mM NaADP; 1 mM AlF₄ (P_i analog), 0.1 mM EGTA, 1 mM DTT or in in 20 mM hepes; 400 mM NaCl; 2 mM MgCl₂; 0.1 mM EGTA, 1 mM DTT

Overall, getting the atomic resolution structure of the Myo6 back-folded conformation remains of great interest and if crystallization shows limitations, perhaps cryo-EM studies could be a better strategy to determine the myo6 auto-inhibited state at high resolution in the future.

A.3.c. Structural description of the Myo6 Tail

Determining the structure of the whole Myo6 Tail would be of great interest as it would greatly improve our Myo6 auto-inhibited state model and brings us a clearer understanding of the way certain partners may activate Myo6 or not. Indeed, if small fragments of CBD or DT domains are available, a structure of the whole DT-CBD domain is still missing and it is thus unknown how CBDⁿ and CBD^c would be organized with respect to one another, potentially limiting the accessibility of certain binding interfaces. Using a severely truncated fragment of CBDⁿ, Shang *et al.* 2017 proposed the formation of a GIPC1-Myo6 complex with high oligomerization. In contrast, using larger fragments that also include CBD^c, a 1:1 Myo6/GIPC1 complex was characterized in our lab (Planelles Herrero 2017; see section G.1). Such structures could also help us understand why addition of the LI insert at the N-terminus of

the Myo6 CBD could improve binding affinity of partners, such as Dab2 and LMTK-2 on the CBD C-terminus (Fili *et al.* 2020, Chibalina *et al.* 2007).

A.3.d. Activation

Our study highlights the importance of a proper back-folding equilibrium between on and off states of Myo6 for correct recruitment of Myo6 in cells since mutants biased to favor the open conformation, FLMyo6 L926Q and SAHmimic were over-recruited while Jo-Myo6-In was not recruited to melanosomes. Since FLMyo6 L926Q and SAHmimic interact with partners normally unable to bind to the back-folded Myo6, improper folding could potentially result in misrecruitment resulting in activation of undesired pathway.

But to understand to what extent over-recruitment could be deleterious, a functional assay would be required to look at the effect of Myo6 over-recruitment at a cell compartment. In MNT-1, Myo6 is required for constriction and fission of tubular carriers (Ripoll *et al.* 2018), which is essential for melanosome maturation prior to their delivery to keratinocytes. Additionally, these carriers are involved in protein recycling (Dennis *et al.* 2016). To complete this study, it would now be interesting to monitor fission events frequency using FLMyo6 L926Q open mutants for example or looking at impact on transferrin uptake.

In our case, such a question is particularly tricky as both the L926Q and SAHmimic mutants impact the SAH N-terminus and, as a consequence, the stabilization of the off-state as well as Myo6 dimerization. It is thus difficult to say if pathogenous effect of the L926Q mutation comes from over/misrecruitment of Myo6 or improper dimerization. Actually, mutating the 3HB-SAH region should always be done carefully as it appears to be a challenging task to destabilize back-folding without destabilizing the proximal dimerization by mutating this region. The detailed structure of the Myo6 auto-inhibited state would thus be of great interest to identify how the SAH domain folds on the 3HB in the context of the auto-inhibited state and how pathogenous mutations, such as L926Q, could both trigger Myo6 opening and reduce the dynamics of the 3HB domain. On the basis of such a structure, it would then be easier to identify mutations that would target only the activation equilibrium without impairing dimerization.

We have explored the role of binding partners for differential recruitment of Myo6 and this study suggests the ability of RRL partners such as GIPC1 to recruit Myo6 independently of its activation state, while partners such as Dab2 and TOM1 would require assistance to open Myo6 prior to their binding. We propose that for WWY motif partners, local high concentration of Ca²⁺ ions could timely and spatially control Myo6 recruitment.

Interestingly, [French, Sosnick, and Rock \(2017\)](#) noticed that when Dab2 is artificially addressed to the Golgi apparatus, Myo6 recruitment does not correlate with the amount of Dab2, consistent with our results that have shown a lack of FL Myo6 or Jo-Myo6-In recruitment to melanosomes via Dab2. However, in contrast with our results: when Dab2 is artificially addressed to mitochondria, Dab2 can significantly recruit Myo6 to the mitochondria membrane. It should be noted that if, these three organelles are regulated by different Ca^{2+} flux/potential that could be responsible for differential recruitment of Myo6 by Dab2 depending on the compartment where Dab2 is addressed ([Wuytack, Raeymaekers, and Missiaen 2003](#)). This highlights the fact that the Myo6 recruitment depends on several parameters, and it is also possible that the freeing of the regions that bind Myo6 also depend on the other proteins present on these distinct organelles. To go further in this study, it would thus be of interest to repeat our recruitment assays on different organelles and in particular at the Golgi apparatus membrane.

Impact of other parameters on Myo6 unfolding remains to be explored, notably the role of actin or that of post-translational modifications such as phosphorylation. Indeed, phosphorylation has already been shown to regulate folding of Myo2 ([Craig, Smith, and Kendrick-Jones 1983](#); [Brzeska and Korn 1996](#)), and impacts Myo6 ATPase activity ([De La Cruz, Ostap, and Sweeney 2001](#)) and its recruitment ([Buss et al. 1998](#), [Brooks et al. 2017](#) and [Sahlender et al. 2005](#)). We thus could exclude its general requirement for either activation or back-folding. Considering the key role of CBD for the off-state stability, it would be of great interest to investigate the impact of LI and SI inserts on the off-state stability. Recent results already show that the LI insert does not impair the interaction between the Myo6 CBD and the IQ-DT fragment ([Dos Santos et al. 2022](#)). It would now be interesting to revisit this finding with Motor containing construct.

A.3.e. Proximal dimerization

A.3.e.i. Mechanical consequence of the proximal dimerization

Our study provided a detailed atomic structure for the Myo6 dimerization region, in which two Myo6s associate as an antiparallel dimer through residues 875-940. Compatibility of this dimer with 30-36 nm steps ([Figure 62](#)) and inability of FLMyo6 T888D, R892E and V903D to rescue transferrin uptake support the physiological relevance of this model. Moreover, the ability of GIPC1 to induce gating of FL Myo6, which is lost for the FLMyo6 T888D, R892E and V903D triple mutant, is a strong argument that GIPC1 induces proximal dimerization.

To develop our understanding of the Myo6 function, closer analysis of the mechanical properties of the proximal dimer would be of great interest. Single motility assays suggest that proximal dimerization may be important for Myo6 processivity as no movement could be detected

upon addition of the T888D, R892E and V903D mutations on FLMyo6. Yet, to test the role this dimer may play in cells, looking at the impact of T888D, R892E and V903D on Myo6 ability to stay attached to actin under resisting load would be of particular interest. As detailed description of either the proximal dimer upon GIPC1 binding (this study) or distal dimer upon Dab2 binding (Yu *et al.* 2009) are now available, such a study could now be considered.

A.3.e.ii. CaM recruitment by the proximal dimer

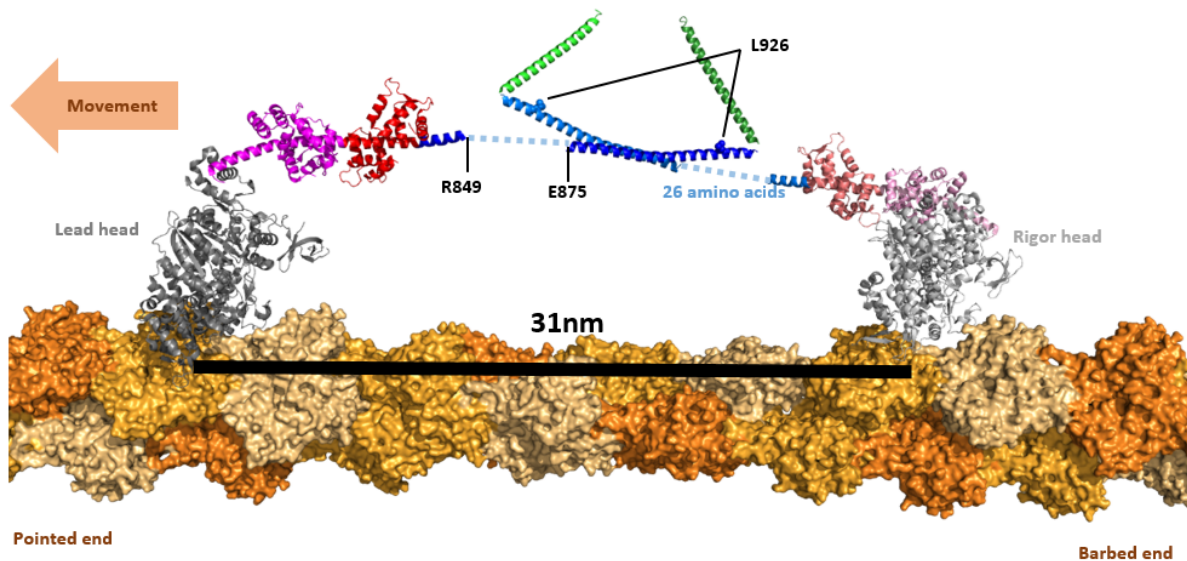


Figure 62: Model of the active FL Myo6 proximal dimer (extracted from Canon *et al.*, in preparation, see section A.2.)

The cryoEM structure of Myo6 bound to actin (PDB: 6BNP, Gurel *et al.* 2017) was used as a basis for placing two myo6 Motor domains in rigor and PPS states (grey) at the desired 31 nm distance. On each side, the N-terminus of the Lever arm bound to 2 light chains (pink, PDB: 3GN4, Mukherjea *et al.* 2009) was aligned to the corresponding residues in the converter. The crystallized dimerization domain (blue) was then arbitrarily placed between the two Lever arms, leaving a gap of 4.6 nm on each side. This gap needs to be filled by a stretch of 26 amino acid residues that would correspond to 3.9 nm if in a theoretical helix, or up to 9.9 nm if fully extended. The rest of the SAH (green) (PDB: 6OBI, Barnes *et al.*, 2019) was connected to the C-terminus of the dimerization region via a kink. The model is compatible with parallel dimerization of the cargo-binding domain.

Additionally, to complete our model (Figure 62), closer look should be taken to the R849-E875 region. Tryptophan fluorescence (Batters *et al.* 2016) and microscale thermophoresis assays (Mukherjea *et al.* 2014) proposed that this fragment could have the ability to bind CaM. For Batters *et al.* 2016, helix 833-856 could fold on the IQ/CaM while Mukherjea *et al.* 2014 proposed that an additional CaM could be recruited by the 834-875 region which would rigidify the proximal dimer Lever arm compared to one with only two Cam on each side. In fact, the zippered Myo6 dimer was shown to

associate with three CaM per HC via HPLC and gel quantification. In our view, folding of residues R849-E875 on IQ/CaM is unlikely as it would result in a shortening of the distance between the two Myo6 heads and thus such a model is not compatible with the 30-36 nm steps previously measured for the molecule (De La Cruz, Ostap, and Sweeney 2001; Rock *et al.* 2001) (Figure 63).

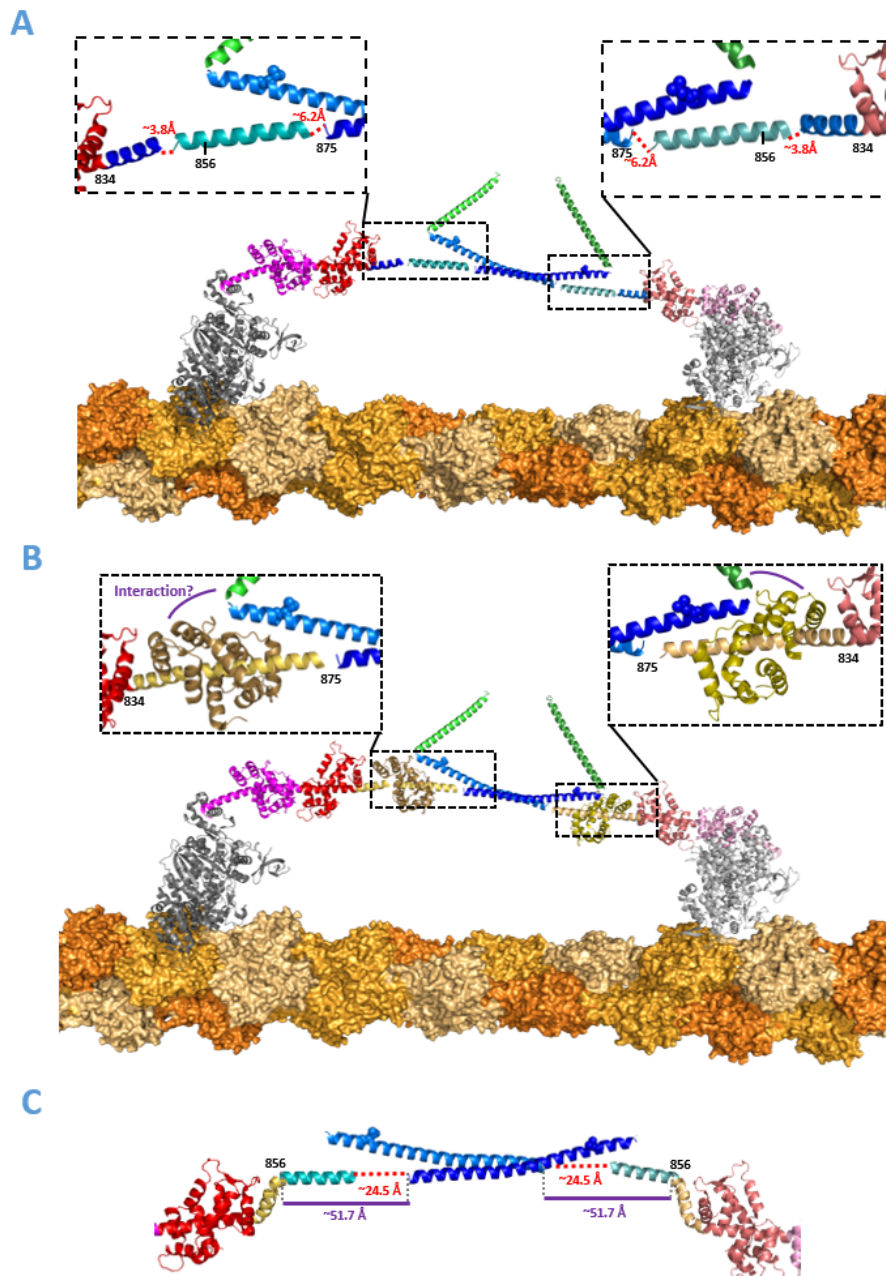


Figure 63: Model of the active FL Myo6 proximal dimer with modelization of the R849-E875 region (A) docking of a 26 amino acid helix composed of alanine was docked between residues 849 and 875. A distance of $\sim 3.8 \text{ \AA}$ was left between R849 and the C-terminus of the poly-Ala helix, which corresponds to the typical distance found between two residues within an α -helix. It should be noted that this docking is imprecise since it was roughly assembled without any alteration of the cryoEM and crystallographic model of the Lever arm and the dimerization region, this should be reviewed in the context of a dynamic motor (molecular dynamic) to

improve this docking. (B) A third CaM could be recruited on residues 834-875 in our model without generating clashes. Close proximity between CaM and the kink between the end of the proximal dimerization area and the SAH (at residue 940) could suggest that interactions may occur here, although such interaction remained to be investigated (C) The 833-856 region is folded on the IQ CaM as proposed by [Batters et al., 2016](#). This leaves a 51.7 Å gap between residues 856 and 875 if the heads are positioned to allow 31 nm steps. Filling this gap would require that the 856-875 region extends fully (a linker would in fact cover ~ 47 Å). This model is thus unlikely as it does not seem compatible with the stepping previously measured for dimeric Myo6.

Exploring putative interaction between CaM and the Myo6 930-950 region may bring insights on the way Myo6 dimerizes. Finally, the crystal structure of Ins2-E875 could provide us with a detailed description of the Myo6 Lever arm when proximal dimerization through residues 875-940 occurs. These findings could provide a clearer description of the Lever arm rigidity and help understand the kind of function the proximal dimer could play in cell.

A.3.e.iii. FLGIPC1 – Myo6 stoichiometry

To prevent GIPC1 auto-inhibition, all our studies were performed using the GIPC1 GH2 domain only. Yet, in physiological context, GIPC1 contains a GH1 domain that can mediate GIPC1 dimerization ([Figure 64](#)) (see results - section A.1.c). Thus, the impact of GIPC1 auto-inhibition and its ability to prevent or to favour Myo6 binding should be monitored using the FL GIPC1. This should also result in the correct description of the real physiological stoichiometry that can occur upon Myo6/GIPC1 recognition. Indeed, Myo6 has been found to exhibit different mechanical properties depending on whether it is functioning as a dimer or an assembly of cargos (see introduction - section E.3). If FL GIPC1 is not compatible with Myo6 binding, the challenge would be to find a way to destabilize the auto-inhibited state of GIPC1 for *in vitro* experiments without perturbing the Myo6/GIPC1 interactions. The most physiological way would be to try adding GIPC1 PDZ partners such as APPL1. This question remains to be explored in future investigations.

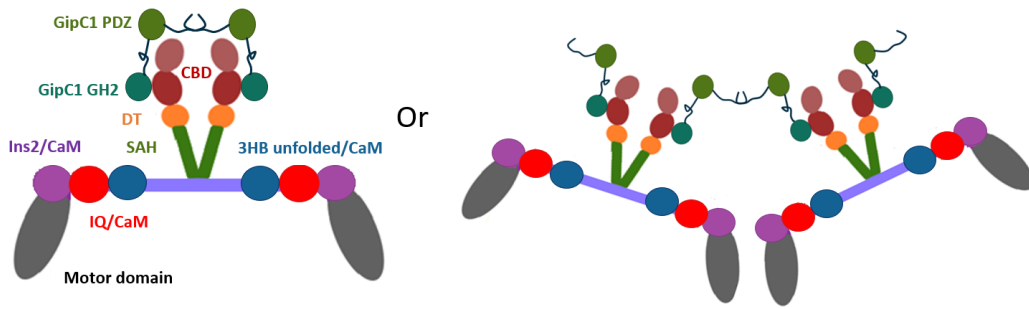


Figure 64: Model of the GIPC1-Myo6 complex that could either form a single dimer or a large oligomer of dimers

Model of Myo6 proximal dimer (light chains not shown). Motor domain in grey, Ins-2 in purple, IQ in red, unfolded 3HB in blue, SAH in light green, DT in orange, CBD in brown. GIPC1 is picture in green. As a dimer, it exhibits two GH2 domain that can bind either to the two cargos binding domain of the same Myo6 proximal dimer (right) or bind to cargo binding domains belonging to two different motors resulting in the formation of large oligomers (right)

A.3.e.iv. Ability of partners to trigger the formation of the Myo6 proximal dimerization

The formation of the Myo6 proximal dimer relies on 3HB unfolding ([Mukherjea et al. 2009](#)) but once the 3HB unfolding has occurred, Myo6 proximal dimerization is exposed, thus in this context, Myo6 may dimerize without assistance of a particular partner. This raises the question of whether all partners of Myo6 could trigger 3HB unfolding and proximal dimerization. Yet, from our study, whether the proximal dimerization can be triggered only by certain partners or whether all partners could trigger proximal dimerization remains an open question.

Through a kinetic study using FRET-based stopped flow, [Dos Santos et al. 2022](#) monitored the dimerization of the Myo6 814-end construct upon NDP52 binding. Interestingly, they found that the dimerization rate is independent of NDP52 concentration. Moreover, they found that Myo6 can gate upon increasing concentrations of actin using a constant concentration of either the NDP52 or Dab2 partners ([Dos Santos et al. 2022](#)). As in this context, the k_{cat} was identical for Myo6 supplemented with Dab2 or NDP52 or Myo6 truncated from the Tail, the authors thus proposed that the partners do not regulate the ATPase level, it mainly promotes exposition of the internal dimerization site normally masked when Myo6 adopts a back-folded conformation ([Fili et al. 2017](#) and [Dos Santos et al. 2022](#)). They thus proposed that the role of the Myo6 partner may be to control whether the Myo6 internal dimerization would occur by either promoting unfolding and exposing the dimerization area, or by its inability to do so. The region they considered to allow internal dimerization was suggested to occur arbitrarily after the SAH, and thus was not the same as the one we identified in our study. In fact, we demonstrated that the proximal dimerization requires the opening of the 3HB to form and whether

Myo6 unfolding automatically results in a 3HB opening in a physiological context remains to be explored.

It should be noted that in contrast with our study, [Dos Santos *et al.* 2022](#) found that Dab2 was able to activate FLMyo6 in actin-activated ATPase assays. Perhaps this difference is due to the 5-fold higher salt concentration used in this experiment or to the lower concentration of F-actin. Further experiments are needed to understand the differences. Still, in our hand, the inability of TOM1 and Dab2 to recruit a constitutively closed Myo6 (Jo-Myo6-In) in contrast with the constitutively open constructs (SAHmimic or L926Q mutant) on melanosome strongly support the fact that not all partners have the ability to bind to the Myo6 auto-inhibited state which would be necessary so that they could trigger unfolding. We thus propose that partners must at least be split in two classes: in the first class, that likely includes at least some of the RRL partners, the partner unfolds Myo6 possibly triggering 3HB unfolding. In the second class, that includes the WWY partners and other CBD^c partners such as DNA ([Fili *et al.* 2017](#)), their binding site being masked in the off-state, they cannot act to unfold and activate on their own. However, they might act to stabilize the Myo6 active form by preventing Myo6 back-folding. However, the identification of partners triggering/stabilizing the proximal dimerization requires further experiments.

In the other hand, [Rai *et al.* 2021; 2022](#) proposed that the Myo6 partners may influence the Myo6 mechanical role in different ways depending on the partner. Indeed, in their hands, using a similar experimental set up, the addition of Dab2 results in the formation of sparse Myo6 dimers minimizing cortical actin reorganization while that of GIPC1 results in the formation of unfolded Myo6 monomers that could mediate long and fast processive runs when assembled in a network via a DNA scaffold. Note that these experiments have been performed in conditions that may not facilitate dimerization (immobilized motor, very low concentration up to ~50 pM). This likely explains why [Rai *et al.*, 2022](#) could only see a 1:1 complex between GIPC1 and Myo6, while our ATPase results pointed out to Myo6 dimerization upon GIPC1 binding. These findings suggest that Dab2 and GIPC1 may have differential impact on Myo6 mechanical properties once unfolded.

It would thus be of interest to see if all partners could promote proximal dimerization to challenge these models. Yet to answer such question, actin activated ATPase assays as performed in our study show limitations: As Dab2 and TOM1 were not able to activate FL Myo6 WT in our ATPase assays, the impact of Dab2 and TOM1 on the Myo6 mechanical properties and in particular on dimerization is unclear. Indeed, all our constitutively opened mutants impaired proximal dimerization and they thus cannot be used to look at the ability of Dab2 or TOM1 to promote gating. Moreover, the impact of TOM1 and Dab2 on the SAHmimic ATPase activity is very similar despite the fact that these two partners were reported to induce different oligomeric states of the motor: TOM1 and Dab2 were proposed to activate Myo6 as a monomer ([Hu *et al.*, 2019](#)) of a distal dimer ([Yu *et al.*, 2009](#)),

respectively. Thus, either distal dimerization does not induce gating making distal dimers indistinguishable from active monomers, or our experimental conditions do not allow the formation of proper distal dimerization, perhaps due to the use of the SAHmimic mutant. Possibly also, more studies on TOM1 or Dab2 are required to ascertain whether they can mediate distal dimerization since the results from the crystal structures are insufficient to assess the stoichiometry of the Myo6-partners in the context of the FLMyo6.

Overall, to have a clear understanding of the impact of the binding of partners on Myo6, a direct measurement of the oligomeric state is required in complement to the ATPase assays.

Actually, to overcome this limitation, we first aimed to perform interferometric scattering mass spectrometry (iSCAMS) (Young *et al.* 2018) taking advantage of the fact that our collaborator Lee Sweeney was able to gain access to an iSCAMS system in the beginning of my PhD. iSCAMS is a recently developed technique that can provide a good estimation of the molecular weight of biomolecules and biomolecule complexes. It relies on illumination of molecule in solution with a coherent light resulting in light reflection and light scattering by the biomolecule. Interference between the reflected and scattered light at the detector results in a contrasted signal enabling imaging while a scattered signal is proportional with the particle volume, enabling molecular weight determination (Young *et al.* 2018) (Figure 65).

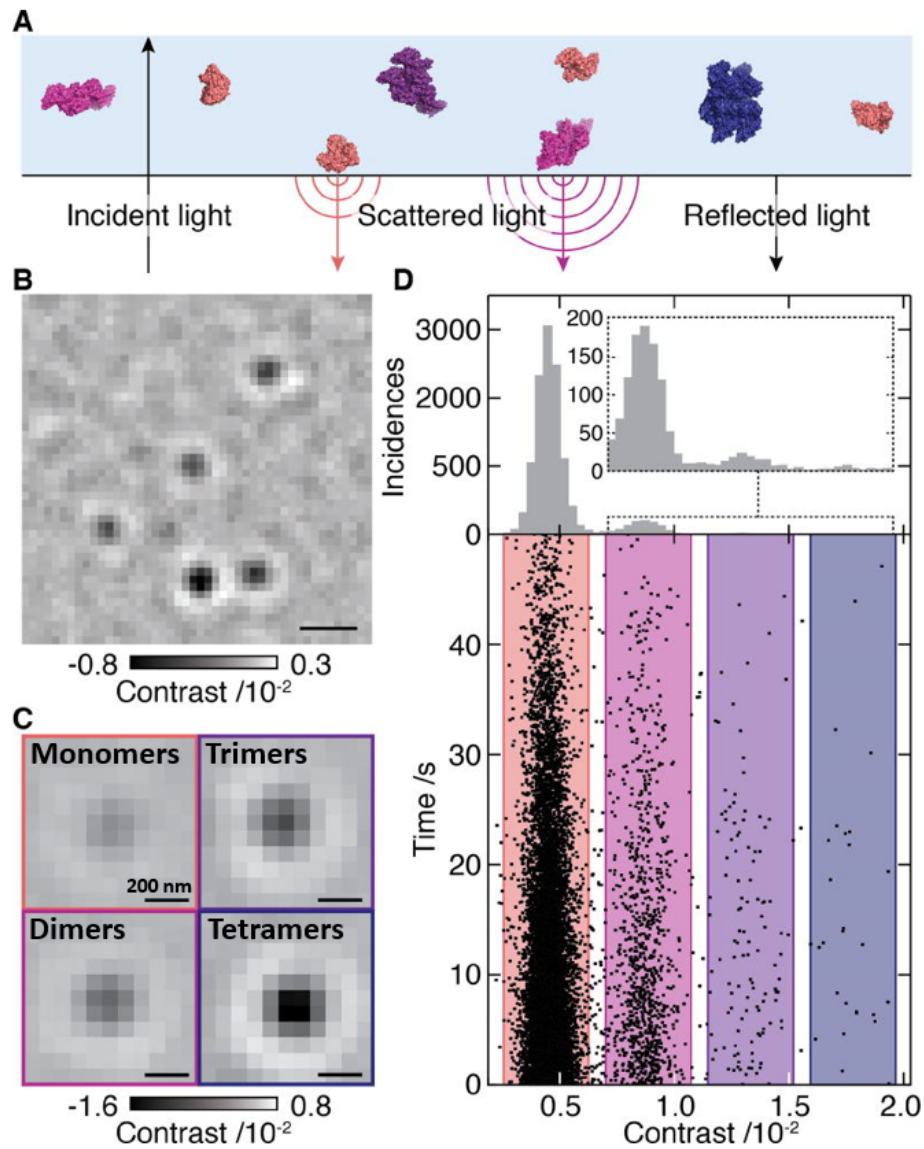


Figure 65: interferometric scattering mass spectrometry principle (adapted from [Young et al. 2018](#))

Characterization of a 12 nM BSA sample in iSCAMS, (A) schematic representation of the iSCAMS experimental approach, (B) Differential interferometric scattering image (scale bar 0.5 μm), (C) Representative image for different oligomeric states (D) Scattering plot of single molecule and corresponding histogram

Yet this technique exhibits several limitations. In particular, it is challenging to detect particles below 50 kDa and concentrations must be low enough so that a signal can be detected for single particles near the refractive interface. The detection limit was a first issue to overcome in our experiments as the Myo6 partners we were working with were too small to be detected on their own (GIPC GH2 weights ~12 kDa, TOM1₂₀₇₋₄₉₂ weights ~33 kDa and Dab2 weights ~17 kDa).

I thus fused these partners to bigger proteins. The Myo6 adaptor constructs cloned in fusion with monomericYFP (27 kDa) ([Shaner et al. 2004](#)), mNeongreen (26.5 kDa) ([Shaner et al. 2013](#)) or MICAL-2₁₋₆₂₃ (71 kDa) ([Giridharan and Caplan 2014](#)) were used to try to reach a detectable signal. The

purified proteins and experimental protocol were then sent to our collaborator Lee Sweeney where the iSCAMS experiments were carried out by Peter Hook. These assays were carried out using different nucleotides, salt concentrations, Myo6 constructs (promoting either closure or opening). Despite several experiments, the results obtained were inconclusive: the association between Myo6 and its adaptors was only rarely seen, and we were not able to detect more than ~4 % of 2:2 complexes between Myo6 and any tested partners. We propose that iSCAMS was inconclusive for our case perhaps due to the low Myo6 concentration required. Actually, a recent study trying to measure the oligomeric state of Myo7a-M7BP complex faced the same limitation that we did as they could only measure a 1:1 complex in iSCAMS despite the very high affinity of the Myo7a-M7BP complex (~6 nM) ([Liu et al. 2021](#)).

We therefore decided now to switch from iSCAMS to analytical ultracentrifugation (AUC) which allows the use of higher concentration of proteins and can detect small proteins. AUC can provide us on stoichiometry of Myo6 in complex with its various partners using Motor less fragments. These experiments should give us clearer answer regarding Myo6-partners stoichiometry. We will put these data in perspective with the ATPase assays performed by our collaborator to clarify whether partners can instruct the Myo6 motor of unique mechanical functions.

Finally, additional ATPase assays could be conceived to look at the impact of the WWY partners on proximal dimerization. Perhaps, repeating actin activated ATPase assays in higher salt conditions could be sufficient to enable TOM1 or Dab2 binding. Another way could be the addition of Ca^{2+} . Indeed, Ca^{2+} addition results in enhanced TOM1 binding to Myo6. However, a complication comes from the fact that Ca^{2+} addition must be transient as it was shown to result in loss of coordination between the two heads of a dimer ([Morris et al. 2003](#)). Although difficult to implement, such study is important as they would provide us with a more complete characterization of the way partners could provide Myo6 with unique mechanical functions.

A.3.f. Conservation of the proximal dimerization among species

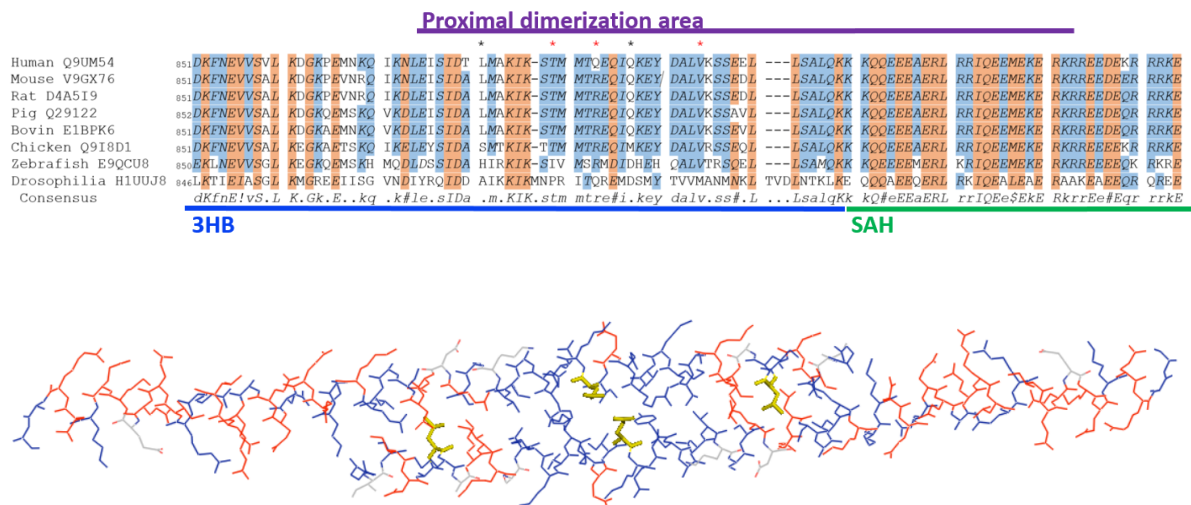


Figure 66: Sequence alignment of the 851-949 (human gene numbering) amino acids among species. Red corresponds to conserved residues, blue to residues conserved in at least 6 out of 8 species. Top: * marks residues inside the dimerization area that are poorly conserved. * marks the residues mutated that are sufficient to disrupt proximal dimerization. Bottom: residues colored depending on their conservation in the crystal structure, residues poorly conserved inside the dimerization interface are plotted in yellow

To complete our study, it would be interesting to explore the conservation of the proximal dimerization among species and investigate whether proximal dimerization can occur outside the mammalian phylogenetic group (Figure 66). While the proximal dimerization area is overall conserved, *Drosophila* exhibits the most divergent sequence among the 8 species compared in Fig XX. Indeed, two insertions can be found within the proximal dimerization area suggesting that if the Myo6 proximal dimerization occurs in *Drosophila*, some adjustment in the structure are likely occurring compared to the structure we have solved. It is however not possible to say whether this would not favor dimerization or if the adjustments would remain local.

Additionally, chicken, zebrafish and *drosophila* Myo6 exhibit two divergent residues compared to the human sequence crystallized: Leu881 is replaced with Ser, His or Ala respectively. If Ser and Ala seems compatible with the structure, a bulk residue such as His could result in steric hindrance and make formation of the dimer destabilized. In addition, Gln896 in the human sequence is replaced with Met or Asp. To understand the impact of these sequence changes on the formation and stability of the proximal dimerization, ATPase assays to monitor gating through different species could be performed.

A.3.g. Endogenous recruitment of Myo6 to melanosome

The Myo6 partner OPTN was proposed to be involved in Myo6 mediated tubular carrier fission during melanosome maturation as OPTN silencing similarly to SiMyo6, decreases fission events without decreasing tubule formation in MNT-1 (Ripoll *et al.* 2018). However, OPTN silencing does not impact Myo6 localization to melanosome suggesting that if OPTN may be required for Myo6 in melanosomes it may not be required for Myo6 recruitment to melanosomes (Ripoll *et al.* 2018). In contrast, the I1072A mutation reported in our study drastically reduces Myo6 recruitment to melanosomes. The I1072A mutation has previously been reported to drastically reduce ubiquitin binding to the Myo6 MyUb binding site through pull-down assay, (He *et al.* 2016) while keeping the overall MyUb domain fold as showing by NMR (He *et al.* 2016). It is thus tempting to speculate that recruitment to melanosomes requires Myo6 interaction with ubiquitylated cargos.

He *et al.*, 2016 shows that ubiquitin chains exhibiting the highest affinity for Myo6 MyUb binding sites are the K63-linked chains. Considering the importance of residue I1072 for Myo6 recruitment to melanosomes, we decided to check whether K63-diUbiquitin could activate Myo6. I produced the K63-diUbiquitin homemade following the previously published protocol (Komander *et al.* 2008). DNA encoding for enzymes required for K63link ubiquitin preparation and Ubiquitin DNA were a kind gift for the Komander's lab. We confirmed the ability of K63-diUbiquitin to bind the Myo6 Tail by microscale thermophoresis ($K_D \sim 10 \mu\text{M}$) (Table 13).

	Adaptor	Myo6 Tail	K_D	n
Interaction with K63-diUbiquitin	K63-diUbiquitin	YFP ^{CBD}	$10 \pm 6 \mu\text{M}$	1
	K63-diUbiquitin	YFP ^{CBD} _{I1072A}	n.b	1

Table 13: K63-diUbiquitin binding to the Myo6 CBD

Microscale thermophoresis experiment performed in 20 mM Tris pH8.5, 100 mM KCl, 1 mM DTT, 0.05 % tween

We then sent the protein to our collaborator Lee Sweeney to evaluate its ability to activate Myo6 in actin activated ATPase assays but remarkably the K63-diUbiquitin was not able to activate wild-type FLMyo6 in contrast to what was seen for GIPC1 (Figure 67).

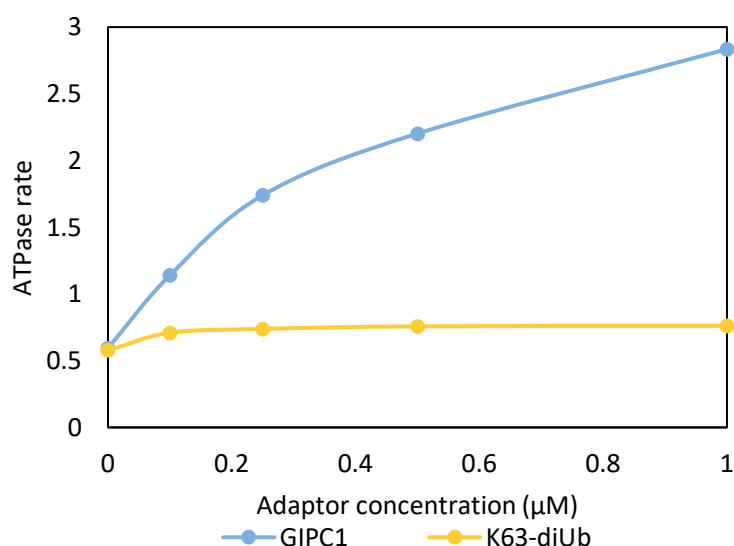


Figure 67: K63-diUbiquitin is unable to increase the Myo6 ATPase rate.

Actin-activated ATPase rate ($s^{-1}.Head^{-1}$) of 250 nM FLMyo6 wild-type upon increasing concentration of K63-diUb or GIPC1 GH2 (from 0 to 1 µM) ($n=6$) on 40 µM F-actin in 10 mM MOPS7, 10 mM KCl, 1 mM DTT, 1 mM MgCl₂, 1 mM EGTA

Thus, while we cannot exclude that ubiquitylated cargos could help recruit Myo6 to melanosome, it seems that another partner would be required to activate it, possibly the RRL partner OPTN. Importantly, it should be noted that OPTN can be ubiquitylated (UbOPTN). Interestingly, [He et al. 2016](#) reported, through a pull-down assay, that Myo6's ability to bind UbOPTN is drastically reduced by the I1072A mutant. This could be the reason why even our constitutively open construct FLMyo6 (SAHmimic.I1072A) or FLMyo6 (L926Q.I1072A) were not able to fully rescue Myo6 recruitment to melanosomes. Indeed, the Myo6 affinity for ubiquitylated partners present at the surface of melanosomes such as OPTN may still be impaired by the mutant. Overall, while our study is not sufficient to describe how endogenous recruitment of Myo6 to melanosomes occur, it has provided interesting insights and tools for further study on the role of Myo6 in melanosome maturation.

Conclusions

The work presented in this thesis offers new insights on Myo6 regulation.

In our study, we highlight the importance of Myo6 back folding for regulation of its activity in cell. Although some Myo6 back-folding is possible using Motor-less Myo6 construct (or FLMyo6 in nucleotide free state) (Fili *et al.* 2017; 2020; Dos Santos *et al.* 2022; Batters *et al.* 2016), our study identifies that the presence of ADP.P_i analog within Myo6 motor greatly enhances the stability of the Myo6 back-folded state since the presence of ADP.P_i analog prevents Myo6 opening in high salt concentration and should thus be sufficient to maintain Myo6 back-folded in a physiological context. Our study also demonstrates that interactions between the head and the Tail involve a highly conserved loop within the CBD^c that has been previously reported to bind DNA, making DNA binding to Myo6 auto-inhibited state unlikely, consistently with what has been proposed previously (Fili *et al.* 2017).

As a consequence, not all partners can directly interact with the Myo6 auto-inhibited state to trigger Myo6 recruitment and activation. In particular, the WWY motif partners Dab2 and TOM1 were shown to be unable to bind to the Myo6 auto-inhibited state in *in vitro* and cell-based assays and considering the fact that the WWY motif is particularly buried in our model, it is tempting to propose that none of the Myo6 WWY partners may be able to trigger unfolding. In this context, a signal triggering unfolding must be required to allow recruitment of these partners offering spatial and temporal control of their binding to Myo6. Indeed, in cells, it has been shown that the ability of Dab2 to recruit Myo6 depends on the cell compartment where it is localized (French, Sosnick, and Rock 2017). This signal might be for example a Ca²⁺ ion concentration variation. Indeed, a recent study has proven the ability of Ca²⁺ ion to unfold Myo6 (Rai *et al.* 2022) as previously proposed (Batters *et al.* 2016). In our study we confirm through a pull-down assay that Ca²⁺ addition indeed improves Myo6 binding to the WWY partner TOM1, further supporting this hypothesis.

In contrast, we demonstrate that the Myo6 RRL motif partner GIPC1 can efficiently bind to the Myo6 auto-inhibited state, as GIPC1 can recruit both FLMyo6 and Jo-Myo6-In to melanosome. GIPC1 can then trigger unfolding and activation, consistent with a recent study showing GIPC1's ability to unfold FLMyo6 in a FRET assays (Rai *et al.* 2022) and supporting a different role of partners for Myo6 activation.

Although GIPC1 GH2 domain has been proposed either to oligomerize Myo6 (Shang *et al.* 2017) or to stabilize an active monomer of Myo6 (Rai *et al.* 2022), here we demonstrate GIPC1's ability to trigger Myo6 gating, reflecting its ability to promote Myo6 self-dimerization, which was further supported by the fact that a triple mutant specifically designed by our team to impair Myo6 proximal

dimerization disrupts GIPC1's ability to promote Myo6 gating. Due to its ability to oligomerize the Myo6 Tail in AUC and crystal structure (Shang *et al.* 2017), and to speed up Myo6 in *in vitro* motility assays (Rai *et al.* 2022), the Myo6-GIPC1 complex has been proposed to act as a transporter. Yet, a strong gating between the Myo6 heads might be optimal for anchoring function of the motor (Sweeney and Houdusse 2007), our study opens the possibility that GIPC1 may mediate Myo6 anchoring function against load. Actually, as proposed for NDP52, it is possible that the Myo6 stoichiometry induced by GIPC1 binding may be regulated by local concentration offering ability for Myo6 to work either as a transporter or an anchor through its binding to the same partner. Thus, studying the impact of GIPC1 concentrations on Myo6 mechanical properties and the impact of GIPC1 on Myo6's anchoring ability may be of great interest in the future.

Our data also support the idea that each partner may impact Myo6 mechanical properties in a different manner: although we could not compare TOM1 and Dab2's impact to GIPC1 on Myo6 wild-type ATPase activity in our ATPase assay, comparison of their ability to activate the constitutively open mutant SAHmimic revealed that even in the context of an open construct TOM1 and Dab2 cannot fully activate Myo6 as opposed to GIPC1, suggesting a differential impact of these partners on Myo6 activity. Although, this point still requires investigation, the idea is further supported by crystal structures showing diverse stoichiometries for Myo6 Tail – partner complexes depending on the partner bound (Shang *et al.* 2017; Hu *et al.* 2019; Biancospino *et al.* 2019; He *et al.* 2016; Yu *et al.* 2009) and supported by functional assays showing that in similar conditions, Dab2 can dimerize Myo6 and mediate a sparse motility while in contrast, GIPC1 stabilizes a monomer and speeds up the motor in ensemble motility assays (Rai *et al.* 2021; 2022).

Moreover, thanks to their incompatibility with the Myo6 auto-inhibited state, CBD^c partners sequester CBD^c, preventing its rebinding to the Myo6 head, thus, stabilizing Myo6 active form following unfolding. This is consistent with previous competitive experiments with DNA, Dab2 and NDP52 (Fili *et al.* 2020; 2017). While the GIPC1 binding is compatible with the Myo6 auto-inhibited state, its ability to sequester Myo6 CBD to stabilize an active form may not be as strong as the one of DNA or Dab2 and remains to be investigated. In this context, it may be interesting for the motor to bind several partners at once for optimal functioning or for switching for one mechanical role to another.

Our study of the Myo6 auto-inhibited state provides a clearer definition of the Myo6 back-folded state overall shape and dimensions. Consequently, a hinge between the 3HB and SAH must exist to allow Myo6 to fold back making the SAH N-terminus a critical area for the stabilization of the Myo6 auto-inhibited state. The unusual high occurrence of apolar residues within the N-terminus part of the SAH domain of Myo6 may have a role in the auto-inhibited state stability. Thereby, mutations of apolar residues in this region results in Myo6 opening (SAHmimic (Mukherjea *et al.* 2014) or L926Q deafness mutant (Brownstein *et al.* 2014)).

But both the SAHmimic ([Mukherjea et al. 2014](#)) and L926Q mutations (this study) were shown to also have an impact on the Myo6 proximal dimerization by limiting the 3HB dynamics and unfolding required for proximal dimerization. These findings thus demonstrate the close coordination that must exist between the Myo6 3HB and the SAH domain. It also highlights the crucial role of this region for Myo6 regulation and emphasizes the difficulty to study it, since a particular mutation in this region can impact dimerization as well as opening. A more detailed description of the interactions existing between the Myo6 3HB and the SAH domain would thus be of great interest. Overall, even if our cell-based assays demonstrated that L926Q and SAHmimic mutations can lead to overrecruitment of the motor, it must not necessarily enhance Myo6 functions as they also make the motor dysfunctional and may instead act as dominant negative which is further supported by the fact that SAHmimic is unable to rescue Myo6 function for Golgi maintenance and transferrin uptake, even when artificially dimerized ([Mukherjea et al. 2009](#)).

Finally, our study offers a new model for Myo6 self-dimerization. The step size that myosins are able to take on actin has initially been proposed to be proportional to the size of its Lever arm, yet the discovery of Myo6 has challenged this hypothesis since despite its short canonical Lever arm, Myo6 was found able to take large steps on actin (see section E.5). Several models were proposed and debated to explain this step size, involving either a distal dimerization mediated by partners ([Yu et al. 2009](#)) and providing Myo6 with a highly flexible Lever arm or internal dimerization mediated either by SAH ([Kim et al. 2010](#)) or 3HB ([Mukherjea et al. 2009](#)) domains. Here thanks to a crystal structure, our study demonstrates the ability of Myo6 to undergoes anti-parallel dimerization through residues 875-940. Importantly, an atomic model of the Myo6 dimer can thus be built thanks to this information. It is compatible with a distance of 31 nm between the two heads of the Myo6 dimer which explains how the motor can step on actin using ~30 nm steps. This model is further supported by the fact that motility assays demonstrated that a triple mutant (that does not interfere with the 3HB fold but disrupts proximal dimerization renders Myo6 unable to step on actin. Finally, the inability of our triple mutant anti-proximal dimerization to rescue Myo6 mediated transferrin uptake supports the importance of proximal dimerization for endocytosis.

Chapter 2: Inhibition of Myosin motor by small molecules binding in the 50 kDa cleft

Introduction

A. Conventional myosins (Myo2): therapeutical targets

Due to the long coiled-coil domain that mediates dimerization of the myosin heavy chain, Myo2s are constitutive hexamers (2 heavy chains and 4 light chains, which comprise 2 essential light chains (ELC) and 2 regulatory light chains (RLC)) (Figure 68). These dimers can then associate and form large fibers to pursue their cellular functions.

Historically, several myosin fragments were defined based on proteolysis. Chymotrypsin cleaves myosin in heavy meromyosin (HMM), which contains the Motor domain plus the Lever arm and the beginning of the coiled coil, and light meromyosin (LMM), which contains the remaining C-terminus. HMM can be cleaved by papain in subfragment S1 (Motor domain plus Lever arm) and S2 (remaining part of the coiled coil) (Lowey *et al.* 1969) (Figure 68). S1 is sufficient to produce force and slides actin filaments, although it is monomeric.

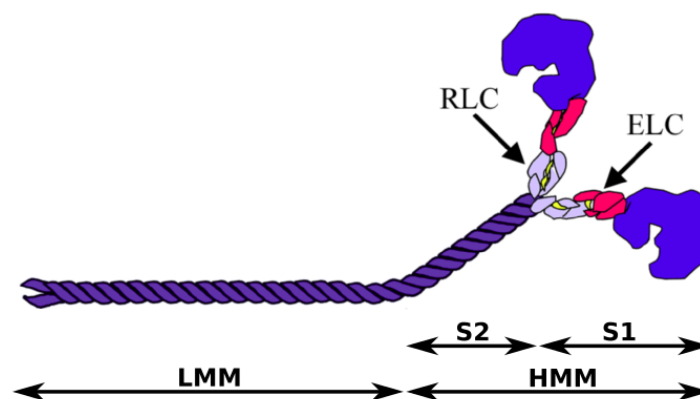


Figure 68: Myo2 subfragments (Planelles Herrero 2017)

Schematic representation of Myo2 with (from right to left) the Motor domain in blue, the Lever arm bound to the essential light chain (ELC) in pink and the regulatory light chain (RLC) in lilac and the long coiled coil Tail in purple. The delimitation of the subfragments 1 (S1) and 2 (S2), the heavy meromyosin (HMM) and the light meromyosin (LMM) are depicted.

There are several isoforms of class II myosin whose heavy chains are encoded by:

- MYH1, MYH2, MYH3, MYH4, MYH7B, MYH8, MYH13, MYH15 for skeletal muscle contraction
- MYH6 and MYH7 for cardiac muscle contraction
- MYH11 for smooth muscle contraction
- MYH9, MYH10, MYH14 for non-muscle cells
- Uncharacterized pseudogene MYH16

A.1. Sarcomeric Myo2

Skeletal (SkMyo2) and cardiac (CardMyo2) muscles Myo2 associate with actin in a contractile unit called the sarcomere (Figure 69). The sarcomere is composed of an alternation of thick myosin filaments and thin actin filaments that give a striated aspect to cardiac and striated muscles. CardMyo2 is specifically found in the heart tissue, and its contraction mediates heartbeat, while SkMyo2 is found in all striated muscles and mediates voluntary contraction. In both cases, contraction of the sarcomere is controlled by the actin-associated proteins troponin and tropomyosin.

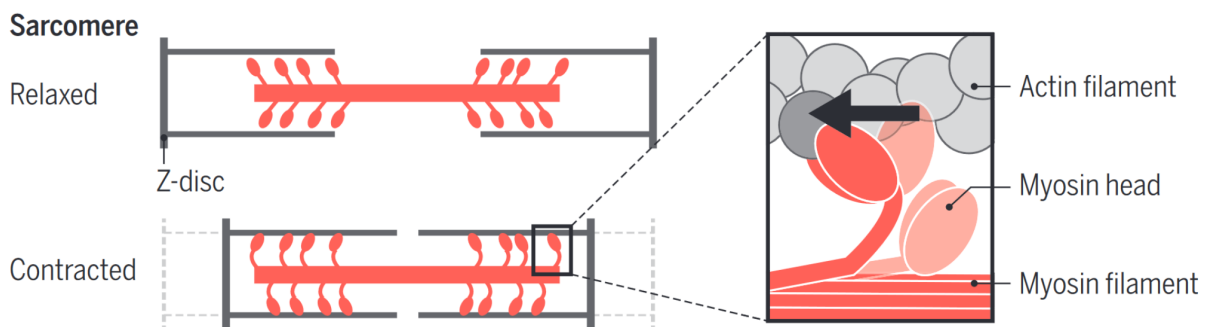


Figure 69: Overall sarcomere organization (Warshaw, 2016)

Overall sarcomere organization with the thick myosin filaments in red and the thin actin filaments in grey. The Z-disc delineates the lateral borders of the sarcomere. During the powerstroke, Myo2 generates force resulting in association of the Myo2 head with the actin filament and the contraction of the sarcomere.

SkMyo2s isoforms can be fast (MYH1, MYH2, MYH3, MYH4, MYH8, MYH13) or slow (MYH7B and MYH15), and their abundance varies depending on the muscle and on stage of development. Thus, we can find slow (Type I) or fast (Type IIa, IIb, IIx/d) fibers in the muscle, depending on the isoform of Myo2 that is incorporated in it. Actually, different kind of fibers can be found at once in a muscle, but their proportion vary, allowing fine regulation of muscle contraction depending on the specific function of the muscle, and on its position in the body (Figure 70). CardMyo2s are also split into isoforms exhibiting different mechanical properties: α -CardMyo2 (MYH6 gene) is 2-3-fold faster than β -CardMyo2 (MYH7 gene) and is expressed mainly in the atria, while β -CardMyo2 is mainly expressed in ventricle (Walklate et al. 2021).

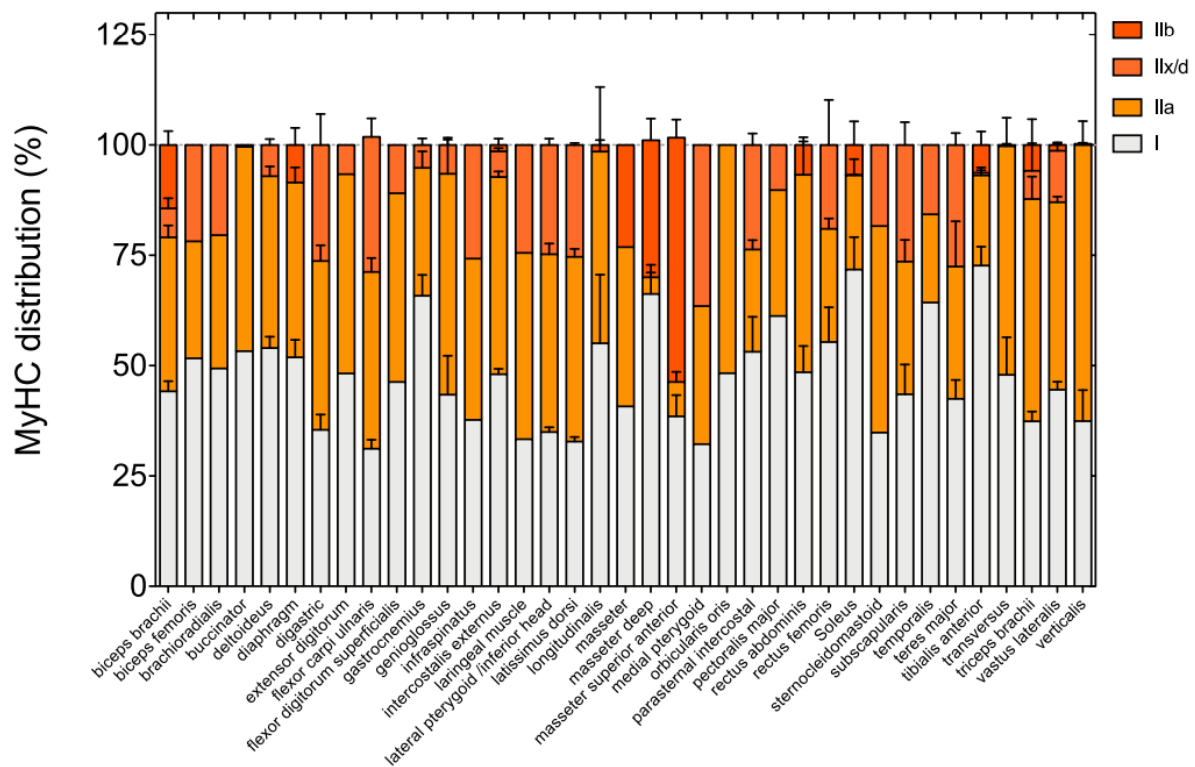


Figure 70: Relative abundance of Myo2 isoforms in human muscles (Gyimesi *et al.* 2020)
Myo2 isoform distribution in different human muscle type (literature-based analysis). The slow Myo2 isoform (I) is present in all muscles and represents at least ~30% of the Myo2. Fast Myo2 isoforms are available in various proportion depending on the muscle type.

Due to their central role in striated muscle contractions, sarcomeric Myo2 dysfunction has been linked to many muscle diseases. Typically, spasticity or Duchenne muscular dystrophy are due to improper contraction of the striated muscle (Mhandire *et al.* 2022; Wieters *et al.* 2021).

Furthermore, β -CardMyo2 mutations have directly been linked to **hypertrophic cardiomyopathy**. Hypertrophic cardiomyopathy is the most common genetic heart disease and results in hypertrophy and hypercontractility of the left ventricle, representing a high risk of heart failure or stroke (Geisterfer-Lowrance *et al.* 1996; Dadson, Hauck, and Billia 2017). Interestingly, β -CardMyo2 mutations result in ~40% of hypertrophic cardiomyopathy (Spudich 2015), making β -CardMyo2 a particularly interesting therapeutic target to fight hypertrophic cardiomyopathy.

Moreover, mutations in the α -CardMyo2 Lever arm seem to be involved in an autosomal dominant form of **atrial septal defect**, one of the most common forms of congenital heart malformations (Ching *et al.* 2005). Mutations in SkMyo2 SH1 can cause abnormal formation of type IIa fibers, and has thus been associated with **hereditary inclusion body myopathy** that causes proximal muscle weakness and atrophy (Martinsson *et al.* 2000). A mutation on SkMyo2 Motor domain was reported to cause **myositis** (immune-mediated muscle inflammation) in horses (Finno *et al.* 2018).

A.2. Smooth muscle Myo2

Smooth muscle Myo2 (SmMyo2) enables involuntary smooth muscle contraction without adopting a sarcomere organization as opposed to CardMyo2 and SkMyo2. It participates in the contraction of blood vessels, digestive track and lung muscles. Concerning the regulation of force production, SmMyo2 differs from sarcomeric myosin: in SmMyo2, force production is regulated by phosphorylation of the light chain (Craig, Smith, and Kendrick-Jones 1983). Mutations of SmMyo2 are involved in circulatory system diseases such as non-syndromic thoracic aortic aneurysm and dissection (TAAD) (Pomianowski and Elefteriades 2013), and urinary and intestinal diseases such as **Berdon syndrome** (Gauthier *et al.* 2015; Yetman *et al.* 2018). Additionally, smooth muscle hypercontractility has been associated with **asthma** (Dowell *et al.* 2014).

A.3. Non-muscle Myo2

Non-muscle Myo2s (NM2A encoded by MYH9, NM2B encoded by MYH10 and NM2C encoded by MYH14), as muscle Myo2, can associate in filaments to perform their functions. The force produced is used for cytokinesis, cell morphology, cell migration, cell adhesion and signaling (reviewed in Newell-Litwa, Horwitz, and Lamers 2015). Proper functioning of NM2s appears to be vital for organism development. Typically, it has been found that depletion of NM2A in mice results in embryo death within 6.5 days (Conti *et al.* 2004). Moreover, a mutation in NM2B results in hearts developing outside of the mice bodies (Ma and Adelstein 2014).

Still in mice, the L458R mutation in NM2B leads to **cyanosis and respiratory distress** due to extracellular matrix rearrangement in their lungs (Kim *et al.* 2018). Aberrant splicing of NM2C has been identified in **myotonic dystrophy type 1** (the most common form of muscular dystrophy), suggesting implication of NM2C in the disease (Rinaldi *et al.* 2012). NM2A mutations result in a **rare platelet disorder** known as MYH9 syndrome (Kelley *et al.* 2000; Heath *et al.* 2001; Kunishima *et al.* 2001; Seri *et al.* 2003) due to NM2A aggregation. Such condition can lead to hearing loss, cataracts and nephritis (Seri *et al.* 2003).

Additionally, because of its role in cytokinesis, NM2C could be required for tumor cell division (Kawamoto, and Adelstein 2006). NM2A has been associated to breast cancer invasiveness as reduced expression of NM2A results in reduced invasion of MCF-7 breast cancer cells (Derycke *et al.* 2011). In contrast, in squamous cell carcinomas (SCCs), NM2A was found to act as a tumor suppressor (Schramek *et al.* 2014), since the knock-out of NM2A accelerates tumor progression.

Moreover, genetic studies of families suffering from **hearing loss** associated eight NM2C mutations and one NM2A mutation to non-syndromic hearing loss (Donaudy *et al.* 2004; Kim *et al.*

2016; Kim *et al.* 2017; Choi *et al.* 2011; Lalwani *et al.* 2000). In mice, NM2A is located in the stereocilia of inner ear hair cells (Mhatre *et al.* 2006), and NM2C is mainly found, distinctly of NM2A, in the organ of Corti, the *stria vascularis*, and in the cells surrounding the *scala media* (Lalwani *et al.* 2000), reinforcing the role of NM2A and NM2C in hearing, although their precise functions could be different and remain unclear.

B. Targeting myosin Motors against diseases

Therefore, specific targeting of certain myosin isoforms against diseases appears of particular interest. The potential of myosins as therapeutical targets has already been addressed (Trivedi *et al.* 2020). However, due to the high similarity of their Motor domains, and to the ubiquitous expression of many myosin classes in cells, specific targeting of one myosin class or of one specific member of a myosin class is particularly challenging. Yet, it is an unavoidable challenge to be overcome for the development of efficient therapies without impairing vital functions such as respiration or heartbeat.

	Study ID	status	Phase	drug	diseases
CardMyo2	NCT02929329	completed	Phase 3	Omecamtiv Mercabil	Heart failure
	NCT03759392	completed	Phase 3		Heart Failure With Reduced Ejection Fraction
	NCT00941681	completed	Phase 2		Heart Failure
	NCT02695420	completed	Phase 2		Heart Failure With Reduced Ejection Fraction
	NCT00682565	completed	Phase 2		Heart Failure Myocardial Ischemia Angina Pectoris
	NCT01786512	completed	Phase 2		Heart failure
	NCT01300013	completed	Phase 2		Heart failure
	NCT05186818	recruiting	Phase 3		Aficamten
	NCT04848506	enrolling by invitation	Phase 2	Hypertrophic Cardiomyopathy	
	NCT05174416	recruiting	Phase 3	Mavacamten	Hypertrophic Cardiomyopathy
	NCT03470545	completed	Phase 3		Hypertrophic cardiomyopathy
	NCT05414175	recruiting	Phase 3		Hypertrophic cardiomyopathy
	NCT04766892	recruiting	Phase 2		Heart Failure With Preserved Ejection Fraction
	NCT04349072	active	Phase 3		Hypertrophic Obstructive Cardiomyopathy
	NCT03496168	active	Phase 2		Hypertrophic Cardiomyopathy
	NCT03723655	enrolling by invitation	Phase 2/3		Hypertrophic Cardiomyopathy
NCT04572893	recruiting	Phase 2	Danicamtiv		Cardiomyopathy
SkMyo2	NCT05291091	recruiting	Phase 2	EDG-5506	Becker Muscular Dystrophy

Table 14: clinical trials studies on myosin modulators (www.clinicaltrials.gov)

Clinical trials references on (www.clinicaltrials.gov) and concerning a myosin modulator. Most of them concern CardMyo2 and show the potential of myosin modulator to cure diseases

To date, several myosin inhibitors and activators exhibiting various specificities have been reported (see section B.2.). The majority are directed toward the Myo2s. In particular, several of them, targeting CardMyo2, are now in clinical trials. The β -CardMyo2 inhibitor Mavacamten has been approved by the FDA in April, 2022, highlighting the potential of myosins as druggable targets (Table 14).

B.1. Five allosteric pockets found in myosin Motor domain

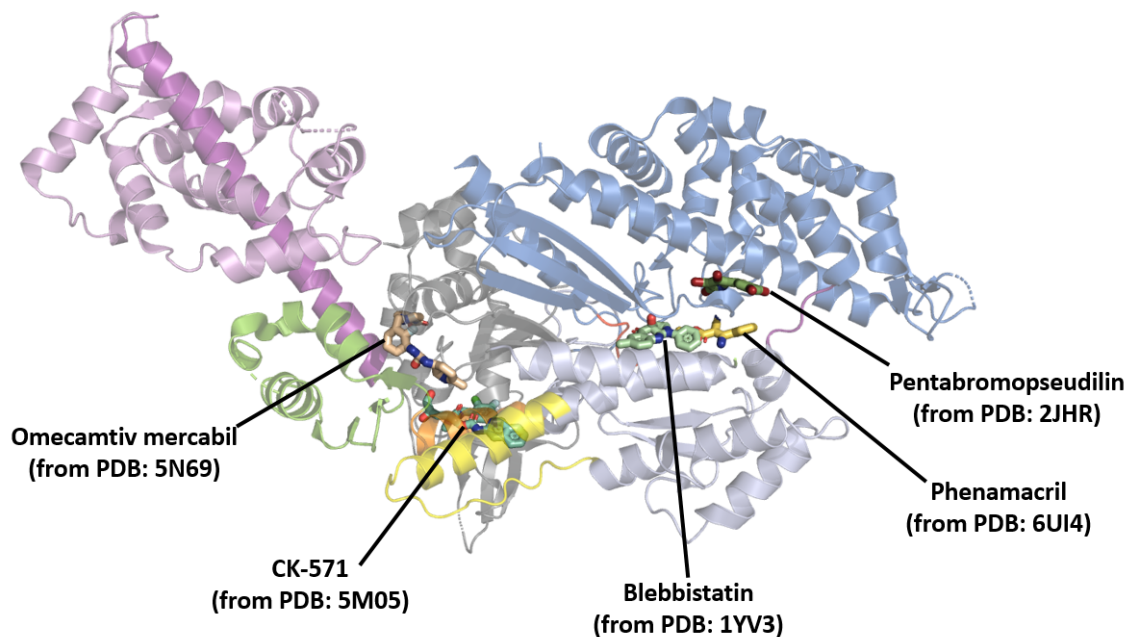


Figure 71: Allosteric binding pockets within the myosin Motor

β -CardMyo2 Motor domain plus essential light chain (MDE) from structure PDB: 5N69 (Planelles-Herrero et al. 2017) is displayed with its Lever arm in purple, its converter in green, its SH1 in orange, its relay in yellow, its upper-50 in blue and its lower-50 in light blue. Omecamtiv mercabil (PDB: 5N69; Planelles-Herrero et al. 2017), CK-571 (PDB: 5M05; Sirigu et al. 2016), Blebbistatin (PDB: 1YV3; Allingham et al. 2005), Pentabromopseudilin (PDB: 2JHR; Fedorov et al. 2009) and phenamacril (PDB: 6UI4; Zhou et al. 2020) are represented in sticks in their allosteric binding pocket.

Thanks to the structures obtained from myosin-drug co-crystals (Planelles-Herrero et al. 2017; Sirigu et al. 2016; Allingham, Smith, and Rayment 2005; Fedorov et al. 2009; Zhou et al. 2020), five different allosteric pockets in the myosin Motor domain have been described. Drug interactions are mainly hydrophobic and most likely to happen during the pre-powerstroke state (see General introduction; section D: the pre-powerstroke happens at the end of the recovery stroke). The CK-571 binding pocket is an exception as it exists in an intermediate state along the recovery stroke. In the pre-powerstroke state, myosin has low affinity for actin and does not generate force, thus blocking

myosin Motors in this state would inhibit force production. Importantly, compounds that facilitate the transition between pre-powerstroke and Pi release states can allow more heads to participate in powerstroke initiation, and they can function as muscle activators, as described for Omecamtiv mercabil (Planelles-Herrero *et al.* 2017) (see section B.2.a.).

B.2. Myosin modulators overview

Over the past decades, several myosin modulators have emerged and were recently reviewed (Manstein and Preller 2020).

B.2.a. myosin activators

Few myosin activators have been described: **Omecamtiv mercabil** (OM) is a specific activator of CardMyo2 (Malik *et al.* 2011) that stabilizes the pre-powerstroke state of the motor cycle, as suggested by kinetics studies and that binds in between the converter and the N-terminus subdomain as shown with a crystal structure (Malik *et al.* 2011; Y. Liu *et al.* 2015; Swenson *et al.* 2017; Planelles-Herrero *et al.* 2017). It was thus proposed to facilitate CardMyo2 binding to actin and the initiation of the powerstroke (Planelles-Herrero *et al.* 2017). Additionally, **EMD 57033** (Radke *et al.* 2014) and **Danicamtiv** (Voors *et al.* 2020) were described as CardMyo2 activators although their binding site(s) and deTailed mechanism(s) of action remains unknown. **EMD 57033** (Radke *et al.*, 2014) has been proposed through docking to bind near the Lever arm similarly to what was found for OM.

B.2.b. myosin inhibitors

2,3-butanedione monoxime (BDM) was the first myosin inhibitor described against myosins (Higuchi and Takemori 1989). It was proposed to act as a SkMyo2 inhibitor with a K_i in the millimolar range. Yet more recent studies suggest numerous off-target interactions of BDM in cells (reviewed in Manstein and Preller 2020). Several small molecules have been described since then as Myo2 inhibitors, including **N-benzyl-p-toluene sulfonamide** (BTS), a SkMyo2 inhibitor exhibiting ~5 μ M of half maximal inhibitory concentration (IC_{50}) (Cheung *et al.* 2002); the fluorescent dye **3-[4-(3-phenyl-2-pyrazolin-1-yl) benzene-1- sulfonylamido]-phenylboronic acid** (PPBA) (Hiratsuka 1994; 2006); the antipsychotic drug **trifluoperazine** (TFP) (Sellers, Wang, and Chantler 2003); and (3-(N-butylethanimidoyl) ethyl)-4-hydroxy-2 H-chromen-2-one, **BHC** (Brawley *et al.* 2020). Additionally, **Mavacamten** and **Aficamten** were identified recently as specific CardMyo2 inhibitors (Green *et al.* 2016; Kawas *et al.* 2017; Chuang *et al.* 2021) and both drugs are currently in phase 3 of clinical trials, although their binding site(s) and the basis of their specificity remain to be further characterized.

CK-571 was described as a specific inhibitor of SmMyo2 exhibiting a particularly high affinity ($IC_{50} \sim 9$ nM). The crystal structure reveals that CK-571 binding near the SH1 traps the Motor in an intermediate state of the recovery stroke, thus prevents actin binding and force production (Sirigu *et al.* 2016). Intriguingly, even if all the residues involved in CK-571 binding are conserved in Myo2, only SmMyo2 is inhibited, emphasizing that subtle changes among these allosteric machines can be sufficient for gaining selectivity. This supports the potential of selective myosin Motor inhibition for the development of various treatments.

Few inhibitors were also found against unconventional myosins: **2,4,6-triiodophenol** (TIP) was proposed as a low affinity inhibitor of unconventional Myo6 (Heissler *et al.* 2012) and **Myo-Vin1** (Islam *et al.* 2010) as a ~ 6 μ M inhibitor of unconventional Myo5. Perhaps the best characterized unconventional myosin inhibitor is **Phenamacril**. Phenamacril, a fungicide, has been identified as a specific submicromolar inhibitor of unconventional Myo1. Even among Myo1, phenamacril exhibits a certain specificity: Myo1s from plant pathogen *Fusarium* are efficiently inhibited by phenamacril while human Myo1c isn't (Wollenberg *et al.* 2019). The crystal structure of *F. graminearum* Myo1 in complex with Phenamacril was recently solved at 2.65 Å (PDB: 6UI4; Zhou *et al.* 2020) revealing that the compound binds to the 50 kDa cleft. The authors identified Met375 as a key residue for phenamacril inhibition and selectivity among Myo1s, as the introduction of the methionine in position 375 in Myo1 isoforms that are not usually inhibited by phenamacril renders them inhibited.

The **Halogenated pseudilins** were uniquely described as inhibitors of both unconventional and conventional myosins. Halogenated pseudilins were first described in 2009 as myosin inhibitors (Fedorov *et al.* 2009) able to inhibit myosins of class I, II and V in the micromolar range, but not able to inhibit myosins of class VI and class VII (Preller *et al.* 2011; Chinthalapudi *et al.* 2011; Fedorov *et al.* 2009). Crystal structures allow deTailed description of the binding site of halogenated pseudilins near the actin loops (PDB: 2XO8, 2XEL, 2JHR). Although halogenated pseudilins are not specific for one myosin isoform, chlorinated and brominated pseudilins were shown to exhibit preference either for Myo1 or Myo5, respectively (Preller *et al.* 2011). These findings assess the potential of halogenated pseudilin derivatives for selective inhibition of myosins in the future, especially considering the fact that actin loops exhibit variability among classes (Robert-Paganin *et al.* 2020), and this could be exploited for the development of specific inhibitors. The risk of off-target binding should be carefully considered, however, as several non-myosin molecules were reported to be inhibited by pseudilin (Kunfermann *et al.* 2014; Zhang *et al.* 2011).

The most well characterized inhibitor is **blebbistatin** (Straight *et al.* 2003) (see section C.); a Myo2 specific inhibitor whose potential for development of therapy has already been addressed (Rauscher *et al.* 2018; Roman, Guedes, *et al.* 2018).

C. Blebbistatin

Blebbistatin (Figure 72) was first discovered as an inhibitor of furrow ingression through cell division (Straight *et al.* 2003) and named according to its ability to block cell blebbing (Straight *et al.* 2003). Blebbistatin has the ability to inhibit Myo2 in a submicromolar/micromolar range (Straight *et al.* 2003) without blocking RLC phosphorylation by MLCK (myosin light chain kinase) (Straight *et al.* 2003; Zhang *et al.* 2017; Wang *et al.* 2008). Steady-state ATPase assays show that blebbistatin is able to efficiently inhibit SkMyo2 S1 activity both in basal and actin-activated assays (Kovács *et al.* 2004). It can even inhibit Myo2 coming from the invertebrate organisms *Dictyostelium discoideum* (DictyMyo2), *Argopecten irradians* (ScallopMyo2) (Limouze *et al.* 2004) and *Tarantula* (Zhao, Padrón, and Craig 2008).

Blebbistatin contains one asymmetric carbon whose geometry appears to be particularly important for Myo2 inhibition: only the (-)-blebbistatin enantiomer have been reported to inhibit Myo2s: (+)-blebbistatin does not inhibit SmMyo2 activity, while the racemic mix does (Wang *et al.* 2008) and (-)-blebbistatin inhibits specifically skMyo2 over (+)-blebbistatin in steady-state ATPase assays (Verhasselt, Roman, De Wever, *et al.* 2017).

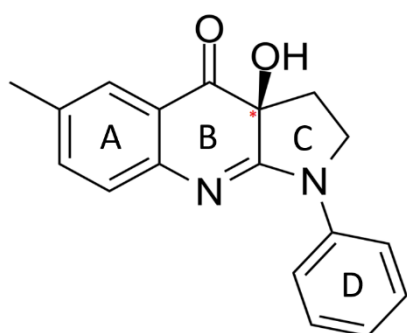


Figure 72: (-)-Blebbistatin scaffold
Red star marks the asymmetric carbon

C.1. Specificity

A closer look at blebbistatin's ability to inhibit Myo2 ATPase activity confirms selectivity for myosins of class II over myosins of class I, V, X and XV (Straight *et al.* 2003; Limouze *et al.* 2004; Zhang *et al.* 2017), but also shows specificity within the Myo2 class: IC₅₀ can vary from submicromolar for SkMyo2, to 4-80 μM for SmMyo2 (Limouze *et al.* 2004; Wang *et al.* 2008; Zhang *et al.* 2017; Eddinger *et al.* 2007). Such a poor inhibition of SmMyo2 is surprising, considering that its sequence is highly similar to the well inhibited NM2A and NM2B (Figure 73).

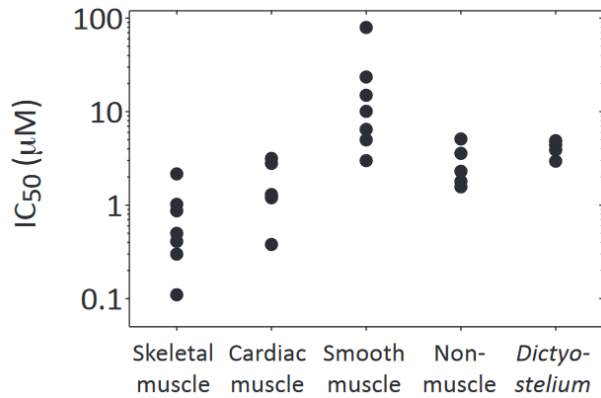


Figure 73: Blebbistatin IC₅₀ for various Myo2 isoforms (Rauscher *et al.* 2018)

Summary of IC₅₀ measured for Myo2 different isoform in various publications (Képiró *et al.* 2014; Várkuti *et al.* 2016; Verhasselt, Roman, De Wever, *et al.* 2017; Verhasselt, Stevens, *et al.* 2017; Limouze *et al.* 2004; Zhang *et al.* 2017; Dou, Arlock, and Arner 2007; Farman *et al.* 2008; Wang *et al.* 2008; Eddinger *et al.* 2007)

Specificity has also been investigated in cells using a crosslinkable version of blebbistatin: azidoblebbistatin. Azidoblebbistatin exhibits the same inhibitory and solubility properties as blebbistatin, but, under illumination at 310 nm, azidoblebbistatin forms a covalent bond with its binding pocket. Proteins interacting with azidoblebbistatin in Dd cells treated with 5 µM of drug were identified by cell extract fluorescence and mass spectroscopy analysis after cell illumination at 310 nm. Myo2 was found to be the main partner of azidoblebbistatin. Additionally, few other, non-myosin proteins were able to interact with azidoblebbistatin, but with much lower affinity (>50 µM vs. 6 µM) (Képiró *et al.* 2014).

C.2. Solubility and permeability

Blebbistatin is able to cross cell membranes and to inhibit contraction of the muscle tissue within minutes after administration, with an IC₅₀ that is similar to the one found on isolated Myo2 Motors, showing the good capacity of blebbistatin to cross the plasma membrane and to diffuse in biological tissue (Dou, Arlock, and Arner 2007).

However, blebbistatin suffers from poor solubility: blebbistatin starts to precipitate over 10 µM in water (Kolega 2004; Sakamoto *et al.* 2005; Képiró *et al.* 2014). In the presence of DMSO, the limiting concentrations are ~7.5 µM at 0.1 % DMSO and ~80 µM at 10 % DMSO (Képiró *et al.* 2014). Solubility is thus in the range of the IC₅₀, which can be problematic in cells when precipitation can damage the model under study (Swift *et al.* 2012). This issue has been overcome by the development of the highly soluble blebbistatin derivative 3'-hydroxyblebbistatin (Verhasselt, Roman, De Wever, *et al.* 2017) and also aminoblebbistatin (Várkuti *et al.* 2016).

C.3. Fluorescence

Blebbistatin is fluorescent (emission peak at 410 nm), which can be an advantage for monitoring the drug, but can also be damaging, notably for cell imaging at this wavelength. Yet, the very bright fluorescence found in cell imaging mostly comes from blebbistatin precipitate rather than the soluble part, thus fluorescence will not be an issue as far as the solubility of the blebbistatin derivative is high enough to avoid precipitation. This is supported by the fact that 3'-hydroxyblebbistatin does not cause undesired fluorescence signal in cell imaging ([Verhasselt, Roman, De Wever, et al. 2017](#)).

C.4. Blebbistatin stability and toxicity

C.4.a. Blebbistatin is cytotoxic under blue light and UV

When bovine aortic endothelial cells (BAECs) are supplemented with blebbistatin and illuminated at **450-490 nm or 365 nm**, cell death overcomes within hours, and proportionally to the blebbistatin concentration (0-20 μM), even after very short illumination time (1 s). Similarly, 10 - 200 μM blebbistatin was found to be phototoxic following illumination with blue light (**390 – 470 nm**) to various cancer cell lines: FEMX-1, LNCaP, Du145, U87 and F11-hTERT ([Mikulich, Kavaliauskiene, and Juzenas 2012](#)). In contrast, illumination of BAECs supplemented with blebbistatin had no toxic effect at **510 – 560 nm** or **590 – 650 nm**: cells continue to migrate and remain alive with a correct shape, even after 12h. These data suggest that if 20 μM blebbistatin is not toxic on its own, it becomes toxic after illumination at 450 – 490 nm or 365 nm ([Kolega 2004](#)).

Yet, it should also be noted that even without blue or UV illumination, blebbistatin can result in cell death if it is used at high concentrations and/or for long times: over 50 μM blebbistatin, significant toxicity can be seen after 24 h in F11-hTERT, FEMX-I, Du145 and LNCaP ([Mikulich, Kavaliauskiene, and Juzenas 2012](#)). Moreover, 4 different pancreatic adenocarcinoma cell lines ([Duxbury, Ashley, and Whang 2004](#)) remain viable up to 200 μM blebbistatin, but 50% cell death is reached using 400 μM .

C.4.b. Blebbistatin is inactivated by blue light and UV

Interestingly, once illuminated by UV, blebbistatin is no longer able to inhibit NM2A/B ATPase activity, or to disrupt actin filament sliding and actin network organisation in cells, suggesting that photodegradation induces loss of blebbistatin pharmaceutical activity ([Kolega 2004](#); [Sakamoto et al.](#)

2005; Ramamurthy *et al.* 2004). Actually, illumination of blebbistatin in blue light (425 nm) even results in an increase of NM2B ATPase activity from ~ 0.17 to $\sim 0.36 \text{ s}^{-1}$ (Ramamurthy *et al.* 2004).

C.4.c. Blebbistatin requires careful use

These findings make blebbistatin use and blebbistatin mechanism study particularly challenging. Each illumination wavelength used for experiments need a careful check to avoid inactivation or toxicity. In particular, ATP binding to myosin upon blebbistatin addition cannot be studied by tryptophan fluorescence quenching, as such an experiment requires fluorescence measurement at 295 nm, which will result in blebbistatin degradation within 1 s, compromising the subsequent observations (Ramamurthy *et al.* 2004). It should be noted that illumination at 310 nm has no impact on blebbistatin stability, thus crosslink experiments using azidoblebbistatin at 310 nm still look trustworthy (Képiró *et al.* 2014).

Despite all its flaws, with careful choice of illumination wavelength and use of « moderate » concentrations, blebbistatin is not too harmful for cell viability and has already allowed great findings concerning Myo2 functions and related diseases. Myo2 inhibition by blebbistatin was found to be beneficial for various medical indications reviewed in Rauscher *et al.* 2018 : notably, NM2 inhibition can reduce infiltration of leukemia cells in the central nervous system, methamphetamine seeking and lung carcinoma migration. SmMyo2 inhibition can reduce thrombus formation and blood pressure. CardMyo2 inhibition can reduce cardiac hypercontractility, and SkMyo2 inhibition can reduce spasticity. It was also suggested that blebbistatin's sensitivity to blue light could make it a photodynamic agent against cancer (Mikulich, Kavaliauskiene, and Juzenas 2012).

C.5. Blebbistatin degradation mechanism

C.5.a. UV-blue light illumination modifies the spectral properties of blebbistatin

In order to identify the reaction product resulting from UV-blue light illumination, evolution of blebbistatin spectral properties was analyzed. The absorption spectra of blebbistatin shows a peak at 430 nm that decreases after illumination in either blue (450 - 490 nm) or UV (365nm) for 1 h (Figure 74). Surprisingly, the profiles differ depending on the wavelength used. If blue light has been used, a double peak appears; if UV light was used, absorbance slightly increases between 300 and 380 nm. In contrast, illumination at 510 – 560 or 590 – 650 nm results in no modification within the absorbance spectrum consistent with the absence of change in toxicity (Kolega 2004).

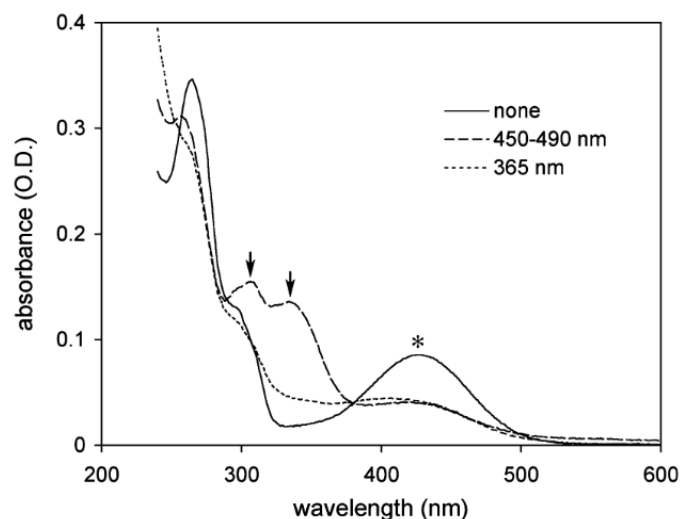


Figure 74: Blebbistatin photodegradation (Kolega 2004)

*Blebbistatin absorption spectra after 1 h illumination at 365 nm, 450 nm, or not illuminated. Arrows mark absorbance peaks that appear within the spectra after illumination at 450-490 nm and * marks an absorbance peak that decreases following 450-490 or 365 nm illumination. Overall, these data show that light exposure alters the structural integrity of Blebbistatin resulting in a modification of its spectral properties.*

C.5.b. The photoinactivation product is not responsible for toxicity

Interestingly, addition of photodegraded blebbistatin to BAECs does not result in cell death, not even 50 μM for 18 h. Hence, Blebbistatin phototoxicity after illumination may come from a short life intermediate product, such as radicals that might be the same for UV and blue light illumination (Kolega 2004). Indeed, ROS liberation was detected after blebbistatin and blue light illumination using dihydrorhodamine 123 (ROS sensor). It should be noted that, in contrast, the Singlet Oxygen Sensor Green was not oxidized, which gives us insights on the degradation mechanism of blebbistatin (Mikulich, Kavaliauskiene, and Juzenas 2012).

Also of interest, the kinetics of degradation of blebbistatin do not depend only on light exposure, but also on buffer conditions: no degradation was seen on PBS or 100% DMSO after 30-minute exposure to 480 nm light, but degradation occurs in water (Verhasselt, Roman, Bracke, et al. 2017). Verhasselt, Roman, Bracke, et al. (2017) proposed that degradation may be promoted by hydroxyl or peroxy radicals in water that will ultimately result in oxidative degradation of blebbistatin.

C.5.c. Development of photostable derivatives

Finally, detailed analysis of blebbistatin reaction with blue light using femtosecond transient absorption spectroscopy and chemoselective ROS fluorescent probes results in the proposition of a reactional mechanism (Li *et al.* 2018) for degradation mediated by blue light (Figure 75).

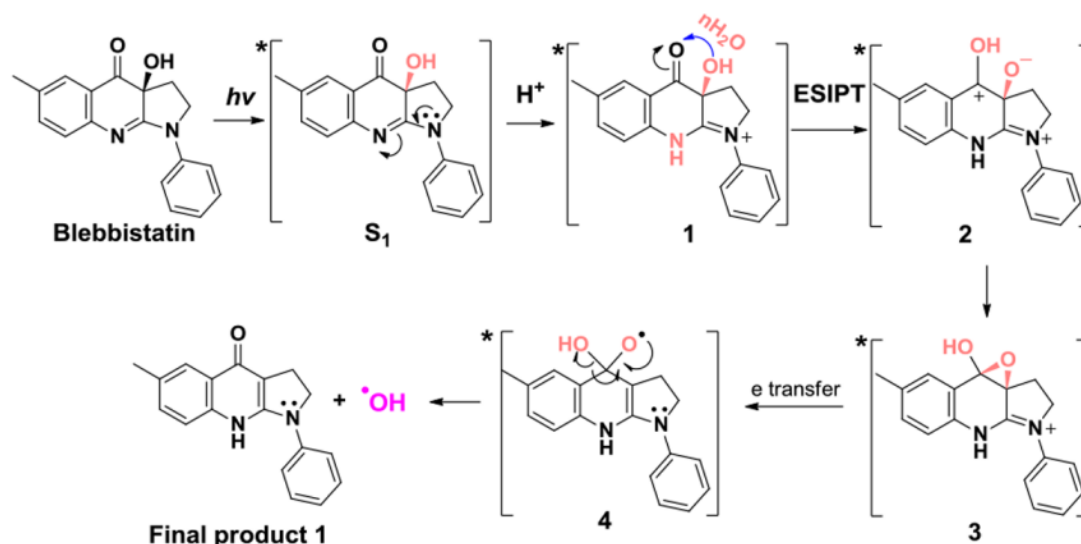


Figure 75: Putative photochemical mechanism for blebbistatin photo-inactivation upon 416 nm illumination (Li *et al.* 2018)

Water-dependent mechanism consisting in a water-dependent protonation followed by an excited state intramolecular proton transfer (ESIPT). Finally, electron transfer results in liberation of the toxic $\cdot OH$ radical.

Liberation of the hydroxyl radical during the photo-inactivation of blebbistatin had been previously proposed (Verhasselt, Roman, Bracke, *et al.* 2017).

In this context an electron withdrawing group could prevent or minimize blebbistatin oxidative degradation. Indeed, *para* substitution of the blebbistatin D-cycle by an electron-withdrawing group: azido, nitro, chloro or amino, abolishes blebbistatin's sensitivity to blue light (no change in absorbance spectra after 15 minutes of illumination at 480 nm). After HeLa cells are treated with *para*-Nitroblebbistatin or *para*-Aminoblebbistatin and illuminated at 480nm, cell mortality was similar to the non-treated control, while treatments with blebbistatin and *para*-Chloroblebbistatin result in stronger mortality, characteristic of blue light phototoxicity (Várkuti *et al.* 2016; Képiró *et al.* 2014).

Addition of these electron-withdrawing groups also results in loss of fluorescence at 410 nm, which is much more convenient for fluorescence experiments to avoid interferences (Várkuti *et al.* 2016; Képiró *et al.* 2014). *Para*-Nitroblebbistatin and *para*-Aminoblebbistatin also keep good pharmaceutical activity: they can efficiently inhibit SkMyo2 and Dicty Myo2 in steady-state ATPase assays, even if *para*-Aminoblebbistatin exhibits a higher IC_{50} against SkMyo2 ($0.47 \pm 0.06 \mu M$)

compared to blebbistatin and *para*-Nitroblebbistatin ($0.11 \pm 0.009 \mu\text{M}$ and $0.1 \pm 0.004 \mu\text{M}$, respectively) (Várkuti *et al.* 2016; Képiró *et al.* 2014).

para-Aminoblebbistatin is 40-fold more soluble than blebbistatin making the former particularly well suited for use in cells despite its higher IC_{50} (Várkuti *et al.* 2016). In contrast, the blebbistatin-like solubility of *para*-Nitroblebbistatin limits its use in cells.

C.6. Blebbistatin inhibition mechanism

To understand how blebbistatin inhibits Myo2 ATPase activity, detailed studies of its impact on various steps of the Myo2 kinetic cycle have been pursued by several groups.

C.6.a. Blebbistatin does not disturb ATP binding and hydrolysis

The fluorescence of the ATP analog MantATP increases when it binds to Myosin. Experiments with MantATP have consistently shown that Blebbistatin does not compete against the nucleotide, as an increase in fluorescence can be seen both with and without excess of blebbistatin using NM2A (Limouze *et al.* 2004), NM2B (Ramamurthy *et al.* 2004) and SkMyo2 (Kovács *et al.* 2004). Moreover, blebbistatin doesn't seem to impact basal $[\gamma\text{-}^{32}\text{P}]\text{ATP}$ hydrolysis of NM2B either (Ramamurthy *et al.* 2004).

C.6.b. Blebbistatin reduces P_i release

Ramamurthy *et al.* (2004) employed a fluorescent phosphate binding protein in a stopped flow apparatus to measure P_i release rates after incubation of NM2B, actin and ATP. They noticed that Blebbistatin could only block P_i release for 1 s. Past that time, normal P_i release rate was recovered, which is explained by the 425 nm wavelength used as excitation for the phosphate binding protein in their experiments. Illumination at that wavelength results in blebbistatin inactivation within 1 s as described in sections C.4. and C.5. Overall, blebbistatin seems to impact the Myo2 P_i burst without interfering with binding of the nucleotide.

C.6.c. Blebbistatin reduces actin binding

Addition of Blebbistatin to cosedimentation experiments using Myo2 S1 and actin during steady state ATP hydrolysis results in blebbistatin mainly present in the supernatant and a slightly smaller fraction of S1 bound to actin (Kovács *et al.* 2004). This was further confirmed using pyrene-

actin fluorescence quenching, in which a large excess of blebbistatin prevented NM2B to rebind to actin after ATP-induced dissociation (Ramamurthy *et al.* 2004).

Thin filaments (actin, tropomyosin and troponin filaments) have the ability to bind to myosin thick filaments in the presence of calcium. Addition of calcium to mixes containing thin and thick filaments results in formation of granulates and lots of thin and thick filaments interacting in negative staining. When a homogenate of *Tarantula* muscles containing both thin and thick filaments was incubated with 100 μM blebbistatin prior to addition of calcium, neither macroscopic granulates or thin-thick filaments bound to each other were seen on negative staining, as opposed to the controls, suggesting that blebbistatin prevents actin-myosin interaction (Zhao, Padrón, and Craig 2008).

These findings are in line with blebbistatin stabilizing the pre-powerstroke (MgADP.Pi) state, a state characterized by low affinity for actin (Ramamurthy *et al.* 2004).

C.6.d. Blebbistatin might slightly reduce ADP release

Recently, a crystal structure of DictyMyo2 bound to blebbistatin and ADP has been proposed to correspond to the Myo2 ADP release state (Ewert *et al.* 2020), proposing an impact of blebbistatin on ADP release. However, in kinetic studies, the impact of blebbistatin on ADP release seems rather limited compared to its impact on P_i release and actin binding:

Impact of blebbistatin on ADP dissociation from acto-NM2B can be monitored using mant-ADP fluorescence. Addition of blebbistatin excess results in lower ADP dissociation rate ($\sim 1.3 \text{ s}^{-1}$ instead of 1.8 s^{-1}). But DMSO was found to reduce ADP dissociation rate to $\sim 1.4 \text{ s}^{-1}$ on its own. It is thus unclear if blebbistatin effect on ADP release is significant or not (Ramamurthy *et al.* 2004). Overall, the impact of blebbistatin on ADP release, if significant, remains much subtler than its effect on P_i release and actin binding. This is further supported by the fact that in actin cosedimentation, a large majority of blebbistatin is found in the supernatant (i.e., bound to low actin affinity states of the Myo2 motor) (see section C.6.c.).

C.6.e. Blebbistatin does not promote motor dissociation from actin

No significant effect on Myo2 S1 binding rate and affinity to actin was reported upon addition of blebbistatin in excess for the Myo2 high affinity states: rigor (NF) (Kovács *et al.* 2004 on SkMyo2 and Ramamurthy *et al.* 2004 on NM2B) or ADP (Ramamurthy *et al.* 2004 on NM2B) using transient pyrene fluorescence assay. Lack of impact of blebbistatin on S1 actin dissociation thus suggests no effect of the blebbistatin on the actin bound motor.

C.6.f. Blebbistatin must stabilize the pre-powerstroke state

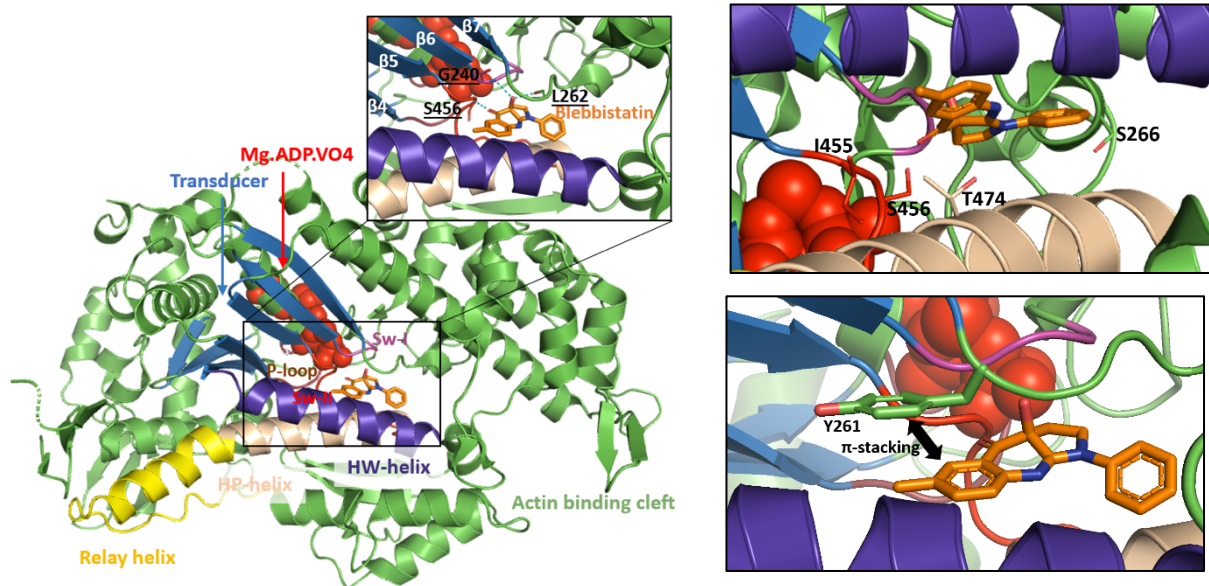
From these studies, it thus appears that blebbistatin must stabilize the pre-powerstroke of the Motor in which P_i is not yet released from the Motor and the actin affinity is low to inhibit Myo2 activity.

Stabilization of the pre-powerstroke state by blebbistatin was supported by a study in the context of Myo2 thick filaments. The structure of the thick filament depends on the nucleotide state of myosin: MgADP. P_i results in helical order while NF or ADP Motors leads to disordered filaments: this can be clearly identified by electron microscopy and Fourier transform. Treatment with 100 μ M blebbistatin for 2h slows down filament loss of order upon nucleotide loss through apyrase addition consistent with the stabilization of the MgADP. P_i state stabilization by blebbistatin. This treatment is also able to reorder a disordered MgADP filament into a helical order filament consistent with the fact that blebbistatin has the ability to promote a pre-powerstroke like state even without P_i addition. It should be noted that blebbistatin addition is not able to reorganize a disordered NF filament onto a helical order one (Zhao, Padrón, and Craig 2008).

C.7. Blebbistatin site

The first structure of Myo2 bound to blebbistatin was solved at 2 Å resolution using X-ray crystallography (Allingham, Smith, and Rayment 2005). The Dictyostelium myosin Motor in the pre-powerstroke state using MgADP. VO4 (MgADP. P_i analog) allowed direct comparison of the structure in the apo and bound state and showed that blebbistatin does not induce any major conformational change within the pre-powerstroke structure (r.m.s.d = 0.407 Å). Blebbistatin lies in the 50 kDa cleft in between the upper-50 and the lower-50, close to the P_i pocket, switch I, switch II and P-loop. It interacts with the Φ LL motif, HP and HW helix of the lower-50 mainly through apolar contacts: benzyl ring (D-ring) is enclosed by Dicty residues Leu262, Phe466, Glu467 and Val630. Tetrahydropyrrolo ring (C-ring) with Ser456 and Ile471 and methylquinolinone (A and B-rings) with Tyr261, Thr474, Tyr634, Gln637 and Leu641 (Allingham, Smith, and Rayment 2005). Movement of Leu262 and Tyr634 side chains are required to allow blebbistatin binding in its tight pocket (Allingham, Smith, and Rayment 2005). The specificity for the (-)-blebbistatin can be easily understood on the basis of the structure as the chiral alcohol group is able to form a hydrogen bond with the Leu262 carbonyl and Gly240 amine. An additional hydrogen bond can be found between the Ser456 amine and the blebbistatin carbonyl (Figure 76). It should be noted that this allosteric pocket might be occupied by many other myosin inhibitors. Indeed, BHC (Brawley *et al.* 2020), aficamten (Chuang *et al.* 2021), TIP (Heissler *et al.* 2012)

and PPBA (Hiratsuka *et al.* 2006) were all proposed to occupy the same binding site, although this needs confirmation with high resolution crystal structures.



Dicty nb	U50		Sw-II	HP			HW			
	238-240	261-263	455-456	466-467	470-471	474	630	634	637	641
Dicty	RFG	YLL	<u>I</u> S	FE	CI	T	V	Y	Q	L
NM2A	RFG	YLL	IA	FE	CI	T	V	Y	Q	L
NM2B	RFG	YLL	IA	FE	CI	T	V	Y	<u>S</u>	L
NM2C	RFG	YLL	IA	FE	CI	T	V	Y	<u>S</u>	L
Cardiac	RFG	YLL	IA	FE	CI	T	V	<u>H</u>	<u>N</u>	L
Smooth	RFG	YLL	IA	FE	CI	T	V	Y	Q	L
Skeletal	RFG	YLL	IA	<u>L</u> E	CI	T	V	<u>F</u>	<u>N</u>	L
Myo1	RFG	YLL	<u>I</u> Y	FE	CI/II	<u>C</u>	V/A	<u>F</u>	<u>S</u>	L
Myo5	RFG	YLL	<u>I</u> Y	FE	CI	<u>A</u>	V	<u>F</u>	<u>S</u>	<u>I</u>
Myo10	RFG	YLL	<u>I</u> F	FE	<u>N</u> I	<u>A</u>	V	<u>F</u>	<u>S</u>	L
Myo15	RFG	YLL	<u>I</u> Y	FE	CI	<u>A</u>	V	<u>F</u>	<u>S</u>	L

Figure 76: Blebbistatin binding site

(Top) Blebbistatin in its allosteric pocket in the DictyMyo2 Motor domain, zoom pictures key residues surrounding blebbistatin (PDB:1YV3, Allingham, Smith, and Rayment 2005). Blue dotted lines represent hydrogen bonds.

(Bottom) The table highlights the conservation of the myosin residues within the blebbistatin allosteric pocket. In particular, one residue is poorly conserved in switch-2 (sw-II, red) resulting in the loss of the blebbistatin inhibition for unconventional Myo1, Myo5 and Myo10.

Key residues for blebbistatin binding are not conserved in several unconventional myosins which leads to the specificity of blebbistatin for Myo2s: in particular, Ser456 is replaced by aromatics residues in myosin I, V, X (Allingham, Smith, and Rayment 2005). In fact, mutation of this residue in SmMyo2 or NM2 into Phe results in severe loss of blebbistatin inhibition (although it alters the normal ATPase activity of NM2B (which increases) and NM2C (which decreases)) (Zhang *et al.* 2017).

Mutations Ala454Tyr, Trp, Arg, Glu in NM2A-HMM results as well in loss of blebbistatin inhibition in ATPase assays. Other mutations such as Smooth Ser266Leu (highly conserved in Myo2 and Myo1) and Thr474Ala (highly conserved in Myo2, Cys in Myo1 or Ala in Myo5) did not impair blebbistatin ability to inhibit smooth (Zhang *et al.* 2017). Blebbistatin has no effect on *Drosophila melanogaster* cells (Straight *et al.* 2003) due to Met466 in *Drosophila* Myo2 instead of Ile455 in DictyMyo2 (Heissler, Chinthalapudi, and Sellers 2015). Similarly, the Ile455Met mutant in NM2A-HMM results in a reduction of the inhibition (although it is less severe than for Ala454Phe) (Zhang *et al.* 2017).

However, these studies are not sufficient to explore the rules of specificity in this site as blebbistatin (and derivatives) exhibit various inhibition among Myo2 (Allingham, Smith, and Rayment 2005). Thus, to understand the specificity, small changes within the pocket and in its close proximity should be further investigated. Especially considering how tight the pocket is, indeed the blebbistatin pocket is only 417.77 \AA^3 (Roman, Guedes, *et al.* 2018).

Moreover, the blebbistatin pocket is rather buried inside the Myo2 Motor. The structure of blebbistatin in complex with the Myo2 Motor cannot reveal how blebbistatin reaches its binding site and detach from it. As blebbistatin inhibition is reversible upon blebbistatin wash out, blebbistatin must find its way out of the pocket. Roman *et al.* (2018) proposed a potential tunnel that may enable blebbistatin access to its binding site. Identification of the blebbistatin tunnel using CAVER results in the identification of a tight access tunnel making drug access and dissociation within the pre-powerstroke very constrained by the tunnel residues (Roman *et al.* 2018) (Figure 77). How blebbistatin enters and dissociates from the Motor thus remains an open question.

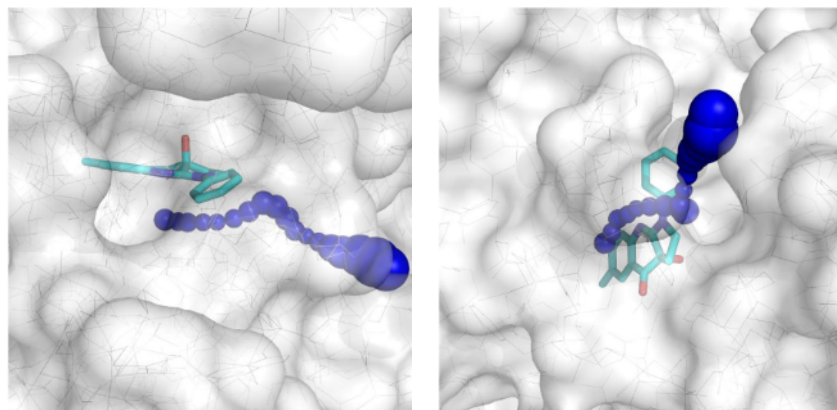


Figure 77: Blebbistatin tunnel within the DictyMyo2 pre-powerstroke Motor (Roman *et al.* 2018)

Blue spheres correspond to the blebbistatin tunnel detected by CAVER in top and side views. The protein surface is pictured in white and blebbistatin is pictured in cyan. The tunnel presented is very tight which emphasizes the difficulty for Blebbistatin to access its binding pocket in a pre-powerstroke state.

C.8. Developing efficient blebbistatin inhibitors

In order to improve blebbistatin potency and selectivity several groups work on development of blebbistatin derivatives focusing on specific features of the molecule. Indeed, if the B-ring appears as a highly critical part of the molecule since it carries the carbonyl and hydroxyl groups that mediate the three polar contacts, A-ring, C-ring and D-ring seem to let more room for optimization, their potential has thus been explored.

C.8.a. A-cycle modification

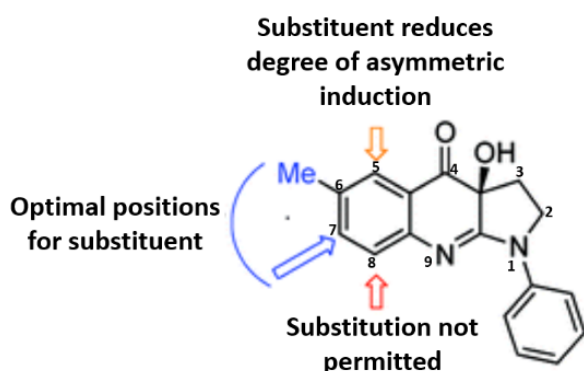


Figure 78: Identification of most promising positions for A-ring substitution (Lucas-Lopez *et al.* 2008)

Blebbistatin A-ring binds in the deepest part of the actin binding cleft. By synthesizing A-ring derivatives and cocrystallizing them with DictyMyo2 at 2-2.2 Å, Lucas-Lopez *et al.* (2008) shows that removing or changing the position of the methyl substituent on the A-ring from C6 to C5 results in a lower inhibition perhaps due to a shift of the overall molecule by ~ 1 Å driven by the A-ring structure which notably results in weaker H-bond formation between the blebbistatin carbonyl and the myosin backbone (from 3.1 to 3.4 Å). Moving the methyl group to C7 also slightly decreases the inhibition efficiency but does not result in blebbistatin corpse shift in the crystal structure. Moving the hydroxyl to C8 disrupts the ability of blebbistatin to inhibit skMyo2. Lucas-Lopez *et al.* (2008) proposed thus that cycle A optimization should be done though C6 and C7 modification without touching C5 and C8. Based on interactive modelling, the authors proposed that enhancing π -stacking between A-ring and Tyr261 through branching of an aromatic cycle on C6 and C7 would be a promising way to improve blebbistatin potency (Figure 78). To assess this hypothesis, (Verhasselt, Stevens, *et al.* 2017) thus synthesized new derivatives with bigger A-ring. However, none of them resulted in gain in inhibition potency and they exhibited worse solubility than blebbistatin.

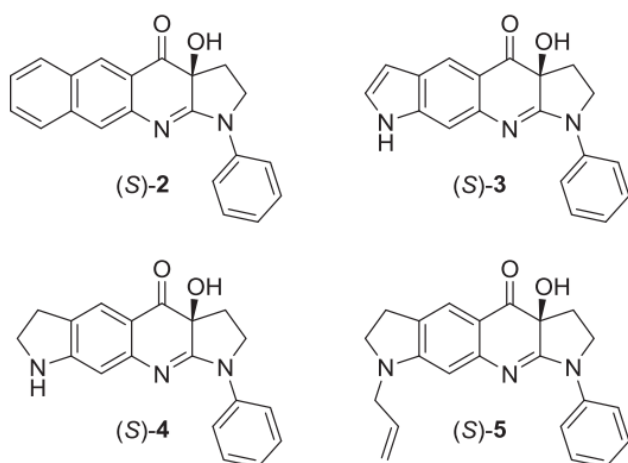


Figure 79: A-ring derivatives from (Verhasselt, Stevens, *et al.* 2017)

C.8.b. C-ring substitution

There is a very limited room for modification on blebbistatin's C-ring, yet an arginine in close proximity could result in an extra H-bond for a short-to-medium size substitute (Roman, Verhasselt, *et al.* 2018) (Figure 80). Roman, Verhasselt, *et al.* (2018) thus proposed a serie of 4 derivatives. They however result in severe or complete loss of inhibition. Thus C-ring modification does not seem to be the most promising approach for optimizing the potency of blebbistatin.

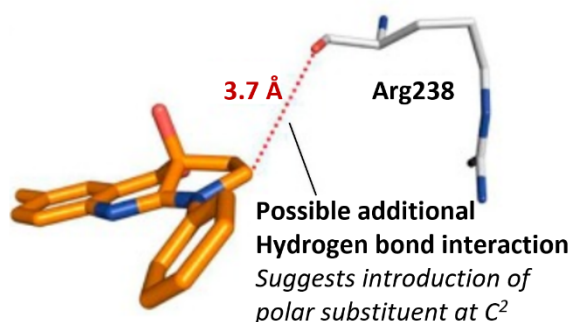
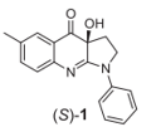
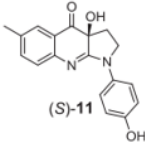
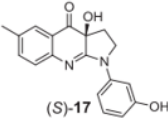
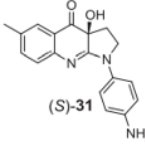
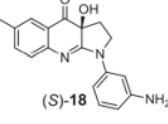
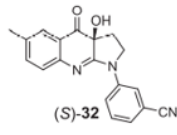
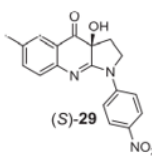
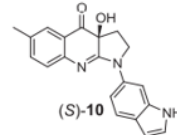
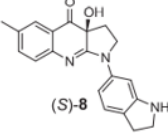
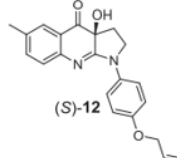
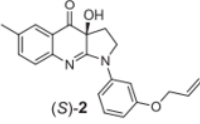
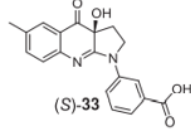
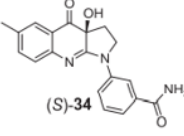
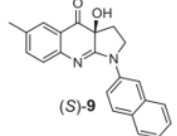
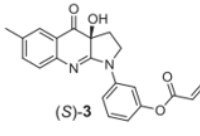


Figure 80: The Arg238 backbone is close to the blebbistatin C-ring and was proposed as a potential way to mediate additional polar contact in the allosteric pocket (Roman, Verhasselt, *et al.* 2018)

C.8.c. D-ring substitution

Addition of small groups in D-ring meta position (cyano, hydroxyl or amino) can still inhibit SkMyo2 but are less efficient than blebbistatin (IC₅₀ 10-20-fold higher) while bigger groups: carbamoyl and carboxy results in no inhibition (Verhasselt, Roman, De Wever, *et al.* 2017)(Figure 81).

Compound	Relative potency to (S)-1	Compound	Relative potency to (S)-1
Parent compound			
 (S)-1	1.0 ± 0.2		
Small substituents			
 (S)-11	0.16 ± 0.04	 (S)-17	0.11 ± 0.01
 (S)-31	0.19 ± 0.01	 (S)-18	0.15 ± 0.01
Medium-sized substituents			
 (S)-32	0.04 ± 0.01	 (S)-29	2.5 ± 0.2
 (S)-10	0.12 ± 0.02	 (S)-8	0.11 ± 0.02
 (S)-12	2.3 ± 0.3	 (S)-2	0.23 ± 0.05
Large substituents			
 (S)-33	<0.02	 (S)-34	<0.02
 (S)-9	<0.02	 (S)-3	0.04 ± 0.01

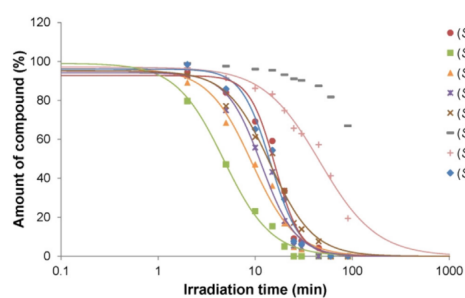


Figure 81: D-ring derivatives of blebbistatin (Verhasselt, Roman, Bracke, *et al.* 2017)

(Top) derivative scaffold and potency compared to blebbistatin. (Bottom) Stability of the various derivatives upon 480 nm illumination. Most molecules are quickly degraded after 10 minutes. S-29 (pNitroBlebbistatin) is the most stable construct.

Actually, the most successful modification of the blebbistatin scaffold was reached through para substitutions of the D-ring (see section C.5.c.). They resulted in improved stability, solubility and fewer toxicity (Várkuti *et al.* 2016; Verhasselt, Roman, De Wever, *et al.* 2017; Képiró *et al.* 2014). Strikingly, from all the derivatives described up to date, only two of them exhibit an improved potency compared to blebbistatin (propenoxyBlebb (S-12) and pNitroBlebb (S-29) exhibit a 2.3 and 2.5-fold potency improvement respectively) (Verhasselt, Roman, Bracke, *et al.* 2017).

Interestingly, Gyimesi *et al.* (2021) pointed out that, if pNitroBlebb exhibits an improved potency for SkMyo2, this is not true for the other Myo2 isoforms tested (Gyimesi *et al.* 2021), resulting in a relative specificity. Although it is not sufficient to call pNitroBlebb a specific inhibitor of SkMyo2, it highlights the potential of development of blebbistatin derivatives with both increased potency and selectivity.

Objectives

To further understand the specificity of the blebbistatin binding pocket among myosins, we started a collaboration with András Málnási Csizmadia's group as they were developing a blebbistatin derivative (MPH-220) that showed good stability, no detectable cytotoxicity and exquisite specificity for fast SkMyo2, characteristics that make it a good drug candidate against spasticity. Indeed, they further demonstrate that MPH-220 is an efficient muscle relaxant with no detectable side effects on the cardiac and respiratory functions in mice (Gyimesi *et al.* 2020). MPH-220 differs from blebbistatin in two points: the A-ring was replaced by a methylthiophen moiety, and the D-ring was substituted by a morpholino group in *para* (Figure 82).

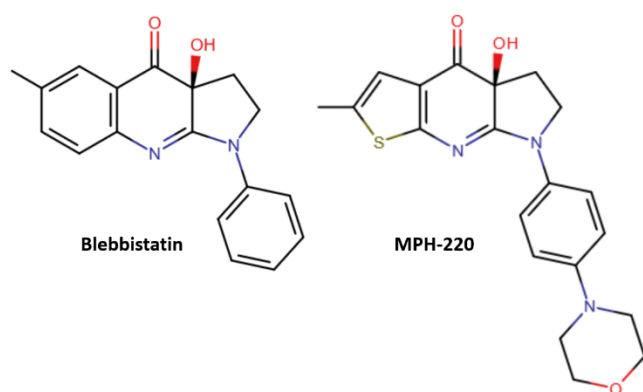


Figure 82: Comparison between blebbistatin and MPH-220.

MPH-220 differs from Blebbistatin by its A-ring (methylthiophen) and by the substitution of its D-ring with a morpholino group

Thus, our objectives consisted in solving the crystal structure of SkMyo2 in complex with MPH-220, and in studying the basis of its specificity.

Results and discussion

A. Study of MPH-220: a specific SkMyo2 inhibitor

A.1. Crystallization of the promising specific skeletal inhibitor: MPH220

András Málnási Csizmadia group provided us the MPH-220 molecule and purified SkMyo2 S1 subfragment, extracted from psoas muscle from rabbits. As no crystallization condition had yet been published for SkMyo2 in the pre-powerstroke state, we first tried to characterize the solubility of SkMyo2 supplemented with 2 mM Mg.ADP.VO₄ in crystallization trials. VO₄ acts as a high affinity analog P_i, which more strongly stabilizes the myosin Motor domain in its pre-powerstroke state. Crystallization was performed with or without *in situ* proteolysis with trypsin (Dong *et al.* 2007).

Indeed, because of the additional flexibility of the Lever arm of Myo2, obtaining crystals of SkMyo2 S1 would be even more challenging compared to crystallizing the more compact SkMyo2 MD or MDE fragments; and in the case of a myosin Motor, trypsin digestion could lead to removal of part or the totality of the Lever arm. So doing, I managed to obtain crystals of SkMyo2 MDE bound to MPH-220 that diffracted up to 2.1 Å (Table 15). The electron density map that I obtained by molecular replacement indeed corresponds to SkMyo2 in its pre-powerstroke. From the initial refinement maps, clear difference density was identified, both for Mg.ADP.VO₄ in the active site, and for MPH-220 in the allosteric pocket described for blebbistatin. Yet, as I went on with refinement, the structure revealed that the crystal contained a degraded form of MPH-220. Indeed, the electron density indicated that MPH-220 had lost its hydroxyl function, whose expected position is pointed by a red arrow on the Figure 83.

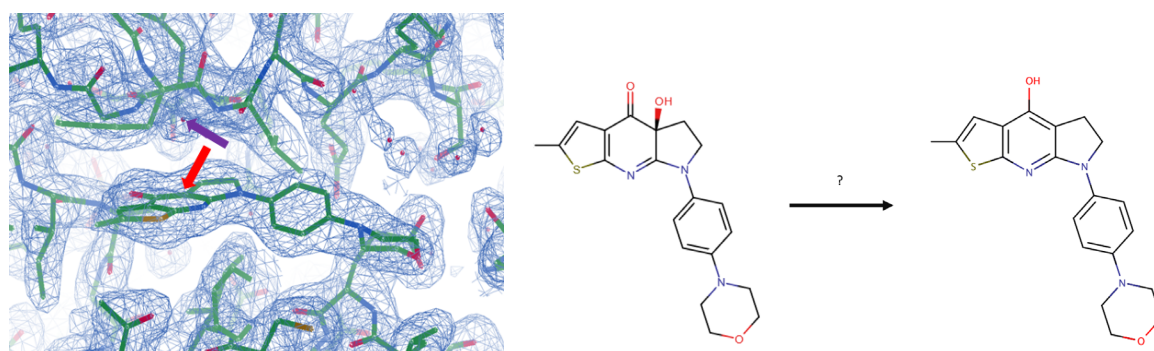


Figure 83: Degraded MPH-220 within the SkMyo2 Motor

(Left) Degraded MPH-220 fitted in the electron density of SkMyo2-MPH220 crystal structure at 2.1 Å. The red arrow shows the expected position for the hydroxyl function; the purple arrow shows an unexpected water molecule nearby the degradation site which does not appear in the published structures with blebbistatin. (Right) Putative degradation product of MPH-220 where the hydroxyl group is missing.

SkMyo2 ADP-VO4 MPH-220 degraded	
Wavelength	0.98010 Å
Resolution range	98.04 - 2.149 (2.16 – 2.15)
Space group	P 21 21 21
Unit cell	48.253 118.408 174.813 90.00 90.00 90.00
Total reflections	904552 (43593)
Unique reflections	66524 (3326)
Multiplicity	13.6 (13.1)
Completeness (%)	100 (98.48)
Mean I/sigma(I)	9.2 (1.5)
Wilson B-factor	38.42
R-merge	0.181 (1.747)
R-meas	0.188 (1.816)
R-pim	0.072 (0.678)
CC1/2	0.998 (0.684)
Reflections used in refinement	55602 (1113)
Reflections used for R-free	2765 (1056)
R-work	0.1914 (0.1979)
R-free	0.2268 (0.2242)
CC(work)	0.947
CC(free)	0.928
Number of non-hydrogen atoms	7826
macromolecules	7321
ligands	71
solvent	434
Protein residues	967
RMS(bonds)	0.008
RMS(angles)	0.94
Ramachandran favored (%)	96.99%
Ramachandran allowed (%)	2.9%
Ramachandran outliers (%)	0.11%
Rotamer outliers (%)	2.14%
Clashscore	3.67
Average B-factor	44.13
ligands	31.12

Table 15: Data collection and refinement statistics of the crystal structure of SkMyo2 bound to degraded MPH-220

Similarly, for blebbistatin, photodegradation was found to promote loss of the hydroxyl group (Li *et al.* 2018) (see section C.5.c). Yet, we were surprised as András Málnási Csizmadia's group monitored the Mw of MPH-220 over time by mass spectroscopy and could not detect degradation or toxicity after incubation with human fibroblast for 120 hours. Thus, the compound seemed stable in a physiological context, and light does not seem sufficient to degrade the compound.

We first wondered whether the degradation had occurred prior or after MPH-220 binding to skMyo2. I thus co-crystallized Myo2 with the putative degraded form of MPH-220 produced by our collaborators (as presented in the Figure 83). The best crystal I obtained with the degraded form was diffracting to ~3.7 Å only, and I found no density for the compound, so the procedure was inconclusive. In parallel, András Málnási Csizmadia's group couldn't detect any inhibition of SkMyo2 ATPase activity

by the putative degraded form. It should be noted that, as the hydroxyl group mediates two key polar contacts between blebbistatin and Myo2 (see section C.7.), it is not surprising that loss of the hydroxyl group leads to loss of inhibitory activity. Therefore, the degradation as we observed is more likely to happen once the drug is bound to Myo2.

Interestingly, additional density likely corresponding to a water molecule was found nearby the degradation site (marked by a purple arrow on the [Figure 83](#)). This density is not seen in any myosin-Blebbistatin crystals determined so far (PDB: 1YV3, [Allingham, Smith, and Rayment 2005](#), PDB: 3MYK, [Frye et al. 2010](#), PDB: 3MYH, [Frye et al. 2010](#), PDB: 3MJX, [Fedorov et al. 2009](#), PDB: 6Z7U, [Ewert et al. 2020](#)). We propose that this water molecule could come from the hydroxyl lost by MPH-220.

To understand the origin of the degradation in SkMyo2 MPH-220 crystals, we thus hypothesized that:

- MPH-220 could be degraded by radiation damage due to X-ray
- MPH-220 could react with one or some of the ingredients in the crystallization solution
- MPH-220 degradation could be caused by exposure to light, as is the case for blebbistatin

A.1.a. Radiation damage

We contacted the beamline scientist of proxima-2 (Synchrotron SOLEIL) William Shepard to discuss with him the possibility of radiation damage of MPH-220. As the overall radiation dose at proxima-2 is way below the Garman limit (30 MGy), and as sulphur is much more prone to radiation damage than a hydroxyl group, radiation damage did not seem likely in this case.

To confirm this hypothesis, I prepared new crystals of SkMyo2 with MPH-220 with limited exposure to light. The newly obtained crystals were then shot at proxima-2 beamline (Synchrotron SOLEIL) using different radiation doses (~1.9MGy and ~0.4MGy) for each one. Two crystals diffracting at 2.1 Å and 2.5 Å were obtained, yet all datasets corresponded to the degraded form of MPH-220 even at the low dose of ~0.4MGy, making the hypothesis of MPH-220 degradation through radiation damage very unlikely.

A.1.b. SkMyo2 –non degraded MPH-220 structure

Finally, a third crystal, diffracting to 3.2 Å, was obtained. This time the crystal contained the complete MPH-220 at both ~1.9MGy and ~0.4Mgy ([Figure 84](#)). Data were analyzed and published on [Gyimesi et al. 2020](#) (PDB: 6YSY).

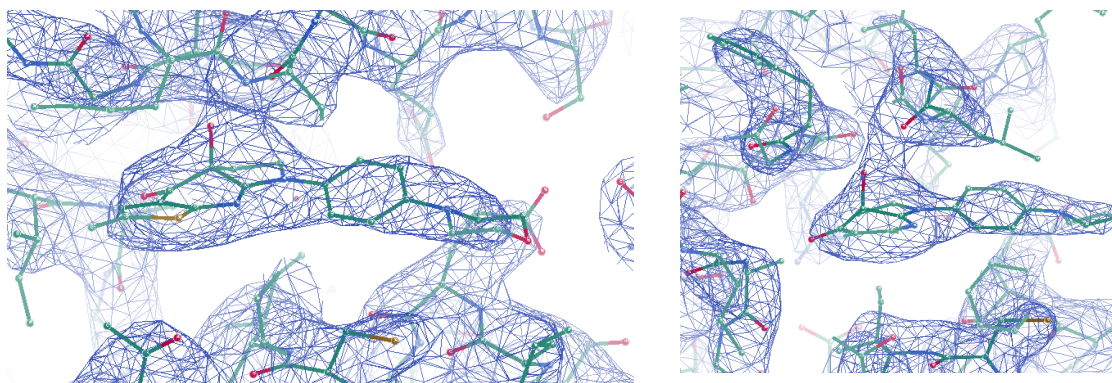


Figure 84: MPH-220 fitted in SkMyo2 blebbistatin allosteric pocket (6YSY)

Nice electron density (in blue) can be seen for MPH-220. All the features of MPH-220 seems present within the density and in particular the hydroxyl group.

Growing crystals on limited light exposure might have been helpful to prevent degradation, as I managed to get one crystal containing the non-degraded form of MPH-220. Yet, it may not be a key parameter on its own, as even by limited light exposure, degradation was seen in certain crystals. Overall, for discovering what leads to MPH-220 degradation, further investigations were needed.

A.1.c. Dithiothréitol (DTT) in combination with light responsible of MPH-220 degradation

We next looked at the impact of crystallization reagents on the dehydroxylation of MPH-220. The crystallization condition contained ~35-37% PEG 600, 0.1 M HEPES-NaOH, pH 7.2, and a high concentration of reducing reagent (20 mM DTT).

Dehydroxylation of blebbistatin by light can be easily followed by monitoring light absorbance (Kolega 2004). We looked at the ability of different parameters to either slow down or aggravate blebbistatin photodegradation by following absorbance from 300 to 500 nm of different time points under exposure to white light.

With the help of Helena Sirkia, engineer in our team, we monitored the effect of the original SkMyo2 protein buffer, of pH (from 6.5 to 9.8), of DTT and of the usual crystallization additives 3% methanol, 3% ethanol and 3% dichloromethane on blebbistatin stability.

When blebbistatin is degraded upon light exposure the spectral properties of blebbistatin evolve (see section C.4.): the absorption peak at ~400-450 nm decreases, and the absorption peak at 330-350 nm increases.

In our hands, in either SkMyo2 buffer protein or water, when exposed to white light, blebbistatin degradation is rather slow. During the first 3h, absorption at 400-450 nm decreased, but no increase can be seen on the 330-350 nm range. After ~18h, a clear absorbance peak starts to emerge at 330-350nm, in particular in the SkMyo2 buffer (Figure 85).

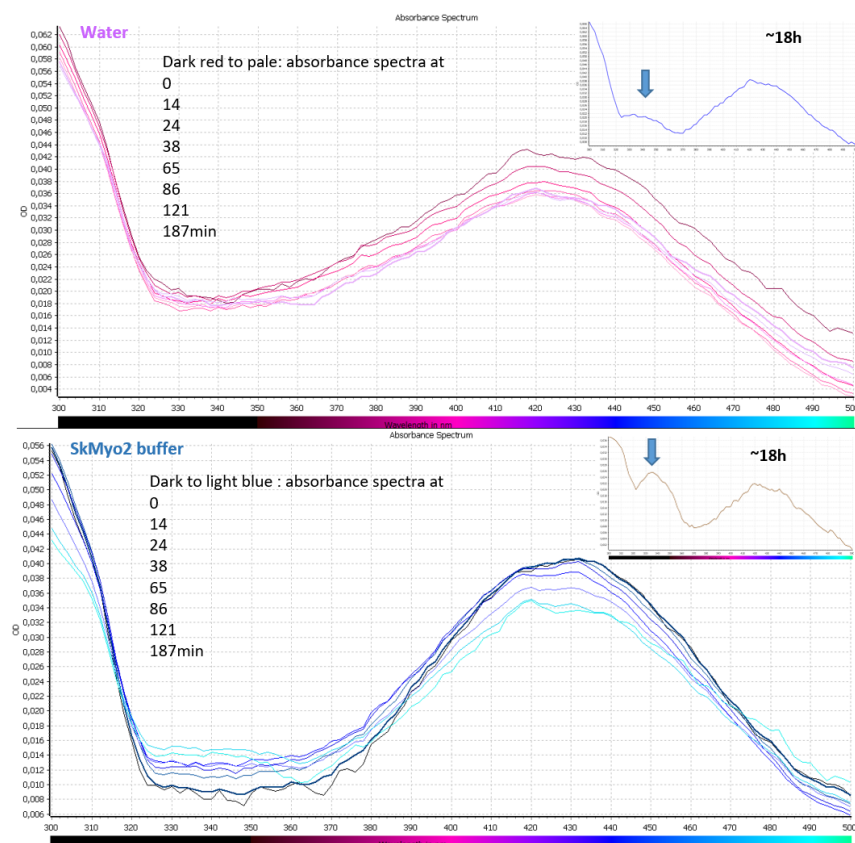


Figure 85: Absorption of 10 μM blebbistatin in water or SkMyo2 buffer

Absorption spectra of blebbistatin in water (top panel) or SkMyo2 buffer (bottom panel). Blebbistatin absorption spectra after 0 to 187min exposure to white light are plotted. The spectra of Blebbistatin after 18h exposure to white light is plotted is inserted at the top left corner of each panel. On this spectrum, a clear absorbance peak (marked by a blue arrows) resulting from blebbistatin degradation can be detected at $\sim 340\text{nm}$. Degradation seems more severe in SkMyo2 buffer than in water.

We thus repeated this experiment to compare the effect of pH (from 6.5 to 9.8), of DTT (20 μM or 5 mM), of 3% methanol, of 3% ethanol and of 3% dichloromethane on the absorption spectrum of blebbistatin after $\sim 18\text{h}$. All the tested condition resulted in aggravation of blebbistatin degradation compared to the control (Blebbistatin in water). Higher absorbance peaks can be seen between 330 and 350 nm for all the tested reagents (Figure 86).

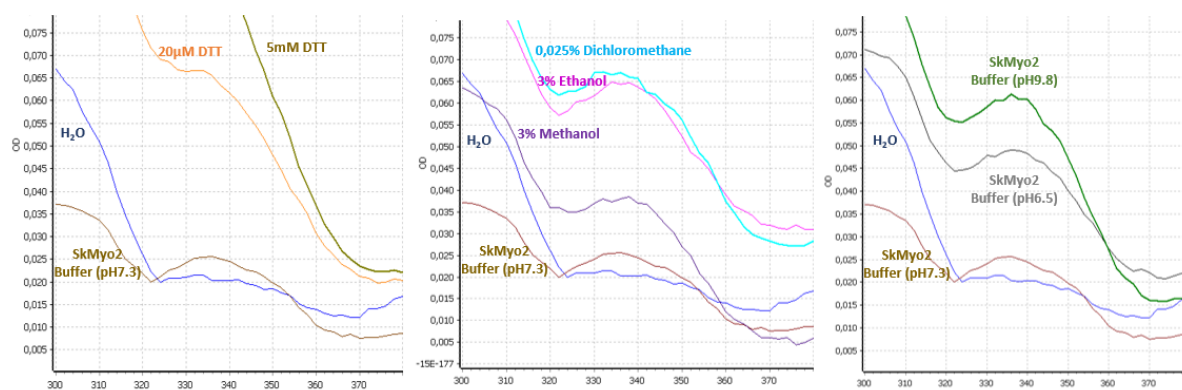


Figure 86: Absorption of 10 μM blebbistatin supplemented with various reagents after 18h in white light.

Absorption spectra of blebbistatin in water supplemented with 20 μM DTT, 5 mM DTT, 3 % Methanol, 3 % Ethanol, 0.025 % Dichloromethane or in SkMyo2 buffer at pH 7.3, 6.5 or 9.8. Spectra of Blebbistatin in water or in SkMyo2 buffer a pH7.3 after 18h are plotted as reference to see which condition(s) could aggravate or slow down Blebbistatin degradation. All conditions tested result in a large peak at 340 nm pointed out to a degradation of the Blebbistatin. Worst conditions seem to be the addition of 5 mM DTT.

From these data, a neutral pH is the most adapted to avoid hydroxyl loss, but high DTT concentration as used on the crystallization condition can be deleterious as 5 mM DTT results in the biggest absorbance increase at 350 nm. Interestingly, repeating the same experiment in the dark, 5 mM DTT does not promote blebbistatin degradation. Thus, a combination of DTT and light exposure is more likely to be the explanation for the degradation seen in our crystal structure.

This certainly makes co-crystallization of SkMyo2 with blebbistatin derivatives in this crystallization condition more difficult. Indeed, I had found that DTT was essential to reduce the multiplicity of these crystals, and to improve the resolution to which they could diffract. Special care should thus be taken to prevent as much as possible light exposure when using DTT with blebbistatin derivatives.



Figure 87: Example of crystallization drops for SkMyo2 MPH-220 crystals with (right) and without (left) 20 mM DTT

Detailed crystallization protocol can be found in the method of the [Gyimesi et al. 2020 paper](#).

Overall, this does not seem to be a major issue in the physiological context. As mentioned above, no MPH-220 mediated toxicity was found on cultured fibroblasts (see section A.1). Additionally, MPH-220 gives good results on rat muscle relaxation ([Gyimesi *et al.* 2020](#), see section A.2.).

A.2. Article describing MPH-220 specificity and potential for spasticity treatment

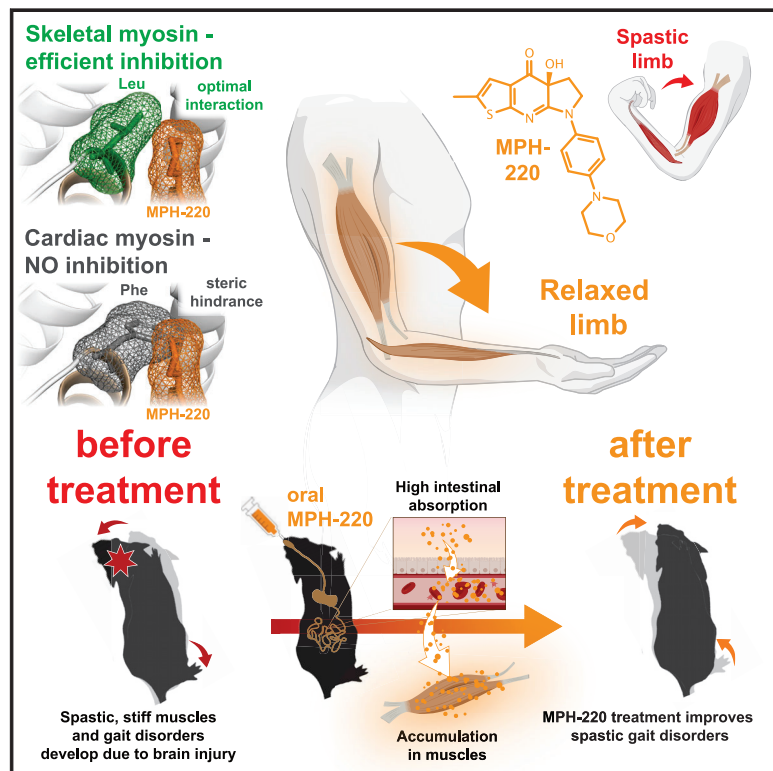
We thus published an article in October 2020 describing MPH-220 specificity and its potential for treating spasticity:

Gyimesi M, Horváth ÁI, Túrós D, Suthar SK, Péntes M, Kurdi C, **Canon L**, Kikuti C, Ruppel KM, Trivedi DV, Spudich JA, Lőrincz I, Rauscher AÁ, Kovács M, Pál E, Komoly S, Houdusse A, Málnási-Csizmadia A. Single Residue Variation in Skeletal Muscle Myosin Enables Direct and Selective Drug Targeting for Spasticity and Muscle Stiffness.

Cell. 2020 Oct 15;183(2):335-346.e13. doi: 10.1016/j.cell.2020.08.050. Epub 2020 Oct 8. PMID: 33035452; PMCID: PMC7596007.

Single Residue Variation in Skeletal Muscle Myosin Enables Direct and Selective Drug Targeting for Spasticity and Muscle Stiffness

Graphical Abstract



Authors

Máté Gyimesi, Ádám I. Horváth, Demeter Túrós, ..., Sámuel Komoly, Anne Houdusse, András Málnási-Csizmadia

Correspondence

mate.gyimesi@elte.hu (M.G.), malna@elte.hu (A.M.-C.)

In Brief

Therapeutic muscle relaxation is currently achieved pharmacologically via indirect mechanisms by modulation of the nervous system. Selective targeting of skeletal muscle has not been possible because myosin isoforms in skeletal muscle and the heart are structurally very similar. Using a rational, structure-based approach, Gyimesi et al. design a small-molecule muscle relaxant that specifically inhibits the skeletal, but not the cardiac, myosin 2 isoform. With their new drug candidate, they show how spasticity and muscle stiffness might be relieved pharmacologically without cardiac or nervous system side effects.

Highlights

- A key residue variation of fast skeletal myosin allows selective targeting
- A rationally designed inhibitor (MPH-220) specifically blocks skeletal muscle
- The inhibitor-bound myosin atomic structure reveals mechanism of selectivity
- MPH-220 improves gait disorders in spastic animal model after brain injury



Article

Single Residue Variation in Skeletal Muscle Myosin Enables Direct and Selective Drug Targeting for Spasticity and Muscle Stiffness

Máté Gyimesi,^{1,2,*} Ádám I. Horváth,¹ Demeter Túrós,¹ Sharad Kumar Suthar,^{1,3} Máté Péntes,¹ Csilla Kurdi,¹ Louise Canon,⁴ Carlos Kikuti,⁴ Kathleen M. Ruppel,⁵ Darshan V. Trivedi,⁵ James A. Spudich,⁵ István Lőrincz,³ Anna Á. Rauscher,^{1,2} Mihály Kovács,^{1,6} Endre Pál,⁷ Sámuel Komoly,⁷ Anne Houdusse,⁴ and András Málnási-Csizmadia^{1,6,8,*}

¹MTA-ELTE Motor Pharmacology Research Group, Pázmány Péter sétány 1/c, 1117 Budapest, Hungary

²Motorpharma, Ltd., Szilágyi Erzsébet fasor 27, 1026 Budapest, Hungary

³Printnet, Ltd., Kisgömb utca 25-27, 1135 Budapest, Hungary

⁴Structural Motility, Institut Curie, Paris Université Sciences et Lettres, Sorbonne Université, CNRS UMR144, 75005 Paris, France

⁵Department of Biochemistry, Stanford University School of Medicine, Beckman Center B400, 279 W. Campus Drive, Stanford, CA 94305, USA

⁶Department of Biochemistry, Eötvös Loránd University, Pázmány Péter sétány 1/c, 1117 Budapest, Hungary and Brunszvik u. 2, 2462 Martonvásár, Hungary

⁷Department of Neurology, University of Pécs, Rét utca 2, 7623 Pécs, Hungary

⁸Lead Contact

*Correspondence: mate.gyimesi@elte.hu (M.G.), malna@elte.hu (A.M.-C.)

<https://doi.org/10.1016/j.cell.2020.08.050>

SUMMARY

Muscle spasticity after nervous system injuries and painful low back spasm affect more than 10% of global population. Current medications are of limited efficacy and cause neurological and cardiovascular side effects because they target upstream regulators of muscle contraction. Direct myosin inhibition could provide optimal muscle relaxation; however, targeting skeletal myosin is particularly challenging because of its similarity to the cardiac isoform. We identified a key residue difference between these myosin isoforms, located in the communication center of the functional regions, which allowed us to design a selective inhibitor, MPH-220. Mutagenic analysis and the atomic structure of MPH-220-bound skeletal muscle myosin confirmed the mechanism of specificity. Targeting skeletal muscle myosin by MPH-220 enabled muscle relaxation, in human and model systems, without cardiovascular side effects and improved spastic gait disorders after brain injury in a disease model. MPH-220 provides a potential nervous-system-independent option to treat spasticity and muscle stiffness.

INTRODUCTION

Spasticity—characterized by involuntary increased tone of skeletal muscles—is a common sensorimotor disorder in patients with brain and spinal cord injuries after stroke, trauma, cerebral palsy, or in multiple sclerosis and several myopathies of different etiologies (Li, 2017; Trompetto et al., 2014). Spasticity-related physical and mental conditions of patients often permanently disable self-supporting life management and ability to work (Martin et al., 2014; Rychlik et al., 2016). Economic burden for post-stroke patients with spasticity is 4-fold higher than those for patients without spasticity (Zorowitz et al., 2013), which includes direct costs of medications and hospitalization and indirect costs of caregiver assignments and independent daily-life-facilitating instruments.

Spasticity develops as a consequence of complex rearrangements of supraspinal inputs, which transforms the synaptic regu-

lation of motoneurons that drives muscle contraction. The resulting exaggerated stretch reflex is accompanied with disrupted balance in regulation from the premotor cortex and reticular formation of the brainstem, which finally leads to aberrantly increased potentiation of motoneurons and hypercontraction of muscles (Enslin et al., 2020; Mukherjee and Chakravarty, 2010; Trompetto et al., 2014).

Current muscle relaxants in medical practice target the central nervous system (e.g., baclofen [GABA_B agonist] and tizanidine [α 2 agonist]), the neuromuscular junction (botulinum toxins), or the sarcoplasmic reticulum in muscle cells (dantrolene; Figure 1A). Due to their aspecific mechanism of action, centrally acting muscle relaxants have a wide range of neurological and cardiovascular side effects (drowsiness, dizziness, depression, and low blood pressure; Meleger, 2006; Smit and Slim, 2008) and low levels of efficacy (Orsnes et al., 2000), which often necessitate the application of an intrathecal pump surgically



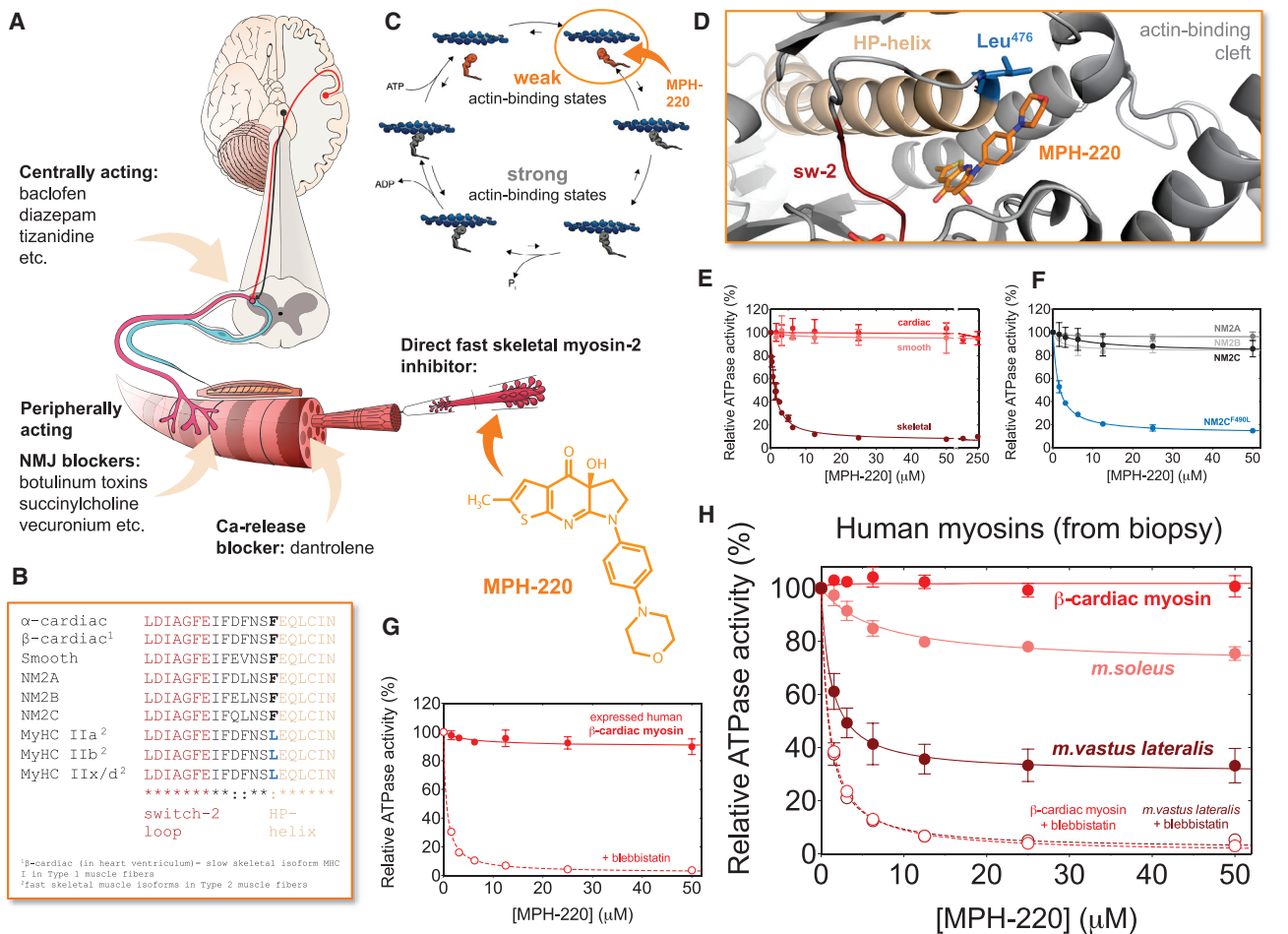


Figure 1. MPH-220 Inhibits Skeletal Muscle Myosin with Extreme Selectivity Independently of the Nervous System

(A) Current muscle relaxants target the central nervous system or act peripherally, whereas MPH-220 directly inhibits myosin. (B) Human myosin-2 isoforms contain phenylalanine (black F) at the beginning of the HP-helix between the switch-2 loop (red) and the relay region, except for fast skeletal myosin isoforms, where this position is leucine (blue L; cf. Figure S1). (C) MPH-220 was designed to bind into the blebbistatin-binding cavity of the motor domain, to enable inhibition in the actin-detached state. (D) Close-up view of the communication center of the functional regions (actin-binding cleft, switch-2 loop of the active site, and the relay region, except for fast skeletal myosin isoforms, where this position is leucine (blue L; cf. Figure S1). (E) Actin-activated ATPase inhibition of three myosin-2 isoforms (cf. Table S1). (F) Actin-activated ATPase inhibition of NM2A, NM2B, NM2C and the NM2C^{F490L} variant. (G) Actin-activated ATPase inhibition of expressed human β -cardiac myosin with MPH-220 and blebbistatin. (H) Actin-activated ATPase inhibition of human muscle myosin samples from biopsies of *m. soleus*, *m. vastus lateralis*, and heart ventricle. In contrast to MPH-220, blebbistatin fully inhibited *m. vastus lateralis* sample and β -cardiac myosin samples. Mean \pm SD are shown in all ATPase experiments; n = 3–9. See also Figures S1 and S2.

implanted inside the body (Medical Advisory, 2005). Systemic treatment with botulinum toxins is impossible due to their lethal effect on respiratory and cardiac functions, and local treatments are painful, costly, and often ineffective (Careta et al., 2015; Pavone et al., 2016). Dantrolene has been associated with severe hepatotoxicity and genotoxicity (NIH, 2012); therefore, its clinical use is now restricted to life-threatening malignant hyperthermia. Surgical treatment of severe spasticity is limited to selective dorsal rhizotomy, when the sensory roots that transfer abnormal information from the muscles to the spinal cord are transected. However, the advantage of dorsal rhizotomy over oral medica-

tions is only marginal, because the treatment often leads to paralysis, chronic back pain, sensory dysfunction, inflammation, constipation, and cyst formation in the spinal column (cf. NICE interventional guidance 373).

Besides nervous-system-injury-related spasticity, permanent muscle spasms emerge as the leading source of prolonged pain in non-specific low back pain and chronic musculoskeletal pain disorder, fibromyalgia, altogether affecting more than 10% of global population (Marques et al., 2017; Vos et al., 2012). Although treatments of muscle spasm in these syndromes with systemic muscle relaxants are statistically effective,

recommendations for their use in clinics underline precautions due to the reported adverse side effects resulting from non-specific targeting of the nervous system (Tofferi et al., 2004; van Tulder et al., 2003).

These considerations emphasize the unmet medical need for the development of a new-generation anti-spastic drug, which directly targets the effector protein of muscle contraction while avoiding neurological and cardiovascular side effects. Nervous-system-independent inhibition of muscle contraction in spastic patients could also overcome the need for targeting the otherwise disrupted synaptic balance of neuronal regulation.

Selective inhibition of skeletal muscles, however, raises the challenge of developing a small molecule that distinguishes between the structurally and sequentially highly similar myosin-2 isoforms. The ideal candidate inhibits only skeletal muscle fast isoforms (MyHC Ila,b,x/d), because the slow isoform in skeletal muscles (myosin heavy chain [MyHC I]) expressed from the *MYH7* gene is identical to β -cardiac myosin, the most abundant motor in the ventricles of the heart (Coluccio, 2020; Figures 1B and S1).

RESULTS

In order to relax muscle fibers, we aimed to arrest the actomyosin force-generation cycle in the actin-detached weak actin-binding state (Takács et al., 2010), when myosin heads are decoupled from actin filaments (Málnási-Csizmadia and Kovács, 2010; Sweeney and Hammers, 2018; Figure 1C). Using rational pharmacological design in a model MyHC Ila myosin structure, we developed and optimized a small-molecule inhibitor (MPH-220) into the myosin-2 class-specific blebbistatin-binding pocket (Allingham et al., 2005; Kovács et al., 2004; Limouze et al., 2004; Straight et al., 2003; Figures 1D and S2). MPH-220 enabled selective inhibition of fast skeletal myosin-2 isoforms (further referred to as skeletal myosins; Figure S1) isolated from rabbit psoas muscle, whereas—even at extremely high concentrations—it did not inhibit the ATPase activity of slow skeletal/ β -cardiac myosin (further referred to as cardiac myosin) isolated from left ventricle of porcine heart or smooth muscle myosin-2 (Figure 1E; Table S1) or any non-muscle myosin-2 (NM2) isoforms (Figure 1F; Table S1). Sequence analysis of the inhibitor binding site revealed an important difference between the cardiac and skeletal myosins near the morpholine ring of MPH-220 at a location playing a key role in the myosin force-generation pathway (Málnási-Csizmadia and Kovács, 2010). The drug-interacting amino acid is uniquely and invariably leucine in fast skeletal myosin heavy chains (Leu⁴⁷⁶ in human MyHC Ila), whereas this position is occupied by phenylalanine in all other myosin-2 isoforms (Figures 1B and S1). We hypothesized that this structural difference can be the basis for the extreme selectivity of MPH-220 toward skeletal myosins. Therefore, we assessed the role of a Phe/Leu exchange through mutational analysis of human non-muscle myosin-2C (NM2C), which is not inhibited by MPH-220 in the wild-type form, possibly due to the presence of Phe⁴⁹⁰ in the corresponding position. According to our hypothesis, the expressed NM2C^{F490L} variant became sensitive to MPH-220 (Figure 1F), corroborating that the single-amino-acid change determines the observed selectivity.

Considering the selective inhibitory nature of MPH-220 on myosin samples (Figures 1E and 1F) and its potential to become a new-generation anti-spastic drug candidate, we performed ATPase inhibition assays on human myosin samples. Expressed human β -cardiac myosin was essentially unaffected by MPH-220, however, the non-selective myosin-2 inhibitor, blebbistatin, completely blocked its ATPase activity (Figure 1G; Table S1). We further tested MPH-220 on skeletal and cardiac myosin samples isolated from patient-derived biopsies (Figure 1H; Table S1). In line with their myosin-2 isoform composition, skeletal myosin samples from *m.vastus lateralis* and *m.soleus*—containing 56% and 28% fast isoforms in human muscles (Figure S1)—were inhibited by 70% and 29%, respectively, confirming the hypothesis that only the fast isoform fraction is targeted by MPH-220. More importantly, β -cardiac myosin isolated from human heart left ventricle was unaffected by MPH-220 (Figure 1H; Table S1). By contrast, blebbistatin reduced the activity of *m.vastus lateralis* and cardiac myosin samples by more than 90%, confirming that MPH-220 inhibition is proportional to the ratio of fast myosin isoform in different tissues (Figure 1H; Table S1). These results provide the basis for future safe systemic administration of MPH-220 to human patients. Left ventricle human biopsy contains cca. 10% α -cardiac myosin isoform (expressed from the *MYH6* gene [Figure S1; Miyata et al., 2000], which also contains Phe in the proximal part of HP-helix Phe⁴⁷⁴). The lack of inhibition of myosin samples from the biopsies confirms that α -cardiac myosin could not be inhibited by MPH-220. We also note that gene products of MYH1, MYH2, and MYH4 encoding fast skeletal muscle myosin heavy chains IIX/d, Ila, and IIb, respectively, are not expressed in adult human heart in significant amount (England and Loughna, 2013; NCBI Gene Expression database).

In order to further analyze the molecular background of selectivity, we crystalized fast skeletal muscle myosin (isolated from high-quality rabbit *m.psoas*) in the presence of MPH-220 (Figures 2A and S3). The crystal structure confirmed that MPH-220 binds to the blebbistatin-binding cleft and its morpholine ring is in close proximity to Leu⁴⁷⁶. This residue is at the N terminus of the so-called HP-helix of the L50 subdomain (Cope et al., 1996), which is preceded by the switch-2 loop and followed by the relay region of the motor. Comparison of the MPH-220-bound skeletal and blebbistatin-bound *Dictyostelium* myosin-2 structures confirms that, although the tricyclic cores of the inhibitors, including the chiral OH, are positioned similarly, Phe⁴⁶⁶ of the HP-helix in *Dictyostelium* myosin-2 comes into steric hindrance with MPH-220 (Figure 2B). Likewise, the position of this Phe in cardiac myosin structure also causes steric hindrance with MPH-220 (Planelles-Herrero et al., 2017; Figure 2C). This steric hindrance based on crystal structures together with the biochemical results strongly support that the unique Leu in the HP-helix of fast skeletal muscle myosin isoforms is responsible for the extreme selectivity of MPH-220. This mechanism for selective inhibition among myosin-2 isoforms is analogous to how blebbistatin is selective for myosin-2s due to the presence of the switch-2 Ser/Ala residue in myosin-2s (Allingham et al., 2005), whereas this position is occupied by Tyr/Phe in myosins from other classes that are uninhibited by blebbistatin. The resolved crystal structure also confirmed that MPH-220 selects and stabilizes the pre-powerstroke state. Overall, the structure

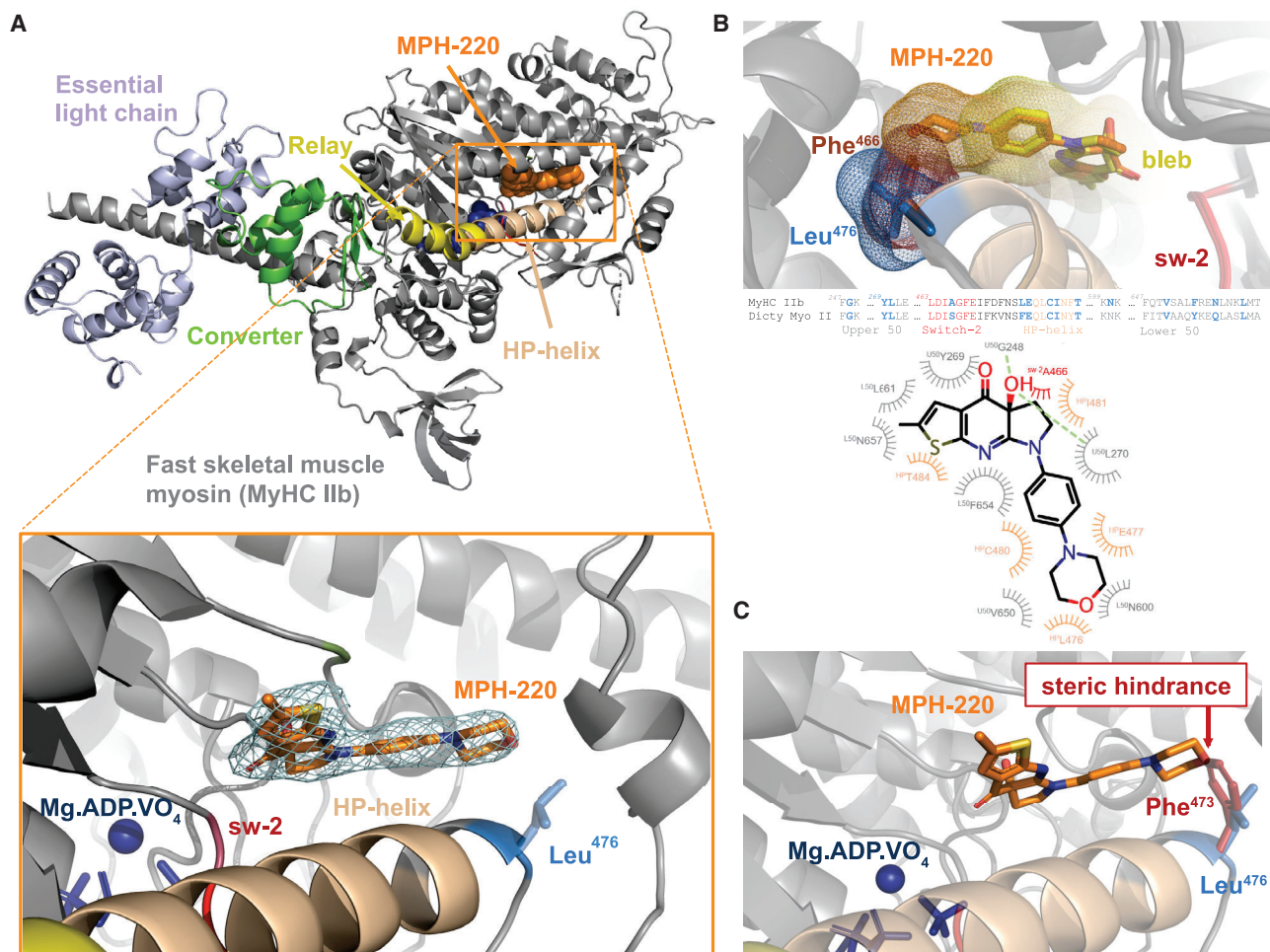


Figure 2. Crystal Structure of MPH-220-Bound Fast Skeletal Muscle Myosin

(A) Cartoon representation of the heavy chain (gray) of rabbit skeletal muscle myosin-2 in Mg.ADP.VO₄ (spheres, blue) pre-powerstroke state with the essential light chain bound to the lever arm. MPH-220 binds to the bottom of the actin-binding cleft close to the HP-helix, with its morpholine ring in close proximity of Leu⁴⁷⁶. Blue mesh, electron density corresponding to MPH-220 at sigma 1.0.

(B) Comparison of the MPH-220 (orange) binding site in MyHC IIb (gray/beige) and the blebbistatin (yellow) binding site in *Dictyostelium* myosin-2 (dark gray/brown; PDB: 1YV3; Allingham et al., 2005). The chiral OH groups of both inhibitors interact with the same residues Gly²⁴⁸ and Leu²⁷⁰ (Gly²⁴⁰ and Leu²⁶² in *Dictyostelium*). Mesh, surfaces based on Van-der-Waals radii, calculated with PyMol. (Bottom) Residues involved in compound binding in LigPlot+ v2.2 (Laskowski and Swindells, 2011) representation are shown; U50, upper 50-kDa subdomain; L50, lower 50-kDa subdomain (gray); sw-2, switch-2 loop (red); HP, HP-helix (beige). Hydrogen bonds (up to 3.2 Å) are shown as green lines.

(C) MPH-220-bound MyHC IIb structure with superimposed cardiac HP-helix illustrates the steric clash between the morpholine ring of MPH-220 and the cardiac HP-helix Phe⁴⁷³ (red) residue.

See also Figure S3.

validated the *in silico* approach to design molecules for selective inhibitor development (Figure S3).

We further studied the effect of MPH-220 on muscle force generation in living animals (Figure 3A). In agreement with the ATPase inhibitory properties, the S(−) enantiomer of MPH-220 was drastically more effective than the R(+) enantiomer when animals were treated orally with MPH-220 (Figure S4). Consequently, the force-relaxing effect of the racemic mixture was significantly lower than that of the S(−) enantiomer. Although the racemic mixture caused maximum 40% reduction, the S(−) enantiomer could decrease hindleg force by 70% in a concentra-

tion-dependent manner (Figures 3B and 3C). The 30% residual isometric force level for S(−)-MPH-220 is in line with the presence of uninhabitable slow skeletal muscle isoforms in rat hindleg muscles. This attribute is of high importance because, unlike centrally acting muscle relaxants, MPH-220 would never cause overdose-related patient immobilization due to the remaining slow myosin-mediated muscle tone. Importantly, the decreased force persisted for more than 10 h (Figure 3C), which indicates optimal properties for pharmacological development. The force-relaxing effect after oral administration was only marginally slower than that after intraperitoneal injection (Figure S4), which

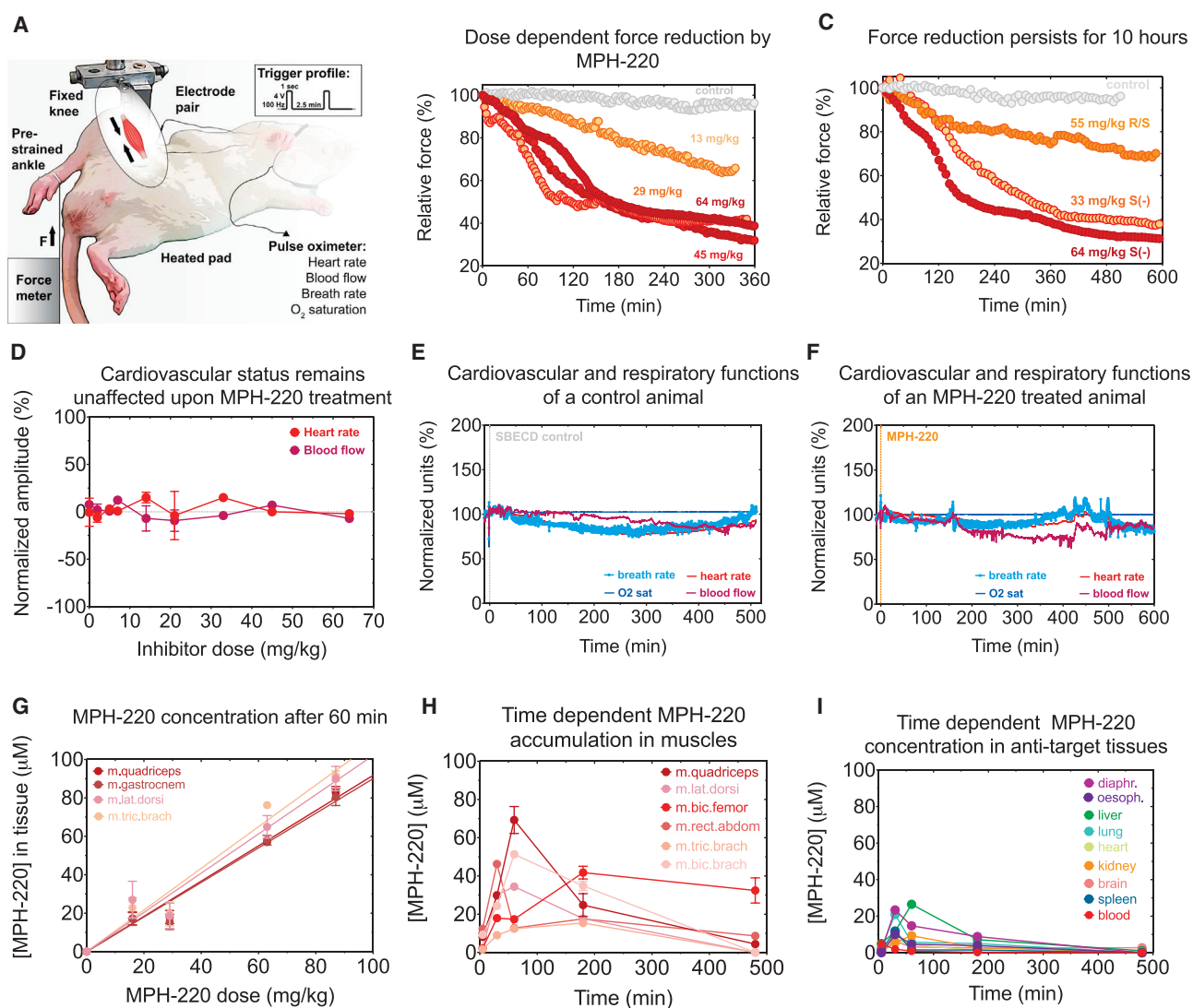


Figure 3. MPH-220 Reduces Skeletal Muscle Force without Cardiovascular Effects

(A) Isometric force of rat hindleg was measured while vital functions were detected by a non-invasive pulse oximeter. (B and C) Dose-dependent force reduction after MPH-220 treatment persisted for more than 10 h. (D) Heart rate (red circle) and pulse distention—reflecting local blood flow at the carotid artery—(maroon circle) show the maximal signal deflections during the measurements (60–600 min) on 1–4 animals/dose. (E and F) Cardiovascular and respiratory functions as a function of time after treatment with sulfbutyl-ether- β -cyclodextrin (SBECD) control or MPH-220. Note that permanent oxygen level is maintained by O₂-supplemented isoflurane anesthesia. (G) Dose-dependent MPH-220 accumulation in rat muscle tissues 60 min after oral treatment. Mean \pm SD are shown; n = 2–3. (H and I) Time-dependent MPH-220 accumulation in rat tissues after 35 mg/kg intraperitoneal (i.p.) treatment. Mean \pm SD are shown; n = 2–11. See also Figure S4.

indicated optimal absorption properties of MPH-220. High endothelial permeability was further confirmed by Caco-2 assay, which showed that MPH-220 is highly permeable with significantly faster transfer rate in the absorptive direction over the excipitive direction (Figure S4).

Although skeletal muscle relaxation could be efficiently achieved by MPH-220, cardiac function was not perturbed in the concentration range that was effective in skeletal muscle force relaxation experiments (Figures 3F and S4). More impor-

tantly, neither cardiac nor respiratory functions differed significantly from the excipient control during the 10-h experiments, suggesting a reasonable safety range between the effective and toxic doses of MPH-220 (Figures 3E and 3F). The maximum 25% decrease in heart rate and blood flow parameters is most probably due to the 10-h-long anesthesia without food and drink after an overnight starvation period and not the effect of myosin inhibition (Figure S4). Moreover, the identical direction of the change in heart rate and blood flow parameters solely reflects

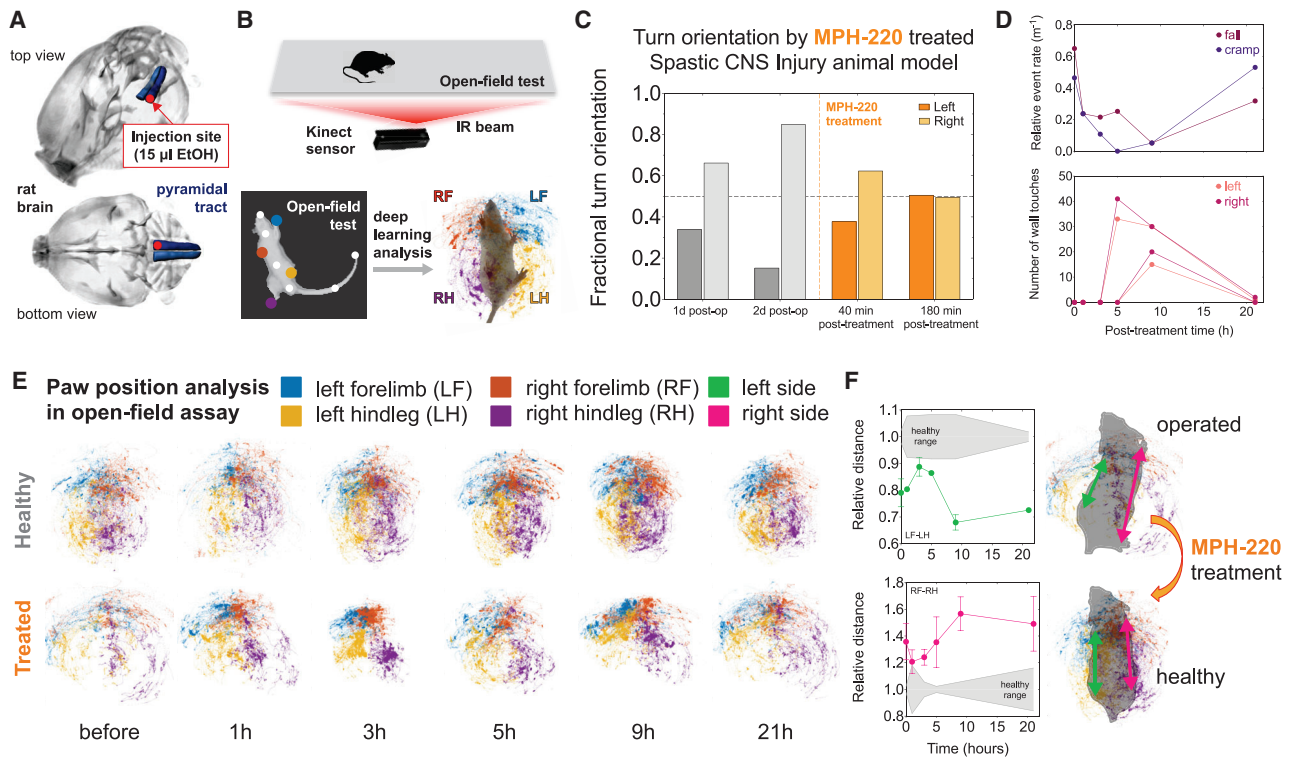


Figure 4. MPH-220 Efficiently Improves Gait Functions of Spastic Rats after Brain Injury

(A) Position of pyramidal tract lesion (red dots).
 (B) Open-field gait analysis was performed by deep-learning algorithms coupled to sub-millimeter 3D movement detection. Dots represent the determined positions; right and left forelimbs (RF and LF) and right and left hindlegs (RH and LH).
 (C) Fractional turn orientation of spastic rat before (gray) and after (orange) 15 mg/kg MPH-220 treatment.
 (D) Falling and spontaneous cramping rates normalized to the total distance traveled (upper) and the number of touches on the cylinder wall (lower) after 20 mg/kg MPH-220 treatment.
 (E) Paw position distribution of the healthy (upper) and treated (lower) animals before and after 20 mg/kg MPH-220 treatment in slow regime.
 (F) Averaged distances between the left (upper) and right (lower) fore- and hindlimbs in each frame of the 3D recordings relative to the healthy values. Mean \pm SD are shown.
 See also [Figure S5](#).

slowing down the heart during anesthesia, because cardiac myosin inhibition preceding heart failure increases heart rate while drastically lowering blood flow, as shown with the non-selective inhibitor, AmBleb ([Figure S4](#)).

We also examined MPH-220 distribution in rat tissues in a time-dependent manner and observed a dose-dependent, few-fold accumulation of MPH-220 in skeletal muscle samples over other tissues, including brain, heart, kidney, and blood ([Figures 3G–3I](#)). Accumulation in skeletal muscle persists after 3 h when MPH-220 is completely eliminated from blood and other tissues, whereas its concentration in target muscles is still in the effective concentration range (10-fold higher than the determined inhibitory constant [IC_{50}]). MPH-220 concentration was only temporarily elevated in the liver, which metabolizes MPH-220. We note that MPH-220 concentration in the diaphragm was much lower compared to other striated muscle samples, which explains the lack of respiratory dysfunctions after MPH-220 treatments. This feature is expected to prove even more favorable in human patients due to the substantially higher ratio of MyHC I slow isoforms in human diaphragm ([Figure S1](#)). The

pronounced accumulation of MPH-220 in skeletal muscles might be the result of high concentration of fast skeletal myosin isoforms, which bind the inhibitor with high affinity. This hypothesis is supported by the significantly lower accumulation of the R(+) enantiomer, which further explains the 4-fold weaker force relaxation by the R(+) enantiomer (cf. [Figure S4A](#)). The species-specific MyHC distribution ([Figure S1](#)) also emphasizes the need for testing these pharmacodynamic properties of MPH-220 in larger animals (dogs and mini pigs), which—unlike rodents—have higher slow isoform proportions, more similar to human tissues.

Direct and efficient targeting of skeletal muscle contraction by MPH-220 raises the possibility of the development of a new-generation, nervous-system-independent, anti-spastic drug. Therefore, we investigated the efficiency of MPH-220 to improve spasticity-related gait disorders in rats with brain injury. We applied the recently developed spastic cerebral palsy animal model to provoke paralysis-coupled spasticity in rats ([Figure 4A](#); [Yu et al., 2013](#)), and gait disorders were analyzed by non-invasive methods focusing on the motoric functions of rats combined with neural-network-based deep-learning movement analysis

(Figure 4B; Video S1). Similarly to human patients with stroke or brain trauma, rats showed individually variable gait patterns with different degrees of palsy in the lower limbs. Thus, we analyzed the effect of MPH-220 treatment individually on each animal and focused on treatment-induced changes in spasticity-related gait components.

Rat-A could not use the right forelimb and the left hindleg due to paralysis-coupled spasticity, which resulted in an almost complete one-sided circling behavior in the open-field box 2 days after the surgery (Video S2). 40 min after MPH-220 treatment, the ratio of left turns increased from 15% to 38%, which further improved to 51% 3 h after the treatment (Figure 4C). Even though rat-A walked significantly less after treatment, it was obvious that a major improvement was achieved: after relaxing spasticity in its left hindleg, rat-A was able to use this leg and make quasi-normal steps (Video S3). Rat-B and C also had paralysis-coupled spasticity in the hindlegs, although to a lower degree than rat-A. The most obvious spasticity-related feature in the open-field test was the random falling and the spontaneous cramping of the right hindleg of rat-C (Video S4). Importantly, the relative frequency of both symptoms decreased drastically after MPH-220 treatment (Figure 4D). Besides these serious gait abnormalities, rat-B and C could not stand up in the cylinder assay before MPH-220 treatment. In agreement with the kinetics observed in the open-field assay, 3 and 5 h after oral MPH-220 treatment, both rats could stand up in the cylinder, touching the wall with both forepaws with the same number of events as their healthy littermates (Figure 4D). Next morning, the positive effects on falling and cramping frequencies and on the ability to stand up in the cylinder disappeared as MPH-220 was excreted from their bodies. Rat-D showed spastic gait disorders only in the right hindleg without signs of severe palsy, and all other legs remained unaffected. This animal could not use the right hindleg normally due to stiff muscles, which resulted in abnormal positioning of all four paws (Figures 4E and S5). The spastic leg was offset from the body axis, which hindered normal progression of the limb during walking and resulted in lopsided gait patterns with tilted body axis (Figures 4F and S5; Video S5). After MPH-220 treatment, the gait of this animal improved significantly as it started to use both hindlegs normally. The improved movement was the consequence of relaxed spasticity in the hindlegs, which enabled the animal to pull its leg into the body axis, thereby making normal walking steps (Figures 4E, 4F, and S5; Video S5). The enhanced gait functions remained persistent for 5 h, when paw positions and body symmetry were close to those of the healthy animals. Similarly to the other experiments, the effect relapsed to the pre-treatment state after 21 h. These effects could be reproduced 5 and 12 days after the first treatment, corroborating the specific anti-spastic effect of MPH-220 treatment.

Beside the individual patterns of spastic behavior that could be improved by MPH-220 treatment, deep-learning analysis was used to assess the over-ground locomotion of all animals during 15 min of free movement in the open-field test. We used 28 parameters characterizing the 3D position of the limbs and body axis in three movement-speed regimes (Figure S5) to quantify the locomotor features based on pose-estimating deep-learning algorithms and exposed these to a principal-components analysis (PCA). In the global PCA space—including all

three speed regimes—the major gait component (PC1) was significantly different from the healthy range, indicating that pyramidal tract damage-induced spastic walk asymmetry is reflected in the major principal gait component (Figure 5A). Most importantly, MPH-220 treatment significantly decreased PC1 scores, the effect of which was maximal at 3 h and no longer detected after 21 h. Importantly, PC1 scores were significantly different from the untreated level, however, the treated values did not differ significantly from the healthy range, which confirms that MPH-220 ameliorated gait pattern of the treated animals to that of the healthy rats. However, when we analyzed the three speed regimes separately, we found that pyramid tract damage mostly affected PC1 in the slow and medium-speed regimes, whereas PC2 and PC3 were significantly affected in the fast regime (Figures 5B and S5). More importantly, PC1 could be significantly improved by MPH-220 treatment in the slow- and medium-speed regimes, and PC3 was significantly improved in the fast regime. We identified the major parameters that predominantly contributed to PC1 and PC3 in the slow, medium, and fast regimes and found a marked difference in the parameter sets defining PC1 and PC3 (Figures 5C, 5D, and S5). Analysis of these components revealed that, in the slow- and medium-speed regimes, MPH-220 treatment has the largest effect on the volumes of the ellipsoids representing paw positions and on the distances between their centers, both suggesting a much-ordered stepping pattern and straightened body axis (Figure 5E). On the other hand, in the fast regime, MPH-220 has the most pronounced effect on the angles of the ellipsoids, which indicates that the treated rats could keep their legs closer to the body axis similarly to the healthy running pattern. These results further solidify that MPH-220 is capable of treating the spastic component of movement abnormalities after brain injury, exhibiting a promising potential to address the unmet medical need for effective anti-spastic therapies.

DISCUSSION

Our biochemical and *in vivo* results demonstrate that MPH-220 selectively inhibits fast skeletal myosin-2 isoforms, which enables effective improvements of spastic gait disorders after brain damage as a consequence of efficient reduction of muscle force. These findings emphasize that nervous-system-injury-derived muscle spasticity can be treated by directly targeting the effector protein of muscle contraction, thereby avoiding adverse neurological and cardiovascular side effects that are characteristic of currently used muscle relaxants. Moreover, as MPH-220 proved a promising candidate for further anti-spastic drug development, we tested its pharmacological properties by investigating its off-target effects on human enzymes, including kinase panels and G-protein-coupled and nuclear hormone receptors (Figure S6). We also demonstrate that MPH-220 is not mutagenic and not cytotoxic (Figure S6), which, together with its high-absorption properties, confirms that MPH-220 is safe and possesses optimal attributes for further drug development as a new-generation anti-spastic drug candidate.

Although we acknowledge that MPH-220 may cause general muscle weakness as observed in our animal disease model, we believe that this effect will be significantly less

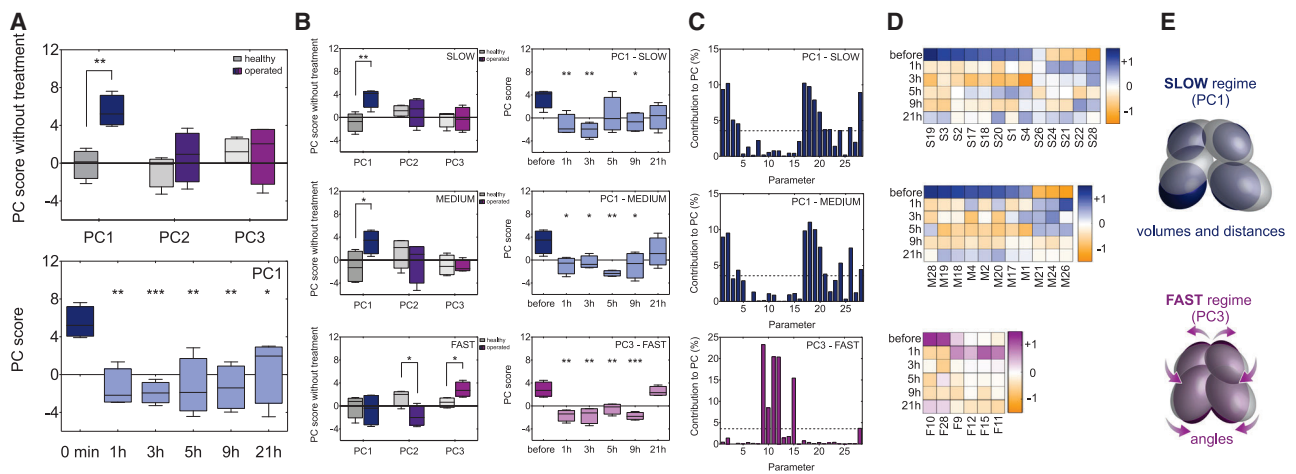


Figure 5. Principal-Component Analysis of Spastic Rats Reveals Details of Improved Gait Components after MPH-220 Treatment

(A and B) Box and whiskers (min to max) representation of global (A) and speed-specific (B) principal-component (PC) analysis of gait parameters of healthy (gray) and operated (colored) animals before (darker) and after (lighter) MPH-220 treatment.

(C) Parameter contributions to PC1 in the slow and medium regimes and to PC3 in the fast regimes (cf. Figure S5).

(D) Heatmap of major parameters contributing to PC1 (blue-orange) and PC3 (purple-orange; cf. Figure S5).

(E) Schematic representation of MPH-220 effects on paw positions in slow and fast regimes.

See also Figure S5.

pronounced in human patients due to the higher ratio of MyHC I slow skeletal muscle myosin isoform. In human skeletal muscles, the presence of 40%–60% MyHC I isoform, which is not inhibited by MPH-220, highlights another important aspect of this type of muscle relaxation as opposed to nervous-system-targeting medications. Although general weakness of aspecific muscle groups may appear by using both types of muscle relaxants, the MPH-220-based anti-spastic effect is not expected to cause complete immobilization of patients due to the residual muscle tone from the uninhibited slow isoform fraction. Another concern may arise regarding extraocular muscles, which express MYH13 gene product containing Leu required for MPH-220 inhibition (Figure S1). Nevertheless, in adult human extraocular muscles, significant amount of α -cardiac myosin heavy chain is expressed (Kjellgren et al., 2003); therefore, these muscles will also not be completely immobilized by MPH-220. However, these effects might be investigated during future clinical trials. Moreover, based on the complex pathophysiology of spasticity development (Trompetto et al., 2014), we suppose that early treatment with an effective anti-spastic drug will significantly delay the onset and markedly reduce the severity of spastic symptoms after nervous system injuries.

Besides traumatic brain and spinal cord injuries in stroke and cerebral palsy, spasticity is also a common symptom in several other diseases of broad etiology (Table 1). Spasticity is a major component of upper motor neuron lesion syndromes, including multiple sclerosis, amyotrophic lateral sclerosis, spastic paraplegia, multiple system atrophy, and atypical Parkinsonism, and also a characteristic symptom in several skeletal muscle myopathies, such as myotonia congenita, myotonia fluctuans, or certain neurodegenerative diseases. Altogether, spasticity in these syndromes affect nearly

1% of the human population (cca. 55 million spastic patients), and more than 10% of people suffer from often-painful muscle stiffness in low back pain and fibromyalgia (Marques et al., 2017; Vos et al., 2012). Consequently, a nervous-system-independent, safe, and effective treatment is a significant unmet need from both clinical and socio-economical perspectives. Therefore, MPH-220 is a promising anti-spastic drug candidate to improve quality of life and may contribute to extended life expectancy (Blair et al., 2019; Gillard et al., 2015; Slaman et al., 2014; Yi et al., 2019) of these patients and would provide new therapeutic protocols for clinicians in these diverse indications.

STAR★METHODS

Detailed methods are provided in the online version of this paper and include the following:

- KEY RESOURCES TABLE
- RESOURCE AVAILABILITY
 - Lead Contact
 - Materials Availability
 - Data and Code Availability
- EXPERIMENTAL MODEL AND SUBJECT DETAILS
 - Animals
 - Human muscle biopsies
- METHOD DETAILS
 - Materials
 - Proteins
 - ATPase measurement
 - Molecular dynamics simulation
 - Crystallization and data processing
 - Structure determination and refinement

Table 1. Prevalence of Diseases with Broad Etiologies in which Muscle Spasticity Is One of the Major Characteristic Symptoms

Disease	Background	Symptom	Prevalence (per 100,000)	Patient Number	Ratio of Spasticity
Stroke	blood flow disruption in the brain either by a blood clot or by hemorrhage	weakness, paralysis, spasticity, coordination and balance problems, memory problems	100–600 (Kim et al., 2015; Yi et al., 2020)	30 million	38%–46% (Lundström et al., 2008; Opheim et al., 2014; Urban et al., 2010; Wissel et al., 2013; 11–14 million spastic patients)
Multiple sclerosis (MS)	autoimmune disease attacking the myelin sheaths of nerve fibers	fatigue, gait difficulties, numbness, spasticity, weakness, vision problems	300–400 in US (Wallin et al., 2019)	2.3 million	50% ^a (1.5–2 million spastic patients)
Cerebral palsy (CP)	brain development disorders or disruption, due to genetic mutations, infections, trauma, or injury	muscle stiffness, spasticity, ataxia, tremors, gait disorders	150–300 (Kruse et al., 2009; Pulgar et al., 2019; Van Naarden Braun et al., 2016)	17 million	70%–75% (Novak, 2014; Pulgar et al., 2019; 12 to 13 million spastic patients)
Amyotrophic lateral sclerosis (ALS)	degeneration of cortical motor neurons, the motor nuclei of the brainstem, and the anterior horn cells of the spinal cord	muscle weakness, atrophy, spasticity	4 to 5 (Xu et al., 2020)	14–15,000 (US) ^b	40% (Meyer et al., 2019; 6,000 spastic patients)
Traumatic brain injury (TBI)	blow or jolt to the head or a head injury that disrupts normal functions	paralysis, sensory impairments, headaches, coordination, spasticity	1% (up to 15%; Dewan et al., 2018), 475,000 children/year (US; Enslin et al., 2020)	1.7–2 million new TBI/year in US (Enslin et al., 2020), 68–71 million worldwide (Dewan et al., 2018)	5%–19% (Bose et al., 2015; Verplancke et al., 2005; 30–35 million spastic patients)
Multiple system atrophy (MSA)	progressive neurodegenerative disease with alpha-synuclein accumulation in glia (form of atypical Parkinsonism)	slow movement, muscle stiffness, spasticity, incoordination, tremors, bladder control problems	2–6 (Bjornsdottir et al., 2013)		
Spastic paraplegia	defects in transport of proteins, lipids through long nerve fibers (axons)	progressive gait disorder, spasticity	3–6		
Myotonia congenita (Becker disease)	abnormality of skeletal muscle membranes resulting in hyperexcitability	painless spasm, difficulty relaxing muscles (myotonia), rigidity, abnormally enlarged muscles (hypertrophy)	1 to 2 (Romitti et al., 2015)		
Spinal cord injury or tumors	nerve damage due to, e.g., thoracic spine herniated discs damage the nerves	pain, increased reflexes in legs that can cause spasticity, muscle weakness, numbness or tingling	2–8 (Witiw and Fehlings, 2015)		

^aWHO Atlas multiple sclerosis resources in the world 2008 (http://www.who.int/mental_health/neurology)

^bNIH amyotrophic lateral sclerosis (ALS) brochure (<https://www.ninds.nih.gov/Disorders>)

- Isometric force measurement
- Non-invasive measurement of cardiovascular and respiratory functions
- Concentration measurement from tissue samples
- Spasticity animal model
- Neural network based deep-learning analysis of movements in open-field tests
- Cylinder assay
- Safety panel measurements

● QUANTIFICATION AND STATISTICAL ANALYSIS

SUPPLEMENTAL INFORMATION

Supplemental Information can be found online at <https://doi.org/10.1016/j.cell.2020.08.050>.

ACKNOWLEDGMENTS

We would like to thank Prof. Árpád Dobolyi for help in rat operations; Máté Winternitz, Noémi Karnok, Kinga Oravec, and Henrietta Hóf for technical assistance; and beam line scientists of PX2A (SOLEIL synchrotron) for excellent support during data collection. We also thank Prof. James R. Sellers (NIH-NHLBI), Ádám Miklósi (ELTE), and Csaba Szalontai (ELTE) for detailed discussions and helpful comments on the manuscript and Prof. Matthias Preller (MHH) for helpful discussions regarding MD simulations. This study has been supported by the Hungarian National Research, Development and Innovation Office (NVKP 16-1-2016-0051 to M.G., A.Á.R., and A.M.-C.) and the Hungarian Ministry of Finance (GINOP-2.1.7-15-2016-02580 to M.G. and A.Á.R.). L.C. is the recipient of a PhD fellowship from Ligue Contre le Cancer IP/SC-16058. A.H. was supported by grants from CNRS, FRM DCM20181039553, ANR-17-CE11-0029-01, and AFM 21805. The A.H. team is part of the Labex CelTisPhyBio:11-LBX-0038, which is part of the IDEX PSL (ANR-10-IDEX-0001-02 PSL). D.V.T., K.M.R., and J.A.S. are supported by National Institutes of Health grants R01 GM033289 and R01 HL117138. D.V.T. is supported by an American Heart Association postdoctoral fellowship (17POST33411070).

AUTHOR CONTRIBUTIONS

Conceptualization, M.G., S.K., and A.M.-C.; Formal Analysis, M.G., Á.I.H., D.T., S.K.S., C. Kurdi, L.C., C. Kikuti, I.L., A.H., and A.M.-C.; Funding Acquisition, M.G., J.A.S., A.Á.R., M.K., S.K., and A.M.-C.; Investigation, M.G., Á.I.H., D.T., S.K.S., M.P., C. Kurdi, L.C., C. Kikuti, K.M.R., D.V.T., I.L., E.P., and A.M.-C.; Methodology Development, M.G., M.P., L.C., C. Kikuti, I.L., A.H., and A.M.-C.; Supervision, M.G., M.K., and A.M.-C.; Validation, M.G., Á.I.H., D.T., and A.M.-C.; Visualization, M.G. and A.M.-C.; Writing, M.G. and A.M.-C.; Software Development, D.T.; Crystallization and Structure Determination, L.C.; Structure Refinement, C. Kikuti; Preparation of Human Cardiac Myosin Sample, K.M.R. and D.V.T.; Supervision for Human Cardiac Myosin Sample, J.A.S.; Writing – Review & Editing, A.Á.R. and M.K.; Funding Acquisition for Crystallization and Structure Determination, A.H.

DECLARATION OF INTERESTS

The authors declare the following competing interests: employment, A.M.-C. and M.G. are owners of Motorpharma, Ltd. and A.Á.R. and M.G. are part-time employed by Motorpharma, Ltd.; related patents, PCT/EP2017/051829, WO/2017/129782, HU1800129A2, PCT/HU2019/050017, WO/2019/202346A2, and WO/2019/202346A3; J.A.S. is a cofounder and member of the scientific advisory boards of Cytokinetics and MyoKardia, biotechnology companies developing small molecules that target the sarcomere for the treatment of various muscle diseases; K.M.R. is on the scientific advisory board at MyoKardia; and J.A.S., D.V.T., and K.M.R. are cofounders of Kainomyx Inc., a biotechnology company focused on developing small molecules to target tropical diseases.

Received: May 23, 2020
Revised: July 24, 2020
Accepted: August 27, 2020
Published: October 8, 2020

SUPPORTING CITATIONS

The following references appear in the Supplemental Information: Billington et al. (2013); Várkuti et al., 2016; Kovács et al. (2003); Wang et al. (2003); Zhang et al. (2017).

REFERENCES

- Allingham, J.S., Smith, R., and Rayment, I. (2005). The structural basis of blebbistatin inhibition and specificity for myosin II. *Nat. Struct. Mol. Biol.* *12*, 378–379.
- Berman, H., Henrick, K., and Nakamura, H. (2003). Announcing the worldwide Protein Data Bank. *Nat. Struct. Biol.* *10*, 980.
- Billington, N., Wang, A., Mao, J., Adelstein, R.S., and Sellers, J.R. (2013). Characterization of three full-length human nonmuscle myosin II paralogs. *J. Biol. Chem.* *288*, 33398–33410.
- Bjornsdottir, A., Gudmundsson, G., Blondal, H., and Olafsson, E. (2013). Incidence and prevalence of multiple system atrophy: a nationwide study in Iceland. *J. Neurol. Neurosurg. Psychiatry* *84*, 136–140.
- Blair, E., Langdon, K., McIntyre, S., Lawrence, D., and Watson, L. (2019). Survival and mortality in cerebral palsy: observations to the sixth decade from a data linkage study of a total population register and National Death Index. *BMC Neurol.* *19*, 111.
- Bose, P., Hou, J., and Thompson, F.J. (2015). Traumatic brain injury (TBI)-induced spasticity: neurobiology, treatment, and rehabilitation. In *Brain Neurotrauma: Molecular, Neuropsychological, and Rehabilitation Aspects*, F.H. Kobeissy, ed. (CRC).
- Bricogne, G., Blanc, E., Brandl, M., Flensburg, C., Keller, P., Paciorek, W., Roversi, P., Sharff, A., Smart, O.S., Vonrhein, C., et al. (2017). BUSTER version 2.10.3 (Global Phasing).
- Careta, M.F., Delgado, L., and Patriota, R. (2015). Report of allergic reaction after application of botulinum toxin. *Aesthet. Surg. J.* *35*, NP102–NP105.
- Coluccio, L.M. (2020). Myosins and disease. *Adv. Exp. Med. Biol.* *1239*, 245–316.
- Cope, M.J., Whisstock, J., Rayment, I., and Kendrick-Jones, J. (1996). Conservation within the myosin motor domain: implications for structure and function. *Structure* *4*, 969–987.
- Dewan, M.C., Rattani, A., Gupta, S., Baticulon, R.E., Hung, Y., Punchak, M., Agrawal, A., Adeleye, A.O., Shrimel, M.G., Rubiano, A.M., et al. (2018). Estimating the global incidence of traumatic brain injury. *J. Neurosurg.* *130*, 1080–1097.
- Emsley, P., and Cowtan, K. (2004). Coot: model-building tools for molecular graphics. *Acta Crystallogr. D Biol. Crystallogr.* *60*, 2126–2132.
- England, J., and Loughna, S. (2013). Heavy and light roles: myosin in the morphogenesis of the heart. *Cell. Mol. Life Sci.* *70*, 1221–1239.
- Enslin, J.M.N., Rohlwink, U.K., and Figaji, A. (2020). Management of spasticity after traumatic brain injury in children. *Front. Neurol.* *11*, 126.
- Gillard, P.J., Sucharew, H., Kleindorfer, D., Belagaje, S., Varon, S., Alwell, K., Moomaw, C.J., Woo, D., Khatri, P., Flaherty, M.L., et al. (2015). The negative impact of spasticity on the health-related quality of life of stroke survivors: a longitudinal cohort study. *Health Qual. Life Outcomes* *13*, 159.
- Gotoh, T., Miyazaki, Y., Sato, W., Kikuchi, K., and Bentley, W.E. (2001). Proteolytic activity and recombinant protein production in virus-infected Sf-9 insect cell cultures supplemented with carboxyl and cysteine protease inhibitors. *J. Biosci. Bioeng.* *92*, 248–255.
- Gourinath, S., Himmel, D.M., Brown, J.H., Reshetnikova, L., Szent-Györgyi, A.G., and Cohen, C. (2003). Crystal structure of scallop Myosin s1 in the

- pre-power stroke state to 2.6 a resolution: flexibility and function in the head. *Structure* 11, 1621–1627.
- Gyimesi, M., Kintszes, B., Bodor, A., Perczel, A., Fischer, S., Bagshaw, C.R., and Málnási-Csizmadia, A. (2008). The mechanism of the reverse recovery step, phosphate release, and actin activation of Dictyostelium myosin II. *J. Biol. Chem.* 283, 8153–8163.
- Heissler, S.M., and Manstein, D.J. (2011). Comparative kinetic and functional characterization of the motor domains of human nonmuscle myosin-2C isoforms. *J. Biol. Chem.* 286, 21191–21202.
- Kawana, M., Sarkar, S.S., Sutton, S., Ruppel, K.M., and Spudich, J.A. (2017). Biophysical properties of human β -cardiac myosin with converter mutations that cause hypertrophic cardiomyopathy. *Sci. Adv.* 3, e1601959.
- Kim, A.S., Cahill, E., and Cheng, N.T. (2015). Global stroke belt: geographic variation in stroke burden worldwide. *Stroke* 46, 3564–3570.
- Kjellgren, D., Thornell, L.E., Andersen, J., and Pedrosa-Domellöf, F. (2003). Myosin heavy chain isoforms in human extraocular muscles. *Invest. Ophthalmol. Vis. Sci.* 44, 1419–1425.
- Kovács, M., Wang, F., Hu, A., Zhang, Y., and Sellers, J.R. (2003). Functional divergence of human cytoplasmic myosin II: kinetic characterization of the non-muscle IIA isoform. *J. Biol. Chem.* 278, 38132–38140.
- Kovács, M., Tóth, J., Hetényi, C., Málnási-Csizmadia, A., and Sellers, J.R. (2004). Mechanism of blebbistatin inhibition of myosin II. *J. Biol. Chem.* 279, 35557–35563.
- Kruse, M., Michelsen, S.I., Flachs, E.M., Brønnum-Hansen, H., Madsen, M., and Uldall, P. (2009). Lifetime costs of cerebral palsy. *Dev. Med. Child Neurol.* 51, 622–628.
- Laskowski, R.A., and Swindells, M.B. (2011). LigPlot+: multiple ligand-protein interaction diagrams for drug discovery. *J. Chem. Inf. Model.* 51, 2778–2786.
- Li, S. (2017). Spasticity, motor recovery, and neural plasticity after stroke. *Front. Neurol.* 8, 120.
- Limouze, J., Straight, A.F., Mitchison, T., and Sellers, J.R. (2004). Specificity of blebbistatin, an inhibitor of myosin II. *J. Muscle Res. Cell Motil.* 25, 337–341.
- Lundström, E., Terént, A., and Borg, J. (2008). Prevalence of disabling spasticity 1 year after first-ever stroke. *Eur. J. Neurol.* 15, 533–539.
- Maier, J.A., Martinez, C., Kasavajhala, K., Wickstrom, L., Hauser, K.E., and Simmerling, C. (2015). ff14SB: improving the accuracy of protein side chain and backbone parameters from ff99SB. *J. Chem. Theory Comput.* 11, 3696–3713.
- Málnási-Csizmadia, A., and Kovács, M. (2010). Emerging complex pathways of the actomyosin powerstroke. *Trends Biochem. Sci.* 35, 684–690.
- Margossian, S.S., and Lowey, S. (1982). Preparation of myosin and its subfragments from rabbit skeletal muscle. *Methods Enzymol.* 85, 55–71.
- Marques, A.P., Santo, A.S.D.E., Berssaneti, A.A., Matsutani, L.A., and Yuan, S.L.K. (2017). Prevalence of fibromyalgia: literature review update. *Rev. Bras. Reumatol. Engl.* 57, 356–363.
- Martin, A., Abogunrin, S., Kurth, H., and Dinet, J. (2014). Epidemiological, humanistic, and economic burden of illness of lower limb spasticity in adults: a systematic review. *Neuropsychiatr. Dis. Treat.* 10, 111–122.
- Mathis, A., Mamidanna, P., Cury, K.M., Abe, T., Murthy, V.N., Mathis, M.W., and Bethge, M. (2018). DeepLabCut: markerless pose estimation of user-defined body parts with deep learning. *Nat. Neurosci.* 21, 1281–1289.
- McCoy, A.J., Grosse-Kunstleve, R.W., Adams, P.D., Winn, M.D., Storoni, L.C., and Read, R.J. (2007). Phaser crystallographic software. *J. Appl. Cryst.* 40, 658–674.
- Medical Advisory, S.; Medical Advisory Secretariat (2005). Intrathecal baclofen pump for spasticity: an evidence-based analysis. *Ont. Health Technol. Assess. Ser.* 5, 1–93.
- Meleger, A.L. (2006). Muscle relaxants and antispasticity agents. *Phys. Med. Rehabil. Clin. N. Am.* 17, 401–413.
- Meyer, T., Funke, A., Münch, C., Kettemann, D., Maier, A., Walter, B., Thomas, A., and Spittel, S. (2019). Real world experience of patients with amyotrophic lateral sclerosis (ALS) in the treatment of spasticity using tetrahydrocannabinol:cannabidiol (THC:CBD). *BMC Neurol.* 19, 222.
- Miyata, S., Minobe, W., Bristow, M.R., and Leinwand, L.A. (2000). Myosin heavy chain isoform expression in the failing and nonfailing human heart. *Circ. Res.* 86, 386–390.
- Mukherjee, A., and Chakravarty, A. (2010). Spasticity mechanisms - for the clinician. *Front. Neurol.* 1, 149.
- Nath, T., Mathis, A., Chen, A.C., Patel, A., Bethge, M., and Mathis, M.W. (2019). Using DeepLabCut for 3D markerless pose estimation across species and behaviors. *Nat. Protoc.* 14, 2152–2176.
- NIH (2012). Dantrolene. In *LiverTox: Clinical and Research Information on Drug-Induced Liver Injury* (National Institute of Diabetes and Digestive and Kidney Diseases).
- Novak, I. (2014). Evidence-based diagnosis, health care, and rehabilitation for children with cerebral palsy. *J. Child Neurol.* 29, 1141–1156.
- Opheim, A., Danielsson, A., Alt Murphy, M., Persson, H.C., and Sunnerhagen, K.S. (2014). Upper-limb spasticity during the first year after stroke: stroke arm longitudinal study at the University of Gothenburg. *Am. J. Phys. Med. Rehabil.* 93, 884–896.
- Orsnes, G.B., Sørensen, P.S., Larsen, T.K., and Ravnborg, M. (2000). Effect of baclofen on gait in spastic MS patients. *Acta Neurol. Scand.* 101, 244–248.
- Pavone, V., Testa, G., Restivo, D.A., Cannavò, L., Condorelli, G., Portinaro, N.M., and Sessa, G. (2016). Botulinum toxin treatment for limb spasticity in childhood cerebral palsy. *Front. Pharmacol.* 7, 29.
- Paxinos, G., and Watson, C. (2007). *The Rat Brain in Stereotaxic Coordinates*, Sixth Edition (Academic/Elsevier).
- Planelles-Herrero, V.J., Hartman, J.J., Robert-Paganin, J., Malik, F.I., and Houdusse, A. (2017). Mechanistic and structural basis for activation of cardiac myosin force production by omecamtiv mecarbil. *Nat. Commun.* 8, 190.
- Pollard, C.E., Abi Gerges, N., Bridgland-Taylor, M.H., Easter, A., Hammond, T.G., and Valentin, J.P. (2010). An introduction to QT interval prolongation and non-clinical approaches to assessing and reducing risk. *Br. J. Pharmacol.* 159, 12–21.
- Pratt, S.J.P., and Lovering, R.M. (2014). A stepwise procedure to test contractility and susceptibility to injury for the rodent quadriceps muscle. *J. Biol. Methods* 1, e8.
- Pulgar, S., Bains, S., Gooch, J., Chambers, H., Noritz, G.H., Wright, E., Sawhney, T.G., Pyenson, B., and Ferro, C. (2019). Prevalence, patterns, and cost of care for children with cerebral palsy enrolled in Medicaid managed care. *J. Manag. Care Spec. Pharm.* 25, 817–822.
- Romitti, P.A., Zhu, Y., Puzhankara, S., James, K.A., Nabukera, S.K., Zamba, G.K., Ciafaloni, E., Cunniff, C., Druschel, C.M., Mathews, K.D., et al.; MD STARnet (2015). Prevalence of Duchenne and Becker muscular dystrophies in the United States. *Pediatrics* 135, 513–521.
- Rychlik, R., Kreimendahl, F., Schnur, N., Lambert-Baumann, J., and Dressler, D. (2016). Quality of life and costs of spasticity treatment in German stroke patients. *Health Econ. Rev.* 6, 27.
- Seidel, J.C. (1980). Fragmentation of gizzard myosin by alpha-chymotrypsin and papain, the effects on ATPase activity, and the interaction with actin. *J. Biol. Chem.* 255, 4355–4361.
- Slaman, J., Roebroek, M., van der Slot, W., Twisk, J., Wensink, A., Stam, H., and van den Berg-Emons, R.; LEARN 2 MOVE Research Group (2014). Can a lifestyle intervention improve physical fitness in adolescents and young adults with spastic cerebral palsy? A randomized controlled trial. *Arch. Phys. Med. Rehabil.* 95, 1646–1655.
- Smit, C.A., and Slim, E.J. (2008). Heart conduction problems in a tetraplegic patient caused by a single therapeutic dosage of Baclofen. *Spinal Cord* 46, 317–318.
- Sommese, R.F., Sung, J., Nag, S., Sutton, S., Deacon, J.C., Choe, E., Leinwand, L.A., Ruppel, K., and Spudich, J.A. (2013). Molecular consequences of the R453C hypertrophic cardiomyopathy mutation on human β -cardiac myosin motor function. *Proc. Natl. Acad. Sci. USA* 110, 12607–12612.

- Spudich, J.A., and Watt, S. (1971). The regulation of rabbit skeletal muscle contraction. I. Biochemical studies of the interaction of the tropomyosin-troponin complex with actin and the proteolytic fragments of myosin. *J. Biol. Chem.* *246*, 4866–4871.
- Straight, A.F., Cheung, A., Limouze, J., Chen, I., Westwood, N.J., Sellers, J.R., and Mitchison, T.J. (2003). Dissecting temporal and spatial control of cytokinesis with a myosin II inhibitor. *Science* *299*, 1743–1747.
- Sweeney, H.L., and Hammers, D.W. (2018). Muscle contraction. *Cold Spring Harb. Perspect. Biol.* *10*, a023200.
- Takács, B., Billington, N., Gyimesi, M., Kintses, B., Málnási-Csizmadia, A., Knight, P.J., and Kovács, M. (2010). Myosin complexed with ADP and blebbistatin reversibly adopts a conformation resembling the start point of the working stroke. *Proc. Natl. Acad. Sci. USA* *107*, 6799–6804.
- Tofferi, J.K., Jackson, J.L., and O'Malley, P.G. (2004). Treatment of fibromyalgia with cyclobenzaprine: A meta-analysis. *Arthritis Rheum.* *51*, 9–13.
- Tong, C.W., Stelzer, J.E., Greaser, M.L., Powers, P.A., and Moss, R.L. (2008). Acceleration of crossbridge kinetics by protein kinase A phosphorylation of cardiac myosin binding protein C modulates cardiac function. *Circ. Res.* *103*, 974–982.
- Trompetto, C., Marinelli, L., Mori, L., Pelosin, E., Currà, A., Molfetta, L., and Abbruzzese, G. (2014). Pathophysiology of spasticity: implications for neurorehabilitation. *BioMed Res. Int.* *2014*, 354906.
- Trybus, K.M. (2000). Biochemical studies of myosin. *Methods* *22*, 327–335.
- Urban, P.P., Wolf, T., Uebele, M., Marx, J.J., Vogt, T., Stoeter, P., Bauermann, T., Weibrich, C., Vucurevic, G.D., Schneider, A., and Wissel, J. (2010). Occurrence and clinical predictors of spasticity after ischemic stroke. *Stroke* *41*, 2016–2020.
- Vagin, A., and Teplyakov, A. (2010). Molecular replacement with MOLREP. *Acta Crystallogr. D Biol. Crystallogr.* *66*, 22–25.
- Van Naarden Braun, K., Doernberg, N., Schieve, L., Christensen, D., Goodman, A., and Yeargin-Allsopp, M. (2016). Birth prevalence of cerebral palsy: a population-based study. *Pediatrics* *137*, 1–9.
- van Tulder, M.W., Touray, T., Furlan, A.D., Solway, S., and Bouter, L.M. (2003). Muscle relaxants for non-specific low back pain. *Cochrane Database Syst. Rev.* (2), CD004252.
- Várkuti, B., H., Képiró, M., Horváth, I., Á., Végner, L., Ráti, S., Zsigmond, Á., Hegyi, G., Lenkei, Z., Varga, M., and Málnási-Csizmadia, A. (2016). A highly soluble, non-phototoxic, non-fluorescent blebbistatin derivative. *Scientific Reports* *6*, 26141.
- Verplancke, D., Snape, S., Salisbury, C.F., Jones, P.W., and Ward, A.B. (2005). A randomized controlled trial of botulinum toxin on lower limb spasticity following acute acquired severe brain injury. *Clin. Rehabil.* *19*, 117–125.
- Vonrhein, C., Flensburg, C., Keller, P., Sharff, A., Smart, O., Paciorek, W., Womack, T., and Bricogne, G. (2011). Data processing and analysis with the autoPROC toolbox. *Acta Crystallogr. D Biol. Crystallogr.* *67*, 293–302.
- Vos, T., Flaxman, A.D., Naghavi, M., Lozano, R., Michaud, C., Ezzati, M., Shibuya, K., Salomon, J.A., Abdalla, S., Aboyans, V., et al. (2012). Years lived with disability (YLDs) for 1160 sequelae of 289 diseases and injuries 1990–2010: a systematic analysis for the Global Burden of Disease Study 2010. *Lancet* *380*, 2163–2196.
- Wallin, M.T., Culpepper, W.J., Campbell, J.D., Nelson, L.M., Langer-Gould, A., Marrie, R.A., Cutter, G.R., Kaye, W.E., Wagner, L., Tremlett, H., et al.; US Multiple Sclerosis Prevalence Workgroup (2019). The prevalence of MS in the United States: a population-based estimate using health claims data. *Neurology* *92*, e1029–e1040.
- Wang, F., Kovacs, M., Hu, A., Limouze, J., Harvey, E.V., and Sellers, J.R. (2003). Kinetic mechanism of non-muscle myosin IIB: functional adaptations for tension generation and maintenance. *J. Biol. Chem.* *278*, 27439–27448.
- Wang, J., Wolf, R.M., Caldwell, J.W., Kollman, P.A., and Case, D.A. (2004). Development and testing of a general amber force field. *J. Comput. Chem.* *25*, 1157–1174.
- Waterhouse, A., Bertoni, M., Bienert, S., Studer, G., Tauriello, G., Gumienny, R., Heer, F.T., de Beer, T.A.P., Rempfer, C., Bordoli, L., et al. (2018). SWISS-MODEL: homology modelling of protein structures and complexes. *Nucleic Acids Res.* *46* (W1), W296–W303.
- Wissel, J., Manack, A., and Brainin, M. (2013). Toward an epidemiology of poststroke spasticity. *Neurology* *80* (3, Suppl 2), S13–S19.
- Witiw, C.D., and Fehlings, M.G. (2015). Acute spinal cord injury. *J. Spinal Disord. Tech.* *28*, 202–210.
- Xu, L., Liu, T., Liu, L., Yao, X., Chen, L., Fan, D., Zhan, S., and Wang, S. (2020). Global variation in prevalence and incidence of amyotrophic lateral sclerosis: a systematic review and meta-analysis. *J. Neurol.* *267*, 944–953.
- Yi, Y.G., Jung, S.H., and Bang, M.S. (2019). Emerging issues in cerebral palsy associated with aging: a physiatrist perspective. *Ann. Rehabil. Med.* *43*, 241–249.
- Yi, X., Luo, H., Zhou, J., Yu, M., Chen, X., Tan, L., Wei, W., and Li, J. (2020). Prevalence of stroke and stroke related risk factors: a population based cross sectional survey in southwestern China. *BMC Neurol.* *20*, 5.
- Yu, Y., Li, L., Shao, X., Tian, F., and Sun, Q. (2013). Establishing a rat model of spastic cerebral palsy by targeted ethanol injection. *Neural Regen. Res.* *8*, 3255–3262.
- Zhang, Y., Li, L., Zhao, Y., Han, H., Hu, Y., Liang, D., Yu, B., and Kou, J. (2017). The myosin II inhibitor, blebbistatin, ameliorates FeCl₃-induced arterial thrombosis via the GSK3 β -NF- κ B pathway. *Int. J. Biol. Sci.* *13*, 630–639.
- Zorowitz, R.D., Gillard, P.J., and Brainin, M. (2013). Poststroke spasticity: sequelae and burden on stroke survivors and caregivers. *Neurology* *80* (3, Suppl 2), S45–S52.

STAR★METHODS

KEY RESOURCES TABLE

REAGENT or RESOURCE	SOURCE	IDENTIFIER
Bacterial Strains		
<i>Salmonella typhimurium</i> TA98 (<i>hisD3052</i>)	Xenometrix AG	Cat# A10-210
<i>Salmonella typhimurium</i> TA100 (<i>hisG46</i>)	Xenometrix AG	Cat# A10-210
Biological Samples		
Lyophilized rat liver S9, Phenobarbital/ β -Naphthoflavone induced	Xenometrix AG	Cat# A10-210-S2-P
Adult Human Left Ventricular tissue sample	AnaBios Corporation	Cat# Car-148/F
Adult Human Muscle Biopsies	This paper, University of Pécs	N/A
Critical Commercial Assays		
gpcrMAX	DiscoverX® Profiling service, Eurofins	Cat# 86-0115
Caco-2	Absorption and Permeability Services, Eurofins Discovery	Cat# 4560, 4561, 4482, 4483
Predictor™ hERG Fluorescence Polarization Assay	SelectScreen Profiling, Thermo Fisher Scientific	Cat# PBH5698
SelectScreen Kinase Profiling	SelectScreen Profiling, Thermo Fisher Scientific	Cat# A24800, A24801, A28578, A30526, A30527, A30528, A33688, A33689, A33690, PV3382, PV3412, PV3430, PV3432, PV3444, PV3459, PV3639, PV3707, PV3721
SelectScreen Nuclear Receptor Profiling	SelectScreen Profiling, Thermo Fisher Scientific	Cat# A15930, A15931, A15932
CyQUANT™ LDH Cytotoxicity assay	Thermo Fisher Scientific	Cat# C20301
Deposited Data		
Crystal structure of rabbit skeletal muscle myosin MyHC IIb	This paper	PDB: 6YSY
Experimental Models: Cell Lines		
Human Adult Dermal Fibroblasts, adult (HDFa)	GIBCO, Thermo Fisher Scientific	Cat# C0135C
Human Lung Fibroblasts, (HLF)	Cell Applications Inc.	Cat# 506-05a
Sf9 cells in Sf-900 II SFM	GIBCO, Thermo Fisher Scientific	Cat# 11496-015
C2C12 mouse muscle myoblast	ATCC	Cat# CRL-1772
Experimental Models: Organisms/Strains		
Wistar albino rat, Han:WIST SPF	Toxi-Coop Ltd.	N/A
Recombinant DNA		
Plasmid: pFastBac1/NM2A/ α -actinin/FLAG	This paper, Biomatik Co.	N/A
Plasmid: pFastBac1/NM2B/ α -actinin/FLAG	This paper, Biomatik Co.	N/A
Plasmid: pFastBac1/NM2C/ α -actinin/FLAG	This paper, Biomatik Co.	N/A
Plasmid: pFastBac1/NM2C-F490L/ α -actinin/FLAG	This paper, Biomatik Co.	N/A
Plasmid: AdEasy/MYH7/GFP	Spudich Lab., Stanford University, (Kawana et al., 2017)	N/A
Software and Algorithms		
MATLAB 2019	MathWorks	https://www.mathworks.com/
Prism 8	GraphPad	https://www.graphpad.com:443/scientific-software/prism
Illustrator CS6	Adobe Systems	https://www.adobe.com/
Photoshop CS6	Adobe Systems	https://www.adobe.com/
MassLynx	Waters Ltd.	https://www.waters.com/

RESOURCE AVAILABILITY

Lead Contact

Further information and requests for resources and reagents should be directed to and will be fulfilled by the Lead Contact, András Málnási-Csizmadia (malna@elte.hu)

Materials Availability

MPH-inhibitors generated in this study will be made available on request, but we may require a payment and/or a completed Materials Transfer Agreement as there is potential for commercial application.

Data and Code Availability

The published article includes all datasets generated or analyzed during this study. The accession number for the skeletal myosin bound to MPH-220, Mg.ADP.VO₄ reported in this paper is PDB: 6YSY. The atomic model is available in the PDB ([Berman et al., 2003](#)).

EXPERIMENTAL MODEL AND SUBJECT DETAILS

Animals

200–250 g male Wistar rats were obtained from Toxi-Coop Ltd. (Hungary) or Animal Facility, Basic Medical Science Center at Semmelweis University (Hungary). Animals were maintained in standard housing conditions with 12–12-hour light-dark periods and were allowed free access to dry rat food and water. All procedures were conducted in accordance with the ARRIVE guidelines and the guidelines set by the European Communities Council Directive (86/609 EEC) and approved by the Animal Care and Use Committee of the Eötvös University (registration number: 48/1/2015) under the permission numbers: PE/EA/142-5/2020, PE/EA/143-7/2020.

Human muscle biopsies

Human muscle biopsy samples were prepared, processed and measured in accordance with the Recommended Standards for Muscle Biopsies by the European Reference Network for Neuromuscular Diseases and the European Commission and approved by the Regional Research Ethics Committee of the Coordination Centre of Clinical Studies of University of Pécs under the permission number: 8340–PTE 2020. *M.vastus* samples were obtained from female (60%) and male (40%) patients with normal creatine kinase (CK) levels and no or non-specific changes in muscle fibers. *M.soleus* sample was obtained from a female patient with normal creatine kinase (CK) level and non-specific changes in muscle fibers. 50% of patients had undergone electromyography (EMG) examination before biopsy preparation. Neither of the patients had received medications that would affect muscle protein compositions: obtained treatments include antihypertensive medicines, anti-inflammatory drugs and vitamin products.

METHOD DETAILS

Materials

All chemicals were purchased from Sigma-Aldrich (Germany) if otherwise not stated. Sulphobutyl-ether- β -cyclodextrin (Dexolve™ (SBECD)) was obtained from Cyclolab (Hungary). HPLC-grade acetonitrile, chloroform and water were purchased from VWR (PA, USA). Blebbistatin was purchased from Sellekchem (TX, USA), AmBleb [Várkuti et al., 2016](#) is product of Motorpharma Ltd., and isoflurane was purchased from Rotacher-Medical GmbH (Germany). Ames Microplate Format Mutagenicity Assay kit was purchased from Xenometrix (Switzerland).

Proteins

Rabbit actin was prepared as described previously from rabbit muscle acetone powder (Pel-Freez Biologicals Llc., AR, USA) ([Spudich and Watt, 1971](#)). Briefly, 5–6 g muscle acetone powder was soaked into ice cold G-actin Buffer (20 ml/g powder; 2 mM Tris pH 7.7, 0.2 mM CaCl₂, 0.2 mM ATP, 2 mM DTT) and was stirred on ice for 40 min. After stirring wet acetone powder was filtered using filter paper. 2 mM MgCl₂ and 50 mM KCl were added to the filtered solution and further incubated at room temperature for 30 min. KCl was added to the final concentration 0.5 M and was stirred for further 60 min. Solution was centrifuged (40,000 rpm, 90 min, 4°C) and pellet was homogenized in G-buffer and excessively dialyzed against G-buffer. After dialysis, solution was centrifuged (40,000 rpm, 90 min, 4°C) and the supernatant was frozen in liquid nitrogen in 1 mL aliquots. Skeletal muscle myosin subfragment-1 (S1) was prepared from rabbit *m.psoas* according to an earlier published protocol ([Margossian and Lowey, 1982](#)) by α -chymotryptic digestion (0.25 mg/ml α -chymotrypsin, 10 min, 25°C; reaction was stopped with 3 mM PMSF). Psoas S1 prep was further purified on MonoS 5/50 GL column to produce high-quality prep for crystallization. Cardiac muscle myosin S1 was isolated from left ventricle of porcine heart following cardiac myofibril preparation protocol ([Tong et al., 2008](#)) by α -chymotryptic digestion (0.05 mg/ml α -chymotrypsin, 10 min, 25°C; reaction was stopped with 3 mM PMSF). Human cardiac muscle myosin subfragment-1 (S1) was prepared from adult human left ventricular tissue samples obtained from ethically consented donors (AnaBios Corporation) according to earlier published protocol ([Margossian and Lowey, 1982](#)) by α -chymotryptic digestion (0.25 mg/ml

α -chymotrypsin, 9 min, 25°C; reaction was stopped with 3 mM PMSF). Smooth muscle myosin S1 was prepared from chicken gizzard (Trybus, 2000) by activated papain digestion (Seidel, 1980) (0.2 mg/ml papain, 12 min, 25°C; reaction was stopped with 5 mM sodium iodoacetate). Human skeletal muscle myosin was prepared similarly to rabbit skeletal muscle myosin (Margossian and Lowey, 1982). Briefly, biopsies were washed in Rigor Buffer (20 mM MOPS pH 7.4, 40 mM KCl, 2 mM MgCl₂) and myosin was extracted in Myosin Extraction Buffer (20 mM MOPS pH 7.4, 500 mM KCl). Extracted myosin was precipitated in 21-volume ultrapure water with 1 mM EDTA. Myosin was collected in tabletop centrifuge, dissolved in Myosin Extraction Buffer and kept on ice until the measurement. The Sf9 codon optimized sequences for NM2 motor domains (Met¹-Arg⁷⁷⁵ for NM2A, Met¹-Arg⁷⁸² for NM2B (B0) and Met¹-Arg⁷⁹⁹ for NM2C (C0)) fused to an Ala-Ser linker and an artificial α -actinin lever arm: (amino acid sequence: AS-EQTKS-DYLLKRANELVQWINDKQASLESRDFGDSIE-SVQSFMNAHKEYKKTEKPPKQEVSELEAIYNSLQTKLRLLIKREPFVAPAGLTPNEIDST-WSALEKAEQEHAELRIELKRQKKIAVLLQKYNRILKLENWATTKSVYLGSNETGDSI-TAVQAKLKNLEAFDGCQSLEGQSNDDLSI-LAQLTELNYNGVPELTERKDTFFAQW-TGVKSSAETYKNTLLAELERLQKIED) as described earlier for NM2C (Heissler and Manstein, 2011) with C-terminal FLAG-tag after an Ala-Leu linker (amino acid sequence: AL-DYKDDDDK) sequences were synthesized and cloned into pFastBac1 expression vector. The NM2C-F490L construct was also synthesized by Biomatik Co in pFastBac1 expression vector. The pFastBac1/NM2 constructs were overexpressed in Sf9 cells after bacmid preparation from DH10Bac cells. To reduce proteolytic digestion during expression, Pepstatin-A (0.1 mg/l) was added to Sf9 cells (Gotoh et al., 2001). Expressed human β -cardiac myosin S1 (Kawana et al., 2017) was prepared as earlier described (Sommese et al., 2013).

ATPase measurement

Steady-state ATPase measurements were carried out in 50 μ L volume in a flat bottom 384-well plate (Nunc-Thermo Fischer) using NADH-PK/LDH coupled assay described previously (Gyimesi et al., 2008). Briefly, myosin samples were mixed with 2% pyruvate kinase/lactate dehydrogenase (PK/LDH) mixture (Sigma P0294), 1 mM phosphoenol-pyruvate (PEP) and 200 μ M NADH at 25°C in the presence of 0.5 mM ATP and 25 μ M F-actin in ATPase buffer (10 mM MOPS pH 7.0, 4 mM MgCl₂, 2 mM β -mercaptoethanol) for 15 minutes. Absorbance was followed at 340 nm wavelength to follow the decrease of NADH in Microplate Spectrophotometer (BioTek Epoch). ATPase activity was calculated from linear regression of the time dependent absorbance data collected at 340 nm. Different concentrations of inhibitors were added to the reaction in 0.5 μ L DMSO (1% of total volume). DMSO and actin-controls were measured for each measurement set.

Molecular dynamics simulation

Simulations were carried out using the AMBER16 program suite. The ff14SB force field (Maier et al., 2015) was used in all subsequent simulations to model protein interactions. The initial structure of the Fast Human Skeletal myosin-2 motor domain was modeled using structural homology with the SWISS-MODEL server (Waterhouse et al., 2018) using the Human Cardiac myosin-2 motor domain (PDB: 5N69). ADP.VO₄ was substituted to ADP.PO₄. Coordinates and partial charges for MPH-220 were refined using *antechamber* of the AMBERTOOLS package with the AM1 semi-empirical Hamiltonian. Force field parameters for the MPH-220 atoms were adopted from GAFF force field (Wang et al., 2004) based on structural similarity following the suggestions of the *parmchk2* program. We determined the initial position of MPH-220 by RMSD least-square fitting the model's structure with the blebbistatin-*Dyctostelium* motor domain (PDB: 3BZ9) binding pocket. The initial position was then determined by RMSD least-square fitting the tricyclic ring of MPH-220 to blebbistatin's tricyclic ring. The water molecules resolved by crystallography were retained and the model was expanded in an 8-Ångstrom clearance dodecahedron box with TIP3P water molecules for explicit solvation and counterions were added to neutralize the system's net charge. The complex was minimized with 2000 steps steepest descent followed by 4000 steps of conjugate gradient method while applying 10 kcal/(mol Å²) to all atoms except water molecules. The minimization continued with the same protocol while removing the restraint from all H atoms. The same restraints were applied for the following steps. The complex was heated in 3 100-K 20-ps steps to 300 K under NVT conditions, then subsequently equilibrated to 1 bar in 20 ps under NPT conditions. NPT conditions were applied in all further steps. The system was cooled back to 10 K in the next 20 ps. Restraints from this point were only applied to the protein backbone. The system was heated back to 300 K in 10 ps and the simulation was continued for 1 ns. The restraint force was then gradually reduced in 1 ns simulations steps to 5, 1, 0.5 and 0 kcal/(mol Å²). The simulation was then allowed to continue and equilibrate under NPT conditions for a further 200 ns to obtain the final structures. The trajectories were sampled every 50 ps during the simulation.

Crystallization and data processing

MyCH IIb-MPH-220 crystals were obtained by vapor diffusion using a protein solution at 10 mg/ml containing 10 mM MOPS pH 7.3; 50 mM NaCl; 3 mM MgCl₂; 0.2 mM ATP; 3 mM NaN₃; 1 mM DTT; 0.1 mM EGTA; 0.1 mM PMSF; 1 μ g/ml leupeptin, 2mM MgADP, 2mM VO₄, 0.5 mM MPH-220 against a reservoir containing 35% PEG600, 20mM DTT; 100mM HEPES pH 7.0; 5% DMSO at 291K. Optimization of crystallization conditions was performed with trypsin *in situ* proteolysis. Crystals were frozen then shot in the Proxima2 beamline (synchrotron Soleil). X-ray diffraction images were processed with AutoProc (Vornrhein et al., 2011). The crystal belongs to the P2₁2₁2₁ space group with one molecule per asymmetric unit. The data collection and refinement statistics are presented in Figure S3.

Structure determination and refinement

Structure of the motor domain was initially solved by molecular replacement using 1QVI (Gourinath et al., 2003) as a search model in Molrep (Vagin and Teplyakov, 2010), and completed with a second search for the lever arm and its essential light chain from 5N69 (Planelles-Herrero et al., 2017) with Phaser (McCoy et al., 2007). Refinement constraints for the ligand were automatically generated with Grade (Bricogne et al., 2017). The final model was obtained after several cycles of building in Coot (Emsley and Cowtan, 2004) and refinement with the latest 2019 release of BUSTER-TNT (Bricogne et al., 2017).

Isometric force measurement

Isometric force of rat left hindleg was measured by a force meter (Supertech Ltd.) after the hindleg was fixed and stimulated according to earlier published protocol (Pratt and Lovering, 2014). A non-elastic wire was attached to the ankle of the rat and pulled until pre-strained position. Spike^(R) software controlled stimulator (BioStim, Supertech Ltd.) was used to trigger the *n. femoralis* through metal electrodes with 100 Hz, 1 s, 4V, 2.5 minute intervals. Data detection was performed with CED Micro 1401 data acquisition interface. Inhibitors were either dissolved in 200 μ L DMSO for intraperitoneal injection or in 1ml 30% SBECD solution (dissolved in GIBCOTM Dulbeccos's Phosphate Buffered Saline (D-PBS)) for oral administration.

Non-invasive measurement of cardiovascular and respiratory functions

Cardiovascular and respiratory functions were measured using a non-invasive pulse oximeter (MouseOx Plus, Starr Life Sciences Corp., PA, USA). Blood flow parameters shown on figures corresponds to the measured pulse distention, which is the measure of change in blood vessel volumes in the light path of the sensor, which reflects local blood pressure changes. Rats were anesthetized and the neck region was trimmed using a small animal trimmer to facilitate accurate measurements by size specific collar sensor.

Concentration measurement from tissue samples

Animals were treated *i.p.* or *per os* with MPH-220, over-anesthetized and tissue samples were collected and frozen at -80°C . Tissue samples were thawed and homogenized in D-PBS, and chloroform was added to the homogenate. Samples were thoroughly shaken, vortexed and sonicated. After sonication, samples were centrifuged and the chloroform layer was collected. Chloroform extraction was repeated two more times. Chloroform was evaporated in a fume-hood. After chloroform drying, water-acetonitrile solution (50%/50%) was added to the samples, which were again vortexed and sonicated again. Samples were centrifuged and supernatants were collected and transferred into ultra-centrifuge vials and ultracentrifuged at 60,000 rpm, 10°C for 60 minutes before HPLC-MS injection. Peak area of compound in HPLC was determined at 400 nm and concentration of compound was determined from the calibration curve. HPLC-MS conditions were the following: Merck Purosphere STAR RP-18 endcapped 250 mm X 4.6 mm column, mobile phase: isocratic 50% H_2O (0.1% TFA) – 50% ACN (0.09% TFA), injection volume: 20 μ L HPLC, flow rate: 0.5 ml/min, run time: 25 min, detection at 260, 280, 300, 400 and 450 nm, capillary voltage: 3.5 kV, cone voltage: 30 V.

Spasticity animal model

Targeted brain damage was performed to establish a rat model of spastic cerebral palsy. Briefly, animals were pre-anesthetized with 4% isoflurane, which was reduced to 2% after the fixation of the animal on the stereotactic apparatus. First, a 2 cm-long longitudinal incision between ears was carried out, which was followed by the cleaning of the surface of the skull by hydrogen peroxide to visualize the Bregma point. Injection coordinates were determined based on The Rat Brain in Stereotaxic Coordinates, 6th Edition (Paxinos and Watson, 2007): ML -0.8 mm, AP -10 mm and DV 9.7 mm from the dura. A 25 μ L Neuros Syringe (Hamilton, NV, USA) with needle size 22G was used to gently inject 15 μ L ethanol for left pyramidal tract lesion. After the injection the syringe was left in place for 10 minutes, followed by its removal from the brain and the sealing of the wound.

Neural network based deep-learning analysis of movements in open-field tests

The over-ground locomotion of the animals was recorded in an 80 by 80 cm wide plastic open-field box using an 8 mm thick transparent Plexiglas as the bottom panel over the course of 15 minutes. The arena was placed on a custom-made wooden frame in order to raise it 1 m above the ground level, while keeping the transparent bottom unobstructed. A Microsoft Kinect V2 for XBOX ONE (2013) RGB-D sensor was secured approx. 80 cm below the Plexiglas facing upward to capture depth information from inside the open-field arena (Figure 4B). The Kinect sensor was connected to a Windows PC (i5-9500F, GeForce GTX 1050 2 GB, 16GB DDR4) placed in a separate room via the official adaptor (Kinect Adaptor for Windows PC) and a USB extension cable. The Kinect for Windows SDK V2.0.1410.19000 API-s were used to control the Kinect sensor in MATLAB v. R2019b with the Image Acquisition Toolbox Support Package for Kinect for Windows Sensor add-on.

An in-house MATLAB program was used to calibrate the spatial position of the device by measuring the relative distance of the four corners of the arena to the sensor to ensure uniform depth information values in the whole arena during experiments. Another in-house MATLAB program was used for image acquisition by the infrared depth camera (512 \times 424 / 30 FPS) and the RGB camera (1920 \times 1080 / 30 FPS) simultaneously. Video recordings from the depth camera were stored in .mj2 archives using lossless 16-Bit Motion JPEG 2000 compression, while the RGB camera recordings were stored in MP4 formats to allow easy viewer access. The depth video recordings were subjected to a preprocessing MATLAB script to correct the erroneous depth estimates arising

from the time-of-flight depth sensing, such as flying pixels and multipath interference. The modified archives were scaled to preserve intensity values of the region of interest (rat in the arena) and exported as 8-Bit uncompressed AVI videos for further use.

A Resnet-50 deep convolutional neural network was trained to predict distinct body parts (nose, neck, center, right forelimb, left forelimb, right hindlimb, left hindlimb, base of the tail) of the animals on the 8-Bit depth recordings using the DeepLabCut toolbox (Mathis et al., 2018) in the Google Colaboratory python environment. The network training parameters were identical as described in Nath et al. (2019) with the provided pre-trained resnet_v1_50 architecture using stochastic gradient descent optimizer, multi-step learning rate (0.005 until 10000 epochs, 0.02 until 430.000, 0.002 until 500.000), batch size of 1, train-test split of 0.3, and no early stopping. We used ~1000 manually annotated frames for the final training and validation sets (training on 500.000 epochs achieved 1.75 mean pixel error for the training and 7.33 mean pixel error for the validation set). A custom MATLAB script was then used to process the previously modified depth archives (25.000 frames / recording) in conjunction with the error corrected numerical output (X and Y coordinates) of the deep learning algorithm of each labeled body part. The animals were first segmented based on the pixel intensity deviation relative to the background. Each frame was then translated and rotated based on the position and angle of the axis between the center of mass of the animal and the position of its nose to create egocentric recording. This transformation and rotation was then carried out on the body part labels as well. The 3 dimensional position of each limb was calculated by combining the transformed output coordinates of the deep neural net with the depth information of the labeled body parts on each frame of the preprocessed and transformed depth recordings. The three dimensional movement maps were exported to further analyses.

In the final algorithm 95% CI least-squares elliptical fittings were computed on the 3D movement maps of each individual limb of the animals and the gait parameters were calculated (Table S3). Centroid displacement thresholds on moving average function of 100 frames were used to calculate distinct locomotion regimes (1st Regime: < 0.6 pixel deviation, 2nd Regime: > 0.6 and < 1.2 pixel deviation, 3rd Regime: > 1.2 pixel deviation.). The gait parameters were scaled using the Z-score method and subjected to principal component analysis and the results were represented in the 3D PC space together with the 95% CI ellipsoids.

Cylinder assay

Motor functions of spastic rats were tested in an open-top, 21 cm diameter, clear plastic cylinder. Forelimb activity was calculated from number of touches of each forelimb against the wall of the arena. Forelimb touch was defined when the whole palm touched the sidewall of the cylinder. Number of sidewall touches was counted for 3 minutes.

Safety panel measurements

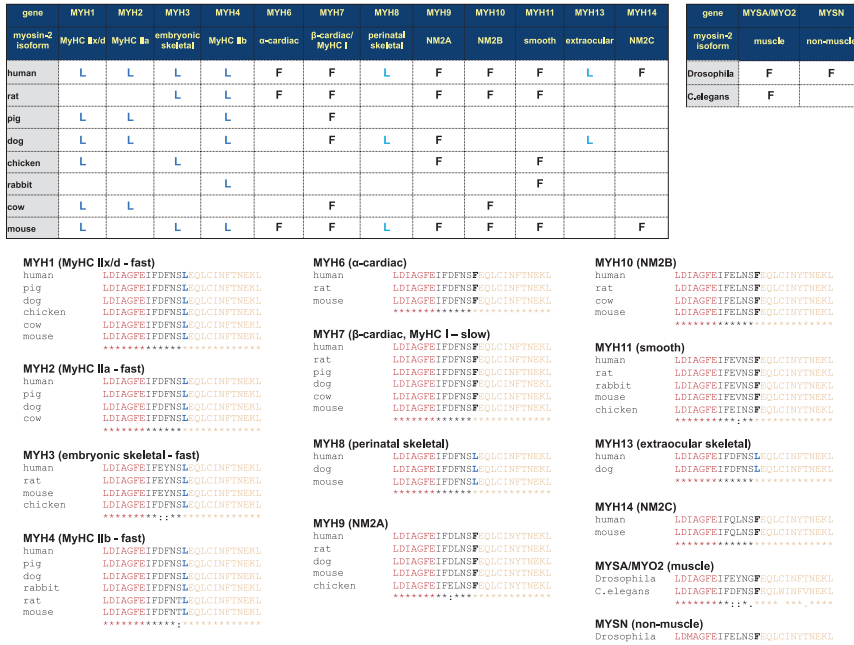
G-protein coupled receptor inhibition and activation was tested in the gpcrMAX panel of DiscoverX® Profiling service (Eurofins). Caco-2 assays were carried out by Absorption and Permeability Services at Eurofins Discovery. Predictor™ hERG Fluorescence Polarization Assay, SelectScreen Kinase Profiling and SelectScreen Nuclear Receptor Profiling was carried out by Thermo Fisher Scientific. Ames MPF™ (Xenometrix, Switzerland) reverse mutagenicity assay was performed according to the manufacturer's guide on TA98 and TA100 bacterial strains in the absence and presence of phenobarbital/β-naphthoflavone-induced rat liver S9 fraction. Cytotoxicity measurements were performed with CyQUANT™ LDH Cytotoxicity assay (Thermo Fisher) according to the manufacturer's protocols with human adult dermal (GIBCO, Thermo Fisher) and lung (Cell Applications Inc., CA, USA) fibroblast strains.

QUANTIFICATION AND STATISTICAL ANALYSIS

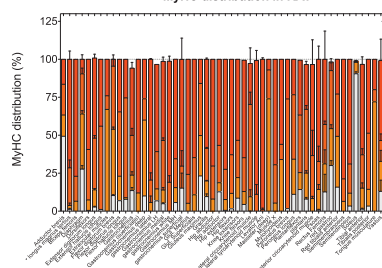
Unless otherwise specified, data are presented as means with standard deviations. Principal component analysis data are presented as box and whiskers representation with min to max whiskers in GraphPad Prism software (Graphpad Software Inc.). ATPase activity analysis, IC₅₀ and maximal inhibition analysis, single exponential fitting and t tests for significance analysis were performed by GraphPad Prism software (Graphpad Software Inc.). Tissue concentration determination was based on standard curve fitting and area under curve analysis by MassLynx software (Waters Ltd.). Principal component analysis was performed by MATLAB software (MathWorks). We did not apply statistical methods to predetermine sample sizes for animal experiments and kept the used subject numbers at a minimum to conform with ARRIVE and 3R principles. Further details of statistical analysis can be found in the figure legends or in the [Method Details](#) section.

Supplemental Figures

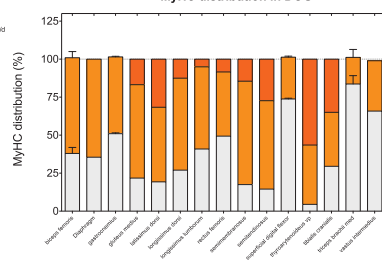
A



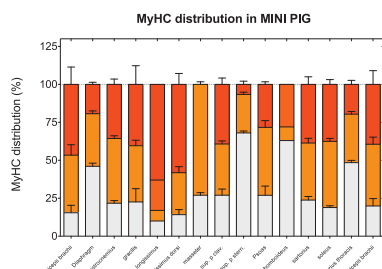
B



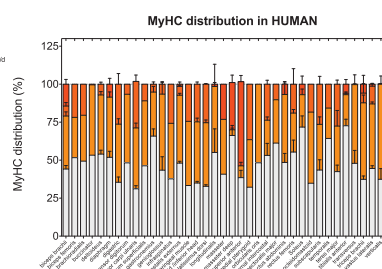
C



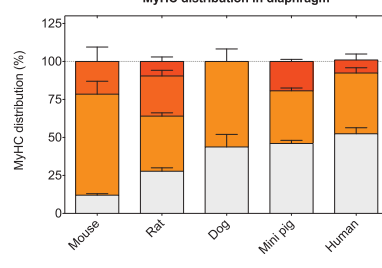
D



E



F



(legend on next page)

Figure S1. Sequence Analysis of Myosin-2 Isoforms from Different Species, Related to Figure 1

(A) The tables show the amino acid residue at the starting point of the HP-helix in myosin-2 isoforms expressed from different MYH genes in eight vertebrate species and the muscle and non-muscle myosin-2 isoforms in *D. melanogaster* and *C. elegans* invertebrate species. The alignments below the tables represent the sequence environment of the relevant Leu (blue L) or Phe (black F) residue, including the switch-2 loop (red) and the N-terminal part of the HP-helix (light orange). These data clearly show that all fast skeletal myosin-2 isoforms in all species contain Leu in the morpholine-interacting position, while Phe is present in all slow type myosin-2 s including both cardiac isoforms at this position. The characteristic difference is even more pronounced when comparing the neighboring residues in the HP-helix, which are practically invariant in all myosin isoforms and species. (B-F) Myosin-2 isoform distribution within different muscle types in different species. Literature-based analysis of myosin-2 isoform composition – determined by SDS-PAGE or immune/enzyme histochemistry – of different muscles in rat (B), dog (C), mini pig (D) and human (E) show significant differences in the proportion of the slow isoform (MyHC I, gray) between the species. While rat muscles contain predominantly fast isoforms (MyHC IIa, IIb, IIx/d, orange), the ratio of fast isoforms in human muscles is between 40%–70%. Distributions in dogs and mini-pigs are in between the rat and human levels. These differences bear important consequences on the expected effect size in different species and may require unique consideration of dosage in non-clinical studies on different species (e.g., rats versus dogs/pigs). The relatively high proportion of slow isoform in human muscles also has important positive consequence on the effect profile of an MPH-220 based anti-spastic drug, because overdosing-related complete muscle tone loss is not expected to occur due to the residual non-inhibited slow myosin contractions. This latter condition confers a huge advantage over the currently used nervous system targeting muscle relaxants, where temporary but complete immobility can occur in case of slight overdose. The large difference in slow isoform proportion can also be seen in the diaphragm of different species (F), which indicates that MPH-220 will be even safer for respiratory functions in humans than in rats.

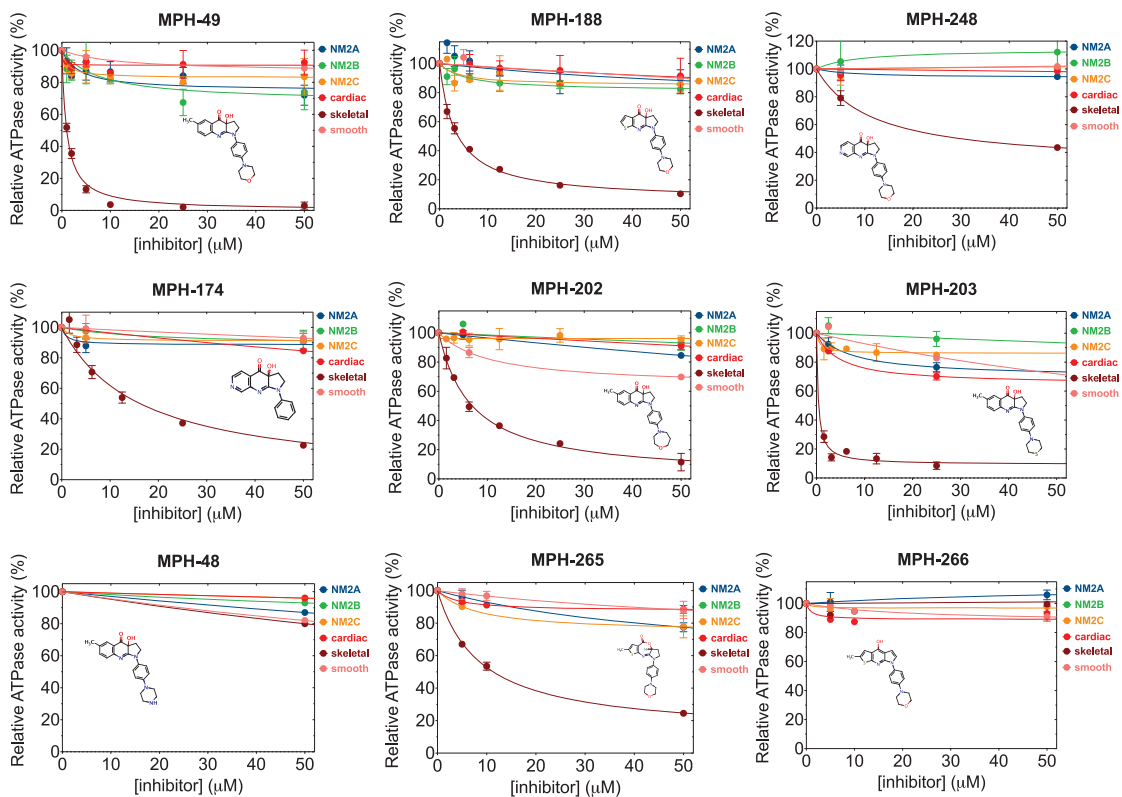


Figure S2. Inhibitory Properties of Different MPH-220 Derivatives, Related to Figure 1

Relative ATPase activities are shown for different MPH-220 derivatives tested during the development of MPH-220. MPH-49 is the morpholine derivative of blebbistatin, which shows selective inhibition; however, its solubility remained blebbistatin-like (less than 50 μM in aqueous solutions). MPH-188 and MPH-248 are morpholine derivatives on different scaffolds of the patented MPH-family. MPH-188 showed drastic improvement in solubility (1 mM in aqueous solutions), but its IC_{50} value for skeletal myosin was slightly worse than that of MPH-220. MPH-248 retained skeletal myosin specificity of the pyridine ring containing core (MPH-174), but its total inhibition and IC_{50} values remained worse than those of MPH-220. We found that the morpholino group (MPH-49) was superior to homomorpholine (MPH-202), thiomorpholine (MPH-203) or piperazine (MPH-48). The IC_{50} of MPH-203 was promising; however, its solubility was even lower than that of MPH-49, suggesting that the optimal ring structure for selective and efficient inhibition is the morpholine ring. We also tried to modify the ring structure of the tricyclic core, but neither modification showed improved properties, confirming that MPH-220 is the optimal structure. Mean \pm SD are shown in all ATPase experiments; $n = 3-9$.

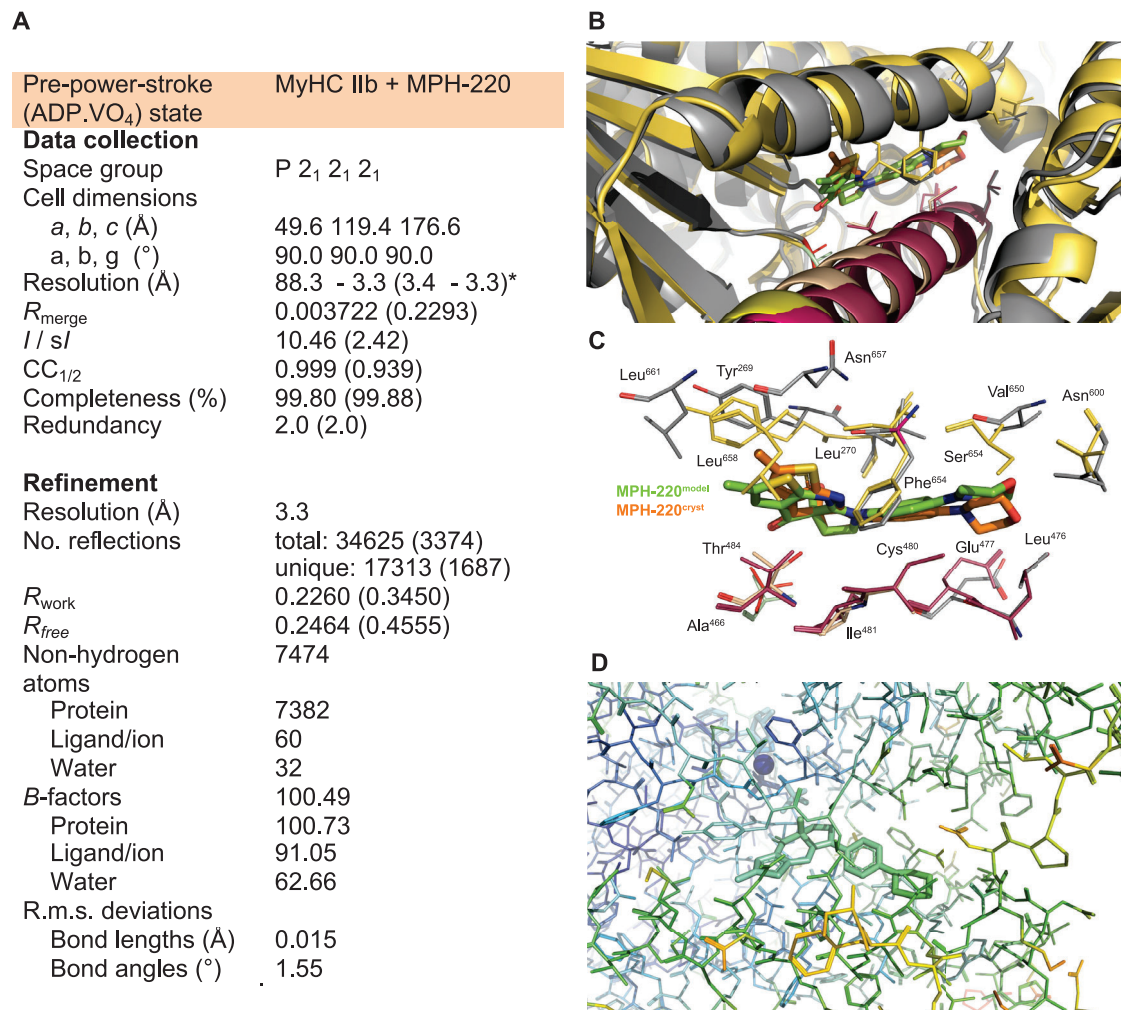


Figure S3. Crystal Structure Refinement Statistics and Comparison of Crystal and Modeled Structures Used for Inhibitor Development, Related to Figure 2

(A) Data collection and refinement statistics (molecular replacement). Data from one crystal. *Values in parentheses are for highest-resolution shell. (B) Cartoon representation of the crystal structure of MyHC IIb (gray/beige), and the superimposed modeled structure of MyHC IIa from molecular dynamic simulations (yellow/maroon). MPH-220 binding site reveals that the position and orientation of MPH-220 in the crystal structure (orange) and in the modeled structure (green) is similar. Amino acid residue carbons in gray (crystal structure) and maroon (model), and carbons for MPH-220 in orange (crystal structure) and green (model) are shown. (C) Close-up of the MPH-220 binding site reveals that HP-helix position is well predicted; in particular, Leu⁴⁷⁶ position is very similar. The alignment also reveals a moderate shift in MPH-220 position between the homology model and the crystal structure; in particular we see slightly different position and orientation of the morpholino group. Still, the homology model predicts well the sub-pocket explored by this cycle; residues Leu⁴⁷⁶, Glu⁴⁷⁷, Cys⁴⁸⁰, Asn⁶⁰⁰ and Val⁶⁵⁰ interact indeed with the morpholino group in both crystal structure and homology model. These results confirm that the modeled structure that we used for inhibitor development (cf. Figures 1 and S2) is reliable and the results from those experiments are trustworthy. (D) Close-up view of the crystal structure with bound MPH-220 colored according to B-factors from 21.1 Å² (dark blue) to 125.2 Å² (red). ADP, VO₄ and MPH-220 are represented by thicker lines, the sphere represents the Mg²⁺ ion.

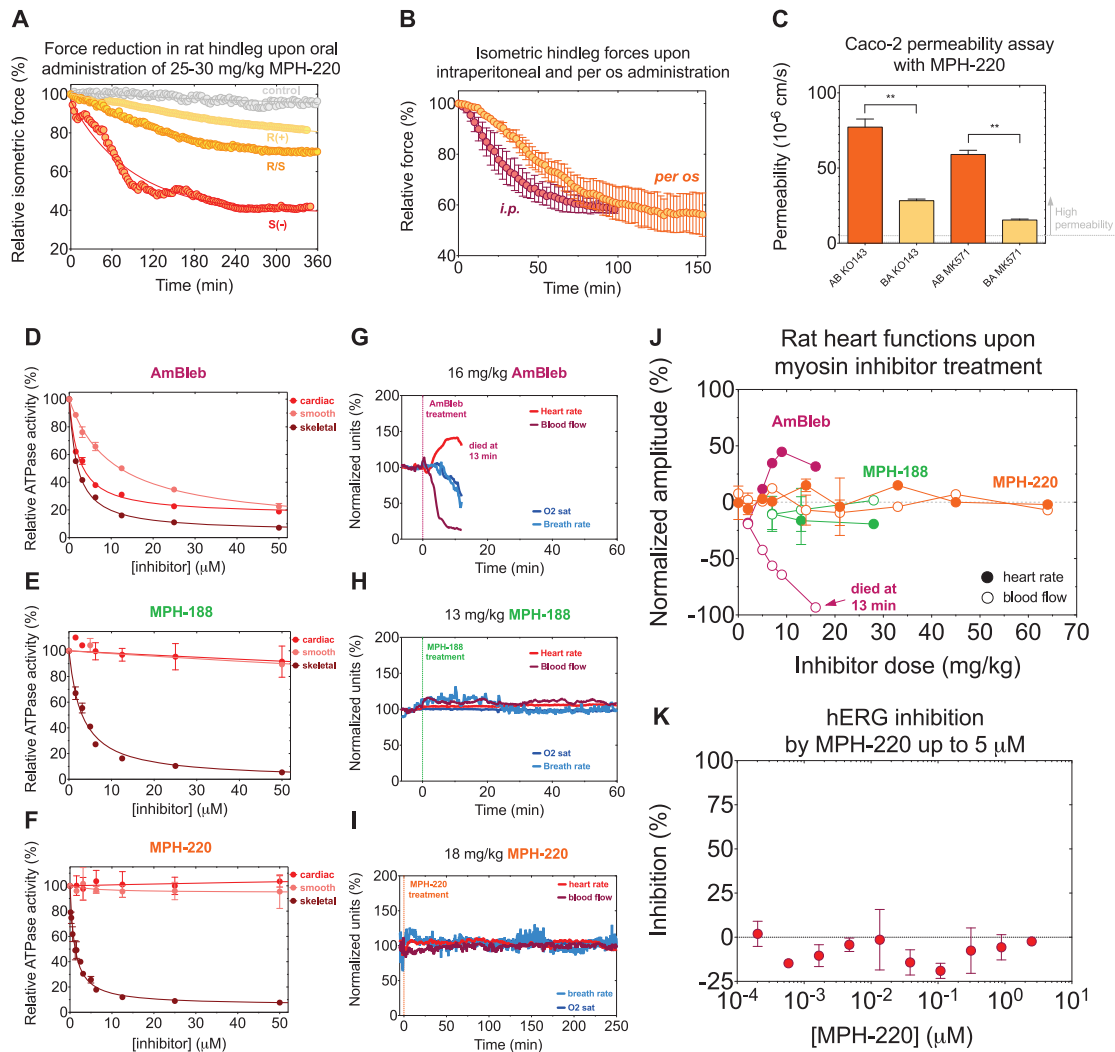
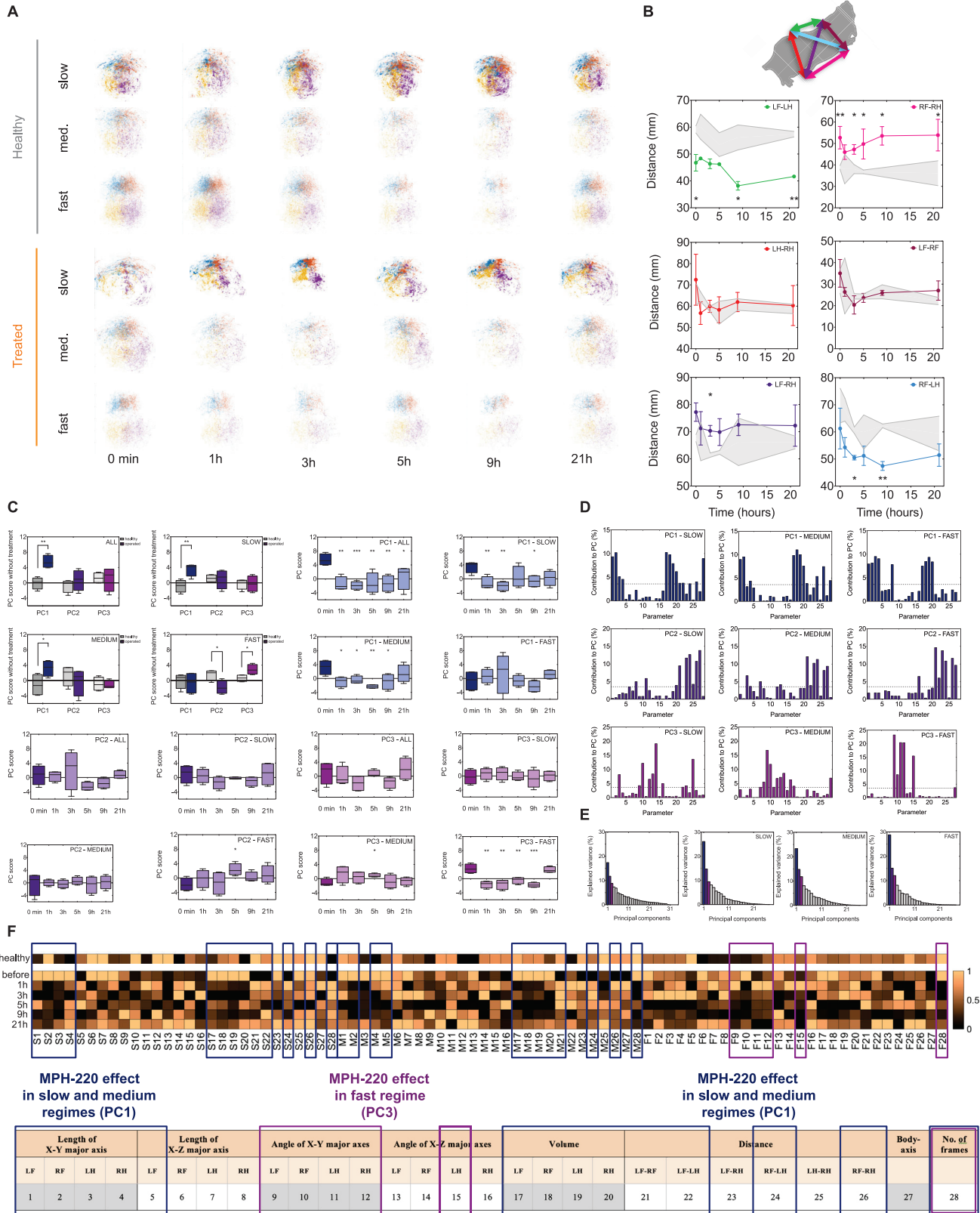


Figure S4. MPH-220 Effects on Isometric Force and Vital Functions, Related to Figure 3

(A) Isometric force reduction in rat hindleg after oral MPH-220 treatment: $\Delta F_{S(-)} = 58\%$, $\Delta F_{R(+)} = 36\%$, $\Delta F_{R/S} = 32\%$, $\tau_{S(-)} = 88$ min, $\tau_{R(+)} = 121$ min, $\tau_{R/S} = 461$ min; muscle fatigue in the control animals: $\Delta F_{\text{contr}} = 8\%$, $\tau_{\text{contr}} = 323$ min. (B) 18 mg/kg MPH-220 was administered to anesthetized rats by intraperitoneal injection in 200 μL DMSO (pink circles) or orally through a gavage tube in 30% SBECD (orange circles). Isometric force decrease rates were very similar ($\tau_{i.p.} = 34$ min) except that oral administration resulted in a 17-minute leg phase – corresponding to absorption of MPH-220 – followed by force decrease phase ($\tau_{p.o.} = 53$ min). Mean \pm SD are shown; $n = 2$. These observations support high gastrointestinal permeability of MPH-220, which was further confirmed by *in vitro* Caco-2 permeability assay (C). (C) Caco-2 permeability assay in the apical-to-basolateral (AB, orange) and basolateral-to-apical (BA, light orange) direction in the presence of two different transporter inhibitors. Mean \pm SD are shown; $n = 2$ (D-F) ATPase activity of skeletal (brown), cardiac (red) and smooth (pink) muscle myosins, measured in the presence of non-selective para-aminoblebbistatin (AmBleb) (D), MPH-188 (E) and MPH-220 (F). Mean \pm SD are shown; $n = 3-12$. (G-I) All three inhibitors were administered to rats in different concentration ranges and cardiovascular (heart rate, blood flow) and respiratory functions (breath rate, oxygen saturation) were monitored. 16 mg/kg AmBleb killed the animals within 15 minutes due to heart failure (G), while neither 13 mg/kg MPH-188 (H) nor 18 mg/kg MPH-220 (I) had any significant effect on cardiovascular and respiratory functions. Note that we measured MPH-220 effect on longer timescales (parallel with force measurements). (J) We repeated the experiments several times and found that MPH-220 does not affect cardiac functions to a greater extent than the solvent excipient during the long anesthetic period (*cf.* Figures 2E and 2F). Data are mean \pm SD, $n = 1-4$. (K) hERG potassium channel inhibition measurement up to 5 μM MPH-220. We measured hERG inhibition up to 5 μM , because the concentrations of MPH-220 in cardiac tissue even upon treatment with high doses (up to 130 mg/kg) were in this concentration range (3-7 μM). At this concentration range we did not observe inhibition of hERG potassium channels and we did not observe any concentration dependence of inhibition on cardiomyocytes, which would otherwise potentiate a drug candidate for QT prolongation leading to life-threatening arrhythmias (Pollard et al., 2010). Mean \pm SEM are shown; $n = 2$.



(legend on next page)

Figure S5. Gait Analysis of MPH-220-Treated Rats, Related to Figures 4 and 5

(A) Paw position distribution of healthy (upper three rows) and treated (lower three rows) animals in the three speed-regimes (slow (less than 0.036 m/s), medium (0.036-0.072 m/s) and high (more than 0.072 m/s)), 1, 3, 5, 9 and 21 hours after the first measurement (healthy control) or before and 1, 3, 5, 9 and 21 hours after 20 mg/kg oral MPH-220 treatment. (B) Averaged distances between the paws in each frame of the 3D recordings in healthy (gray band) and treated (colored dots) animals; green: left fore- and hindlimbs, pink: right fore- and hindlimbs, red: left and right hindlimbs, maroon: left and right forelimbs, purple: left fore- and right hindlimbs, blue: right fore- and left hindlimbs. Schematic representation of distances is shown above the plots. Statistical analyses show that left fore- and hindlimbs are significantly closer in the operated rats than in the healthy animals, however, 1-5 hours after MPH-220 treatment the difference becomes insignificant. The right fore- and hindlimbs are significantly farther in the operated rats before treatment, which becomes non-significant 1 hour after MPH-220 treatment. These together indicate that MPH-220 treatment resulted in a significantly straightened body axis. Data are mean \pm SD; n = 2. (C) Principal component (PC) analysis: PC1, PC2 and PC3 scores of healthy (gray) and operated (colored bars) rats in all, slow, medium-speed and fast movement regimes (upper left quartet). PC1 (blue, upper right quartet), PC2 (eggplant, lower left quartet) and PC3 (purple, lower right quartet) scores before (darker) and after (lighter) 20 mg/kg oral MPH-220 treatment in all, slow, medium-speed and fast movement regimes. Boxplots with min-to-max whiskers, n = 4. (D) Parameter contributions to PC1 (upper row), PC2 (middle row) and PC3 (lower row) in the slow (left column), medium-speed (middle column) and fast (right column) movement regimes. Dotted lines represent the threshold for major contributions to PC (3.57%). Boxplots with min-to-max whiskers, n = 4. (E) Explained variance in all, slow, medium-speed and fast movement regimes; PC1, PC2 and PC3 are colored according to panels C-D. (F) The computed gait parameters were scaled (Z-score) and averaged. The columns represent the individual gait parameters (1-28, defined below the heatmap) in the slow (S1-28), medium-speed (M1-28) and fast (F1-28) movement regimes. The separate row represents the average of healthy animals at zero minute, and the other six rows represent the parameter scores before and 1, 3, 5, 9 and 21 hours after MPH-220 treatment (n = 4). PC analysis revealed that in the slow regime MPH-220 has the largest effect on X-y axis length and the consequent volumes of the ellipsoids representing paw positions in 3D and certain distances between the centers of ellipsoids (blue brackets) contributing to PC1; in the fast regime MPH-220 has the largest effect on the angles of the ellipsoids (purple brackets) contributing to PC3. Parameter description used in PCA calculations: video recordings were analyzed in three walking speed categories. The numbers encode different parameters of the ellipsoids fitted to data points from 3D position analysis. LF: left front limb, RF: right front limb, LH: left hind limb, RH: right hind limb.

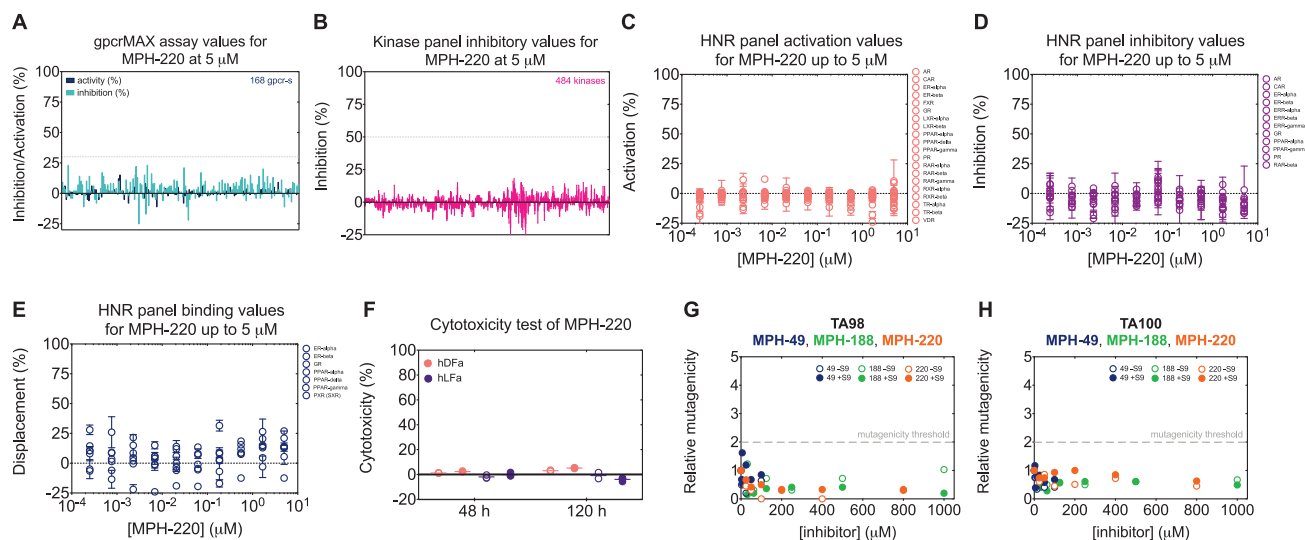


Figure S6. Safety Profiling of MPH-220 Supports Further Drug Development due to Lack of Mutagenicity and Interaction with Off-Target Enzymes, Related to STAR Methods

(A) We tested the effects of 5 μM MPH-220 on 186 different human G-protein-coupled-receptors (GPCRs) covering 60 different receptor families including adrenergic, dopamine, P2Y and serotonin receptor families (by DiscoverX-Eurofins). According to the highly selective nature of MPH-220, neither GPCR was inhibited or activated above 30%, which is a standard reference threshold for hit compounds. (B) Beside the gpcrMAX panel, inhibition of 484 kinases was measured in the presence of 5 μM MPH-220. Neither kinase was inhibited by more than 20%, which indicates that MPH-220 does not interfere with the signal transduction pathways in human cells. This Select Screen Kinase Profiling panel (by Thermo Fisher) contains all available wild-type and the most abundant mutant forms of human kinases. (C-E) MPH-220 was also tested on 23 human hormone nuclear receptors (HNR) at 5 μM concentration (by Thermo Fisher). In agreement with the kinase and GPCR results, all investigated receptors remained unaffected by MPH-220 due to the lack of significant binding to any of the HNRs. Mean \pm SEM are shown; $n = 2$ in (A-E). (F) Cytotoxicity was measured with CyQUANTTM LDH Cytotoxicity assay on human adult dermal fibroblast (hDFa, pink) and human adult lung (hLFa, purple) fibroblast cell lines in the presence of 20 μM (open circles) and 50 μM (closed circles) MPH-220 for 48 and 120 hours. MPH-220 was not toxic to either fibroblast strain at any time point or concentration, confirming its safe use in further developments. As one of the most important requirements for a lead compound, mutagenicity was measured by the OECD/FDA approved Ames reverse mutagenicity assay using the two most sensitive bacterial strains for testing frameshift (TA98, G) and base-pair substitution (TA100 H) mutation both in the absence (open circles) and presence (closed circles) of activated rat liver S9 fraction. Relative mutagenicity did not show MPH-220 concentration dependency and, more importantly, experiments on neither strain resulted in any data points above the threshold (gray dotted line). Besides MPH-220 we also tested the mutagenicity of the other two morpholine derivatives of MPH-220 (*cf.* Figure S2) to elucidate whether the lack of mutagenicity is associated with the morpholine group. Neither MPH-49 nor MPH-188 showed concentration dependent increase in mutagenicity levels and, more importantly, neither showed in data points above the OECD/FDA threshold. Lack of mutagenicity was observed for both TA98 and TA100 *S. typhimurium* strains both in the absence and presence of liver S9 fraction, suggesting that neither the inhibitors nor their major metabolites are mutagenic, which supports safe development of MPH-220 toward human clinical phases.

A.3. MPH-220 may induce rearrangements within the Myo2 Motor

Finally, we aimed at comparing SkMyo2 with or without MPH-220 bound to characterize the rearrangements required for MPH-220 binding. I managed to obtain the structure of SkMyo2 in the pre-powerstroke state at 3.2 Å in the same crystallization condition (Table 16).

SkMyo2 ADP-VO4	
Wavelength	0.98010 Å
Resolution range	71.7 - 3.215 (3.33 - 3.215)
Space group	P 21 21 21
Unit cell	51.1107 120.103 178.75 90 90 90
Total reflections	36400 (3617)
Unique reflections	18232 (1811)
Multiplicity	13.2 (13.0)
Completeness (%)	97.73 (99.94)
Mean I/sigma(I)	10.51 (2.44)
Wilson B-factor	69.39
R-merge	0.05155 (0.2647)
R-meas	0.0729 (0.3743)
R-pim	0.05155 (0.2647)
CC1/2	0.997 (0.862)
Reflections used in refinement	18226 (1811)
Reflections used for R-free	899 (82)
R-work	0.1976 (0.2691)
R-free	0.2429 (0.3975)
CC(work)	0.956 (0.869)
CC(free)	0.930 (0.661)
Number of non-hydrogen atoms	7416
macromolecules	7322
ligands	41
solvent	53
Protein residues	914
RMS(bonds)	0.016
RMS(angles)	1.63
Ramachandran favored (%)	96.99
Ramachandran allowed (%)	2.79
Ramachandran outliers (%)	0.22
Rotamer outliers (%)	2.40
Clashscore	3.89
Average B-factor	75.72
ligands	64.76

Table 16: Data collection and refinement statistics of the SkMyo2 pre-powerstroke state crystal

As for blebbistatin bound to DictyMyo2, MPH-220 binding to SkMyo2 does not result in large changes in the 50 kDa cleft within the motor (RMSD = 0.205 Å aligning the allosteric pocket with or without MPH-220). The most notable change consists in Leu270 moving out of the cleft to allow MPH-220 to bind as described for blebbistatin (Allingham, Smith, and Rayment 2005) (Figure 88).

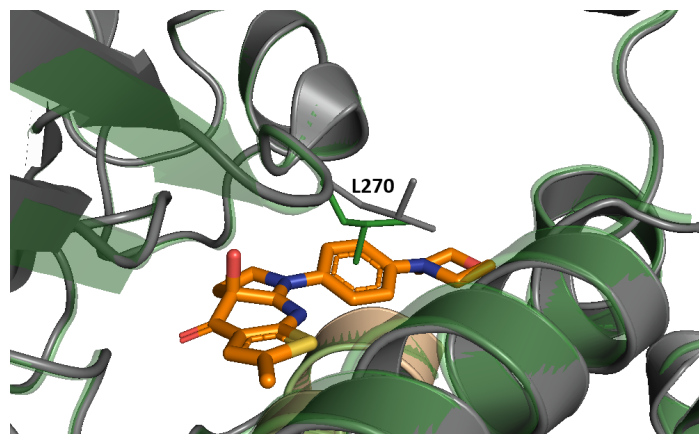


Figure 88: Superimposition of SkMyo2 allosteric pocket with MPH-220 (PDB:6YSY) and without MPH-220.

MPH-220 is pictured in orange, SkMyo2 bound to MPH-220 is pictured in grey and SkMyo2 without MPH-220 is pictured in green.

Yet, strikingly, although the changes in MPH-220 pocket are small, they promote a 3.8 Å difference in the priming of the Lever arm. More precisely, no change was found in the switch-II, the transducer is tilted by 0.8 Å, the relay is shifted by 1.6 Å, the N-terminus subdomain by 1.1 Å, the Converter by 2.5 Å, and finally, the Lever arm is tilted by 3.8 Å (Figure 89). This suggests that MPH-220 could stabilize a state slightly different than the one obtained without drug. Yet whether this finding is due to crystal constraints or whether it is relevant in the context of MPH-220 inhibition and is this change proper to MPH-220 or can be more generally be applied to all blebbistatin derivatives requires further investigation.

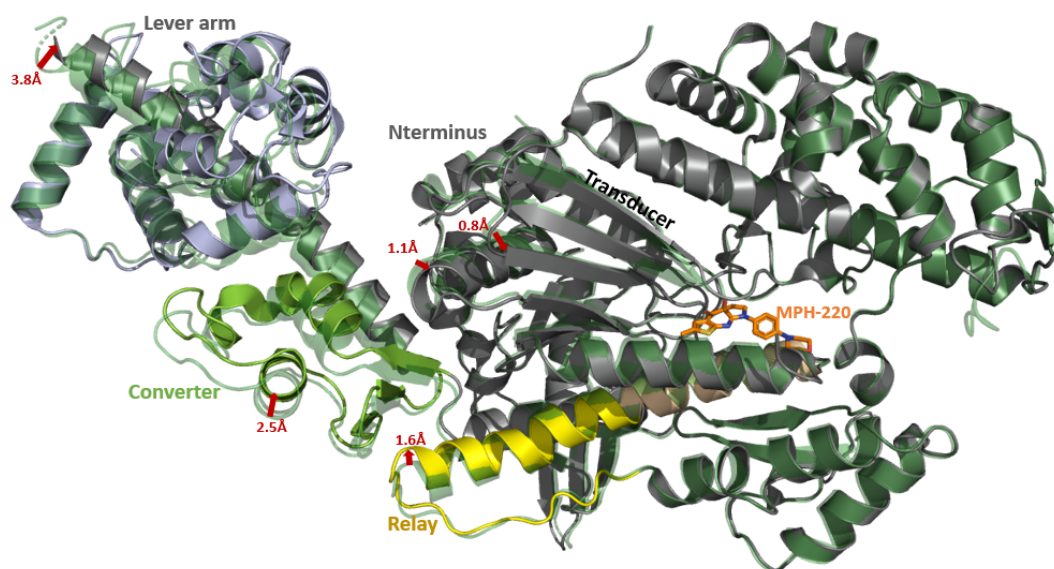


Figure 89: Superimposition of SkMyo2 with MPH-220 (PDB: 6YSY) and without MPH-220.

MPH-220 is pictured in orange, SkMyo2 bound to MPH-220 is pictured in grey and SkMyo2 without MPH-220 is pictured in green.

B. Perspectives

B.1. Potential of blebbistatin derivatives for specific myosin targeting

As we show in [Gyimesi et al. 2020](#), the difference in sequence of only one residue within the blebbistatin allosteric pocket is sufficient to reach high selectivity among different types of Myo2. Thereby selective inhibitors of SkMyo2 (skeletalstatins) ([Figure 90](#)), also obtained by para-substitution of blebbistatin D-ring with a morpholino group (or two other bulk groups) were recently described the same strategy as MPH-220 by another group ([Radnai et al. 2021](#)).

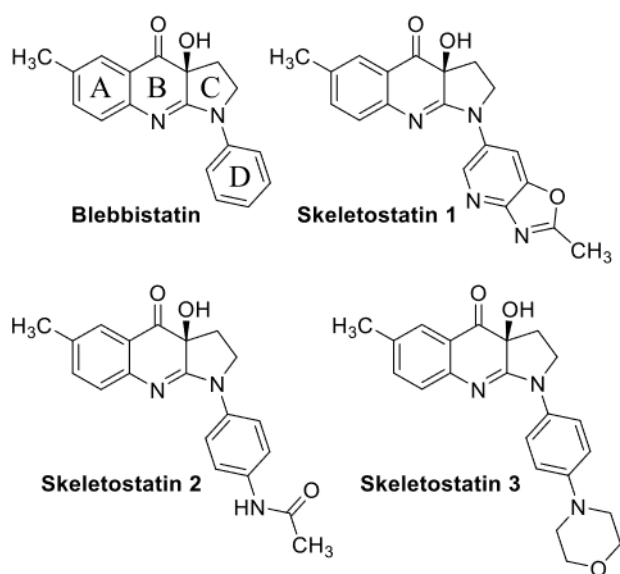


Figure 90: comparison of skeletalstatin and blebbistatin ([Radnai et al. 2021](#))

This emphasizes the potential of the blebbistatin pocket for development of specific inhibitors and could lead to the development of blebbistatin derivatives targeting specifically CardMyo2, SmMyo2 or NM2A/B/C, notably by exploiting the differences found in the least conserved part of the pocket, which is the HW-helix ([Table 17](#)). Actually, even AmBlebb, pNitroBlebb and blebbistatin which are known as inhibitors of Myo2s exhibit relative specificity among them ([Figure 91](#)).

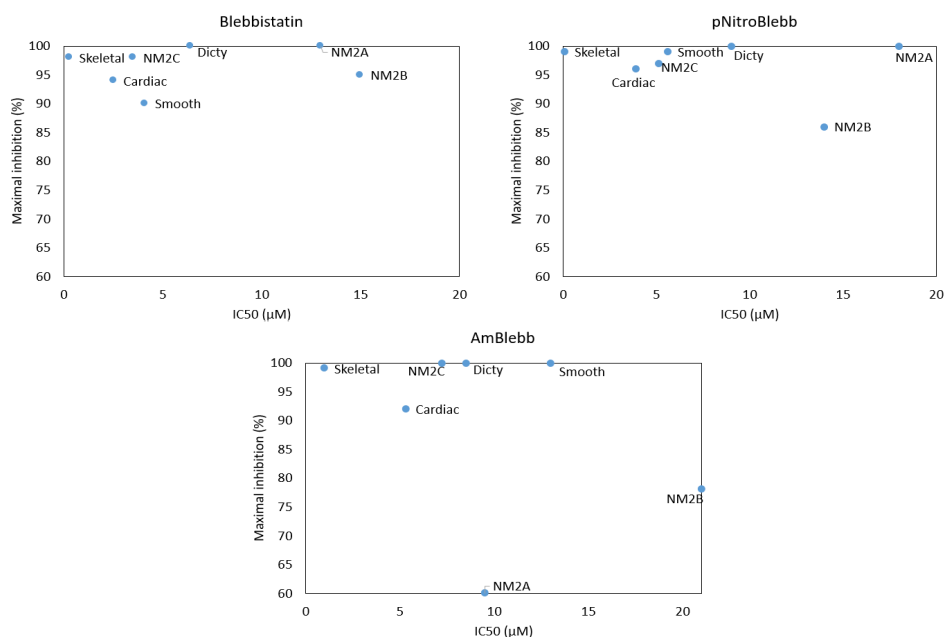


Figure 91: Inhibition of different Myo2 subclasses by blebbistatin, paraNitroBlebbistatin and Amino-Blebbistatin (Gyimesi *et al.* 2021).

For those three compounds, inhibition of NM2A and NM2B is weaker, in particular for AmBlebb. We also noticed that AmBlebb inhibits DictyMyo2 better than SmMyo2, while pNitroBlebb does the opposite. SkMyo2 is the best inhibited Myo2 of all the myosins and the second best IC₅₀ is always found for CardMyo2. Although these differences are not sufficient for making any of these drugs a specific inhibitor of one Myo2 isoform, understanding the origin of these differences and how we can use them for future development of inhibitors is of particular interest.

Thus, our team will continue the collaboration with András Málnási-Csizmadia. Indeed, in the course of the development of MPH-220, they synthesized and characterized the inhibition efficiency of more than 144 molecules. A close look at the difference in their activity for different myosins coupled with co-crystal structures of a selected subset of inhibitors may now lead to a better understanding of the rules of selectivity within the Blebbistatin pocket.

Actually, such knowledge could also be used for the development of specific and potent inhibitors of certain unconventional myosins such as Myo6 for which key residues for blebbistatin binding are rather conserved.

Dicty nb	U50		Sw-II	HP			HW			
	238-240	261-263	455-456	466-467	470-471	474	630	634	637	641
Dicty	RFG	YLL	<u>I</u> S	FE	CI	T	V	Y	Q	L
NM2A	RFG	YLL	IA	FE	CI	T	V	Y	Q	L
NM2B	RFG	YLL	IA	FE	CI	T	V	Y	<u>S</u>	L
NM2C	RFG	YLL	IA	FE	CI	T	V	Y	<u>S</u>	L
Cardiac	RFG	YLL	IA	FE	CI	T	V	<u>H</u>	<u>N</u>	L
Smooth	RFG	YLL	IA	FE	CI	T	V	Y	Q	L
Skeletal	RFG	YLL	IA	<u>L</u> E	CI	T	V	<u>F</u>	<u>N</u>	L
Myo6	RFG	YLL	IA	FE	CI	<u>C</u>	V	<u>F</u>	Q	L

Table 17: Conservation of key residues for blebbistatin binding between conventional myosins and unconventional Myo6

Nevertheless, it should be noted that blebbistatin itself is unable to inhibit Myo6, highlighting the fact that looking only at this subset of residues is not sufficient to predict inhibition. Additional parameters should be considered to identify key parameters influencing binding of blebbistatin and binding of its derivatives, and to understand the rules of selectivity and potency within the Blebbistatin pocket.

Moreover, [Roman, Guedes, et al. \(2018\)](#) pointed out the current difficulty in predicting the efficiency of blebbistatin derivatives *in silico* as no correlation could be found between IC₅₀ and docking scores in their study (with or without taking water molecules into account).

B.2. Blebbistatin pocket entrance: a parameter than still requires investigation

An important parameter to be considered is the tightness of the blebbistatin tunnel (see introduction section C.7.). Indeed, the drug must be able of both reaching the blebbistatin binding pocket and stay bound to it to efficiently inhibit a myosin motor.

Looking at surface residues in the outer part of the 50 kDa cleft (putative blebbistatin entrance tunnel), important differences can be found among Myo2s, notably the charge distribution at the surface, which differs from one Myo2 to another:

In particular, in part A ([Figure 92](#)), bulky and hydrophobic residues can be found at the entrance of the 50 kDa cleft for CardMyo2 and SkMyo2: Ser272 and Val463 from Dicty are replaced by Leu and Phe, respectively, suggesting more difficult access for small molecules, and in particular polar molecules in SkMyo2 and CardMyo2 across this part of the cleft.

In part B ([Figure 92](#)), we noticed the formation of a polar contact between _{Sm}Glu422/_{NM2C}Glu441 and _{Sm}Arg273/_{NM2C}Arg293 in SmMyo2 and NM2C that could restrict flexibility of

the Upper-50 and hinder entrance of small molecules, in particular rather apolar molecules. In contrast, CardMyo2 and SkMyo2 exhibit a Gly instead of a Glu, leaving more space for ligand entrance.

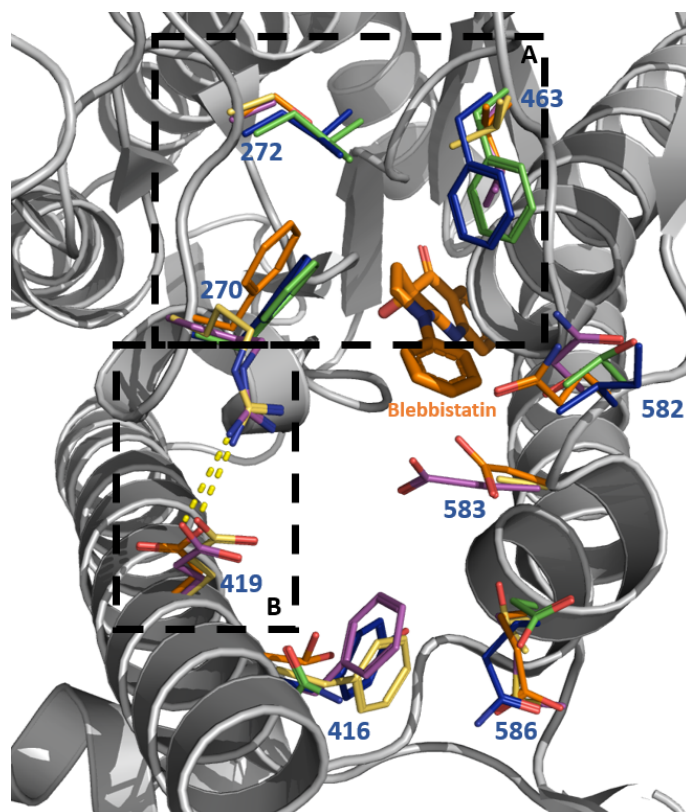


Figure 92: Residues variability at the entrance of the 50 kDa cleft.

DictyMyo2 bound to blebbistatin (PDB: 1YV3) is pictured in grey with side chains in orange. NM2C side chains are pictured in purple, SmMyo2 side chains in yellow, SkMyo2 side chains are pictured in blue and CardMyo2 side chains are pictured in green. Residue numbers correspond to DictyMyo2 numbers.

Yet, deTailed understanding of the way blebbistatin can enter its pocket and of the relative importance of these surface residues remains to be obtained. To that aim, molecular simulations of Myo2s pre-powerstroke dynamics and mutagenesis assays could greatly help understanding how blebbistatin and its derivatives manage to enter in the site and how residue changes within the entrance of the pocket can impact blebbistatin and blebbistatin derivatives inhibition. Coupled with a deTailed analysis of blebbistatin pocket bound to derivatives exhibiting different specificities (see section B.1.), this knowledge could lead to a greater understanding of the criteria that determines the specificity of a compounds in such a tight pocket. Perhaps helping the development of future specific inhibitors against myosins.

Conclusions

The work presented in this chapter offers new insights on the potential of Blebbistatin allosteric pocket for the development of specific myosin inhibitors.

Thanks to our collaboration with András Málnási-Csizmadia's lab, we had the opportunity to take part in the characterization of the antispastic drug MPH-220. This Blebbistatin derivative has been initially found in a series of more than 144 Blebbistatin derivatives as a highly specific SkMyo2 inhibitor. It diverges from Blebbistatin by its A-ring: the Blebbistatin methylphenyl is replaced by a methylthiophen moiety resulting in improved solubility. But the most significant change for specificity was the *para* substitution of the D-ring with a morpholino group. Indeed, more recently independent development of SkMyo2 inhibitors results in the development of skeletostatins, *i.e.*, blebbistatin derivatives characterized by a morpholino group of the D-ring in *para* (Radnai *et al.*, 2022). As revealed by the crystallographic structure of the complex between rabbit SkMyo2 and MPH-220, in the allosteric pocket, the morpholino group comes 3.1 Å close to Leu476 at the extremity of the HP-helix which corresponds to a phenylalanine in all other Myo2s. Thus, binding of MPH-220 to any other Myo2 would result in a steric clash between this phenylamine, explaining the striking specificity of MPH-220 for SkMyo2. This explanation was further supported by the fact that introduction of mutation Phe490Leu in NM2C Motor rescues MPH-220 ability to inhibit NM2C.

Through characterization of MPH-220 and SkMyo2, we also gain insights on Blebbistatin photodegradation process, which can be accelerated by the addition of alcohol reagents, or DTT. On this basis, we proposed that MPH-220 degradation can be due to the high concentration of DTT used in the crystallization drops. Yet, this does not seem to be an issue in physiological conditions as András Málnási-Csizmadia's lab confirms the efficiency and non-toxicity of the drug in mice, assess its high drugability.

Finally, this study attests of the potential of the Blebbistatin allosteric pocket for specific targeting of Myo2 motors. Indeed, if only MPH-220 results in strong selectivity for SkMyo2, several Blebbistatin derivatives exhibit a relative selectivity among Myo2s, starting with AmBlebb. Our collaboration with András Málnási-Csizmadia is now continuing to unpack the origin of specificity of a series of Blebbistatin derivatives through co-crystallization assays in CardMyo2, SmMyo2 and SkMyo2. The Blebbistatin allosteric pocket is rather buried, in the inner part of the 50 kDa cleft of the motor. Thus, to fully understand what rules blebbistatin derivatives specificity among Myo2, the Blebbistatin tunnel should be looked at as well. We already identified several residues at the entrance of the 50 kDa cleft that greatly differ among Myo2s and could at least in part explain why myosins with very similar Blebbistatin pockets are not equally inhibited by Blebbistatin.

Gathering all this information should help understanding why unconventional myosins which exhibit a rather conserved blebbistatin pocket compared to Myo2, such as Myo6, are not inhibited by Blebbistatin, and that understanding could eventually lead to the development of a new Myo6 inhibitor in the future.

General conclusion

Myosin motors are allosteric machines whose force is essential for key processes in cells. Thus, their malfunctions have been associated with many diseases. Understanding how the force produced by these motors can be modulated is thus of outstanding interest. During my PhD, using a structural approach, I aimed at dissecting how the unique molecular functions of Myo6 can be regulated by Myo6 binding partners, how a pathogenous mutant could perturb this process and how the small allosteric effector MPH-220 can specifically inhibit fast SkMyo2.

Using this structural approach, I managed to solve the structure of the anti-spastic drug MPH-220 bound to the Motor domain of SkMyo2. These X-ray crystallographic data offer an unambiguous electron density for MPH-220 within the blebbistatin pocket. Thus, our structural data, together with the ATPase characterization of the NM2C F/L mutant, clearly demonstrated that the morpholino cycle of MPH-220 is incompatible with the presence of a phenylalanine at the N-terminus of the HP-helix of the myosin motor. Thanks to these findings we were thus able to understand the origin of the exquisite specificity of MPH-220 for SkMyo2. Yet such structural approach can be particularly challenging to put in place, especially in the case of allosteric proteins whose conformational changes can greatly complicate their structural characterization. In particular, the crystallographic approach that I used in an attempt to obtain the structure of Myo6 in its auto-inhibited state remains unsuccessful. If the fusion of the Jo and the In tag with the Myo6 N- and C-terminus (respectively) successfully improved the stability of the auto-inhibited state, the crystals obtained with Jo-Myo6-In remained very small and exhibited no X-ray diffraction at the synchrotron beamline proxima-2 (SOLEIL synchrotron). Overall, it seems that the crystallographic approach may not be the most appropriate in this case. In contrast, negative staining EM gave us a very encouraging result since a first ~ 17 Å 3D reconstruction of the Jo-Myo6-In was obtained using this technique suggesting that in fact cryoEM might be the most promising approach to explore to determine the structure of the Myo6 auto-inhibited state at high resolution in the future.

To offer more complete insights on myosin activity modulation, the structural work was combined with functional assays, experiments in cells and even in living animals thanks to great collaborations with the laboratories of András Málnási-Csizmadia and Lee Sweeney. In this context structural data offers insights enabling to guide the functional assays while the functional assays provide data to confront/validate the hypothesis proposed based on the structural work. Taken all these data together, we gain insights on myosin auto-inhibition and modulation of motor activity using a highly specific inhibitor.

Auto-inhibition is a key regulation mechanism for myosins in general but a clear description of the auto-inhibited state and ways to relieve Auto-inhibition remains poorly understood in most cases. Actually, a high-resolution structure of the auto-inhibited state is only available in the case of SmMyo2 (Heissler *et al.* 2021). Thus, working on Myo6 auto-inhibition was of particular interest for understanding the mechanism of auto-inhibition of myosin motors in general. Previous studies have identified interactions between the CBD and the neck that must mediate Myo6 auto-inhibition (Fili *et al.* 2017, 2020, Batters *et al.* 2016) and showed ability of partners to relieve Myo6 auto-inhibition (Fili *et al.* 2017, 2020, Rai *et al.* 2022). In our study, we addressed the importance of the nucleotide for Myo6 auto-inhibition and demonstrated that in the context of a full-length motor, not all partners are able to activate the motor on their own. Moreover, we highlighted that the deafness mutation L926Q can destabilize the Myo6 auto-inhibited state, making Myo6 accessible for partners that normally cannot relieve Myo6 auto-inhibition such as Dab2 and TOM1. Our work on Myo6 thus highlights the importance of the myosin auto-inhibition for appropriate recruitment of the motor.

Being able to modulate myosin activity with small effectors is also of great interest in order to study motor mechanism, provide tools for biology experiments and also to cure diseases. The study of MPH-220 offers a great example of the potential of myosin allosteric modulator to treat diseases and in particular the potential of the blebbistatin allosteric pocket for developing highly specific inhibitors against Myo2. Moreover, during the course of the development of MPH-220, several blebbistatin derivatives exhibiting different selectivities among Myo2 have been identified by András Málnási-Csizmadia's lab. Characterization of a collection of inhibitor-myosin complexes through co-crystallization could offer insights to dissect the origin of the specificity and guide design of specific inhibitors for distinct Myo2. It may even perhaps provide clues to design Myo6 specific inhibitors in this pocket as this myosin exhibits rather well conserved residues in the blebbistatin pocket although it interestingly is not inhibited by blebbistatin.

Bibliography

- Acharya, Bipul R., Alexander Nestor-Bergmann, Xuan Liang, Shafali Gupta, Kinga Duszyc, Estelle Gauquelin, Guillermo A. Gomez, *et al.* 2018. "A Mechanosensitive RhoA Pathway That Protects Epithelia against Acute Tensile Stress." *Developmental Cell* 47 (4): 439-452.e6. <https://doi.org/10.1016/j.devcel.2018.09.016>.
- Ahmed, Zubair M., Robert J. Morell, Saima Riazuddin, Andrea Gropman, Shahzad Shaukat, Mussaber M. Ahmad, Saidi A. Mohiddin, *et al.* 2003. "Mutations of MYO6 Are Associated with Recessive Deafness, DFNB37." *American Journal of Human Genetics* 72 (5): 1315–22. <https://doi.org/10.1086/375122>.
- Akutsu, Masato, Ivan Dikic, and Anja Bremm. 2016. "Ubiquitin Chain Diversity at a Glance." *Journal of Cell Science* 129 (5): 875–80. <https://doi.org/10.1242/jcs.183954>.
- Alimardani, Maliheh, Seyed Mojtaba Hosseini, Mahmoud Shekari Khaniani, Mohsen Rajati Haghi, Atieh Eslahi, Mashsa Farjami, Javad Chezgi, Sima Mansoori Derakhshan, and Majid Mojarrad. 2019. "Targeted Mutation Analysis of the SLC26A4, MYO6, PJKV and CDH23 Genes in Iranian Patients with AR Nonsyndromic Hearing Loss." *Fetal and Pediatric Pathology* 38 (2): 93–102. <https://doi.org/10.1080/15513815.2018.1547336>.
- Alkowari, Moza K., Diego Vozzi, Shruti Bhagat, Navaneethakrishnan Krishnamoorthy, Anna Morgan, Yousra Hayder, Barathy Logendra, *et al.* 2017. "Targeted Sequencing Identifies Novel Variants Involved in Autosomal Recessive Hereditary Hearing Loss in Qatari Families." *Mutation Research* 800–802 (August): 29–36. <https://doi.org/10.1016/j.mrfmmm.2017.05.001>.
- Allingham, John S., Robert Smith, and Ivan Rayment. 2005. "The Structural Basis of Blebbistatin Inhibition and Specificity for Myosin II." *Nature Structural & Molecular Biology* 12 (4): 378–79. <https://doi.org/10.1038/nsmb908>.
- Alonso-Matilla, Roberto, Sathish Thiyagarajan, and Ben O'Shaughnessy. 2019. "Sliding Filament and Fixed Filament Mechanisms Contribute to Ring Tension in the Cytokinetic Contractile Ring." *Cytoskeleton (Hoboken, N.J.)* 76 (11–12): 611–25. <https://doi.org/10.1002/cm.21558>.
- Altman, David, Debanjan Goswami, Tama Hasson, James A. Spudich, and Satyajit Mayor. 2007. "Precise Positioning of Myosin VI on Endocytic Vesicles in Vivo." *PLoS Biology* 5 (8): e210. <https://doi.org/10.1371/journal.pbio.0050210>.
- Altman, David, H. Lee Sweeney, and James A. Spudich. 2004. "The Mechanism of Myosin VI Translocation and Its Load-Induced Anchoring." *Cell* 116 (5): 737–49. [https://doi.org/10.1016/s0092-8674\(04\)00211-9](https://doi.org/10.1016/s0092-8674(04)00211-9).
- Ameen, Nadia, and Gerard Apodaca. 2007. "Defective CFTR Apical Endocytosis and Enterocyte Brush Border in Myosin VI-Deficient Mice." *Traffic (Copenhagen, Denmark)* 8 (8): 998–1006. <https://doi.org/10.1111/j.1600-0854.2007.00587.x>.
- Arden, Susan D., David A. Tumbarello, Tariq Butt, John Kendrick-Jones, and Folma Buss. 2016. "Loss of Cargo Binding in the Human Myosin VI Deafness Mutant (R1166X) Leads to Increased Actin Filament Binding." *The Biochemical Journal* 473 (19): 3307–19. <https://doi.org/10.1042/BCJ20160571>.
- Aschenbrenner, Laura, TinThu Lee, and Tama Hasson. 2003. "Myo6 Facilitates the Translocation of Endocytic Vesicles from Cell Peripheries." *Molecular Biology of the Cell* 14 (7): 2728–43. <https://doi.org/10.1091/mbc.e02-11-0767>.
- Au, Josephine Sui-Yan, Claudia Puri, Gudrun Ihrke, John Kendrick-Jones, and Folma Buss. 2007. "Myosin VI Is Required for Sorting of AP-1B-Dependent Cargo to the Basolateral Domain in Polarized MDCK Cells." *The Journal of Cell Biology* 177 (1): 103–14. <https://doi.org/10.1083/jcb.200608126>.
- Avraham, K. B., T. Hasson, K. P. Steel, D. M. Kingsley, L. B. Russell, M. S. Mooseker, N. G. Copeland, and N. A. Jenkins. 1995. "The Mouse Snell's Waltzer Deafness Gene Encodes an Unconventional Myosin Required for Structural Integrity of Inner Ear Hair Cells." *Nature Genetics* 11 (4): 369–75. <https://doi.org/10.1038/ng1295-369>.
- Bahloul, Amel, Guillaume Chevreux, Amber L. Wells, Davy Martin, Jocelyn Nolt, Zhaohui Yang, Li-Qiong Chen, *et al.* 2004. "The Unique Insert in Myosin VI Is a Structural Calcium-Calmodulin Binding Site." *Proceedings of the National Academy of Sciences of the United States of America* 101 (14): 4787–92. <https://doi.org/10.1073/pnas.0306892101>.
- Balasanyan, Varuzhan, Kaori Watanabe, William P. Dempsey, Tommy L. Lewis, Le A. Trinh, and Don B. Arnold. 2017. "Structure and Function of an Actin-Based Filter in the Proximal Axon." *Cell Reports* 21 (10): 2696–2705. <https://doi.org/10.1016/j.celrep.2017.11.046>.

- Barnes, C. Ashley, Yang Shen, Jinfa Ying, Yasuharu Takagi, Dennis A. Torchia, James R. Sellers, and Ad Bax. 2019. "Remarkable Rigidity of the Single α -Helical Domain of Myosin-VI As Revealed by NMR Spectroscopy." *Journal of the American Chemical Society* 141 (22): 9004–17. <https://doi.org/10.1021/jacs.9b03116>.
- Batters, Christopher, Dario Brack, Heike Ellrich, Beate Aeverbeck, and Claudia Veigel. 2016. "Calcium Can Mobilize and Activate Myosin-VI." *Proceedings of the National Academy of Sciences of the United States of America* 113 (9): E1162-1169. <https://doi.org/10.1073/pnas.1519435113>.
- Bement, W. M., T. Hasson, J. A. Wirth, R. E. Cheney, and M. S. Mooseker. 1994. "Identification and Overlapping Expression of Multiple Unconventional Myosin Genes in Vertebrate Cell Types." *Proceedings of the National Academy of Sciences of the United States of America* 91 (14): 6549–53. <https://doi.org/10.1073/pnas.91.14.6549>.
- Berggren, K., E. Chernokalskaya, T. H. Steinberg, C. Kemper, M. F. Lopez, Z. Diwu, R. P. Haugland, and W. F. Patton. 2000. "Background-Free, High Sensitivity Staining of Proteins in One- and Two-Dimensional Sodium Dodecyl Sulfate-Polyacrylamide Gels Using a Luminescent Ruthenium Complex." *Electrophoresis* 21 (12): 2509–21. [https://doi.org/10.1002/1522-2683\(20000701\)21:12<2509::AID-ELPS2509>3.0.CO;2-9](https://doi.org/10.1002/1522-2683(20000701)21:12<2509::AID-ELPS2509>3.0.CO;2-9).
- Berman, Helen, Kim Henrick, and Haruki Nakamura. 2003. "Announcing the Worldwide Protein Data Bank." *Nature Structural Biology* 10 (12): 980. <https://doi.org/10.1038/nsb1203-980>.
- Biancospino, Matteo, Gwen R. Buel, Carlos A. Niño, Elena Maspero, Rossella Scotto di Perrotolo, Andrea Raimondi, Lisa Redlingshöfer, *et al.* 2019. "Clathrin Light Chain A Drives Selective Myosin VI Recruitment to Clathrin-Coated Pits under Membrane Tension." *Nature Communications* 10 (1): 4974. <https://doi.org/10.1038/s41467-019-12855-6>.
- Blaine, Judith, Kayo Okamura, Hector Giral, Sophia Breusegem, Yupanqui Caldas, Andrew Millard, Nicholas Barry, and Moshe Levi. 2009. "PTH-Induced Internalization of Apical Membrane NaPi2a: Role of Actin and Myosin VI." *American Journal of Physiology. Cell Physiology* 297 (6): C1339-1346. <https://doi.org/10.1152/ajpcell.00260.2009>.
- Blanc, Florian, Tatiana Isabet, Hannah Benisty, H. Lee Sweeney, Marco Cecchini, and Anne Houdusse. 2018. "An Intermediate along the Recovery Stroke of Myosin VI Revealed by X-Ray Crystallography and Molecular Dynamics." *Proceedings of the National Academy of Sciences of the United States of America* 115 (24): 6213–18. <https://doi.org/10.1073/pnas.1711512115>.
- Boal, Frédéric, Rana Mansour, Marion Gayral, Estelle Saland, Gaëtan Chicanne, Jean-Marie Xuereb, Marlène Marcellin, *et al.* 2015. "TOM1 Is a PI5P Effector Involved in the Regulation of Endosomal Maturation." *Journal of Cell Science* 128 (4): 815–27. <https://doi.org/10.1242/jcs.166314>.
- Bond, Lisa M., Andrew A. Peden, John Kendrick-Jones, James R. Sellers, and Folma Buss. 2011. "Myosin VI and Its Binding Partner Optineurin Are Involved in Secretory Vesicle Fusion at the Plasma Membrane." *Molecular Biology of the Cell* 22 (1): 54–65. <https://doi.org/10.1091/mbc.E10-06-0553>.
- Bonnet, J., J. Cartannaz, G. Tourcier, C. Contreras-Martel, J. P. Kleman, C. Morlot, T. Vernet, and A. M. Di Guilmi. 2017. "Autocatalytic Association of Proteins by Covalent Bond Formation: A Bio Molecular Welding Toolbox Derived from a Bacterial Adhesin." *Scientific Reports* 7 (1): 43564. <https://doi.org/10.1038/srep43564>.
- Brawley, Jhonnathan, Emily Etter, Dante Heredia, Amarawan Intasiri, Kyle Nennecker, Joshua Smith, Brandon M. Welcome, *et al.* 2020. "Synthesis and Evaluation of 4-Hydroxycoumarin Imines as Inhibitors of Class II Myosins." *Journal of Medicinal Chemistry* 63 (19): 11131–48. <https://doi.org/10.1021/acs.jmedchem.0c01062>.
- Bricogne, G., E. Blanc, M. Brandl, C. Flensburg, P. Keller, W. Paciorek, P. Roversi, *et al.* 2017. "BUSTER Version X.Y.Z. Cambridge, United Kingdom: Global Phasing Ltd."
- Briggs, Sherri B., Ashley M. Blouin, Erica J. Young, Gavin Rumbaugh, and Courtney A. Miller. 2017. "Memory Disrupting Effects of Nonmuscle Myosin II Inhibition Depend on the Class of Abused Drug and Brain Region." *Learning & Memory (Cold Spring Harbor, N.Y.)* 24 (2): 70–75. <https://doi.org/10.1101/lm.043976.116>.
- Brooks, Andrew B. E., Daniel Humphreys, Vikash Singh, Anthony C. Davidson, Susan D. Arden, Folma Buss, and Vassilis Koronakis. 2017. "MYO6 Is Targeted by Salmonella Virulence Effectors to Trigger PI3-Kinase Signaling and Pathogen Invasion into Host Cells." *Proceedings of the National Academy of Sciences of the United States of America* 114 (15): 3915–20. <https://doi.org/10.1073/pnas.1616418114>.
- Brownstein, Zippora, Amal Abu-Rayyan, Daphne Karfunkel-Doron, Serena Sirigu, Bella Davidov, Mordechai Shohat, Moshe Frydman, Anne Houdusse, Moien Kanaan, and Karen B. Avraham. 2014. "Novel Myosin Mutations for Hereditary Hearing Loss Revealed by Targeted Genomic Capture and Massively Parallel Sequencing." *European Journal of Human Genetics: EJHG* 22 (6): 768–75. <https://doi.org/10.1038/ejhg.2013.232>.

- Bryant, Zev, David Altman, and James A. Spudich. 2007. "The Power Stroke of Myosin VI and the Basis of Reverse Directionality." *Proceedings of the National Academy of Sciences* 104 (3): 772–77. <https://doi.org/10.1073/pnas.0610144104>.
- Brzeska, H., and E. D. Korn. 1996. "Regulation of Class I and Class II Myosins by Heavy Chain Phosphorylation." *The Journal of Biological Chemistry* 271 (29): 16983–86. <https://doi.org/10.1074/jbc.271.29.16983>.
- Bunn, R. C., M. A. Jensen, and B. C. Reed. 1999. "Protein Interactions with the Glucose Transporter Binding Protein GLUT1CBP That Provide a Link between GLUT1 and the Cytoskeleton." *Molecular Biology of the Cell* 10 (4): 819–32. <https://doi.org/10.1091/mbc.10.4.819>.
- Buss, F., S. D. Arden, M. Lindsay, J. P. Luzio, and J. Kendrick-Jones. 2001. "Myosin VI Isoform Localized to Clathrin-Coated Vesicles with a Role in Clathrin-Mediated Endocytosis." *The EMBO Journal* 20 (14): 3676–84. <https://doi.org/10.1093/emboj/20.14.3676>.
- Buss, F., J. Kendrick-Jones, C. Lionne, A. E. Knight, G. P. Côté, and J. Paul Luzio. 1998. "The Localization of Myosin VI at the Golgi Complex and Leading Edge of Fibroblasts and Its Phosphorylation and Recruitment into Membrane Ruffles of A431 Cells after Growth Factor Stimulation." *The Journal of Cell Biology* 143 (6): 1535–45. <https://doi.org/10.1083/jcb.143.6.1535>.
- Capmany, Anahi, Azumi Yoshimura, Rachid Kerdous, Valentina Caorsi, Aurianne Lescure, Elaine Del Nery, Evelyne Coudrier, Bruno Goud, and Kristine Schauer. 2019. "MYO1C Stabilizes Actin and Facilitates the Arrival of Transport Carriers at the Golgi Complex." *Journal of Cell Science* 132 (8): jcs225029. <https://doi.org/10.1242/jcs.225029>.
- Caporizzo, Matthew A., Claire E. Fishman, Osamu Sato, Ryan M. Jamiolkowski, Mitsuo Ikebe, and Yale E. Goldman. 2018. "The Antiparallel Dimerization of Myosin X Imparts Bundle Selectivity for Processive Motility." *Biophysical Journal* 114 (6): 1400–1410. <https://doi.org/10.1016/j.bpj.2018.01.038>.
- Chen, Ping-Hung, Nawal Bendris, Yi-Jing Hsiao, Carlos R. Reis, Marcel Mettlen, Hsuan-Yu Chen, Sung-Liang Yu, and Sandra L. Schmid. 2017. "Crosstalk between CLCb/Dyn1-Mediated Adaptive Clathrin-Mediated Endocytosis and Epidermal Growth Factor Receptor Signaling Increases Metastasis." *Developmental Cell* 40 (3): 278–288.e5. <https://doi.org/10.1016/j.devcel.2017.01.007>.
- Chen, Tiane, Ann Hubbard, Rakhilya Murtazina, Jennifer Price, Jianbo Yang, Boyoung Cha, Rafiqueel Sarker, and Mark Donowitz. 2014. "Myosin VI Mediates the Movement of NHE3 down the Microvillus in Intestinal Epithelial Cells." *Journal of Cell Science* 127 (Pt 16): 3535–45. <https://doi.org/10.1242/jcs.149930>.
- Cheung, A., J. A. Dantzig, S. Hollingworth, S. M. Baylor, Y. E. Goldman, T. J. Mitchison, and A. F. Straight. 2002. "A Small-Molecule Inhibitor of Skeletal Muscle Myosin II." *Nature Cell Biology* 4 (1): 83–88. <https://doi.org/10.1038/ncb734>.
- Chibalina, Margarita V., Matthew N. J. Seaman, Christopher C. Miller, John Kendrick-Jones, and Folma Buss. 2007. "Myosin VI and Its Interacting Protein LMTK2 Regulate Tubule Formation and Transport to the Endocytic Recycling Compartment." *Journal of Cell Science* 120 (Pt 24): 4278–88. <https://doi.org/10.1242/jcs.014217>.
- Ching, Yung-Hao, Tushar K. Ghosh, Steve J. Cross, Elizabeth A. Packham, Louise Honeyman, Siobhan Loughna, Thelma E. Robinson, *et al.* 2005. "Mutation in Myosin Heavy Chain 6 Causes Atrial Septal Defect." *Nature Genetics* 37 (4): 423–28. <https://doi.org/10.1038/ng1526>.
- Chinthalapudi, Krishna, Manuel H. Taft, René Martin, Sarah M. Heissler, Matthias Preller, Falk K. Hartmann, Hemma Brandstaetter, *et al.* 2011. "Mechanism and Specificity of Pentachloropseudilin-Mediated Inhibition of Myosin Motor Activity." *The Journal of Biological Chemistry* 286 (34): 29700–708. <https://doi.org/10.1074/jbc.M111.239210>.
- Chittenden, Thomas W., Jane Pak, Renee Rubio, Hailing Cheng, Kristina Holton, Niall Prendergast, Vladimir Glinkii, *et al.* 2010. "Therapeutic Implications of GIPC1 Silencing in Cancer." *PLoS One* 5 (12): e15581. <https://doi.org/10.1371/journal.pone.0015581>.
- Choi, Byung-Ok, Sung Hee Kang, Young Se Hyun, Sumaria Kanwal, Sun Wha Park, Heasoo Koo, Sang-Beom Kim, *et al.* 2011. "A Complex Phenotype of Peripheral Neuropathy, Myopathy, Hoarseness, and Hearing Loss Is Linked to an Autosomal Dominant Mutation in MYH14." *Human Mutation* 32 (6): 669–77. <https://doi.org/10.1002/humu.21488>.
- Chuan, Peiyang, James A. Spudich, and Alexander R. Dunn. 2011. "Robust Mechanosensing and Tension Generation by Myosin VI." *Journal of Molecular Biology* 405 (1): 105–12. <https://doi.org/10.1016/j.jmb.2010.10.010>.
- Chuang, Chihyuan, Scott Collibee, Luke Ashcraft, Wenye Wang, Mark Vander Wal, Xiaolin Wang, Darren T. Hwee, *et al.* 2021. "Discovery of Aficamten (CK-274), a Next-Generation Cardiac Myosin Inhibitor for the Treatment of Hypertrophic Cardiomyopathy." *Journal of Medicinal Chemistry* 64 (19): 14142–52. <https://doi.org/10.1021/acs.jmedchem.1c01290>.

- Coffin, Allison B., Alain Dabdoub, Matthew W. Kelley, and Arthur N. Popper. 2007. "Myosin VI and Villa Distribution among Inner Ear Epithelia in Diverse Fishes." *Hearing Research* 224 (1–2): 15–26. <https://doi.org/10.1016/j.heares.2006.11.004>.
- Collaco, Anne, Robert Jakab, Peter Hegan, Mark Mooseker, and Nadia Ameen. 2010. "Alpha-AP-2 Directs Myosin VI-Dependent Endocytosis of Cystic Fibrosis Transmembrane Conductance Regulator Chloride Channels in the Intestine." *The Journal of Biological Chemistry* 285 (22): 17177–87. <https://doi.org/10.1074/jbc.M110.127613>.
- Coluccio, Lynne M., ed. 2020a. *Myosins: A Superfamily of Molecular Motors*. Vol. 1239. Advances in Experimental Medicine and Biology. Cham: Springer International Publishing. <https://doi.org/10.1007/978-3-030-38062-5>.
- . 2020b. "Myosins and Disease." *Advances in Experimental Medicine and Biology* 1239: 245–316. https://doi.org/10.1007/978-3-030-38062-5_12.
- Conti, Mary Anne, Sharona Even-Ram, Chengyu Liu, Kenneth M. Yamada, and Robert S. Adelstein. 2004. "Defects in Cell Adhesion and the Visceral Endoderm Following Ablation of Nonmuscle Myosin Heavy Chain II-A in Mice." *The Journal of Biological Chemistry* 279 (40): 41263–66. <https://doi.org/10.1074/jbc.C400352200>.
- Côté, Jean-François, and Kristiina Vuori. 2002. "Identification of an Evolutionarily Conserved Superfamily of DOCK180-Related Proteins with Guanine Nucleotide Exchange Activity." *Journal of Cell Science* 115 (Pt 24): 4901–13. <https://doi.org/10.1242/jcs.00219>.
- Coureux, Pierre-Damien, H. Lee Sweeney, and Anne Houdusse. 2004. "Three Myosin V Structures Delineate Essential Features of Chemo-Mechanical Transduction." *The EMBO Journal* 23 (23): 4527–37. <https://doi.org/10.1038/sj.emboj.7600458>.
- Coureux, Pierre-Damien, Amber L. Wells, Julie Ménétrey, Christopher M. Yengo, Carl A. Morris, H. Lee Sweeney, and Anne Houdusse. 2003. "A Structural State of the Myosin V Motor without Bound Nucleotide." *Nature* 425 (6956): 419–23. <https://doi.org/10.1038/nature01927>.
- Craig, R., R. Smith, and J. Kendrick-Jones. 1983. "Light-Chain Phosphorylation Controls the Conformation of Vertebrate Non-Muscle and Smooth Muscle Myosin Molecules." *Nature* 302 (5907): 436–39. <https://doi.org/10.1038/302436a0>.
- Cruz, Daniel F., Carlos M. Farinha, and Agnieszka Swiatecka-Urban. 2019. "Unraveling the Function of Lemur Tyrosine Kinase 2 Network." *Frontiers in Pharmacology* 10: 24. <https://doi.org/10.3389/fphar.2019.00024>.
- Dadson, Keith, Ludger Hauck, and Filio Billia. 2017. "Molecular Mechanisms in Cardiomyopathy." *Clinical Science (London, England: 1979)* 131 (13): 1375–92. <https://doi.org/10.1042/CS20160170>.
- Dance, Amber L., Matthew Miller, Shinobu Seragaki, Prafulla Aryal, Breanne White, Laura Aschenbrenner, and Tama Hasson. 2004. "Regulation of Myosin-VI Targeting to Endocytic Compartments." *Traffic (Copenhagen, Denmark)* 5 (10): 798–813. <https://doi.org/10.1111/j.1600-0854.2004.00224.x>.
- De La Cruz, E. M., E. M. Ostap, and H. L. Sweeney. 2001. "Kinetic Mechanism and Regulation of Myosin VI." *The Journal of Biological Chemistry* 276 (34): 32373–81. <https://doi.org/10.1074/jbc.M104136200>.
- Delevoe, Cédric. 2014. "Melanin Transfer: The Keratinocytes Are More than Gluttons." *The Journal of Investigative Dermatology* 134 (4): 877–79. <https://doi.org/10.1038/jid.2013.487>.
- DeLuca-Flaherty, C., D. B. McKay, P. Parham, and B. L. Hill. 1990. "Uncoating Protein (Hsc70) Binds a Conformationally Labile Domain of Clathrin Light Chain LCa to Stimulate ATP Hydrolysis." *Cell* 62 (5): 875–87. [https://doi.org/10.1016/0092-8674\(90\)90263-e](https://doi.org/10.1016/0092-8674(90)90263-e).
- Deng, Chunchu, Mehri Moradi, Sebastian Reinhard, Changhe Ji, Sibylle Jablonka, Luisa Hennlein, Patrick Lüningschrör, Sören Doose, Markus Sauer, and Michael Sendtner. 2021. "Dynamic Remodeling of Ribosomes and Endoplasmic Reticulum in Axon Terminals of Motoneurons." *Journal of Cell Science* 134 (22): jcs258785. <https://doi.org/10.1242/jcs.258785>.
- Dennis, Megan K., Cédric Delevoe, Amanda Acosta-Ruiz, Ilse Hurbain, Maryse Romao, Geoffrey G. Hesketh, Philip S. Goff, et al. 2016. "BLOC-1 and BLOC-3 Regulate VAMP7 Cycling to and from Melanosomes via Distinct Tubular Transport Carriers." *The Journal of Cell Biology* 214 (3): 293–308. <https://doi.org/10.1083/jcb.201605090>.
- Deol, M. S., and M. C. Green. 1966. "Snell's Waltzer, a New Mutation Affecting Behaviour and the Inner Ear in the Mouse." *Genetical Research* 8 (3): 339–45. <https://doi.org/10.1017/s0016672300010193>.
- Derycke, Lara, Christophe Stove, Anne-Sophie Vercutter-Edouart, Olivier De Wever, Laurent Dollé, Nathalie Colpaert, Herman Depypere, Jean-Claude Michalski, and Marc Bracke. 2011. "The Role of Non-Muscle Myosin IIA in Aggregation and Invasion of Human MCF-7 Breast Cancer Cells." *The International Journal of Developmental Biology* 55 (7–9): 835–40. <https://doi.org/10.1387/ijdb.113336ld>.

- Donaudy, Francesca, Rik Snoeckx, Markus Pfister, Hans-Peter Zenner, Nikolaus Blin, Mariateresa Di Stazio, Antonella Ferrara, *et al.* 2004. "Nonmuscle Myosin Heavy-Chain Gene MYH14 Is Expressed in Cochlea and Mutated in Patients Affected by Autosomal Dominant Hearing Impairment (DFNA4)." *American Journal of Human Genetics* 74 (4): 770–76. <https://doi.org/10.1086/383285>.
- Dong, Aiping, Xiaohui Xu, Aled M. Edwards, Midwest Center for Structural Genomics, Structural Genomics Consortium, Changsoo Chang, Maksymilian Chruszcz, *et al.* 2007. "In Situ Proteolysis for Protein Crystallization and Structure Determination." *Nature Methods* 4 (12): 1019–21. <https://doi.org/10.1038/nmeth1118>.
- Dos Santos, Ália, Natalia Fili, Yukti Hari-Gupta, Rosemarie E. Gough, Lin Wang, Marisa Martin-Fernandez, Jesse Aaron, Eric Wait, Teng-Leong Chew, and Christopher P. Toseland. 2022. "Binding Partners Regulate Unfolding of Myosin VI to Activate the Molecular Motor." *The Biochemical Journal* 479 (13): 1409–28. <https://doi.org/10.1042/BCJ20220025>.
- Dou, Ying, Per Arlock, and Anders Arner. 2007. "Blebbistatin Specifically Inhibits Actin-Myosin Interaction in Mouse Cardiac Muscle." *American Journal of Physiology. Cell Physiology* 293 (3): C1148–1153. <https://doi.org/10.1152/ajpcell.00551.2006>.
- Dowell, Maria L., Tera L. Lavoie, Julian Solway, and Ramaswamy Krishnan. 2014. "Airway Smooth Muscle: A Potential Target for Asthma Therapy." *Current Opinion in Pulmonary Medicine* 20 (1): 66–72. <https://doi.org/10.1097/MCP.0000000000000011>.
- Dunn, Thomas A., Shenglin Chen, Dennis A. Faith, Jessica L. Hicks, Elizabeth A. Platz, Yidong Chen, Charles M. Ewing, *et al.* 2006. "A Novel Role of Myosin VI in Human Prostate Cancer." *The American Journal of Pathology* 169 (5): 1843–54. <https://doi.org/10.2353/ajpath.2006.060316>.
- Duxbury, Mark S., Stanley W. Ashley, and Edward E. Whang. 2004. "Inhibition of Pancreatic Adenocarcinoma Cellular Invasiveness by Blebbistatin: A Novel Myosin II Inhibitor." *Biochemical and Biophysical Research Communications* 313 (4): 992–97. <https://doi.org/10.1016/j.bbrc.2003.12.031>.
- Dye, Natalie A., Marko Popović, K. Venkatesan Iyer, Jana F. Fuhrmann, Romina Piscitello-Gómez, Suzanne Eaton, and Frank Jülicher. 2021. "Self-Organized Patterning of Cell Morphology via Mechanosensitive Feedback." *eLife* 10 (March): e57964. <https://doi.org/10.7554/eLife.57964>.
- Eaton, Suzanne, and Fernando Martin-Belmonte. 2014. "Cargo Sorting in the Endocytic Pathway: A Key Regulator of Cell Polarity and Tissue Dynamics." *Cold Spring Harbor Perspectives in Biology* 6 (10): a016899. <https://doi.org/10.1101/cshperspect.a016899>.
- Eddinger, Thomas J., Daniel P. Meer, Amy S. Miner, Joel Meehl, Arthur S. Rovner, and Paul H. Ratz. 2007. "Potent Inhibition of Arterial Smooth Muscle Tonic Contractions by the Selective Myosin II Inhibitor, Blebbistatin." *The Journal of Pharmacology and Experimental Therapeutics* 320 (2): 865–70. <https://doi.org/10.1124/jpet.106.109363>.
- Emsley, Paul, and Kevin Cowtan. 2004. "Coot: Model-Building Tools for Molecular Graphics." *Acta Crystallographica. Section D, Biological Crystallography* 60 (Pt 12 Pt 1): 2126–32. <https://doi.org/10.1107/S0907444904019158>.
- Endres, Nicholas F., Craig Yoshioka, Ronald A. Milligan, and Ronald D. Vale. 2006. "A Lever-Arm Rotation Drives Motility of the Minus-End-Directed Kinesin Ncd." *Nature* 439 (7078): 875–78. <https://doi.org/10.1038/nature04320>.
- Ewert, Wiebke, Peter Franz, Georgios Tsiavaliaris, and Matthias Preller. 2020. "Structural and Computational Insights into a Blebbistatin-Bound Myosin•ADP Complex with Characteristics of an ADP-Release Conformation along the Two-Step Myosin Power Stroke." *International Journal of Molecular Sciences* 21 (19): E7417. <https://doi.org/10.3390/ijms21197417>.
- Farman, Gerrie P., Kittipong Tachampa, Ryan Mateja, Olivier Cazorla, Alain Lacampagne, and Pieter P. de Tombe. 2008. "Blebbistatin: Use as Inhibitor of Muscle Contraction." *Pflugers Archiv: European Journal of Physiology* 455 (6): 995–1005. <https://doi.org/10.1007/s00424-007-0375-3>.
- Fedorov, Roman, Markus Böhl, Georgios Tsiavaliaris, Falk K. Hartmann, Manuel H. Taft, Petra Baruch, Bernhard Brenner, *et al.* 2009. "The Mechanism of Pentabromopseudilin Inhibition of Myosin Motor Activity." *Nature Structural & Molecular Biology* 16 (1): 80–88. <https://doi.org/10.1038/nsmb.1542>.
- Fili, Natalia, Yukti Hari-Gupta, Bjork Aston, Ália Dos Santos, Rosemarie E. Gough, Bana Alamad, Lin Wang, Marisa L. Martin-Fernandez, and Christopher P. Toseland. 2020. "Competition between Two High- and Low-Affinity Protein-Binding Sites in Myosin VI Controls Its Cellular Function." *The Journal of Biological Chemistry* 295 (2): 337–47. <https://doi.org/10.1074/jbc.RA119.010142>.
- Fili, Natalia, Yukti Hari-Gupta, Ália Dos Santos, Alexander Cook, Simon Poland, Simon M. Ameer-Beg, Maddy Parsons, and Christopher P. Toseland. 2017. "NDP52 Activates Nuclear Myosin VI to Enhance RNA

- Polymerase II Transcription." *Nature Communications* 8 (1): 1871. <https://doi.org/10.1038/s41467-017-02050-w>.
- Fili, Natalia, and Christopher P. Toseland. 2019. "Unconventional Myosins: How Regulation Meets Function." *International Journal of Molecular Sciences* 21 (1): E67. <https://doi.org/10.3390/ijms21010067>.
- Finno, Carrie J., Giuliana Gianino, Sudeep Perumbakkam, Zoë J. Williams, Matthew H. Bordbari, Keri L. Gardner, Erin Burns, Sichong Peng, Sian A. Durward-Akhurst, and Stephanie J. Valberg. 2018. "A Missense Mutation in MYH1 Is Associated with Susceptibility to Immune-Mediated Myositis in Quarter Horses." *Skeletal Muscle* 8 (1): 7. <https://doi.org/10.1186/s13395-018-0155-0>.
- Fotin, Alexander, Yifan Cheng, Piotr Sliz, Nikolaus Grigorieff, Stephen C. Harrison, Tomas Kirchhausen, and Thomas Walz. 2004. "Molecular Model for a Complete Clathrin Lattice from Electron Cryomicroscopy." *Nature* 432 (7017): 573–79. <https://doi.org/10.1038/nature03079>.
- Frank, Deborah J., Tatsuhiko Noguchi, and Kathryn G. Miller. 2004. "Myosin VI: A Structural Role in Actin Organization Important for Protein and Organelle Localization and Trafficking." *Current Opinion in Cell Biology* 16 (2): 189–94. <https://doi.org/10.1016/j.ceb.2004.02.001>.
- French, Alexander R., Tobin R. Sosnick, and Ronald S. Rock. 2017. "Investigations of Human Myosin VI Targeting Using Optogenetically Controlled Cargo Loading." *Proceedings of the National Academy of Sciences of the United States of America* 114 (9): E1607–16. <https://doi.org/10.1073/pnas.1614716114>.
- Frye, Jeremiah J., Vadim A. Klenchin, Clive R. Bagshaw, and Ivan Rayment. 2010. "Insights into the Importance of Hydrogen Bonding in the Gamma-Phosphate Binding Pocket of Myosin: Structural and Functional Studies of Serine 236." *Biochemistry* 49 (23): 4897–4907. <https://doi.org/10.1021/bi1001344>.
- Gateva, Gergana, Elena Kremneva, Theresia Reindl, Tommi Kotila, Konstantin Kogan, Laurène Gressin, Peter W. Gunning, Dietmar J. Manstein, Alphée Michelot, and Pekka Lappalainen. 2017. "Tropomyosin Isoforms Specify Functionally Distinct Actin Filament Populations In Vitro." *Current Biology: CB* 27 (5): 705–13. <https://doi.org/10.1016/j.cub.2017.01.018>.
- Gauthier, Julie, Bouchra Ouled Amar Bencheikh, Fadi F. Hamdan, Steven M. Harrison, Linda A. Baker, Françoise Couture, Isabelle Thiffault, *et al.* 2015. "A Homozygous Loss-of-Function Variant in MYH11 in a Case with Megacystis-Microcolon-Intestinal Hypoperistalsis Syndrome." *European Journal of Human Genetics: EJHG* 23 (9): 1266–68. <https://doi.org/10.1038/ejhg.2014.256>.
- Geisbrecht, Erika R., and Denise J. Montell. 2002. "Myosin VI Is Required for E-Cadherin-Mediated Border Cell Migration." *Nature Cell Biology* 4 (8): 616–20. <https://doi.org/10.1038/ncb830>.
- Geisterfer-Lowrance, A. A., M. Christe, D. A. Conner, J. S. Ingwall, F. J. Schoen, C. E. Seidman, and J. G. Seidman. 1996. "A Mouse Model of Familial Hypertrophic Cardiomyopathy." *Science (New York, N.Y.)* 272 (5262): 731–34. <https://doi.org/10.1126/science.272.5262.731>.
- Gibson, Daniel G., Lei Young, Ray-Yuan Chuang, J. Craig Venter, Clyde A. Hutchison, and Hamilton O. Smith. 2009. "Enzymatic Assembly of DNA Molecules up to Several Hundred Kilobases." *Nature Methods* 6 (5): 343–45. <https://doi.org/10.1038/nmeth.1318>.
- Giridharan, Sai Srinivas Panapakkam, and Steve Caplan. 2014. "MICAL-Family Proteins: Complex Regulators of the Actin Cytoskeleton." *Antioxidants & Redox Signaling* 20 (13): 2059–73. <https://doi.org/10.1089/ars.2013.5487>.
- Gotoh, Nanami, Qingshang Yan, Zhaopeng Du, Daniel Biemesderfer, Michael Kashgarian, Mark S. Mooseker, and Tong Wang. 2010. "Altered Renal Proximal Tubular Endocytosis and Histology in Mice Lacking Myosin-VI." *Cytoskeleton (Hoboken, N.J.)* 67 (3): 178–92. <https://doi.org/10.1002/cm.20435>.
- Gourinath, S., Daniel M. Himmel, Jerry H. Brown, Ludmilla Reshetnikova, Andrew G. Szent-Györgyi, and Carolyn Cohen. 2003. "Crystal Structure of Scallop Myosin S1 in the Pre-Power Stroke State to 2.6 Å Resolution: Flexibility and Function in the Head." *Structure (London, England: 1993)* 11 (12): 1621–27. <https://doi.org/10.1016/j.str.2003.10.013>.
- Green, Eric M., Hiroko Wakimoto, Robert L. Anderson, Marc J. Evanichik, Joshua M. Gorham, Brooke C. Harrison, Marcus Henze, *et al.* 2016. "A Small-Molecule Inhibitor of Sarcomere Contractility Suppresses Hypertrophic Cardiomyopathy in Mice." *Science (New York, N.Y.)* 351 (6273): 617–21. <https://doi.org/10.1126/science.aad3456>.
- Gurel, Pinar S., Laura Y. Kim, Paul V. Ruijgrok, Tosan Omabegho, Zev Bryant, and Gregory M. Alushin. 2017. "Cryo-EM Structures Reveal Specialization at the Myosin VI-Actin Interface and a Mechanism of Force Sensitivity." *ELife* 6 (December): e31125. <https://doi.org/10.7554/eLife.31125>.
- Gwon, Youngdae, Tae-In Kam, Seo-Hyun Kim, Sungmin Song, Hyejin Park, Bitna Lim, Haneul Lee, Weontae Lee, Dong-Gyu Jo, and Yong-Keun Jung. 2018. "TOM1 Regulates Neuronal Accumulation of Amyloid- β Oligomers by Fc γ RIIb2 Variant in Alzheimer's Disease." *The Journal of Neuroscience: The Official Journal of the Society for Neuroscience* 38 (42): 9001–18. <https://doi.org/10.1523/JNEUROSCI.1996-17.2018>.

- Gyimesi, Máté, Ádám I. Horváth, Demeter Túrós, Sharad Kumar Suthar, Máté Péntes, Csilla Kurdi, Louise Canon, *et al.* 2020. "Single Residue Variation in Skeletal Muscle Myosin Enables Direct and Selective Drug Targeting for Spasticity and Muscle Stiffness." *Cell* 183 (2): 335-346.e13. <https://doi.org/10.1016/j.cell.2020.08.050>.
- Gyimesi, Máté, Anna Á Rauscher, Sharad Kumar Suthar, Kamirán Á Hamow, Kinga Oravec, István Lórin, Zsolt Borhegyi, *et al.* 2021. "Improved Inhibitory and Absorption, Distribution, Metabolism, Excretion, and Toxicology (ADMET) Properties of Blebbistatin Derivatives Indicate That Blebbistatin Scaffold Is Ideal for Drug Development Targeting Myosin-2." *The Journal of Pharmacology and Experimental Therapeutics* 376 (3): 358-73. <https://doi.org/10.1124/jpet.120.000167>.
- Haleblian, Mary, Kyle Morris, and Corinne Smith. 2017. "Structure and Assembly of Clathrin Cages." *Sub-Cellular Biochemistry* 83: 551-67. https://doi.org/10.1007/978-3-319-46503-6_20.
- Hariadi, Rizal F., Mario Cale, and Sivaraj Sivaramakrishnan. 2014. "Myosin Lever arm Directs Collective Motion on Cellular Actin Network." *Proceedings of the National Academy of Sciences* 111 (11): 4091-96. <https://doi.org/10.1073/pnas.1315923111>.
- Hari-Gupta, Yukti, Natalia Fili, Ália Dos Santos, Alexander W. Cook, Rosemarie E. Gough, Hannah C. W. Reed, Lin Wang, *et al.* 2022. "Myosin VI Regulates the Spatial Organisation of Mammalian Transcription Initiation." *Nature Communications* 13 (1): 1346. <https://doi.org/10.1038/s41467-022-28962-w>.
- Hasson, T., P. G. Gillespie, J. A. Garcia, R. B. MacDonald, Y. Zhao, A. G. Yee, M. S. Mooseker, and D. P. Corey. 1997. "Unconventional Myosins in Inner-Ear Sensory Epithelia." *The Journal of Cell Biology* 137 (6): 1287-1307. <https://doi.org/10.1083/jcb.137.6.1287>.
- Hasson, T., and M. S. Mooseker. 1994. "Porcine Myosin-VI: Characterization of a New Mammalian Unconventional Myosin." *The Journal of Cell Biology* 127 (2): 425-40. <https://doi.org/10.1083/jcb.127.2.425>.
- Hasson, Tama. 2003. "Myosin VI: Two Distinct Roles in Endocytosis." *Journal of Cell Science* 116 (Pt 17): 3453-61. <https://doi.org/10.1242/jcs.00669>.
- He, Fahu, Hans-Peter Wollscheid, Urszula Nowicka, Matteo Biancospino, Eleonora Valentini, Aaron Ehlinger, Filippo Acconcia, Elisa Magistrati, Simona Polo, and Kylie J. Walters. 2016a. "Myosin VI Contains a Compact Structural Motif That Binds to Ubiquitin Chains." *Cell Reports* 14 (11): 2683-94. <https://doi.org/10.1016/j.celrep.2016.01.079>.
- Heath, K. E., A. Campos-Barros, A. Toren, G. Rozenfeld-Granot, L. E. Carlsson, J. Savige, J. C. Denison, *et al.* 2001. "Nonmuscle Myosin Heavy Chain IIA Mutations Define a Spectrum of Autosomal Dominant Macrothrombocytopenias: May-Hegglin Anomaly and Fechtner, Sebastian, Epstein, and Alport-like Syndromes." *American Journal of Human Genetics* 69 (5): 1033-45. <https://doi.org/10.1086/324267>.
- Hegan, Peter S., Anthony A. Lanahan, Michael Simons, and Mark S. Mooseker. 2015. "Myosin VI and Cardiomyopathy: Left Ventricular Hypertrophy, Fibrosis, and Both Cardiac and Pulmonary Vascular Endothelial Cell Defects in the Snell's Waltzer Mouse." *Cytoskeleton (Hoboken, N.J.)* 72 (8): 373-87. <https://doi.org/10.1002/cm.21236>.
- Heissler, Sarah M., Amandeep S. Arora, Neil Billington, James R. Sellers, and Krishna Chinthlapudi. 2021. "Cryo-EM Structure of the Autoinhibited State of Myosin-2." *Science Advances* 7 (52): eabk3273. <https://doi.org/10.1126/sciadv.abk3273>.
- Heissler, Sarah M., Krishna Chinthalapudi, and James R. Sellers. 2015. "Kinetic Characterization of the Sole Nonmuscle Myosin-2 from the Model Organism *Drosophila Melanogaster*." *FASEB Journal: Official Publication of the Federation of American Societies for Experimental Biology* 29 (4): 1456-66. <https://doi.org/10.1096/fj.14-266742>.
- Heissler, Sarah M., and James R. Sellers. 2014. "Myosin Light Chains: Teaching Old Dogs New Tricks." *Bioarchitecture* 4 (6): 169-88. <https://doi.org/10.1080/19490992.2015.1054092>.
- . 2016. "Various Themes of Myosin Regulation." *Journal of Molecular Biology* 428 (9 Pt B): 1927-46. <https://doi.org/10.1016/j.jmb.2016.01.022>.
- Heissler, Sarah M., Jayashankar Selvadurai, Lisa M. Bond, Roman Fedorov, John Kendrick-Jones, Folma Buss, and Dietmar J. Manstein. 2012. "Kinetic Properties and Small-Molecule Inhibition of Human Myosin-6." *FEBS Letters* 586 (19): 3208-14. <https://doi.org/10.1016/j.febslet.2012.07.014>.
- Hewage, Navindi, and David Altman. 2018. "A Role for Myosin VI in Retinal Pigment Epithelium Phagocytosis." *Biochemical and Biophysical Research Communications* 504 (4): 759-64. <https://doi.org/10.1016/j.bbrc.2018.09.006>.
- Higuchi, H., and S. Takemori. 1989. "Butanedione Monoxime Suppresses Contraction and ATPase Activity of Rabbit Skeletal Muscle." *Journal of Biochemistry* 105 (4): 638-43. <https://doi.org/10.1093/oxfordjournals.jbchem.a122717>.

- Hiratsuka, Toshiaki. 2006. "The Interaction of Phe472 with a Fluorescent Inhibitor Bound to the Complex of Myosin Subfragment-1 with Nucleotide." *Biochemistry* 45 (4): 1234–41. <https://doi.org/10.1021/bi051373l>.
- Houdusse, A., and C. Cohen. 1996. "Structure of the Regulatory Domain of Scallop Myosin at 2 Å Resolution: Implications for Regulation." *Structure (London, England: 1993)* 4 (1): 21–32. [https://doi.org/10.1016/s0969-2126\(96\)00006-8](https://doi.org/10.1016/s0969-2126(96)00006-8).
- Hu, Shichen, Yujiao Guo, Yingli Wang, Ying Li, Tao Fu, Zixuan Zhou, Yaru Wang, Jianping Liu, and Lifeng Pan. 2019. "Structure of Myosin VI/Tom1 Complex Reveals a Cargo Recognition Mode of Myosin VI for Tethering." *Nature Communications* 10 (1): 3459. <https://doi.org/10.1038/s41467-019-11481-6>.
- Hu, Shichen, Yingli Wang, Yukang Gong, Jianping Liu, Ying Li, and Lifeng Pan. 2018. "Mechanistic Insights into Recognitions of Ubiquitin and Myosin VI by Autophagy Receptor TAX1BP1." *Journal of Molecular Biology* 430 (18 Pt B): 3283–96. <https://doi.org/10.1016/j.jmb.2018.06.030>.
- Huttenlocher, A., R. R. Sandborg, and A. F. Horwitz. 1995. "Adhesion in Cell Migration." *Current Opinion in Cell Biology* 7 (5): 697–706. [https://doi.org/10.1016/0955-0674\(95\)80112-x](https://doi.org/10.1016/0955-0674(95)80112-x).
- Inoue, Akira, Osamu Sato, Kazuaki Homma, and Mitsuo Ikebe. 2002. "DOC-2/DAB2 Is the Binding Partner of Myosin VI." *Biochemical and Biophysical Research Communications* 292 (2): 300–307. <https://doi.org/10.1006/bbrc.2002.6636>.
- Inoue, Takeshi, Takahide Kon, Reiko Ohkura, Hisashi Yamakawa, Osamu Ohara, Jun Yokota, and Kazuo Sutoh. 2008. "BREK/LMTK2 Is a Myosin VI-Binding Protein Involved in Endosomal Membrane Trafficking." *Genes to Cells: Devoted to Molecular & Cellular Mechanisms* 13 (5): 483–95. <https://doi.org/10.1111/j.1365-2443.2008.01184.x>.
- Ishida, Morié, Saki P. Arai, Norihiko Ohbayashi, and Mitsunori Fukuda. 2014. "The GTPase-Deficient Rab27A(Q78L) Mutant Inhibits Melanosome Transport in Melanocytes through Trapping of Rab27A Effector Protein Slac2-a/Melanophilin in Their Cytosol: Development of a Novel Melanosome-Targeting Tag." *The Journal of Biological Chemistry* 289 (16): 11059–67. <https://doi.org/10.1074/jbc.M114.552281>.
- Islam, Kabirul, Harvey F. Chin, Adrian O. Olivares, Lauren P. Saunders, Enrique M. De La Cruz, and Tarun M. Kapoor. 2010. "A Myosin V Inhibitor Based on Privileged Chemical Scaffolds." *Angewandte Chemie (International Ed. in English)* 49 (45): 8484–88. <https://doi.org/10.1002/anie.201004026>.
- Iwaki, M., S. F. Wickham, K. Ikezaki, T. Yanagida, and W. M. Shih. 2016. "A Programmable DNA Origami Nanospring That Reveals Force-Induced Adjacent Binding of Myosin VI Heads." *Nature Communications* 7 (December): 13715. <https://doi.org/10.1038/ncomms13715>.
- Jana, Siddhartha S., Sachiyo Kawamoto, and Robert S. Adelstein. 2006. "A Specific Isoform of Nonmuscle Myosin II-C Is Required for Cytokinesis in a Tumor Cell Line." *The Journal of Biological Chemistry* 281 (34): 24662–70. <https://doi.org/10.1074/jbc.M604606200>.
- Jbireal, Jbireal M. Ali, Carina Strell, Bernd Niggemann, Kurt Zänker, and Frank Entschladen. 2010. "The Selective Role of Myosin VI in Lymphoid Leukemia Cell Migration." *Leukemia Research* 34 (12): 1656–62. <https://doi.org/10.1016/j.leukres.2010.04.018>.
- Jonge, Janeska J. de, Christopher Batters, Thomas O'Loughlin, Susan D. Arden, and Folma Buss. 2019. "The MYO6 Interactome: Selective Motor-Cargo Complexes for Diverse Cellular Processes." *FEBS Letters* 593 (13): 1494–1507. <https://doi.org/10.1002/1873-3468.13486>.
- Jumper, John, Richard Evans, Alexander Pritzel, Tim Green, Michael Figurnov, Olaf Ronneberger, Kathryn Tunyasuvunakool, et al. 2021. "Highly Accurate Protein Structure Prediction with AlphaFold." *Nature* 596 (7873): 583–89. <https://doi.org/10.1038/s41586-021-03819-2>.
- Karolczak, Justyna, Iuliia Pavlyk, Łukasz Majewski, Magdalena Sobczak, Paweł Niewiadomski, Yuriy Rzhpetskyy, Agata Sikorska, et al. 2015. "Involvement of Unconventional Myosin VI in Myoblast Function and Myotube Formation." *Histochemistry and Cell Biology* 144 (1): 21–38. <https://doi.org/10.1007/s00418-015-1322-6>.
- Katoh, Masaru. 2013. "Functional Proteomics, Human Genetics and Cancer Biology of GIPC Family Members." *Experimental & Molecular Medicine* 45 (June): e26. <https://doi.org/10.1038/emm.2013.49>.
- Kawas, Raja F., Robert L. Anderson, Sadie R. Bartholomew Ingle, Yonghong Song, Arvinder S. Sran, and Hector M. Rodriguez. 2017. "A Small-Molecule Modulator of Cardiac Myosin Acts on Multiple Stages of the Myosin Chemomechanical Cycle." *The Journal of Biological Chemistry* 292 (40): 16571–77. <https://doi.org/10.1074/jbc.M117.776815>.
- Kelleher, J. F., M. A. Mandell, G. Moulder, K. L. Hill, S. W. L'Hernault, R. Barstead, and M. A. Titus. 2000. "Myosin VI Is Required for Asymmetric Segregation of Cellular Components during C. Elegans Spermatogenesis." *Current Biology: CB* 10 (23): 1489–96. [https://doi.org/10.1016/s0960-9822\(00\)00828-9](https://doi.org/10.1016/s0960-9822(00)00828-9).

- Kellerman, K. A., and K. G. Miller. 1992. "An Unconventional Myosin Heavy Chain Gene from *Drosophila Melanogaster*." *The Journal of Cell Biology* 119 (4): 823–34. <https://doi.org/10.1083/jcb.119.4.823>.
- Kelley, M. J., W. Jawien, T. L. Ortel, and J. F. Korczak. 2000. "Mutation of MYH9, Encoding Non-Muscle Myosin Heavy Chain A, in May-Hegglin Anomaly." *Nature Genetics* 26 (1): 106–8. <https://doi.org/10.1038/79069>.
- Képiró, Miklós, Boglárka H. Várkuti, László Végner, Gergely Vörös, György Hegyi, Máté Varga, and András Málnási-Csizmadia. 2014. "Para-Nitroblebbistatin, the Non-Cytotoxic and Photostable Myosin II Inhibitor." *Angewandte Chemie (International Ed. in English)* 53 (31): 8211–15. <https://doi.org/10.1002/anie.201403540>.
- Kesavapany, Sashi, Kwok-Fai Lau, Steven Ackerley, Steven J. Banner, Stephen J. A. Shemilt, Jonathan D. Cooper, P. Nigel Leigh, Christopher E. Shaw, Declan M. McLoughlin, and Christopher C. J. Miller. 2003. "Identification of a Novel, Membrane-Associated Neuronal Kinase, Cyclin-Dependent Kinase 5/P35-Regulated Kinase." *The Journal of Neuroscience: The Official Journal of the Society for Neuroscience* 23 (12): 4975–83.
- Kim, Bong Jik, Jin Hee Han, Hye-Rim Park, Min Young Kim, Ah Reum Kim, Seung-Ha Oh, Woong-Yang Park, Doo Yi Oh, Seungmin Lee, and Byung Yoon Choi. 2018. "A Clinical Guidance to DFNA22 Drawn from a Korean Cohort Study with an Autosomal Dominant Deaf Population: A Retrospective Cohort Study." *The Journal of Gene Medicine* 20 (6): e3019. <https://doi.org/10.1002/jgm.3019>.
- Kim, Bong Jik, Ah Reum Kim, Jin Hee Han, Chung Lee, Doo Yi Oh, and Byung Yoon Choi. 2017. "Discovery of MYH14 as an Important and Unique Deafness Gene Causing Prelingually Severe Autosomal Dominant Nonsyndromic Hearing Loss." *The Journal of Gene Medicine* 19 (4). <https://doi.org/10.1002/jgm.2950>.
- Kim, Byeong-Won, Seung Beom Hong, Jun Hoe Kim, Do Hoon Kwon, and Hyun Kyu Song. 2013. "Structural Basis for Recognition of Autophagic Receptor NDP52 by the Sugar Receptor Galectin-8." *Nature Communications* 4: 1613. <https://doi.org/10.1038/ncomms2606>.
- Kim, Hyeongjun, Jen Hsin, Yanxin Liu, Paul R. Selvin, and Klaus Schulten. 2010a. "Formation of Salt Bridges Mediates Internal Dimerization of Myosin VI Medial Tail Domain." *Structure (London, England: 1993)* 18 (11): 1443–49. <https://doi.org/10.1016/j.str.2010.09.011>.
- Kim, Hyun-Taek, Wenguang Yin, Young-June Jin, Paolo Panza, Felix Gunawan, Beate Grohmann, Carmen Buettner, et al. 2018. "Myh10 Deficiency Leads to Defective Extracellular Matrix Remodeling and Pulmonary Disease." *Nature Communications* 9 (1): 4600. <https://doi.org/10.1038/s41467-018-06833-7>.
- Kim, Sang-Joo, Seokwon Lee, Hong-Joon Park, Tae-Hun Kang, Borum Sagong, Jeong-In Baek, Se-Kyung Oh, Jae Young Choi, Kyu-Yup Lee, and Un-Kyung Kim. 2016. "Genetic Association of MYH Genes with Hereditary Hearing Loss in Korea." *Gene* 591 (1): 177–82. <https://doi.org/10.1016/j.gene.2016.07.011>.
- Kleeff, Jörg, Yong Huang, Samuel C. Mok, Arthur Zimmermann, Helmut Friess, and Markus W. Büchler. 2002. "Down-Regulation of DOC-2 in Colorectal Cancer Points to Its Role as a Tumor Suppressor in This Malignancy." *Diseases of the Colon and Rectum* 45 (9): 1242–48. <https://doi.org/10.1007/s10350-004-6399-2>.
- Kneussel, Matthias, Noelia Sánchez-Rodríguez, Michaela Mischak, and Frank F. Heisler. 2021. "Dynein and Musklin Control Myosin VI Delivery towards the Neuronal Nucleus." *iScience* 24 (5): 102416. <https://doi.org/10.1016/j.isci.2021.102416>.
- Ko, Young Wook, Joo Yeon Ko, Young Suck Ro, and Jeong Eun Kim. 2022. "Oral-Facial-Digital Syndrome Type 1: A Case Report and Review." *Annals of Dermatology* 34 (2): 132–35. <https://doi.org/10.5021/ad.2022.34.2.132>.
- Kolega, J. 2004. "Phototoxicity and Photoinactivation of Blebbistatin in UV and Visible Light." *Biochemical and Biophysical Research Communications* 320 (3): 1020–25. <https://doi.org/10.1016/j.bbrc.2004.06.045>.
- Komander, David, Christopher J. Lord, Hartmut Scheel, Sally Swift, Kay Hofmann, Alan Ashworth, and David Barford. 2008. "The Structure of the CYLD USP Domain Explains Its Specificity for Lys63-Linked Polyubiquitin and Reveals a B Box Module." *Molecular Cell* 29 (4): 451–64. <https://doi.org/10.1016/j.molcel.2007.12.018>.
- Komander, David, and Michael Rape. 2012. "The Ubiquitin Code." *Annual Review of Biochemistry* 81: 203–29. <https://doi.org/10.1146/annurev-biochem-060310-170328>.
- Kovács, Mihály, Judit Tóth, Csaba Hetényi, András Málnási-Csizmadia, and James R. Sellers. 2004. "Mechanism of Blebbistatin Inhibition of Myosin II." *The Journal of Biological Chemistry* 279 (34): 35557–63. <https://doi.org/10.1074/jbc.M405319200>.

- Krementsov, Dmitry N., Elena B. Kremetsova, and Kathleen M. Trybus. 2004. "Myosin V: Regulation by Calcium, Calmodulin, and the Tail Domain." *The Journal of Cell Biology* 164 (6): 877–86. <https://doi.org/10.1083/jcb.200310065>.
- Kruppa, Antonina J., Chieko Kishi-Itakura, Thomas A. Masters, Joanna E. Rorbach, Guinevere L. Grice, John Kendrick-Jones, James A. Nathan, Michal Minczuk, and Folma Buss. 2018. "Myosin VI-Dependent Actin Cages Encapsulate Parkin-Positive Damaged Mitochondria." *Developmental Cell* 44 (4): 484-499.e6. <https://doi.org/10.1016/j.devcel.2018.01.007>.
- Kunfermann, Andrea, Matthias Witschel, Boris Illarionov, René Martin, Matthias Rottmann, H. Wolfgang Höffken, Michael Seet, *et al.* 2014. "Pseudilins: Halogenated, Allosteric Inhibitors of the Non-Mevalonate Pathway Enzyme IspD." *Angewandte Chemie (International Ed. in English)* 53 (8): 2235–39. <https://doi.org/10.1002/anie.201309557>.
- Kunishima, S., T. Matsushita, T. Kojima, N. Amemiya, Y. M. Choi, N. Hosaka, M. Inoue, *et al.* 2001. "Identification of Six Novel MYH9 Mutations and Genotype-Phenotype Relationships in Autosomal Dominant Macrothrombocytopenia with Leukocyte Inclusions." *Journal of Human Genetics* 46 (12): 722–29. <https://doi.org/10.1007/s100380170007>.
- Lalwani, A. K., J. A. Goldstein, M. J. Kelley, W. Luxford, C. M. Castelein, and A. N. Mhatre. 2000. "Human Nonsyndromic Hereditary Deafness DFNA17 Is Due to a Mutation in Nonmuscle Myosin MYH9." *American Journal of Human Genetics* 67 (5): 1121–28. [https://doi.org/10.1016/S0002-9297\(07\)62942-5](https://doi.org/10.1016/S0002-9297(07)62942-5).
- Lehka, Lilya, Małgorzata Topolewska, Dominika Wojton, Olena Karatsai, Paloma Alvarez-Suarez, Paweł Pomorski, and Maria Jolanta Rędownicz. 2020. "Formation of Aberrant Myotubes by Myoblasts Lacking Myosin VI Is Associated with Alterations in the Cytoskeleton Organization, Myoblast Adhesion and Fusion." *Cells* 9 (7): E1673. <https://doi.org/10.3390/cells9071673>.
- Li, Hui, Fusheng Zhou, Hongyan Wang, Da Lin, Gang Chen, Xianbo Zuo, Liangdan Sun, Xuejun Zhang, and Sen Yang. 2015. "Knockdown of Myosin VI by Lentivirus-Mediated Short Hairpin RNA Suppresses Proliferation of Melanoma." *Molecular Medicine Reports* 12 (5): 6801–6. <https://doi.org/10.3892/mmr.2015.4261>.
- Li, Jianchao, and Mingjie Zhang. 2020. "Cargo Binding by Unconventional Myosins." *Advances in Experimental Medicine and Biology* 1239: 21–40. https://doi.org/10.1007/978-3-030-38062-5_3.
- Li, Ming-De, Nai-Kei Wong, Jia Xiao, Ruixue Zhu, Liangliang Wu, Sheng-Yao Dai, Feng Chen, *et al.* 2018. "Dynamics of Oxygen-Independent Photocleavage of Blebbistatin as a One-Photon Blue or Two-Photon Near-Infrared Light-Gated Hydroxyl Radical Photocage." *Journal of the American Chemical Society* 140 (46): 15957–68. <https://doi.org/10.1021/jacs.8b10235>.
- Li, Sunan, Gui-Jing Xiong, Ning Huang, and Zu-Hang Sheng. 2020. "The Cross-Talk of Energy Sensing and Mitochondrial Anchoring Sustains Synaptic Efficacy by Maintaining Presynaptic Metabolism." *Nature Metabolism* 2 (10): 1077–95. <https://doi.org/10.1038/s42255-020-00289-0>.
- Limouze, John, Aaron F. Straight, Timothy Mitchison, and James R. Sellers. 2004. "Specificity of Blebbistatin, an Inhibitor of Myosin II." *Journal of Muscle Research and Cell Motility* 25 (4–5): 337–41. <https://doi.org/10.1007/s10974-004-6060-7>.
- Lister, Ida, Stephan Schmitz, Matthew Walker, John Trinick, Folma Buss, Claudia Veigel, and John Kendrick-Jones. 2004. "A Monomeric Myosin VI with a Large Working Stroke." *The EMBO Journal* 23 (8): 1729–38. <https://doi.org/10.1038/sj.emboj.7600180>.
- Liu, Huanting, and James H. Naismith. 2008. "An Efficient One-Step Site-Directed Deletion, Insertion, Single and Multiple-Site Plasmid Mutagenesis Protocol." *BMC Biotechnology* 8 (December): 91. <https://doi.org/10.1186/1472-6750-8-91>.
- Liu, Jun, Dianne W. Taylor, Elena B. Kremetsova, Kathleen M. Trybus, and Kenneth A. Taylor. 2006. "Three-Dimensional Structure of the Myosin V Inhibited State by Cryoelectron Tomography." *Nature* 442 (7099): 208–11. <https://doi.org/10.1038/nature04719>.
- Liu, Rong, Neil Billington, Yi Yang, Charles Bond, Amy Hong, Verl Siththanandan, Yasuharu Takagi, and James R. Sellers. 2021a. "A Binding Protein Regulates Myosin-7a Dimerization and Actin Bundle Assembly." *Nature Communications* 12 (1): 563. <https://doi.org/10.1038/s41467-020-20864-z>.
- Liu, Yingying, Howard D. White, Betty Belknap, Donald A. Winkelmann, and Eva Forgacs. 2015. "Omecamtiv Mecarbil Modulates the Kinetic and Motile Properties of Porcine β -Cardiac Myosin." *Biochemistry* 54 (10): 1963–75. <https://doi.org/10.1021/bi5015166>.
- Llinas, Paola, Tatiana Isabet, Lin Song, Virginie Ropars, Bin Zong, Hannah Benisty, Serena Sirigu, *et al.* 2015. "How Actin Initiates the Motor Activity of Myosin." *Developmental Cell* 33 (4): 401–12. <https://doi.org/10.1016/j.devcel.2015.03.025>.

- Louvet, Emilie, and Piergiorgio Percipalle. 2009. "Transcriptional Control of Gene Expression by Actin and Myosin." *International Review of Cell and Molecular Biology* 272: 107–47. [https://doi.org/10.1016/S1937-6448\(08\)01603-1](https://doi.org/10.1016/S1937-6448(08)01603-1).
- Lowey, S., H. S. Slayter, A. G. Weeds, and H. Baker. 1969. "Substructure of the Myosin Molecule. I. Subfragments of Myosin by Enzymic Degradation." *Journal of Molecular Biology* 42 (1): 1–29. [https://doi.org/10.1016/0022-2836\(69\)90483-5](https://doi.org/10.1016/0022-2836(69)90483-5).
- Lu, Qing, Fei Ye, Zhiyi Wei, Zilong Wen, and Mingjie Zhang. 2012. "Antiparallel Coiled-Coil-Mediated Dimerization of Myosin X." *Proceedings of the National Academy of Sciences of the United States of America* 109 (43): 17388–93. <https://doi.org/10.1073/pnas.1208642109>.
- Lucas-Lopez, Cristina, John S. Allingham, Tomas Lebl, Christopher P. A. T. Lawson, Ruth Brenk, James R. Sellers, Ivan Rayment, and Nicholas J. Westwood. 2008. "The Small Molecule Tool (S)-(-)-Blebbistatin: Novel Insights of Relevance to Myosin Inhibitor Design." *Organic & Biomolecular Chemistry* 6 (12): 2076–84. <https://doi.org/10.1039/b801223g>.
- Lumb, K. J., C. M. Carr, and P. S. Kim. 1994. "Subdomain Folding of the Coiled Coil Leucine Zipper from the BZIP Transcriptional Activator GCN4." *Biochemistry* 33 (23): 7361–67. <https://doi.org/10.1021/bi00189a042>.
- Ma, Xiaoming, Jiqi Yan, Wei Chen, Peng Du, Jiaming Xie, Hongpei Yu, and Haorong Wu. 2015. "Knockdown of Myosin VI Inhibits Proliferation of Hepatocellular Carcinoma Cells In Vitro." *Chemical Biology & Drug Design* 86 (4): 723–30. <https://doi.org/10.1111/cbdd.12544>.
- Ma, Xuefei, and Robert S. Adelstein. 2014. "A Point Mutation in Myh10 Causes Major Defects in Heart Development and Body Wall Closure." *Circulation. Cardiovascular Genetics* 7 (3): 257–65. <https://doi.org/10.1161/CIRCGENETICS.113.000455>.
- Magistrati, Elisa, Giorgia Maestrini, Carlos A. Niño, Mariana Lince-Faria, Galina Beznoussenko, Alexandre Mironov, Elena Maspero, Mónica Bettencourt-Dias, and Simona Polo. 2022. "Myosin VI Regulates Ciliogenesis by Promoting the Turnover of the Centrosomal/Satellite Protein OFD1." *EMBO Reports* 23 (3): e54160. <https://doi.org/10.15252/embr.202154160>.
- Majewski, Lukasz, Jolanta Nowak, Magdalena Sobczak, Olena Karatsai, Serhiy Havrylov, Robert Lenartowski, Malgorzata Suszek, Marta Lenartowska, and Maria Jolanta Redowicz. 2018. "Myosin VI in the Nucleus of Neurosecretory PC12 Cells: Stimulation-Dependent Nuclear Translocation and Interaction with Nuclear Proteins." *Nucleus (Austin, Tex.)* 9 (1): 125–41. <https://doi.org/10.1080/19491034.2017.1421881>.
- Majewski, Łukasz, Magdalena Sobczak, Serhiy Havrylov, Jolanta Józwiak, and Maria Jolanta Rędownicz. 2012. "Dock7: A GEF for Rho-Family GTPases and a Novel Myosin VI-Binding Partner in Neuronal PC12 Cells." *Biochemistry and Cell Biology = Biochimie Et Biologie Cellulaire* 90 (4): 565–74. <https://doi.org/10.1139/o2012-009>.
- Majewski, Łukasz, Magdalena Sobczak, Anna Wasik, Krzysztof Skowronek, and Maria Jolanta Rędownicz. 2011. "Myosin VI in PC12 Cells Plays Important Roles in Cell Migration and Proliferation but Not in Catecholamine Secretion." *Journal of Muscle Research and Cell Motility* 32 (4–5): 291–302. <https://doi.org/10.1007/s10974-011-9279-0>.
- Makioka, Kouki, Tsuneo Yamazaki, Masamitsu Takatama, Masaki Ikeda, Shigeo Murayama, Koichi Okamoto, and Yoshio Ikeda. 2016. "Immunolocalization of Tom1 in Relation to Protein Degradation Systems in Alzheimer's Disease." *Journal of the Neurological Sciences* 365 (June): 101–7. <https://doi.org/10.1016/j.jns.2016.03.035>.
- Malik, Fady I., James J. Hartman, Kathleen A. Elias, Bradley P. Morgan, Hector Rodriguez, Katjusa Brejc, Robert L. Anderson, et al. 2011. "Cardiac Myosin Activation: A Potential Therapeutic Approach for Systolic Heart Failure." *Science (New York, N.Y.)* 331 (6023): 1439–43. <https://doi.org/10.1126/science.1200113>.
- Manalastas-Cantos, K., P. V. Konarev, N. R. Hajizadeh, A. G. Kikhney, M. V. Petoukhov, D. S. Molodenskiy, A. Panjkovich, et al. 2021. "ATSAS 3.0: Expanded Functionality and New Tools for Small-Angle Scattering Data Analysis." *Journal of Applied Crystallography* 54 (1): 343–55. <https://doi.org/10.1107/S1600576720013412>.
- Manceva, Slobodanka, Tianming Lin, Huy Pham, John H. Lewis, Yale E. Goldman, and E. Michael Ostap. 2007. "Calcium Regulation of Calmodulin Binding to and Dissociation from the Myo1c Regulatory Domain." *Biochemistry* 46 (42): 11718–26. <https://doi.org/10.1021/bi700894h>.
- Mangold, Sabine, Suzanne J. Norwood, Alpha S. Yap, and Brett M. Collins. 2012. "The Juxtamembrane Domain of the E-Cadherin Cytoplasmic Tail Contributes to Its Interaction with Myosin VI." *Bioarchitecture* 2 (5): 185–88. <https://doi.org/10.4161/bioa.22082>.

- Manstein, Dietmar J., J. C. M. Meiring, E. C. Hardeman, and Peter W. Gunning. 2020. "Actin-Tropomyosin Distribution in Non-Muscle Cells." *Journal of Muscle Research and Cell Motility* 41 (1): 11–22. <https://doi.org/10.1007/s10974-019-09514-0>.
- Manstein, Dietmar J., and Matthias Preller. 2020. "Small Molecule Effectors of Myosin Function." *Advances in Experimental Medicine and Biology* 1239: 61–84. https://doi.org/10.1007/978-3-030-38062-5_5.
- Martin, J. C., B.-S. Herbert, and B. A. Hocevar. 2010. "Disabled-2 Downregulation Promotes Epithelial-to-Mesenchymal Transition." *British Journal of Cancer* 103 (11): 1716–23. <https://doi.org/10.1038/sj.bjc.6605975>.
- Martini, Alessandra Cadete, Angela Gomez-Arboledas, Stefania Forner, Carlos J. Rodriguez-Ortiz, Amanda McQuade, Emma Danhash, Jimmy Phan, *et al.* 2019. "Amyloid-Beta Impairs TOM1-Mediated IL-1R1 Signaling." *Proceedings of the National Academy of Sciences of the United States of America* 116 (42): 21198–206. <https://doi.org/10.1073/pnas.1914088116>.
- Martinsson, T., A. Oldfors, N. Darin, K. Berg, H. Tajsharghi, M. Kyllerman, and J. Wahlstrom. 2000. "Autosomal Dominant Myopathy: Missense Mutation (Glu-706 --> Lys) in the Myosin Heavy Chain IIa Gene." *Proceedings of the National Academy of Sciences of the United States of America* 97 (26): 14614–19. <https://doi.org/10.1073/pnas.250289597>.
- Masters, Thomas A., and Folma Buss. 2017. "Filopodia Formation and Endosome Clustering Induced by Mutant Plus-End-Directed Myosin VI." *Proceedings of the National Academy of Sciences of the United States of America* 114 (7): 1595–1600. <https://doi.org/10.1073/pnas.1616941114>.
- Masters, Thomas A., David A. Tumbarello, Margarita V. Chibalina, and Folma Buss. 2017. "MYO6 Regulates Spatial Organization of Signaling Endosomes Driving AKT Activation and Actin Dynamics." *Cell Reports* 19 (10): 2088–2101. <https://doi.org/10.1016/j.celrep.2017.05.048>.
- Matthews, B. W. 1968. "Solvent Content of Protein Crystals." *Journal of Molecular Biology* 33 (2): 491–97. [https://doi.org/10.1016/0022-2836\(68\)90205-2](https://doi.org/10.1016/0022-2836(68)90205-2).
- McCoy, A. J., R. W. Grosse-Kunstleve, P. D. Adams, M. D. Winn, L. C. Storoni, and R. J. Read. 2007. "Phaser Crystallographic Software." *Journal of Applied Crystallography* 40 (4): 658–74. <https://doi.org/10.1107/S0021889807021206>.
- Melchionda, S., N. Ahituv, L. Bisceglia, T. Sobe, F. Glaser, R. Rabionet, M. L. Arbones, *et al.* 2001. "MYO6, the Human Homologue of the Gene Responsible for Deafness in Snell's Waltzer Mice, Is Mutated in Autosomal Dominant Nonsyndromic Hearing Loss." *American Journal of Human Genetics* 69 (3): 635–40. <https://doi.org/10.1086/323156>.
- Ménétreay, Julie, Amel Bahloul, Amber L. Wells, Christopher M. Yengo, Carl A. Morris, H. Lee Sweeney, and Anne Houdusse. 2005. "The Structure of the Myosin VI Motor Reveals the Mechanism of Directionality Reversal." *Nature* 435 (7043): 779–85. <https://doi.org/10.1038/nature03592>.
- Ménétreay, Julie, Tatiana Isabet, Virginie Ropars, Monalisa Mukherjea, Olena Pylypenko, Xiaoyan Liu, Javier Perez, Patrice Vachette, H. Lee Sweeney, and Anne M. Houdusse. 2012. "Processive Steps in the Reverse Direction Require Uncoupling of the Lead Head Lever arm of Myosin VI." *Molecular Cell* 48 (1): 75–86. <https://doi.org/10.1016/j.molcel.2012.07.034>.
- Ménétreay, Julie, Paola Llinas, Jérôme Cicolari, Gaëlle Squires, Xiaoyan Liu, Anna Li, H. Lee Sweeney, and Anne Houdusse. 2008. "The Post-Rigor Structure of Myosin VI and Implications for the Recovery Stroke." *The EMBO Journal* 27 (1): 244–52. <https://doi.org/10.1038/sj.emboj.7601937>.
- Ménétreay, Julie, Paola Llinas, Monalisa Mukherjea, H. Lee Sweeney, and Anne Houdusse. 2007. "The Structural Basis for the Large Powerstroke of Myosin VI." *Cell* 131 (2): 300–308. <https://doi.org/10.1016/j.cell.2007.08.027>.
- Mentes, Ahmet, Andrew Huehn, Xueqi Liu, Adam Zwolak, Roberto Dominguez, Henry Shuman, E. Michael Ostap, and Charles V. Sindelar. 2018. "High-Resolution Cryo-EM Structures of Actin-Bound Myosin States Reveal the Mechanism of Myosin Force Sensing." *Proceedings of the National Academy of Sciences of the United States of America* 115 (6): 1292–97. <https://doi.org/10.1073/pnas.1718316115>.
- Merino, Felipe, Sabrina Pospich, Johanna Funk, Thorsten Wagner, Florian Küllmer, Hans-Dieter Arndt, Peter Bieling, and Stefan Raunser. 2018. "Structural Transitions of F-Actin upon ATP Hydrolysis at near-Atomic Resolution Revealed by Cryo-EM." *Nature Structural & Molecular Biology* 25 (6): 528–37. <https://doi.org/10.1038/s41594-018-0074-0>.
- Mhandire, Doreen Z., David P. Burns, Angela L. Roger, Ken D. O'Halloran, and Mai K. ElMallah. 2022. "Breathing in Duchenne Muscular Dystrophy: Translation to Therapy." *The Journal of Physiology* 600 (15): 3465–82. <https://doi.org/10.1113/JP281671>.

- Mhatre, Anand N., Yan Li, Graham Atkin, Abdel Maghnoij, and Anil K. Lalwani. 2006. "Expression of Myh9 in the Mammalian Cochlea: Localization within the Stereocilia." *Journal of Neuroscience Research* 84 (4): 809–18. <https://doi.org/10.1002/jnr.20993>.
- Mikulich, Aliaksandr, Simona Kavaliauskiene, and Petras Juzenas. 2012. "Blebbistatin, a Myosin Inhibitor, Is Phototoxic to Human Cancer Cells under Exposure to Blue Light." *Biochimica Et Biophysica Acta* 1820 (7): 870–77. <https://doi.org/10.1016/j.bbagen.2012.04.003>.
- Millo, Hadas, Kevin Leaper, Vasiliki Lazou, and Mary Bownes. 2004. "Myosin VI Plays a Role in Cell-Cell Adhesion during Epithelial Morphogenesis." *Mechanisms of Development* 121 (11): 1335–51. <https://doi.org/10.1016/j.mod.2004.06.007>.
- Mishra, Sanjay K., Peter A. Keyel, Matthew J. Hawryluk, Nicole R. Agostinelli, Simon C. Watkins, and Linton M. Traub. 2002. "Disabled-2 Exhibits the Properties of a Cargo-Selective Endocytic Clathrin Adaptor." *The EMBO Journal* 21 (18): 4915–26. <https://doi.org/10.1093/emboj/cdf487>.
- Misra, S., B. M. Beach, and J. H. Hurley. 2000. "Structure of the VHS Domain of Human Tom1 (Target of Myb 1): Insights into Interactions with Proteins and Membranes." *Biochemistry* 39 (37): 11282–90. <https://doi.org/10.1021/bi0013546>.
- Mitra, Sharmistha, C. Alicia Traughber, Mary K. Brannon, Stephanie Gomez, and Daniel G. S. Capelluto. 2013. "Ubiquitin Interacts with the Tollip C2 and CUE Domains and Inhibits Binding of Tollip to Phosphoinositides." *The Journal of Biological Chemistry* 288 (36): 25780–91. <https://doi.org/10.1074/jbc.M113.484170>.
- Mok, S. C., W. Y. Chan, K. K. Wong, K. K. Cheung, C. C. Lau, S. W. Ng, A. Baldini, C. V. Colitti, C. O. Rock, and R. S. Berkowitz. 1998. "DOC-2, a Candidate Tumor Suppressor Gene in Human Epithelial Ovarian Cancer." *Oncogene* 16 (18): 2381–87. <https://doi.org/10.1038/sj.onc.1201769>.
- Mok, S. C., K. K. Wong, R. K. Chan, C. C. Lau, S. W. Tsao, R. C. Knapp, and R. S. Berkowitz. 1994. "Molecular Cloning of Differentially Expressed Genes in Human Epithelial Ovarian Cancer." *Gynecologic Oncology* 52 (2): 247–52. <https://doi.org/10.1006/gyno.1994.1040>.
- Morris, Carl A., Amber L. Wells, Zhaohui Yang, Li-Qiong Chen, Corradina V. Baldacchino, and H. Lee Sweeney. 2003. "Calcium Functionally Uncouples the Heads of Myosin VI." *The Journal of Biological Chemistry* 278 (26): 23324–30. <https://doi.org/10.1074/jbc.M208957200>.
- Morris, Shelli M., Susan D. Arden, Rhys C. Roberts, John Kendrick-Jones, Jonathan A. Cooper, J. Paul Luzio, and Folma Buss. 2002. "Myosin VI Binds to and Localises with Dab2, Potentially Linking Receptor-Mediated Endocytosis and the Actin Cytoskeleton." *Traffic (Copenhagen, Denmark)* 3 (5): 331–41. <https://doi.org/10.1034/j.1600-0854.2002.30503.x>.
- Morriswood, Brooke, Grigory Ryzhakov, Claudia Puri, Susan D. Arden, Rhys Roberts, Calliope Dendrou, John Kendrick-Jones, and Folma Buss. 2007. "T6BP and NDP52 Are Myosin VI Binding Partners with Potential Roles in Cytokine Signalling and Cell Adhesion." *Journal of Cell Science* 120 (Pt 15): 2574–85. <https://doi.org/10.1242/jcs.007005>.
- Mukherjea, Monalisa, M. Yusuf Ali, Carlos Kikuti, Daniel Safer, Zhaohui Yang, Helena Sirkia, Virginie Ropars, Anne Houdusse, David M. Warshaw, and H. Lee Sweeney. 2014a. "Myosin VI Must Dimerize and Deploy Its Unusual Lever arm in Order to Perform Its Cellular Roles." *Cell Reports* 8 (5): 1522–32. <https://doi.org/10.1016/j.celrep.2014.07.041>.
- Mukherjea, Monalisa, Paola Llinas, HyeonJun Kim, Mirko Travaglia, Daniel Safer, Julie Ménétrey, Clara Franzini-Armstrong, Paul R. Selvin, Anne Houdusse, and H. Lee Sweeney. 2009a. "Myosin VI Dimerization Triggers an Unfolding of a Three-Helix Bundle in Order to Extend Its Reach." *Molecular Cell* 35 (3): 305–15. <https://doi.org/10.1016/j.molcel.2009.07.010>.
- Mulkearns, Erin E., and Jonathan A. Cooper. 2012. "FCH Domain Only-2 Organizes Clathrin-Coated Structures and Interacts with Disabled-2 for Low-Density Lipoprotein Receptor Endocytosis." *Molecular Biology of the Cell* 23 (7): 1330–42. <https://doi.org/10.1091/mbc.E11-09-0812>.
- Müller, Mirco, Ralph P. Diensthuber, Igor Chizhov, Peter Claus, Sarah M. Heissler, Matthias Preller, Manuel H. Taft, and Dietmar J. Manstein. 2013. "Distinct Functional Interactions between Actin Isoforms and Nonsarcomeric Myosins." *PloS One* 8 (7): e70636. <https://doi.org/10.1371/journal.pone.0070636>.
- Naccache, Samia N., Tama Hasson, and Arie Horowitz. 2006a. "Binding of Internalized Receptors to the PDZ Domain of GIPC/Synectin Recruits Myosin VI to Endocytic Vesicles." *Proceedings of the National Academy of Sciences of the United States of America* 103 (34): 12735–40. <https://doi.org/10.1073/pnas.0605317103>.
- Narendra, Derek, Atsushi Tanaka, Der-Fen Suen, and Richard J. Youle. 2008. "Parkin Is Recruited Selectively to Impaired Mitochondria and Promotes Their Autophagy." *The Journal of Cell Biology* 183 (5): 795–803. <https://doi.org/10.1083/jcb.200809125>.

- Newell-Litwa, Karen A., Rick Horwitz, and Marcelo L. Lamers. 2015. "Non-Muscle Myosin II in Disease: Mechanisms and Therapeutic Opportunities." *Disease Models & Mechanisms* 8 (12): 1495–1515. <https://doi.org/10.1242/dmm.022103>.
- Nishikawa, So, Ikuo Arimoto, Keigo Ikezaki, Mitsuhiro Sugawa, Hiroshi Ueno, Tomotaka Komori, Atsuko H. Iwane, and Toshio Yanagida. 2010. "Switch between Large Hand-over-Hand and Small Inchworm-like Steps in Myosin VI." *Cell* 142 (6): 879–88. <https://doi.org/10.1016/j.cell.2010.08.033>.
- Noguchi, Tatsuhiko, Marta Lenartowska, and Kathryn G. Miller. 2006. "Myosin VI Stabilizes an Actin Network during Drosophila Spermatid Individualization." *Molecular Biology of the Cell* 17 (6): 2559–71. <https://doi.org/10.1091/mbc.e06-01-0031>.
- Odrionitz, Florian, and Martin Kollmar. 2007. "Drawing the Tree of Eukaryotic Life Based on the Analysis of 2,269 Manually Annotated Myosins from 328 Species." *Genome Biology* 8 (9): R196. <https://doi.org/10.1186/gb-2007-8-9-r196>.
- Ogbu, Stella C., Phillip R. Musich, Jinyu Zhang, Zhi Q. Yao, Philip H. Howe, and Yong Jiang. 2021. "The Role of Disabled-2 (Dab2) in Diseases." *Gene* 769 (February): 145202. <https://doi.org/10.1016/j.gene.2020.145202>.
- Oka, Shin-Ichiro, Timothy F. Day, Shin-Ya Nishio, Hideaki Moteki, Maiko Miyagawa, Shinya Morita, Shuji Izumi, *et al.* 2020. "Clinical Characteristics and In Vitro Analysis of MYO6 Variants Causing Late-Onset Progressive Hearing Loss." *Genes* 11 (3): E273. <https://doi.org/10.3390/genes11030273>.
- O'Loughlin, Thomas, Thomas A. Masters, and Folma Buss. 2018. "The MYO6 Interactome Reveals Adaptor Complexes Coordinating Early Endosome and Cytoskeletal Dynamics." *EMBO Reports* 19 (4): e44884. <https://doi.org/10.15252/embr.201744884>.
- Onishi, Mashun, Koji Yamano, Miyuki Sato, Noriyuki Matsuda, and Koji Okamoto. 2021. "Molecular Mechanisms and Physiological Functions of Mitophagy." *The EMBO Journal* 40 (3): e104705. <https://doi.org/10.15252/emboj.2020104705>.
- Osterweil, Emily, David G. Wells, and Mark S. Mooseker. 2005. "A Role for Myosin VI in Postsynaptic Structure and Glutamate Receptor Endocytosis." *The Journal of Cell Biology* 168 (2): 329–38. <https://doi.org/10.1083/jcb.200410091>.
- Pal, Krishnendu, Alexandre A. Pletnev, Shamit K. Dutta, Enfeng Wang, Ruizhi Zhao, Aradhita Baral, Vinod Kumar Yadav, *et al.* 2014. "Inhibition of Endoglin-GIPC Interaction Inhibits Pancreatic Cancer Cell Growth." *Molecular Cancer Therapeutics* 13 (10): 2264–75. <https://doi.org/10.1158/1535-7163.MCT-14-0291>.
- Park, Hyekeun, Anna Li, Li-Qiong Chen, Anne Houdusse, Paul R. Selvin, and H. Lee Sweeney. 2007. "The Unique Insert at the End of the Myosin VI Motor Is the Sole Determinant of Directionality." *Proceedings of the National Academy of Sciences* 104 (3): 778–83. <https://doi.org/10.1073/pnas.0610066104>.
- Park, Hyekeun, Bhagavathi Ramamurthy, Mirko Travaglia, Dan Safer, Li-Qiong Chen, Clara Franzini-Armstrong, Paul R. Selvin, and H. Lee Sweeney. 2006. "Full-Length Myosin VI Dimerizes and Moves Processively along Actin Filaments upon Monomer Clustering." *Molecular Cell* 21 (3): 331–36. <https://doi.org/10.1016/j.molcel.2005.12.015>.
- Patra, Chitta Ranjan, Chamila N. Rupasinghe, Shamit K. Dutta, Santanu Bhattacharya, Enfeng Wang, Mark R. Spaller, and Debabrata Mukhopadhyay. 2012. "Chemically Modified Peptides Targeting the PDZ Domain of GIPC as a Therapeutic Approach for Cancer." *ACS Chemical Biology* 7 (4): 770–79. <https://doi.org/10.1021/cb200536r>.
- Penengo, Lorenza, Marina Mapelli, Andrea G. Murachelli, Stefano Confalonieri, Laura Magri, Andrea Musacchio, Pier Paolo Di Fiore, Simona Polo, and Thomas R. Schneider. 2006. "Crystal Structure of the Ubiquitin Binding Domains of Rabex-5 Reveals Two Modes of Interaction with Ubiquitin." *Cell* 124 (6): 1183–95. <https://doi.org/10.1016/j.cell.2006.02.020>.
- Peterson, M. D., W. M. Bement, and M. S. Mooseker. 1993. "An In Vitro Model for the Analysis of Intestinal Brush Border Assembly. II. Changes in Expression and Localization of Brush Border Proteins during Cell Contact-Induced Brush Border Assembly in Caco-2BBE Cells." *Journal of Cell Science* 105 (Pt 2) (June): 461–72. <https://doi.org/10.1242/jcs.105.2.461>.
- Phichith, Denis, Mirko Travaglia, Zhaohui Yang, Xiaoyan Liu, Alan B. Zong, Daniel Safer, and H. Lee Sweeney. 2009a. "Cargo Binding Induces Dimerization of Myosin VI." *Proceedings of the National Academy of Sciences of the United States of America* 106 (41): 17320–24. <https://doi.org/10.1073/pnas.0909748106>.
- Piehl, Michelle, Corinna Lehmann, Anna Gumpert, Jean-Pierre Denzot, Dominique Segretain, and Matthias M. Falk. 2007. "Internalization of Large Double-Membrane Intercellular Vesicles by a Clathrin-Dependent Endocytic Process." *Molecular Biology of the Cell* 18 (2): 337–47. <https://doi.org/10.1091/mbc.e06-06-0487>.

- Planelles Herrero, Vicente José. 2017. "Bases Mécanistiques et Structurales de La Régulation de l'activité Des Myosines." These de doctorat, Paris 6. <https://www.theses.fr/2017PA066465>.
- Planelles-Herrero, Vicente J., James J. Hartman, Julien Robert-Paganin, Fady I. Malik, and Anne Houdusse. 2017. "Mechanistic and Structural Basis for Activation of Cardiac Myosin Force Production by Omecamtiv Mecarbil." *Nature Communications* 8 (1): 190. <https://doi.org/10.1038/s41467-017-00176-5>.
- Polo, Simona, Pier Paolo Di Fiore, and Sara Sigismund. 2014. "Keeping EGFR Signaling in Check: Ubiquitin Is the Guardian." *Cell Cycle (Georgetown, Tex.)* 13 (5): 681–82. <https://doi.org/10.4161/cc.27855>.
- Pomianowski, Pawel, and John A. Elefteriades. 2013. "The Genetics and Genomics of Thoracic Aortic Disease." *Annals of Cardiothoracic Surgery* 2 (3): 271–79. <https://doi.org/10.3978/j.issn.2225-319X.2013.05.12>.
- Powers, Joseph D., Sage A. Malingen, Michael Regnier, and Thomas L. Daniel. 2021. "The Sliding Filament Theory Since Andrew Huxley: Multiscale and Multidisciplinary Muscle Research." *Annual Review of Biophysics* 50 (May): 373–400. <https://doi.org/10.1146/annurev-biophys-110320-062613>.
- Preller, Matthias, Krishna Chinthalapudi, Renee Martin, Hans-Joachim Knolker, and Dietmar J. Manstein. 2011. "Inhibition of Myosin ATPase Activity by Halogenated Pseudilins: A Structure-Activity Study." *Journal of Medicinal Chemistry* 54 (11): 3675–85. <https://doi.org/10.1021/jm200259f>.
- Punjani, Ali, John L. Rubinstein, David J. Fleet, and Marcus A. Brubaker. 2017. "CryoSPARC: Algorithms for Rapid Unsupervised Cryo-EM Structure Determination." *Nature Methods* 14 (3): 290–96. <https://doi.org/10.1038/nmeth.4169>.
- Puri, C., M. V. Chibalina, S. D. Arden, A. J. Kruppa, J. Kendrick-Jones, and F. Buss. 2010. "Overexpression of Myosin VI in Prostate Cancer Cells Enhances PSA and VEGF Secretion, but Has No Effect on Endocytosis." *Oncogene* 29 (2): 188–200. <https://doi.org/10.1038/onc.2009.328>.
- Pylypenko, Olena, Lin Song, Ai Shima, Zhaohui Yang, Anne M. Houdusse, and H. Lee Sweeney. 2015. "Myosin VI Deafness Mutation Prevents the Initiation of Processive Runs on Actin." *Proceedings of the National Academy of Sciences of the United States of America* 112 (11): E1201-1209. <https://doi.org/10.1073/pnas.1420989112>.
- Pylypenko, Olena, Lin Song, Gaelle Squires, Xiaoyan Liu, Alan B. Zong, Anne Houdusse, and H. Lee Sweeney. 2011. "Role of Insert-1 of Myosin VI in Modulating Nucleotide Affinity." *The Journal of Biological Chemistry* 286 (13): 11716–23. <https://doi.org/10.1074/jbc.M110.200626>.
- Qiu, Yueping, Jincheng Wang, Hui Li, Bo Yang, Jijia Wang, Qiaojun He, and Qinjie Weng. 2022. "Emerging Views of OPTN (Optineurin) Function in the Autophagic Process Associated with Disease." *Autophagy* 18 (1): 73–85. <https://doi.org/10.1080/15548627.2021.1908722>.
- Quintero, Omar A., Judy E. Moore, and Christopher M. Yengo. 2012. "Basics of the Cytoskeleton: Myosins." In *Cytoskeleton and Human Disease*, edited by Maria Kavallaris, 73–100. Totowa, NJ: Humana Press. https://doi.org/10.1007/978-1-61779-788-0_4.
- Radke, Michael B., Manuel H. Taft, Britta Stapel, Denise Hilfiker-Kleiner, Matthias Preller, and Dietmar J. Manstein. 2014. "Small Molecule-Mediated Refolding and Activation of Myosin Motor Function." *ELife* 3 (February): e01603. <https://doi.org/10.7554/eLife.01603>.
- Radnai, Laszlo, Matthew Surman, Madalyn Hafenbreidel, Erica J. Young, Rebecca F. Stremel, Li Lin, Bilel Bdiri, et al. 2021. "Discovery of Selective Inhibitors for In Vitro and In Vivo Interrogation of Skeletal Myosin II." *ACS Chemical Biology* 16 (11): 2164–73. <https://doi.org/10.1021/acscchembio.1c00067>.
- Rai, Ashim, Rachit Shrivastava, Duha Vang, Michael Ritt, Fredrik Sadler, Shreyas Bhaban, Murti Salapaka, and Sivaraj Sivaramakrishnan. 2022. "Multimodal Regulation of Myosin VI Ensemble Transport by Cargo Adaptor Protein GIPC." *The Journal of Biological Chemistry* 298 (3): 101688. <https://doi.org/10.1016/j.jbc.2022.101688>.
- Rai, Ashim, Duha Vang, Michael Ritt, and Sivaraj Sivaramakrishnan. 2021. "Dynamic Multimerization of Dab2-Myosin VI Complexes Regulates Cargo Processivity While Minimizing Cortical Actin Reorganization." *The Journal of Biological Chemistry* 296 (June): 100232. <https://doi.org/10.1074/jbc.RA120.012703>.
- Ramamurthy, Bhagavathi, Christopher M. Yengo, Aaron F. Straight, Timothy J. Mitchison, and H. Lee Sweeney. 2004. "Kinetic Mechanism of Blebbistatin Inhibition of Nonmuscle Myosin IIb." *Biochemistry* 43 (46): 14832–39. <https://doi.org/10.1021/bi0490284>.
- Rauscher, Anna Á, Máté Gyimesi, Mihály Kovács, and András Málnási-Csizmadia. 2018. "Targeting Myosin by Blebbistatin Derivatives: Optimization and Pharmacological Potential." *Trends in Biochemical Sciences* 43 (9): 700–713. <https://doi.org/10.1016/j.tibs.2018.06.006>.
- Rayment, I., W. R. Rypniewski, K. Schmidt-Bäse, R. Smith, D. R. Tomchick, M. M. Benning, D. A. Winkelmann, G. Wesenberg, and H. M. Holden. 1993. "Three-Dimensional Structure of Myosin Subfragment-1: A Molecular Motor." *Science (New York, N.Y.)* 261 (5117): 50–58. <https://doi.org/10.1126/science.8316857>.

- Rejman, Joanna, Alessandra Bragonzi, and Massimo Conese. 2005. "Role of Clathrin- and Caveolae-Mediated Endocytosis in Gene Transfer Mediated by Lipo- and Polyplexes." *Molecular Therapy: The Journal of the American Society of Gene Therapy* 12 (3): 468–74. <https://doi.org/10.1016/j.ymthe.2005.03.038>.
- Rief, M., R. S. Rock, A. D. Mehta, M. S. Mooseker, R. E. Cheney, and J. A. Spudich. 2000. "Myosin-V Stepping Kinetics: A Molecular Model for Processivity." *Proceedings of the National Academy of Sciences of the United States of America* 97 (17): 9482–86. <https://doi.org/10.1073/pnas.97.17.9482>.
- Rinaldi, F., C. Terracciano, V. Pisani, R. Massa, E. Loro, L. Vergani, S. Di Girolamo, et al. 2012. "Aberrant Splicing and Expression of the Non Muscle Myosin Heavy-Chain Gene MYH14 in DM1 Muscle Tissues." *Neurobiology of Disease* 45 (1): 264–71. <https://doi.org/10.1016/j.nbd.2011.08.010>.
- Ripoll, Léa, Xavier Heiligenstein, Ilse Hurbain, Lia Domingues, Florent Figon, Karl J. Petersen, Megan K. Dennis, et al. 2018. "Myosin VI and Branched Actin Filaments Mediate Membrane Constriction and Fission of Melanosomal Tubule Carriers." *The Journal of Cell Biology* 217 (8): 2709–26. <https://doi.org/10.1083/jcb.201709055>.
- Ritt, Michael, and Sivaraj Sivaramakrishnan. 2018. "Engaging Myosin VI Tunes Motility, Morphology and Identity in Endocytosis." *Traffic (Copenhagen, Denmark)*, June. <https://doi.org/10.1111/tra.12583>.
- Robblee, James P., Adrian O. Olivares, and Enrique M. de la Cruz. 2004. "Mechanism of Nucleotide Binding to Actomyosin VI: Evidence for Allosteric Head-Head Communication." *The Journal of Biological Chemistry* 279 (37): 38608–17. <https://doi.org/10.1074/jbc.M403504200>.
- Robert-Paganin, Julien, Daniel Auguin, and Anne Houdusse. 2018. "Hypertrophic Cardiomyopathy Disease Results from Disparate Impairments of Cardiac Myosin Function and Auto-Inhibition." *Nature Communications* 9 (1): 4019. <https://doi.org/10.1038/s41467-018-06191-4>.
- Robert-Paganin, Julien, Olena Pylypenko, Carlos Kikuti, H. Lee Sweeney, and Anne Houdusse. 2020. "Force Generation by Myosin Motors: A Structural Perspective." *Chemical Reviews* 120 (1): 5–35. <https://doi.org/10.1021/acs.chemrev.9b00264>.
- Rock, Ronald S., Bhagavathi Ramamurthy, Alexander R. Dunn, Sara Beccafico, Bhadrash R. Rami, Carl Morris, Benjamin J. Spink, Clara Franzini-Armstrong, James A. Spudich, and H. Lee Sweeney. 2005. "A Flexible Domain Is Essential for the Large Step Size and Processivity of Myosin VI." *Molecular Cell* 17 (4): 603–9. <https://doi.org/10.1016/j.molcel.2005.01.015>.
- Rock, Ronald S., Sarah E. Rice, Amber L. Wells, Thomas J. Purcell, James A. Spudich, and H. Lee Sweeney. 2001. "Myosin VI Is a Processive Motor with a Large Step Size." *Proceedings of the National Academy of Sciences* 98 (24): 13655–59. <https://doi.org/10.1073/pnas.191512398>.
- Rogez, Benoit, Laeschkir Würthner, Anastasiia B. Petrova, Felix B. Zierhut, Dario Saczko-Brack, Maria-Ana Huergo, Christopher Batters, Erwin Frey, and Claudia Veigel. 2019. "Reconstitution Reveals How Myosin-VI Self-Organises to Generate a Dynamic Mechanism of Membrane Sculpting." *Nature Communications* 10 (1): 3305. <https://doi.org/10.1038/s41467-019-11268-9>.
- Roman, Bart I., Rita C. Guedes, Christian V. Stevens, and Alfonso T. García-Sosa. 2018. "Recovering Actives in Multi-Antitarget and Target Design of Analogs of the Myosin II Inhibitor Blebbistatin." *Frontiers in Chemistry* 6: 179. <https://doi.org/10.3389/fchem.2018.00179>.
- Roman, Bart I., Sigrid Verhasselt, Christophe W. Mangodt, Olivier De Wever, and Christian V. Stevens. 2018. "Synthesis of C-Ring-Modified Blebbistatin Derivatives and Evaluation of Their Myosin II ATPase Inhibitory Potency." *Bioorganic & Medicinal Chemistry Letters* 28 (13): 2261–64. <https://doi.org/10.1016/j.bmcl.2018.05.041>.
- Ropars, Virginie, Zhaohui Yang, Tatiana Isabet, Florian Blanc, Kaifeng Zhou, Tianming Lin, Xiaoyan Liu, et al. 2016. "The Myosin X Motor Is Optimized for Movement on Actin Bundles." *Nature Communications* 7 (September): 12456. <https://doi.org/10.1038/ncomms12456>.
- Rosenfeld, Steven S., and H. Lee Sweeney. 2004. "A Model of Myosin V Processivity." *The Journal of Biological Chemistry* 279 (38): 40100–111. <https://doi.org/10.1074/jbc.M402583200>.
- Ross, Jennifer L., M. Yusuf Ali, and David M. Warshaw. 2008. "Cargo Transport: Molecular Motors Navigate a Complex Cytoskeleton." *Current Opinion in Cell Biology* 20 (1): 41–47. <https://doi.org/10.1016/j.ceb.2007.11.006>.
- Roth, Stephan, and Rainer Heintzmann. 2016. "Optical Photon Reassignment with Increased Axial Resolution by Structured Illumination." *Methods and Applications in Fluorescence* 4 (4): 045005. <https://doi.org/10.1088/2050-6120/4/4/045005>.
- Ryan, Thomas A., and David A. Tumbarello. 2018. "Optineurin: A Coordinator of Membrane-Associated Cargo Trafficking and Autophagy." *Frontiers in Immunology* 9: 1024. <https://doi.org/10.3389/fimmu.2018.01024>.

- Sahlender, Daniela A., Rhys C. Roberts, Susan D. Arden, Giulietta Spudich, Marcus J. Taylor, J. Paul Luzio, John Kendrick-Jones, and Folma Buss. 2005. "Optineurin Links Myosin VI to the Golgi Complex and Is Involved in Golgi Organization and Exocytosis." *The Journal of Cell Biology* 169 (2): 285–95. <https://doi.org/10.1083/jcb.200501162>.
- Sakai, Tsuyoshi, Hyun Suk Jung, Osamu Sato, Masafumi D. Yamada, Dong-Ju You, Reiko Ikebe, and Mitsuo Ikebe. 2015. "Structure and Regulation of the Movement of Human Myosin VIIA." *The Journal of Biological Chemistry* 290 (28): 17587–98. <https://doi.org/10.1074/jbc.M114.599365>.
- Sakamoto, Takeshi, John Limouze, Christian A. Combs, Aaron F. Straight, and James R. Sellers. 2005. "Blebbistatin, a Myosin II Inhibitor, Is Photoinactivated by Blue Light." *Biochemistry* 44 (2): 584–88. <https://doi.org/10.1021/bi0483357>.
- Sampaio-Silva, Juliana, Ana Carla Batissoco, Rafaela Jesus-Santos, Osório Abath-Neto, Luciano Cesar Scarpelli, Patricia Yoshie Nishimura, Layla Testa Galindo, Ricardo Ferreira Bento, Jeanne Oiticica, and Karina Lezirovitz. 2018. "Exome Sequencing Identifies a Novel Nonsense Mutation of MYO6 as the Cause of Deafness in a Brazilian Family." *Annals of Human Genetics* 82 (1): 23–34. <https://doi.org/10.1111/ahg.12213>.
- Schramek, Daniel, Ataman Sendoel, Jeremy P. Segal, Slobodan Beronja, Evan Heller, Daniel Oristian, Boris Reva, and Elaine Fuchs. 2014. "Direct in Vivo RNAi Screen Unveils Myosin IIa as a Tumor Suppressor of Squamous Cell Carcinomas." *Science (New York, N.Y.)* 343 (6168): 309–13. <https://doi.org/10.1126/science.1248627>.
- Schröder, Rasmus R. 2020. "The Structure of Acto-Myosin." *Advances in Experimental Medicine and Biology* 1239: 41–59. https://doi.org/10.1007/978-3-030-38062-5_4.
- Schrödinger, L., and W. DeLano. 2020. "PyMOL. Retrieved from [Http://www.pymol.org/pymol](http://www.pymol.org/pymol)."
- Sckolnick, Maria, Elena B. Kremontsova, David M. Warshaw, and Kathleen M. Trybus. 2016. "Tropomyosin Isoforms Bias Actin Track Selection by Vertebrate Myosin Va." *Molecular Biology of the Cell* 27 (19): 2889–97. <https://doi.org/10.1091/mbc.E15-09-0641>.
- Seet, Li-Fong, and Wanjin Hong. 2005. "Endofin Recruits Clathrin to Early Endosomes via TOM1." *Journal of Cell Science* 118 (Pt 3): 575–87. <https://doi.org/10.1242/jcs.01628>.
- Seki, Yuta, Yuki Miyasaka, Sari Suzuki, Kenta Wada, Shumpei P. Yasuda, Kunie Matsuoka, Yasuhiro Ohshiba, *et al.* 2017. "A Novel Splice Site Mutation of Myosin VI in Mice Leads to Stereociliary Fusion Caused by Disruption of Actin Networks in the Apical Region of Inner Ear Hair Cells." *PloS One* 12 (8): e0183477. <https://doi.org/10.1371/journal.pone.0183477>.
- Seki, Yuta, Hiroshi Shitara, Rie Ishii, Takafumi Ouchi, Shumpei P. Yasuda, and Yoshiaki Kikkawa. 2021. "Myosin VI Haploinsufficiency Reduced Hearing Ability in Mice." *Neuroscience* 478 (December): 100–111. <https://doi.org/10.1016/j.neuroscience.2021.09.023>.
- Self, T., T. Sobe, N. G. Copeland, N. A. Jenkins, K. B. Avraham, and K. P. Steel. 1999. "Role of Myosin VI in the Differentiation of Cochlear Hair Cells." *Developmental Biology* 214 (2): 331–41. <https://doi.org/10.1006/dbio.1999.9424>.
- Sellers, James R., Fei Wang, and Peter D. Chantler. 2003. "Trifluoperazine Inhibits the MgATPase Activity and in Vitro Motility of Conventional and Unconventional Myosins." *Journal of Muscle Research and Cell Motility* 24 (8): 579–85. <https://doi.org/10.1023/b:jure.0000009969.04562.58>.
- Seri, Marco, Alessandro Pecci, Filomena Di Bari, Roberto Cusano, Maria Savino, Emanuele Panza, Alessandra Nigro, *et al.* 2003. "MYH9-Related Disease: May-Hegglin Anomaly, Sebastian Syndrome, Fechtner Syndrome, and Epstein Syndrome Are Not Distinct Entities but Represent a Variable Expression of a Single Illness." *Medicine* 82 (3): 203–15. <https://doi.org/10.1097/01.md.0000076006.64510.5c>.
- Shaner, Nathan C., Robert E. Campbell, Paul A. Steinbach, Ben N. G. Giepmans, Amy E. Palmer, and Roger Y. Tsien. 2004. "Improved Monomeric Red, Orange and Yellow Fluorescent Proteins Derived from *Discosoma* Sp. Red Fluorescent Protein." *Nature Biotechnology* 22 (12): 1567–72. <https://doi.org/10.1038/nbt1037>.
- Shaner, Nathan C., Gerard G. Lambert, Andrew Chammas, Yuhui Ni, Paula J. Cranfill, Michelle A. Baird, Brittney R. Sell, *et al.* 2013. "A Bright Monomeric Green Fluorescent Protein Derived from *Branchiostoma lanceolatum*." *Nature Methods* 10 (5): 407–9. <https://doi.org/10.1038/nmeth.2413>.
- Shang, Guijun, Chad A. Brautigam, Rui Chen, Defen Lu, Jesús Torres-Vázquez, and Xuewu Zhang. 2017. "Structure Analyses Reveal a Regulated Oligomerization Mechanism of the PlexinD1/GIPC/Myosin VI Complex." *eLife* 6 (May): e27322. <https://doi.org/10.7554/eLife.27322>.
- Shrivastava, Rachit, Ashim Rai, Murti Salapaka, and Sivaraj Sivaramakrishnan. 2019. "Stiffness of Cargo-Motor Linkage Tunes Myosin VI Motility and Response to Load." *Biochemistry* 58 (47): 4721–25. <https://doi.org/10.1021/acs.biochem.9b00422>.

- Singla, Veena, Miriam Romaguera-Ros, Jose Manuel Garcia-Verdugo, and Jeremy F. Reiter. 2010. "Ofd1, a Human Disease Gene, Regulates the Length and Distal Structure of Centrioles." *Developmental Cell* 18 (3): 410–24. <https://doi.org/10.1016/j.devcel.2009.12.022>.
- Sirigu, Serena, James J. Hartman, Vicente José Planelles-Herrero, Virginie Ropars, Sheila Clancy, Xi Wang, Grace Chuang, *et al.* 2016. "Highly Selective Inhibition of Myosin Motors Provides the Basis of Potential Therapeutic Application." *Proceedings of the National Academy of Sciences of the United States of America* 113 (47): E7448–55. <https://doi.org/10.1073/pnas.1609342113>.
- Sivaramakrishnan, Sivaraj, and James A. Spudich. 2009. "Coupled Myosin VI Motors Facilitate Unidirectional Movement on an F-Actin Network." *The Journal of Cell Biology* 187 (1): 53–60. <https://doi.org/10.1083/jcb.200906133>.
- Sobczak, Magdalena, Vira Chumak, Paweł Pomorski, Emilia Wojtera, Łukasz Majewski, Jolanta Nowak, Junji Yamauchi, and Maria Jolanta Rędownicz. 2016. "Interaction of Myosin VI and Its Binding Partner DOCK7 Plays an Important Role in NGF-Stimulated Protrusion Formation in PC12 Cells." *Biochimica Et Biophysica Acta* 1863 (7 Pt A): 1589–1600. <https://doi.org/10.1016/j.bbamcr.2016.03.020>.
- Song, Chun Feng, Kasim Sader, Howard White, John Kendrick-Jones, and John Trinick. 2010. "Nucleotide-Dependent Shape Changes in the Reverse Direction Motor, Myosin VI." *Biophysical Journal* 99 (10): 3336–44. <https://doi.org/10.1016/j.bpj.2010.09.014>.
- Spink, Benjamin J., Sivaraj Sivaramakrishnan, Jan Lipfert, Sebastian Doniach, and James A. Spudich. 2008. "Long Single Alpha-Helical Tail Domains Bridge the Gap between Structure and Function of Myosin VI." *Nature Structural & Molecular Biology* 15 (6): 591–97. <https://doi.org/10.1038/nsmb.1429>.
- Spitzer, Michaela, Jan Wildenhain, Juri Rappsilber, and Mike Tyers. 2014. "BoxPlotR: A Web Tool for Generation of Box Plots." *Nature Methods* 11 (2): 121–22. <https://doi.org/10.1038/nmeth.2811>.
- Spudich, Giuletta, Margarita V. Chibalina, Josephine Sui-Yan Au, Susan D. Arden, Folma Buss, and John Kendrick-Jones. 2007a. "Myosin VI Targeting to Clathrin-Coated Structures and Dimerization Is Mediated by Binding to Disabled-2 and PtdIns(4,5)P₂." *Nature Cell Biology* 9 (2): 176–83. <https://doi.org/10.1038/ncb1531>.
- Spudich, J. A. 2001. "The Myosin Swinging Cross-Bridge Model." *Nature Reviews. Molecular Cell Biology* 2 (5): 387–92. <https://doi.org/10.1038/35073086>.
- Spudich, James A. 2015. "The Myosin Mesa and a Possible Unifying Hypothesis for the Molecular Basis of Human Hypertrophic Cardiomyopathy." *Biochemical Society Transactions* 43 (1): 64–72. <https://doi.org/10.1042/BST20140324>.
- Spudich, James A., and Sivaraj Sivaramakrishnan. 2010. "Myosin VI: An Innovative Motor That Challenged the Swinging Lever arm Hypothesis." *Nature Reviews. Molecular Cell Biology* 11 (2): 128–37. <https://doi.org/10.1038/nrm2833>.
- Straight, Aaron F., Amy Cheung, John Limouze, Irene Chen, Nick J. Westwood, James R. Sellers, and Timothy J. Mitchison. 2003. "Dissecting Temporal and Spatial Control of Cytokinesis with a Myosin II Inhibitor." *Science (New York, N.Y.)* 299 (5613): 1743–47. <https://doi.org/10.1126/science.1081412>.
- Svergun, D. I., M. V. Petoukhov, and M. H. Koch. 2001. "Determination of Domain Structure of Proteins from X-Ray Solution Scattering." *Biophysical Journal* 80 (6): 2946–53. [https://doi.org/10.1016/S0006-3495\(01\)76260-1](https://doi.org/10.1016/S0006-3495(01)76260-1).
- Swarup, Ghanshyam, and Zuberwasim Sayyad. 2018. "Altered Functions and Interactions of Glaucoma-Associated Mutants of Optineurin." *Frontiers in Immunology* 9: 1287. <https://doi.org/10.3389/fimmu.2018.01287>.
- Sweeney, H. L., S. S. Rosenfeld, F. Brown, L. Faust, J. Smith, J. Xing, L. A. Stein, and J. R. Sellers. 1998. "Kinetic Tuning of Myosin via a Flexible Loop Adjacent to the Nucleotide Binding Pocket." *The Journal of Biological Chemistry* 273 (11): 6262–70. <https://doi.org/10.1074/jbc.273.11.6262>.
- Sweeney, H. Lee, and David W. Hammers. 2018. "Muscle Contraction." *Cold Spring Harbor Perspectives in Biology* 10 (2): a023200. <https://doi.org/10.1101/cshperspect.a023200>.
- Sweeney, H. Lee, and Anne Houdusse. 2007. "What Can Myosin VI Do in Cells?" *Current Opinion in Cell Biology* 19 (1): 57–66. <https://doi.org/10.1016/j.ceb.2006.12.005>.
- . 2010. "Structural and Functional Insights into the Myosin Motor Mechanism." *Annual Review of Biophysics* 39: 539–57. <https://doi.org/10.1146/annurev.biophys.050708.133751>.
- Sweeney, H. Lee, Anne Houdusse, and Julien Robert-Paganin. 2020. "Myosin Structures." *Advances in Experimental Medicine and Biology* 1239: 7–19. https://doi.org/10.1007/978-3-030-38062-5_2.
- Swenson, Anja M., Wanjian Tang, Cheavar A. Blair, Christopher M. Fetrow, William C. Unrath, Michael J. Previs, Kenneth S. Campbell, and Christopher M. Yengo. 2017. "Omecamtiv Mecarbil Enhances the Duty Ratio of Human β -Cardiac Myosin Resulting in Increased Calcium Sensitivity and Slowed Force Development

- in Cardiac Muscle." *The Journal of Biological Chemistry* 292 (9): 3768–78. <https://doi.org/10.1074/jbc.M116.748780>.
- Swift, Luther M., Huda Asfour, Nikki G. Posnack, Ara Arutunyan, Matthew W. Kay, and Narine Sarvazyan. 2012. "Properties of Blebbistatin for Cardiac Optical Mapping and Other Imaging Applications." *Pflugers Archiv: European Journal of Physiology* 464 (5): 503–12. <https://doi.org/10.1007/s00424-012-1147-2>.
- Szent-Györgyi, Andrew G. 2004. "The Early History of the Biochemistry of Muscle Contraction." *The Journal of General Physiology* 123 (6): 631–41. <https://doi.org/10.1085/jgp.200409091>.
- Talebi, Farah, Farideh Ghanbari Mardasi, Javad Mohammadi Asl, and Masoomeh Sayahi. 2017. "Next-Generation Sequencing Identifies Three Novel Missense Variants in ILDR1 and MYO6 Genes in an Iranian Family with Hearing Loss with Review of the Literature." *International Journal of Pediatric Otorhinolaryngology* 103 (December): 103–8. <https://doi.org/10.1016/j.ijporl.2017.09.018>.
- Teckchandani, Anjali, Erin E. Mulkearns, Timothy W. Randolph, Natalie Toida, and Jonathan A. Cooper. 2012. "The Clathrin Adaptor Dab2 Recruits EH Domain Scaffold Proteins to Regulate Integrin B1 Endocytosis." *Molecular Biology of the Cell* 23 (15): 2905–16. <https://doi.org/10.1091/mbc.E11-12-1007>.
- Terasaki, A. G., M. Ohnuma, and I. Mabuchi. 1997. "Identification of Actin-Binding Proteins from Sea Urchin Eggs by F-Actin Affinity Column Chromatography." *Journal of Biochemistry* 122 (1): 226–36. <https://doi.org/10.1093/oxfordjournals.jbchem.a021733>.
- Terwilliger, Thomas C., Ralf W. Grosse-Kunstleve, Pavel V. Afonine, Nigel W. Moriarty, Peter H. Zwart, Li Wei Hung, Randy J. Read, and Paul D. Adams. 2008. "Iterative Model Building, Structure Refinement and Density Modification with the PHENIX AutoBuild Wizard." *Acta Crystallographica. Section D, Biological Crystallography* 64 (Pt 1): 61–69. <https://doi.org/10.1107/S090744490705024X>.
- Thirumurugan, Kavitha, Takeshi Sakamoto, John A. Hammer, James R. Sellers, and Peter J. Knight. 2006. "The Cargo-Binding Domain Regulates Structure and Activity of Myosin 5." *Nature* 442 (7099): 212–15. <https://doi.org/10.1038/nature04865>.
- Thureau, A., P. Roblin, and J. Pérez. 2021. "BioSAXS on the SWING Beamline at Synchrotron SOLEIL." *Journal of Applied Crystallography* 54 (6): 1698–1710. <https://doi.org/10.1107/S1600576721008736>.
- Tian, Tao, Yajie Lu, Jun Yao, Xin Cao, Qinjun Wei, and Qi Li. 2018. "Identification of a Novel MYO6 Mutation Associated with Autosomal Dominant Non-Syndromic Hearing Loss in a Chinese Family by Whole-Exome Sequencing." *Genes & Genetic Systems* 93 (5): 171–79. <https://doi.org/10.1266/ggs.18-00006>.
- Tickle, I.J., C. Flensburg, P. Keller, W. Paciorek, A. Sharff, C. Vornrhein, and G. Bricogne. 2018. "STARANISO. Cambridge, United Kingdom: Global Phasing Ltd."
- Tomatis, Vanesa M., Andreas Papadopoulos, Nancy T. Malintan, Sally Martin, Tristan Wallis, Rachel S. Gormal, John Kendrick-Jones, Folma Buss, and Frédéric A. Meunier. 2013. "Myosin VI Small Insert Isoform Maintains Exocytosis by Tethering Secretory Granules to the Cortical Actin." *The Journal of Cell Biology* 200 (3): 301–20. <https://doi.org/10.1083/jcb.201204092>.
- Trivedi, Darshan V., Suman Nag, Annamma Spudich, Kathleen M. Ruppel, and James A. Spudich. 2020. "The Myosin Family of Mechanoenzymes: From Mechanisms to Therapeutic Approaches." *Annual Review of Biochemistry* 89 (June): 667–93. <https://doi.org/10.1146/annurev-biochem-011520-105234>.
- Tsygankova, Oxana M., and James H. Keen. 2019. "A Unique Role for Clathrin Light Chain A in Cell Spreading and Migration." *Journal of Cell Science* 132 (10): jcs224030. <https://doi.org/10.1242/jcs.224030>.
- Tumbarello, David A., Paul T. Manna, Mark Allen, Mark Bycroft, Susan D. Arden, John Kendrick-Jones, and Folma Buss. 2015. "The Autophagy Receptor TAX1BP1 and the Molecular Motor Myosin VI Are Required for Clearance of Salmonella Typhimurium by Autophagy." *PLoS Pathogens* 11 (10): e1005174. <https://doi.org/10.1371/journal.ppat.1005174>.
- Tumbarello, David A., Bennett J. Waxse, Susan D. Arden, Nicholas A. Bright, John Kendrick-Jones, and Folma Buss. 2012. "Autophagy Receptors Link Myosin VI to Autophagosomes to Mediate Tom1-Dependent Autophagosome Maturation and Fusion with the Lysosome." *Nature Cell Biology* 14 (10): 1024–35. <https://doi.org/10.1038/ncb2589>.
- Umeki, Nobuhisa, Hyun Suk Jung, Tsuyoshi Sakai, Osamu Sato, Reiko Ikebe, and Mitsuo Ikebe. 2011. "Phospholipid-Dependent Regulation of the Motor Activity of Myosin X." *Nature Structural & Molecular Biology* 18 (7): 783–88. <https://doi.org/10.1038/nsmb.2065>.
- Umeki, Nobuhisa, Hyun Suk Jung, Shinya Watanabe, Tsuyoshi Sakai, Xiang-dong Li, Reiko Ikebe, Roger Craig, and Mitsuo Ikebe. 2009. "The Tail Binds to the Head-Neck Domain, Inhibiting ATPase Activity of Myosin VIIA." *Proceedings of the National Academy of Sciences of the United States of America* 106 (21): 8483–88. <https://doi.org/10.1073/pnas.0812930106>.
- Varadi, Mihaly, Stephen Anyango, Mandar Deshpande, Sreenath Nair, Cindy Natassia, Galabina Yordanova, David Yuan, et al. 2022. "AlphaFold Protein Structure Database: Massively Expanding the Structural Coverage

- of Protein-Sequence Space with High-Accuracy Models." *Nucleic Acids Research* 50 (D1): D439–44. <https://doi.org/10.1093/nar/gkab1061>.
- Várkuti, Boglárka H., Miklós Képiró, István Ádám Horváth, László Végner, Szilvia Ráti, Áron Zsigmond, György Hegyi, Zsolt Lenkei, Máté Varga, and András Málnási-Csizmadia. 2016. "A Highly Soluble, Non-Phototoxic, Non-Fluorescent Blebbistatin Derivative." *Scientific Reports* 6 (May): 26141. <https://doi.org/10.1038/srep26141>.
- Venugopal, Parvathy, Lucia Gagliardi, Cecily Forsyth, Jinghua Feng, Kerry Phillips, Milena Babic, Nicola K. Poplawski, *et al.* 2020. "Two Monogenic Disorders Masquerading as One: Severe Congenital Neutropenia with Monocytosis and Non-Syndromic Sensorineural Hearing Loss." *BMC Medical Genetics* 21 (1): 35. <https://doi.org/10.1186/s12881-020-0971-z>.
- Verhasselt, Sigrid, Bart I. Roman, Marc E. Bracke, and Christian V. Stevens. 2017. "Improved Synthesis and Comparative Analysis of the Tool Properties of New and Existing D-Ring Modified (S)-Blebbistatin Analogs." *European Journal of Medicinal Chemistry* 136 (August): 85–103. <https://doi.org/10.1016/j.ejmech.2017.04.072>.
- Verhasselt, Sigrid, Bart I. Roman, Olivier De Wever, Kristof Van Hecke, Rik Van Deun, Marc E. Bracke, and Christian V. Stevens. 2017. "Discovery of (S)-3'-Hydroxyblebbistatin and (S)-3'-Aminoblebbistatin: Polar Myosin II Inhibitors with Superior Research Tool Properties." *Organic & Biomolecular Chemistry* 15 (9): 2104–18. <https://doi.org/10.1039/c7ob00006e>.
- Verhasselt, Sigrid, Christian V. Stevens, Tom Van den Broecke, Marc E. Bracke, and Bart I. Roman. 2017. "Insights into the Myosin II Inhibitory Potency of A-Ring-Modified (S)-Blebbistatin Analogs." *Bioorganic & Medicinal Chemistry Letters* 27 (13): 2986–89. <https://doi.org/10.1016/j.bmcl.2017.05.008>.
- Viret, Christophe, Aurore Rozières, and Mathias Faure. 2018. "Novel Insights into NDP52 Autophagy Receptor Functioning." *Trends in Cell Biology* 28 (4): 255–57. <https://doi.org/10.1016/j.tcb.2018.01.003>.
- Volkov, V. V., D. I. Svergun, and IUCr. 2003. "Uniqueness of Ab Initio Shape Determination in Small-Angle Scattering." Text. *Journal of Applied Crystallography*. International Union of Crystallography. April 16, 2003. <https://doi.org/10.1107/S0021889803000268>.
- Vonrhein, Clemens, Claus Flensburg, Peter Keller, Andrew Sharff, Oliver Smart, Wlodek Paciorek, Thomas Womack, and Gérard Bricogne. 2011. "Data Processing and Analysis with the AutoPROC Toolbox." *Acta Crystallographica. Section D, Biological Crystallography* 67 (Pt 4): 293–302. <https://doi.org/10.1107/S0907444911007773>.
- Voors, Adriaan A., Jean-François Tamby, John G. Cleland, Michael Koren, Leslie B. Forgoth, Dinesh Gupta, Lars H. Lund, *et al.* 2020. "Effects of Danicamtiv, a Novel Cardiac Myosin Activator, in Heart Failure with Reduced Ejection Fraction: Experimental Data and Clinical Results from a Phase 2a Trial." *European Journal of Heart Failure* 22 (9): 1649–58. <https://doi.org/10.1002/ejhf.1933>.
- Vreugde, Sarah, Carmelo Ferrai, Annarita Miluzio, Ehud Hauben, Pier Carlo Marchisio, Massimo P. Crippa, Mario Bussi, and Stefano Biffo. 2006. "Nuclear Myosin VI Enhances RNA Polymerase II-Dependent Transcription." *Molecular Cell* 23 (5): 749–55. <https://doi.org/10.1016/j.molcel.2006.07.005>.
- Wagner, Wolfgang, Kristina Lippmann, Frank F. Heisler, Kira V. Gromova, Franco L. Lombino, Mona K. Roesler, Yvonne Pechmann, *et al.* 2019. "Myosin VI Drives Clathrin-Mediated AMPA Receptor Endocytosis to Facilitate Cerebellar Long-Term Depression." *Cell Reports* 28 (1): 11–20.e9. <https://doi.org/10.1016/j.celrep.2019.06.005>.
- Walklate, Jonathan, Cecilia Ferrantini, Chloe A. Johnson, Chiara Tesi, Corrado Poggesi, and Michael A. Geeves. 2021. "Alpha and Beta Myosin Isoforms and Human Atrial and Ventricular Contraction." *Cellular and Molecular Life Sciences: CMLS* 78 (23): 7309–37. <https://doi.org/10.1007/s00018-021-03971-y>.
- Wang, Dong, Libing Zhu, Min Liao, Tengyue Zeng, Wenli Zhuo, Shunliang Yang, and Weizhen Wu. 2016. "MYO6 Knockdown Inhibits the Growth and Induces the Apoptosis of Prostate Cancer Cells by Decreasing the Phosphorylation of ERK1/2 and PRAS40." *Oncology Reports* 36 (3): 1285–92. <https://doi.org/10.3892/or.2016.4910>.
- Wang, Hong, and David L. Brautigan. 2002. "A Novel Transmembrane Ser/Thr Kinase Complexes with Protein Phosphatase-1 and Inhibitor-2." *The Journal of Biological Chemistry* 277 (51): 49605–12. <https://doi.org/10.1074/jbc.M209335200>.
- Wang, Hong Hui, Hideyuki Tanaka, Xiaoran Qin, Tiejun Zhao, Li-Hong Ye, Tuyoshi Okagaki, Takeshi Katayama, *et al.* 2008. "Blebbistatin Inhibits the Chemotaxis of Vascular Smooth Muscle Cells by Disrupting the Myosin II-Actin Interaction." *American Journal of Physiology. Heart and Circulatory Physiology* 294 (5): H2060–2068. <https://doi.org/10.1152/ajpheart.00970.2007>.
- Wang, Hua, Surong Dong, Yun Liu, Feng Ma, Jian Fang, Wentao Zhang, Shihe Shao, Hongxing Shen, and Jingpeng Jin. 2020. "DAB2 Suppresses Gastric Cancer Migration by Regulating the Wnt/ β -Catenin and Hippo-YAP

- Signaling Pathways." *Translational Cancer Research* 9 (2): 1174–84. <https://doi.org/10.21037/tcr.2019.12.96>.
- Wang, Jing, Shaobo Ke, Yi Gong, Yuxin Cai, Lingling Xia, Zhenguo Shi, Hu Qiu, Wei Shi, Qiushuang Wang, and Yongshun Chen. 2022. "Circ_0011385 Knockdown Inhibits Cell Proliferation, Migration and Invasion, Whereas Promotes Cell Apoptosis by Regulating MiR-330-3p/MYO6 Axis in Colorectal Cancer." *Biomedical Journal*, January, S2319-4170(22)00007-5. <https://doi.org/10.1016/j.bj.2022.01.007>.
- Wang, Jinghan, Jun Shen, Luo Guo, Cheng Cheng, Renjie Chai, Yilai Shu, and Huawei Li. 2019. "A Humanized Mouse Model, Demonstrating Progressive Hearing Loss Caused by MYO6 p.C442Y, Is Inherited in a Semi-Dominant Pattern." *Hearing Research* 379 (August): 79–88. <https://doi.org/10.1016/j.heares.2019.04.014>.
- Wang, Lei, Marion Failler, Wenxiang Fu, and Brian D. Dynlacht. 2018. "A Distal Centriolar Protein Network Controls Organelle Maturation and Asymmetry." *Nature Communications* 9 (1): 3938. <https://doi.org/10.1038/s41467-018-06286-y>.
- Wang, Tuanlao, Ning Sheng Liu, Li-Fong Seet, and Wanjin Hong. 2010. "The Emerging Role of VHS Domain-Containing Tom1, Tom1L1 and Tom1L2 in Membrane Trafficking." *Traffic (Copenhagen, Denmark)* 11 (9): 1119–28. <https://doi.org/10.1111/j.1600-0854.2010.01098.x>.
- Wang, Wen-Lun, Wei-Lun Chang, Hsiao-Bai Yang, Yu-Chi Wang, I.-Wei Chang, Ching-Tai Lee, Chi-Yang Chang, Jaw-Town Lin, and Bor-Shyang Sheu. 2016. "Low Disabled-2 Expression Promotes Tumor Progression and Determines Poor Survival and High Recurrence of Esophageal Squamous Cell Carcinoma." *Oncotarget* 7 (44): 71169–81. <https://doi.org/10.18632/oncotarget.8460>.
- Wang, Zishu, Mingzhen Ying, Qiong Wu, Rui Wang, and Yumei Li. 2016. "Overexpression of Myosin VI Regulates Gastric Cancer Cell Progression." *Gene* 593 (1): 100–109. <https://doi.org/10.1016/j.gene.2016.08.015>.
- Warner, Claire L., Abigail Stewart, J. Paul Luzio, Karen P. Steel, Richard T. Libby, John Kendrick-Jones, and Folma Buss. 2003. "Loss of Myosin VI Reduces Secretion and the Size of the Golgi in Fibroblasts from Snell's Waltzer Mice." *The EMBO Journal* 22 (3): 569–79. <https://doi.org/10.1093/emboj/cdg055>.
- Watabe-Uchida, Mitsuko, Keisha A. John, Justyna A. Janas, Sarah E. Newey, and Linda Van Aelst. 2006. "The Rac Activator DOCK7 Regulates Neuronal Polarity through Local Phosphorylation of Stathmin/Op18." *Neuron* 51 (6): 727–39. <https://doi.org/10.1016/j.neuron.2006.07.020>.
- Waxse, Bennett J., Prabuddha Sengupta, Geoffrey G. Hesketh, Jennifer Lippincott-Schwartz, and Folma Buss. 2017. "Myosin VI Facilitates Connexin 43 Gap Junction Accretion." *Journal of Cell Science* 130 (5): 827–40. <https://doi.org/10.1242/jcs.199083>.
- Weeks, Stephen D., Kimberly C. Grasty, Lisa Hernandez-Cuebas, and Patrick J. Loll. 2009. "Crystal Structures of Lys-63-Linked Tri- and Di-Ubiquitin Reveal a Highly Extended Chain Architecture." *Proteins* 77 (4): 753–59. <https://doi.org/10.1002/prot.22568>.
- Wells, A. L., A. W. Lin, L. Q. Chen, D. Safer, S. M. Cain, T. Hasson, B. O. Carragher, R. A. Milligan, and H. L. Sweeney. 1999. "Myosin VI Is an Actin-Based Motor That Moves Backwards." *Nature* 401 (6752): 505–8. <https://doi.org/10.1038/46835>.
- Westbrook, Jules A., David A. Cairns, Jianhe Peng, Valerie Speirs, Andrew M. Hanby, Ingunn Holen, Steven L. Wood, et al. 2016. "CAPG and GIPC1: Breast Cancer Biomarkers for Bone Metastasis Development and Treatment." *Journal of the National Cancer Institute* 108 (4). <https://doi.org/10.1093/jnci/djv360>.
- White, Eileen. 2015. "The Role for Autophagy in Cancer." *The Journal of Clinical Investigation* 125 (1): 42–46. <https://doi.org/10.1172/JCI73941>.
- White, Jesse, Sujit Suklabaidya, Mai Tram Vo, Young Bong Choi, and Edward W. Harhaj. 2022. "Multifaceted Roles of TAX1BP1 in Autophagy." *Autophagy*, May, 1–10. <https://doi.org/10.1080/15548627.2022.2070331>.
- Wieters, Frederique, Carolin Weiss Lucas, Matthias Gruhn, Ansgar Büschges, Gereon R. Fink, and Markus Aswendt. 2021. "Introduction to Spasticity and Related Mouse Models." *Experimental Neurology* 335 (January): 113491. <https://doi.org/10.1016/j.expneurol.2020.113491>.
- Wollenberg, Rasmus D., Manuel H. Taft, Sven Giese, Claudia Thiel, Zoltán Balázs, Henriette Giese, Dietmar J. Manstein, and Teis E. Sondergaard. 2019. "Phenamacril Is a Reversible and Noncompetitive Inhibitor of Fusarium Class I Myosin." *The Journal of Biological Chemistry* 294 (4): 1328–37. <https://doi.org/10.1074/jbc.RA118.005408>.
- Wollscheid, Hans-Peter, Matteo Biancospino, Fahu He, Elisa Magistrati, Erika Molteni, Michela Lupia, Paolo Soffientini, et al. 2016. "Diverse Functions of Myosin VI Elucidated by an Isoform-Specific α -Helix Domain." *Nature Structural & Molecular Biology* 23 (4): 300–308. <https://doi.org/10.1038/nsmb.3187>.
- Wood, Katherine M., and Corinne J. Smith. 2021. "Clathrin: The Molecular Shape Shifter." *The Biochemical Journal* 478 (16): 3099–3123. <https://doi.org/10.1042/BCJ20200740>.

- Wu, Di, Weiyuan Huang, Zhenhang Xu, Shuo Li, Jie Zhang, Xiaohua Chen, Yan Tang, *et al.* 2020. "Clinical and Genetic Study of 12 Chinese Han Families with Nonsyndromic Deafness." *Molecular Genetics & Genomic Medicine* 8 (4): e1177. <https://doi.org/10.1002/mgg3.1177>.
- Wu, Xufeng, and John A. Hammer. 2014. "Melanosome Transfer: It Is Best to Give and Receive." *Current Opinion in Cell Biology* 29 (August): 1–7. <https://doi.org/10.1016/j.ceb.2014.02.003>.
- Wuytack, Frank, Luc Raeymaekers, and Ludwig Missiaen. 2003. "PMR1/SPCA Ca²⁺ Pumps and the Role of the Golgi Apparatus as a Ca²⁺ Store." *Pflugers Archiv: European Journal of Physiology* 446 (2): 148–53. <https://doi.org/10.1007/s00424-003-1011-5>.
- Xiao, Shuyan, Mary K. Brannon, Xiaolin Zhao, Kristen I. Fread, Jeffrey F. Ellena, John H. Bushweller, Carla V. Finkielstein, Geoffrey S. Armstrong, and Daniel G. S. Capelluto. 2015. "Tom1 Modulates Binding of Tollip to Phosphatidylinositol 3-Phosphate via a Coupled Folding and Binding Mechanism." *Structure (London, England: 1993)* 23 (10): 1910–20. <https://doi.org/10.1016/j.str.2015.07.017>.
- Xue, Yuanyuan, Xinde Hu, Daqi Wang, Di Li, Yige Li, Fang Wang, Mingqian Huang, *et al.* 2022. "Gene Editing in a Myo6 Semi-Dominant Mouse Model Rescues Auditory Function." *Molecular Therapy: The Journal of the American Society of Gene Therapy* 30 (1): 105–18. <https://doi.org/10.1016/j.ymthe.2021.06.015>.
- Yamakami, Megumi, Tamotsu Yoshimori, and Hideyoshi Yokosawa. 2003. "Tom1, a VHS Domain-Containing Protein, Interacts with Tollip, Ubiquitin, and Clathrin." *The Journal of Biological Chemistry* 278 (52): 52865–72. <https://doi.org/10.1074/jbc.M306740200>.
- Yamauchi, Junji, Yuki Miyamoto, Jonah R. Chan, and Akito Tanoue. 2008. "ErbB2 Directly Activates the Exchange Factor Dock7 to Promote Schwann Cell Migration." *The Journal of Cell Biology* 181 (2): 351–65. <https://doi.org/10.1083/jcb.200709033>.
- Yang, An, Xin Liu, Ping Liu, Yunzhang Feng, Hongbo Liu, Shen Gao, Limin Huo, Xinyan Han, Jurong Wang, and Wei Kong. 2021. "LncRNA UCA1 Promotes Development of Gastric Cancer via the MiR-145/MYO6 Axis." *Cellular & Molecular Biology Letters* 26 (1): 33. <https://doi.org/10.1186/s11658-021-00275-8>.
- Yang, Quanfu. 2019. "MicroRNA-5195-3p Plays a Suppressive Role in Cell Proliferation, Migration and Invasion by Targeting MYO6 in Human Non-Small Cell Lung Cancer." *Bioscience, Biotechnology, and Biochemistry* 83 (2): 212–20. <https://doi.org/10.1080/09168451.2018.1540288>.
- Yetman, Anji T., Lois Starr, Jennifer Sanmann, Megan Wilde, Mary Murray, and Jonathan W. Cramer. 2018. "Clinical and Echocardiographic Prevalence and Detection of Congenital and Acquired Cardiac Abnormalities in Girls and Women with the Turner Syndrome." *The American Journal of Cardiology* 122 (2): 327–30. <https://doi.org/10.1016/j.amjcard.2018.03.357>.
- Yoong, Li-Foong, Hui-Keem Lim, Heidi Tran, Simone Lackner, Zhihao Zheng, Pengyu Hong, and Adrian W. Moore. 2020. "Atypical Myosin Tunes Dendrite Arbor Subdivision." *Neuron* 106 (3): 452–467.e8. <https://doi.org/10.1016/j.neuron.2020.02.002>.
- Yoshida, Hiroyuki, Wenjun Cheng, Jamie Hung, Denise Montell, Erika Geisbrecht, Daniel Rosen, Jinsong Liu, and Honami Naora. 2004. "Lessons from Border Cell Migration in the Drosophila Ovary: A Role for Myosin VI in Dissemination of Human Ovarian Cancer." *Proceedings of the National Academy of Sciences of the United States of America* 101 (21): 8144–49. <https://doi.org/10.1073/pnas.0400400101>.
- You, Weiqiang, Gewen Tan, Nengquan Sheng, Jianfeng Gong, Jun Yan, Di Chen, Huizhen Zhang, and Zhigang Wang. 2016. "Downregulation of Myosin VI Reduced Cell Growth and Increased Apoptosis in Human Colorectal Cancer." *Acta Biochimica Et Biophysica Sinica* 48 (5): 430–36. <https://doi.org/10.1093/abbs/gmw020>.
- Young, Gavin, Nikolas Hundt, Daniel Cole, Adam Fineberg, Joanna Andrecka, Andrew Tyler, Anna Olerinyova, *et al.* 2018. "Quantitative Mass Imaging of Single Biological Macromolecules." *Science (New York, N.Y.)* 360 (6387): 423–27. <https://doi.org/10.1126/science.aar5839>.
- Yu, Cong, Wei Feng, Zhiyi Wei, Yohei Miyanoiri, Wenyu Wen, Yanxiang Zhao, and Mingjie Zhang. 2009. "Myosin VI Undergoes Cargo-Mediated Dimerization." *Cell* 138 (3): 537–48. <https://doi.org/10.1016/j.cell.2009.05.030>.
- Yu, Cong, Jizhong Lou, Jingjing Wu, Lifeng Pan, Wei Feng, and Mingjie Zhang. 2012. "Membrane-Induced Lever arm Expansion Allows Myosin VI to Walk with Large and Variable Step Sizes." *The Journal of Biological Chemistry* 287 (42): 35021–35. <https://doi.org/10.1074/jbc.M111.328781>.
- Yu, Hui, Zhenghong Zhu, Jianhua Chang, Jialei Wang, and Xiaoyong Shen. 2015. "Lentivirus-Mediated Silencing of Myosin VI Inhibits Proliferation and Cell Cycle Progression in Human Lung Cancer Cells." *Chemical Biology & Drug Design* 86 (4): 606–13. <https://doi.org/10.1111/cbdd.12528>.
- Zakrzewski, Przemysław, Marta Lenartowska, and Folma Buss. 2021. "Diverse Functions of Myosin VI in Spermiogenesis." *Histochemistry and Cell Biology* 155 (3): 323–40. <https://doi.org/10.1007/s00418-020-01954-x>.

- Zakrzewski, Przemysław, Anna Suwińska, Robert Lenartowski, Maria Jolanta Rędownicz, Folma Buss, and Marta Lenartowska. 2020. "Myosin VI Maintains the Actin-Dependent Organization of the Tubulobulbar Complexes Required for Endocytosis during Mouse Spermiogenesis†‡." *Biology of Reproduction* 102 (4): 863–75. <https://doi.org/10.1093/biolre/ioz232>.
- Zhang, Baichen, Kristin M. Watts, Dana Hodge, Lisa M. Kemp, David A. Hunstad, Leslie M. Hicks, and Audrey R. Odom. 2011. "A Second Target of the Antimalarial and Antibacterial Agent Fosmidomycin Revealed by Cellular Metabolic Profiling." *Biochemistry* 50 (17): 3570–77. <https://doi.org/10.1021/bi200113y>.
- Zhang, Hai-Man, Huan-Hong Ji, Tong Ni, Rong-Na Ma, Aibing Wang, and Xiang-Dong Li. 2017. "Characterization of Blebbistatin Inhibition of Smooth Muscle Myosin and Nonmuscle Myosin-2." *Biochemistry* 56 (32): 4235–43. <https://doi.org/10.1021/acs.biochem.7b00311>.
- Zhang, Li-Juan, Li Xia, Shu-Lin Liu, En-Ze Sun, Qiu-Mei Wu, Li Wen, Zhi-Ling Zhang, and Dai-Wen Pang. 2018. "A 'Driver Switchover' Mechanism of Influenza Virus Transport from Microfilaments to Microtubules." *ACS Nano* 12 (1): 474–84. <https://doi.org/10.1021/acsnano.7b06926>.
- Zhang, Xinyu, Zhiquan Huang, Yongjie Hu, and Liu Liu. 2016. "Knockdown of Myosin 6 Inhibits Proliferation of Oral Squamous Cell Carcinoma Cells." *Journal of Oral Pathology & Medicine: Official Publication of the International Association of Oral Pathologists and the American Academy of Oral Pathology* 45 (10): 740–45. <https://doi.org/10.1111/jop.12448>.
- Zhao, Fa-Qing, Raúl Padrón, and Roger Craig. 2008. "Blebbistatin Stabilizes the Helical Order of Myosin Filaments by Promoting the Switch 2 Closed State." *Biophysical Journal* 95 (7): 3322–29. <https://doi.org/10.1529/biophysj.108.137067>.
- Zhou, Yeyun, Jared L. Johnson, Richard A. Cerione, and Jon W. Erickson. 2013. "Prenylation and Membrane Localization of Cdc42 Are Essential for Activation by DOCK7." *Biochemistry* 52 (25): 4354–63. <https://doi.org/10.1021/bi301688g>.
- Zhou, Yuxin, X. Edward Zhou, Yuanping Gong, Yuanye Zhu, Xiaoman Cao, Joseph S. Brunzelle, H. Eric Xu, Mingguo Zhou, Karsten Melcher, and Feng Zhang. 2020. "Structural Basis of Fusarium Myosin I Inhibition by Phenamacril." *PLoS Pathogens* 16 (3): e1008323. <https://doi.org/10.1371/journal.ppat.1008323>.
- Zimmermann, Dennis, Alicja Santos, David R. Kovar, and Ronald S. Rock. 2015. "Actin Age Orchestrates Myosin-5 and Myosin-6 Run Lengths." *Current Biology: CB* 25 (15): 2057–62. <https://doi.org/10.1016/j.cub.2015.06.033>.
- Zorca, Cornelia E., Lark Kyun Kim, Yoon Jung Kim, Matthew R. Krause, Daniel Zenklusen, Charalampos G. Spilianakis, and Richard A. Flavell. 2015. "Myosin VI Regulates Gene Pairing and Transcriptional Pause Release in T Cells." *Proceedings of the National Academy of Sciences of the United States of America* 112 (13): E1587–1593. <https://doi.org/10.1073/pnas.1502461112>.

RÉSUMÉ

Les nanomoteurs des cellules Eucaryotes leur permettent d'accomplir des tâches mécaniques complexes, nécessaires à la génération de tensions dans des emplacements cellulaires précis. La formation ou le transport de vésicules dans des voies d'endocytose et de sécrétion peuvent par exemple en résulter. Parmi ces moteurs, les myosines sont capables, à partir de l'hydrolyse de l'ATP, de générer de la force en association avec des filaments d'actine. Les myosines se divisent en plusieurs classes impliquées dans un large panel de fonctions et de pathologies. Leur dysfonctionnement peut entraîner de nombreuses maladies dont la spasticité, l'asthme, la cardiomyopathie, la surdité ou encore de nombreux cancers... (Coluccio, 2020)

En ce sens, le projet de thèse est centré d'une part **(I)** sur l'étude de la régulation du moteur de myosine VI (Myo6) impliqué dans la surdité ainsi que de nombreux cancers (Dunn *et al.*, 2006 ; Li *et al.*, 2015 ; Ma *et al.*, 2015 ; You *et al.*, 2018 ; Yang, 2019 ; Yang *et al.*, 2021). En effet, la Myo6 est unique parmi tous les membres de la superfamille des myosines car elle se déplace sur les filaments d'actine dans la direction opposée à toutes les autres myosines. Cette spécificité lui permet d'accomplir des rôles cellulaires uniques qui ne peuvent être effectués par aucune autre myosine. **(II)** D'autre part, le projet de thèse a été consacré à l'étude de la poche blebbistatin (Straight *et al.*, 2003), une poche d'inhibition au sein du domaine moteur (Roman *et al.*, 2018) afin d'en explorer le potentiel pour le développement d'inhibiteurs spécifiques.

Cette thèse contribue donc :

(I) à la compréhension des processus de régulation de l'activité de la Myo6 via une approche alliant biologie structurale, essais biophysiques et biologie cellulaire.

Une telle régulation passe par l'existence d'un état auto-inhibé de la Myo6 (Spink *et al.*, 2008 ; Fili *et al.*, 2017 ; Fili *et al.*, 2020), état dans lequel cette dernière consomme peu d'ATP et diffuse librement dans le cytosol afin que le moteur ne soit activé qu'au niveau du site requis pour son recrutement. L'étude biophysique de cet état a permis de mieux comprendre comment le stabiliser ou le déstabiliser *in vitro* et nous a permis d'obtenir un premier modèle de l'état auto-inhibé en utilisant la microscopie électronique. Cette étude nous a également permis de mieux comprendre le rôle différentiel des partenaires cellulaires de la Myo6 pour son activation. Des mutants favorisant l'activation ou la formation de l'état auto-inhibé de la Myo6 ont été développés sur la base de cette étude. Leur capacité à être recrutés par différents partenaires de la Myo6 a ainsi pu être étudié dans des cellules de mélanome humain (MNT-1), ces essais confirment un recrutement différentiel par les partenaires et suggère le recrutement non spécifique des mutants favorisant l'activation.

(II) à la compréhension de l'origine de la spécificité du MPH-220, modulateur allostérique n'ayant une activité d'inhibition que sur la myosine-2 du muscle squelettique. Cet inhibiteur a été analysé à la lumière d'une approche cristallographique.

Cette étude décrit que la spécificité de cet inhibiteur a fort potentiel pour le développement d'un nouveau traitement contre la spasticité repose sur un seul résidu non conservé dans la poche allostérique des autres myosines-2 (Gyimesi *et al.*, 2020).

MOTS CLÉS

myosine VI ; auto-inhibition ; surdité ; myosine II ; MPH-220 ; spasticité ; blebbistatin ; biologie structurale

ABSTRACT

The eukaryotic cell nanomotors are able to perform complex mechanical tasks, necessary for tension generation in precise cellular locations. Vesicles formation and transport in the endocytic and secretory pathways can for example result from it. Among these motors, myosins are able, from the hydrolysis of ATP, to generate force in association with actin filaments. Myosins are divided into many classes involved in a wide range of functions and pathologies. Their dysfunction can lead to many diseases including spasticity, asthma, cardiomyopathy, deafness or many cancers... (Coluccio 2020).

Thus, the thesis project is centered on the one hand **(I)** on the study of the regulation of myosin VI (Myo6), a nanomotor involved in deafness as well as many cancers (Dunn *et al.* 2006; Li *et al.* 2015; Ma *et al.* 2015; You *et al.* 2018; Yang 2019; Yang *et al.* 2021). Myo6 is unique among all members of the myosin superfamily because it moves on actin filaments in the opposite direction to all other myosins. This specificity allows it to perform unique cellular roles that cannot be performed by any other myosin. **(II)** On the other hand, the thesis project focused on the study of the blebbistatin pocket (Straight *et al.* 2003), an inhibitor pocket within the myosin motor domain, in order to explore its potential for the development of specific inhibitors.

This thesis therefore contributes to:

(I) Understanding the processes regulating the activity of Myo6 via an approach combining structural biology, biophysical tests and cell biology.

Such regulation involves the existence of an auto-inhibited state of Myo6 (Spink *et al.* 2008; Fili *et al.* 2017; 2020), a state in which the latter consumes little ATP and diffuses freely into the cytosol so that the motor is activated only at the site required for its recruitment. The biophysical study of this state has made it possible to better understand how to stabilize or destabilize it in vitro and has enabled us to obtain a first model of the auto-inhibited state using negative staining electron microscopy. This study also allowed us to better understand the differential role of cellular partners of Myo6 for its activation. Mutants promoting the activation or formation of the auto-inhibited state of Myo6 have been developed based on this study. Their ability to be recruited by different partners of Myo6 could thus be studied in human melanoma cells (MNT-1), these tests confirm a differential recruitment by the partners and suggest non-specific recruitment of mutants promoting activation.

(II) Understanding the origin of the specificity of the MPH-220, an allosteric modulator derived from the well-known myosin inhibitor blebbistatin and able to specifically inhibit skeletal Myosin-2 from a crystallographic approach.

This study describes that the specificity of this inhibitor with high potential for the development of new treatment against spasticity is based on a single non-conserved residue in the Blebbistatin allosteric pocket of the other myosins-2 (Gyimesi *et al.* 2020).

KEYWORDS

myosin VI; auto-inhibition; deafness; myosin II; MPH-220; spasticity; blebbistatin; structural biology